

NAT'L INST. OF STAND & TECH R.I.C.

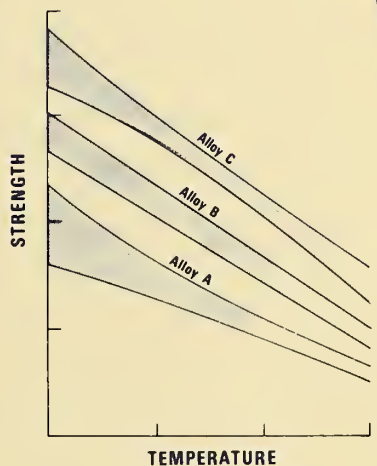
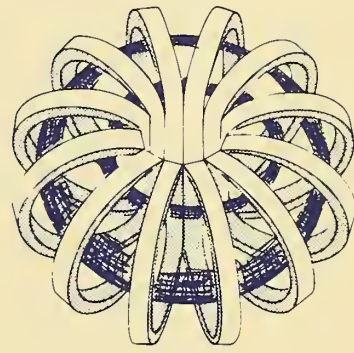
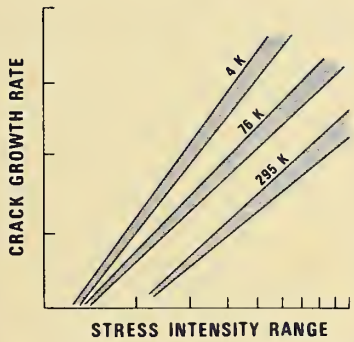


A11104 046430

**NATIONAL INSTITUTE OF STANDARDS &
TECHNOLOGY**
Research Information Center
Gaithersburg, MD 20899

TECHNICAL REPORTS

MATERIALS STUDIES FOR
MAGNETIC FUSION ENERGY
APPLICATIONS AT LOW TEMPERATURES - IV



To
Department of Energy
Office of Fusion Energy
Washington, D.C. 20545

By
Fracture and Deformation Division
National Bureau of Standards
Boulder, CO 80303

QC
100
J56
81-1645
1981
c.2

TECHNICAL REPORTS

**MATERIALS STUDIES FOR
MAGNETIC FUSION ENERGY
APPLICATIONS AT LOW TEMPERATURES - IV**

Edited By

**R.P. Reed and N.J. Simon
Fracture and Deformation Division
National Bureau of Standards
Boulder, CO 80303**

April 1981

Sponsored By

**Department of Energy
Office of Fusion Energy
Washington, D.C. 20545**



U.S. DEPARTMENT OF COMMERCE, Malcolm Baldrige, Secretary

NATIONAL BUREAU OF STANDARDS, Ernest Ambler, Director

CONTENTS

	<u>Page</u>
SUMMARY	v
PROGRAM DESCRIPTION	vii
HIGHLIGHTS OF RESULTS	1
STRUCTURAL ALLOYS	
STRUCTURAL ALLOYS PROGRAM	11
STRUCTURAL ALLOYS FOR SUPERCONDUCTING MAGNETS IN FUSION ENERGY SYSTEMS	17
STRENGTH AND TOUGHNESS RELATIONSHIP FOR INTERSTITIALLY STRENGTHENED AISI 304 STAINLESS STEELS AT 4 K	37
TENSILE AND FRACTURE PROPERTIES OF MANGANESE-MODIFIED Fe-18Cr-8Ni TYPE AUSTENITIC STAINLESS STEELS	77
INTERSTITIAL CARBON AND NITROGEN EFFECTS ON THE CRYOGENIC FATIGUE CRACK GROWTH OF AISI 304 TYPE STAINLESS STEELS	101
ANOMALOUS YIELDING, TRANSFORMATION, AND RECOVERY EFFECTS IN AISI 304L STAINLESS STEELS	131
LOW-TEMPERATURE DEPENDENCE OF YIELDING IN AISI 316 STAINLESS STEELS	147
LOW-TEMPERATURE DEFORMATION OF 5083-0 ALUMINUM ALLOY	185
EFFECTS OF CARBON AND NITROGEN ON THE ELASTIC CONSTANTS OF STAINLESS STEEL 304	203
LOW-TEMPERATURE VARIABILITY OF STAINLESS-STEEL-304 ELASTIC CONSTANTS	215
PREDICTED SINGLE-CRYSTAL ELASTIC CONSTANTS OF STAINLESS STEEL 304	227
ELASTIC-CONSTANT/TEMPERATURE BEHAVIOR OF THREE HARDENED MARAGING STEELS	237
TEMPERATURE BEHAVIOR OF YOUNG'S MODULI OF FORTY ENGI- NEERING ALLOYS	257
WELDING AND CASTING	
EVALUATION OF WELDMENTS AND CASTINGS FOR LIQUID HELIUM SERVICE	273
STRENGTH AND TOUGHNESS OF FULLY AUSTENITIC STAINLESS STEEL FILLER METALS AT 4 K	289
WELD PROCESS STUDY FOR 316 L STAINLESS STEEL WELD METAL FOR LIQUID HELIUM SERVICE	303
FRACTURE TOUGHNESS PROPERTIES OF WELDS IN ALUMINUM ALLOY 5083-0 AT 4 K	323
THE INFLUENCE OF FERRITE AND NITROGEN ON MECHANICAL PROP- ERTIES OF CF8M CAST STAINLESS STEEL	337
METALLOGRAPHY OF δ -FERRITE IN AUSTENITIC STAINLESS STEEL CASTINGS	357
DEFORMATION AND FRACTURE OF STAINLESS STEEL CASTINGS AND WELDMENTS AT 4 K	415
EVALUATION OF WELD FILLERS TO JOIN NITROGEN STRENGTHENED AUSTENITIC STAINLESS STEELS FOR CRYOGENIC APPLICA- TIONS (FUSION AND MHD ENERGY)	453

NONMETALLICS	
NONMETALLICS FOR MAGNET SYSTEMS	467
<u>NONMETALLIC MATERIALS: STANDARDIZATION</u>	
STANDARDIZING NONMETALLIC COMPOSITE MATERIALS FOR CRYOGENIC APPLICATIONS	477
<u>NONMETALLIC MATERIALS: RESEARCH AND CHARACTERIZATION</u>	
THERMAL CONDUCTIVITY OF G-10CR AND G-11CR INDUSTRIAL LAMINATES AT LOW TEMPERATURES (PART III)	495
FRACTURE ANALYSIS OF COMPRESSION DAMAGE IN GLASS FABRIC/ EPOXY, G-10CR, 295 K to 4 K	507
STATIC AND DYNAMIC YOUNG'S MODULI OF TWO FIBER-REINFORCED COMPOSITES	589
RADIATION EFFECTS ON COMPOSITES AND NONMETALLIC MATERIALS	597
<u>NONMETALLIC MATERIALS: TECHNOLOGY TRANSFER</u>	
CONTRIBUTIONS TO TECHNOLOGY FORECAST '81	605
COMMENT ON "MECHANICAL PROPERTIES OF PLASTIC COMPOSITES.."	609
THE MANUFACTURE OF RADIATION RESISTANT LAMINATES	613
TECHNOLOGY TRANSFER	
NBS-DoE WORKSHOP: MATERIALS AT LOW TEMPERATURES	641
ORGANIZATIONAL CONTACTS	646
ACKNOWLEDGMENT	647

SUMMARY

This report contains results of a research program to produce material property data that will facilitate design and development of cryogenic structures for the superconducting magnets of magnetic fusion energy power plants and prototypes. The program was conceived and developed jointly by the staffs of the National Bureau of Standards and the Office of Fusion Energy of the Department of Energy; it is managed by NBS and sponsored by DoE. Research is conducted at NBS and at various other laboratories through subcontracts with NBS.

The reports presented here summarize the fourth year of work on the low temperature materials research program. Highlights of the results are presented first. Research results are given for the four main program areas: structural alloys, weldings and castings, nonmetallics, and technology transfer. Objectives, approaches, and achievements are summarized in an introduction to each program area.

The major portion of the program has been the evaluation of the low temperature mechanical and physical properties of stainless steel base metal and welds, with particular emphasis on the nitrogen-strengthened stainless steels. Aluminum alloys have received some consideration also. Work has been done on the production and standardization of nonmetallics, primarily industrial laminates, for low temperature applications and on the measurement of their properties at cryogenic temperatures. A brief description is given of the fourth NBS/DoE Vail workshop held in October 1980.

Note: Certain commercial equipment, instruments, or materials are identified in this paper to specify the experimental procedure adequately. In no case does such identification imply recommendation or endorsement by the National Bureau of Standards, nor does it imply that the material or equipment identified is necessarily the best available for the purpose. Papers by non-NBS authors have not been reviewed or edited by NBS. Therefore, the National Bureau of Standards accepts no responsibility for comments or recommendations contained therein.

PROGRAM DESCRIPTION

The overall objective of the program is to assist in the design, construction, and safe operation of low temperature magnetic fusion energy (MFE) systems, especially superconducting magnets, through effective materials research and materials technology transfer. The specific steps taken to achieve this objective are: (1) evaluation of low temperature materials research needs specific to MFE devices; (2) development and monitoring of a research program to acquire the necessary data; and (3) rapid dissemination of the data to potential users through personal contacts, publications, and workshops.

Efforts directed at the first specific objective began with the publication of the Survey of Low Temperature Materials for Magnetic Fusion Energy in March 1977. A recent publication updating part of this survey, entitled Structural Alloys for Superconducting Magnets in Fusion Energy Systems, is included in this volume. Through continuous interactions with all low temperature design, construction, and measurement programs, such as the Large Coil Project, we are aware of new problems as they arise. This year's contribution to the second objective is described in Table 1 in the form of an outline of the research projects. The results appear later in this report. The third objective is satisfied, in part, by these annual reports and by the series of NBS-DoE Workshops on Materials at Low Temperatures, which are held each fall in Vail, Colorado. Starting in fiscal year 1981, handbook pages presenting the available data for specific materials will be added to the annual report.

Table 1. Outline of the NBS/DoE program on material studies for magnetic fusion energy applications at low temperatures.

<u>Program Area</u>	<u>Organization</u>	<u>Program Description</u>
<u>A. Structural Alloys</u>		
1. Characterization	NBS	Measurement of elastic, tensile, fracture toughness and fatigue crack growth rate properties as a function of temperature for selected austenitic stainless steels and 5083 aluminum. Assessment of effects of grain size, martensitic transformations and alloying on low temperature behavior.
2. Alloy development	NBS	Assessment of low temperature properties of selected austenitic alloys containing varying concentrations of C, N and Mn with a Fe-Cr-Ni base.
3. Characterization and modeling of martensitic start temperatures	U. Wisconsin	Study to assess, empirically, the relation between alloy content and the temperature at which martensite forms on cooling for commercial grades of AISI 300 series stainless steels.
<u>B. Welds and Castings</u>		
1. Stainless steel welds	NBS	Evaluate the strength and toughness of several fully austenitic weld metals provided by suppliers in the United States, Austria, Sweden, and the Soviet Union at 4 K. (Four alloys with 16-20% Cr, 16-20% Ni, 4-7% Mn and 2-5% refractory elements (Mo, W and/or Nb) had strength and toughness combinations comparable to base metal properties.)
2. Aluminum welds	NBS	Evaluate the strength and fracture toughness of GMA welds using 5183 wire in 51 mm thick 5083-0 plates that were provided by five aluminum fabricators. (Property variations were minimal despite significant differences in welding procedures.)

3. Stainless steel castings	ESCO NBS	Produce stainless steel castings (grade CF8M) with varied ferrite and nitrogen contents to study the effects of ferrite and nitrogen on the strength and toughness at 4 K. (This year's efforts consisted of manufacture of the castings, tests at room temperature and 77 K, and metallographic studies to be followed by evaluation in liquid helium next year.)
-----------------------------	-------------	--

C. Nonmetallics for Magnet Structures

1. Standardization	NBS	Continue cooperation with industry to establish and refine cryogenic grade specifications for insulating laminates and coding systems for laminates.
3. Characterization	NBS	Measure thermal conductivity of composite components at cryogenic temperatures to aid in establishing models for predicting the thermal conductivity of a variety of laminates. Investigate failure modes of laminates under compression at cryogenic temperatures. Develop dynamic methods of measuring elastic constants of composite laminates.

D. Technology Transfer

1. NBS/DoE Workshop	NBS	An annual workshop to present research results to the fusion community, to discuss new problems, and to promote interaction between interested parties. Handbook data pages on stainless steels will be produced, starting in FY '81.
---------------------	-----	---

HIGHLIGHTS OF RESULTS

HIGHLIGHTS OF RESULTS

STRUCTURAL ALLOYS:

Stainless Steel 304--Characterization and Alloy Development

The study of this alloy series has been emphasized because of its favorable cryogenic properties, extensive service record, and availability. Stainless 304 has been used in several designs for the Large Coil Project (LCP). Previous work has shown that adding nitrogen increases the tensile strength and austenitic stability of the 304 series at low temperatures. Carbon has a similar effect, but the addition of carbon is limited owing to sensitization (chromium carbide precipitation). It would be desirable to optimize the properties of the alloy for different requirements by varying the composition, and this objective has motivated the studies described below.

1. Carbon and nitrogen (C+N) weight percent were varied systematically in a series of heats for which fracture toughness and tensile yield strength were measured at 4 K. Fracture toughness dropped linearly with increasing C+N content, but strength increased as C+N content increased.
2. The effects of C+N content and temperature upon fatigue crack growth were also measured. Low C+N content was found to correlate with better crack resistance at 4 K. The improved crack resistance for low C+N contents at 4 K, compared with that at room temperature was shown to be due to a transition to transgranular fracture at cryogenic temperatures from intergranular at room temperature.

3. Although interstitial nitrogen strengthens the 304 alloy series, the resulting alloys are harder to fabricate. Since the addition of manganese is expected to improve fabricability, a series of heats with manganese content varying from 1 to 6 weight percent and nitrogen content of 0.1 to 0.2 weight percent were tested for fracture toughness and tensile yield strength. The results gave much lower fracture toughness than expected, except for the heat with 6 percent manganese. These anomalous results may indicate the presence of previously unrecognized factors in alloy production that affect fracture toughness significantly at cryogenic temperatures. Research to elucidate these factors is continuing.
4. Yield strength of a selected heat of 304L was measured as a function of temperature. The measurements showed that yield strength does not increase monotonically with decreasing temperature, as is the case for the austenitically stable stainless 310.
5. Effects of C+N content on the elastic constants of 304 steels were measured at room temperature, and the variability among the elastic constants of alloys of the 304 series was measured down to 4 K.

Stainless Steel 316

The low temperature flow strength of stainless 316 was measured. The formation of bcc martensite that occurs at low temperatures or as the result of strain influences this property.

Aluminum Alloys

The yield strength and stress-strain curves of the aluminum alloy 5083-0 were measured down to 4 K. Serrated yielding was observed at 4 K and room temperature, though not at 76 K. The mechanism causing this effect is different at 4 K than at room temperatures.

The magnesium present in this alloy increases the strength at both room and cryogenic temperatures. Previously unpublished data on alloys 5154 and 5052, which have different magnesium content, are presented to illustrate this trend further.

WELDING AND CASTING:

Research has focused on the metallurgical factors that determine strength and toughness of weldments and castings in stainless steel and aluminum alloys.

1. Since it is known that ferrite reduces the fracture toughness of weldments at 4 K, although ferrite reduces microfissuring, work on the development of 0 percent ferrite filler materials has been undertaken. A series of experimental filler alloys was tested at 4 K. Some were found to have a good combination of strength and toughness, comparable to that of the base metal, but a few problems with microfissuring remain.
2. The effects of differing weld processes were studied for 316L weldments. The cleanliness of the process correlated well with good fracture toughness at 4 K, so it was concluded that the impurity level may have a strong effect on cryogenic properties of welds.

3. To support LCP magnet design and construction, a number of qualifying and test weldments of stainless steel were tested for fracture toughness and tensile strength.
4. The evaluation of 5183 welds in 5083 aluminum alloys was completed during the past fiscal year. The fracture toughness of weldments at 4 K was found to be essentially the same for welds furnished by different suppliers or produced by different processes.
5. Work has begun on a study of the more fundamental aspects of the structure of duplex austenite/ferrite steels and on how this structure is related to fracture and deformation in weldments and castings at cryogenic temperatures. Castings are being studied for two reasons: (a) there is interest in their use as structural elements for superconducting magnets and (b) the factors affecting fracture and deformation modes are more easily observed because their ferrite structure is coarser than that of weldments.

A series of CF8M castings with varied ferrite and nitrogen content was produced this year, and the production techniques are reported. This series will be used to study the effects of ferrite and nitrogen in a controlled manner in the current fiscal year. Meanwhile, during the past year, available weldments and castings were subjected to a detailed metallographic study. Fracture and deformation modes were determined for these specimens, and the effect of ferrite structure on these modes was analyzed.

NONMETALLICS:

Standardization

Efforts to refine and improve the specifications of cryogenic grades of glass-fabric-reinforced bisphenol A epoxy industrial laminates have continued. These established grades are known as G-10CR and G-11CR. Recently it was found that G-11CR does not have the radiation resistance that was initially expected from its composition and curing process. Therefore, this grade has been dropped. The standardization of glass-mat reinforced laminate products is in progress.

Characterization

The thermal conductivity of the epoxy matrix material used in G-10CR and G-11CR was measured, and the results revealed considerable inhomogeneity in the bulk resin. Efforts to compare thermal conductivity measurements made at the National Bureau of Standards with those made by CERN on a laminate of European manufacture indicated a sizeable discrepancy at room temperature. Work on this problem will be continuing during the present fiscal year.

Modes of failure in compressive fracture of laminates at cryogenic temperatures were studied. Compressive stresses of insulators predominate in superconducting magnets.

Dynamic elastic moduli were measured for two fiber-reinforced composites, and the results were compared with static methods.

Results of studies on radiation effects on composites are presented in a section from a review paper.

TECHNOLOGY TRANSFER:

The annual NBS/DoE Workshop on Materials at Low Temperatures at Vail, Colorado in October 1980 was attended by about seventy representatives

of the materials and magnet design communities. Again, the meeting was viewed constructively; it served as a focal point to identify and discuss magnet construction or design problems related to materials. For a few who have become recently involved in cryogenic applications, the workshop served an educational role.

STRUCTURAL ALLOYS

STRUCTURAL ALLOYS PROGRAM

R. P. Reed
Fracture and Deformation Division
National Bureau of Standards
Boulder, Colorado

ABSTRACT

An overview of the structural alloys program is presented. Selection and properties of the alloys under study are discussed, and the objectives of the program in the current fiscal year (1981) are set forth.

The objectives of the structural alloys project are twofold: (1) to characterize the physical and mechanical properties of structural alloys at 4 K to obtain typical properties that can be used for material selection and design estimates and (2) to develop, in collaboration with industry, a stronger, tough, weldable austenitic steel for use as a structural alloy for superconducting magnets.

The structural-alloys-project results from this past year are summarized:

Characterization: The tensile yield strength as a function of temperature (4-330 K) was measured for a thick plate of 5083-0 aluminum alloy.

The temperature dependence of the flow strength of AISI 316 was measured and the influences of martensitic transformations, adiabatic heating, magnetic transitions, and grain size were assessed.

Measurements on fatigue and creep of metastable AISI 304 were initiated.

The fatigue crack growth rate of a series of Fe-18Cr-8Ni alloys with varying C and N concentrations was measured and assessed.

Measurements of elastic constants of stainless and maraging steels, of the variability of AISI 304 elastic properties and a review of the temperature dependence of elastic constants of engineering alloys are presented.

Alloy Development: The tensile yield and ultimate strengths and the fracture toughness of a series of Fe-18Cr-7Ni-0.03C alloys with varying Mn and N concentrations were measured at 295, 76, and 4 K. Fracture toughness results obtained for the low (1-4 wt. %) Mn alloys were anomalous when compared with the Fe-18Cr-8Ni-(C+N) alloy series measured the previous year.

This year (fiscal year 1981), the tensile flow strength of 2219-T87 aluminum alloy will be measured at a series of temperatures ranging from 4 to 300 K. Additional tensile measurements will be conducted on 5083-0 aluminum alloy to assess the influence of grain size on strength and to assess, more accurately, the temperature dependence of the flow strength. The study of the role of martensitic transformation on low-temperature fatigue and creep of AISI 304 steel will continue. Finally, to pursue the development of a stronger, but tough, austenitic steel, the causes for the lower toughness at 4 K of Fe-18Cr-7Ni-1-4Mn-N steels of the last alloy series need to be understood. Metallography, electron microscopy, scanning electron microscopy, and scanning transmission electron microscopy will be used to study the fracture surfaces, crack development, and impurity segregation of these alloys. Subsequently, an alloy heat of selected composition will be prepared.

The program has concentrated on four alloy series: AISI 304 (Fe-18Cr-8Ni), AISI 316 (Fe-16Cr-10Ni-2Mo), 5083-0 (Al-0.7Mn-4.45Mg-0.015Cr) and 2219 (Al-6Cu-0.3Mn-0.1V-0.18Zr-0.06Ti). These alloys are most commonly used for 4 K applications and are thought to represent the best base alloy materials.

The stainless steels have a relatively high Young's modulus, low thermal and electrical conductivity, and excellent toughness. Also, the major fabricators have good experience in welding stainless steel. Aluminum alloys are light, less expensive, and have been used extensively (alloy 5083) in the construction of LNG containment systems. Toughness and strength do not decrease between 110 K and 4 K for these aluminum alloys.

AISI 304 is susceptible to martensitic transformation on cooling or on application of applied stress at low temperatures. Martensitic transformation tends to act as a deformation mode, therefore its presence tends to reduce the resistance of the alloy to applied stress at low temperatures, and the result is low initial flow strengths. However, we have not obtained evidence that the martensitic transformations act to degrade fracture toughness or ultimate tensile strength.

The alloy AISI 316 is less susceptible to martensitic transformation and the dependence of strength on temperature for this steel is more predictable.

The addition of nitrogen to austenitic stainless steel dramatically increases the low-temperature yield strength of the steel. There is an attendant decrease of toughness. The aim of the alloy development program is to establish a composition of Fe-Cr-Ni-Mn-C-N that will provide a stronger and tough structural alloy at 4 K. Two correlations have been established to assist this process: (1) At 4 K the tensile yield strength has been demonstrated to be inversely related to the fracture toughness (J-integral). (2) The total concentration of C+N from about 0.10 to 0.30 wt. % is linearly related to the tensile yield strength at 4 K.

The aluminum alloys do not exhibit low-temperature phase or magnetic transitions. Consequently, both their physical and mechanical properties are well behaved at very low temperatures. The fracture toughness of the aluminum alloys is considerably lower than stainless steel values. However, there is a range of slow, stable crack growth following crack initiation at the critical J-integral fracture toughness and additional research is required to characterize the range of stable crack growth.

STRUCTURAL ALLOYS FOR SUPERCONDUCTING MAGNETS
IN FUSION ENERGY SYSTEMS

H. I. McHenry and R. P. Reed
Fracture and Deformation Division
National Bureau of Standards
Boulder, Colorado 80303

STRUCTURAL ALLOYS FOR SUPERCONDUCTING MAGNETS IN FUSION ENERGY SYSTEMS

H.I. McHENRY and R.P. REED

Thermophysical Properties Division, National Bureau of Standards, Boulder, Colorado 80302, USA

Received 15 March 1979

The behaviour of selected alloys for superconducting magnet structures in fusion energy systems is reviewed with emphasis on the following austenitic stainless steels (AISI grades 304, 310S and 316), nitrogen-strengthened austenitic stainless steels (types 304LN, 316 LN and 21Cr–6Ni–9Mn) and aluminum alloys (grades 5083, 6061 and 2219). The mechanical and physical properties of the selected alloys at 4 K are reviewed. Welding, the properties of weldments, and other fabrication considerations are briefly discussed. The available information suggests that several commercial alloys have adequate properties at 4 K and sufficient fabrication characteristics for the large magnet structures needed for fusion energy systems.

1. Introduction

Alloys will be used for the main structural members of the superconducting magnet systems needed for fusion devices. Designs of tokamak and mirror machines that require superconducting magnets are currently in the conceptual stage (except for MFTF), but many design features that strongly influence materials selection are reasonably well established. The principal features governing alloy selection for structural applications are the enormous size and stored energy of the magnet systems, the extremely high forces exerted by the magnets, the massive structural elements needed to restrain these forces, the limited space available for the structure, and the need for accessibility to install and periodically remove the blanket and shield systems – systems that are completely surrounded by magnets and the support structure. These features result in the need for alloys with sufficient strength and stiffness to perform the required structural functions within the space available, sufficient fatigue and fracture resistance to operate safely, and sufficient fabricability to permit manufacture and assembly of the components.

The choice of materials is further restricted by the adverse operating environment of the magnet system. The alloys are subjected to temperatures down to

4 K and must not be susceptible to low temperature embrittlement. The presence of high magnetic fields of controlled shape cautions against the use of ferromagnetic materials in certain applications because they would be subjected to higher forces due to the magnetic field and would result in field distortion. The rapid magnetic field changes associated with cyclic operation of the poloidal field coils cause heat inputs to the structure from eddy current losses. Consequently, alloys with high electrical resistivity are usually preferred. The radiation environment eliminates use of alloying elements, such as cobalt, which transmute to long half-life products. With this exception, radiation does not appear to be a significant factor in the selection of structural alloys because dosage levels sufficient to degrade structural performance probably cause unacceptable deterioration of other system materials. Finally, the microstructure of the material must be stable when exposed to the operating strains, temperature, and radiation; e.g. the martensite transformation in metastable austenitic stainless steels produces a brittle, ferromagnetic phase and the attendant volume expansion causes localized areas of stress concentration.

The constraints on materials selection caused by size requirements, space limitations and operating environment significantly reduce the number of candidate alloys. Further limitations arise due to con-

siderations related to experience, cost and availability. Currently, the leading candidates are the austenitic stainless steels and aluminum alloys. In this paper the properties of the alloys considered most suitable for liquid helium applications are reviewed with emphasis on their properties at 4 K and on their fabrication characteristics relevant to fusion magnet systems.

This review draws heavily on research conducted at the National Bureau of Standards; particularly a three-year program on materials for superconducting machinery sponsored by the Defense Advanced Research Projects Agency [1], a survey of low temperature materials for magnetic fusion energy [2], and a continuing program on materials for fusion energy magnets [3] sponsored by the Office of Fusion Energy of the US Department of Energy. For background relating to the properties discussed the reader is referred to reviews by Fickett [4] on the physical basis for each property and by McHenry [5] on fracture mechanics and its application to cryogenic structures.

2. Annealed austenitic stainless steels

Austenitic chromium–nickel stainless steels, including the nitrogen-strengthened grades discussed in more detail in section 3, are the most widely proposed alloys for structural applications in superconducting magnet systems. These steels have the best combination of strength, stiffness and toughness at 4 K. The physical properties also offer advantages over competing materials. Specifically, the modulus is high, the thermal expansion is close to that of the copper-stabilized conductor, magnetic permeability is low and the electrical and thermal conductivities are low. The principal disadvantages are the high cost of construction and problems arising from microstructural stability and control.

The AISI 300-series stainless steels, particularly types 304 and 304L, are widely used in cryogenic applications. The designations and compositions of commonly used grades are summarized in table 1. These grades have moderate strength, excellent toughness, good fabrication characteristics and are available in a variety of product forms. The ASTM specifications for the various product forms are listed in table 2. Several 300-series grades not listed in table 1 are cover-

Table 1
Compositions of austenitic stainless steels suitable for liquid helium service

AISI type no.	Composition (%)			
	Cr	Ni	C, max	Other
304	18–20	8–10.5	0.08	
304L	18–20	8–12	0.03	
316	16–18	10–14	0.08	2–3 Mo
316L	16–18	19–22	0.03	2–3 Mo
310	24–26	19–22	0.25	1.5 Si, max
310S	24–26	19–22	0.08	1.5 Si, max

For each grade Mn = 2.0 max; S = 0.030 max; Si = 1.0 max; P = 0.045 max.

ed by ASTM specifications and can meet ASME Pressure Vessels Code requirements for cryogenic vessels. These grades are not described in this chapter because they offer no particular advantage for superconducting magnet structures and consequently their service experience and property data at 4 K are limited.

The alloys listed in table 1 can be compared with respect to AISI 304, the basic 19Cr–9Ni stainless steel. AISI 316 contains 2–3% Mo and slightly higher nickel and thus has greater austenite stability than AISI 304. AISI 304L and 316L are low carbon modifications of 304 and 316, respectively; low carbon is desirable to avoid sensitization, the grain boundary precipitation of Cr-carbides. Type 310S is a 25Cr–20Ni alloy that has lower carbon (0.08% C) than AISI 310 (0.25% C). The high alloy content

Table 2
ASTM specifications for various product forms of austenitic stainless steels

Product form	ASTM Specifications
Plates, sheet and strip	A240
Forgings	A473
Bars and sections	A479
Seamless tubes	A213
Welded tubes	A249
Seamless and welded tubes	A269
Small diameter tubing	A632
Bolts, screws, studs	A320
Nuts	A194

provides austenite stability and greater strength and thus 310S is useful where dimensional stability, non magnetic behavior and higher strength are desirable.

The low temperature properties of the 300-series austenitic stainless steels have been compiled in cryogenic handbooks [6,7], in a review article by Brickner and Defilippi [8], and in suppliers' publications [9,10]. In this section the general trends in strength, toughness and fatigue resistance are summarized as a function of temperature. Care should be taken in using the data presented here or in data compilations because there are significant heat-to-heat variations in the mechanical properties of the 300-series stainless steels, particularly in the yield strength and toughness. The principal causes of these variations are interstitial content, i.e. carbon and nitrogen, and mechanical deformation history, i.e. resulting grain size. The influence of nitrogen within the limits of 0–0.08 wt% is particularly significant with the higher nitrogen contents causing substantial increases in yield strength.

2.1. Tensile properties

The yield and ultimate strengths of AISI grades 304, 310 and 316 are compared in fig. 1 for temperatures ranging from 4 to 300 K. Notice that type 304 has the lowest yield strength and the highest ultimate strength at all temperatures. This is due in part to the martensite transformation which occurs more readily in 304 than in 316 or 310. Since the transformation is strain induced, the yield strength is not significantly influenced by martensite, but the ultimate strength is increased.

The yield and ultimate strengths of AISI grades 304 and 304L are compared in fig. 2. Type 304 exhibits a slightly greater increase in strength than type 304L as temperature is reduced. The loss of strength associated with reduced carbon content is considered to be characteristic of all the stainless steels, i.e. 304L vs. 304, 316L vs. 316 and 310S vs. 310, and is attributed to the strengthening effect of carbon.

The ductility of the annealed 300-series stainless steels is generally excellent at cryogenic temperatures. Elongation and reduction-of-area tend to drop with decreasing temperatures, but values generally exceed 30%.

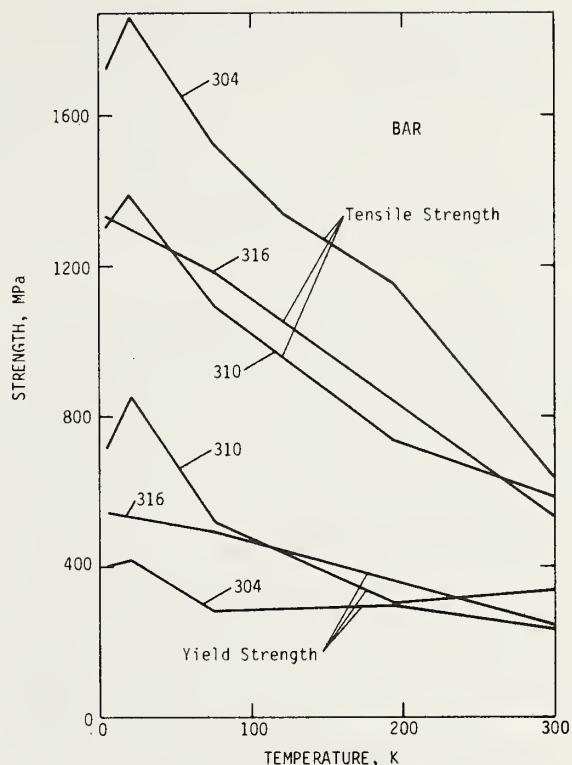


Fig. 1. Tensile and yield strengths of three austenitic stainless steels – AISI types 304, 310 and 316 – at temperatures between 4 and 300 K [6].

2.2. Toughness

The austenitic stainless steels retain excellent toughness at cryogenic temperatures. The Charpy V-notch impact toughness does decrease with temperature but in all cases known to the authors the toughness far exceeds the 0.38 mm lateral expansion requirement of the ASME Boiler and Pressure Vessel Code [11] and a ductile-to-brittle transition is not exhibited. The minimum temperature for Charpy testing is about 20 K, because adiabatic heating causes specimen temperatures in excess of 20 K even when the test temperature is 4 K.

Slow strain-rate tests using notched tensile specimens indicate that notch sensitivity does not develop at 4 K [6]. The data summarized in fig. 3 indicate that the notch-to-unnotched ratio of tensile strengths is approximately equal to 1 and the ratio of notched tensile strength to unnotched yield strength generally exceeds 2.

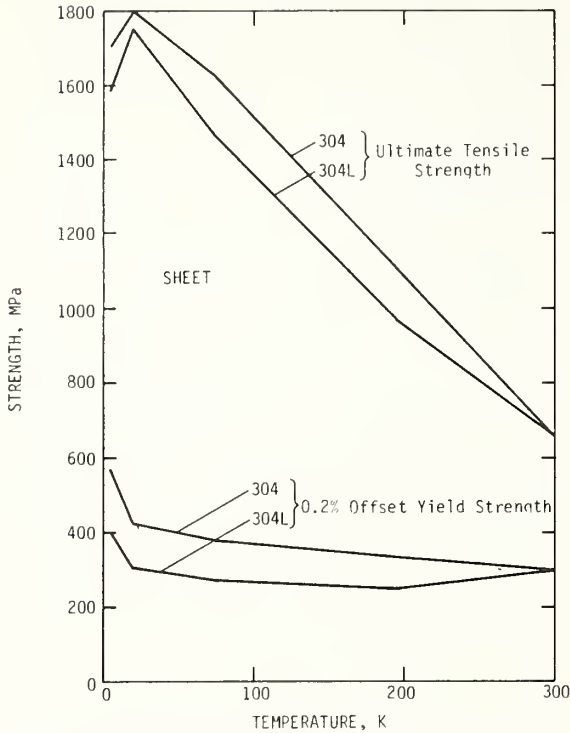


Fig. 2. Tensile properties of two austenitic stainless steels – AISI types 304 and 304L – at temperatures between 4 and 300 K [6].

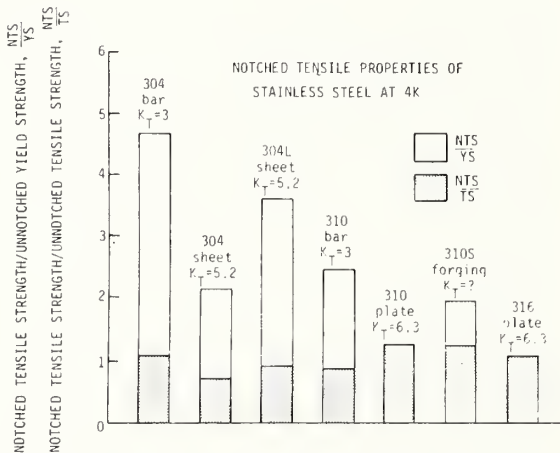


Fig. 3. Notched tensile properties of five austenitic stainless steels – AISI types 304, 304L, 310, 310S and 316 – at 4 K [6]. K_T is the stress concentration factor of the notch.

Tobler [12] used J -integral methods to measure the fracture toughness of AISI grades 310 and 316 at temperatures to 4 K. The toughness, $K_{Ic}(J)$, at 4 K is 230 $\text{MPa}\sqrt{\text{m}}$ for 310S and 460 $\text{MPa}\sqrt{\text{m}}$ for 316, and in both alloys the toughness at 4 K exceeds the toughness at room temperature. The ratio of toughness to yield strength is sufficiently high to ensure gross ductile deformation prior to fracture.

2.3. Fatigue

Strain cycling fatigue properties at 300, 76 and 4 K have been measured for AISI grades 304L and 310 by Nachtigall [13] and for grades 304L and 316 by Shepic and Schwartzberg [14]. The results for 304L, which were essentially the same in both investigations, and for 316 are shown in fig. 4. The fatigue resistance of 310 and 316 were superior to that of 304L, particularly in low cycle fatigue (less than 10^4 cycles). For each alloy the fatigue resistance at low temperatures is superior to the fatigue resistance at room temperature except at the highest strain ranges where failure occurred in less than 1000 cycles.

The fatigue crack growth behavior of AISI grades 304, 304L, 310S and 316 has been determined at 295, 76 and 4 K by Tobler and Reed [15]. The data for 304L are shown in fig. 5. Notice that the growth rates are essentially the same at 76 and 4 K; similar behavior was observed in each of the other alloys. Also, the growth rates at 76 and 4 K are slower than those at room temperature. The best-fit lines through the 304L data at 295 K and at 76 and 4 K form the

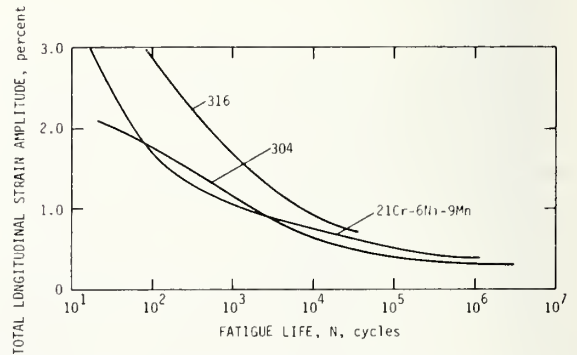


Fig. 4. Fatigue behavior of three austenitic stainless steels – AISI types 304 and 316 and a 21Cr-6Ni-9Mn alloy – at 4 K [14].

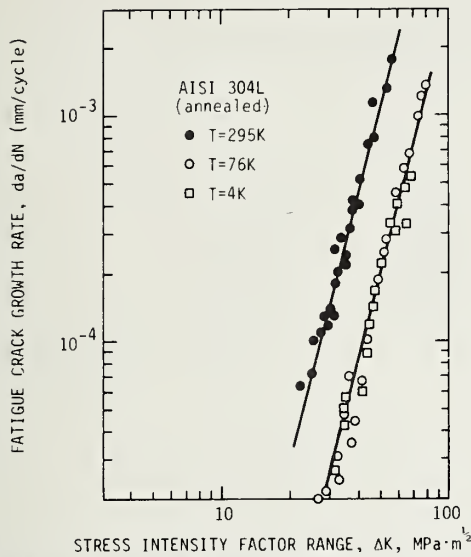


Fig. 5. Fatigue crack growth rates of AISI type 304L austenitic stainless steel at 295, 76 and 4 K [15].

approximate scatter bands for the data on 304, 310S and 316 at 295, 76 and 4 K. Thus, it can be concluded that alloy content and temperature have minimal influence on the fatigue crack growth behavior of the 300-series stainless steels.

2.4. Physical properties

The physical properties of the 300-series stainless steels at 295, 76 and 4 K are summarized in table 3.

Table 3
Physical Properties of austenitic stainless steels

Property	Units	AISI 304			AISI 310			AISI 316		
		295 K	4 K	Ref.	295K	4 K	Ref.	295 K	4 K	Ref.
Density	g/cm ³	7.9	—	19	7.9	—	19	8.0	—	19
Young's modulus	GN/m ²	189	204	16	184	199	16	217	234	16
Shear modulus	GN/m ²	740	800	16	700	770	16	830	910	16
Poisson's ratio	—	0.290	0.271	16	0.307	0.296	16	0.298	0.281	16
Thermal conductivity	W/m · K	13	0.3	7	nearly the same for 304, 310 and 316					
Expansion	cm/cm · K × 10 ⁻⁶	15.8	10.2	7	nearly the same for 304, 310 and 316					
Specific heat	J/kg · K	480	0.5	7	nearly the same for 304, 310 and 316					
Electrical resistivity	μ Ωcm	70.4	49.6	17	87.3	68.5	17	75.0	53.9	17
Magnetic permeability		1.02	1.09	18	1.003	1.10	18	1.003	1.02	18

The thermal properties have been taken from the best-fit lines used in the LNG Materials Handbook [7], and the original sources are given for the elastic properties [16], electrical resistivity [17], and magnetic permeability [18].

3. Annealed nitrogen-strengthened austenitic stainless steels

Nitrogen has a pronounced effect on the yield strength of austenitic stainless steels, particularly at cryogenic temperatures. For example, the yield strength of 304 N (AISI 304 with deliberate additions of nitrogen) is approximately three times greater than the yield strength of 304 at 76 K, the ultimate strengths are approximately equal and the elongation of the 304N is superior at temperatures below 220 K [20]. This remarkable improvement in mechanical properties occurs in many nitrogen-strengthened grades. Consequently, significant interest is developing in these alloys for future applications in superconducting magnet systems.

The designations and compositions of the commercially available grades that offer promise for liquid helium applications are summarized in table 4. Several other nitrogen-strengthened grades have been developed and are covered by ASTM specifications such as A240 and A412. However, the availability and property data on these grades are limited. Several additional grades are commonly used in Europe where

Table 4
Compositions of nitrogen-strengthened austenitic stainless steels suitable for liquid helium service

Type	Nominal composition (%)					
	Cr	Ni	Mn	C, max	N	Other
AISI 304N	18 –20	8 –10.5	2.0, max	0.08	0.10–0.16	–
304LN	18 –20	8 –12	2.0, max	0.03	0.10–0.16	–
AISI 316N	16 –18	10 –14	2.0, max	0.08	0.10–0.16	–
316LN	16 –18	10 –14	2.0, max	0.03	0.10–0.16	–
ASTM XM11 *	18 –21	5 – 7	8–10	0.04	0.15–0.40	–
ASTM XM19 *	20.5–23.5	11.5–13.5	4– 6	0.06	0.20–0.40	Cb 0.10–0.30 V 0.10–0.30 Mo 1.5 –3.0

* ASTM A412.

nitrogen is deliberately added to several of the common Cr–Ni 300-series stainless steels. The equivalent AISI designations for these European grades are 304LN and 316LN.

Two basic types of nitrogen-strengthened stainless

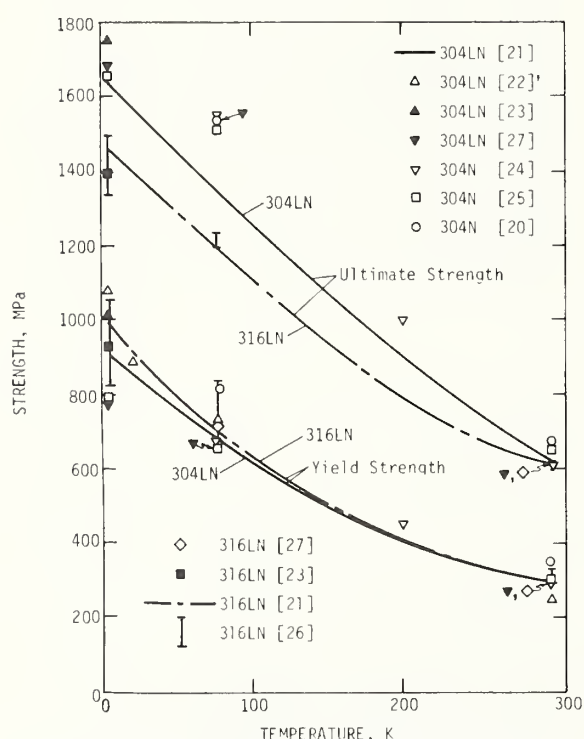


Fig. 6. Tensile and yield strengths of nitrogen-strengthened 300-series stainless steels at temperatures between 4 and 300 K [20–27].

steels are suitable for cryogenic service: the Cr–Ni–N and the Cr–Ni–Mn–N alloys. The Cr–Ni–N alloys are 300-series stainless steels with deliberate additions of nitrogen. In the US specifications, the nitrogen range is 0.10–0.16% for 304N and 316N. The corresponding European specifications permit nitrogen levels to 0.25%. The manganese in Cr–Ni–Mn–N alloys provides austenite stability and can thus be used to replace part of the Ni content. Manganese also increases the solubility of nitrogen in austenite and thus permits higher nitrogen levels –0.4% maximum nitrogen is typical.

3.1. Tensile properties

The yield and ultimate strengths of the Cr–Ni–N 300-series stainless steels are summarized in fig. 7. The solid lines and the broken lines represent the data of Randak et al. [21] for 304LN and 316LN, respectively. The various symbols depict the data for seven other investigations [20, 22–27], each on one of the following alloys: 304LN, 304N and 316LN. As in the case for 304 and 316, fig. 1, alloys 304N and 304LN have approximately 20% greater ultimate strength at cryogenic temperatures than alloy 316LN. All three alloys have essentially the same yield strength at and below room temperature. There is relatively little scatter in the yield strength data considering that data on 17 heats from a variety of sources are plotted. The nitrogen contents of the 17 heats range from 0.09 to 0.17%.

Of the four nitrogen-strengthened Cr–Ni–Mn stain-

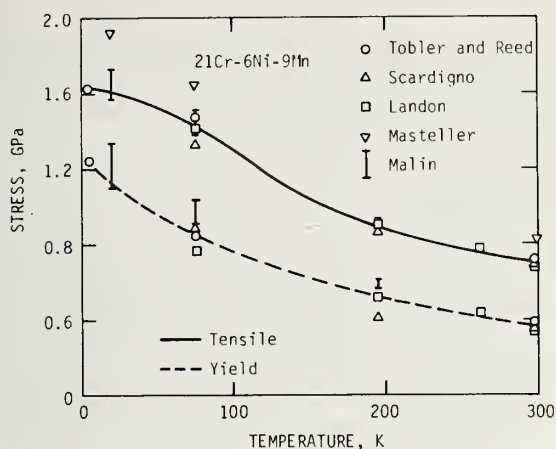


Fig. 7. Tensile and yield strengths of 21Cr-6Ni-9Mn stainless steel at temperatures between 4 and 300 K [28].

less steels listed in table 4, the 21Cr-6Ni-9Mn alloy has been most thoroughly evaluated [28-32]. The tensile and yield strength data are summarized in Fig. 6. This alloy typically has about 25% greater yield strength than the Cr-Ni-N alloys. Representative tensile data on the other nitrogen-strengthened Cr-Ni-Mn alloys that have been tested at 4 K indicate that yield strength increases and ductility decreases with decreasing temperature; and thus, fracture resistance must be considered when selecting these alloys for liquid helium service.

3.2. Toughness

The nitrogen-strengthened stainless steels have excellent toughness at room temperature. However, as shown in fig. 8, significant toughness losses generally occur as the temperature is reduced [25]. Read and Reed [25] observed significant variations in the toughness of a single piece of 21Cr-12Ni-5Mn alloy. As-received mill-annealed material having an intergranular microconstituent had a plane strain fracture toughness at 4 K of 111 MPa \sqrt{m} . A high temperature (1177°C, 1.5 h) anneal dissolved the microconstituent and increased the toughness to 176 MPa \sqrt{m} . Thus, certain nitrogen-strengthened grades can be used at 4 K, but care should be taken to ensure that the alloy selected has satisfactory toughness at 4 K for the applicable melting practice, product form and heat treatment.

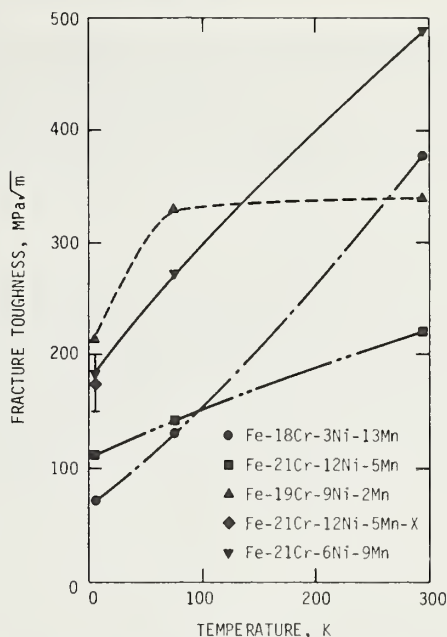


Fig. 8. Fracture toughness of four nitrogen-strengthened austenitic stainless steels at temperatures between 4 and 300 K [25].

3.3. Fatigue

The strain cycling fatigue behavior of 21Cr-6Ni-9Mn has been measured at 295, 76 and 4 K by Shepic and Schwartzberg [14]. The results at 4 K, shown in fig. 4, indicate that the 21Cr-6Ni-9Mn alloy has fatigue strength better than 304L but not as good as 316. Thus, the significantly higher strength of the nitrogen-strengthened grade does not result in a comparable improvement in fatigue life.

The fatigue crack growth behavior of several nitrogen-strengthened grades has been studied at cryogenic temperatures [25,28]. The results for the high nitrogen Cr-Ni-Mn alloys depend largely on the relative austenite stability of the alloys. For the least stable alloy evaluated, 18Cr-3Ni-13Mn, the fatigue crack growth rates at 4 K are 50 times faster than those for the most stable alloy evaluated, 21Cr-12Ni-5Mn, and 10 times faster than the growth rates for 21Cr-6Ni-9Mn. For the 21Cr-12Ni-5Mn alloy, the fatigue crack growth rates fall within the same scatter band as the 300 series ($N < 0.08\%$) alloys at 4 K. For the Cr-Ni alloys, comparison of 304 and 304L with 304N and 304LN shows that the nitrogen-strengthened

alloys have growth rates at 4 K about 4 to 5 times higher than the lower nitrogen grades. In contrast, the 316 alloy, which has greater austenite stability than 304, has essentially the same growth rates at 4 K as the 316LN alloy.

3.4. Physical properties

In general, the physical properties of the nitrogen-strengthened stainless steels are similar to the 300-series alloys, as summarized in table 3. In general, the nitrogen contributes to austenite stability and thus reduces the magnetic permeability induced in some alloys by deformation at low temperatures. Anomalous behavior has been observed in high manganese alloys by Ledbetter [33] in the elastic behavior and by Ledbetter and Collings [34] in the magnetic susceptibility.

4. Fabrication characteristics of austenitic stainless steels

The fabricability of austenitic stainless steels is certainly sufficient for fusion magnet systems as attested by the widespread use of stainless steels in

a variety of industries. Fabrication characteristics that should receive special consideration for fusion magnet applications are briefly reviewed in this section.

4.1. Welding

The austenitic stainless steels, with and without nitrogen strengthening, are readily weldable by all of the common welding processes, providing the appropriate consumables and procedures are used. The service experience with welded assemblies of the alloys has been satisfactory at cryogenic temperatures. The American Welding Society, AWS, designation system, which is similar to the AISI system for wrought products, is generally used to classify stainless steel filled metals. The AWS designations and chemical compositions of the filler metals commonly used for cryogenic applications are summarized in table 5. The strength of stainless steel welds at 4 K generally exceeds the corresponding base metal strength, but toughness is usually significantly lower. Three phenomena that affect the strength and toughness of the as-deposited weld metal take on added significance at cryogenic temperatures: sensitization, ferrite content and nitrogen pickup. In addition, heat treatment

Table 5
Compositions of filler metals for welding austenitic stainless steels

AWS type covered electrodes	Composition (%)			
	Cr	Ni	C, max	Other
E308	18 -21	9 -11	0.08	
E308L	18 -21	9 -11	0.04	
E310	25 -28	20 -22.5	0.20	0.75 Si, max
E16-8-2	14.5-16.5	7.5- 9.5	0.10	0.50 Si, max; 1-2 Mo
E316	17 -20	11 -14	0.08	2-2.5 Mo
E316L	17 -20	11 -14	0.04	2-2.5 Mo
E330	14 -17	33 -37	0.25	
Rod and bare electrodes				
ER308	19.5-22	9-11	0.08	
ER308L	19.5-22	9-11	0.03	
ER310	25 -28	20-22.5	0.08-0.15	
ER316	18 -20	11-14	0.08	2-3 Mo
ER316L	18 -20	11-14	0.03	2-3 Mo

For covered electrodes: Mn = 2.5, max; Si = 0.9, max; P = 0.04, max; S = 0.03 max.

For rod and bare electrodes: Mn = 1.0-2.5; Si = 0.25-0.60; P = 0.03; S = 0.03, max.

generally has a stronger influence on the weld metal than the base metal.

Sensitization, the grain boundary precipitation of Cr carbides, reduces weld metal toughness at low temperatures [35]. Consequently, weld metals with extra low carbon, such as 308L and 316L, are commonly used for cryogenic applications. Sensitization is most extreme if the weldment is given prolonged exposure in the temperature range 500–800°C. However, the underlying weld beads in multipass weldments may receive sufficient exposure to these temperatures to cause significant toughness reductions in stainless steels with greater than 0.03% carbon. Subsequent annealing of the welds at temperatures greater than 950°C dissolves the carbides and improves the toughness.

The ferrite content of as-deposited weld metals can be estimated by using the Schaeffler constitution diagram. To avoid microfussuring the weld metal chemistry is generally balanced to provide 4–10% ferrite. However, for cryogenic service there is concern that the ferrite, which is a bcc phase and therefore brittle at low temperatures, may embrittle the weld metal. Szumachowski and Reid [36] have shown that ferrite reduces toughness at 76 K for a wide range of stainless steel weld metals. Read, McHenry and Steinmeyer [35] have evaluated the

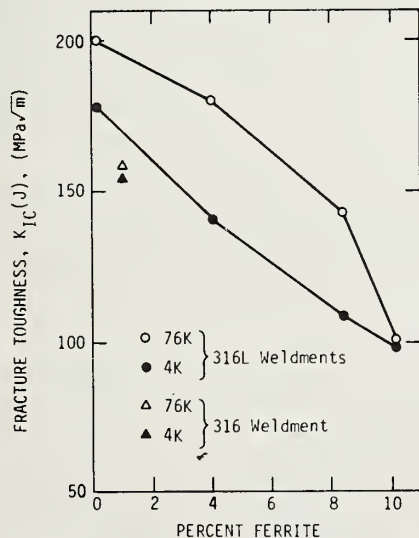


Fig. 9. Fracture toughness of AWS 316L weld metal at 4 K as a function of ferrite content [35].

effect of ferrite content on the fracture toughness of shielded metal arc welds of AWS 316L; the results at 76 and 4 K are shown in fig. 9.

Nitrogen increases the yield strength and decreases the toughness of stainless steel weld metals. When conventional (low N) filler metals are used, nitrogen variations in the range 0.04–0.13% may occur depending on the amount of air which enters the arc shielding medium. The greatest variations in nitrogen pickup are associated with gas metal arc welding where the nitrogen content ranges from 0.04 to 0.13% depending on the type of gas coverage and the electrode stickout. Smaller variations are attributed to electrode coatings; lime coatings generally give better coverage and less nitrogen pickup than titania coatings.

4.2. Heat treatment

One of the principal advantages of annealed austenitic stainless steels is that heat treatment is generally not required. The possible exceptions are annealing at 1000–1100°C following severe forming operations and stress relief at 420–480°C to reduce peak residual stresses and improve dimensional stability.

Heat treatment of stainless steel welds has been studied by Bennett and Dillon [37] for AWS types 308, 308L and 310. Heat treating or slow cooling in the sensitization range causes significant toughness loss at 76 K in types 308 and 310, but does not affect 308L. Stress relieving at 840°C followed by furnace cooling causes about a 50% toughness loss in each alloy (20–32 J as-welded and 8–20 J stress-relieved). Stress relieving at 950°C followed by furnace cooling caused a 50% toughness loss in 310, no change in 308L, and mixed results ($\pm 40\%$ toughness change) in 308. Annealing at 1070°C followed by water quenching improved the toughness of 308 and 308L, but decreased the toughness of 310. The beneficial effect of a full anneal on toughness at 76 K has also been reported by Krivobok and Thomas [38], McConnell and Brady [39] and DeLong [40].

4.3. Castings

The austenitic stainless steels are widely used for manufacturing corrosion resistant castings. The casting alloys equivalent to AISI types 304 and 316 are ACI (Alloy Casting Institute) types CF8 and CF8M, respect-

ively. The ferrite content of these alloys may vary from 0 to 40% due to chemistry variations within the allowable ranges. Ferrite levels in this range are likely to be unacceptable because of low fracture toughness and high permeability. Ferrite-free castings require the use of higher nickel content alloys such as ACI grades CK20 (corresponding to AISI grade 310). A 16Cr–20Ni–10Mn–2.2Mo alloy has been used for liquid hydrogen [41] and liquid helium bubble chambers [42,43]; the alloy retains excellent strength (550 MPa yield strength) and ductility at temperatures to 2.5 K [43].

4.4. Machining, forming and forging

Machining: Annealed austenitic stainless steels are more difficult to machine than carbon steels or aluminum alloys because of their relatively high tensile strength, work hardening rates, and low thermal conductivity. These properties cause poor finishes, heat buildup and excessive tool wear. As a result, it is necessary to use heavier feeds, slower speeds, better quality tool bits, more rigid machines and more power.

Forming: The candidate stainless steels have excellent formability. Alloys with more austenite stability than types 304 or 316 may be needed if severe forming operations are required. The nitrogen-strengthened 21Cr–6Ni–9Mn alloy is reported to have excellent austenite stability; even after 60% reduction at room temperature the permeability is less than 1.02 [44].

Forging: The austenitic stainless steels can be forged into shapes suitable for many magnet applications, e.g. forged pancake billets for ring rolling coil forms. Stainless steels are more difficult to forge than most common structural alloys because of their high strength at elevated temperatures. Within the family of austenitic stainless steels, the forgeability of types 304 and 316 is highly rated [45].

4.5. Inspection

During fabrication of fusion magnet systems, the stainless steel material and components are likely to be inspected using conventional methods. The only problem peculiar to the proposed designs is the need for heavy-section stainless steel welds. These welds cannot be effectively inspected for the presence of

cracks or crack-like defects. Radiography is of limited use because of its inability to reliably detect cracks. Ultrasonic methods do not work effectively because of the high noise levels and large and variable attenuation arising from the large-grain-size welds. Standards are needed to assure that the defect sizes that can be reliably detected do not adversely affect structural integrity.

5. Aluminum alloys

Aluminum alloys have been proposed for many structural applications in fusion magnet systems. Their principal advantages are: low as-fabricated cost, light weight, non-magnetic behavior, stable microstructure, and good retention of strength and toughness at cryogenic temperatures. The main disadvantages of aluminum alloys are low strength in weldments, high electrical and thermal conductivity, and an unfavorable elastic modulus (too low) and thermal expansion (too high) for many applications.

For fusion magnet structures the preferred aluminum alloys are 5083, 2219 and 6061. The composition ranges for these alloys are summarized in table 6. Alloy 5083 is generally used in the annealed condition (5083-0) and has a typical yield strength of 171 MPa (25 ksi) at 4 K. Alloy 2219 is generally used in a heat treated condition (T851, T87, etc.), and in the T851 temper has a typical yield strength of 482 MPa (70 ksi) at 4 K. Alloy 6061 is usually used in the heat treated condition (T6, T651, etc.), and in the T6 temper has a typical yield strength of 380 MPa (55 ksi) at 4 K. Although each of these alloys is readily weldable, only 5083 retains full strength in the welded condition and is the best choice for most large welded components. Alloy 2219 has the highest strength of the three alloys and is recommended for bolted construction where space or weight need to be conserved.

Several other aluminum alloys have excellent properties at 4 K and may be used for special applications. Commercially pure aluminum (alloy 1100) and the 3003 alloy have excellent formability. Alloy 3003 has been widely used for cryogenic applications and is the best choice when brazing is used for joining. The high strength alloys such as 2014 and 7005 may be used for nuts and bolts.

Table 6
Compositions of aluminum alloys suitable for liquid helium service [46]

Type	Composition (%)								
	Si max	Fe max	Cu	Mn	Mg	Cr	Zn max	Ti	Others
1100	1.0	Si + Fe, max	0.05–0.20	0.05, max	–	–	0.10	–	99.00 Al, minimum
2219	0.2	0.3	5.8 –6.8	0.20–0.40	0.02, max	–	0.10	0.02–0.10	0.05–15 V; 0.10–0.25 Zr
3003	0.6	0.7	0.05–0.20	1.0 –1.5	–	–	0.10	–	
5083	0.4	0.4	0.1, max	0.40–1.0	4.0–4.9	0.05–0.25	0.25	0.15, max	
6061	0.4–0.8	0.7	0.15–0.40	0.15, max	0.08–1.2	0.04–0.35	0.25	0.15, max	

The ASTM specifications for aluminum mill products of alloys 5083, 2219 and 6061 are summarized in table 7. For a more complete listing of specifications refer to the Aluminum Standards and Data Book [46]. Procurement of heavy sections may require additional specification requirements on through-thickness ductility [47].

The low temperature properties of aluminum alloys have been compiled in cryogenic handbooks [6,7], in a review article by Kaufman and Wanderer [48] and in suppliers' publications [49]. In this section the general trends in strength, toughness and fatigue resistance are summarized, particularly the data for room temperature and 4 K. The data are taken on relatively few lots of material, but generally the lot-to-lot variations in the mechanical properties of aluminum alloys are relatively small (with respect to stainless steel).

5.1. Tensile properties

The mechanical properties of alloys 5083, 6061 and 2219 at room temperature and 4 K have been determined by Kaufman, Nelson and Wanderer [50] and the results are summarized in table 8. Notice that in all cases the tensile strengths, and to a lesser extent the yield strengths, are superior at 4 K and the ductility values are not significantly changed. The alloys retain good notched-tensile properties at 4 K.

Aluminum alloys having a wide range of strength levels are suitable for liquid helium applications. The yield strengths of commercially pure (CP) aluminum (types 1100-0 and 1099-H14) and the preferred alloys are shown as a function of temperature in fig. 10 [42]. The yield strengths of each alloy gradually increase with decreasing temperature. Strength increases in the following order: annealed CP (1100-0), cold

Table 7
ASTM specifications and availability of aluminum mill products [46]

Product form	Specification ASTM	Available alloys		
		5083	6061	2219
Sheet and plate	B209	x	x	x
Wire, rod, bar; rolled or cold finished	B211		x	x
Wire, rod, bar, shapes, tube	B221	x	x	x
Structural shapes	B308		x	
Pipe	B241		x	
Forgings and forging stock	B247	x	x	x
Structural pipe and tube; extruded	B249		x	

Table 8
Tensile properties of aluminum alloys at room temperature and 4 K [50]

Alloy and temper	Plate thickness (mm)	Orientation	Temp. (K)	TS tensile strength (MPa)	YS yield strength (MPa)	Elongation in 4D (%)	Reduction of area (%)	NTS notch tensile strength (MPa)	NTS/TS	NTS/YS
5083-0	25	L	RT	322	141	19.5	26	372	1.16	2.65
			4	557	178	32	33	429	0.77	2.42
5083-H321	25	L	RT	335	235	15	23	421	1.26	1.80
			4	591	279	29	33	508	0.86	1.82
6061-T651	25	L	RT	309	291	16.5	50	477	1.54	1.64
			4	483	379	25.5	42	619	1.28	1.63
		T	RT	309	278	15.2	42	467	1.51	1.68
			4	485	363	23	33	601	1.24	1.66
2219-T851	25	L	RT	466	371	11	27	547	1.12	1.48
			4	659	484	15	26	703	1.06	1.48
		T	RT	457	353	10.2	22	531	1.16	1.50
			4	659	481	13	21	665	1.01	1.38
2219-T87	25	L	RT	464	387	11.8	28	567	1.22	1.46
			4	674	511	15	23	690	1.03	1.37
A356-T61 casting	19	casting	RT	287	208	8.8	10	354	1.23	1.70
			4	455	331	7.1	9	495	1.09	1.50

worked CP (1099-H14), solution-strengthened Al–Mg alloy (5083-0), cold worked Al–Mg alloy (5083-H321), precipitation hardened Al–Mg–Si alloy (6061-T651) and precipitation hardened Al–Cu alloy (2219-T851). Still higher yield strengths are available in several other

alloys including 2014-T651, 2024-T851 and 7005-T5351.

5.2. Toughness

Aluminum alloys generally retain excellent toughness at cryogenic temperatures. A useful measure of aluminum alloys toughness at 4 K is the notch-yield ratio, i.e. the ratio of notched tensile strength to unnotched yield strength [51]. Ratios substantially greater than one, say 1.5, indicate that the alloys retain the ability to plastically deform and resist crack initiation in the presence of sharp stress concentrations. As shown in table 9, the 5083 and 6061 alloys have notch-yield ratios greater than 1.6 and the higher-strength 2219-T851 and T87 alloys have notch-yield ratios of about 1.4. Significantly lower ratios (1.0–1.25) occur in other high strength alloys such as 2014-T651 and 2024-T851 and in most 7000 series alloys (7005 is an exception), where the ratio is sometimes below 0.4 at cryogenic temperatures [52].

Limited toughness test data are available on aluminum alloys at 4 K. Tobler and Reed [53] measured the fracture toughness of 5083-0 (4.3 cm thick plate)

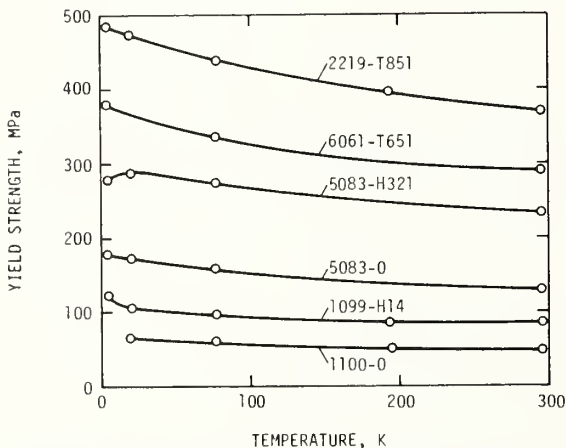


Fig. 10. Yield strengths of six aluminum alloys at temperatures between 4 and 300 K [50].

Table 9
Physical properties of aluminum alloys

Property	Units	5083 (annealed)			Precipitation hardened 6061			Precipitation hardened 2219		
		295 K	4 K	Ref.	295 K	4 K	Ref.	295 K	4 K	Ref.
Specific gravity	g/cm ³	2.66			2.70			2.83		
Young's modulus	GN/m ²	71.5	80.9	58	70.1	77.7	7	77.4	85.7	59
Shear modulus	GN/m ²	26.8	30.7	58	26.4	29.2	7	29.1	32.5	59
Poisson's ratio		0.333	0.318	58	0.338	0.327	7	0.330	0.318	59
Thermal conductivity	W/m · K	120	3.3	7	120–160	3–6	50	120–160	3–6	50
Thermal expansion	K ⁻¹ × 10 ⁻⁶	23	14.1	7	120–160	14.1	7	120–160	14.1	7
Specific heat	J/kg · K	900	0.28	7	120–160	0.28	7	0.28	0.28	7
Electrical resistivity	μ Ω cm	5.66	3.03	17	3.94	1.38	17	5.7	2.9	17

using J -integral procedures and found that toughness increased with decreasing temperature. The $K_{Ic}(J)$ was 47 MPa√m at 4 K in the transverse (TL) orientation. Shepic [54] measured the toughness of 2219-T87 (3.8 cm thick plate) using the ASTM E399 plane strain fracture toughness testing procedures. The K_{Ic} for 2219-T87 at 4 K was 45.5 MPa√m in the transverse (TL), 47.7 MPa√m in the longitudinal (LT) and 28.6 MPa√m in the through-thickness (SL) orientations.

5.3. Fatigue

Strain cycling fatigue tests have been conducted by Nachtigal [13] on 2219-T851 and 2014-T6 alloys at room temperature, 77 and 4 K. For a given strain level, the fatigue lives of both alloys were greater at 4 K than at the higher temperatures for endurance

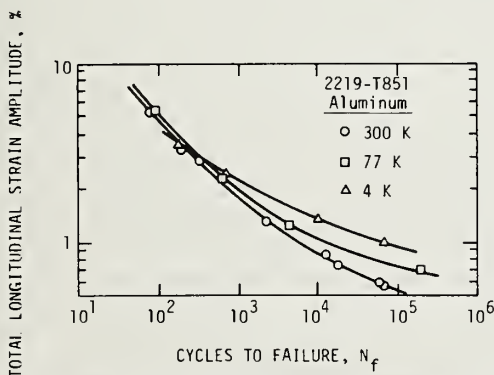


Fig. 11. Fatigue behavior of 2219-T851 aluminum alloy at temperatures of 300, 77 and 4 K [13].

greater than about 500 cycles. The results for 2219-T851 are shown in fig. 11. The Manson-Hirschberg [55] method of universal slopes gave reasonable predictions of fatigue behavior based on the tensile properties at the test temperature.

The fatigue crack growth behavior of 5083-0 [53], 2219-T87 [54] and an Al–6Mg [56] alloys have been determined at 4 K. In each case the results indicate that the growth rates at 4 K are slower than the rates at room temperature.

5.4. Physical properties

The physical properties of the candidate aluminum alloys are summarized in table 9. The thermal properties have been taken from the best-fit lines used in the LNG Materials Handbook [7] and from the compilation on thermal conductivity by Childs, Ericks and Powell [57]. Original sources are given for the elastic properties [58,59] and electrical resistivity [17].

With the exception of magnetic susceptibility, the physical properties of aluminum alloys are not as good as those of stainless steels for fusion magnet applications at 4 K. The elastic modulus is relatively low, and thus when used for coil case applications more of the load must be carried by the conductor assembly. The thermal and electrical conductivities are relatively high, resulting in increased thermal loads particularly from eddy current losses.

6. Fabrication characteristics of aluminum alloys

The relative ease of fabricating large aluminum structures is the principal advantage of aluminum

Table 10
Compositions of aluminum welding rods and electrodes for liquid helium service [46]; composition, % (max unless range given)

Type	Cu	Mg	Mn	Cr	Si	Fe	Zn	Ti	Be	Other	Suggested for welding
1100	0.20	—	0.05	—	Si + Fe = 1.0, max					99.0	—99.5 Al 1100, 3003
2319	5.8–6.8	0.02	0.20–0.40	—	0.20	0.30	0.10	0.10–0.20	0.0008	0.10–0.25	Zr 2219
4043	0.03	0.05	0.05	—	4.5–6.0	0.80	0.10	0.20	0.0008	0.05–0.15	V 1100, 6061
5183	0.10	4.3–5.2	0.50–1.0	0.05–0.25	0.40	0.40	0.25	0.15	0.0008		5083
5356	0.10	4.5–5.5	0.05–0.20	0.05–0.20	Si + Fe = 0.5, max		0.10	0.06–0.20	0.0008		5083, 6061
5556	0.10	4.7–5.5	0.5–1.0	0.05–0.20	Si + Fe = 0.4, max		0.25	0.05–0.20	0.0008		5083, 6061

over stainless steels. In addition the lower weight of aluminum structures may facilitate assembly and erection of the large magnet structures anticipated for fusion energy systems. Fabrication characteristics that should received special consideration for fusion magnet systems are briefly reviewed in this section.

6.1. Welding

Alloys 5083, 6061 and, to a lesser extent 2219, are readily weldable by the gas metal-arc and gas tungsten-arc processes. The compositions of aluminum welding rods and electrodes for these processes are

Table 11
Tensile properties of aluminum alloy weldments at room temperature and 4 K (60)

Alloy and temper	Plate thickness (mm)	Filler alloy	Post-weld thermal treatment	Temp. (K)	TS tensile strength (MPa)	JYS joint yield strength (MPa)	Elongation in 4 D (%)	Reduction of area (%)	Joint efficiency (%)	Location of failure	NTS notch tensile strength (MPa)	NTS TS	NTS JYS	
5083-0	25	5183	no	RT	293	138	21.5	—	100	WM	308	1.05	2.22	
				4	381	174	27	37	69	BM	371	0.98	2.14	
5083-H321	25	5183	no	RT	305	179	14	39	96	HAZ	376	1.23	2.10	
				4	455	246	9.0	14	80	WM	405	0.89	1.65	
5083-H321	25	5356	no	RT	286	167	13.5	47	90	WM	371	1.30	2.22	
				4	455	235	9.0	17	80	HAZ	398	0.87	1.69	
5083-H321	25	5556	no	RT	306	176	14	36	97	WM	370	1.21	2.10	
				4	474	238	13	17	83	WM	399	0.84	1.68	
6061-T6	25	4043	no	RT	214	144	6.0	19	69	HAZ	234	1.10	1.63	
				4	338	259	4.5	9	63	WM	275	0.81	1.06	
				yes	RT	298	247	11	44	96	BM	396	1.31	1.57
6061-T6	25	5356	no	RT	4	452	309	15	16	84	WM	463	1.02	1.50
				RT	225	156	8.0	31	73	WM	323	1.44	2.07	
				4	398	243	13.5	24	74	WM	367	0.92	1.50	
				yes	RT	279	202	9.5	33	90	BM	—	—	—
2219-T851	32	2319	no	RT	4	476	307	19	24	89	WM	419	0.88	1.37
				RT	225	185	2.0	5	50	HAZ	280	1.24	1.52	
				4	411	277	2.5	10	62	HAZ	363	0.88	1.31	
2219-T62	25	2319	yes	RT	395	277	7.5	7	99	HAZ	439	1.11	1.58	
				4	496	355	3.5	5	80	HAZ	570	1.15	1.61	

Note: Location of failures: WM – weld metal; BM – base metal; HAZ – heat affected zone.

summarized in table 10. Annealed 5083 alloy retains full strength in the as-welded condition, but the cold worked and precipitation hardened alloys are weakened by welding. Part of the strength of precipitation hardened alloys can be restored by a post-weld heat treatment.

The tensile properties of aluminum alloy weldments were determined by Nelson, Kaufman and Wanderer [60] and the results for selected alloys at room temperature and 4 K are summarized in table 11. Notice that part of the strength obtained by cold working (5083-H321) and by precipitation hardening (6061-T6 and 2219-T851) is retained by the welded joint. This strength increase is not reflected in design-code allowable stresses [11] which assume as-welded aluminum alloys are in the fully annealed condition. The tensile properties of 6061-T6 and 2219-T62 welds that were subsequently solution treated and aged indicate that substantial strengthening can be achieved by post-weld heat treatments. For most fusion magnet structures, the solution treatment and quenching are not considered practical. The data in table 11 also indicate that the ductility of 2219 weldments is quite low due to localized deformation in the heat affected zone; the ductility and notch-yield ratio of 5556 and 4043 filler metals (as-welded) are low at 4 K; and the best ductility and notch-yield ratios in the as-welded condition at 4 K are provided by the 5083 and 5356 alloys.

6.2. Heat treatment and temper designations

Aluminum alloys are supplied in a wide range of tempers, and for large complex structures, subsequent heat treatments are not generally performed by the fabricator. The tempers are designated by a letter followed by one to three digits. The letter is the basic temper designation: O-annealed, H-strain hardened and T-thermally treated. For the strain hardened tempers, the first digit indicates the hardening operations: H1-strain hardening only, H2-strain hardened and partially annealed and H3-strain hardened and stabilized. The second digit (e.g. H18 is strain-hardened by a cold reduction of 75%) indicates the degree of strain hardening and the third digit is sometimes used for specified variations. For the thermally treated tempers, the first digit indicates the specific sequence of basic treatments; for example, T6 designates solu-

tion heat treated and then artificially aged and T8 designates solution heat treated, cold worked and then artificially aged. Subsequent digits indicate specific variations, such as X51 stress relieved by stretching as in T651 or T851. The reader is referred to the Aluminum Association Handbook [46] for a complete description of the temper designation system.

6.3. Castings

Aluminum alloy castings can be produced by a variety of processes and generally are satisfactory for nonstructural applications at low temperatures. The ASME Code [11] permits use of Al-5 Si (type 43) and Al-7Si-0.3Mg (type 356-T6) for nonwelded structural applications. Nelson, Kaufman and Wanderer [60] evaluated the tensile properties at 4 K of several combinations of castings welded to wrought alloys; in general, superior properties were obtained when the properties of the cast and wrought components were nearly equal.

6.4. Machining, forming and forging

Machining: Aluminum alloys, particularly the heat treated grades, have excellent machinability. Machined and bolted assemblies of high strength aluminum alloys can replace more costly welded stainless steel assemblies. Care should be taken when using steel bolts because the thermal contraction of aluminum alloys on cooling to 4 K exceeds that of steel.

Forming: Aluminum alloys have excellent formability in the annealed or the solution treated conditions.

Forging: Aluminum alloys have the best forgeability of all structural alloys because of their very low strength at forging temperatures of 370–510°C. The size limit on aluminum forgings is significantly greater than that on stainless steels because of the reduced pressures required.

6.5. Inspection

Aluminum alloys and their weldments are readily inspectable by conventional methods: dye-penetrant, ultrasonics and radiography.

7. Alternative alloys

Alternative alloy systems do not provide candidate structural materials for superconducting magnets in fusion energy systems. Consider the following systems:

Nickel base alloys are ferromagnetic, expensive and frequently difficult to fabricate. However, many of these alloys have excellent combinations of strength and toughness at 4 K and may be suitable for special applications [61].

Titanium alloys are brittle at 4 K, expensive and difficult to fabricate [62].

Cobalt base superalloys transmute to long half-life reaction products and are expensive and difficult to fabricate.

Carbon and alloy steels including the ferritic and martensitic stainless steels are ferromagnetic and brittle at 4 K. Even the cryogenic nickel steels are brittle at 4 K [63] except for a specially processed 12Ni alloy [64].

Copper alloys are acceptable, but generally not competitive with the austenitic stainless steels or aluminum alloys.

8. Summary

This review suggests that there are several commercially available alloys that are suitable for construction of large superconducting magnet structures for fusion energy systems. These alloys include annealed austenitic stainless steels, nitrogen strengthened austenitic stainless steels where greater strength is needed, an annealed Al–Mg alloy for welded aluminum construction and precipitation-hardened aluminum alloys for bolted assemblies. For each of these alloys there are enough experimental data and fabrication experience to provide reasonable assurance that the alloys have sufficient strength, ductility and toughness in the liquid helium environment; that the alloys can be fabricated into support structures for superconducting magnets; and finally, that the fabricated structure will retain adequate properties during operation of the fusion energy device.

It should be realized, however, that the depth of understanding, the degree of characterization, and the extent of related experience for these alloys in

the fusion-magnet environment are extremely limited. More work is needed on material behavior at 4 K, particularly in the areas of material variability, processing effects on properties, and the fabrication and mechanical behavior of large, complex, thick-section components.

9. Recommendations

The accumulated knowledge of materials for fusion energy systems should eventually result in a code for the design, construction and inspection of fusion magnets. Adherence to this code should provide assurance that the magnet system provides the intended field and operates in a safe, reliable and efficient manner. Establishment of such a code for large magnets must await further developments in the technology, particularly the experience gained from prototype systems and greater material characterization. However, parts of the code should be set forth as preliminary guidelines to facilitate the orderly development of materials technology for magnet systems.

Design guidelines needed for selection of materials should identify operating loads and conditions and criteria for establishing allowable working stresses for candidate materials. For magnet systems, a description of the operating loads should include the anticipated load history for normal operation, loads due to credible fault conditions and procedures for treating combined loads. The operating conditions of interest are the thermal environment, radiation dosage, magnetic field profile and design life. Allowable working stresses should account for the materials strength variability, the fatigue strength for a specified scatter factor on fatigue cycles, fracture mechanics analysis and a factor of safety based on uncertainties in the loads and stress analysis.

Material procurement and processing should be controlled by a set of specifications which are sufficient to preclude the use of materials in the magnet systems which have properties inferior to those assumed in design. Inspection specifications and standards are needed to provide a high degree of confidence that no defects are present in the raw materials, or introduced during fabrication, which could cause unsatisfactory performance of the magnet system.

References

- [1] R.P. Reed, A.F. Clark and E.C. van Reuth, in: *Advances in Cryogenic Engineering*, vol. 22 (Plenum Press, New York, 1976) 1.
- [2] R.P. Reed, F.R. Fickett, M.B. Kasen and H.I. McHenry, in: *Materials Studies for Magnetic Fusion Energy Applications at Low Temperatures*, vol. 1, NBSIR 78-884 (National Bureau of Standards, Boulder, CO, 1978) 243.
- [3] F.R. Fickett, M.B. Kasen, H.I. McHenry and R.P. Reed, in: *Advances in Cryogenic Engineering*, vol. 24 (Plenum Press, New York, 1979).
- [4] F.R. Fickett, *Properties of Non-superconducting Technical Solids at Low Temperatures*, Proc. Fourth International Conference on Magnet Technology Brookhaven, New York, 1972) 498.
- [5] H.I. McHenry, in: *Advances in Cryogenic Engineering*, vol. 22 (Plenum Press, New York, 1976) 9.
- [6] *Handbook on Materials for Superconducting Machinery*, Metals and Ceramics Information Center, MCIC-HB-04 (Battelle, Columbus, Ohio, 1977).
- [7] D.B. Mann, *LNG Materials and Fluids* (National Bureau of Standards, Boulder, CO, 1978).
- [8] K.G. Brickner and J.D. Defilippi, in: *Handbook of Stainless Steels* (McGraw-Hill, New York, 1977) 20.
- [9] *Low Temperature and Cryogenic Steels*, Materials Manual (U.S. Steel Corp., Pittsburgh, PA, 1966).
- [10] *Materials for Cryogenic Service-Engineering Properties of Austenitic Stainless Steels* (International Nickel Limited, London, 1974).
- [11] *ASME Boiler and Pressure Vessel Code*, Section VIII, Pressure Vessels, (American Society of Mechanical Engineers, New York, 1977).
- [12] R.L. Tobler, in: *Fracture 1977*, vol. 3, Proc. Fourth International Conference on Fracture (Waterloo, Canada, 1977) 839.
- [13] A.J. Nachtigall, in: *Properties of Materials for Liquefied Natural Gas Tankage*, ASTM STP 579 (American Society for Testing and Materials, 1975) 378.
- [14] J.A. Shepic and F.R. Schwartzberg, in: *Materials Studies for Magnetic Fusion Energy Applications at Low Temperatures-1*, NBSIR 78-884 (National Bureau of Standards, Boulder, CO, 1978) 13.
- [15] R.L. Tobler and R.P. Reed, in: *Advances in Cryogenic Engineering*, Vol. 24 (Plenum Press, New York, 1979).
- [16] H.M. Ledbetter, W.F. Weston and E.R. Naimon, *J. Appl. Phys.* 46 (9) (1975) 3855.
- [17] A.F. Clark, G.E. Childs and G.H. Wallace, *Cryogenics* 10 (1970) 295.
- [18] K.R. Efferson and W.J. Leonard, *Magnetic Properties of Some Structural Materials Used in Cryogenic Applications*; ORNL-4150 (Oak Ridge National Laboratory, Oak Ridge, TN, 1976) 126.
- [19] *Metals Handbook*, vol. 1, 8th edn. (American Society for Metals, Metals Park, OH, 1967).
- [20] G.P. Sanderson and D.T. Llewellyn, *J. Iron Steel Inst. Lond.* 27 (1969) 1129.
- [21] V.A. Randak, W. Wesseling, H.E. Bock, H. Steinmaurer and L. Faust, *Stahl Eisen* 91 (1971) 1255.
- [22] R. Voyer and L. Weil, in: *Advances in Cryogenic Engineering*, vol. 11 (Plenum Press, New York, 1966) 447.
- [23] D.C. Larbalestier, Private Communication, University of Wisconsin, Madison, WI (1977).
- [24] C.E. Spaeder, Jr. and W.F. Domis, Project 44.012-062(2), US Steel Corp., Pittsburgh, PA (1969).
- [25] D.T. Read and R.P. Reed, in: *Materials Studies for Magnetic Fusion Energy Applications at Low Temperatures-1*, NBSIR-78-884 (National Bureau of Standards, Boulder, CO, 1978) 91.
- [26] D.B.A. Macmichael, M. Liddle and J.S.H. Ross, *Superconducting AC Generators Trial Rotor Forging Investigation* (International Research and Development Co. Ltd., Newcastle upon Tyne, England, 1978).
- [27] D.T. Read and R.P. Reed, in: *Materials Studies for Magnetic Fusion Energy Low Temperature Applications-II* (National Bureau of Standards, Boulder, CO, 1979).
- [28] R.L. Tobler and R.P. Reed, in: *Elastic Plastic Fracture*, ASTM STP-000, (American Society for Testing Materials, Philadelphia, PA, forthcoming).
- [29] P.F. Scardigno, M.S. Thesis, Naval Postgraduate School, Monterey, CA, NTIS AD/A-004555 (1974).
- [30] P.R. Landon, Unpublished Data, Lawrence Livermore Laboratories, Livermore, Ca (1975).
- [31] R.D. Masteller, NASACR-82638, Martin Marietta Corp., Denver, CO (1970).
- [32] C.O. Malin, NASA SP-5921 (01), Technology Utilization Office, NASA, Washington, D.C. (1970).
- [33] H.M. Ledbetter, *Mater. Sci. Eng.* 29 (1977) 255.
- [34] H.M. Ledbetter and E.W. Collings, in: *Metal Physics of Stainless Steels* (TMS AIME, New York, forthcoming).
- [35] D.T. Read, H.I. McHenry and P.A. Steinmeyer, in: *Materials Studies for Magnetic Fusion Energy Low Temperature Applications*, vol. II (National Bureau of Standards, Boulder, CO, 1979).
- [36] E.R. Szumackowski and H.F. Reid, *Weld. J.* 57 (1978) 325-s.
- [37] V.N. Krivobok and R.D. Thomas, Jr., *Weld. J.* 29 (1950) 493-s.
- [39] J.H. McConnell and R.R. Brady, *Chem. Eng.* 67 (1960) 125.
- [40] W.T. DeLong, *Weld. J.* 53 (1974) 273-s.
- [41] C.L. Goodzeit, in: *Advances in Cryogenic Engineering*, vol. 20 (Plenum Press, New York, 1965) 26.
- [42] D.F. Shaw, *Cryogenics* 4 (1964) 193.
- [43] A.B. Miller, *Cryogenics* 5 (1965) 320.
- [44] *Armco Nitronic 40 Stainless Steel Sheet and Strip* (Armco Steel Corp., Baltimore, MD, 1976).
- [45] J.E. Jenson, ed., *Forging Industry Handbook* (Forging Industry Association, Cleveland, OH, 1966).
- [46] *Aluminum Standards and Data*, Aluminum Association, Inc. Washington, D.C. (1976).
- [47] H.I. McHenry, *Met. Progr.* 93 (3) (1968) 62.
- [48] J.G. Kaufman and E.T. Wanderer, in: *Aluminum*, vol. II: *Design and Applications* (American Society for Metals, Metals Park, OH, 1967) 297.

- [49] Alcoa Aluminum – The Cryogenic Metal, Alcoa, Pittsburgh, PA (1971).
- [50] J.G. Kaufman, K.O. Bogardus and E.T. Wanderer, in: *Advances in Cryogenic Engineering*, vol. 13 (Plenum Press, New York, 1968) 294.
- [51] J.G. Kaufman and E.W. Johnson, in: *Advances in Cryogenic Engineering*, vol. 8 (Plenum Press, New York, 1963) 678.
- [52] M.P. Hanson, G.W. Stickley and H.T. Richards, in: *Low Temperature Properties of High-Strength Aircraft and Missile Materials*, ASTM STP 287 (American Society for Testing and Materials, Philadelphia, PA, 1961) p. 3.
- [53] R.L. Tobler and R.P. Reed, *J. Eng. Mat. Technol.* 99 (1977) 306.
- [54] J.A. Sphetic, in: *Materials Studies for Magnetic Fusion Energy Low Temperature Applications*, vol. II (National Bureau of Standards, Boulder, CO, 1979).
- [55] S.S. Manson, *Exp. Mech.* 5 (1965) 193.
- [56] H.I. McHenry, S.E. Naranjo, D.T. Read and R.P. Reed, in: *Advances in Cryogenic Engineering*, vol. 24 (Plenum Press, New York, 1979).
- [57] G.E. Childs, L.J. Ericks and R.L. Powell, *Thermal Conductivity of Solids at Room Temperature and Below*, NBS Monograph 131 (National Bureau of Standard, Boulder, CO, 1973).
- [58] E.R. Naimon, H.M. Ledbetter and W.F. Weston, *J. Mater. Sci.* 10 (1975) 1309.
- [59] D.T. Read and H.M. Ledbetter, *J. Eng. Mater. Technol.* 99 (1977) 181.
- [60] F.G. Nelson, J.G. Kaufman and E.T. Wanderer, in: *Advances in Cryogenic Engineering*, vol. 14 (Plenum Press, New York, 1969) 71.
- [61] J.M. Wells, R. Kossowsky, W.A. Logsdon and M.R. Daniel, in: *Materials Research for Superconducting Machinery VI*, NTIS No. ADA 036919 (National Bureau of Standards, Boulder, CO, 1976).
- [62] R.L. Tobler, in: *Cracks and Fracture*, ASTM STP 601 (American Society for Testing and Materials, Philadelphia, PA, 1976) 346.
- [63] R.L. Tobler, in: *Materials Research for Superconducting Machinery VI*, NTIS No. ADA 036919 (National Bureau of Standards, Boulder, CO, 1976).
- [64] S. Jin, S.K. Hwang and J.W. Morris, Jr., *Met. Trans.* 6A (1975) 1569.

STRENGTH AND TOUGHNESS RELATIONSHIP FOR INTERSTITIALLY STRENGTHENED
AISI 304 STAINLESS STEELS AT 4 K

R. L. Tobler, D. T. Read, and R. P. Reed
National Bureau of Standards
Boulder, Colorado

ABSTRACT

A study was conducted to determine the effects of carbon and nitrogen on the 4-K fracture properties of Fe-18Cr-10Ni austenitic stainless steels having a base composition corresponding to AISI 304. J-integral fracture toughness tests using 24.5-mm-thick compact specimens (TL orientation) were performed in a liquid helium environment on nine steel heats having carbon plus nitrogen (C+N) contents between 0.067 and 0.325 wt.%. The fracture toughness decreased with increasing C+N content. The K_{IC} estimates obtained at 4 K ranged from 337 to 123 $\text{MPa}\cdot\text{m}^{1/2}$, exhibiting an inverse dependence on tensile yield stress. A computer-aided J-integral test facility was implemented to conduct this study. This new facility improves measurement accuracy, conserves material specimens and testing time, and systematizes test procedures.

INTRODUCTION

Acceptance of the parameter J_{IC} as a measure of the fracture resistance of metals has become widespread in recent years. A large volume of J-integral fracture toughness data on a variety of candidate materials for low temperature applications has been accumulated. The J-integral test has the advantage of being applicable to smaller specimens (up to 100 times smaller) and tougher materials than the plane strain fracture test (K_{IC} test). A disadvantage of the J-integral technique has been its experimental difficulty. Previous test methods have required approximately five specimens and lengthy data reduction procedures [1]. Recently developed single-specimen J-integral test techniques [2] eliminated the multiple-specimen requirement, but the data reduction procedure was still lengthy. In the computer-aided J-integral test, most of the data-reduction procedure is automated; the apparatus produces a plot of the J-integral value versus crack extension from which J_{IC} can be quickly and simply extracted.

The AISI 300 series stainless steels are austenitic Fe-Cr-Ni alloys, offering relatively low strength but excellent cryogenic ductility and toughness [3]. By virtue of favorable mechanical properties, service history, and availability, AISI 304 is perhaps the most widely used cryogenic alloy in the world. But nitrogen-strengthened grades such as AISI 304 N or AISI 304 LN have attracted attention recently as possible substitutes for AISI 304 in applications demanding higher strength. Nitrogen is a relatively inexpensive and effective strengthener. Nitrogen also stabilizes the austenitic structure and reduces the probability of martensitic transformation when stress is applied at cryogenic temperatures.

Carbon has similar effects, but carbon contents in austenitic stainless steels must be held to low levels to prevent sensitization (chromium carbide precipitation) during thermal excursions.

Nitrogen-strengthened austenitic stainless steels are gaining popularity, but some applications are hindered by limited availability, limited service experience, lower fracture toughness, and lack of cryogenic design data. Several mechanical property studies were conducted on these steels [4-18], but most papers are concerned only with room temperature behavior. In the present study, fracture toughness measurements for nine heats of an Fe-18Cr-10Ni stainless steel are reported at 4 K. The carbon and nitrogen (C+N) contents of the nine heats were varied to enable a systematic study of interstitial concentration. The results can be used to predict the strength and toughness of commercial steels of given compositions or to tailor the properties for a particular application by appropriate specification of the steel composition.

MATERIALS

Nine stainless steel plates were procured from the research laboratories of a major steel manufacturer. These plates had a nominal base composition falling within the limits set by ASTM specification A 240 for AISI 304 stainless steel: Fe-18Cr-10Ni-1.5Mn-0.02P-0.02S-0.55Si-0.2Mo-0.2Cu. The carbon and nitrogen levels varied, however, with carbon at 0.03, 0.06, or 0.09 wt.% and nitrogen at 0.04, 0.12, or 0.24 wt.%. The mill chemical analyses are listed in Table I. The nine plates were produced from three 136-kg (300-lb) vacuum-induction-melted heats, split with respect to carbon level, and teemed into 76- x 200- x 360-cm hot-topped cast-iron ingot molds. The ingots were then reheated and soaked at 1561 K (2350°F), hot-rolled to 25.4-mm-thick plates,

and air cooled. The plates were finally annealed at 1332 ± 7 K ($1937^\circ \pm 13^\circ$ F) for 1 h and water quenched. The hardness and grain size measurements are listed in Table I.

METHODS

Since elastic-plastic fracture was anticipated in the test materials, the J_{IC} parameter was measured. The measurement problem in J_{IC} testing is to obtain the required plot of J-integral, J, versus crack extension, Δa , from the directly measured quantities, which are the load, P, on the specimen and the relative displacement, δ , of two measurement points located on the specimen load line on opposite sides of the notch (Fig. 1). The J value is proportional to the area under the (P, δ) curve (Fig. 2) and can be easily determined for any point along the curve. The shaded area in Fig. 2 is proportional to J at the point labeled "a". The principle used to measure Δa is that the crack length, a, is related to the slope of the (P, δ) curve of the specimen for elastic conditions through the known specimen compliance function. The Δa measurement procedure is to partially (about 10%) unload the specimen while recording load displacement changes (Fig. 2 and 3). Subsequent unloadings at increasing crack extension values result in increased compliance. The crack extension at a given unloading is the difference between the crack length measured in that unloading minus the initial crack length measured by an unloading carried out before crack extension.

The cryostat system that was used for computer-aided J-integral testing was described previously by Fowlkes and Tobler [19]. The specimen loading is controlled in conventional fashion by the operator. The computer

is used only in data acquisition and reduction. An analog ramp generator controlled by the operator applies a smoothly varying signal to the test-machine control circuitry to allow unloading-reloading cycles as necessary. The additional equipment needed for computer-aided testing includes a multichannel analog-digital conversion system, the computer itself, a CRT terminal, a dual floppy disk data-storage unit, and a digital plotter (Fig. 4).

Two signals are used to direct the operation of the data acquisition system. One is derived from the output of the ramp generator by which the operator initiates the unloading-reloading cycle. When the ramp generator is activated, a signal transmitted to the processor commands it to begin to acquire and store load- and displacement-change data during the unloading-reloading cycle. Data are stored until the load again reaches the value it had before the unloading. The test continues through as many unloading cycles as desired until the operator activates the quit signal, which directs the processor to await the operator's command, entered at the CRT terminal, to stop the data acquisition procedure and terminate the test.

During the incremental unloading required to measure Δa , displacement changes of the order of 0.05 mm and load changes of the order of 5 kN must be correlated accurately. These changes correspond to a change in the overall displacement signal of about 70 mV and a change in the load signal of about 1 V. Because the analog-to-digital converter used has only 16-bit resolution, the displacement signal cannot be converted directly to digital form with precision sufficient for accurate measurement of this displacement change. The measurement of the small displacement changes that occur during the unloading-reloading cycles is

facilitated by regarding the overall displacement to consist of small changing displacements superimposed on a large reference displacement value. The measurement is accomplished by canceling out the reference part and then converting the small displacement changes to digital form with high resolution. To achieve this cancellation, the overall displacement is converted to digital form at the beginning of each unloading-reloading cycle. This initial value is treated as the reference part. To cancel out this reference part of the displacement signal, a digital-to-analog converter with 14-bit resolution is used to apply a voltage equivalent to the reference part of the displacement signal to one terminal of a differential high-sensitivity analog-to-digital conversion channel. The overall displacement signal is applied to the other input terminal of this channel. This results in the analog-to-digital conversion of a voltage equal to the difference between the instantaneous value of the displacement signal and its value at the beginning of the unloading. This difference signal is the required change-of-displacement signal and is converted to digital form with 16-bit resolution of its 80-mV range. The least significant bit represents about 2.5 μV , which is quite sufficient. The load-change signal is produced in a similar manner by using another digital-to-analog converted signal and converted to digital form with 16-bit resolution at the 1.25-V level. Here the least significant bit represents about 40 μV , which is again quite sufficient.

Approximately 80 load-change and displacement-change data points are obtained for each unloading-reloading cycle over a 30-s period. These data are plotted during the unloading-reloading cycle with a

digital plotter, forming a plot like Fig. 3. From this plot, the presence of excessive noise or other improper behavior in the signals can be easily observed. The load-change and displacement-change data are correlated using a least-squares fit. From the resulting slope, the instantaneous crack length is calculated using the known expression for the compliance of the specimen.

Each $(J, \Delta a)$ datum is plotted by the digital plotter as soon as it is available, forming a plot similar to Fig. 1. This plot allows convenient monitoring of the progress and quality of the test in real time. The values are also displayed on a CRT terminal for transcription. This step will be replaced by an automatic print-out when facilities become available. The least-squares-fit and data-output procedure takes about 12 s.

The record of the completed test consists of the $(J, \Delta a)$, (P, δ) ; and $(\Delta P, \Delta \delta)$ plots, the transcribed $(J, \Delta a)$ data, and three files stored on a floppy disk during the test--one containing the $(J, \Delta a)$ values and a few other key data, one containing all the (P, δ) data, and one containing all the $(\Delta P, \Delta \delta)$ data.

The computer-aided J-integral test facility at NBS is similar to that described by Joyce and Gudas [20]. The differences are in the specific types of equipment used and in the real-time outputs. Real-time is used here to mean during the course of the test, as opposed to after the test is completed.

The procedure for extracting J and Δa from the directly measured load and displacement on a deeply notched, compact tensile specimen is as follows: The electrical signals from the load cell and displacement

gage are amplified by the electronics supplied with the closed-loop servo-hydraulic apparatus used for the test. A plot of load versus displacement similar to Fig. 2 is produced by an x-y plotter throughout the course of the test. Either signal may be displayed on a digital readout. The plot and readout are used by the operator to monitor the progress of the test.

The amplified load and displacement signals are also introduced into an analog-to-digital conversion system to permit calculation of J and Δa . At this point, the overall levels of the signals range between 0 and 10 V. These signals are converted to digital form with a resolution of 16 bits; the least significant bit represents about 0.3 mV. The overall load and displacement values are used for calculating the instantaneous J value, which is proportional to the area under the load-displacement curve. Stored overall-displacement points are separated by 2.5×10^3 . Smaller observed overall-displacement increments are not stored. Computations of the instantaneous J values are made when the overall displacement has increased sufficiently from the previously stored value.

The geometry of the compact specimens tested in this study is shown in Fig. 5. Specimen thickness, B , was 24.5 mm, and width, W , was 50.8 mm. The specimens were machined in the TL orientation as defined by ASTM Method E-399-74 [21]. The specimens were fatigue cracked at 4 K to a crack length between 28.8 and 36 mm ($\frac{a}{W} \approx 0.57$ to 0.71). The specimens were then J-tested in displacement control, and partial unloadings were performed periodically. The J value at each unloading point was calculated using the expression:

$$J = \frac{\lambda A}{Bb}$$

where λ is the Merkle-Corten factor dependent on crack length [22], A is the area under the load-versus-deflection curve at the unloading point, b is the specimen ligament ($b = W - a$), and B is the specimen thickness. J-resistance curves consisting of many sets of J and Δa points were generated, as shown by the example in Fig. 6.

The J_{IC} value for each steel was taken at the intersection of the J-resistance curve with the blunting line. The blunting line is given by $J = 2\sigma_f\Delta a$ where σ_f is the flow stress, which is the average of the yield and ultimate tensile stresses. As shown in Fig. 6, there is an artificial offset of the data from the theoretical blunting line, so a blunting line parallel to the theoretical blunting line but passing through the data was used. Scatter in the J-resistance curves caused uncertainties of about $\pm 12\%$ in the values of J_{IC} .

The validity of J_{IC} results was determined by the size criterion, which requires that [1]:

$$B, b, a \geq \frac{25J_{IC}}{\sigma_f}$$

In all low temperature fracture tests, partial transformation of the paramagnetic austenite to ferromagnetic α' (bcc) martensite was observed (e.g., Ref. 23). The extent of α' transformation was estimated by using a bar-magnet device [24]. Small amounts of ϵ (hcp) martensite may also have formed, but this was not measured.

RESULTS AND DISCUSSION

The computer-aided J-integral methods have now been in use for nine months and have proved quite satisfactory. In comparison with the

multiple specimen and non-computer-aided single-specimen techniques previously used, the new methodology has eliminated about 4 h of data reduction per test and has provided a real-time readout of the test progress and quality. The cost of the complete data-acquisition system, including analog-to-digital converters, processor, digital plotter, and CRT terminal is estimated at about \$25,000.

J_{IC} results were obtained for seven of the austenitic stainless steels tested, but the data for the two lower strength heats (with C+N 0.067 and 0.097 wt.%) were invalid. The maximum J values in these tests exceeded the allowable limits for 24.5-mm-thick specimens. The resistance curves deviated from the blunting line at exceptionally low J values, and the resistance curves obtained could not be analyzed according to conventional techniques because there was no obvious knee at the blunting line-resistance curve intersection. The J_{IC} values for the seven steels at 4 K range from 63 to 499 kJ/m², whereas the yield stresses for the same materials at 4 K range from 329 to 1286 MPa (Table II). Higher toughness in these seven steels is associated with lower interstitial C + N contents, and hence lower strength. All of the steels tested exhibited a ductile dimpled fracture mode at 4 K, as shown by the scanning electron fractographs of Figs. 7 and 8.

Estimates of the plane strain fracture toughness parameter, K_{IC} , which would be observed under linear-elastic conditions, were obtained using the relationship:

$$K_{IC}(J) = \left(\frac{J_{IC} E}{(1 - \nu^2)} \right)^{1/2}$$

where E is Young's modulus, ν is Poisson's ratio, and $K_{IC}(J)$ denotes an estimate of K_{IC} from J_{IC} . The values of E and ν for the stainless

steels at 4 K were estimated to be 206.8 GPa and 0.3 [25], respectively. The calculated K_{IC} estimates are plotted versus C + N content in Fig. 9 and versus yield strength in Fig. 10. As shown, the $K_{IC}(J)$ values decrease linearly with interstitial concentration and are inversely related to yield stress. Therefore nitrogen, which is a particularly effective strengthener, also has a strong influence on fracture toughness at cryogenic temperatures. An expression governing the relationship between fracture toughness and yield stress was derived from Fig. 10:

$$K_{IC}(J) = 500 - 0.3 \sigma_y$$

The data scatter of $K_{IC}(J)$ from this expression is $\pm 20 \text{ MPa}\cdot\text{m}^{1/2}$.

The present results compare well with existing data, some of which are also shown for comparison in Fig. 10. The AISI 304 N datum of Read and Reed [5] falls slightly below the present data, reflecting differences owing to metallurgy or measurement techniques. The Fe-Cr-Ni-Mn-N steels tend to have higher nitrogen contents, higher 4-K strength, and lower toughness compared with the Fe-Cr-Ni-N (AISI 304) steels [4]. Yet, the Fe-Cr-Ni-Mn-N steels in Fig. 10 appear to possess higher toughness than would be expected from the extrapolated trend for Fe-Cr-Ni-N steels. It is uncertain whether this is due to metallurgical effects or measurement bias, since the Fe-Cr-Ni-Mn-N data were obtained by other methods including the multispecimen technique, which have greater J_{IC} uncertainty.

The inverse relationship of σ_y and K_{IC} is well known for linear-elastic fracture toughness data. Now there is appreciable evidence that the inverse relationship holds in the elastic-plastic region as well.

Previous 4-K data for a variety of austenitic stainless steels and uncontrolled metallurgical conditions [5] indicated a linear trend of lesser slope than that shown in Fig. 10. It is advantageous that the present data derive from a controlled alloy series in which strength was varied by interstitial content while other compositional and processing variables were constant.

The approximate amount of α' (bcc) martensite formed during fatigue and fracture at 4 K is plotted as a function of interstitial content in Fig. 11. These results provide only an approximate indication of the extent of phase transformation, because the magnetometer measurements were taken directly from the compact specimen fracture surfaces, which are rough and unmachined. It is clear from Fig. 11 that some martensite forms in all of the steels during testing.

The quantity of martensite that forms would be expected to increase with the plastic-zone size. Referring to Fig. 11, more α' is detected in steel specimens of lower strength, higher toughness, and presumably, larger plastic-zone size. It is not clear at this time whether the formation of martensite plays a significant role in the fracture process of these metastable steels.

Stress-strain curves of various heats at 295, 195, 76 and 4 K are presented in Figures 12-17. At 4 K, all heats exhibited discontinuous yielding. Both the magnitude and the strain of initiation of the yield drops increased with increasing austenite stability and strength. The inflections of the curves at low temperatures result from the martensitic transformation. Notice in Figure 12 that the effect of C + N at 4 K is to increase the early deformation of austenite and that the ultimate tensile strength remains relatively unchanged.

SUMMARY AND CONCLUSIONS

1. New computer-assisted J-integral test methods and facilities have been developed and applied to cryogenic testing.
2. Fracture toughness measurements at 4 K are reported for Fe-18Cr-10Ni austenitic stainless steels having C+N contents ranging from 0.067 to 0.325 wt.%.
3. The fracture toughness at 4 K decreased with increasing C+N content, and the K_{IC} values estimated from J_{IC} (ranging from 123 to 336 $\text{MPa}\cdot\text{m}^{1/2}$) were inversely related to yield stress.

ACKNOWLEDGMENTS

This research was supported by the Naval Ship Research and Development Center (J. Gudas, coordinator) and by the Office of Fusion Energy, DoE (D. Beard, coordinator). T. Whipple, A. Castillo, D. Burkhalter, and D. Beekman assisted in performing the fracture tests.

REFERENCES

1. J. D. Landes and J. A. Begley, "Test Results from J-integral Studies: An Attempt to Establish a J_{IC} Testing Procedure," in Fracture Analysis, ASTM STP 560, American Society for Testing and Materials, Philadelphia, PA (1974), pp. 170-186.
2. G. A. Clarke, W. R. Andrews, P. C. Paris, and D. W. Schmidt, "Single Specimen Tests for J_{IC} Determination," in Mechanics of Crack Growth, ASTM STP 590, American Society for Testing and Materials, Philadelphia, PA (1976), pp. 27-42.
3. R. P. Reed, F. R. Fickett, M. B. Kasen, and H. I. McHenry, "Magnetic Fusion Energy Low Temperature Materials Program: A Survey," in Materials Studies for Magnetic Fusion Energy Applications at Low Temperatures-I, NBSIR 78-884, F. R. Fickett and R. P. Reed, Eds., National Bureau of Standards, Boulder, CO (1978), pp. 245-335.
4. D. T. Read and R. P. Reed, "Toughness, Fatigue Crack Growth, and Tensile Properties of Three Nitrogen-Strengthened Stainless Steels Cryogenic Temperatures," in Materials Studies for Magnetic Fusion Energy Applications at Low Temperatures-I, NBSIR 78-884, F. R. Fickett and R. P. Reed, Eds., National Bureau of Standards, Boulder, CO (1978), pp. 91-154.
5. D. T. Read and R. P. Reed, "Fracture and Strength Properties of Selected Austenitic Stainless Steels at Cryogenic Temperatures," in: Materials Studies for Magnetic Fusion Energy Applications at Low Temperatures-II, NBSIR 79-1609, F. R. Fickett and R. P. Reed, Eds., National Bureau of Standards, Boulder, CO (1979), pp. 81-122.

6. D. T. Read, R. P. Reed, and R. E. Schramm, "Low Temperature Deformation of Fe-18Cr-8Ni Steels," in: Materials Studies for Magnetic Fusion Energy Applications at Low Temperatures-II, NBSIR 79-1609, F. R. Fickett and R. P. Reed, Eds., National Bureau of Standards, Boulder, CO (June 1979), pp. 151-172.
7. D. T. Read and R. P. Reed, "Heating and Strain Rate Effects in AISI 304 L Stainless Steel at 4 K," in: Materials Studies for Magnetic Fusion Energy Applications at Low Temperatures-II, NBSIR 79-1609, F. R. Fickett and R. P. Reed, Eds., National Bureau of Standards, Boulder, CO (1979), pp. 125-147.
- 8.. R. L. Tobler and R. P. Reed, "Tensile and Fracture Behavior of Nitrogen-Strengthened, Chromium-Nickel-Manganese Stainless Steel at Cryogenic Temperatures," in Elastic-Plastic Fracture, ASTM STP 668, American Society for Testing and Materials, Philadelphia, PA (1979), pp. 537-552.
9. P. P. Dessau, "LN₂ and LH₂ Fracture Toughness of Armco Alloy 22-13-5," Report No. TID/SNA-2083, Aerojet Nuclear Systems Company, Sacramento, CA (1971).
10. D. C. Larbalestier and D. Evans, "High Strength Austenitic Stainless Steels for Cryogenic Use," in Proceedings of Sixth International Cryogenic Engineering Conference, IPC Science and Technology Press Ltd., Guildford, Surrey, England (1976), pp. 345-347.
11. R. B. Gunia and G. R. Woodrow, "Nitrogen Improves Engineering Properties of Chromium-Nickel Stainless Steels," J. Mater., JMLSA, 5 (1970), pp. 413-430.
12. R. Voyer and L. Weil, "Tensile and Creep Properties of a High Nitrogen Content 18/10 (AISI 304L) Stainless Steel at Cryogenic Temperatures," in Adv. Cryo. Eng. 11, K. D. Timmerhaus, Ed., Plenum, New York (1965), pp. 447-452.

13. L.-A. Norström, "The Influence of Nitrogen and Grain Size on Yield Strength in Type AISI 316L Austenitic Stainless Steel," Met. Sci., 11 (1977), pp. 208-212.
14. M. K. Booker and V. K. Sikka, "Effects of Composition Variables on the Tensile Properties of Type 304 Stainless Steel," ORNL-5353, Oak Ridge National Laboratory, Oak Ridge, TN (1977), pp. 1-38.
15. P. Soo and W. H. Horton, "The Effect of Carbon and Nitrogen on the Short-Term Tensile Behavior of Types 304 and 316 Stainless Steels," Ward NA 3045-2, Westinghouse Electric Corporation, Madison, PA (1973) pp. 1-48.
16. K. J. Irvine, D. T. Lewellyn, and F. B. Pickering, "High Strength Austenitic Stainless Steels," J. Iron Steel Inst., 199 (1961), pp. 153-175.
17. K. J. Irvine, T. Gladman, and F. B. Pickering, "The Strength of Austenitic Stainless Steels," J. Iron Steel Inst., 207 (1969), pp. 1017-1028.
18. C. E. Spaeder, Jr. and W. F. Domis, "Cryogenic and Elevated-Temperature Mechanical Properties of a High-Nitrogen Type 304 Stainless Steel," Report No. 44012-062-2, United States Steel Corporation, Pittsburgh, PA (1969).
19. C. W. Fowlkes and R. L. Tobler, "Fracture Testing and Results for a Ti-6Al-4V Alloy at Liquid Helium Temperature," Eng. Fract. Mech., 8 (1976), pp. 487-500.
20. J. A. Joyce and J. P. Gudas, "Computer Interactive J_{IC} Testing of Navy Alloys," in Elastic-Plastic Fracture, ASTM STP 668, American Society for Testing and Materials, Philadelphia, PA (1979), pp. 451-468.

21. "Standard Method of Test for Plane Strain Fracture Toughness of Metallic Materials (Designation E399-74)," 1974 Annual Book of ASTM Standards, Part 10, American Society for Testing and Materials, Philadelphia, PA (1974), pp. 432-451.
22. J. G. Merkle and H. T. Corten, "A J-Integral Analysis for the Compact Specimen, Considering Axial Force as Well as Bending Effects," J. Pressure Vessel Tech., Trans. ASME, 6 (1974), pp. 1-7.
23. R. P. Reed and C. J. Guntner, "Stress-Induced Martensitic Transformations in 18Cr-8Ni Steel," Trans. Metall. Soc. AIME 230 (1964), pp. 1713-1720.
24. R. P. Reed and R. P. Mikesell, "The Stability of Austenitic Stainless Steels at Low Temperatures as Determined by Magnetic Measurements," in Adv. Cryo. Eng., 4, K. D. Timmerhaus, Ed., Plenum, New York (1960), pp. 84-100.
25. H. M. Ledbetter, N. V. Frederick, and M. W. Austin, "Elastic-Constant Variability in Stainless Steel 304," J. Appl. Phys., 51 (1980), pp. 305-309.

LIST OF TABLES

Table No.

- I. Stainless steel compositions (wt.%), hardnesses, and grain sizes.
- II. Yield strength and J-integral toughness results for Fe-18Cr-10Ni steels at 4 K.

Table I. Stainless steel compositions (wt.%), hardnesses, and grain sizes.

Heat No.	Fe	Cr	Ni	Mn	P	S	Si	Mo	Cu	C	N	C+N	Hardness, Rockwell 8	Average Grain Size, μm
1 bal.	18.3	10.1	1.57	0.021	0.019	0.50	0.20	0.210	0.028	0.039	0.067	74	85	
2 bal.	"	"	"	"	"	"	"	"	0.058	"	0.097	76	78	
3 bal.	"	"	"	"	"	"	"	"	0.089	"	0.128	79	90	
4 bal.	18.0	9.91	1.50	0.022	0.017	0.57	0.205	0.197	0.037	0.120	0.157	79	105	
5 bal.	"	"	"	"	"	"	"	"	0.067	"	0.187	82	85	
6 bal.	"	"	"	"	"	"	"	"	0.094	"	0.214	82	78	
7 bal.	20.3	9.97	1.42	0.024	0.016	0.55	0.195	0.200	0.030	0.240	0.270	89	98	
8 bal.	"	"	"	"	"	"	"	"	0.057	"	0.297	89	82	
9 bal.	"	"	"	"	"	"	"	"	0.085	"	0.325	91	90	

Table II. Yield strength and J-integral toughness results Fe-18Cr-10Ni steels at 4 K.

Specimen	C+N Content (wt.%)	Yield Strength, σ_y (MPa) ^a	Flow Strength, σ_f (MPa)	$\frac{25 J_{IC}}{\sigma_f}$	J_{IC}	$K_{IC}(J)^*$
				(mm)	(kJ/m ²) ^b	(MPa·m ^{1/2}) ^c
1	0.067	329	892	NA	NA	NA
2	0.097	445	996	NA	NA	NA
3	0.128	530	1029	12.2	499	337
4	0.157	745	1158	6.7	312	266
5	0.187	876	1288	4.5	230	230
6-A	0.214	896	1264	4.3	218	222
6-B	0.214	896	1264	5.3	272	249
7	0.270	1186	1411	1.2	67	124
8-A	0.297	1178	1456	1.5	88	141
8-B	0.297	1178	1456	1.3	78	133
9	0.325	1286	1496	1.1	63	124

*Calculated from the expression $K_{IC}^2 = J_{IC} \cdot E / (1 - \nu^2)$, assuming $E = 206.8$ GPa and $\nu = 0.3$ at $T = 4$ K.

^aTo convert from MPa to ksi, divide by 6.895.

^bTo convert from kJ/m² to in-lb/in², multiply by 5.709.

^cTo convert from MPa· \sqrt{m} to ksi \sqrt{in} , divide by 1.099.

LIST OF FIGURES

- Figure 1. Typical J-integral-versus-crack extension curve.
- Figure 2. Typical load-versus-specimen displacement curve, indicating J-integral area for specimen at point a.
- Figure 3. Calibration curve of load change versus displacement change.
- Figure 4. Flow chart of recording and analyses computer system for fracture testing.
- Figure 5. Specimen geometries used for fracture mechanics tests.
- Figure 6. Typical J-resistance curve for an austenitic stainless steel tested at 4 K.
- Figure 7. Scanning electron microscopy photograph of Fe-18Cr-10Ni; C+N = 0.325 wt.%. The 4-K fracture surface is shown at 200 X and 1000 X.
- Figure 8. Scanning electron microscopy photograph of Fe-18Cr-10Ni; C+N = 0.067 wt.%. The 4-K fracture surface is shown at 200 X and 1000 X.
- Figure 9. Dependence of K_{IC} on C+N content at 4 K.
- Figure 10. Inverse relationship between fracture toughness and yield stress for austenitic stainless steels at 4 K.
- Figure 11. Relative amounts of α' (bcc) martensite formed during tests of compact specimens at 4 K. (Arbitrary Units)
- Figure 12. Engineering stress-strain curves for Fe-18Cr-10Ni steel heat no. 1, representative of low interstitial C+N contents.

- Figure 13. Engineering stress-strain curves for Fe-18Cr-10Ni steel heat no. 4, representative of medium interstitial C+N contents.
- Figure 14. Engineering stress-strain curves for Fe-18Cr-10Ni steel heat no. 8, representative of high interstitial C+N contents.
- Figure 15. True stress-strain curves for Fe-19Cr-10Ni steel heat no. 1 (serrations at 4K are not shown).
- Figure 16. True stress strain curves for Fe-18Cr-10Ni steel heat no. 4 (serrations at 4K are not shown).
- Figure 17. True stress-strain curves for Fe-18Cr-10Ni steel heat no. 8 (serrations at 4K are not shown).

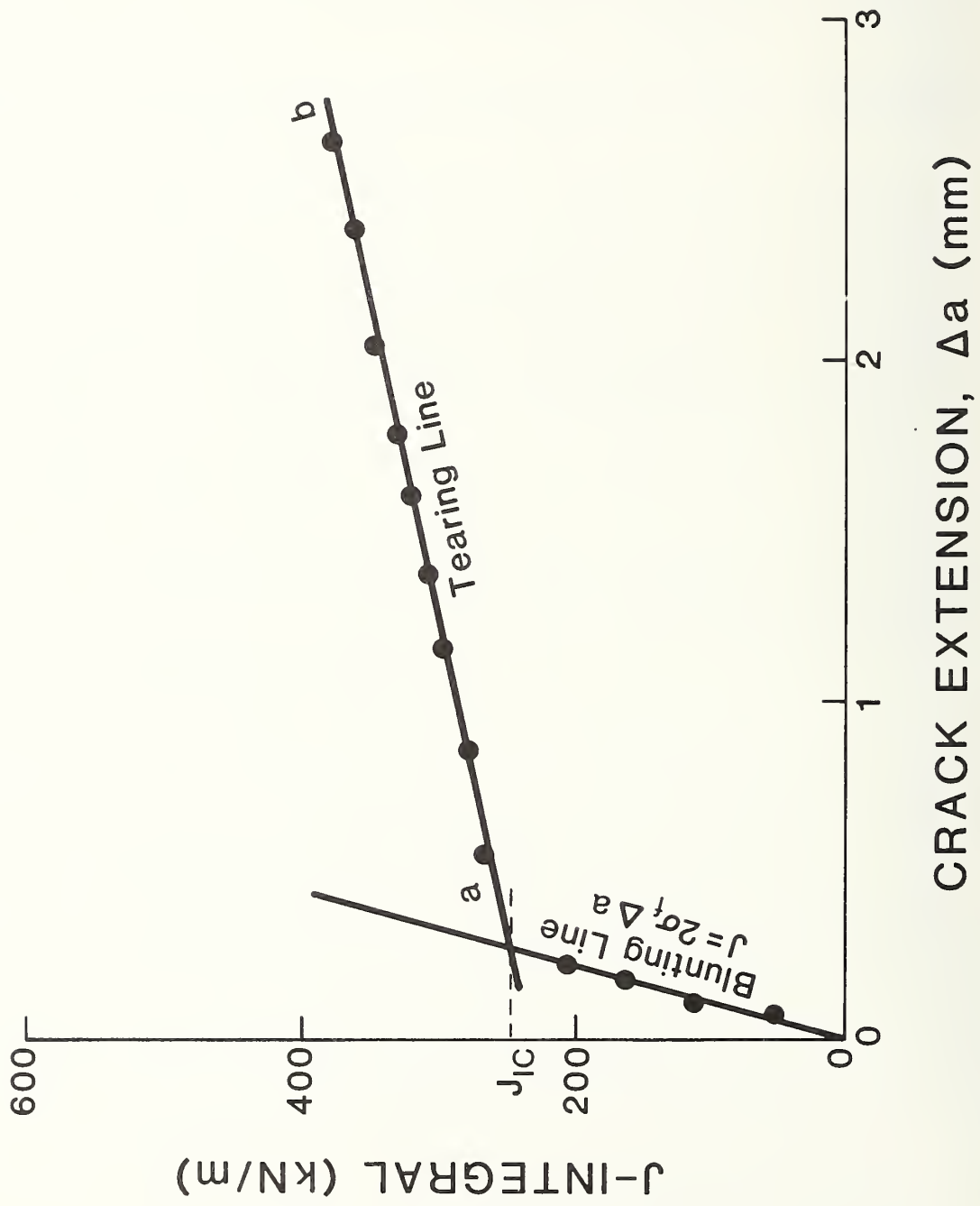
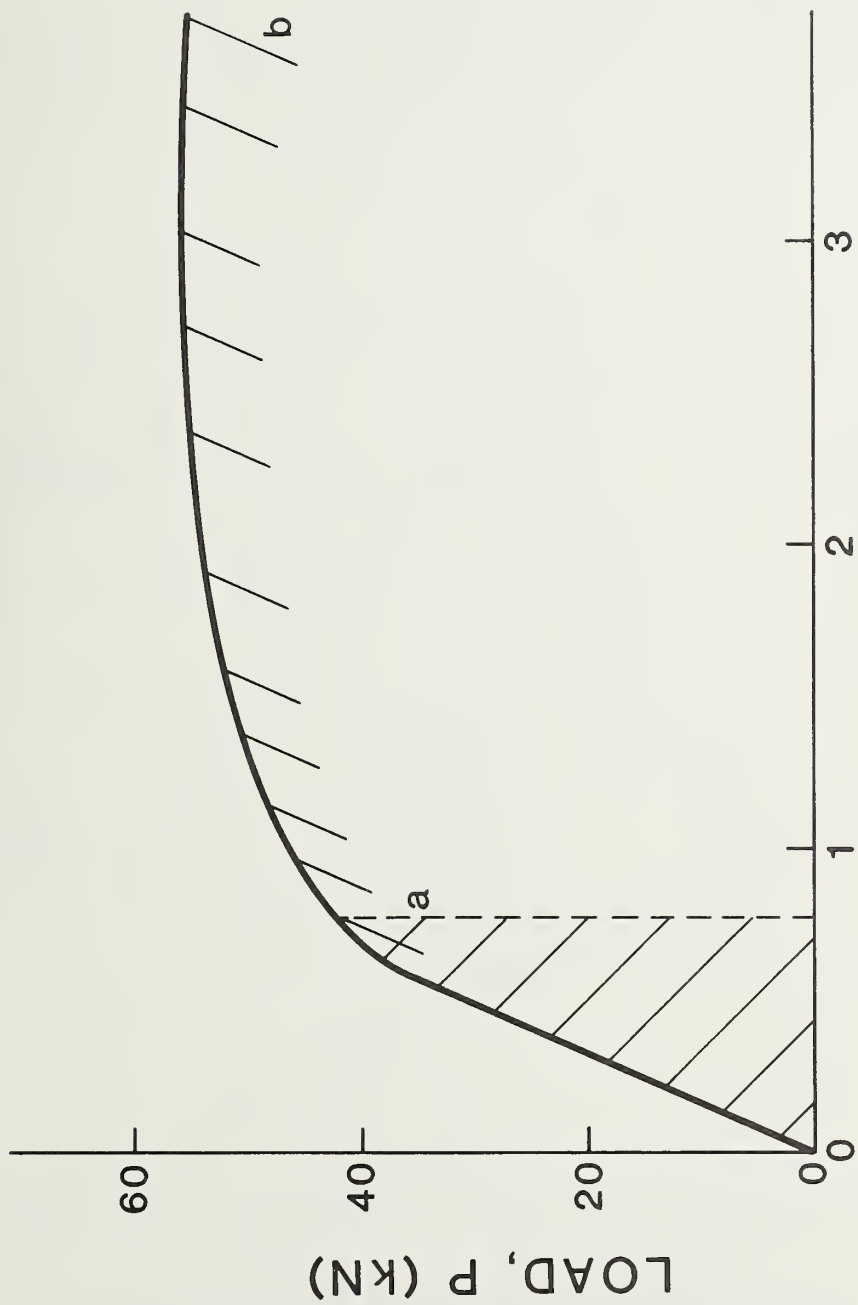


Figure 1. Typical J-integral-versus-crack extension curve.



DISPLACEMENT, δ (mm)

Figure 2. Typical load-versus-specimen displacement curve, indicating J-integral area for specimen at point a.



Figure 3. Calibration curve of load change versus displacement change.

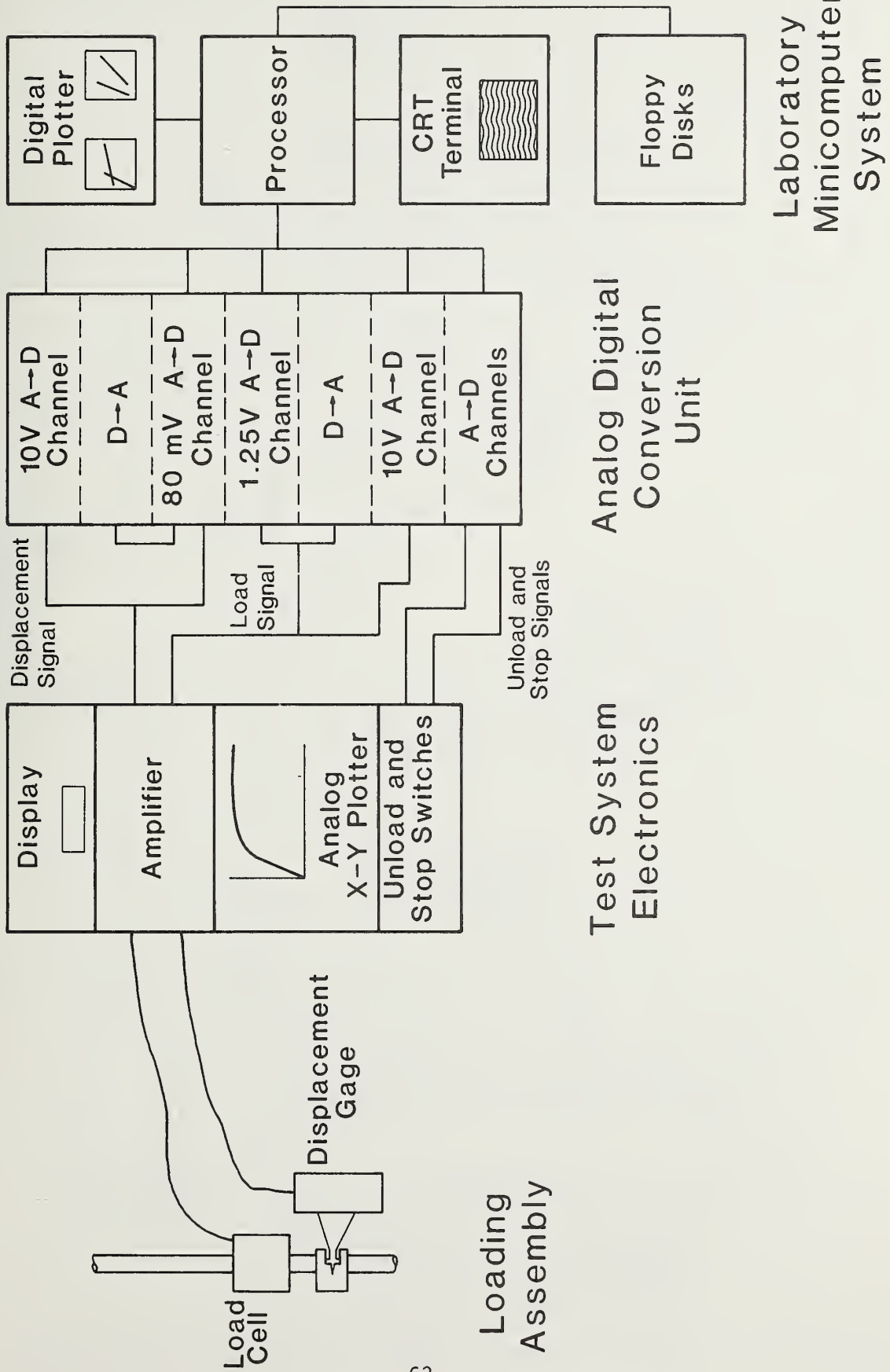
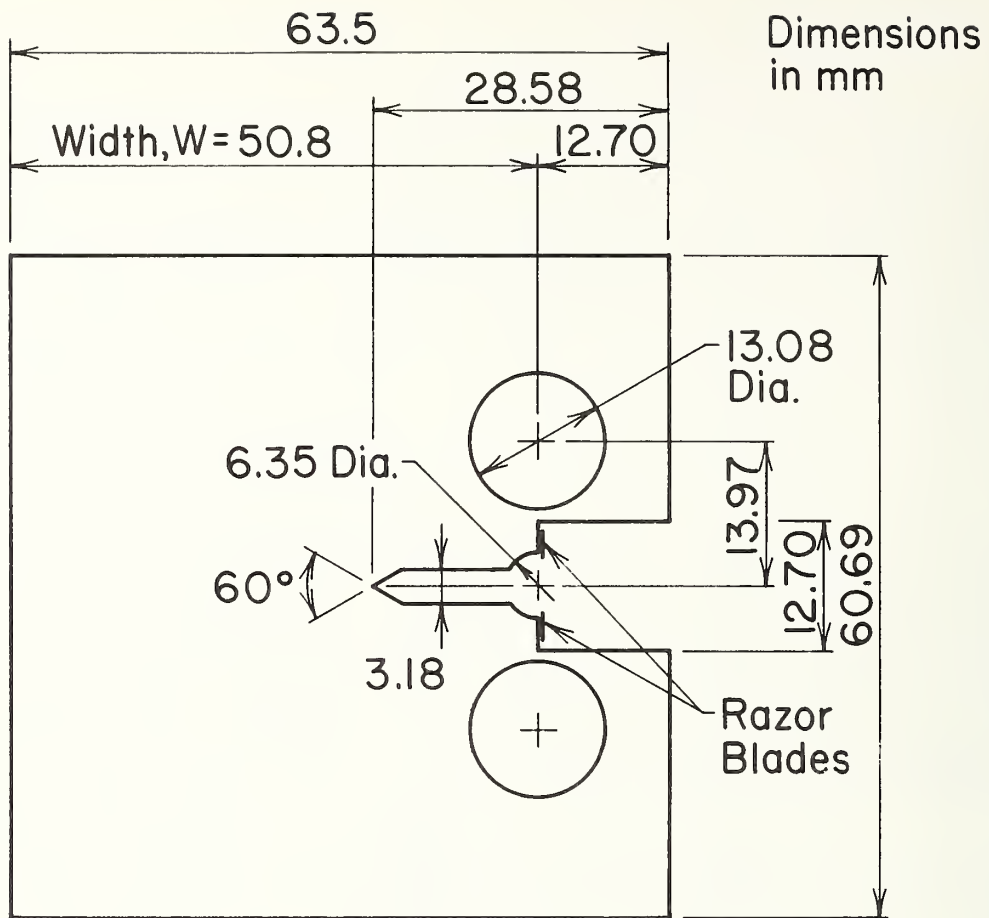
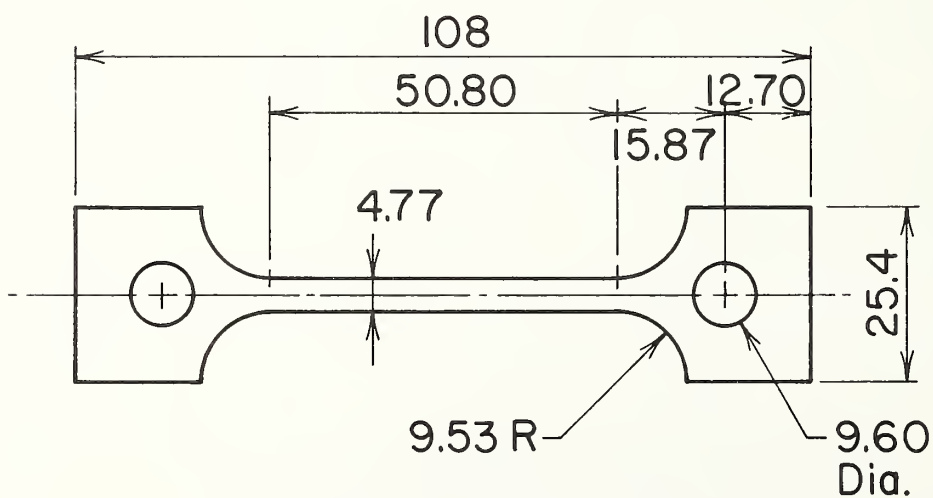


Figure 4. Flow chart of recording and analyses computer system for fracture testing.



COMPACT SPECIMEN
Thickness = 24.5 mm



TENSILE SPECIMEN
Thickness = 2.54 mm

Figure 5. Specimen geometries used for fracture mechanics tests.

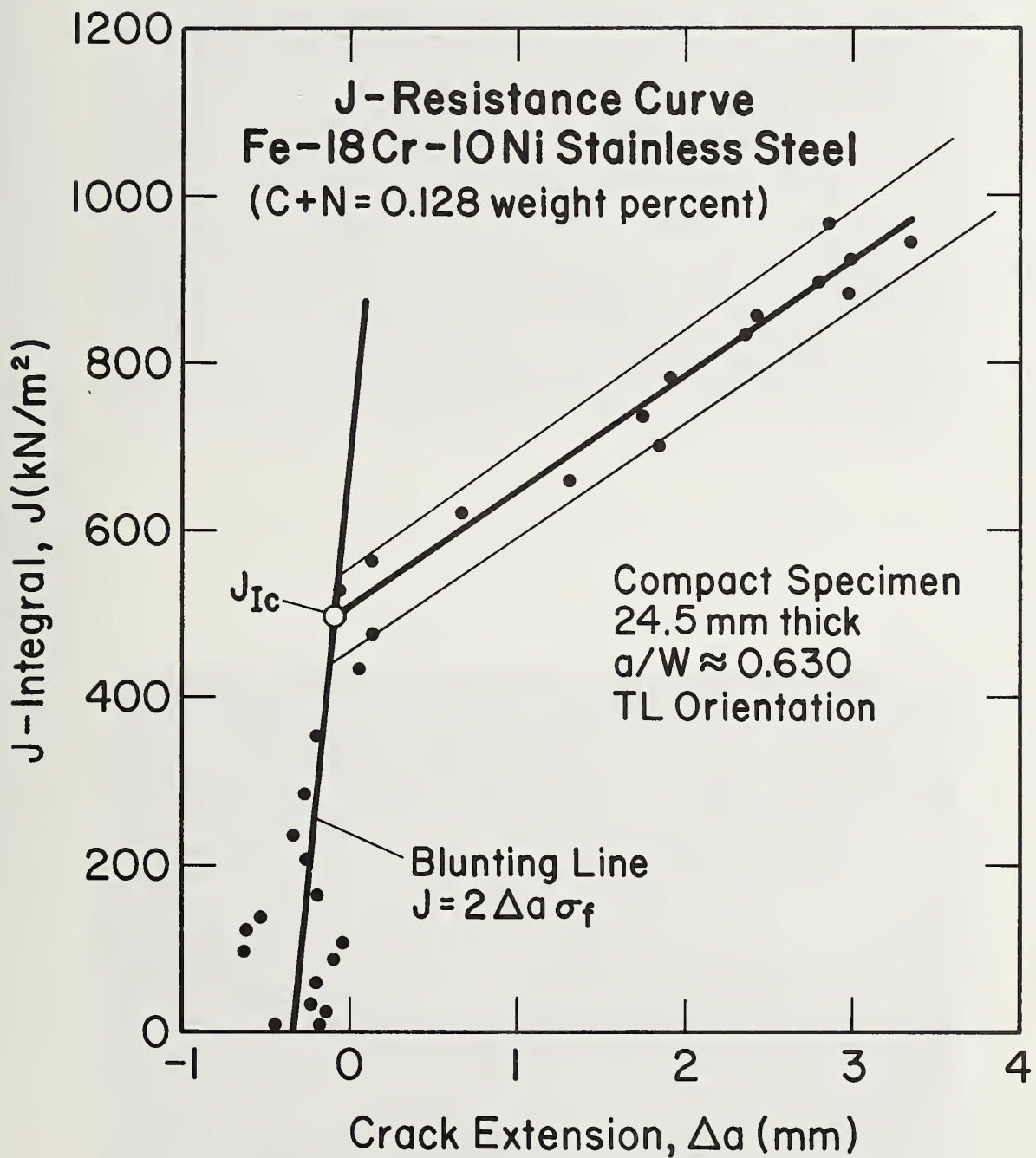


Figure 6. Typical J-resistance curve for an austenitic stainless steel tested at 4 K.



Figure 7. Scanning electron microscopy photograph of Fe-18Cr-10Ni; C+N = 0.325 wt.%. The 4-K fracture surface is shown at 200 X and 1000 X.

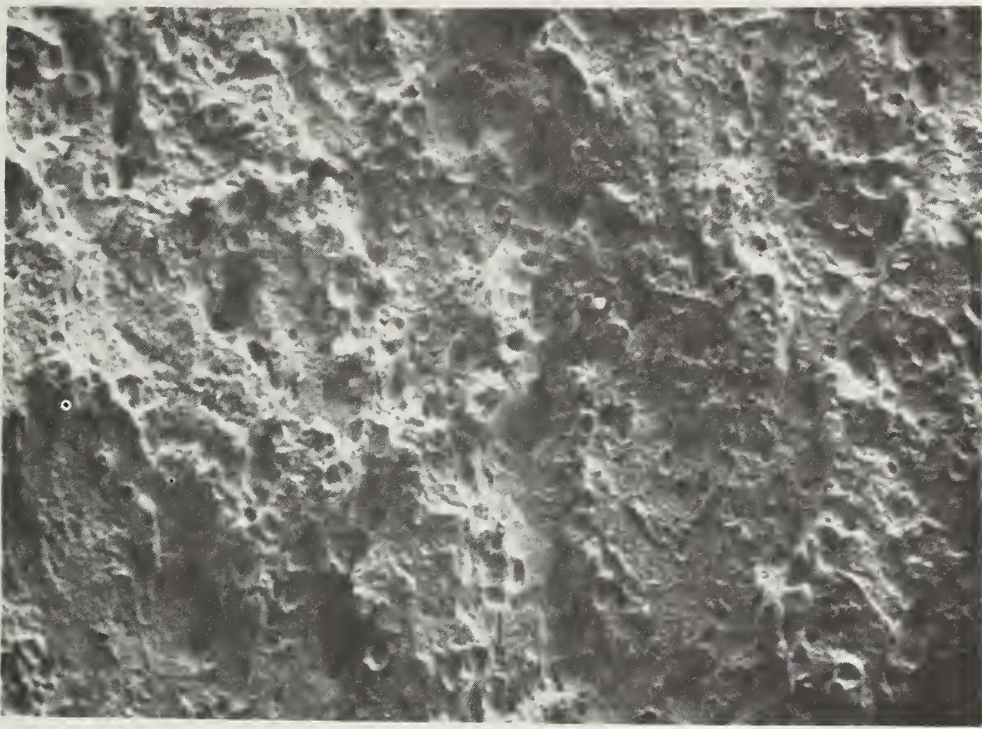


Figure 8. Scanning electron microscopy photograph of Fe-18Cr-10Ni; C+N = 0.067 wt.%. The 4-K fracture surface is shown at 200 X and 1000 X.

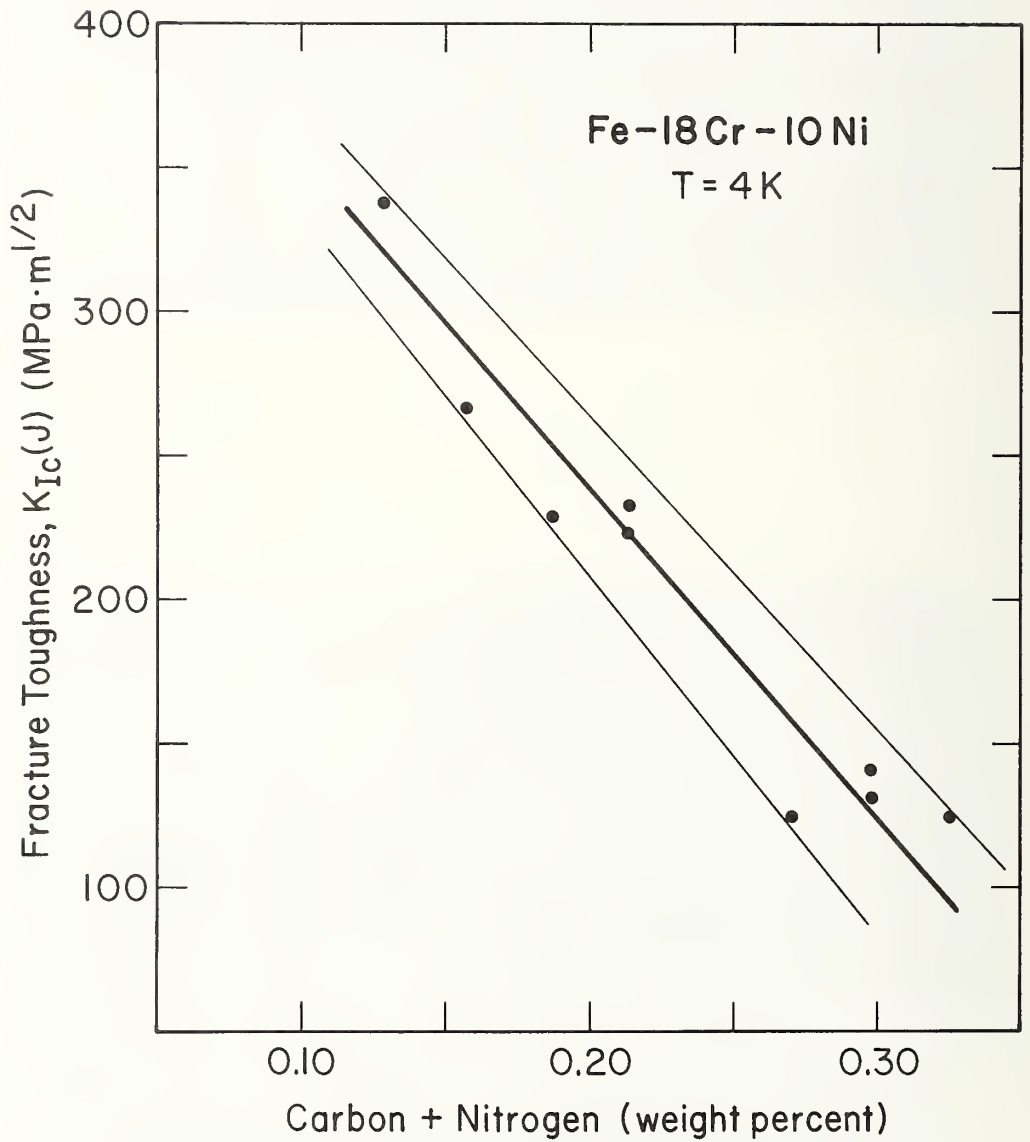


Figure 9. Dependence of K_{Ic} on C+N content at 4 K.

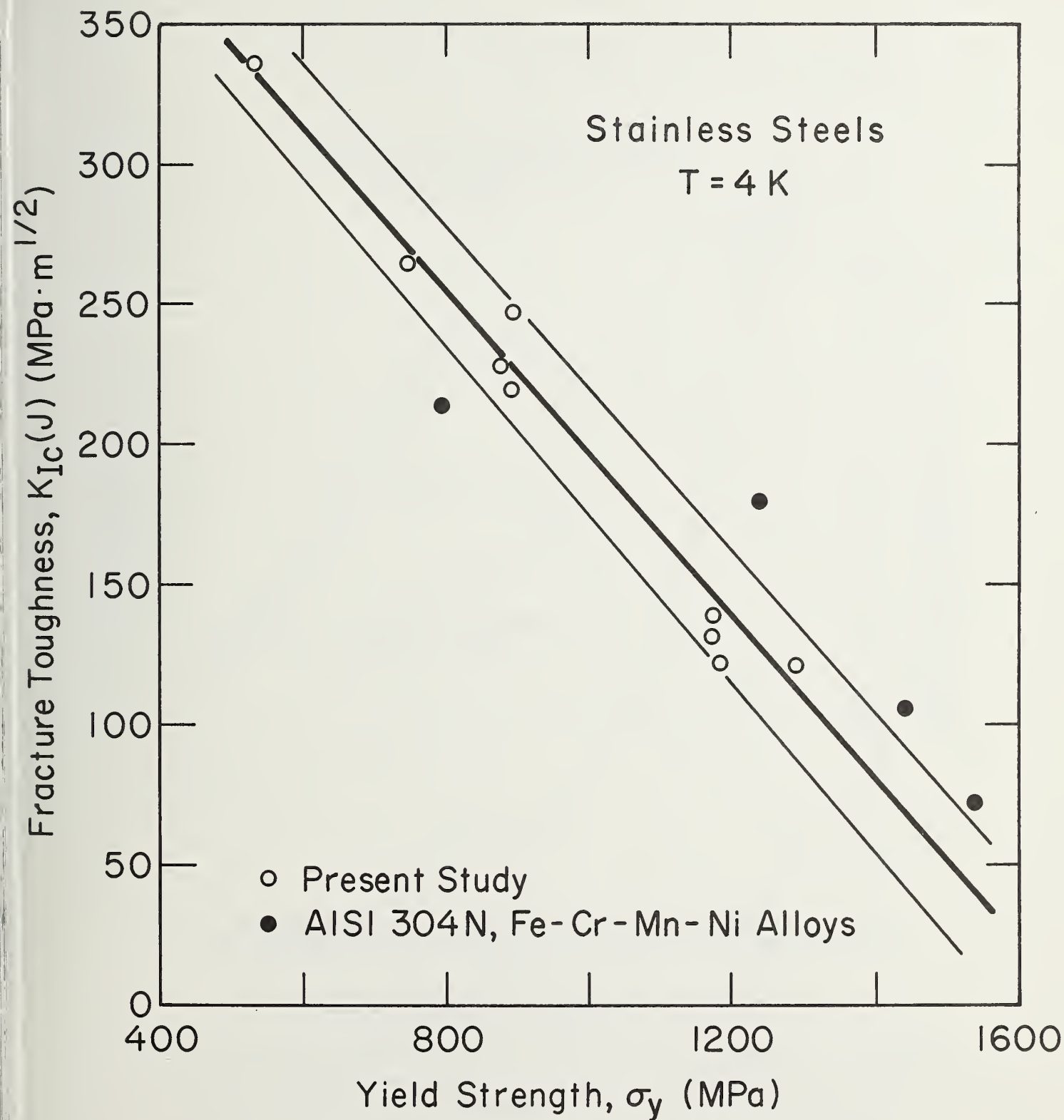


Figure 10. Inverse relationship between fracture toughness and yield stress for austenitic stainless steels at 4 K.

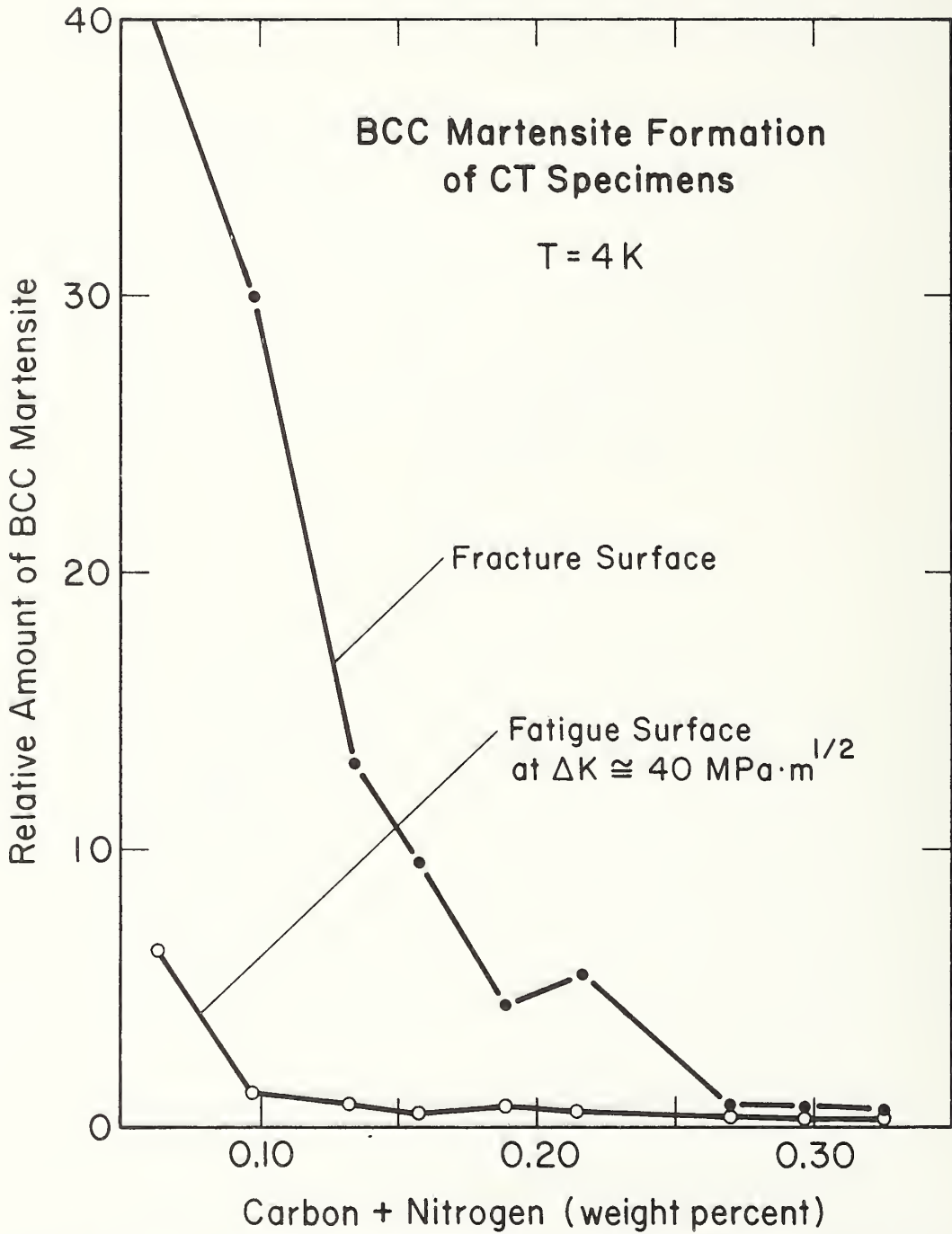


Figure 11. Relative amounts of α' (bcc) martensite formed during tests of compact specimens at 4 K. (Arbitrary Units.)

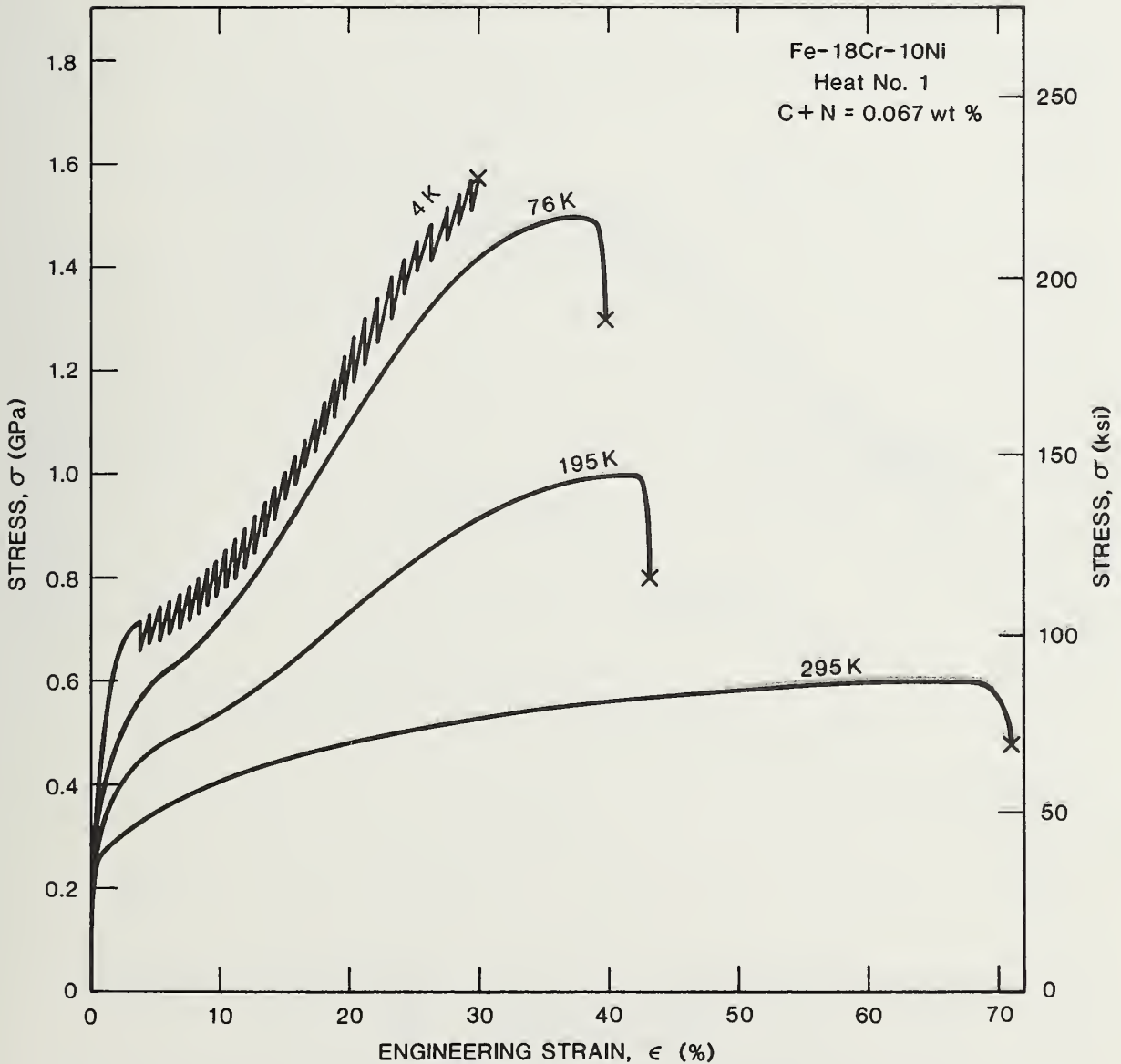


Figure 12. Engineering stress-strain curves for Fe-18Cr-10Ni steel heat no. 1, representative of low interstitial C+N contents.

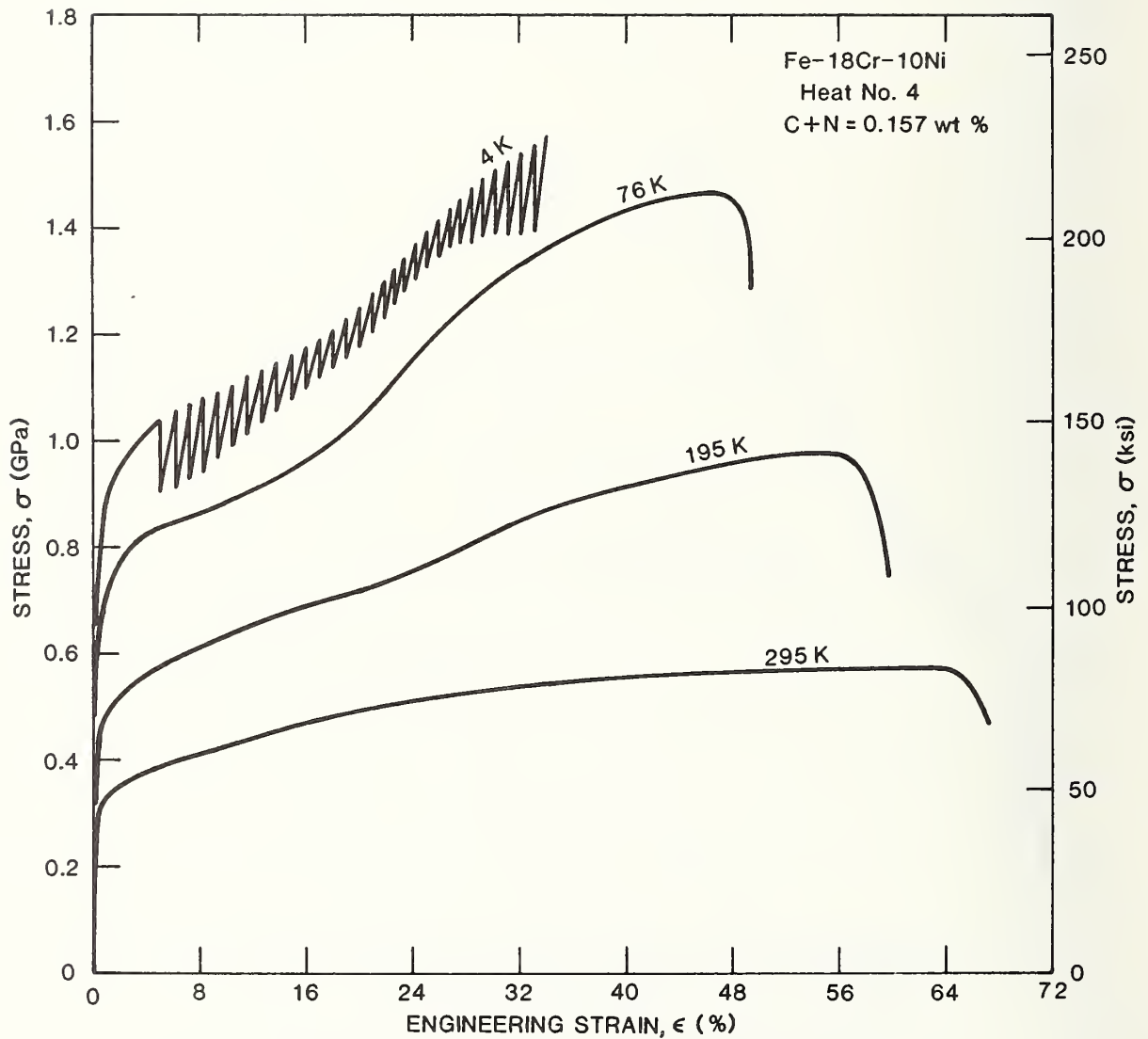


Figure 13. Engineering stress-strain curves for Fe-18Cr-10Ni steel heat no. 4, representative of medium interstitial C+N contents.

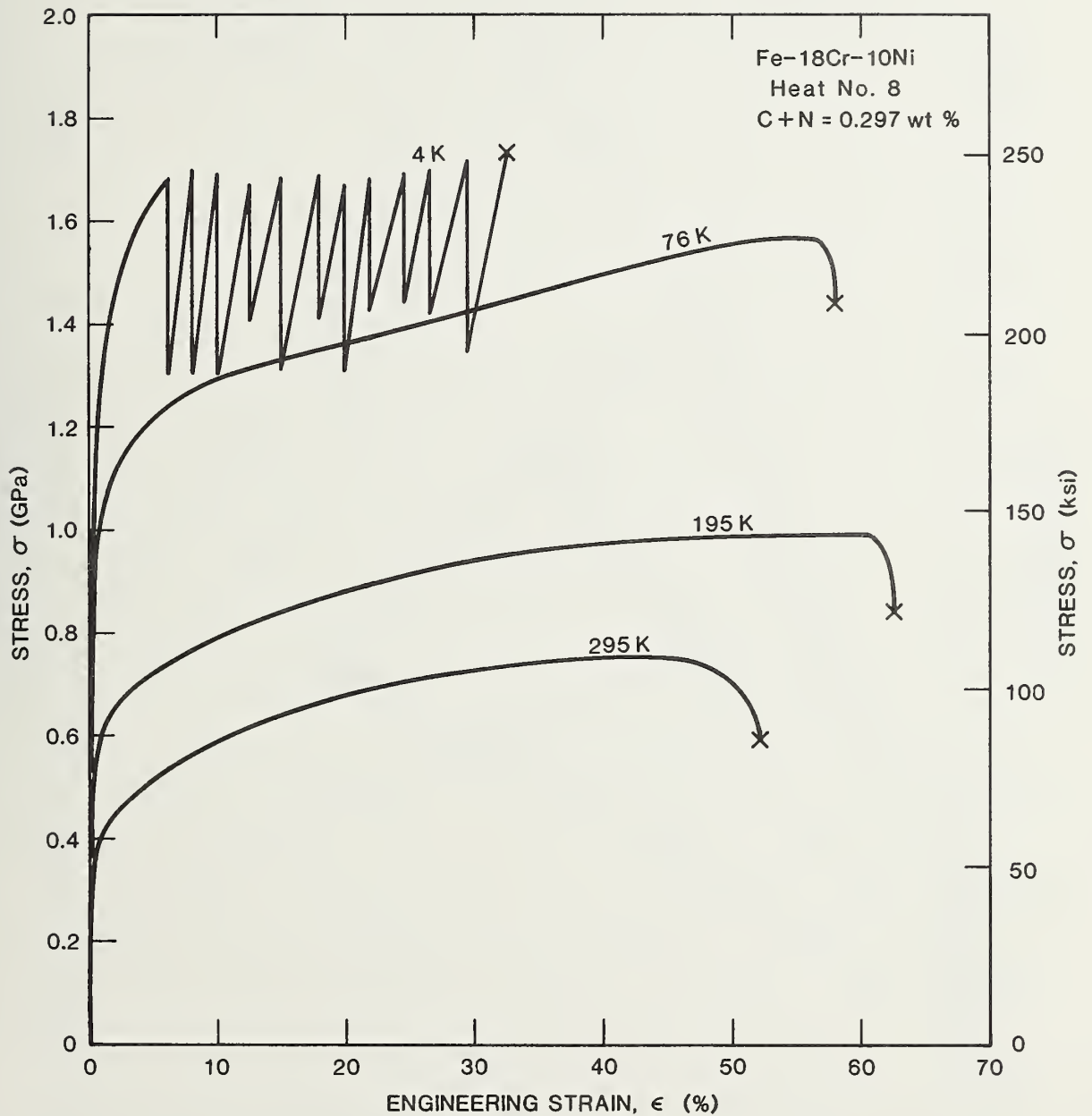


Figure 14. Engineering stress-strain curves for Fe-18Cr-10Ni steel heat no. 8, representative of high interstitial C+N contents.

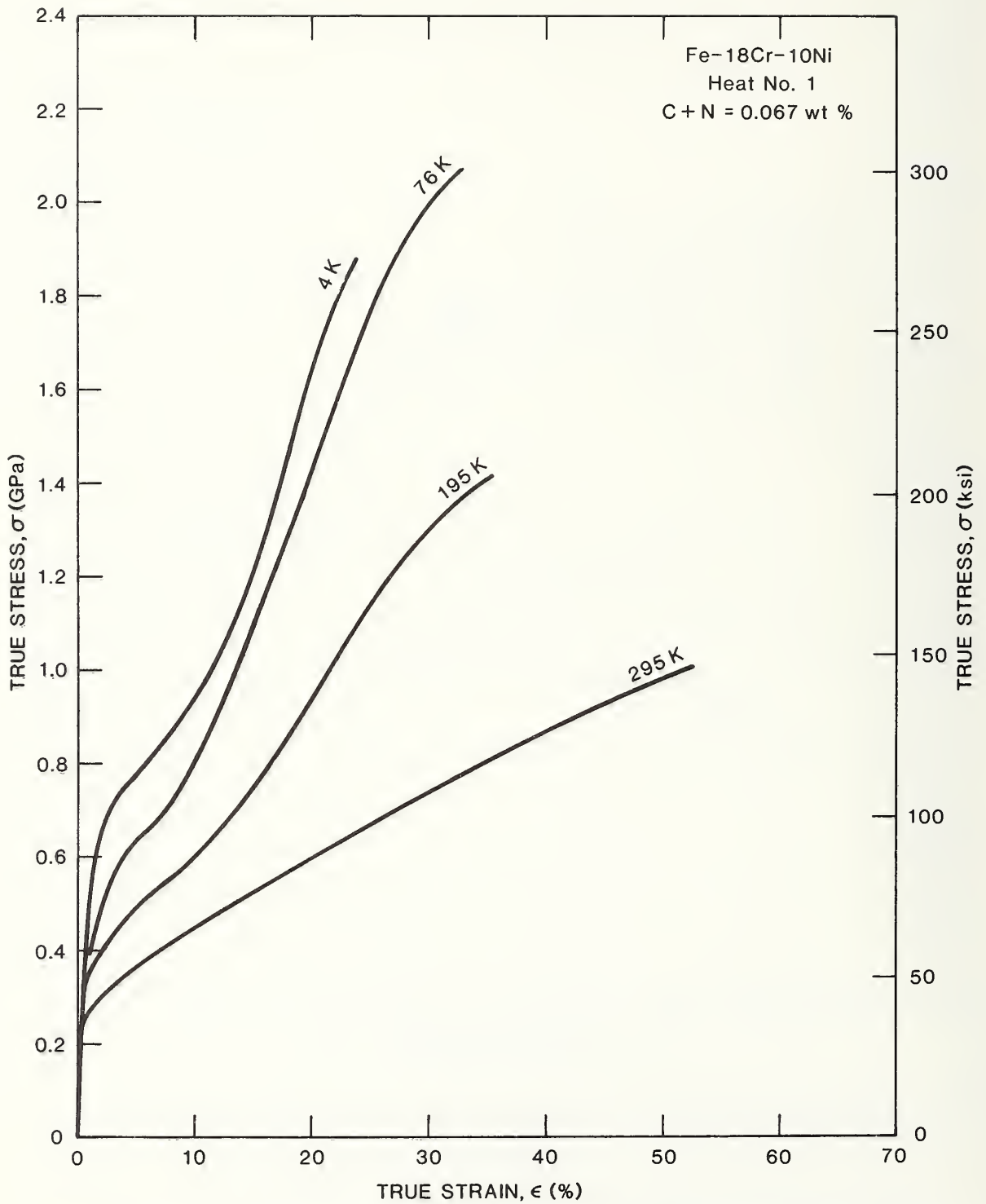


Figure 15. True stress-strain curves for Fe-19Cr-10Ni steel heat no. 1 (serrations at 4K are not shown).

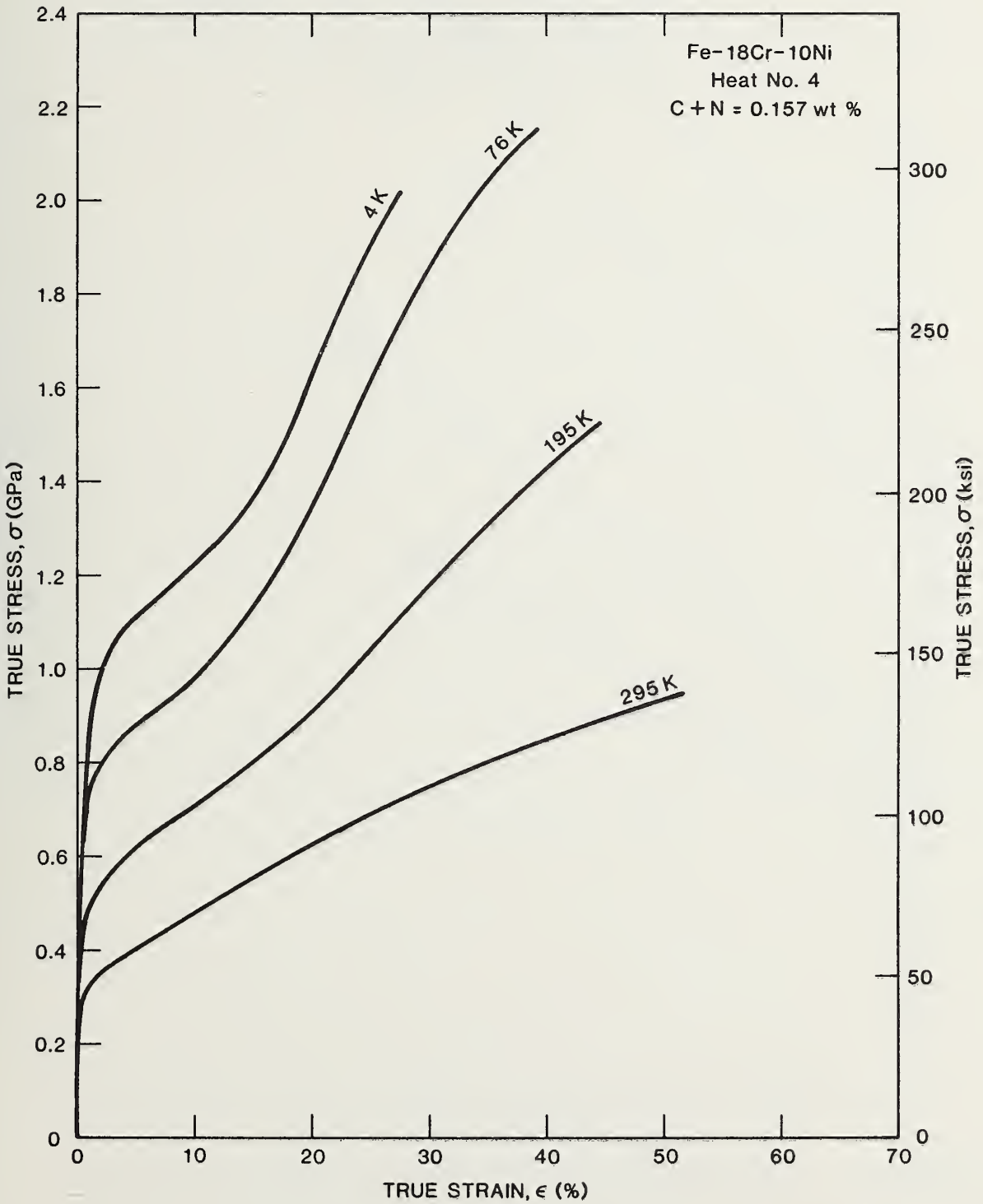


Figure 16. True stress strain curves for Fe-18Cr-10Ni steel heat no. 4 (serrations at 4K are not shown).

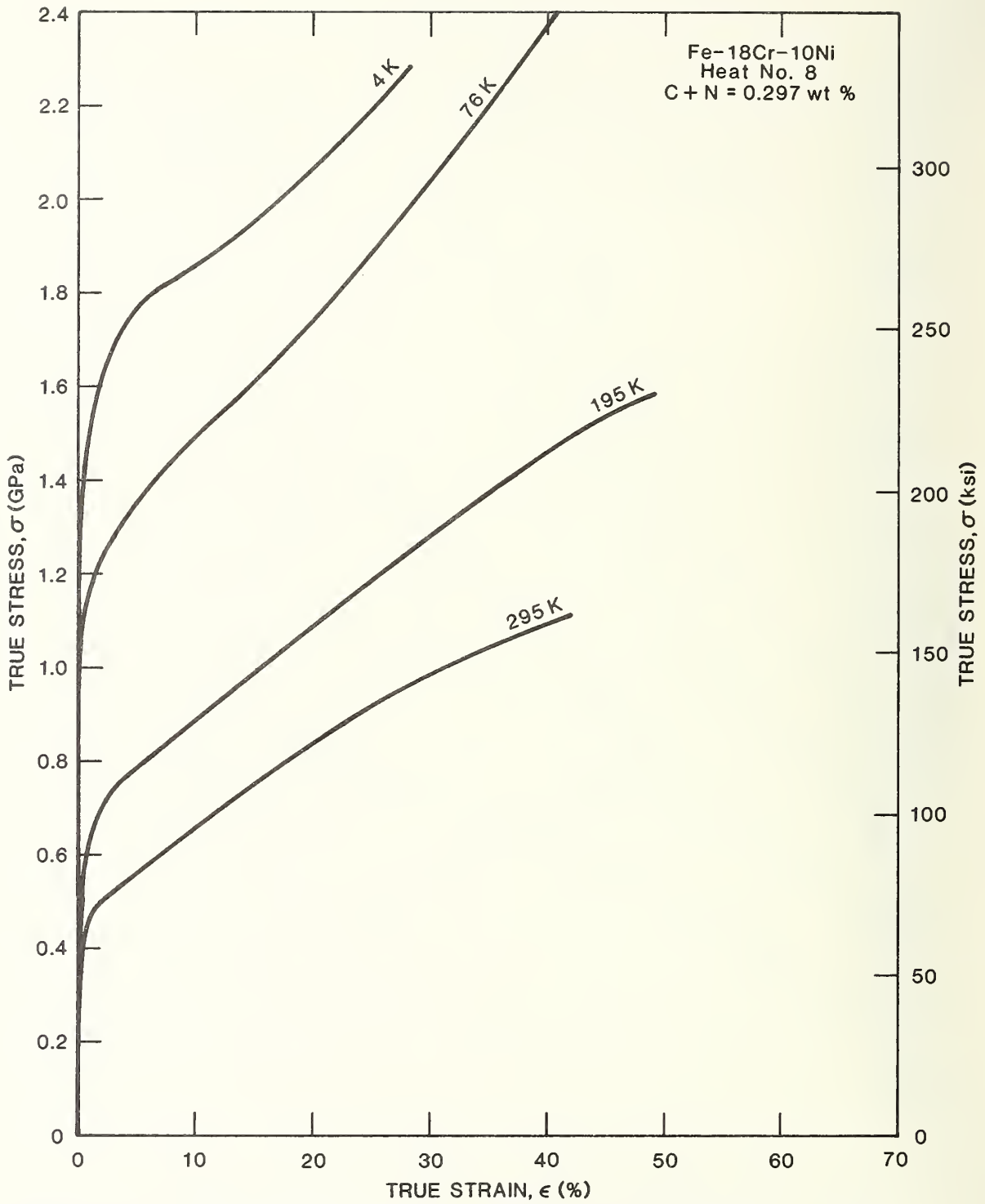


Figure 17. True stress-strain curves for Fe-18Cr-10Ni steel heat no. 8 (serrations at 4K are not shown).

TENSILE AND FRACTURE PROPERTIES OF MANGANESE-MODIFIED
Fe-18Cr-8Ni TYPE AUSTENITIC STAINLESS STEELS

R. L. Tobler and R. P. Reed
Fracture and Deformation Division
National Bureau of Standards
Boulder, Colorado

ABSTRACT

A series of ten low-carbon AISI-304-type austenitic stainless steels having 1 to 6% Mn (by weight) and 0.1 to 0.2% N were produced and tested to determine the effect of these elements on properties at 4 K. Tensile tests (at 295, 76, and 4 K) and J-integral fracture toughness tests (at 4 K) were conducted on developmental steels containing 18.25 to 19.50% Cr, 7.9 to 8.75% Ni, and 0.02 to 0.03% C. All steels were hot-rolled at 1450 K (2150° F) from ingots to 25.4-mm (1-inch) plates. The 4-K yield strengths ranged from 620 MPa (90 ksi) to 1068 MPa (155 ksi), increasing strongly with nitrogen content. Unacceptably low toughness was observed in the low manganese compositions, but the fracture toughnesses of alloys containing 6% Mn were equivalent to those of conventional AISI 304 stainless steels.

INTRODUCTION

The AISI-300 series stainless steels are austenitic Fe-Cr-Ni alloys offering relatively low strength but excellent cryogenic ductility and toughness. Recently, nitrogen-strengthened grades, such as AISI 304 N or AISI 304 LN, have attracted attention as possible substitutes for applications demanding higher strength. Nitrogen is a relatively inexpensive strengthener, and it stabilizes the austenitic structure with respect to martensitic phase transformation. A disadvantage of the nitrogenated grades is that they are more difficult to produce and fabricate. To overcome this disadvantage, manganese additions have been recommended. The potential advantages of manganese-modified type AISI 304 LN steels are (1) consistent fabricability, (2) consistent weldability, and (3) reliable supply in all product forms [1]. It was the purpose of this study to investigate the effects of manganese on the 4-K mechanical properties of nitrogenated AISI 304 L type alloys. Therefore, a series of steels containing 1 to 6% Mn and 0.1 to 0.2% N were prepared, tested, and compared with previous results for Fe-18Cr-10Ni stainless steels [2,3].

MATERIALS

Ten stainless steel plates were obtained from a commercial steel manufacturer. These steels had chemical compositions as listed in table 1 and grain size and hardness values as listed in table 2.

All of these steels were produced from 225 N ingots (12.7 x 12.7 x 17.8 cm) which were hot-rolled at 1450 K (2150° F) to plates approximately 25-mm thick. The plates were annealed at 1340 K (1950° F) for one-half hour, then water quenched and acid pickled. After trimming, the average plate size was 25.4 x 140 x 400 mm.

Figure 1 shows one example of as-received plate. These steels were free from corner checks (edge tears), which sometimes may occur in nitrogen-alloyed austenitic stainless steels. Figure 2 shows an example of corner checks as they appeared in an Fe-18Cr-10Ni-0.03C-0.024N-1.5Mn stainless steel of a previous study [2]. In the previous study a series of nine Fe-18Cr-10Ni-1.5Mn stainless steels were hot-rolled at 1560 K (2350° F) from ingots to 25.4-mm-thick plates, and corner checks were observed in steels having carbon plus nitrogen (C + N) contents of 0.270 wt.% or greater.

EXPERIMENTAL PROCEDURE

Tensile

Tensile tests were conducted using the cryostat described by Reed [4]. Low temperatures were achieved by immersing the specimen and cryostat in liquid nitrogen at 76 K and liquid helium at 4 K. The specimen geometry is shown in fig. 3. The specimens were machined in the transverse orientation. The load-vs-deflection curves were recorded using the outputs from a commercial load cell and strain-gauge extensometer. The specimen yield stress at 0.2% plastic strain, ultimate tensile stress, elongation, and reduction of area were measured. Estimated strain sensitivity is 50 μm at 4 K, and low-temperature accuracy is estimated to be $\pm 500 \mu\text{m}$ at 4 K.

Fracture Toughness

J-integral tests were necessary because austenitic stainless steels typically fail in a ductile (elastic-plastic) mode with gradual crack extension at 4 K. Therefore, single-specimen J-integral tests were used to measure fracture toughness. The technique incorporates a computer to enable digital data acquisition and J-resistance curve plotting during

the tests, as described previously [2,3]. The fracture toughness parameter measured in these tests is J_{IC} , the critical value of the J-integral at the beginning of crack extension, which is a material property enabling quantitative comparisons of ductile materials. J_{IC} also enables an estimate to be made of K_{IC} , which is the plane-strain fracture toughness as conventionally measured by the ASTM E 399 test method.

The compact fracture toughness specimens shown in fig. 3 had a 24.6-mm thickness (B) and 50.8-mm width (W). The notch was machined in the TL orientation, as defined in ASTM E-399-78a [5].

The fracture specimens were fatigue cracked at 76 K to a crack length, a , between 27.25 and 31.44 mm ($\frac{a}{W} \approx 0.535$ to 0.620). The maximum load used in fatigue precracking was 22 kN. The specimens were then loaded in displacement control. As the load increased, partial unloadings were performed periodically. The load reduction during unloading was typically ten percent of the maximum load. Using the crack-length-vs-compliance correlation, the crack length at each unloading was inferred and used to obtain the crack extension increment (Δa) from the difference of the initial precrack length. The J value at each unloading point was calculated using the expression: $J = \frac{\lambda A}{Bb}$ where λ is the Merkle-Corten factor, A is the area under the load-vs-deflection curve at the unloading point, and b is the specimen ligament ($b = W - a$).

J-resistance curves consisting of many sets of J and Δa points were generated. The J_{IC} value for each steel was taken at the intersection of the J-resistance curve with the blunting line. The blunting line is given by $J = 2\sigma_f \Delta a$ where σ_f is the flow stress, which is equal to the

average of the yield and ultimate tensile strengths. It was discovered that the final crack extensions, Δa , measured on the fracture specimens, were 20 to 200% greater than the values inferred by the computer. The error between actual and inferred crack extensions increases as Δa increases, and is lower at the J_{IC} measurement point. Owing to this bias, the J_{IC} values reported here are estimated to be 15% higher than would be expected from multiple specimen tests. Scatter in the J-resistance curves led to uncertainties of $\pm 15\%$ in the values of J_{IC} .

The validity of J_{IC} results was determined by the size criterion, which requires that

$$B, b, a > \frac{25J_{IC}}{\sigma_f}$$

Previous results have shown that valid results at 295 K are impossible for annealed austenitic stainless steels of 25-mm thickness, so a complete temperature dependence of J_{IC} was not attempted. Only 4-K values are reported.

The 4-K J_{IC} values were converted to K_{IC} estimates, denoted $K_{IC}(J)$, using the following equation:

$$K_{IC}(J) = \left(\frac{J_{IC} E}{1-\nu^2} \right)^{1/2}$$

where E is Young's modulus and ν is Poisson's ratio. The values of E and ν at 4 K were estimated as 206.8 GPa and 0.30, respectively.

RESULTS AND DISCUSSION

Tensile Properties

The tensile properties of the steels tested in this study are listed in table 3 and plotted in figs. 4 through 6.

As shown in fig. 4, the yield strength (σ_y) data for the present Fe-18.25 to 19.5Cr-7.90 to 8.75Ni steels (open symbols) agree well with previous data trends for Fe-18Cr-10Ni steels (solid lines). The yield

strength is highly sensitive to interstitial concentration, so differences in other metallurgical parameters (such as processing temperature, grain size, and nickel content) can be neglected for this comparison. The 295-K data confirm a previous conclusion: the yield strength is a linear function of C+N content [2]. The 4-K data also confirm the existence of a kink in the σ_y -versus-C+N plot at C+N contents between 0.127 and 0.157 wt.%. In the previous study, this kink was attributed to the structural instability of the austenitic phase at these interstitial contents [2]. In the present study there is a clear trend of increasing σ_y values with higher Mn contents at C+N contents from 0.131 to 0.138 wt.%. This effect is probably due to the stabilizing effect of Mn additions at this critical interstitial content.

The ultimate tensile strength results of the present study, shown in fig. 5, are also in general agreement with expected trends. The data at room temperature fall on the same trend line that was previously reported for the Fe-18Cr-10Ni stainless steels. The 4-K data show a minor variation owing to the austenite stabilizing effect of Mn modifications. As more manganese is added at a given interstitial concentration level, the austenite is progressively more stable during tests at 4 K; as a result, less martensite is formed during testing and ultimate tensile strength is reduced as Mn concentration is increased to 6%.

Figure 6 shows the spread of the elongation and reduction of area measurements for the ten steels. Not all of the ductility values are typical of commercial stainless steels. In particular, the reduction of area values for the developmental steels containing 1 to 4% Mn are lower compared with values previously reported for Fe-18Cr-10Ni steels [2] or

commercially available AISI 304 LN steels. Only the 6% Mn-modified steels possess ductility values at the expected levels.

Fracture Toughness

The J_{IC} results obtained for one specimen of each of the ten different steel compositions tested are reported in table 4, and the corresponding $K_{IC}(J)$ values are plotted in fig. 7.

As shown in fig. 7, the $K_{IC}(J)$ estimates follow regular trends depending on Mn and N content. Solid lines have been drawn to connect data representing constant Mn contents; for each Mn content the 0.1N composition is represented by the symbol at the lowest yield strength, whereas the 0.2N composition is represented by the higher yield strength, and 0.15N is intermediate. From fig. 7 it is clear that higher N at a given Mn content lowers the $K_{IC}(J)$ value. It is also clear that Mn has a favorable effect, raising both the strength and the toughness of these developmental alloys.

The major observation from fig. 7 is that the 6%-Mn-modified steels have acceptable fracture toughness, whereas the modifications containing 1 to 4% Mn display inferior properties. The 1 and 2% Mn steels are particularly poor, having estimated K_{IC} values as low as $117 \text{ MPa}\cdot\text{m}^{1/2}$. Their load-deflection fracture toughness test records showed a nearly linear-elastic behavior, with regions of fast crack advance (pop-ins). This evaluation is based on comparison of the present results with the previous results for a series of nine Fe-18Cr-10Ni stainless steels containing variable C+N contents (for all of these steels the same J_{IC} test procedures were used). As shown in fig. 7, the 6% Mn-modified steels exhibit an inverse $K_{IC}(J)/\sigma_y$ relationship at 4 K and, within the measurement error indicated by the error bars shown in the figure, the

inverse-linear trend falls along the lower bound of the scatter band of data for the Fe-18Cr-10Ni steels.

The cause of the unexpected, low K_{IC} (J) values of the 1 to 4% Mn grades is not clear, but it may be related to chemical composition or chemical segregation. The nominal compositional variations between the 1 to 2% Mn steels of this study and the Fe-18Cr-10Ni-1.5Mn steels of the previous study include a 1.25 to 2.5% difference in nickel content. Metallurgical factors, such as interstitial segregation, may account for the low fracture toughness of the 1 to 4% Mn steels of the present study. However, light microscopy revealed no evidence of sensitization or other obvious microstructural differences.

Evidence for interstitial (nitrogen) segregation to grain boundaries in the 1, 2, and 4% Mn steels was obtained by scanning electron microscopy performed on the fracture surfaces of the compact specimens subsequent to J_{IC} testing at 4 K. Figure 8 presents typical results. The specimens containing 4% Mn or less exhibited a significant portion of brittle intercrystalline fracture, whereas the three heats containing 6% Mn (heats 72, 76, 78) all showed a more completely dimpled fracture mode. The lower manganese heats (69, 70, 73, and 74) also show more intercrystalline fracture than was observed in the Fe-18Cr-10Ni steels of our previous study. The only apparent distinction between the thermal-mechanical treatments of the two alloy series was the temperature of hot-working of the billet. The hot-rolling temperature of the initial 304 LN alloy series was 1560 K (2350° F) and the rolling temperature of the 1-6 wt.% Mn alloy series was 1450 K (2150° F). Perhaps this higher deformation temperature is required to preclude excessive

nitrogen segregation to grain boundaries. Further research is continuing to identify the distinctions between the two alloy series.

CONCLUSION

The data of this study show that 6% Mn-modified AISI 304 LN stainless steel can be produced, having conventional tensile and fracture toughness properties equivalent to standard AISI 304 LN stainless steel when tested at 4 K. The Mn-modified stainless steel offers potential processing and fabrication advantages when compared with the standard grade, which contains 1 to 2% Mn.

ACKNOWLEDGMENTS

The stainless steel plates were produced by Armco, under the direction of R. H. Espy of Armco's Research and Technology division. Dr. E. L. Brown of NBS contributed valuable metallographic assistance and technical advice, and D. Baxter of NBS conducted many of the tensile and fracture toughness tests. This assistance is gratefully appreciated.

REFERENCES

- [1] Espy, R. H., "Stainless steel alloy development," presented at NBS/DoE Workshop on Materials at Low Temperatures, Vail, CO, October 16-18, 1979.
- [2] Tobler, R. L., and Reed, R. P., "Interstitial carbon and nitrogen effects on the tensile and fracture parameters of AISI 304 stainless steels," in Materials Studies for Magnetic Fusion Energy Applications at Low Temperatures-III. NBSIR 80-1627, R. P. Reed, ed., National Bureau of Standards, Boulder, CO, June 1980, pp. 17-48.

- [3] Tobler, R. L., Read, D. T., and Reed, R. P., "Strength and toughness relationship for interstitially strengthened AISI 304 stainless steels at 4 K," in Materials Studies for Magnetic Fusion Energy Applications at Low Temperatures-IV. NBSIR 81-1645, R. P. Reed and N. J. Simon, eds., National Bureau of Standards, Boulder, CO, June 1981, pp. 37-76.
- [4] R. P. Reed, "A Cryostat for Tensile Tests in the Temperature Range 300 to 4 K," in Advances in Cryogenic Engineering, Vol. 7, Plenum Press, NY (1961), pp. 448-454.
- [5] Standard Method of Test for Plane Strain Fracture Toughness of Metallic Materials (Designation E399-74), in 1974 Annual Book of ASTM Standards, Part 10, American Society for Testing and Materials, Philadelphia, PA (1974), pp. 432-451.

Table 1. Compositions of modified type 304 LN stainless steels.

Item No.	Heat No.	Code No.	C	Mn	P	S	Si	Cr	Ni	Mo	Cu	N
aim			0.020	1.0	0.020	0.010	0.50	18.25	8.75	0.30	0.30	0.10
actual	8069	69	0.025	1.02	0.022	0.013	0.53	18.19	8.68	0.32	0.30	0.11
aim			0.020	2.00	0.020	0.010	0.50	18.25	8.75	0.30	0.30	0.10
actual	8070	70	0.028	2.00	0.021	0.013	0.63	18.10	8.66	0.31	0.28	0.11
aim			0.020	4.00	0.020	0.010	0.50	18.25	8.75	0.30	0.30	0.10
actual	8071	71	0.025	3.85	0.023	0.013	0.59	18.22	8.70	0.31	0.29	0.11
aim			0.020	6.00	0.020	0.010	0.50	18.25	8.75	0.30	0.30	0.10
actual	8072	72	0.021	5.81	0.023	0.014	0.64	18.06	8.62	0.33	0.30	0.11
aim			0.020	1.00	0.020	0.010	0.50	19.50	7.90	0.30	0.30	0.20
actual	8073	73	0.025	1.19	0.023	0.015	0.60	19.36	7.81	0.32	0.28	0.19
aim			0.020	2.00	0.020	0.010	0.50	19.50	7.90	0.30	0.30	0.20
actual	8074	74	0.022	2.01	0.023	0.013	0.64	19.35	7.89	0.32	0.30	0.19
aim			0.020	4.00	0.020	0.010	0.50	19.50	7.90	0.30	0.30	0.20
actual	8075	75	0.024	3.85	0.022	0.014	0.65	19.25	7.84	0.31	0.29	0.19
aim			0.020	6.00	0.020	0.010	0.50	19.50	7.90	0.30	0.30	0.20
actual	8076	76	0.033	5.79	0.024	0.014	0.61	19.48	7.83	0.31	0.31	0.21
aim			0.020	4.00	0.020	0.010	0.50	18.90	8.3	0.30	0.30	0.15
actual	8077	77	0.026	4.03	0.023	0.014	0.62	18.71	8.22	0.31	0.30	0.15
aim			0.020	6.00	0.020	0.010	0.50	18.90	8.3	0.30	0.30	0.15
actual	8078	78	0.031	5.80	0.024	0.014	0.62	18.42	8.29	0.31	0.30	0.15

Table 2. Grain size and hardness (Rockwell B) of tested stainless steels^a.

Code Number	Carbon+Nitrogen (wt. %)	Hardness (R _B)	Av. Grain Size ASTM No. (mm)
69	0.135	82	5.4 (57)
70	0.138	88	5.5 (55)
71	0.135	84	5.8 (49)
72	0.131	84	5.4 (57)
73	0.215	88	5.5 (55)
74	0.212	94	5.5 (55)
75	0.214	90	5.6 (53)
76	0.243	90	5.6 (53)
77	0.176	89	5.6 (53)
78	0.181	90	5.6 (53)

^aGrain size was measured on planes normal to the transverse direction of the plate stock.

Table 3. Tensile properties (one test per temperature).

Specimen	Mn Content Nominal (wt.%)	N Content Nominal (wt.%)	Test Temperature (K)	Yield Strength, σ_y (MPa)*	Ultimate Strength, σ_u (MPa)	Elongation (%)	Reduction of Area (%)
69	1	0.10	295	276	633	66.7	62.5
			76	535	1578	51.1	39.6
			4	616	1724	34.4	23.1
70	2	0.10	295	294	616	60.5	63.6
			76	518	1524	56.3	42.8
			4	661	1616	28.7	21.5
71	4	0.10	295	272	586	40.6	49.5
			76	523	1404	57.2	50.6
			4	722	1581	37.7	31.2
72	6	0.10	295	255	616	62.6	56.5
			76	580	1326	57.6	56.0
			4	755	1506	44.4	34.1
73	1	0.20	295	307	659	53.5	57.8
			76	804	1662	48.3	43.7
			4	883	1808	33.6	30.4
74	2	0.20	295	325	692	52.5	58.0
			76	796	1599	31.2	43.9
			4	956	1524	21.7	19.8
75	4	0.20	295	329	645	55.5	52.1
			76	781	1474	27.8	42.8
			4	986	1668	38.1	31.2
76	6	0.20	295	343	693	62.6	62.8
			76	819	1429	53.6	54.5
			4	1053	1584	33.3	24.9
77	4	0.15	295	334	662	63.5	52.1
			76	706	1485	52.0	50.9
			4	857	1654	38.3	31.4
78	6	0.15	295	321	652	51.2	51.9
			76	710	1393	53.0	52.3
			4	901	1574	41.1	37.0

Table 4. Yield strength, flow strength, and fracture toughness at 4 K.

Specimen	Mn Content Nominal (wt.%)	N Content Nominal (wt.%)	Yield Strength, σ_y (MPa) ^a	Flow Strength, σ_f (MPa)	$\frac{25J_{Ic}}{\sigma_f}$ (mm)	J_{Ic} (kJ/m ²) ^b	K_{Ic} (J) (MPa·m ^{1/2}) ^c
69	1	0.10	616	1170	2.3	108.5	157
70	2	0.10	661	1138	3.6	163.0	192
71	4	0.10	723	1152	4.4	203.0	215
72	6	0.10	755	1130	5.8	260.0	243
73	1	0.20	883	1345	1.1	60.0	117
74	2	0.20	956	1240	1.3	64.0	121
75	4	0.20	986	1327	1.8	98.0	149
76	6	0.20	1053	1318	2.2	115.5	162
77	4	0.15	857	1255	3.7	188.0	206
78	6	0.15	901	1237	3.7	185.0	205

$${}^a_{\sigma_f} = \frac{1}{2} (\sigma_y + \sigma_u)$$

^aTo convert from MPa to ksi, divide by 6.895.

^bTo convert from kJ/m² to in-lb/in², multiply by 5.709.

^cTo convert from MPa·√m to ksi·√in, divide by 1.099.

LIST OF FIGURES

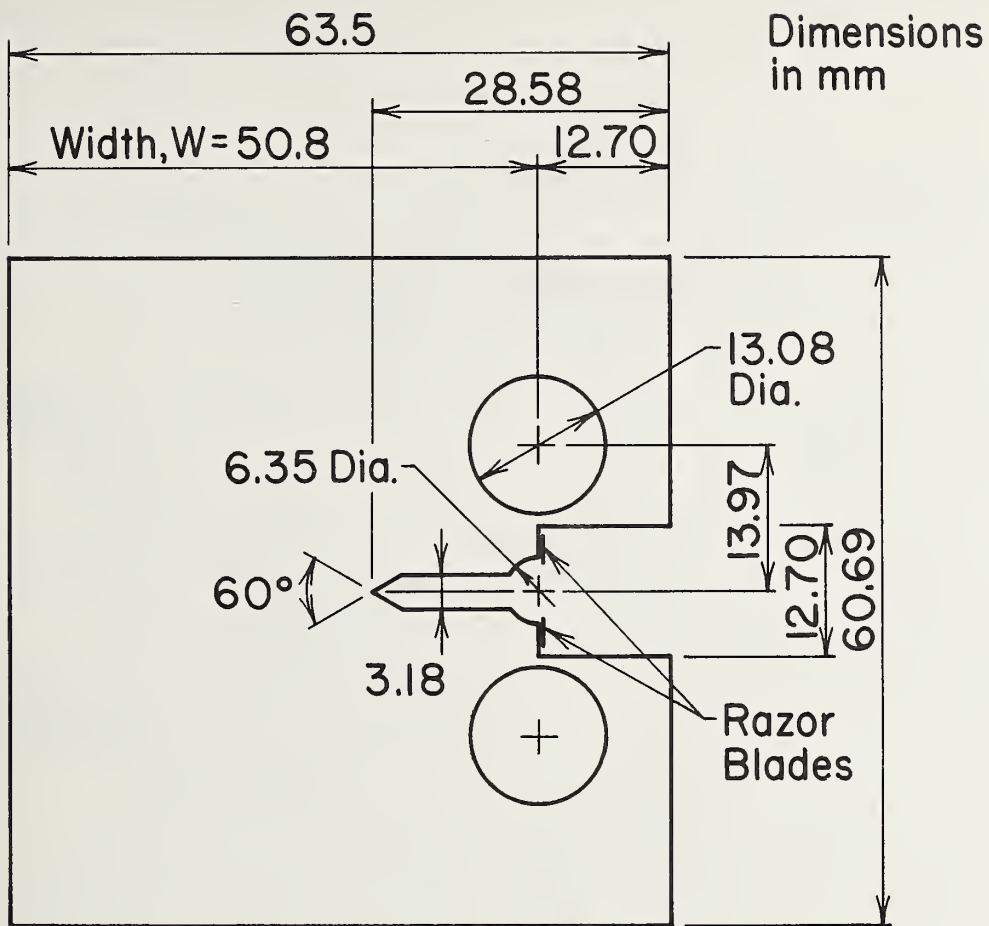
- Figure 1. As-received 25 mm-thick stainless steel plate (heat 76, Fe-19.5Cr-7.83Ni-5.8 Mn), showing freedom from corner checks.
- Figure 2. Corner checks as they appear in hot-rolled nitrogen-modified Fe-18Cr-10Ni stainless steel of a previous study (see text).
- Figure 3. Compact fracture and tensile specimens used in this study.
- Figure 4. Effect of carbon plus nitrogen interstitials on yield strength of stainless steels, with temperature as a parameter.
- Figure 5. Effect of carbon plus nitrogen interstitials on ultimate strength at two test temperatures.
- Figure 6. Ductility of stainless steels.
- Figure 7. Fracture toughness-versus-yield strength results for Mn-N modified steels of the present study, as compared with previous results for AISI 304 type stainless steels.
- Figure 8. Scanning electron micrographs of 4 K fracture surfaces of low toughness (heat 69, top) and high toughness (heat 72, bottom) austenitic stainless steels.



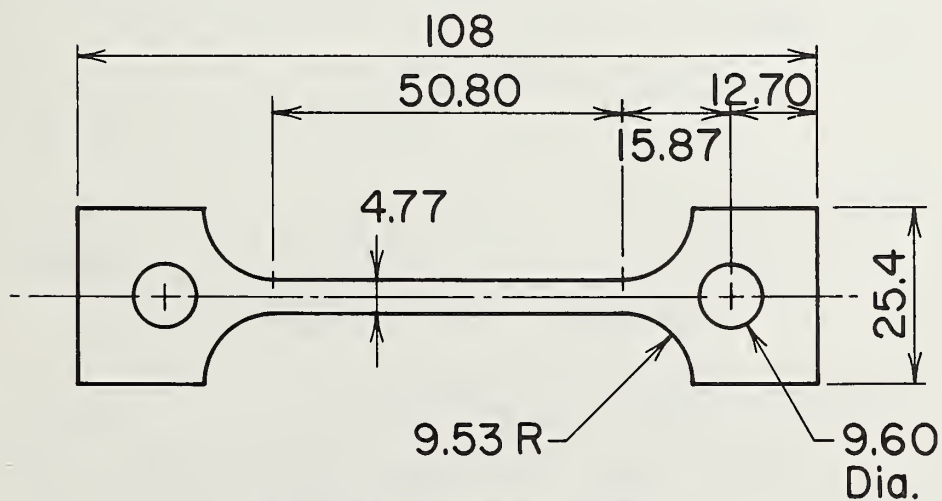
Figure 1. As-received 25 mm-thick stainless steel plates (heat 76, Fe-19.5Cr-7.83Ni-5.8 Mn), showing freedom from corner checks.



Figure 2. Corner checks as they appear in hot-rolled nitrogen-modified Fe-18Cr-10Ni stainless steel of a previous study (see text).



COMPACT SPECIMEN
Thickness = 24.5 mm



TENSILE SPECIMEN
Thickness = 2.54 mm

Figure 3. Compact fracture and tensile specimens used in this study.

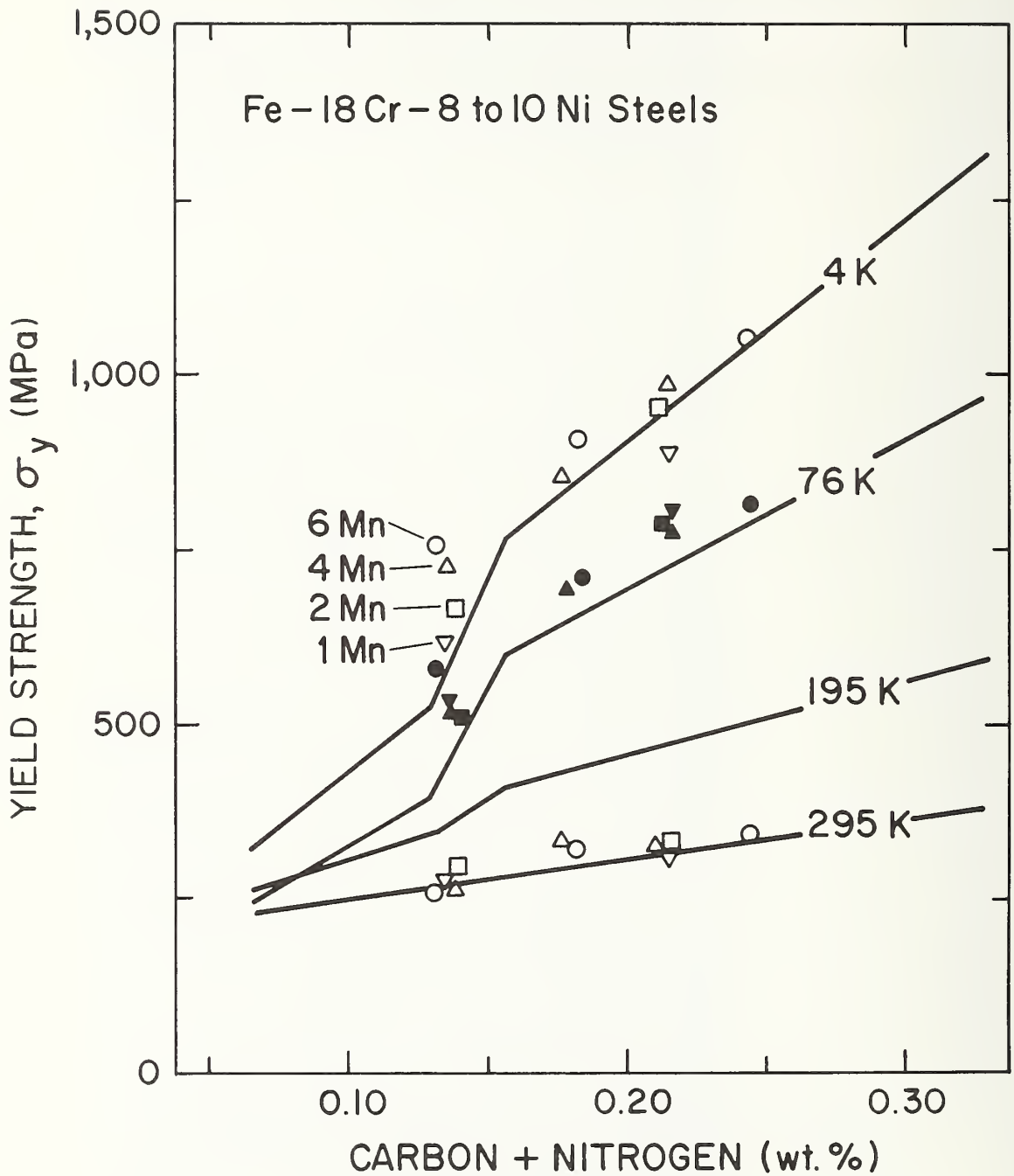


Figure 4. Effect of carbon plus nitrogen interstitials on yield strength of stainless steels, with temperature as a parameter.

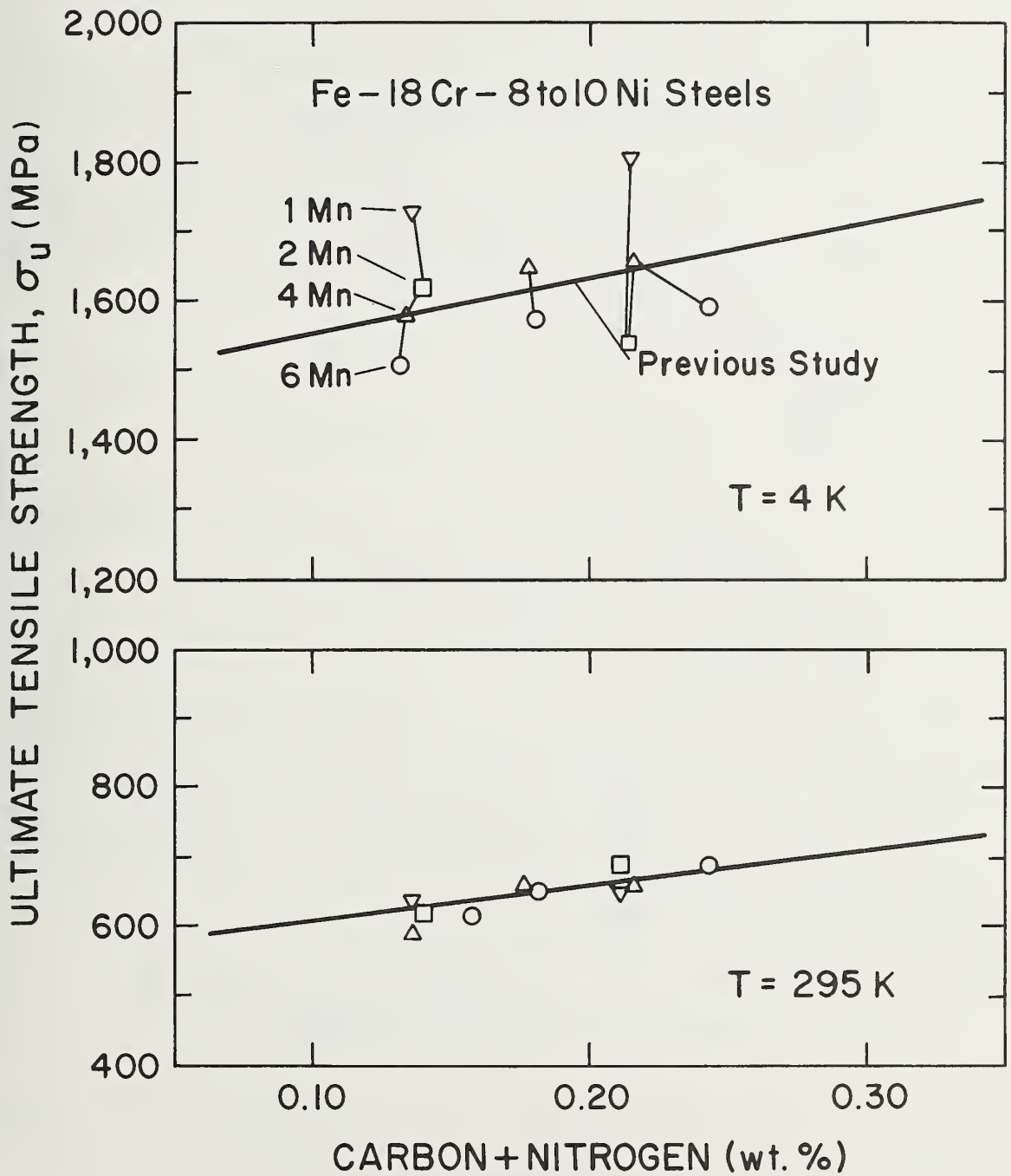


Figure 5. Effect of carbon plus nitrogen interstitials on ultimate strength at two test temperatures.

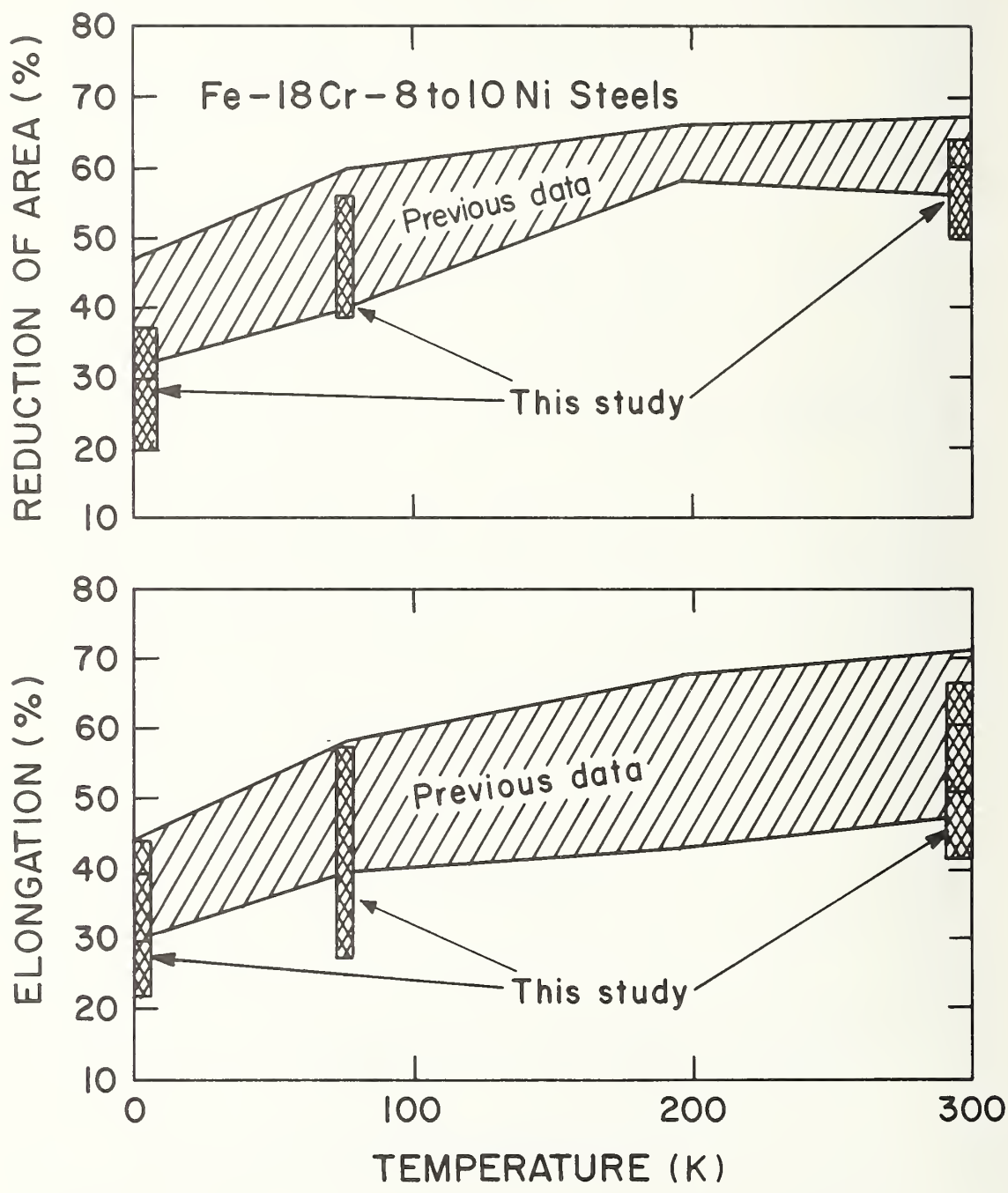


Figure 6. Ductility of stainless steels.

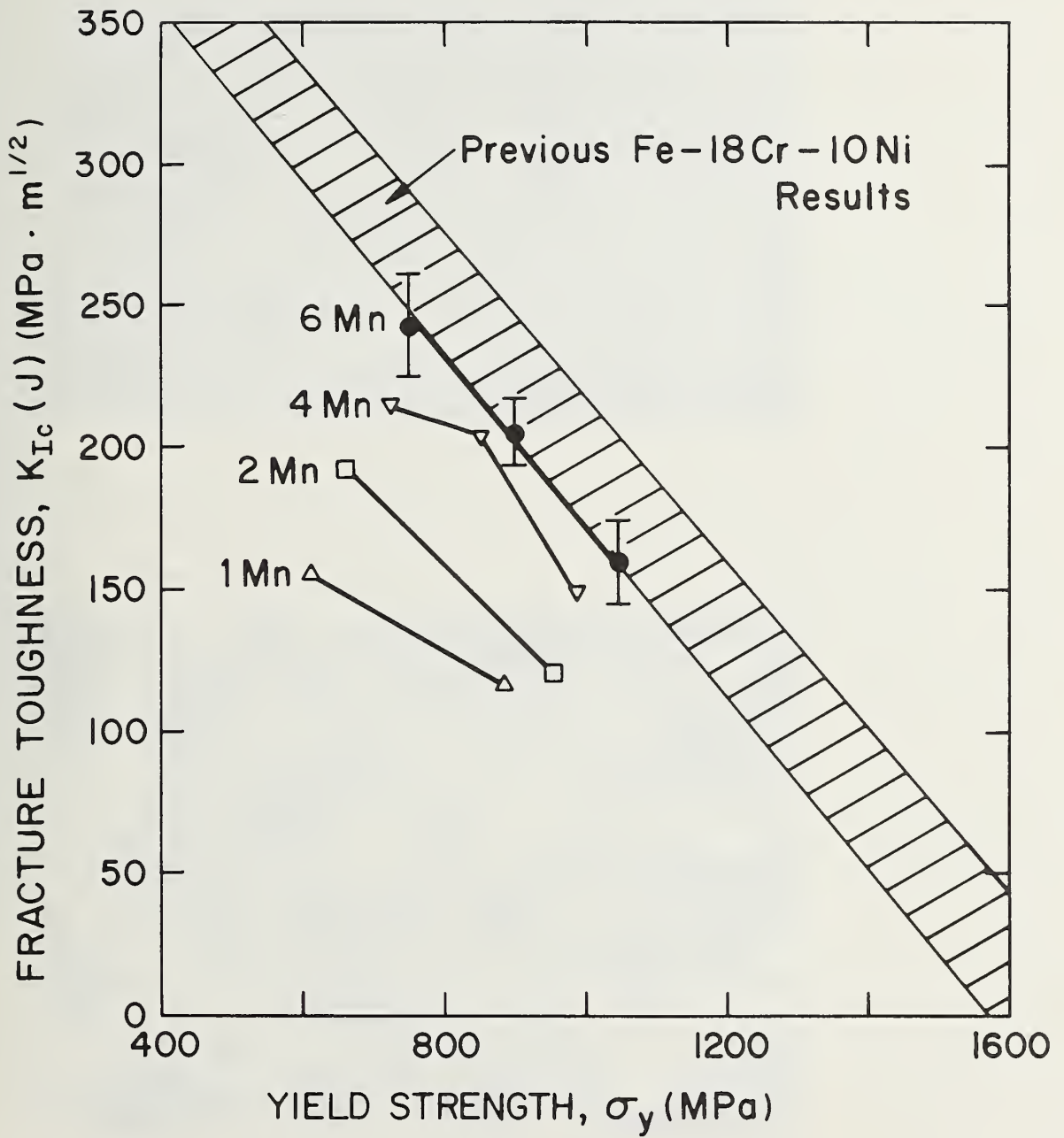


Figure 7. Fracture toughness-versus-yield strength results for Mn-N modified steels of the present study, as compared with previous results for AISI 304 type stainless steels.



(a)

100 μm



(b)

100 μm

Figure 8. Scanning electron micrographs of 4 K fracture surfaces of low toughness (heat 69, top) and high toughness (heat 72, bottom) austenitic stainless steels.

INTERSTITIAL CARBON AND NITROGEN EFFECTS ON THE
CRYOGENIC FATIGUE CRACK GROWTH OF AISI 304 TYPE STAINLESS STEELS

R. L. Tobler and R. P. Reed
Fracture and Deformation Division
National Bureau of Standards
Boulder, Colorado

ABSTRACT

Constant-load-amplitude fatigue crack propagation (FCP) rate measurements are reported for AISI 304 type stainless steels having variable carbon-plus-nitrogen (C+N) contents. Rates at stress-intensity factors from 20 to 70 MPa·m^{1/2} were measured using 25-mm-thick compact specimens. The Fe-18Cr-10Ni steels tested exhibited partial martensitic phase transformations during tests at 76 and 4 K, but not during tests at 295 K. At high C+N contents (0.187 wt.% or greater), the FCP resistance was lower at 4 K than at 295 K. At low C+N contents (0.067 wt.%), the FCP resistance at cryogenic temperature was significantly higher than at room temperature. The improvement in steels of low C+N contents was associated with a transition from partially intergranular failure at 295 K to completely transgranular failure at 76 and 4 K.

INTRODUCTION

When James [1] reviewed the subject of fatigue crack propagation in austenitic stainless steels in 1976, few cryogenic data were available. Since then, fatigue crack propagation rate measurements (da/dN) at intermediate stress intensity factor ranges (ΔK) have shown that stable (nontransforming) austenitic stainless steels display improved resistance to fatigue cracking at extreme cryogenic temperatures, whereas metastable grades are less predictable [2-5]. A metastable stainless steel is one in which the austenitic phase in response to stress or plastic deformation at low temperatures transforms to some degree to body centered cubic (α') or hexagonal (ϵ) martensitic phases.

Metastable AISI 304 stainless steel (Fe-18 to 20Cr-8 to 12Ni) is a common cryogenic structural alloy, whose mechanical properties are highly sensitive to composition; a broad range of mechanical property combinations can be achieved by varying the C+N contents, because these elements significantly stabilize and strengthen the austenitic phase. A previous study described the effects of C+N contents on the 4-K fracture toughness properties of a series of Fe-18Cr-10Ni developmental stainless steels [6]. In the present study, the same series of steels was tested to evaluate fatigue crack propagation behavior.

MATERIALS

Nine stainless steel alloy plates with an Fe-18Cr-10Ni base were tested. These plates had a nominal base composition falling within the limits set by ASTM specification A 240 for AISI 304 stainless steel. The C+N levels varied, however, with carbon at 0.03, 0.06, or 0.09 wt.%, and nitrogen at 0.04, 0.12, or 0.24 wt.%. The nine plates were produced

from three 136-kg (300-lb) vacuum-induction-melted heats, split with respect to carbon level, and teemed into 76 x 200 x 360 cm hot-topped cast-iron ingot molds. The ingots were then reheated and soaked at 1561 K (2350° F), hot-rolled to 25.4-mm-thick plates, and air cooled. The plates were finally annealed at 1332 ± 7 K ($1937^\circ \pm 13^\circ$ F) for 1 h and water quenched. The mill chemical analyses, hardnesses, and grain size measurements are listed in Table I. Tensile properties are listed in Table II.

SPECIMEN

The modified compact specimen geometry of Figure 1 was used (the basic geometry is described in ASTM Method E-399-74 [7]). The modification consisted of mounting knife edges for clip-gage deflection (δ) measurements at the load line. The specimen thickness (B) was 25 mm, and the width-to-thickness ratio (W/B) was 2. The notch was machined in the TL orientation [7], and the crack propagated in a direction parallel to the plate rolling direction.

PROCEDURES

The fatigue tests were performed using a 100-kN servo-hydraulic testing machine and cryostat [8]. Room-temperature tests were conducted in ambient air (295 K) at a relative humidity of 10 to 20%. Cryogenic tests were performed with the specimens submerged in a stainless steel Dewar containing liquid nitrogen (76 K) or liquid helium (4 K).

Specimens tested at 295 and 76 K were precracked at the same temperatures, whereas specimens tested at 4 K were precracked at 76 K. During precracking at 76 K, the number of cycles to initiate a 1.9-mm crack was recorded. The machine was operated in load control, using a

sinusoidal load cycle at frequencies between 20 and 25 Hz. The load, P , was accurate to $\pm 3\%$. The load ratio, $R (P_{\min}/P_{\max})$, was constant at 0.1. The maximum load for a given test was held constant at a value between 22 and 24 kN.

Crack growth-to- a/W ratios of about 0.65 were monitored by specimen compliance (δ/P) measurements. The compliance measurements were correlated with the average crack lengths based on measurements at the specimen edges, quarter points, and center of thickness [5,8]. Crack curvature was such that the average crack length was 93% of the center crack length for $a/W \approx 0.6$. Robert's crack length-compliance solution was corrected (shifted a few percent to agree with the experimental measurements for the final crack length for each test specimen) and then used to infer all other crack lengths from compliance readings taken during fatigue tests [5,8]. A computer was used to fit the a -versus- N curves with third order polynomial expressions, to differentiate the curves to obtain da/dN , and to calculate the corresponding stress intensity factor ranges, ΔK :

$$\Delta K = K_{\max} - K_{\min} = (P_{\max} - P_{\min}) B^{-1} W^{-1/2} [f(a/W)] \quad (1)$$

where $f(a/W)$ is given by Roberts [9]. Data were obtained from one specimen per material per temperature.

Magnetic measurements verified that cyclic loading of the Fe-18Cr-10Ni steels during crack growth experiments at 76 K and 4 K caused formation of α' martensite. The α' martensite is ferromagnetic, whereas the original austenite and ϵ martensite are not. Therefore, by using a torsion bar magnetometer [6] on the compact specimen fatigue surfaces

subsequent to testing, the amount of α' martensitic transformation was determined.

RESULTS

Crack initiation at 76 K

The number of load cycles required to produce a 1.9-mm crack at 76 K for the particular specimen geometry and loading conditions used in the present tests are plotted in Figure 2. As C+N contents are increased, the resistance to crack initiation decreases rapidly at first, but reaches a plateau at C+N = 0.157 or greater. The effect is large, amounting to a five-fold variation of initiation time.

Crack propagation

For the stress intensity factor ranges studied, the FCP rates for Fe-18Cr-10Ni stainless steels conformed to power law equations of the form:

$$da/dN = C(\Delta K)^n \quad (2)$$

where the parameters C and n are material and temperature dependent. Evidence justifying the applicability of this equation to austenitic stainless steels, and to AISI 304 in particular, is presented by James [1] and Brose and Dowling [10]. In the present study, log-log plots of da/dN versus ΔK were constructed to obtain the C and n values that correspond to the ordinate intercepts at $\Delta K = 1$ and the slopes, respectively. Table III lists the C and n values for all material and temperature combinations.

A general presentation of results is shown in Figure 3. The room-temperature data (Fig. 3a) for the present steels form a scatter band

that fits within the larger scatter band drawn by James [1] for many commercial AISI 304 steels tested at different laboratories using ten different specimen geometries and variations of test procedure. The data for the Fe-18Cr-10Ni steel of our study having 0.067 wt.% C+N was also found to be in close agreement with previous measurements for a commercial AISI 304L steel of similar composition [5]. Therefore, our results for laboratory heats are representative of commercial steels.

Figures 3b and 3c show the effect of temperature reductions on the spread of present results. Reducing the temperature to 76 K improves the FCP resistance of many of these steels. At 4 K, however, the high C+N compositions are adversely affected. As indicated in Figure 3c, the 4-K scatter band encompasses the 295-K scatter band for the same steels. The greater variation of fatigue crack growth rates at 4 K is attended by significant differences in austenitic stability and tensile properties (Table II) for these alloys, owing to the effects of C+N at cryogenic temperatures.

Interstitial effects

Figure 4 presents the results for each heat at 295, 76, or 4 K. Four heats were tested at 295 K. As shown in Figure 4a, the rates for heats 1 and 3 are equivalent. The rates for heats 5 and 9 are also equivalent, but lower compared with those of heats 1 and 3. Therefore, higher C+N contents tend to improve fatigue propagation resistance at 295 K. Individual datum points are shown only for heats 1 and 9. The specified C+N contents for these two steels (0.067 and 0.325 wt.%) represent the limits studied, and the indicated data spreads are typical.

Also shown in Figure 4a are results for an AISI 310 stainless steel (Fe-25Cr-20Ni) [5], which fall among the Fe-18Cr-10Ni results. At 295 K, all of these steels are stable with respect to the austenite-to-martensite phase transformation, and all exhibit similar microfailure modes. As shown in Figure 5, the failure modes at 295 K consist of significant portions of intergranular failure. Scanning electron micrographs were taken from the fatigue surfaces where the ΔK value was approximately $40 \text{ MPa}\cdot\text{m}^{1/2}$. In each case, the failures show a number of features, including secondary cracks, coarse transgranular failure zones, and smooth, highly reflective grain-boundary facets. Occasionally, a sample would show delaminations. The exposed grain facets frequently displayed slip-line markings, sometimes twins.

At 76 K (Figure 4b), the effect of C+N content on fatigue crack growth rates is reversed from that at 295 K. The rates for heat 1 are considerably lower than for heats 3, 6, 7, and 9, which are nearly equivalent. Thus, the steel with the lowest C+N level has the lowest rates at 76 K. At 76 K, partial martensitic transformations take place, and transformation is most extensive for heat 1. Significantly, there is also an obvious difference in microfracture mode for heat 1. As shown in Figure 6, the 76-K fatigue surface reveals a completely transgranular microfailure, quite distinct from the partially intergranular mode exhibited by this steel at 295 K. As a result of this transition to a transgranular failure, the 76 K fatigue surfaces for heat 1 are noticeably smoother than those at 295 K. In Figure 6, the tendency to transgranular failure is also somewhat in evidence for heat 3. In fact, as the C+N contents are increased, grain facets gradually become more

prominent on the 76-K fatigue surfaces. Heats 6, 7, and 9 at 76 K exhibit the same degree of intergranular cracking observed in tests at 295 K.

At 4 K (Figure 4c), where all heats were tested, the results were similar to those at 76 K. Again, heat 1 exhibits the lowest fatigue crack growth rates. As C+N contents are increased, the 4-K rates increase rapidly at first, but the effect saturates at $C+N \approx 0.128$ or more, and heats 4 through 9 have equivalent fatigue crack growth resistances at this temperature.

The relative amount of α' (bcc) martensite formed during fatigue testing at 4 K is plotted as a function of interstitial content in Figure 7. These data provide only an approximate indication of the extent of phase transformation, because the magnetometer readings were taken directly from the compact specimen fatigue surfaces, which are unmachined. From Figure 7, it is clear that some martensite forms in all of the alloys fatigued at 4 K. But more martensite forms in the low-strength, low-C+N grades, because these grades are the least stable and also have the largest crack-tip plastic-zone sizes.

Scanning electron microscopy results for specimens fatigued at 4 K are shown in Figure 8. The findings closely parallel those at 76 K: at low C+N contents, the failure mode is completely transgranular, but at high C+N contents there is a partially intergranular failure mode.

Temperature effects

The results for three heats representing low, intermediate, and high C+N contents are replotted in Figure 9, illustrating the temperature dependence of fatigue crack growth resistance.

Heat 1 (C+N = 0.067 wt.%) represents the lowest interstitial content, lowest yield strength, and lowest austenite stability. For this steel, temperature reductions to 76 or 4 K greatly improve the da/dN values at a given ΔK value. The fatigue crack growth rates at 76 and 4 K are nearly equivalent and much lower than those at 295 K. The rates for heat 1 are in excellent agreement with rates previously reported for a commercial AISI 304L and 310 stainless steels [5] at 76 and 4 K. As indicated previously in Figure 5, the improved fatigue crack growth resistance at cryogenic temperatures is associated with a transition from partially intergranular failure (295 K) to transgranular failure (76 and 4 K).

Heat 3 (C+N = 0.128 wt.%) represents intermediate interstitial content, strength, and austenite stability. As shown in Figure 9b, the rates at a given ΔK value decrease slightly between 295 and 76 K and then increase between 76 and 4 K. Thus, temperature effects are minimized at intermediate interstitial content. This concurs with previous reports of temperature-insensitive fatigue crack growth behavior in commercial AISI 304 grade steel [5]. The scanning electron microscopy results for heat 3 show a more well-defined intergranular failure mode at 295 and 4 K, compared with that at 76 K.

Heat 9 (C+N = 0.325 wt.%) represents the highest interstitial content, highest strength, and highest austenite stability. The effect of a temperature reduction to 4 K on this heat is completely opposite to the trend for heat 1, shown in Figure 9c. The 76-K rates are slightly higher or nearly equivalent to the rates at 295 K, but the 4-K rates are two or three times higher. The failure mode for heat 9 is partially intergranular at all test temperatures.

DISCUSSION

It was concluded from previous work that desirable fatigue crack growth resistance at cryogenic temperatures may be achieved with alloys having the austenitic structure and high elastic modulus [5]. Nevertheless, as shown in this paper, a broad range of properties may be displayed within a given austenitic steel family at 4 K, owing to compositional variations.

At room temperature, where the da/dN data represent crack propagation through stable austenite, increasing the C+N level tends to increase fatigue crack growth resistance, in accordance with previous observations [2], although heat-to-heat variations are not very great. The microfailure mode at room temperature always consists of a rough transgranular surface plus a significant portion of intergranular failure. The grain facets corresponding to the intergranular failure are undoubtedly the reflective "cleavage-like" facets observed under low magnification in previous studies of austenitic steels [5].

At cryogenic temperatures, where the strengths of some of the steels were greatly increased and where martensitic transformations occurred in varying degrees, the variation of fatigue-crack-growth resistances was especially great. During tests of these steels at 76 and at 4 K, it can be assumed that the martensitic transformation occurred locally in the plastic zone ahead of the crack, so that transformation preceded material separation. The parameter measured in these tests was the rate of fatigue crack propagation through partially martensitic material.

At low C+N levels, the effects of martensitic transformation are complex: strength is low, strain-hardening capability is high, and a relatively large portion of martensite is formed. Since the martensite

transformation is an energy-absorbing process, a decrease of crack propagation rates may result, as compared to rates under conditions where the austenite is more stable.

At higher C+N contents, the strength level is high and strain hardening capability is low. The amount of phase transformation is reduced, and its effects may be masked by other factors, such as a growing tendency to intergranular fracture. Intergranular fracture may be encouraged at higher C+N contents if the grain boundary energy is reduced by absorbed interstitials or if the grains are hardened relative to the grain boundaries.

These results must be interpreted cautiously, because it is believed that the cyclic stress-strain behavior, not the static tensile properties, govern fatigue behavior [2]. In our work, the effects of C+N contents and martensitic transformation on cyclic stress-strain properties were not studied. The effect of the volumetric expansion accompanying martensitic transformation is also unknown. The volumetric expansion in austenitic stainless steels is about 3%, and this should introduce residual stresses. Separation of the temperature, transformation, strain hardening, and residual stress effects is not easy and is beyond the scope of this study.

A primary purpose of the present work is to compare the fatigue crack growth rates of steels that may be selected for large cryogenic machinery. Nine metastable Fe-18Cr-10Ni steels and an AISI 310 steel are compared. The two alloys having superior fatigue crack growth resistances are the fully stable (AISI 310) and the least stable (AISI 304, heat 1). The 76- and 4-K rates of these two (Fig. 4) are

equivalent and less than the rates at 295 K. The equivalent performances at extreme cryogenic temperatures are surprising since the improvement of the metastable steel is associated with a failure mode transition, whereas the improvement for AISI 310 must be attributed solely to inherent temperature effects on material properties (i.e., there is no failure mode transition for AISI 310).

Fatigue crack propagation at 4 K may be an important design parameter for superconducting magnet structures in some magnetic fusion energy devices. The rates reported here were determined primarily for material characterization, but the results may also be useful for life prediction, with precautions. Owing to the complex nature of the steels tested, the data trends of Table III should not be extrapolated beyond the range of actual data accumulation. The rates in the present study were measured at $R = 0.1$, at constant load amplitude, and at intermediate ΔK . These conditions are not representative of many applications. Before the fatigue life of a component can be accurately predicted, the effects of stress ratio, variable amplitude loading, cycle frequency, and deviations from the power law equation at threshold or very high ΔK levels need to be evaluated. These effects have never been studied at 4 K.

SUMMARY AND CONCLUSION

A study was conducted to determine the effects of interstitial C+N on fatigue crack propagation resistance of AISI 304 type stainless steels at room and cryogenic temperatures. Rate measurements were reported for conditions of constant load amplitude, at a stress ratio of 0.1, and at intermediate ΔK values, using compact specimens of the TL

orientation, taken from 25-mm-thick plate. The C+N content determines the temperature dependence of fatigue crack propagation rates in these alloys:

- (1) At low C+N contents, the rates decrease at cryogenic temperatures, relative to those at 295 K,
- (2) At intermediate C+N contents, the rates are relatively insensitive to temperature, and
- (3) At high C+N contents, the rates increase at cryogenic temperatures, relative to those at 295 K.

The improvement for low C+N contents is associated with a failure mode transition from partially intergranular failure at 295 K to transgranular failure at 76 and 4 K.

REFERENCES

1. James, L. A., "Fatigue crack propagation in austenitic stainless steels," *At. Energy Rev.* 14, 1 (1976), 37-85.
2. Pineau, A. G., and Pelloux, R. M., "Influence of strain-induced martensite transformations on fatigue crack growth rates in stainless steels," *Metall. Trans.*, 5 (1974) 1103-1112.
3. Logsdon, W. A., Wells, J. M., and Kossowsky, R., "Fracture mechanics properties of austenitic stainless steels for advanced cryogenic applications," in: Proceedings of the Second International Conference on Mechanical Behavior of Materials, American Society for Metals, Metals Park, Ohio (1976), 1283-1289.
4. Tobler, R. L. and Reed, R. P., "Fatigue crack growth rates of structural alloys at 4 K," in Advances in Cryogenic Engineering, Vol. 22, K. D. Timmerhaus, R. P. Reed, and A. F. Clark, eds., Plenum, New York (1977), 35-46.
5. Tobler, R. L. and Reed, R. P., "Fatigue crack growth resistance of structural alloys at cryogenic temperatures," in: Advances in Cryogenic Engineering, Vol. 24, K. D. Timmerhaus, R. P. Reed, and A. F. Clark, eds., Plenum, New York (1978), 82-90.
6. Tobler, R. L. and Reed, R. P., "Interstitial carbon and nitrogen effects on the tensile and fracture parameters of AISI 304 stainless steels," in: Materials Studies for Magnetic Fusion Energy Applications at Low Temperatures-III, NBSIR 80-1627, R. P. Reed, ed., Fracture and Deformation Division, National Bureau of Standards, Boulder, Colorado (June 1980), 17-48.

7. Standard test method for plane-strain fracture toughness of metallic materials (designation ANSI/ASTM E399-78a)," in 1979 Annual Book of ASTM Standards, Part 10, American Society for Testing and Materials, Philadelphia (1979), 540-561.
8. Fowlkes, C. W. and Tobler, R. L., "Fracture testing and results for a Ti-6Al-4V alloy at liquid helium temperature," Eng. Fract. Mech. 8 (1976), 487-500.
9. Roberts, E. J., Jr., "Elastic crack-edge displacements for the compact tension specimen," Mater. Res. Stands., 9, No. 2 (1969), 27.
10. Brose, W. R. and Dowling, N. E., "Size effects on the fatigue crack growth rate of type 304 stainless steel," in: Elastic-Plastic Fracture, ASTM STP 668, J. D. Landes, J. A. Begley, and G. A. Clarke, eds., American Society for Testing and Materials, Philadelphia (1979), 720-735.

Table I. Stainless steel compositions (wt.%), hardnesses, and grain sizes.

Heat No.	Fe	Cr	Ni	Mn	P	S	Si	Mo	Cu	C	N	C+N	Hardness, Rockwell B	Average Grain Size (μm)
1	ba1.	18.3	10.1	1.57	0.021	0.019	0.50	0.20	0.210	0.028	0.039	0.067	73.8	85
2	ba1.	"	"	"	"	"	"	"	"	0.058	"	0.097	76.0	78
3	ba1.	"	"	"	"	"	"	"	"	0.089	"	0.128	78.8	90
4	ba1.	18.0	9.91	1.50	0.026	0.017	0.57	0.205	0.197	0.037	0.120	0.157	79.1	105
5	ba1.	"	"	"	"	"	"	"	"	0.067	"	0.187	82.7	85
6	ba1.	"	"	"	"	"	"	"	"	0.094	"	0.214	72.5	78
7	ba1.	20.3	9.97	1.42	0.024	0.016	0.55	0.195	0.200	0.030	0.240	0.270	89.4	98
8	ba1.	"	"	"	"	"	"	"	"	0.057	"	0.297	89.4	82
9	ba1.	"	"	"	"	"	"	"	"	0.085	"	0.325	91.1	90

Table II. Tensile properties (one test per temperature).

Alloy Heat No.	C+N Content (wt.%)	Test Temperature (K)	Yield Strength, σ_y (MPa)*	Ultimate Strength, σ_f (MPa)	Elongation (%)	Red. of Area (%)
1	0.067	295	222	596	71.1	71.1
		76	244	1414	39.6	52.1
		4	329	1454	29.8	43.6
2	0.097	295	241	599	71.0	62.6
		76	316	1444	43.7	56.3
		4	445	1548	32.5	45.6
3	0.128	295	263	624	69.9	65.8
		76	396	1496	44.7	55.2
		4	530	1528	34.4	46.0
4	0.157	295	279	612	67.5	62.3
		76	616	1450	49.4	54.3
		4	745	1570	34.1	42.9
5	0.187	295	312	652	55.5	66.5
		76	688	1494	49.2	54.8
		4	876	1700	34.8	46.1
6	0.214	295	308	654	59.9	63.2
		76	712	1548	50.0	54.0
		4	896	1633	35.4	47.1
7	0.270	295	369	698	50.0	56.0
		76	889	1486	55.2	56.4
		4	1186	1636	31.7	43.1
8	0.297	295	358	740	52.3	67.1
		76	952	1558	58.0	59.9
		4	1178	1735	32.5	41.2
9	0.325	295	376	729	47.7	58.6
		76	919	1530	39.9	39.7
		4	1286	1705	32.7	31.5

*To convert from MPa to ksi, divide by 6.895.

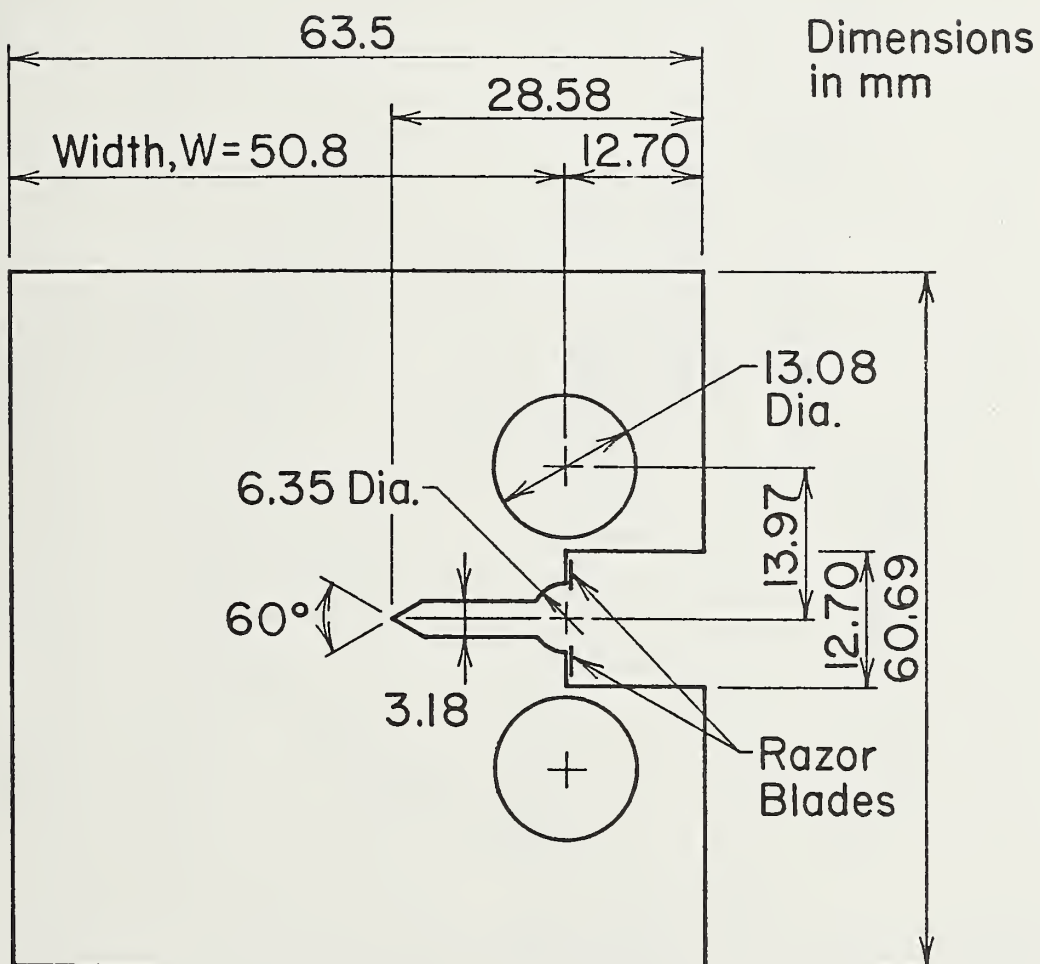
Table III. Power-law fatigue equation [Eq. 2] parameters for austenitic stainless steels ($R = 0.1$), where da/dN is in mm/cycle and ΔK is in $\text{MPa}\cdot\text{m}^{1/2}$.

Material (Heat No.)	Temperature (K)	n	C	ΔK Region ($\text{MPa}\cdot\text{m}^{1/2}$)*
1	295	3.9	3.1×10^{-10}	20-57
	76	4.0	3.7×10^{-11}	24-57
	4	3.4	4.25×10^{-10}	25-55
2	4	3.9	1.7×10^{-10}	25-44
3	295	3.9	3.1×10^{-10}	20-40
	76	3.7	3.4×10^{-10}	25-50
	4	3.8	4.5×10^{-10}	24-64
4	4	3.6	1.1×10^{-9}	25-70
5	295	4.25	3.9×10^{-11}	30-64
	4	3.6	1.1×10^{-9}	35-70
6	76	3.7	3.4×10^{-10}	25-50
	4	3.6	1.1×10^{-9}	25-58
7	76	3.7	3.4×10^{-10}	25-50
	4	3.6	1.1×10^{-9}	25-60
8	4	3.6	1.1×10^{-9}	27-50
9	295	4.25	3.9×10^{-11}	24-64
	76	3.7	3.4×10^{-10}	24-48
	4	3.6	1.1×10^{-9}	24-60
AISI 310 [5]	295	4.4	3.5×10^{-11}	24-35
	295	3.0	4.7×10^{-9}	35-60
	76	3.7	1.1×10^{-10}	25-80
	4	3.7	1.1×10^{-10}	25-80

*To convert from $\text{MPa}\sqrt{\text{m}}$ to $\text{ksi}\sqrt{\text{in}}$, divide by 1.099.

LIST OF FIGURES

- Figure 1. Compact specimen used for fatigue tests.
- Figure 2. Crack initiation results for specific conditions at 76 K.
- Figure 3. General comparison of da/dN vs. ΔK results.
- Figure 4. Fatigue crack propagation behavior as a function of interstitial C+N contents with temperature as a parameter.
- Figure 5. SEM views of the partially intergranular failure modes at 295 K.
- Figure 6. SEM views of the fatigue failure modes at 76 K, showing the transgranular (heat 1) to partially intergranular transition (heat 9).
- Figure 7. Relative amounts of α' (bcc) martensite formed during fatigue tests at 4 K. (Arbitrary units)
- Figure 8. SEM views of the fatigue failure modes at 4 K, showing the transgranular to partially intergranular transition.
- Figure 9. Fatigue crack propagation behavior as a function of temperature, with interstitial C+N contents as a parameter.



COMPACT SPECIMEN
Thickness = 24.5 mm

Figure 1. Compact specimen used for fatigue tests.

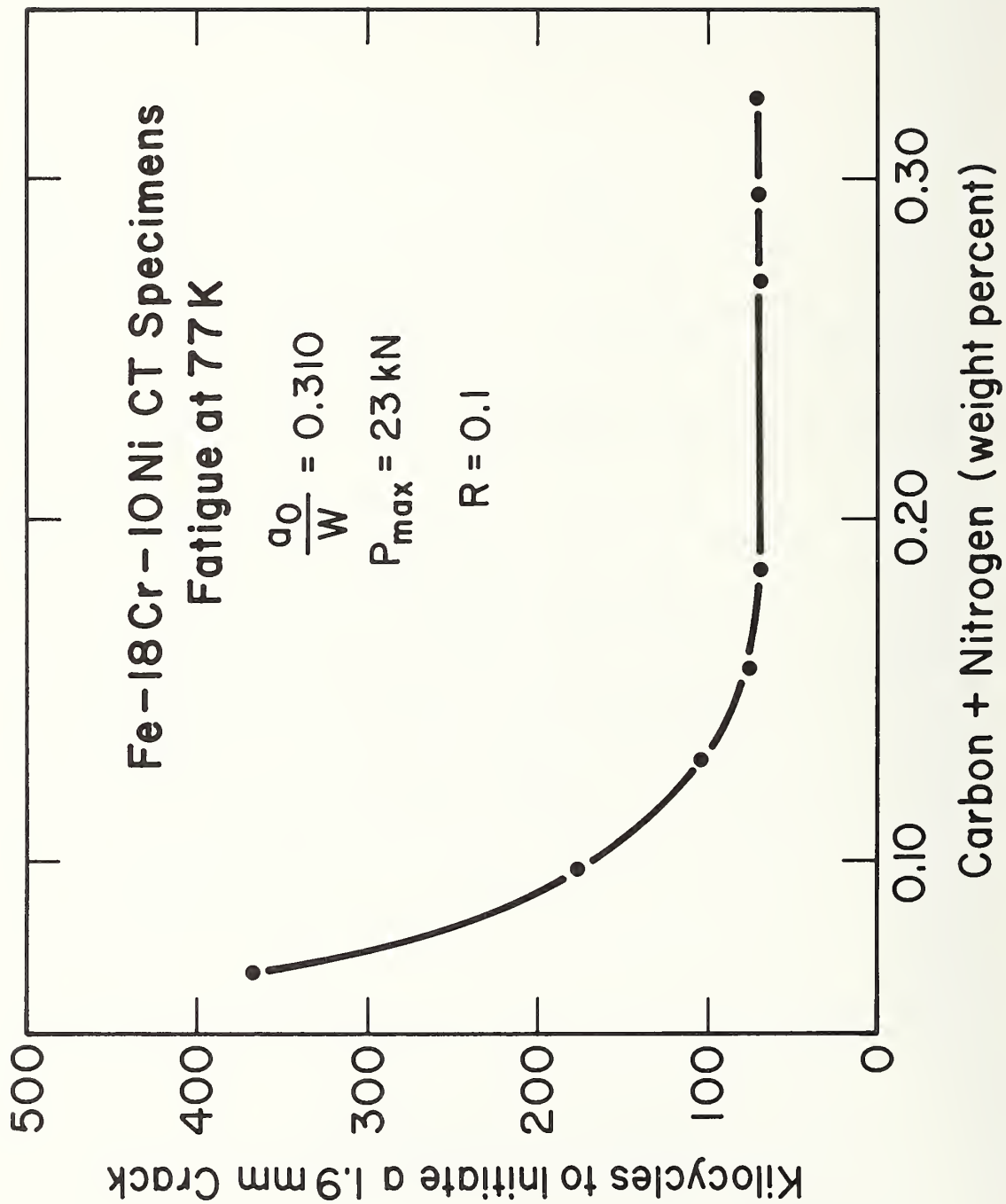


Figure 2. Crack initiation results for specific conditions at 76 K.

Fe-18Cr-10Ni STAINLESS STEELS

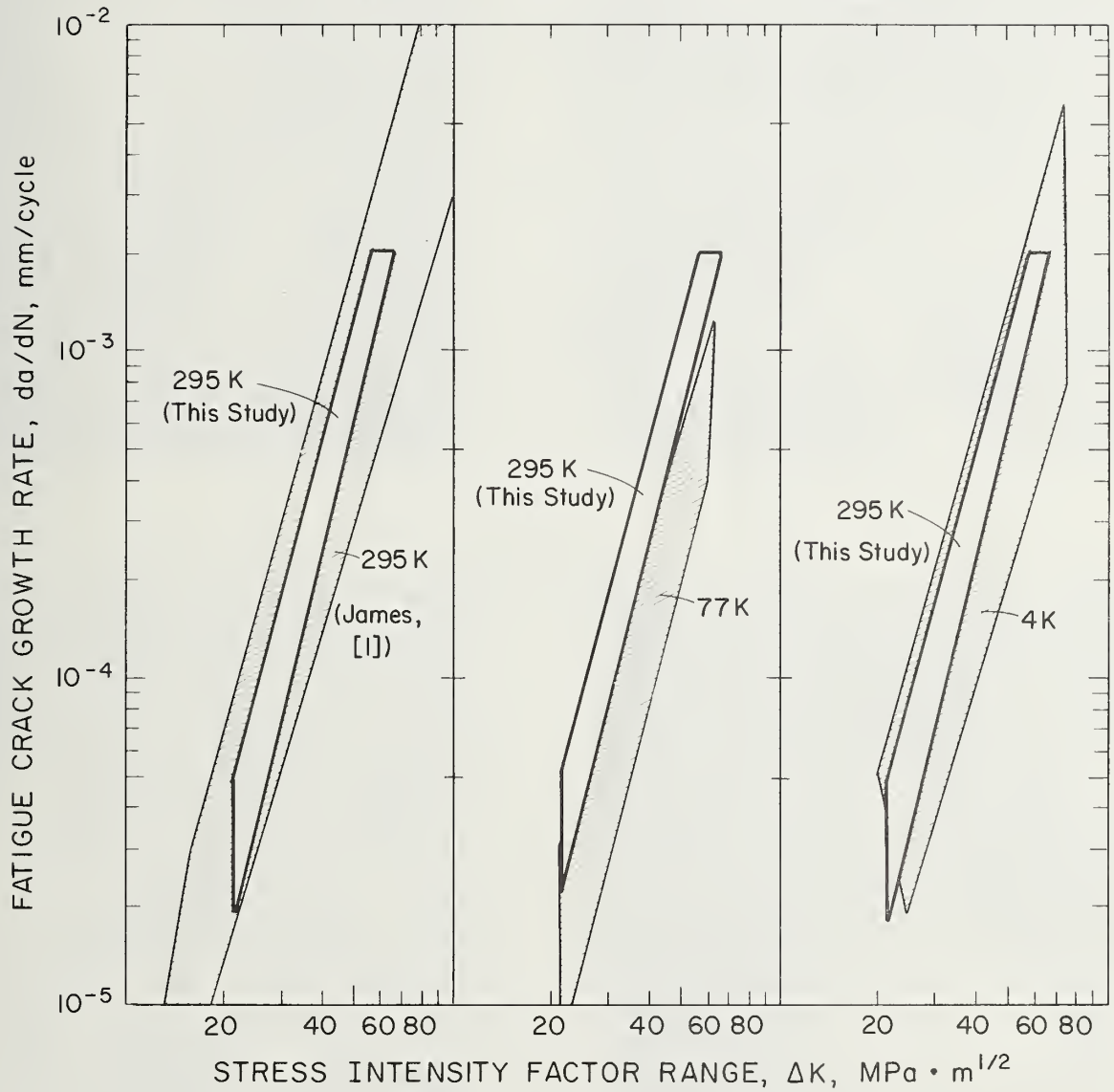


Figure 3. General comparison of da/dN vs. ΔK results.

Fe - 18Cr - 10Ni STAINLESS STEELS

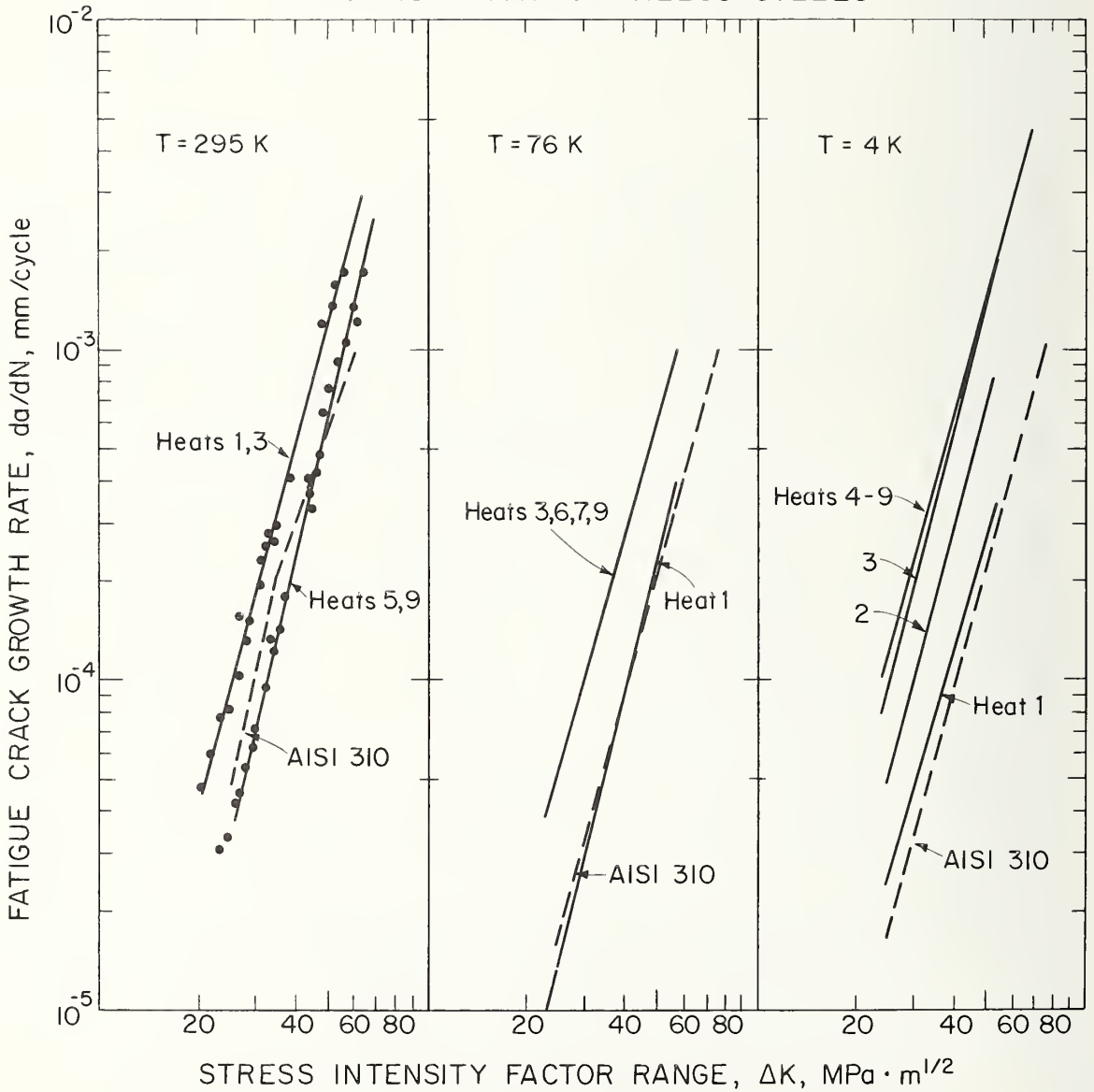


Figure 4. Fatigue crack propagation behavior as a function of interstitial C+N contents with temperature as a parameter.



heat 9



AISI 310



heat 1



heat 1

Figure 5. SEM views of the partially intergranular failure modes at 295 K.



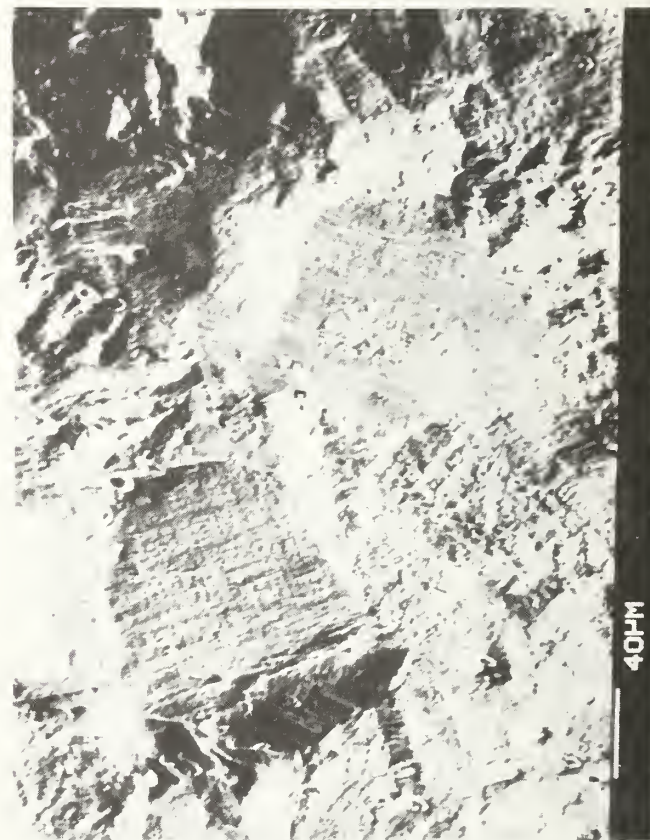
Heat 1



Heat 9



Heat 1



AISI 310

Figure 6. SEM views of the fatigue failure modes at 76 K, showing the transgranular (heat 1) to partially intergranular transition (heat 9).

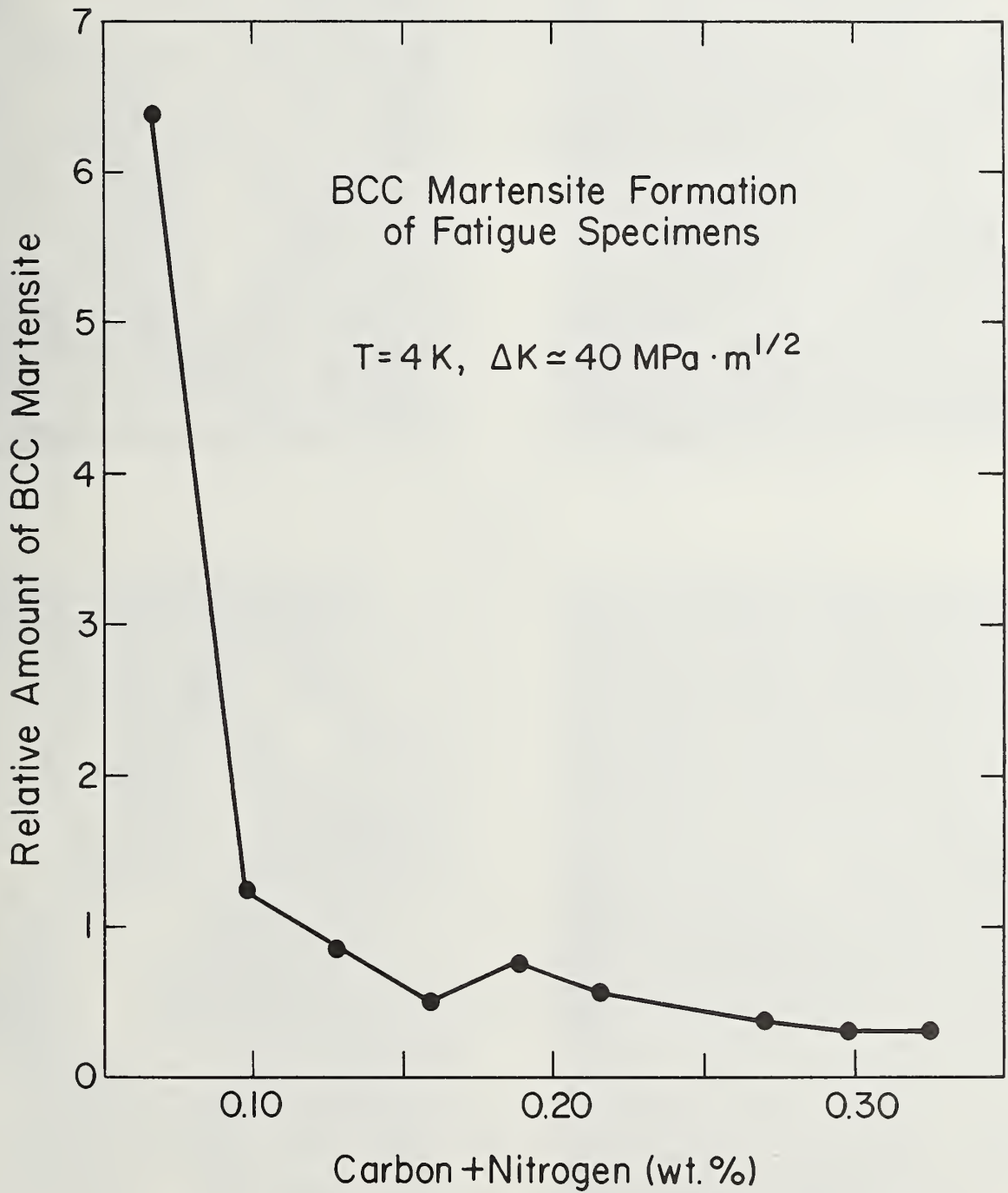


Figure 7. Relative amounts of α' (bcc) martensite formed during fatigue tests at 4 K. (Arbitrary units.)



heat 3



heat 9



heat 1



heat 5

Figure 8. SEM views of the fatigue failure modes at 4 K, showing the transgranular to partially intergranular transition.

Fe-18Cr-10Ni STAINLESS STEELS

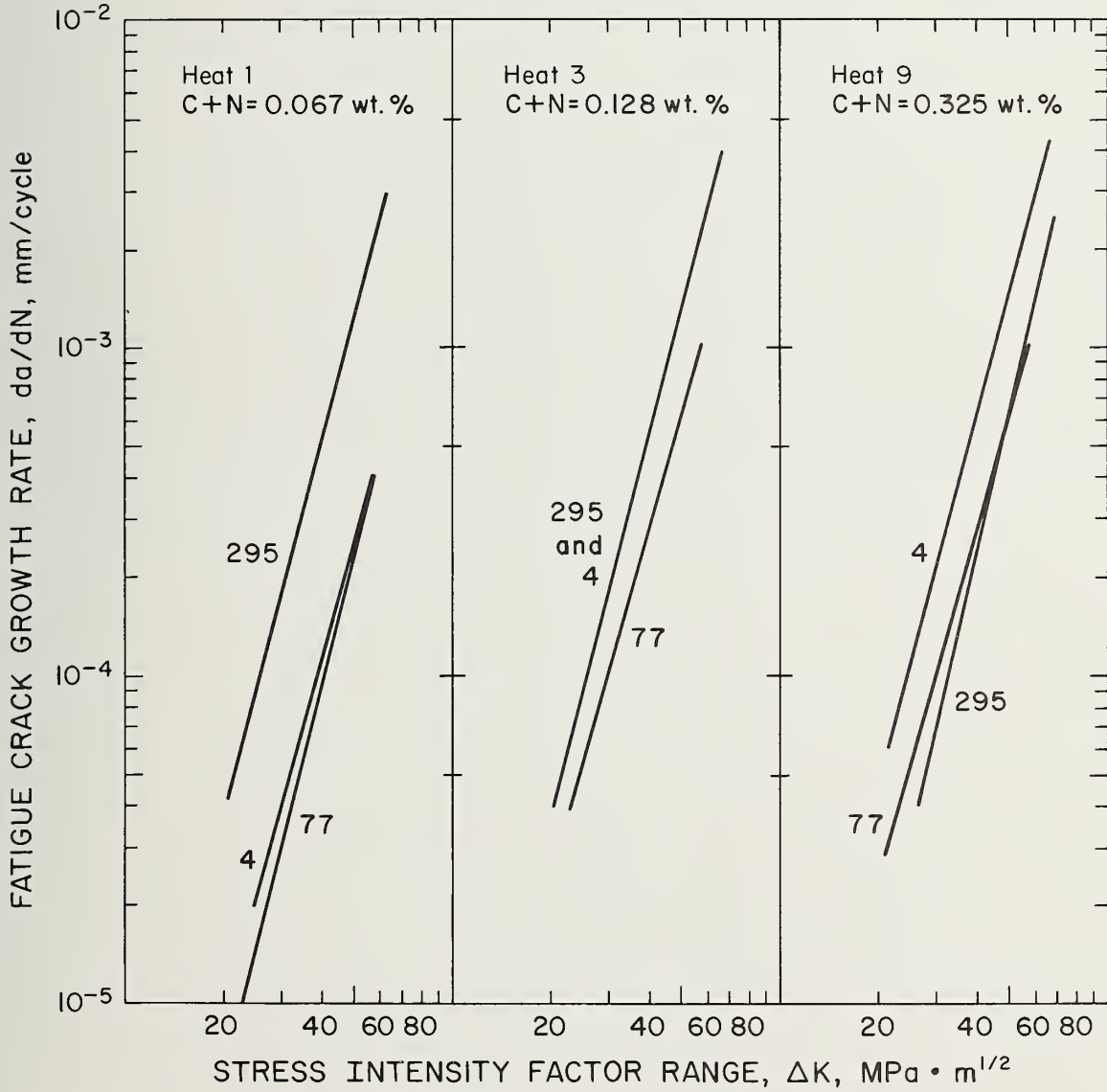


Figure 9. Fatigue crack propagation behavior as a function of temperature, with interstitial C+N contents as a parameter.

ANOMALOUS YIELDING, TRANSFORMATION, AND RECOVERY EFFECTS IN
AISI 304L STAINLESS STEELS

R. L. Tobler, D. H. Beekman, and R. P. Reed
Fracture and Deformation Division
National Bureau of Standards
Boulder, Colorado

ABSTRACT

Experiments describing the temperature dependence of yielding and anomalous stress-strain behaviors of metastable AISI 304L stainless steels were performed. In these steels transformation to α' bcc martensite can be induced by thermal cycling or creep at stresses significantly lower than those required to form α' by simple monotonic tensile loading. A recovery phenomenon is observed for tensile specimens unloaded and warmed to 295 K after plastic strain at 76 K.

INTRODUCTION

Austenitic stainless steels have a metastable face-centered cubic structure (γ). But at room temperature and below both body-centered cubic (α') and hexagonal close-packed (ϵ) structures form during cooling, under applied elastic stress, or during plastic deformation. In the commercial grades of Fe-18Cr-8Ni the martensitic phase transformations may occur during service, depending on alloy content, service temperature, stress history, and metallurgical condition.

Various physical and mechanical property changes occur in conjunction with martensitic transformation in austenitic stainless steels. The most significant consequences of transformation are volumetric expansion (about 2%), magnetic transition from paramagnetic (γ) to ferromagnetic (α'), and mechanical property changes.

In the Fe-Cr-Ni austenitic steels, the martensitic transformation is believed to be responsible for anomalous temperature dependence of the flow strength. Suzuki et al. [1] have suggested that the transition to ϵ is responsible for flow strength decreases at lower temperatures, whereas Olsen and Azrin [2] have produced data that suggest a strong correlation of the decline of flow strength at low temperatures with α' martensite. There are other ramifications of the role of martensitic transformation in plastic deformation of austenite. This paper suggests that thermal cycling and creep behavior are significantly influenced. In particular, preliminary data are presented that suggest that austenitic alloys do creep at low temperatures and that thermal cycling (76-295 K) serves to alter the creep rate.

EXPERIMENTAL PROCEDURE

The materials studied are AISI 304L stainless steels. One of these steels had been previously tested [3]. The second steel has the following composition in weight percent: Fe-18.3Cr-10.1Ni-1.57Mn-0.021P-0.019S-0.50Si-0.20Mo-0.21Cu-0.028C-0.039N. This steel was obtained as a 25-mm-thick plate, having an average grain diameter of 85 μm and a Rockwell hardness of $R_B 74$.

All tests were performed on dog-boned specimens 2.54 x 4.77 mm in cross section, 50.8 mm in gage length, and transversely oriented with respect to the plate rolling direction. Conventional tensile tests used a universal test machine at a crosshead rate of 8.47 $\mu\text{m/s}$. Creep and thermal cycling tests were conducted using a servo-hydraulic test machine in load control.

Clip gage extensometers and inked scribe lines were used to measure strain. Test temperatures were achieved using liquid helium (4 K), liquid nitrogen (76 K), or a vapor cooling system [3].

In thermal cycling and stress tests, the specimens were loaded to a specified stress at 295 K, cooled to 76 K in a Dewar of nitrogen, and then warmed to 295 K in a jet of air after removing the Dewar. This procedure was repeated 10 times in about 0.5 h.

The amount of body-centered cubic (α') martensite formed after various tests was measured using a spring-loaded magnetometer. Five magnetometer readings spaced across the gage length were taken on opposite sides of the specimen, and averaged. The accuracy of the α' martensite determination is estimated at $\pm 0.02\%$. The magnetic readings had been previously associated with volume percent of the α' , a ferromagnetic phase [2].

RESULTS AND DISCUSSION

Tensile yield strength

Yield strength data for AISI 304L stainless steels are plotted as a function of temperature in Fig. 1. A regular trend is expected for stable austenitic stainless steels, whereas the data for AISI 304L demonstrate an irregular temperature dependence: the yield strength increases between 295 and 200 K, then decreases between 200 and 100 K, and finally increases again between 100 and 4 K. The present results follow the trend of Read, Reed, and Schramm [3], who tested a slightly stronger heat (higher carbon content).

Owing to the anomalous behavior demonstrated in Fig. 1, the 76-K yield strength of AISI 304L is only 40 MPa higher than at 295 K. For the thermal cycling and creep experiments described below, this means that for a given applied stress, σ_a , there is not a great difference between the applied stress to yield strength ratio (σ_a/σ_y) at 295 and 76 K.

Behavior during the initial stage of plastic deformation is illustrated by the stress-strain curves shown in Fig. 2 for the steel of reference 3. During the first few percent of plastic strain, the AISI 304L curves at different test temperatures cross over one another. This cross-over behavior is not evident in stress-strain curves for stable stainless steels, such as AISI 310. Stable stainless steels remain completely austenitic in structure, and the elastic moduli and flow strengths at a given strain progressively increase as test temperature is lowered. In contrast, the metastable AISI 304L steel stress-strain curves exhibit early departures from linear elasticity at 100 K (and also at 76 K), so that the proportional limit is lower at

these temperatures than at 199 K. In a study of Fe-18Cr-10Ni stainless steel, an observed decrease of the proportional limit between 243 and 76 K was attributed to ϵ martensite transformation [1]. In these steels, ϵ forms first, followed by α' . Yet strain-induced α' phase transformation was confirmed in the present tests of AISI 304L (see Table 1), and Olsen and Azrin [2] have shown a strong correlation between the stress to initiate α' and σ_y . Furthermore, the higher strain-hardening rates at larger strains have always been correlated with α' formation; in this range of the stress-strain curve the volume fraction of α' is linearly related to strain. Hence at strains above 0.011 for this alloy, there is the gradual transition to a monotonic temperature dependence of flow strengths. Clearly, there is currently conflicting evidence regarding the roles of ϵ and α' on flow strength. The evidence suggests a dual role or possible dual product form for α' : at low strains α' forms at slipband intersections and acts as a "window" for cross-slip, and at higher strains the α' forms within slipbands and acts as a dislocation or deformation barrier.

Creep

Application of a constant stress at constant temperature (76 K) resulted in isothermal martensitic transformation and elongation of AISI 304L specimens. It has been reported that creep occurs in AISI 300 series steels at temperatures as low as 20 K [5]. The purpose of our creep tests was to obtain observations at 295 and 76 K to aid interpretations of the thermal cycling tests described later.

Figure 3 shows a series of creep tests performed at three temperatures. No creep occurred at 4 K at the stress levels indicated, but

significant creep occurred at 76 and 295 K. The creep at 76 K was accompanied by α' martensite formation, as indicated in Table 1.

Thermal cycling at constant stress

One AISI 304L specimen was thermally cycled 10 times between 295 and 76 K with no externally applied stress, but no measurable amount of α' formed. Two additional specimens were thermally cycled 10 times while constant stresses of 100 or 200 MPa were applied. A stress of 100 MPa falls in the elastic region, whereas a stress of 200 MPa causes a small plastic strain of 0.0005. Measurable α' martensite formed in both specimens and there was also a significant elongation of the specimens. As shown in Table 1, greater elongation and martensitic transformation occurred in the specimen at 200 MPa, but the ratio of percent α' martensite to elongation was a factor of three higher for the specimen held at 100 MPa.

The thermal cycling test at 200 MPa took 0.5 h to complete. In comparison, more α' phase transformation and specimen extension resulted from thermal cycling (295 to 76 K) at constant stress than from the 0.5-h, 76 K creep test at the same stress level. However, the ratio of α' to specimen strain was reduced when thermal cycling was combined with creep at 200 MPa (Table 1).

Recovery at room temperature

Figure 4 illustrates a novelty discovered in our tests. The usual strain-hardening behavior for an austenitic stainless steel is depicted by data from specimen 1, which was monotonically loaded in tension at 76 K. Specimen 2 was (1) cooled to 76 K, (2) strained into the plastic range, (3) completely unloaded, (4) warmed to 295 K, (5) cooled to 76 K,

and (6) reloaded at 76 K. The stress-strain curve on reloading at 76 K diverges from the previous unloading line, and plastic flow resumes at a lower stress than expected. In essence, the strain-hardening of the previous loading cycle is partially erased by the intermediate thermal cycle (76 to 295 to 76 K) at zero stress. The proportional limit, observed on each reloading, remains nearly equivalent with each thermal cycle and this can be repeated for a number of cycles.

The effect is apparently linked with microstructural instability. When the same experiments were repeated using metastable AISI 316 and stable AISI 310 steels, the anomalous behavior was observed for metastable AISI 316, but not for stable AISI 310. Therefore, to observe the effect it is necessary (1) to have a metastable steel and (2) to include the thermal cycle to 295 K and back to low temperature.

After a total elongation of 5%, specimen 1 (monotonic loading) contained 5% α' martensite, whereas specimen 2 (repeated stress and thermal cycling) contained 6% α' martensite. This tends to confirm the suspicion that α' martensite forms during each loading cycle at about the same stress level and that warming to room temperature provides sufficient internal recovery to permit additional α' transformation. However, this explanation does complicate the earlier proposed concept that early α' transformation occurs at cross-slip sites, where sufficient dislocation pile-up stresses are presumably generated to induce transformation. Under such circumstances, recovery would not be expected to encourage transformation.

SUMMARY

The results of experiments on metastable AISI 304L stainless steels are:

1. Significant creep occurs at 295 and 76 K, but not at 4 K, at the stress ranges studied.
2. Thermal cycling between 295 and 76 K serves to increase the creep rate.
3. Warming to room temperature produces limited recovery after tensile deformation at 76 K.
4. The role of α' and ϵ martensite transformations in the deformation processes remains unclear.

ACKNOWLEDGMENT

The assistance of D. Baxter of NBS in performing tensile tests is gratefully acknowledged.

REFERENCES

1. Suzuki, T., Kojima, H., Suzuki, K., Hashimoto, T., Koike, S., and Ichihara, M., Plastic deformation and martensitic transformation in an iron-base alloy, Scr. Metall. 10 (1976), pp. 353-358.
2. Olsen, G. B. and Azrin, M., Transformation behavior of TRIP steels, Metall. Trans. A, 9A (1978) 713-721.
3. Read, D. T., Reed, R. P., and Schramm, R. E. (1979), Low temperature deformation of Fe-18Cr-8Ni steel, Metall. Trans. (to be published).
4. Reed, R. P. and Mikesell, R. P., The stability of austenitic stainless steels at low temperatures as determined by magnetic measurements, in Advances in Cryogenic Engineering, Vol. 4, K. D. Timmerhaus, ed. (Plenum, New York, 1960), pp. 84-100.

5. Voyer, R. and Weil, L., Creep properties of 18-10 and 25-20 stainless steels at cryogenic temperatures, in: Advances in Cryogenic Engineering, Vol. 10, K. D. Timmerhaus, ed. (Plenum, New York, 1965), pp. 110-116.

Table 1. Summary of test results.

Test Performed	Spec. No.	Temperature (K)	Stress (MPa) *	Time (h)	α' Martensite (%)	Total Elongation (%)	% α' /Total Elongation
Monotonic loading	X	295	220	NA	0.0	0.2	0
Monotonic loading	16	76	200	NA	0.06	0.05	1.2
Monotonic loading	1	76	237	NA	0.0	0.2	0
Creep only	12	295	200	0.5	0.00	0.34	0
Creep only	14	76	200	0.5	0.09	0.11	0.8
Thermal cycles, constant σ	2	295/76	0	NA	0.00	0.00	0
Thermal cycles, constant σ	8	295/76	100	0.5	0.07	0.04	1.75
Thermal cycles, constant σ	4	295/76	200	0.5	0.15	0.29	0.52

*To convert from MPa to ksi, divide by 6.895

LIST OF FIGURES

- Figure 1. Yield strength of AISI 304L stainless steels, showing irregular temperature dependence.
- Figure 2. Stress-strain curves for AISI 304L steel, showing cross-over behavior.
- Figure 3. Creep test results for AISI 304L at three temperatures.
- Figure 4. Stress-strain curves for AISI 304L specimens illustrating recovery effect after unloading and warming to 295 K.

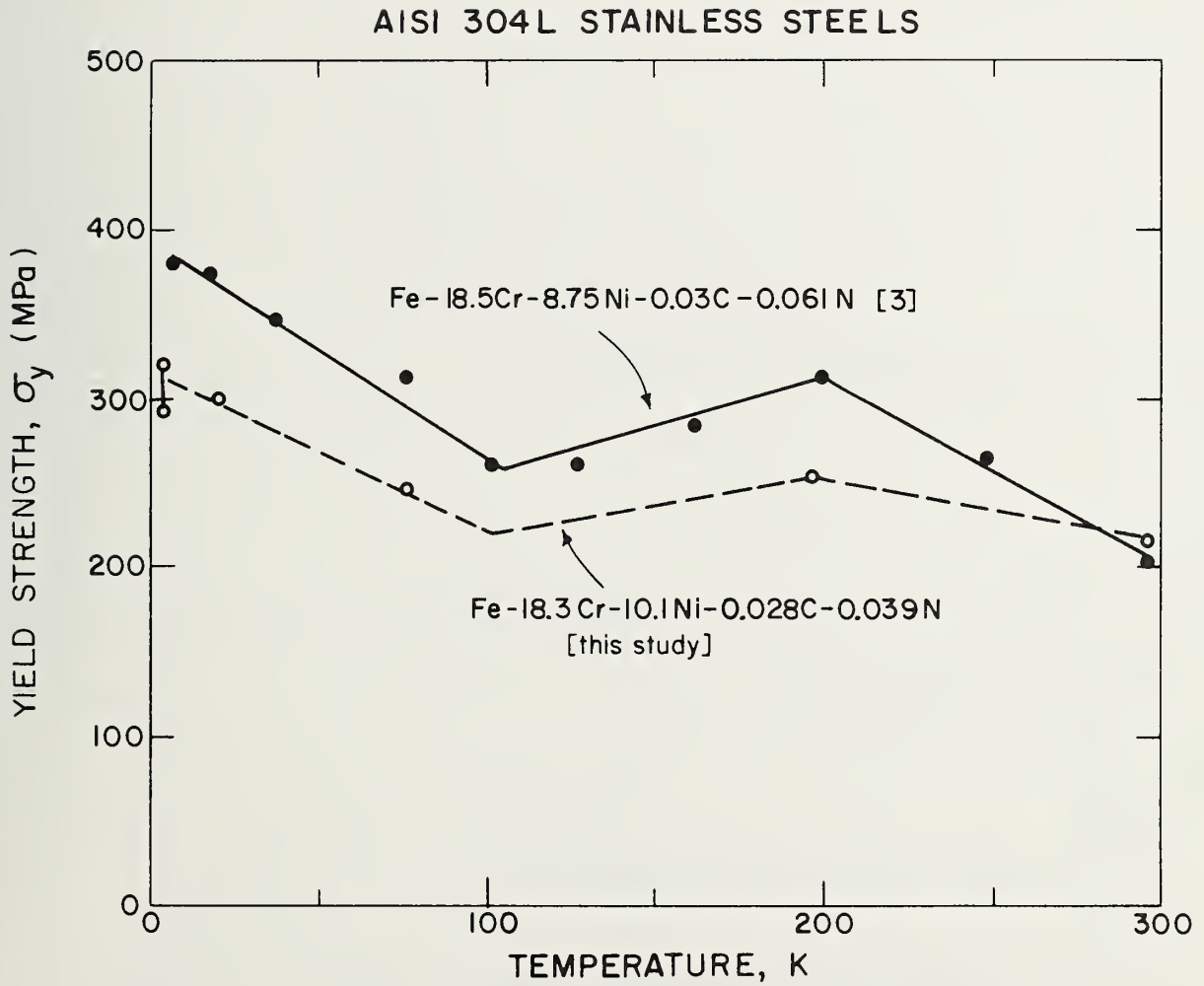


Figure 1. Yield strength of AISI 304L stainless steels, showing irregular temperature dependence.

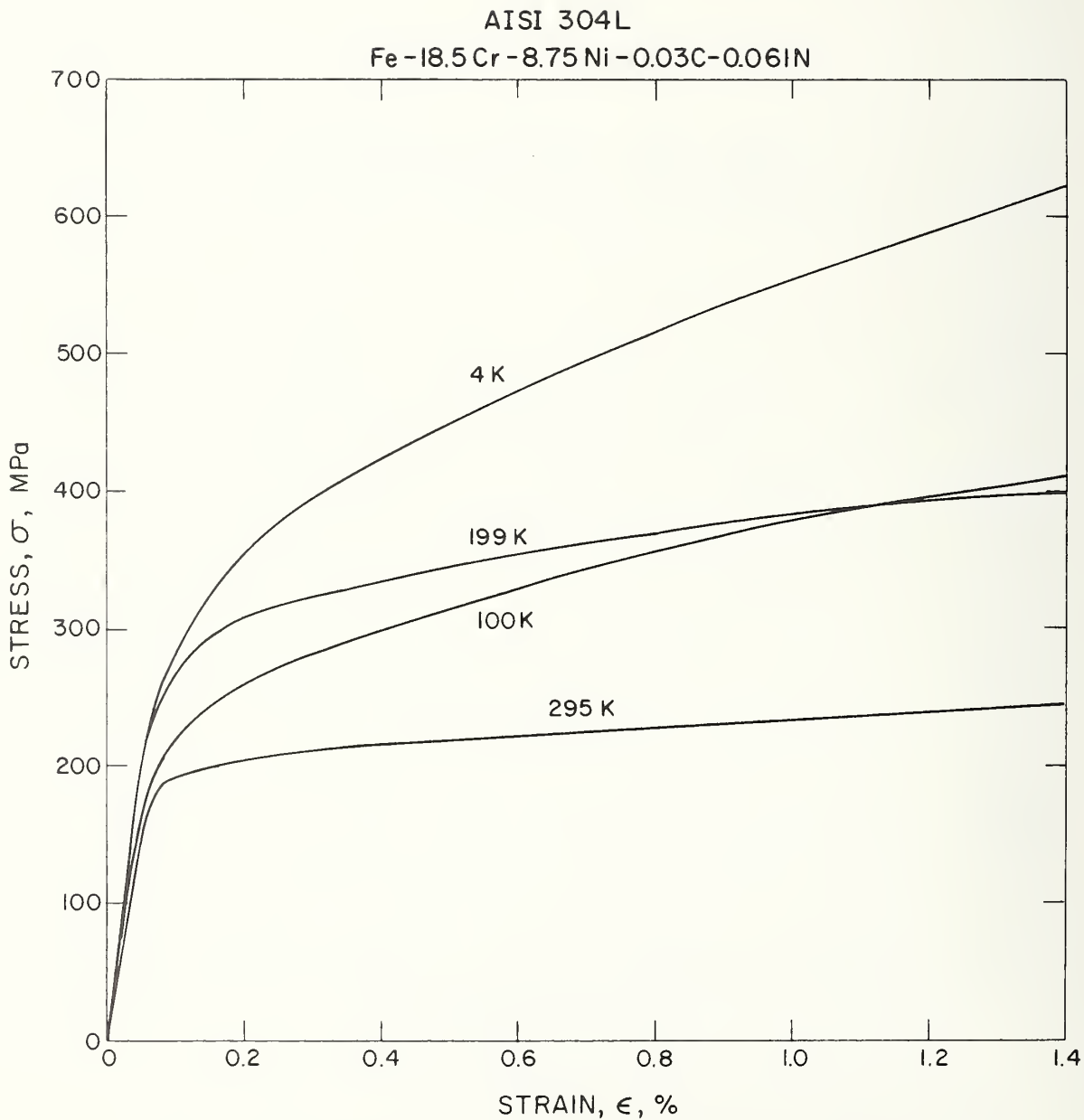


Figure 2. Stress-strain curves for AISI 304L steel, showing cross-over behavior.

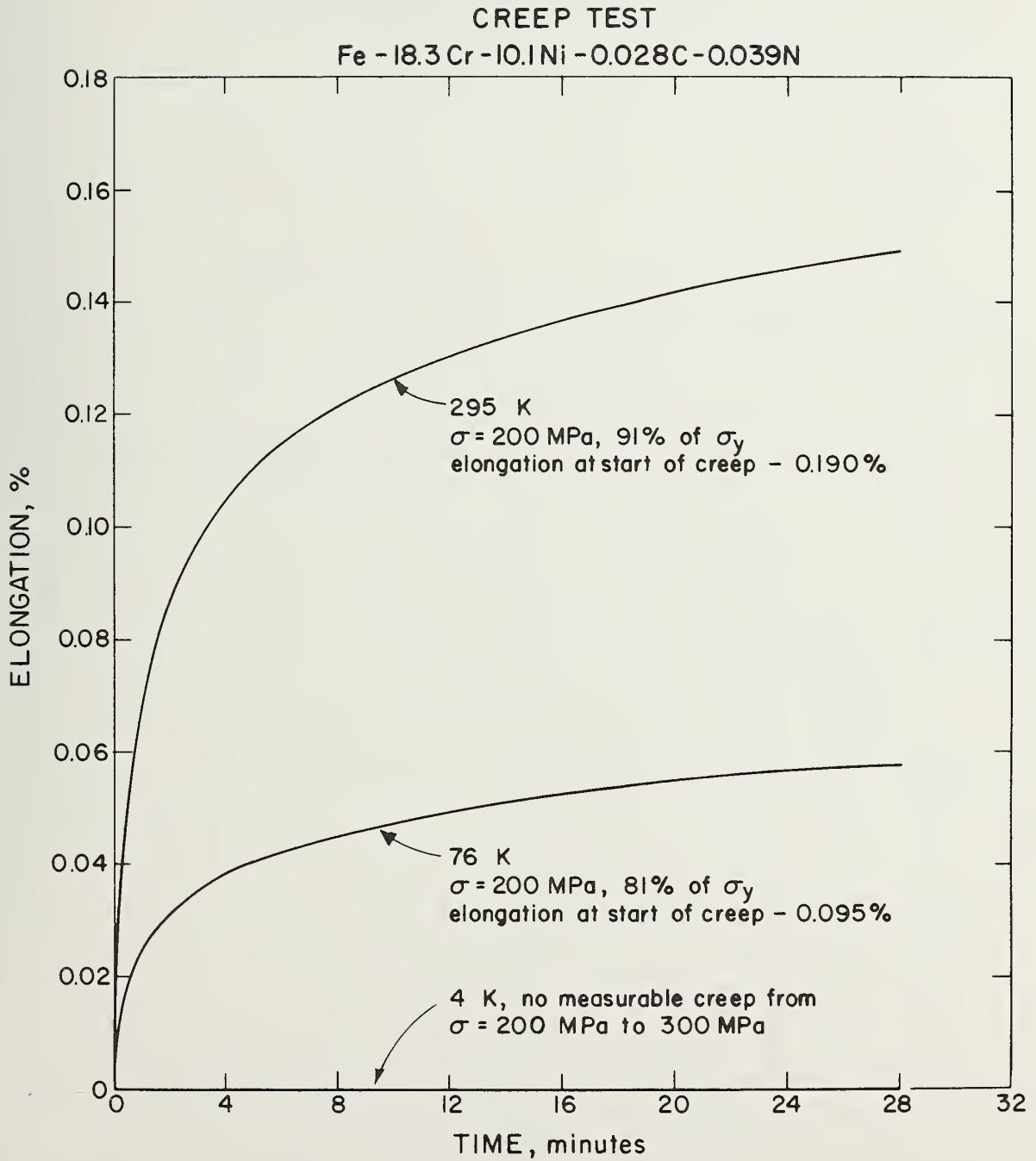


Figure 3. Creep test results for AISI 304L at three temperatures.

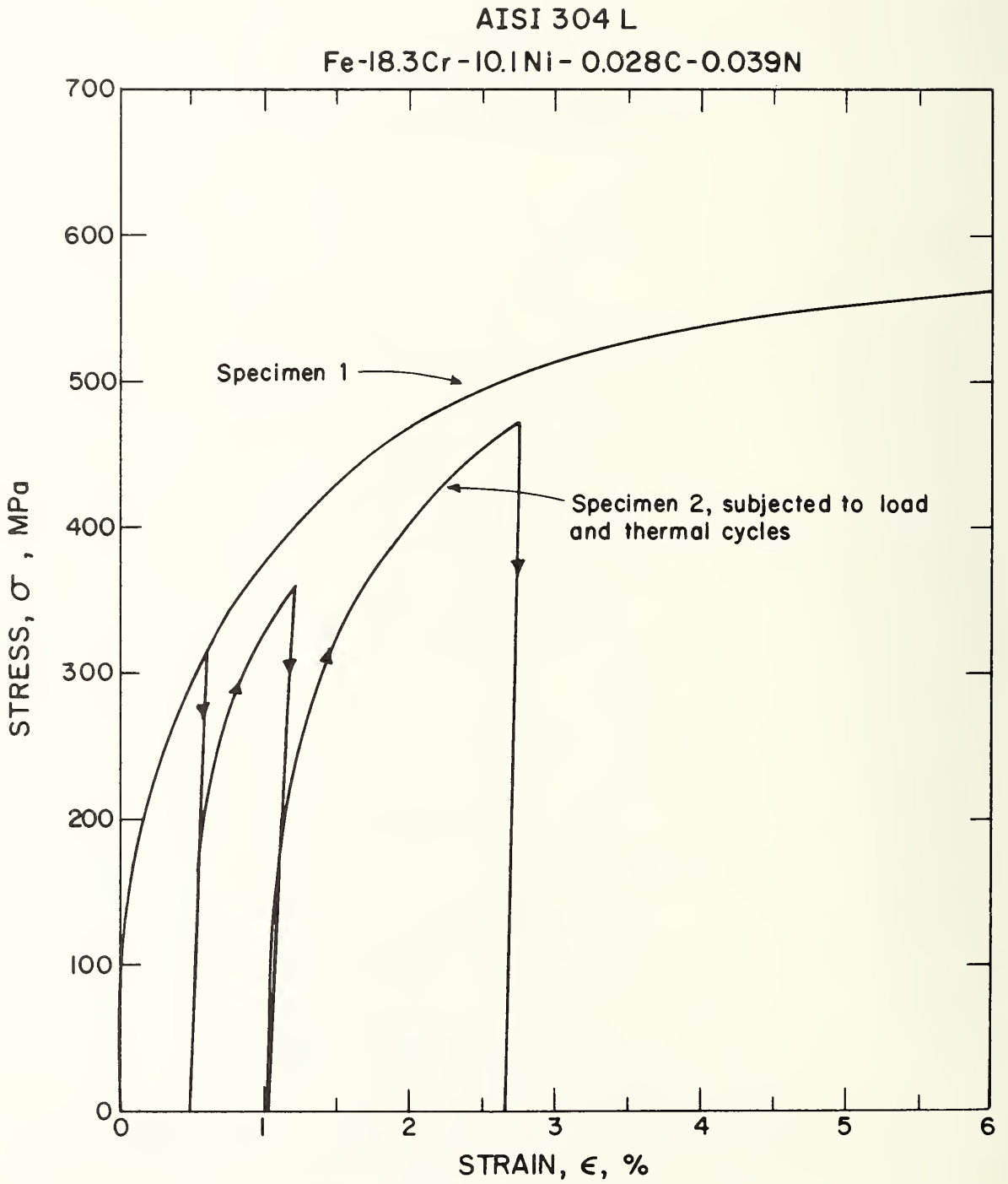


Figure 4. Stress-strain curves for AISI 304L specimens illustrating recovery effect after unloading and warming to 295 K.

LOW-TEMPERATURE DEPENDENCE OF YIELDING IN AISI 316 STAINLESS STEELS

R. L. Tobler and R. P. Reed
Fracture and Deformation Division
National Bureau of Standards
Boulder, Colorado

ABSTRACT

Tensile tests at temperatures between 323 and 4 K were performed on one heat of AISI 316 austenitic stainless steel having the composition Fe-17.34Cr-12.17Ni-1.55Mn-2.16Mo-0.051C. The temperature dependences of the yield and flow strengths at plastic strain increments from 0.2 to 3.65% are analyzed. At the yield strain (0.2%), no body-centered cubic (bcc) martensite phase transformation is detected. At higher strains ($\sim 3.2 \pm 0.6\%$), bcc martensite forms from the parent austenite phase at test temperatures below 190 K, but there are no discontinuities in the temperature dependence of flow strength. A review of data available for three heats of AISI 316 at temperatures between 973 and 4 K reveals that deviations from thermally activated plastic flow theory occur at temperatures below 175 K, apparently depending on heat-to-heat compositional variations. Grain size and magnetic transition effects on the yield strength are discussed.

INTRODUCTION

The mechanical behavior of austenitic stainless steels over a broad range of temperatures is a subject of interest to designers of superconducting and nuclear energy devices. In this paper, the initial yielding and stress-strain behavior of AISI 316 stainless steel are described. AISI 316 stainless steel is a metastable Fe, 16-18Cr, 10-14Ni steel that may undergo a partial austenite-to-martensite phase transformation at low temperatures, the probability of which increases with increasing strain, decreasing temperature, and decreasing alloy content.

Previous studies of Fe-Cr-Ni austenitic stainless steels show that two martensitic phases may be formed: the hexagonal close packed (hcp) ϵ martensite and the body-centered cubic (bcc) α' martensite. The ϵ phase usually forms first; then α' appears [1]. The α' phase is ferromagnetic and easy to detect using a magnetometer [2]. For AISI 316, it is reported that no α' forms spontaneously on cooling to 4 K, but up to 50% α' forms on straining to failure at 4 K [3].

There is apparently conflicting evidence on the role of martensitic phase transformation in affecting the low temperature flow behavior of metastable stainless steels. Suzuki et al., [4] measuring the temperature dependence of the 0.2% offset yield strength in an Fe-18Cr-9Ni stainless steel, report a significant decrease in flow strength when the test temperature is lowered from about 260 K. They argue that ϵ martensite forms first, following an inverse stress dependence at lower temperatures, which results in reduced flow strength. Following ϵ martensite formation, α' martensite forms at slip plane intersections and

the α' lathes along $\langle 110 \rangle$ act as windows for dislocation pileup release; the result is an "easy glide" region of the stress-strain curve. This "easy glide" region had previously been reported by Reed and Guntner [5], who argued that it was caused by strain-induced ϵ martensite, since their x-ray and transmission electron microscopy data for an Fe-18Cr-8Ni alloy indicated an increasing concentration of hcp during easy glide. However, Olson and Azrin [6], studying an Fe-9Cr-8Ni alloy, found an excellent correlation between flow strength reduction at lower temperatures and the initiation of α' martensite. No "easy glide" region of the stress-strain curve was observed.

The effect of grain size on low-temperature flow strength of austenitic stainless steels has not been documented. The characterization of grain size effects is significant in the design of strong and tough steels for low-temperature applications.

Soviet authors [7,8] report the existence of three major anomalies in the temperature dependence of the yield strength for Fe-18Cr-xNi austenitic stainless steels containing 8, 10, or 20% Ni. These anomalies amount to sharp decreases of the yield strength on the order of 100 MPa. The first anomaly occurs between 20 and 4 K and is unexplained. The second anomaly occurs at temperatures between 60 and 35 K and is attributed to the Néel transition (magnetic ordering). The third anomaly occurs in metastable alloys (lower Ni) at temperatures just above the M_S temperature and is attributed to strain-induced martensitic phase transformations. Clearly, continuous flow-strength measurements as a function of temperature should be made to assess these results. Therefore, tensile tests were conducted on a grade of AISI 316 austenitic stainless steel to assess the influence of martensitic transformation, grain size, magnetic transitions, and very low temperature on flow strength.

MATERIALS

The AISI 316 stainless steel tested in this study was purchased in the form of a 38-mm-thick plate. Tensile specimens were machined in the longitudinal orientation in the form of flat coupons having a 50.8-mm gage length and a 2.54- x 4.77-mm-gage cross section. After the specimens were annealed at 1338 K for 0.5 h, they had a Rockwell B (R_B) hardness of 71 and an average grain diameter of 55 μm (ASTM grain size number 5.5). The chemical compositions of this steel (denoted heat 2) and other AISI 316 steels referred in this paper [9-11] are listed in Table 1.

PROCEDURE

Tensile tests were performed on (1) annealed and (2) strained and recrystallized material. The strained and recrystallized material was used to determine grain size effects. All tensile tests were performed at a crosshead rate of 8.5 $\mu\text{m/s}$ using a screw-driven machine and cryostat [1,12]. Test temperatures of 4 and 76 K were achieved with baths of liquid helium and liquid nitrogen. Other temperatures were achieved by controlled thermal conduction using liquid nitrogen reservoirs and heating wires attached to the specimen grips and load train. Current to the heating wires was varied until thermal equilibrium was reached at the specified test temperature, which was accurate to ± 1.5 K. Load-versus-deflection curves were recorded with a commercial load cell and clip-gage extensometer.

Clip-gage extensometers magnify the specimen strain and permit measurement of only the specimen strain within the (2.5-cm) gage length. Estimated flow strength measurement inaccuracies are $\pm 2\%$, but low-temperature specimen-to-specimen variations (including both material and

measurement variations) may reach $\pm 7.5\%$. After plastic strains of 0.2 to 3.65% the specimens were unloaded, warmed to 295 K, and examined for the presence of ferromagnetic α' martensite with a torsion-bar magnetometer [2]. X-ray diffractometer measurements were used to try to detect small concentrations of ϵ martensite. No ϵ martensite was detected and our estimated sensitivity is 2%. The stress-strain curves were calculated in the conventional manner, and the measurement uncertainty of flow strength values is not greater than 3%. As an indication of data scatter, seven tests were performed on the AISI 316 steel at 76 K, resulting in an average yield strength (σ_y) of 448 MPa and an overall spread of ± 7 MPa.

Grain size variations were obtained by recrystallization treatments. Tensile specimens were plastically strained 20 to 30% at 295 or 76 K and then annealed for 0.25 to 0.5 h in an argon atmosphere at 1233 to 1573 K. These treatments produced grain sizes ranging from 22 to 140 μm . Subsequent to recrystallization treatments, the specimen surfaces were cleaned by electropolishing. The recrystallization treatments increased the scatter of yield strength measurements to about ± 15 MPa.

TENSILE YIELD STRENGTH RESULTS

The tensile yield strength (σ_y) and initial stress-strain behavior of the Fe-17Cr-12Ni-2Mo alloy were measured as a function of temperature, grain size, martensitic transformations, and magnetic transitions. These effects are described in this section.

Temperature: As listed in Table 2, twenty-six σ_y measurements were obtained for annealed AISI 316 stainless steel (heat 2) at seventeen temperatures between 323 and 4 K. Magnetometer inspections of the

specimens indicated no α' martensitic transformation for this heat after 0.2% plastic strain, regardless of test temperature. The σ_y data between 295 and 4 K are plotted and compared with previously published data [9,10, 13-16] in Fig. 1. This comparison reveals significant heat-to-heat variations of σ_y , with considerably greater differences at cryogenic temperatures than at room temperature.

Several references cited in Fig. 1 report data at only a few test temperatures, whereas the functional dependence of σ_y on temperature can be identified only by extensive measurements performed over a broad temperature range. Therefore, data for three heats of AISI 316 are replotted in Fig. 2. These data show that σ_y increases progressively as temperature is lowered. Despite minor variations of grain size, strain rate, and composition, the σ_y values for the three heats are nearly equivalent between 973 and 175 K, where the test temperature intervals from different studies overlap. Below 175 K, significant variations of strength begin to emerge. At still lower temperatures, the variations become more obvious until, at 4 K, σ_y correlates with composition: Fe-17.25Cr-13.48Ni (heat 1) exhibits the highest strength, Fe-17.34Cr-12.17Ni (heat 2) exhibits intermediate strength, and Fe-16.72Cr-11.27Ni (heat 3) exhibits the lowest strength. This apparent association of higher strength with higher nickel content may relate to crystal structure stability as discussed below.

Thermally activated plastic flow theory predicts that σ_y should exhibit some dependence upon strain rate. A few experiments were performed on the annealed AISI 316 stainless steel to evaluate this effect. Increasing the crosshead rate by a factor of 100 from 0.85 $\mu\text{m/s}$ to 85 $\mu\text{m/s}$ increased the flow strength at strains lower than 1% by

factors of 6% at 295 K and 3% at 76 K. The effect of crosshead rate on the σ_y at 4 K was negligible. Therefore, strain rate effects do not play a significant part in explaining the variability noted in Fig. 1.

Strength variations may arise between specimens from a single heat of steel owing to inhomogeneity or thermomechanical processing effects. As shown in Fig. 1, Read and Reed's data [13] for a 316 stainless steel at 295, 76, and 4 K are 5 to 17% higher compared with the results of Tobler, Reed, and Burkhalter [9], who tested the same heat. In the former study, the specimens were tested in the as-machined condition, whereas the specimens used in the second study were annealed (1289 K, 1 h) after machining. This annealing step reduced the hardness at 295 K from $R_B 79$ to $R_B 75$ and lowered σ_y by increasing the grain size slightly and removing any residual cold work from the fabrication or machining processes.

An example of within-heat variability is also noted in the present study: the annealed AISI 316 steel specimens had a 76-K σ_y of 448 ± 7 MPa, whereas reprocessed (strained and recrystallized) specimens having a similar grain size ($55 \mu\text{m}$) had a 76-K σ_y of about 480 ± 15 MPa. Thus, process history influences strength. Larger scatter for the recrystallized specimens is to be expected since dislocation density and substructure within the grains depend on prior history and recrystallization temperature.

Grain Size: Figure 3 illustrates the effect of grain size on σ_y at 295, 76, and 4 K. The data at each temperature fit an inverse square root dependence on the average grain diameter, d , which is in reasonable accord with the familiar Hall-Petch equation:

$$\sigma_y = \sigma_i + kd^{-1/2} \quad (1)$$

where σ_i refers to the flow strength in the absence of grain boundaries (the "friction stress") and k is the slope of the σ_y -versus- $d^{-1/2}$ plot and indicates the grain boundary dependence of the yield strength. The values of σ_i and k are given in the figure.

Martensitic transformation: Specimens from this study were screened using a magnetometer, but no α' martensite was detected after 0.2% plastic strain. To force the phase transformation to occur, a series of specimens was loaded to higher strains. Figure 4 presents the strain dependence of α' at 76 K. Notice that a plastic strain of about 2% is necessary for α' to form at 76 K. The dependence of α' on plastic deformation is linear, and this trend continues at least to a strain of 5%. At larger strains, the dependence apparently increases since fractured specimens show between 44 and 52% α' at uniform strains of 40 to 50%.

The stress-strain curves at higher strain increments are presented in Figs. 5 and 6. The quantity of α' martensite formed after either 3.65 or 2.75% plastic strain is negligible for test temperatures between 300 and 190 K, but below 190 K, α' is formed in increasing amounts. In fact, as illustrated in Fig. 7, the percent α' martensite divided by the strain is linearly dependent on test temperature. The curves of Fig. 5 and 6 represent specimens in various states of transformation, containing from 0 to 0.1% α' martensite per unit strain. But the stress-strain curves are regular and free from discontinuities, indicating that the martensitic transformation occurs gradually with no anomalous effects. These findings contrast with the behavior of Fe-18Cr-8Ni and Fe-18Cr-10Ni stainless steels that exhibit: (1) irregular yield and flow strength

temperature dependences owing to the initiation of ϵ and α' phase transformations [7], and (2) suppression of α' martensite at 4 and 20 K, compared with that at 76 K [5].

DISCUSSION

Thermally activated flow: According to classical theory (e.g., Seeger [17]), σ_y may be separated into two components:

$$\sigma_y = \sigma_A + \sigma_T \quad (2)$$

Here σ_A is an athermal stress component determined by metallurgical structure, and σ_T is a thermal stress component governed by lattice vibrations and rate processes. By estimating from Fig. 2, the value of σ_A (uncorrected for shear modulus) for the AISI 316 steel heats 1 and 2 is taken to be 100 MPa, which is the asymptote approached by σ_y at elevated temperatures. From previous work involving thermodynamic and thermally activated plastic flow theories, the following expression was developed for σ_T :

$$\sigma_T = (\sigma_0 - \sigma_A) \exp(-CT) \quad (3)$$

Here σ_0 is the extrapolated value of the yield strength at absolute zero and C is a materials constant comprised of activation energy, entropy, and strain-rate terms. This expression derived from the work of Yaroshevich and Ryvkina, who did not correct the σ_A value for the effect of shear modulus [18].

The applicability of Eq. (3) for AISI 316 stainless steels was tested by plotting $\log(\sigma_y - \sigma_A)$ versus T . Data agreeing with Eq. (3) will produce a single straight line when graphed this way, assuming that

a single mechanism of plastic flow is operative. As demonstrated in Fig. 8, Eq. (3) successfully predicts the experimental results for the three AISI 316 steels down to 175 K, but divergences from the main trend occur for each of the three heats at 175, 150, or 30 K, depending on alloy composition. A graphical solution leads to the following expression for the AISI 316 data (heats 1 and 2) between 975 K and the temperature of divergence:

$$\sigma_y = 100 + 700 \exp(-6.2 \times 10^{-3} T) \quad (4)$$

As a consequence of divergences from the main trend, the experimentally measured 4-K σ_y values for all heats are lower than predicted by Eq. (4). If the trend lines of Fig. 8 are extrapolated, then the measured σ_y values for heats 1 and 2 at 4 K (near absolute zero) are 15 to 45% lower than the extrapolated value of σ_0 , which is 780 MPa. The data for heat 3 suggest an even greater difference.

The reasons for deviations from Eq. (4) are not completely understood. It was suggested previously that dislocation tunneling and magnetic ordering may affect σ_y at temperatures approaching absolute zero [9]. Likewise, adiabatic heating becomes significant as absolute zero is approached. But these processes alone are unable to account for the deviant behavior of AISI 316 heats 2 and 3 at temperatures in the 150- to 175-K range. Moreover, these processes do not account for the apparent sensitivity to alloy composition. As noted in Fig. 1, divergences from Eq. (4) for heats 1, 2, and 3 occur at 30, 150, and 175 K, respectively. This sequence follows the order of decreasing alloy content (Table 1), decreasing stacking fault energy (Table 3), and

decreasing crystal structure stability, as indicated by the M_S and M_D temperatures (Table 3). The possible martensite roles are discussed in the next section. It is also possible that more than one dislocation mechanism is operative, depending on temperature and composition. If a second thermally activated dislocation process becomes rate controlling at sufficiently low temperatures, the change of slopes in Fig. 5 would result.

In Figure 9, the σ_y data for the three AISI 316 stainless steels have been normalized by using the shear modulus and plotted versus test temperature, which is normalized by using the melting point, taken as $T_M = 1658$ K. Values of the shear modulus at cryogenic temperature were taken from Ledbetter [11]. These data indicate that the thermal component of σ_y becomes active at a temperature of 1/3 the melting point. A linear extrapolation of the thermal portion of the yield strength gives a value of about 300 K for the intersection of the two components. The divergences from the thermal components at low temperatures, shown in Figure 8, is also observed here.

Role of martensitic transformation: The nonlinear dependence of $\ln \sigma_T$ (Fig. 8) or σ_y on (Fig. 9) on temperature at very low temperatures may result from strain-induced martensitic transformation.

The M_S and M_D temperatures in Table 3 provide only a relative indication of stability, having been calculated on the basis of the Cr, Ni, Mn, Si, C, and Mo contents. The calculated M_S values are negative, indicating complete stability on cooling to absolute zero, which is consistent with the observation that no α' martensite formed on cooling

to 4 K. Beyond this, a quantitative comparison of the measured and calculated transformation temperatures is impractical because the calculated M_S and M_D temperatures are influenced by trace elements which are neither controlled nor analyzed during steel manufacture.

It is unlikely that the α' transformation can account for the observed deviations since no α' martensite was detected at 0.2% plastic strain. Furthermore, from Fig. 4 it is apparent that no α' is expected to form until a plastic strain of about 2% is reached. However, it is possible that martensitic transformations producing small amounts of ϵ phase may be responsible. From Table 3, the calculated stacking fault energies decrease, but remain positive, with increased deviation of σ_y from linearity. This possibility could not be confirmed, since our metallographic and x-ray inspection methods lacked the required sensitivity to detect a small amount (< 2 %) of ϵ .

In the commercial Fe-18Cr-8Ni austenitic stainless steel grade (AISI 304), the α' martensitic product and, perhaps, the ϵ martensitic product apparently contribute to the anomalous temperature dependence of σ_y and to the "easy glide" portion of the stress-strain curves at temperatures near 77 K [4,5,23]. However, the data represented in Figs. 4-7 suggest that in the alloy of this study (Fe-17Cr-12Ni-2Mo) the temperature dependence of the flow strength (including σ_y) is well behaved and the α' martensitic product, therefore, does not contribute to anomalous behavior.

The nature of the linear relationship between the "normalized" percent bcc martensite (percent magnetic martensite divided by engineering plastic strain) and temperature deserves additional experimental

clarification. It is implied that the temperature of about 190 K represents the onset of strain-induced martensite, and at higher strains and temperatures little magnetic product phase is detected. This behavior has been substantiated by the tests to fracture at 195 and 295 K. However, the nature of the probable family of curves, generated by taking data at larger strains, is not clear. Similar data for AISI 304 steel indicate a gradual deviation from linearity at larger strains, but the existence of a constant temperature of α' initiation [24].

With respect to the role of martensitic products in affecting the temperature dependence of the flow strength of Fe-Cr-Ni alloys at low temperatures, there are two schools of thought: Suzuki et al. [4] argue that the ϵ phase must be responsible for the reduction of σ_y at low temperatures since in their study α' martensite was detected at strengths considerably greater than σ_y . Additionally, they have argued from optical metallography evidence that ϵ martensite forms at strength levels near the measured σ_y . Conversely, Olson and Azrin [6] studied a less stable Fe-9Cr-8Ni alloy and obtained excellent correlation between the temperature dependence of σ_y and the flow strength at which α' martensite was first detected. From the results of this study, it is apparent that the onset of α' strain-induced martensite in austenitic Fe-Cr-Ni alloys does not lead to a reduction of the flow strength at low temperatures. This finding, again, raises the question of the nature of the α' , ferromagnetic martensitic product or products that form(s) during plastic deformation. Conflicting parametric studies and lack of conclusive microscopy preclude assessment of the role of ϵ and α' martensites in affecting low temperature flow strength.

Role of grain size: Data on the effect of grain size for austenitic stainless steels are rare. The present data at room temperature indicate a very slight effect, as evidenced by the low- k value of $191 \text{ MPa} \cdot \mu\text{m}^{-1/2}$. This value is in agreement with the $221 \text{ MPa} \cdot \mu\text{m}^{-1/2}$ value obtained by Norstrom [25] for a 316L stainless steel containing no nitrogen. Low- k values are typical for face-centered cubic alloys at room temperature. At cryogenic temperatures, however, the grain size effect increases significantly. As shown in Fig. 3, the values of σ_i and k at 4 K are greater by factors of 2 and 5, respectively, than the values at 295 K.

In Fig. 10, the temperature dependences of k and σ_i from Eq. (1) are plotted, using the 4- to 295-K data from this study and the 295- to 875-K data of Norstrom [25]. The k is strongly temperature-dependent at low temperatures, but insensitive to temperature above room temperature. The frictional stress, σ_i , increases with decreasing temperature and the $\ln \sigma_i$ is linearly dependent on $T(\text{K})$ for temperatures lower than about 500 K. These data clearly imply that grain size has a significant effect on low-temperature flow strength. From Fig. 10, the quantity $\sigma_y - \sigma_i$ represents the grain boundary contribution to flow strength and about 30% of σ_y at 4 K is contributed by grain-boundary strengthening.

Role of magnetic transition: Similar to other Fe-Cr-Ni austenitic stainless steels, AISI 316 undergoes a magnetic ordering phenomenon characterized by a change from the paramagnetic to the antiferromagnetic state at low temperatures. Accordingly, a peak occurs in the temperature dependence of magnetic susceptibility at T_N , the Néel transition temperature, which corresponds to the onset of antiferromagnetic ordering. Since a decrease of elastic constants occurs at T_N [26,27], it

was suggested that the Néel transition likewise affects dislocation motion and hence tensile properties [7,8]. On the basis of Soviet experimental data [7,8], a sharp decrease of σ_y of about 100 MPa should be expected for our Fe-18Cr-12Ni alloy at temperatures between 60 and 48 K. As shown in Fig. 11, elastic property measurements for Fe-17.5Cr-12.9Ni stainless steel do reveal a noticeable drop in Young's modulus (E), identifying the Néel transition between 40 and 20 K. From Table 3, the calculated predicted value of T_N is 26 K, but the data of Fig. 11 indicate no decrease of σ_y at temperatures corresponding to T_N . From Table 3, T_N values for the three AISI 316 steels of Fig. 8 are nearly equivalent, despite minor compositional differences.

Care must be exercised in these arguments, however. The approximate reduction of E after magnetic transition is about 2%, which is within the possible σ_y data variation. For better assessment, the large grain size contribution should be subtracted from σ_y , and σ_i be examined carefully as a function of temperature.

SUMMARY

Tensile tests were performed on AISI 316 stainless steel (Fe-17.34Cr-12.17Ni) at many temperatures between 323 and 4 K, and the results were compared with data for other AISI 316 heats at temperatures to 973 K. The findings are:

- 1) The existing data for AISI 316 show a monotonic temperature dependence, with σ_y increasing continuously as temperature is lowered between 973 and 4 K.

- 2) Between 973 and 175 K, σ_y data for AISI 316 follow a single equation derived from the theory of thermally activated plastic flow. Below 175 K, deviations occur, apparently depending on chemistry variations which in turn affect phase stability and dislocation dynamics.
- 3) Deformation beyond 0.2% plastic strain is needed to initiate transformation to α' martensite at temperatures below 180 K.
- 4) Reduction of grain size contributes significantly (30% at 4 K) to low-temperature flow strength and at low temperatures the grain size dependence of σ_y follows a Hall-Petch relationship.
- 5) Magnetic transitions do not noticeably affect the deformation of AISI 316.

ACKNOWLEDGMENTS

We thank D. Beard, Office of Fusion Energy, DoE for his support and continued encouragement. D. Beekman and D. Burkhalter of NBS contributed significantly to this study by conducting most of the tensile tests. Discussions with Dr. E. L. Brown of NBS, who contributed valuable metallographic assistance and reviews of the manuscript, are also gratefully acknowledged.

REFERENCES

1. Read, D. T., Reed, R. P., and Schramm, R. E., Low temperature deformation of Fe-18Cr-8Ni steels, in: Materials Studies for Magnetic Fusion Energy Applications at Low Temperatures-II, NBSIR 79-1609, F. R. Fickett and R. P. Reed, eds., National Bureau of Standards, Boulder, CO (June 1979), pp. 151-172.
2. Reed, R. P. and Mikesell, R. P., The stability of austenitic stainless steels at low temperatures as determined by magnetic measurements, in: Adv. Cryo. Eng., 4, K. D. Timmerhaus, ed. Plenum Press, New York (1960), pp. 84-100.

3. Larbalestier, D. C. and King, H. W., Austenitic stainless steels at cryogenic temperatures I, structural stability and magnetic properties, Cryogenics, 13 (1973) 160-168.
4. Suzuki, T., Kojima, H., Suzuki, K., Hashimoto, T, and Ichichara, M., An experimental study of the martensite nucleation and growth in 18/8 stainless steel, Acta Metall., 23 (1972).
5. Reed, R. P. and Guntner, C. J., Stress-induced martensitic transformations in 18Cr-8Ni steel, Trans. AIME, 230 (1969) 1713-1720.
6. Olson, G. B. and Azrin, M., Transformation behavior of TRIP steels, Metall. Trans. A, 9A (1978) 713-721.
7. Ilyichev, V. Ya., Medvedev, Ya. M., Shapovaliev, I. A., and Klimenko, I. N., Low temperature anomaly of the temperature dependence at the flow stresses in iron-chromium-nickel alloys, Phys. Met. Metallogr., 44, No. 1 (1978) 173-176.
8. Verkin, B. I., Ilyichev, V. Ya., and Klimenko, I. N., The low-temperature change of the magnetic structure and plastic properties of Fe-Cr-Ni alloys, in: Adv. Cryo. Eng., 26 Plenum Press, New York (1980), pp. 120-125.
9. Tobler, R. L., Reed, R. P., and Burkhalter, D. S., Temperature dependence of yielding in austenitic stainless steels, in: Adv. Cryo. Eng., 26, Plenum Press, New York (1980), pp. 107-113.
10. Sanderson, G. P. and Llewellyn, D. T., Mechanical properties of standard austenitic stainless steels in the temperature range -196 to +800C, J. Iron Steel Inst., 207 (1969) 1129-1140.
11. Ledbetter, H. M., Sound velocities and elastic constants of austenitic stainless steels, to be published.

12. Reed, R. P., A cryostat for tensile tests in the temperature range 300 to 4 K, in: Adv. Cryo. Eng., 7, K. D. Timmerhaus, ed., Plenum Press, New York (1961), pp. 448-454.
13. Read, D. T. and Reed, R. P., Fracture and strength properties of selected austenitic stainless steels at cryogenic temperatures, to be published, Cryogenics (1980).
14. Baughman, R. A., Gas atmosphere effects on materials, Progress Report #2, AF 33(616), General Electric Co. (November 1958).
15. Tobler R. L., Mikesell, R. P., Durchohz, R. L., Fowlkes, C. W., and Reed, R. P., Fatigue and fracture toughness testing at cryogenic temperatures, NBSIR 74-359, National Bureau of Standards, Boulder, CO (March 1974), pp. 182-308.
16. Hoke, J. H., Mabus, P. G., and Goller, G. N., Mechanical properties of stainless steels at subzero temperatures, Met. Prog. (May 1949) 643-648.
17. Seeger, A., The generation of lattice defects by moving dislocations, and its application to the temperature dependence of the flow-stress of FCC crystals, Phil. Mag., 46 (1955) 1194-1217.
18. Yaroshevich, V. D. and Ryvkina, D. G., Thermal-activation nature of plastic deformation in metals, Sov. Phys.-Solid State (Engl. Transl.) 12, No. 2 (1970) 363-370.
19. Schramm, R. E. and Reed, R. P., Stacking fault energies of seven commercial austenitic stainless steels, Metall. Trans., 6A (1975) 1345-1351.

20. Larbalestier, D. C. and King, H. W., Prediction of the low temperature stability of type 304 stainless steel from a room temperature deformation test, in: Proceedings of the Fourth International Cryogenic Engineering Conference, K. Mendelssohn, ed., IPC Science and Technology Press, Guildford, Surrey, England (1975) pp. 338-340.
21. Williams, I., Williams, R. G., and Capellaro, R. C., Stability of austenitic stainless steels between 4 K and 373 K, in: Proceedings of the Sixth International Cryogenic Engineering Conference, ed. K. Mendelssohn, IPC Science and Technology Press, Guildford, Surrey, England (1976), pp. 337-341.
22. Warnes, L. A. and King, H. W., The low temperature magnetic properties of austenitic Fe-Cr-Ni alloys 2, the prediction of Néel temperatures and maximum susceptibilities, Cryogenics, 16, No. 11 (1976) 659-667.
23. Guntner, C. J. and Reed, R. P., The effect of experimental variables including the martensitic transformation on the low temperature mechanical properties of austenitic stainless steels, Trans. Am. Soc. Met., 55 (1962) 399-419.
24. Starr, C. D., Notes on the plastic critical temperature in strain-induced martensite reaction, Trans. AIME, 197 (1953) 654.
25. Norstrom, L. A., The influence of nitrogen and grain size on yield strength in Type 316L austenitic stainless steel, Met. Sci., 11 (1977) 208-212.
26. Collings, E. W. and Ledbetter, H. M., Sound velocity anomalies near the spin glass transition in an austenitic stainless steel alloy, Phys. Lett., 72A, No. 1, 11 (1979) 53-56.

27. Ledbetter, H. M. and Collings, E. W., Low-temperature magnetic and elastic-constant anomalies in three manganese stainless steels, in: The Metal Science of Stainless Steels, E. W. Collings and H. W. King, eds.

Table 1. Chemical compositions (weight percent) for AISI 316 steel heats referred to in this study.

Heat No. & Reference	Fe	Cr	Ni	Mn	C	P	S	Si	Cu	Mo	Co	N
1 [9]	balance	17.25	13.48	1.86	0.057	0.024	0.019	0.58	--	2.34	--	0.03
2 this study	"	17.34	12.17	1.55	0.051	0.026	0.014	0.68	0.34	2.16	0.19	--
3 [10]	"	16.72	11.27	1.52	0.05	--	--	0.32	--	2.58	--	--
4 [11]	"	17.46	12.93	1.77	0.062	0.030	0.020	0.56	--	2.20	--	--

Table 2. Yield stress measurements at 0.2% plastic strain obtained for AISI 316 (heat 2) of this study.

Test Temperature, T, K	Yield Stress, σ_y , MPa*
323	185
295	204
295	198
295	198
240	244
215	281
194	298
192	306
190	307
164	349
154	368
143	380
125	399
100	428
76	456
76	451
76	445
76	450
76	441
76	447
76	448
60	456
39	487
23	528
4	537
4	527

*To convert from MPa to ksi, divide by 6.895.

Table 3. Calculated stacking fault energies (SFE) and M_S , M_D , and T_N temperatures for AISI 316 steel heats of this study.

Heat No. & Reference	SFE ^a , mJ/M ²	M_S ^b , K	M_D ^c , K	T_N ^d , K
1 [9]	70.4	-226	190	24.7
2 this study	59.6	-126	232	25.5
3 [10]	57.4	- 47	246	7.4
4 [11]	NA	NA	NA	26.4

- a. Calculated from equation (9) of Schramm and Reed [19].
- b. M_S is the temperature at which martensite starts forming spontaneously on cooling, as calculated from the equation of Larbalestier and King [20].
- c. M_D is the temperature above which no deformation induced martensite is possible, as calculated from the equation of Williams, Williams, and Capellaro [21].
- d. T_N is the temperature of the onset of antiferromagnetic ordering, as calculated from the equation of Warnes and King [22].

LIST OF FIGURES

- Fig. 1. Yield strength of AISI 316 stainless steels at low temperatures, illustrating heat-to-heat variability. Heat 1 is from Tobler, Reed, and Burkhalter [9]; heat 3 is from Sanderson and Llewellyn [10].
- Fig. 2. Yield strength data for AISI 316 stainless steels in the elevated-to-cryogenic temperature range, illustrating overall temperature dependence.
- Fig. 3. Effect of grain size on the yield strength at three test temperatures for the Fe-17Cr-12Ni-2Mo alloy.
- Fig. 4. Dependence of bcc (α') martensite on tensile plastic strain. Martensite was detected by using a bar magnet and torsion balance beam.
- Fig. 5. Temperature dependence of the yield and flow stresses for AISI 316 stainless steels, showing no evidence of anomalies despite martensitic phase transformation occurring at higher strain increments and lower test temperatures.
- Fig. 6. Stress-strain curves for AISI 316 stainless steels at various test temperatures, showing no evidence of anomalies despite martensitic phase transformations occurring at higher strain increments and low temperatures.
- Fig. 7. Amount of bcc martensite per unit strain in AISI 316 specimens deformed to plastic strains of 2.75 or 3.65%, indicating clear evidence of martensitic phase transformation at cryogenic temperatures. Extrapolated temperature of 0% bcc martensite is about 180 K.

- Fig. 8. Temperature dependence of the thermal stress component, illustrating applicability of thermally activated plastic flow theory at temperatures between 900 and 175 K.
- Fig. 9. Normalized yield strength versus normalized temperature plot for three AISI 316 stainless steel heats, showing variations in thermal and athermal stress components.
- Fig. 10. Dependence of the tensile yield strength, σ_y ; the Hall-Petch parameter, K ; and the flow strength, σ_i , for AISI 316 steel. High temperature data from Norstrom 25 and σ_i is adjusted to 0.04 weight percent nitrogen.
- Fig. 11. Temperature dependence of yield stress and Young's modulus for AISI 316 stainless steel heats, showing no drop in yield strength at the Néel transition temperature.

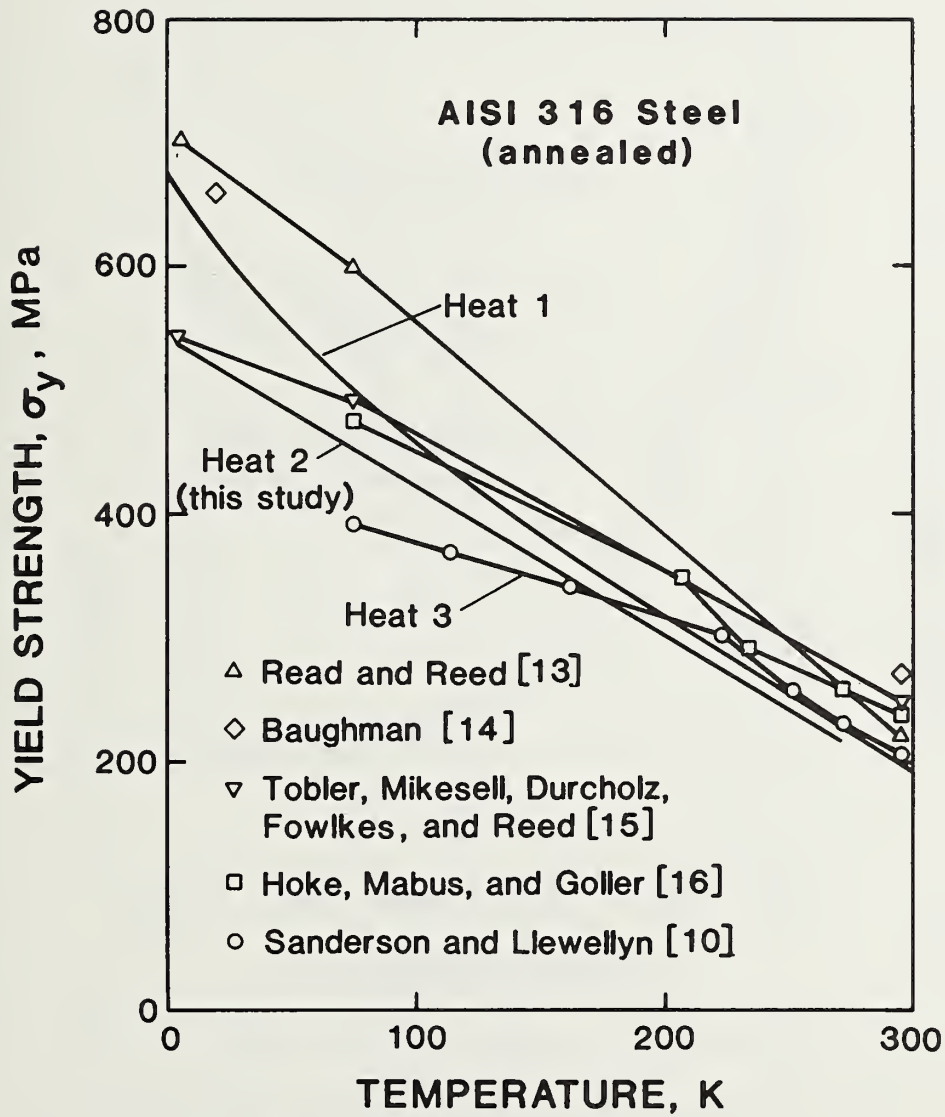


Fig. 1. Yield strength of AISI 316 stainless steels at low temperatures, illustrating heat-to-heat variability. Heat 1 is from Tobler, Reed, and Burkhalter [9]; heat 3 is from Sanderson and Llewellyn [10].

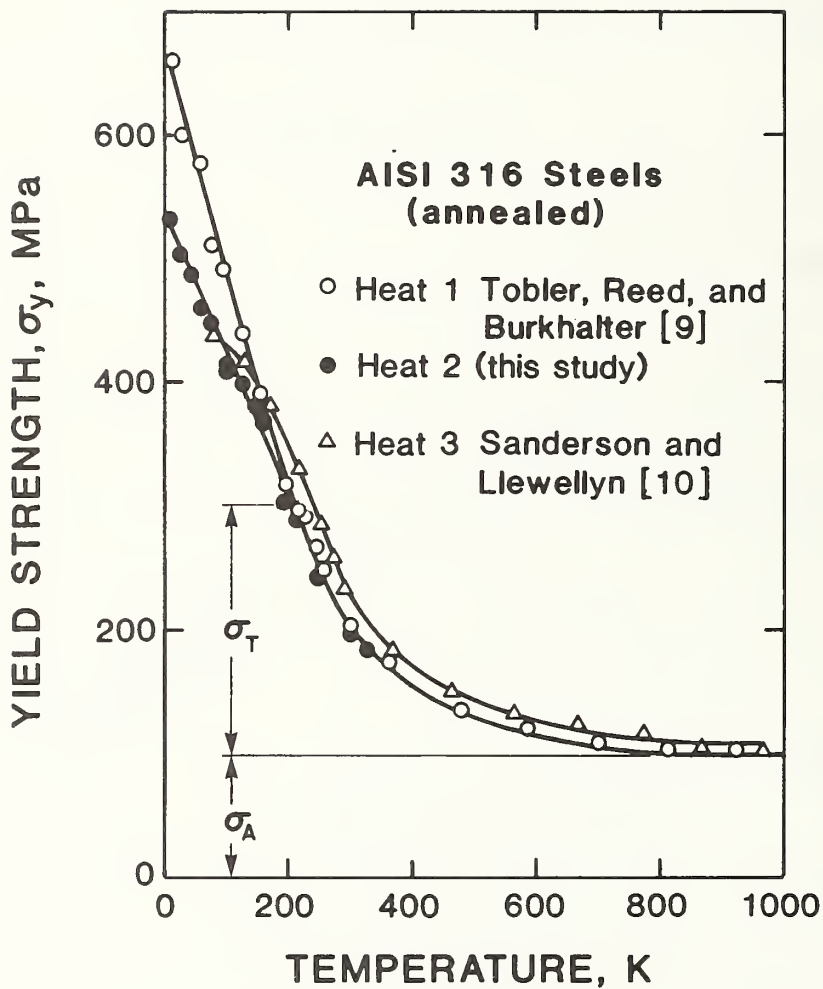


Fig. 2. Yield strength data for AISI 316 stainless steels in the elevated-to-cryogenic temperature range, illustrating overall temperature dependence.

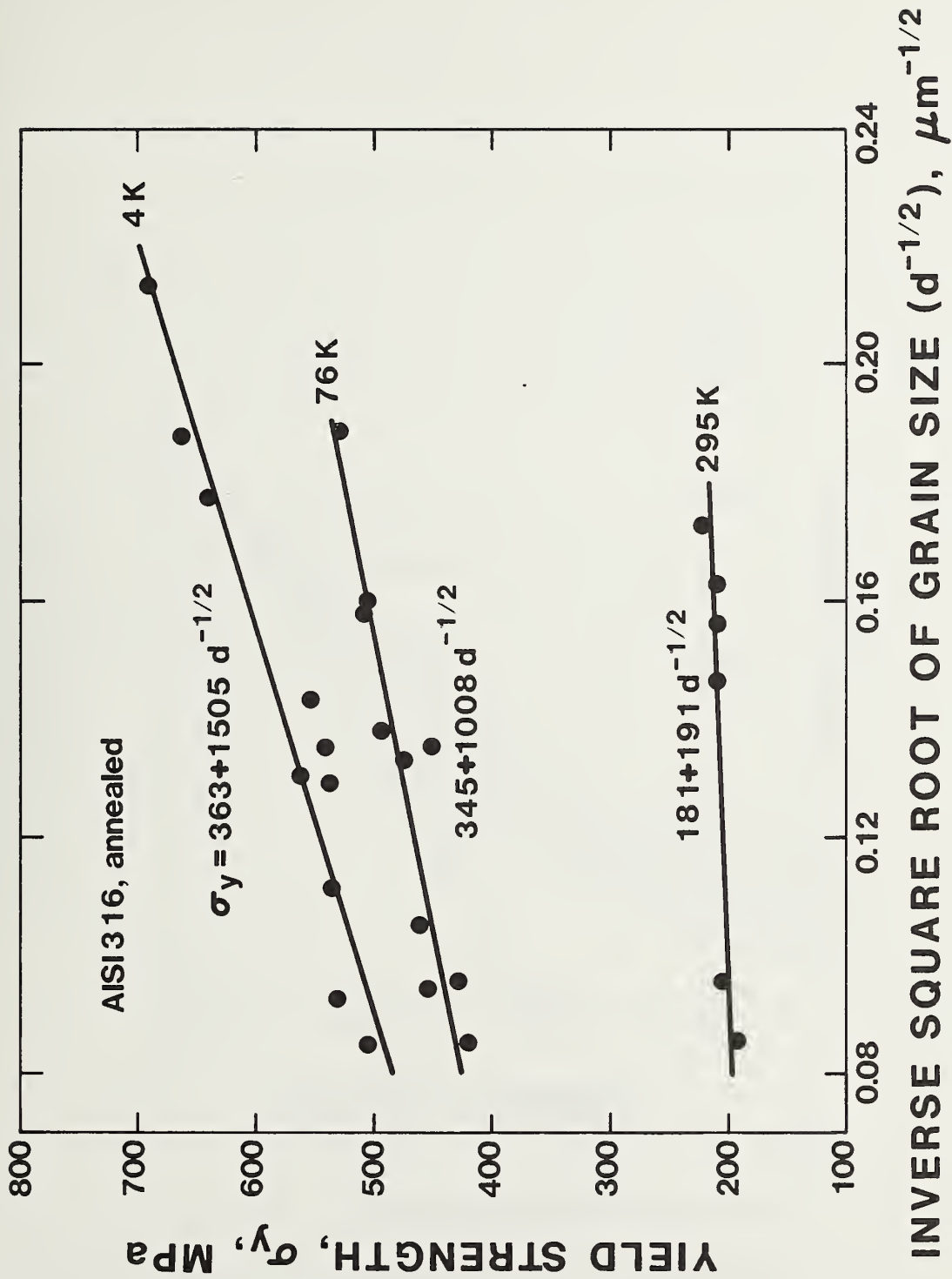


Fig. 3. Effect of grain size on the yield strength at three test temperatures for the Fe-17Cr-12Ni-2Mo alloy.

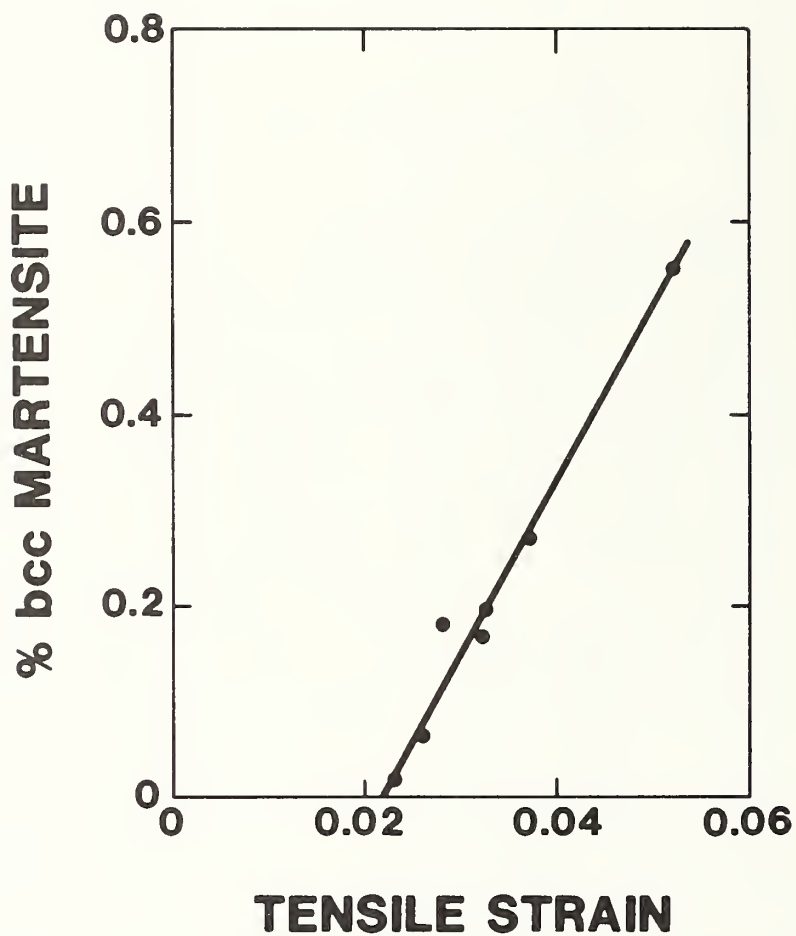


Fig. 4. Dependence of bcc (α') martensite on tensile plastic strain. Martensite was detected by using a bar magnet and torsion balance beam.

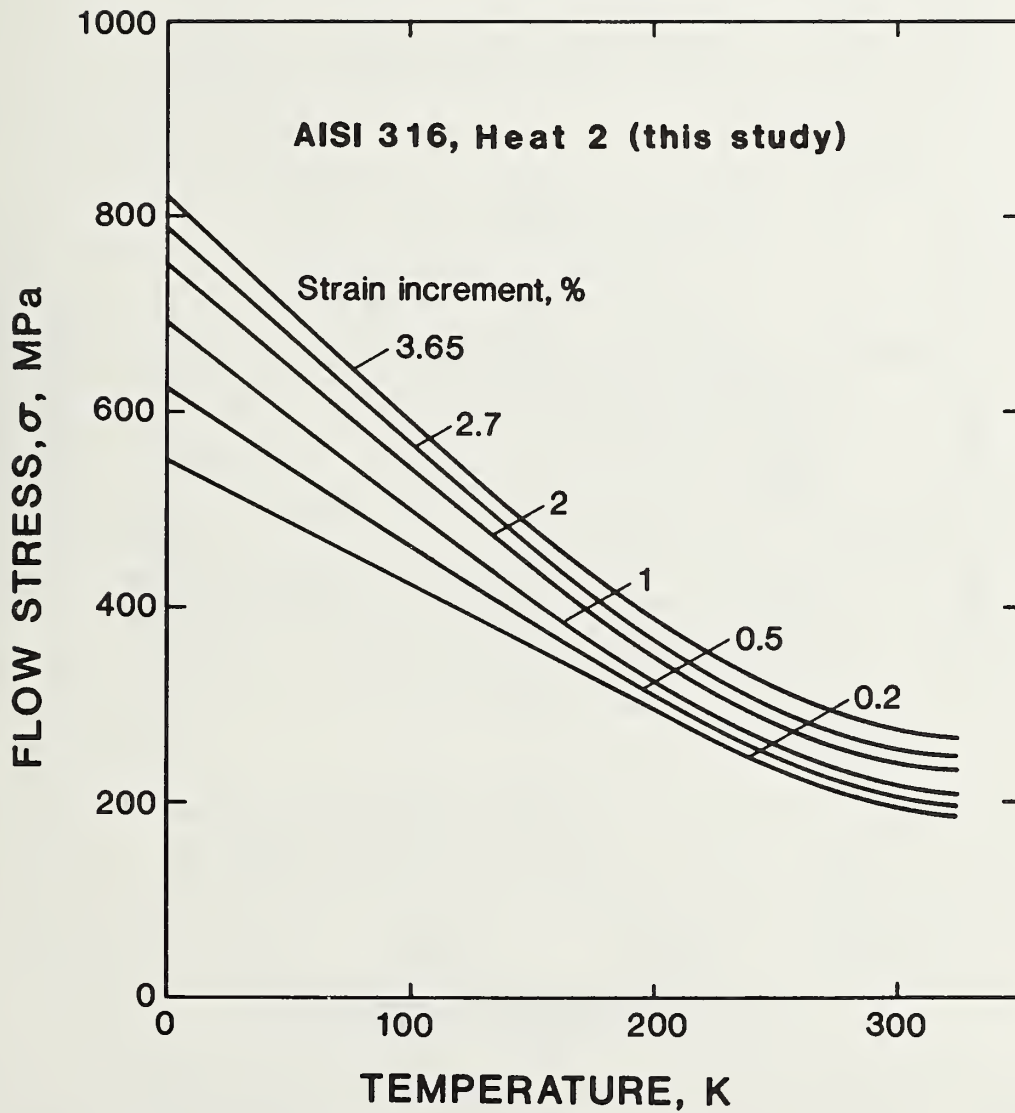


Fig. 5. Temperature dependence of the yield and flow stresses for AISI 316 stainless steels, showing no evidence of anomalies despite martensitic phase transformation occurring at higher strain increments and lower test temperatures.

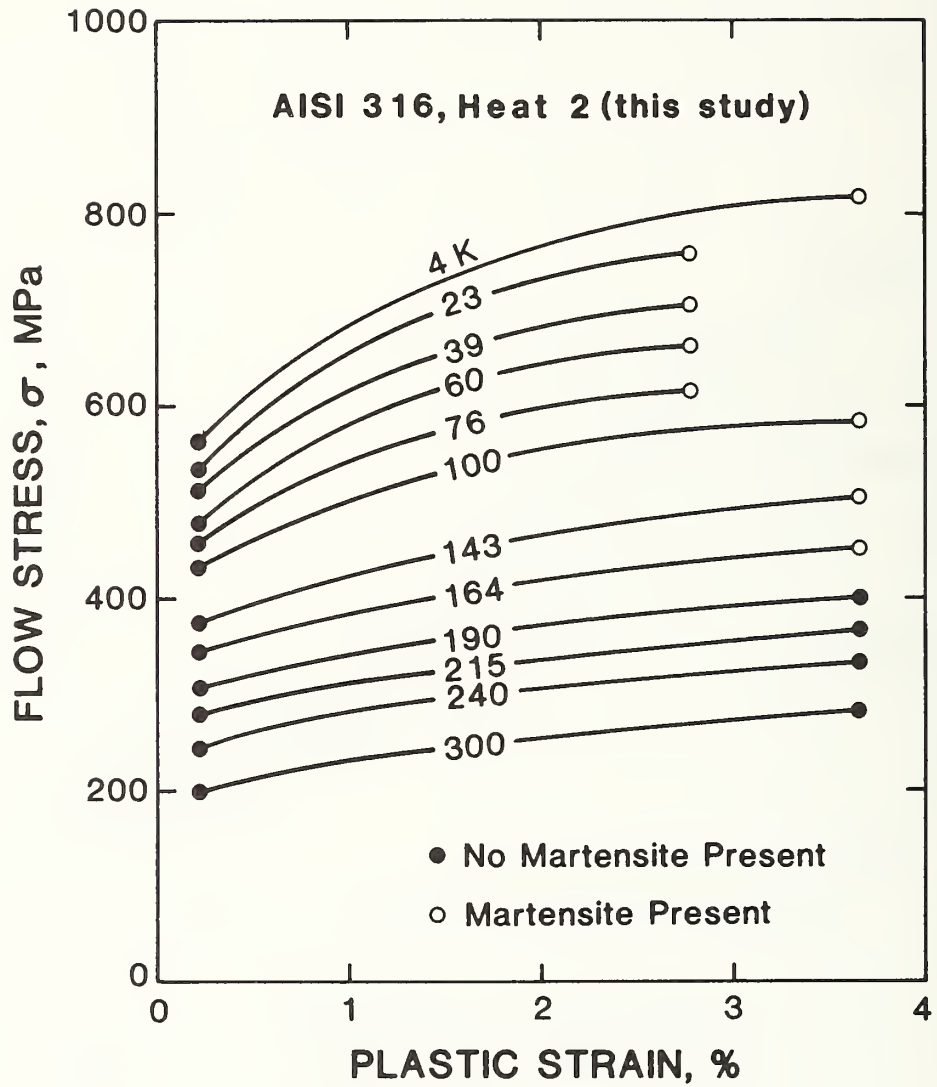


Fig. 6. Stress-strain curves for AISI 316 stainless steels at various test temperatures, showing no evidence of anomalies despite martensitic phase transformations occurring at higher strain increments and low temperatures.

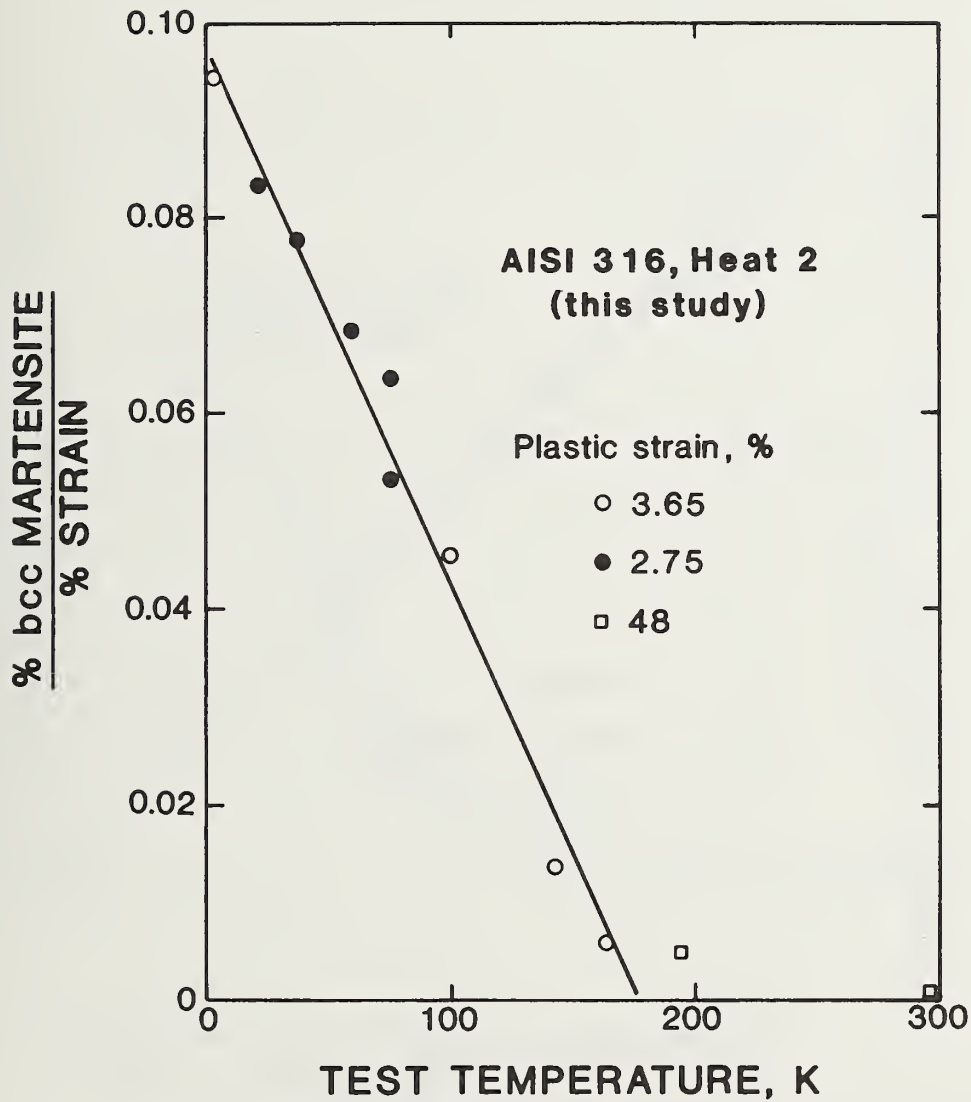


Fig. 7. Amount of bcc martensite per unit strain in AISI 316 specimens deformed to plastic strains of 2.75 or 3.65%, indicating clear evidence of martensitic phase transformation at cryogenic temperatures. Extrapolated temperature of 0% bcc martensite is about 180 K.

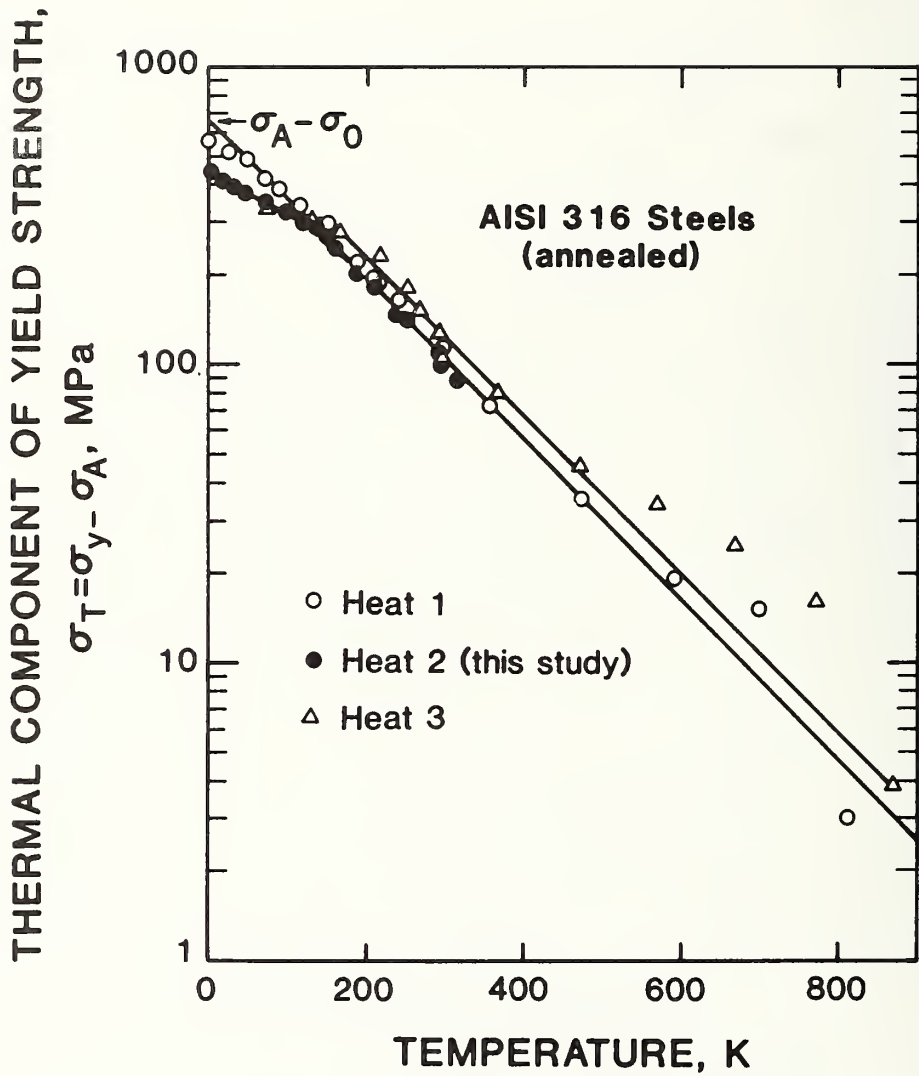


Fig. 8. Temperature dependence of the thermal stress component, illustrating applicability of thermally activated plastic flow theory at temperatures between 900 and 175 K.

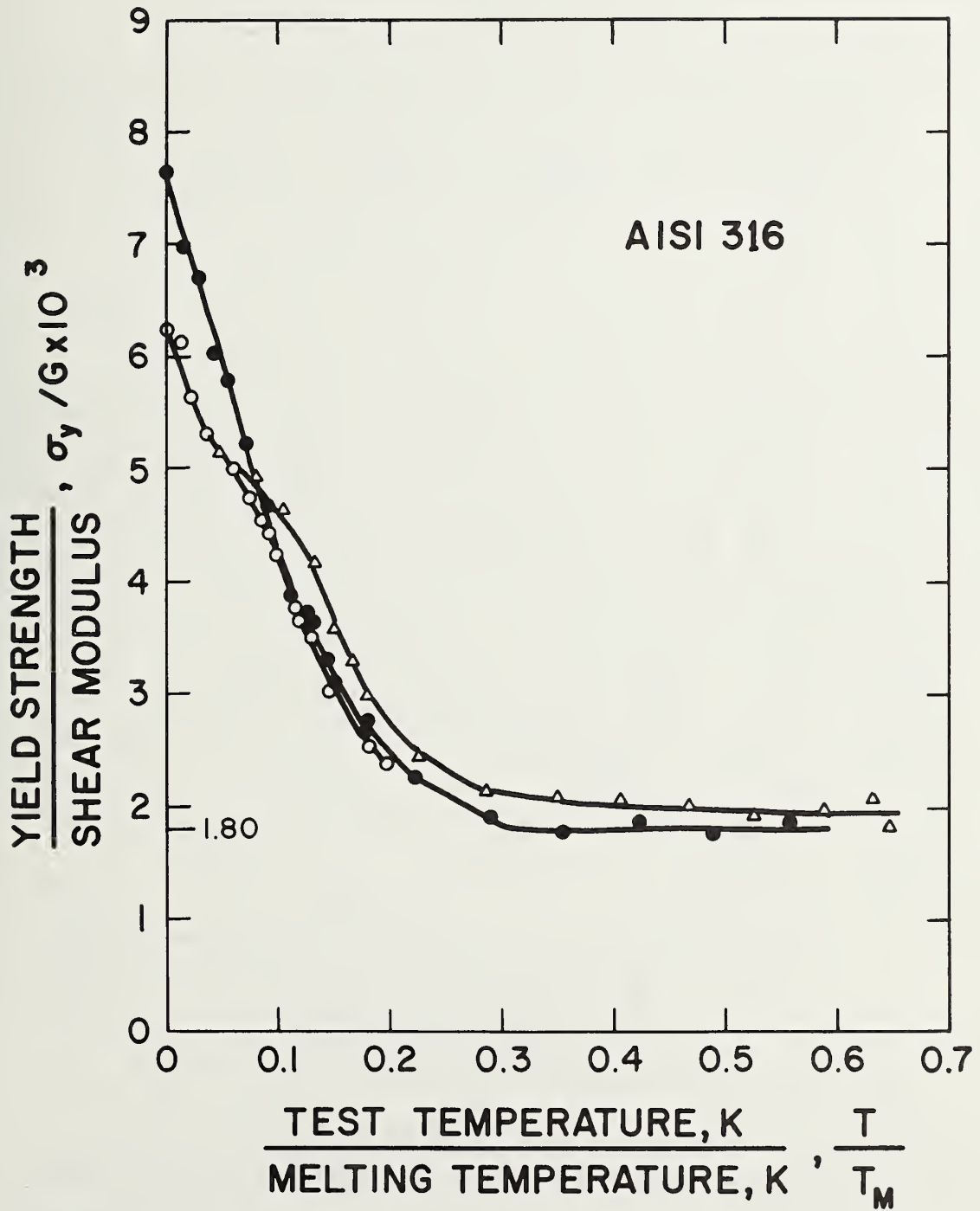


Fig. 9. Normalized yield strength versus normalized temperature plot for three AISI 316 stainless steel heats, showing variations in thermal and athermal stress components.

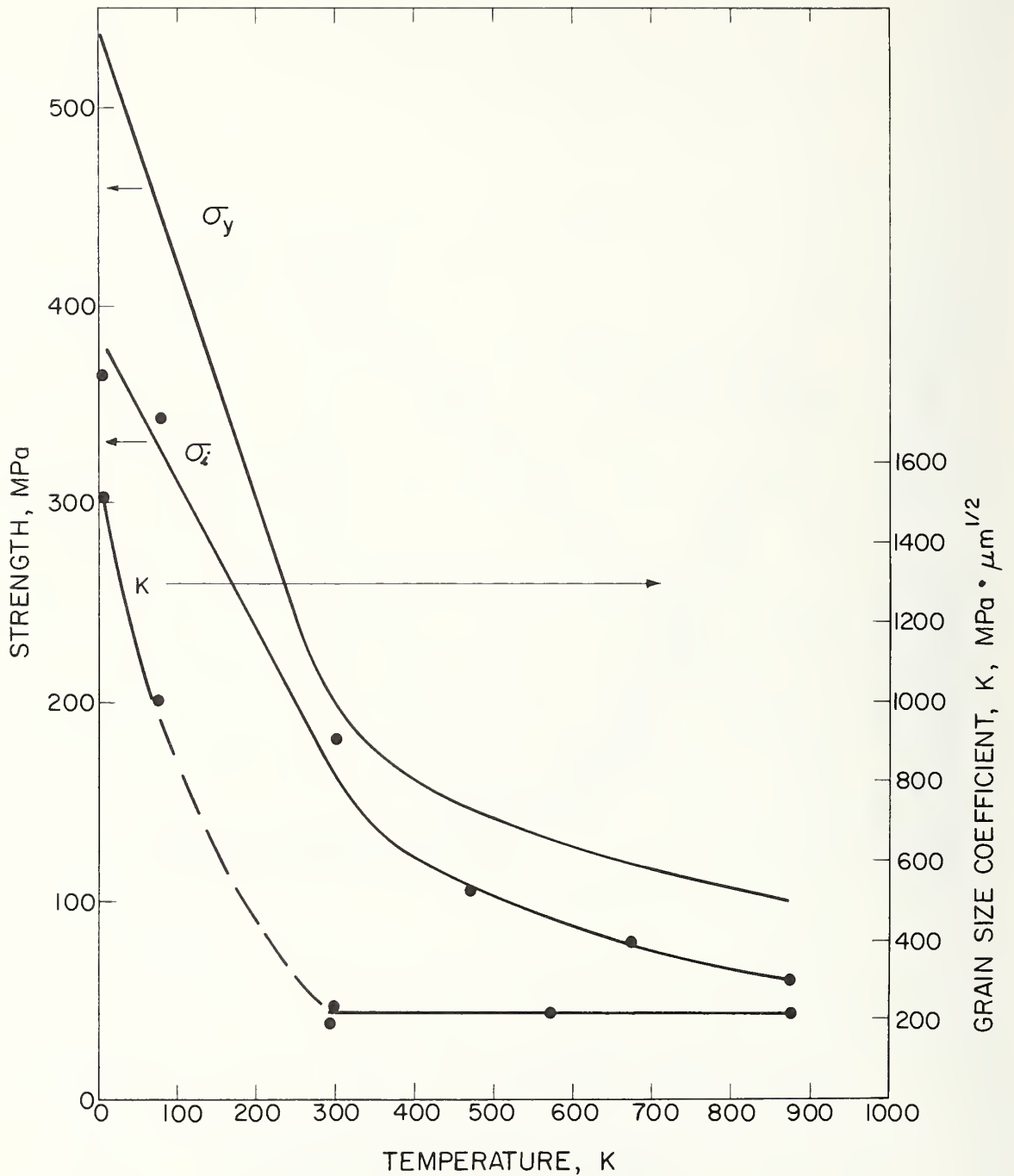


Fig. 10. Dependence of the tensile yield strength, σ_y ; the Hall-Petch parameter, K; and the flow strength, σ_i , for AISI 316 steel. High temperature data from Norstrom 25 and σ_i is adjusted to 0.04 weight percent nitrogen.

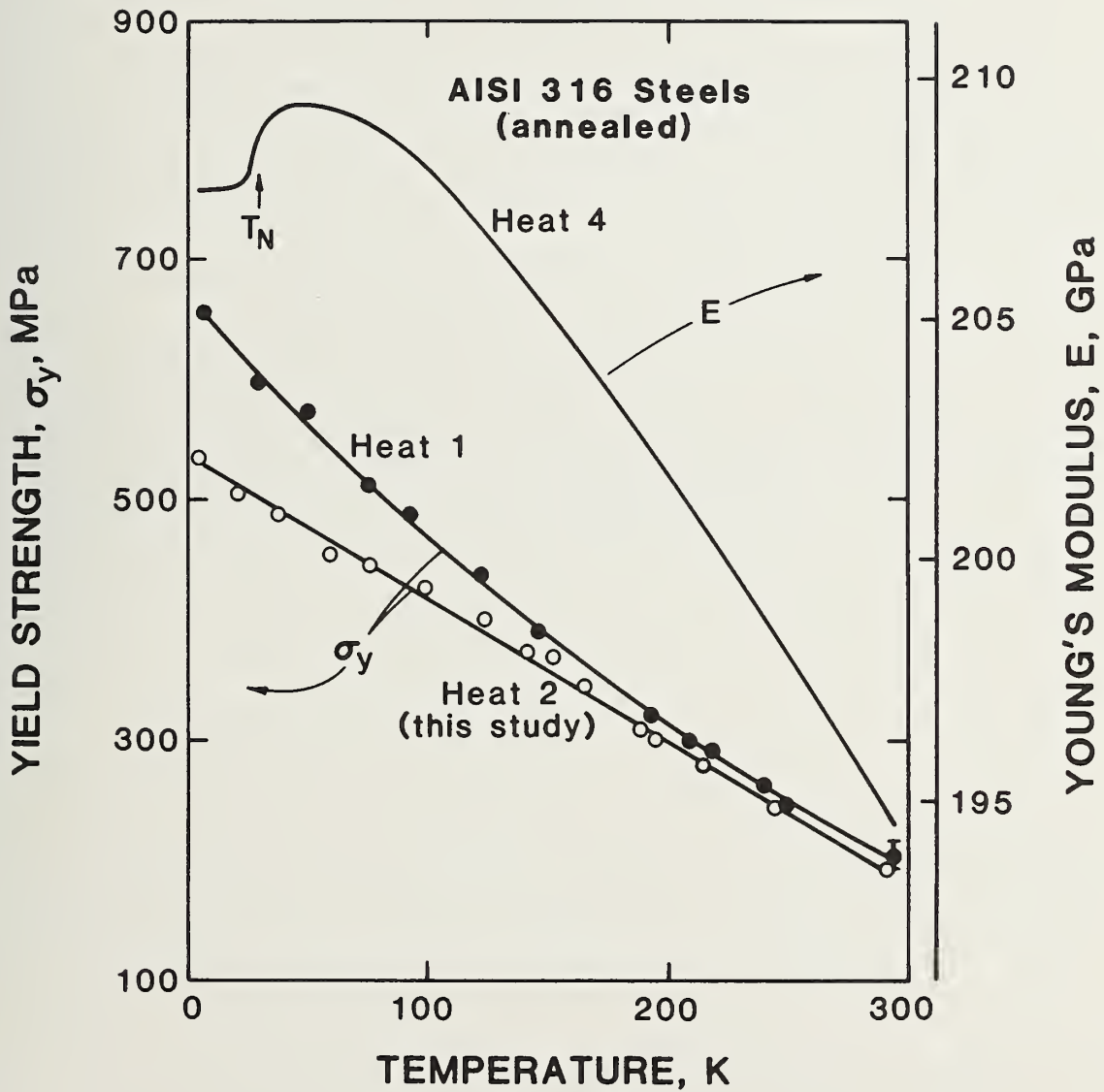


Fig. 11. Temperature dependence of yield stress and Young's modulus for AISI 316 stainless steel heats, showing no drop in yield strength at the Néel transition temperature.

LOW-TEMPERATURE DEFORMATION OF 5083-0 ALUMINUM ALLOY

R. L. Tobler and R. P. Reed
Fracture and Deformation Division
National Bureau of Standards
Boulder, Colorado

ABSTRACT

This paper describes the temperature dependence of the yield strength and stress-strain characteristics for 5083-0 aluminum alloy. New experimental data in the temperature range 4 to 340 K are compared with previously published data extending to the melting point. Thermally activated plastic deformation apparently governs the behavior between 4 and 400 K, but the athermal component is not simply a function of the shear modulus. Aspects of serrated yielding and load-versus-displacement control tensile tests are discussed.

INTRODUCTION

Aluminum alloys have been proposed for structural applications in superconducting magnets for magnetic fusion energy systems. The most widely used aluminum alloy in cryogenic service today is 5083-0 aluminum, which is used extensively in thick sections for the storage of liquefied natural gas. This alloy is strengthened by magnesium in solid solution and is relatively soft, but tough. This provides the advantage, however, that strength can be maintained in the welded joints of structures made with this alloy.

The low-temperature properties of relatively pure aluminum have been reviewed by Reed [1]. The purpose of this study was to characterize the plastic deformation of 5083-0 alloy over a broad temperature range. Although scatter in the studied material prevented determination of the exact form of the temperature dependence of the yield strength, several observations are recorded concerning the effects of temperature, magnesium concentration, and method of testing on the low-temperature strength of aluminum alloys. This work provides a basis for future studies.

PROCEDURE

Material

A 3.8-cm-thick plate of 5083-0 aluminum was obtained from a commercial manufacturer. The ASTM specification B 209-66 gives the chemical composition in weight percent as follows: 4.0-4.9 Mg, 0.3-1.0 Mn, 0.05-0.25 Cr, 0.4 max Si, 0.4 max Fe, 0.10 max Cu, 0.25 max Zn, 0.15 max Ti, and 0.15 max of other impurities. The microstructure consists of elongated grains in the rolling direction, as illustrated in Figure 1. Typical Rockwell hardness of the alloy is R_B 61.

Specimen

Tensile tests were performed using unnotched, longitudinally oriented specimens having a 50.8-mm gage length and 2.54 x 4.80 μm cross section. Specimens were cut from the 3.8-cm-thick plate (at various thickness depths), then annealed at 686 K and furnace cooled.

Apparatus

Most tests were performed using the screw-driven machine and variable temperature cryostat described by Read and Reed [2]. The crosshead rate during these tests was 8.5 $\mu\text{m/s}$. The tensile yield strength was recorded at 0.002 offset specimen strain. The specified test temperatures ranged from 4 to 340 K and were accurate to better than ± 1.5 K. A few tests were also performed using a servo-hydraulic test machine in load control at a loading rate of 0.1 kN/s. Tests were performed at temperatures between 4 and 76 K in a gaseous helium environment and between 76 and 295 K in a gaseous nitrogen atmosphere.

RESULTS AND DISCUSSION

Tensile Yield Strength

In Figure 2, the tensile yield strength between 4 and 300 K is presented. The data scatter is large, with six measurements of the room-temperature yield strength ranging from 137 MPa to 158 MPa. It is thought that this scatter is real and reflects inhomogeneity in the 3.8-cm-thick 5083-0 plate. Unfortunately, the scatter is too large to permit accurate interpretation of the temperature dependence at low temperatures. The trend shown in Figure 2 follows the minimum values measured in this study.

The present results are combined with high temperature results [3] in Figure 3. In the temperature range 150 to 400 K, the yield strength (σ_y) is constant, if one relies on the handbook values in this temperature interval. Normalizing the yield strength by dividing by the shear modulus (G), which is reported by Weston, Naimon, and Ledbetter [4], results in a negative temperature dependence of σ_y/G in this temperature range (Fig. 3). The rather strong thermal contribution to the flow strength is most likely associated with dynamic solute (Mg) segregation to dislocations. Evidence for this effect is the discontinuous yielding observed in the stress-versus-strain behavior of the alloy at room temperature that disappears at 76 K. Owing to the rather strong dynamic strain aging contribution, it is not possible from these data to separate the athermal from the thermal components.

Stress-Strain Behavior

True stress-true strain curves for the 5083-0 aluminum alloy at 295, 76, and 4 K are presented in Figure 4. Here true stress is defined as $P/A_0(1 + \frac{L-L_0}{L_0})$ and true strain equals $\ln(1 + \frac{L-L_0}{L_0})$ where P is load, A_0 is the original cross-sectional area, L_0 is the original gage length, and L is the instantaneous gage length. Serrated yielding phenomena were observed at 4 K and at 295 K, but not at 76 K. In the case of 5083-0 alloy at 4 K, the stress-strain curve was smooth up to a strain of about 4%, at which point the flow became discontinuous. The stress-strain curve at 295 K showed single serrations at 1.8 and 2.5% strain, then continuous serrations from 2.7% strain to fracture.

The serrated yielding at 295 K is well known in aluminum-magnesium alloys as the Portevain-LeChatelier effect, which is accompanied by

Lüders band propagation and is attributed to dynamic strain aging [5]. In the study reported by Lloyd [6], dynamic strain aging was observed at temperatures between 200 and 350 K. In our study, the stress-strain curve at 295 K showed continuous serrations from 3% plastic strain to fracture. The strain at which the serrations begin and the magnitude of the load drops associated with each serration have been demonstrated to be dependent on strain rate, magnesium concentration, and temperature [7].

The serrated yielding at 4 K is attributed to adiabatic heating, a completely different mechanism from that of dynamic strain aging at 295 K. Adiabatic heating is possible because of the low specific heat of the alloy at 4 K [8]. Thus the amount of heat necessary to produce an appreciable temperature rise is relatively low. As a result of heating during plastic deformation, appreciable softening occurs and the deformation becomes unstable. Low thermal conductivity at 4 K (compared with that at 295 K) contributes to a localization of the heat produced until flow occurs.

During testing at 4 K, the load drops suddenly and the flow becomes localized when thermal softening, due to heat generated in plastic straining, is greater than the strain-rate hardening. This instability criterion is more easily satisfied at the lowest temperatures because 1) the volume specific heat is reduced so that relatively large temperature increases are possible in straining and 2) the flow stress is more strongly temperature dependent.

Specimens tested using load control at 4 K were compared with those tested using stroke control. The stress-strain curves obtained are compared in Figure 5. The adiabatic instabilities corresponded to specimen strains of the order of 0.04%. The load-controlled tests did

not produce catastrophic deformation during the discontinuous yields. Instead, each local serration is arrested at some strain and temperature where the flow process becomes stable, owing to local specimen strain hardening which distributes the load over an ever-increasing area that precludes continued temperature increases in the local area in which the process initiated.

Magnesium Strengthening

Tensile yield strength data at low temperatures for three commercial aluminum-magnesium alloys (5083, 5154, and 5052) are presented in Figure 6. The 5083-0 results represent the average data at 295, 76 and 4 K from the present study, whereas the 5154 and 5052 data were previously unpublished [7]. In general, the temperature dependences are very similar and little low-temperature strengthening is apparent. Clearly, the addition of magnesium serves to increase the room-temperature yield strength and this increase is maintained at low temperatures. In Figure 7 the effects from magnesium additions to aluminum are plotted at two test temperatures, 295 and 20 K. Again, the dependence of yield strength on magnesium content at these two temperatures appears very similar. This indicates that, contrary to nitrogen and carbon interstitial contributions to austenitic stainless steels, the addition of magnesium serves to increase the long-range stress fields through solid-solution strengthening and does not affect the thermal contribution to the flow strength. Data scatter in Figure 7 may represent the effects of grain size or relate to lack of solute homogeneity.

SUMMARY

Tensile yield strength was measured for the 3.8-cm-thick plate of aluminum alloy 5083-0 at temperatures ranging from 4 to 340 K. The scatter of yield strength measurements was sizable, preventing an exact determination of the temperature dependence. However, the following results were obtained:

1. The stress-strain behavior of 5083-0 is complex: at 295 K discontinuous yielding from dynamic strain aging occurs; at 4 K discontinuous yielding from adiabatic specimen heating effects occurs.
2. Tensile yield strength is enhanced at room temperature by dynamic strain aging from magnesium solute.
3. The strengthening contribution of magnesium essentially results from its influence on long-range stress fields; little strengthening from short-range solute clustering or precipitation was measurable from comparison of 295 and 20 K data.

ACKNOWLEDGMENTS

We thank D. Beard, Office of Fusion Energy, Department of Energy, for his support and encouragement. D. Beekman and D. Baxter of the National Bureau of Standards, Boulder, Colorado contributed by performing tensile tests, reducing data, and conducting metallographic analyses. Their assistance is gratefully acknowledged.

REFERENCES

1. Reed, R. P., Aluminum: A review of deformation properties of high purity aluminum and dilute aluminum alloys. *Cryogenics*, 12 (1972) 259-291.
2. Read, D. T. and Reed, R. P., Toughness, fatigue crack growth, and tensile properties of three nitrogen-strengthened stainless steels at cryogenic temperatures. The Metal Science of Stainless Steels, E. W. Collings and H. W. King, eds., American Institute of Mining, Metallurgical, and Petroleum Engineers, New York (1979) pp. 92-121.
3. Metals Handbook, Vol. 2, Properties and Selection of Nonferrous Alloys and Pure Metals, American Society for Metals, Metals Park, Ohio (1979).
4. Weston, W. F., Naimon, E. R., and Ledbetter, H. M., Low temperature elastic properties of aluminum 5083-0 and four ferritic nickel steels, in Properties of Materials for Liquefied Natural Gas Tankage, ASTM STP 579, American Society for Testing and Materials, Philadelphia (1975), pp. 297-420.
5. Morris, J. G., Dynamic strain aging in aluminum alloys, *Mater. Sci. Eng.* 13 (1974), 101-108.
6. Lloyd, D. J., The deformation of commercial aluminum-magnesium alloys, *Metall. Trans.* 11A (1980), 1287-1294.
7. Reed, R. P., Unpublished data, National Bureau of Standards, Boulder, Colorado (1980).
8. Read, D. T. and Reed, R. P., Heating effects during tensile tests of AISI 304L stainless steel at 4 K, Advances in Cryogenic Engineering, Vol. 26, Plenum Press, New York (1980), pp. 91-101.

LIST OF FIGURES

- Figure 1. Three-dimensional metallographic representation of aluminum alloy 5083-0.
- Figure 2. Tensile yield strength of 5083-0 aluminum alloy at low temperatures.
- Figure 3. Variation of temperature dependence of tensile yield strength of 5083-0 aluminum alloy from 4 K to the melting temperature.
- Figure 4. Tensile true stress-true strain curves of 5083-0 aluminum alloy at 295, 76, and 4 K.
- Figure 5. Load and displacement controlled tensile stress-strain behavior at 4 K.
- Figure 6. Tensile yield strength at low temperatures from aluminum-magnesium alloys 5083, 5154, and 5052 in the annealed condition.
- Figure 7. Influence of magnesium alloying additions in aluminum on tensile yield strength at 295 and 20 K.

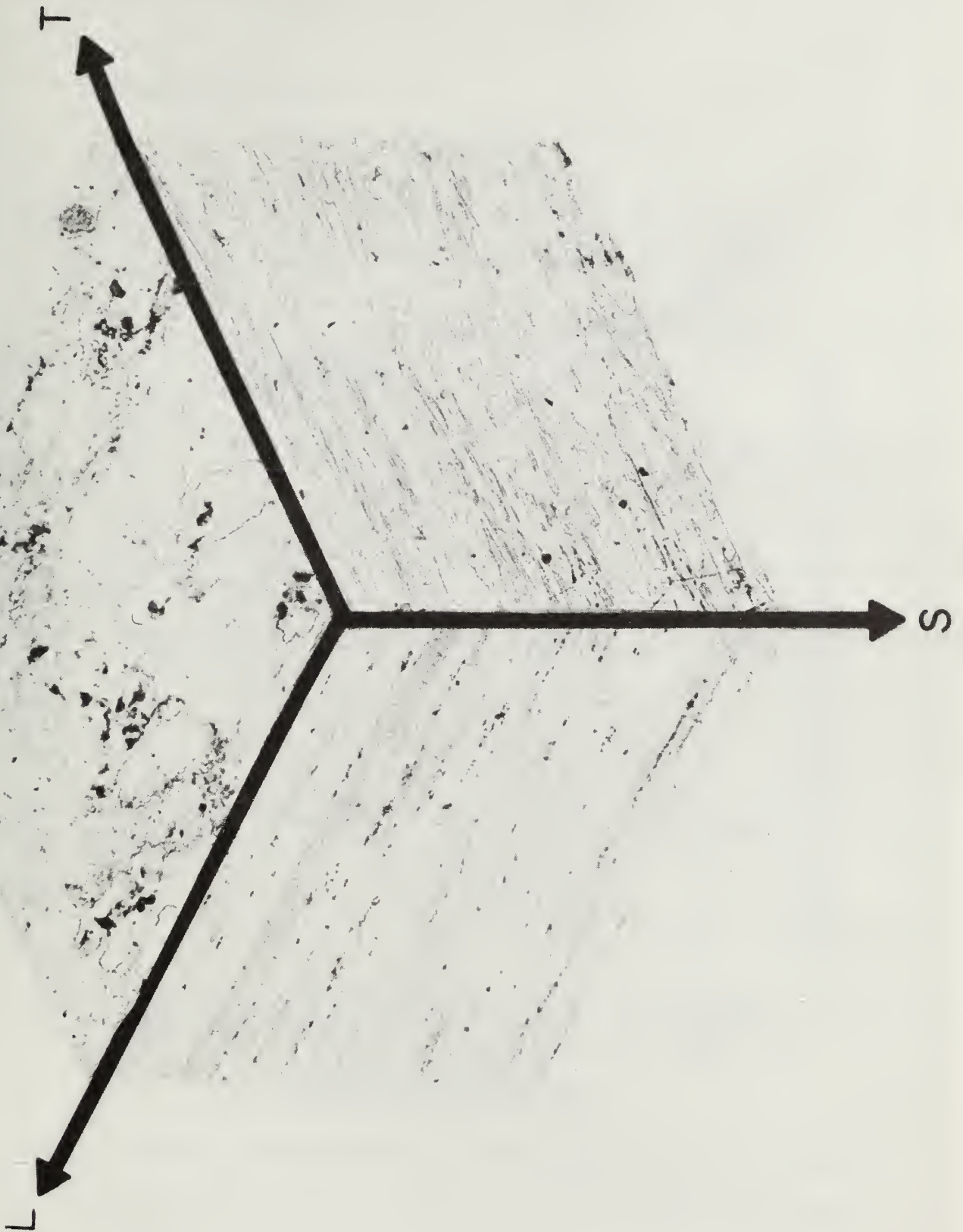


Figure 1. Three-dimensional metallographic representation of aluminum alloy 5083-0.

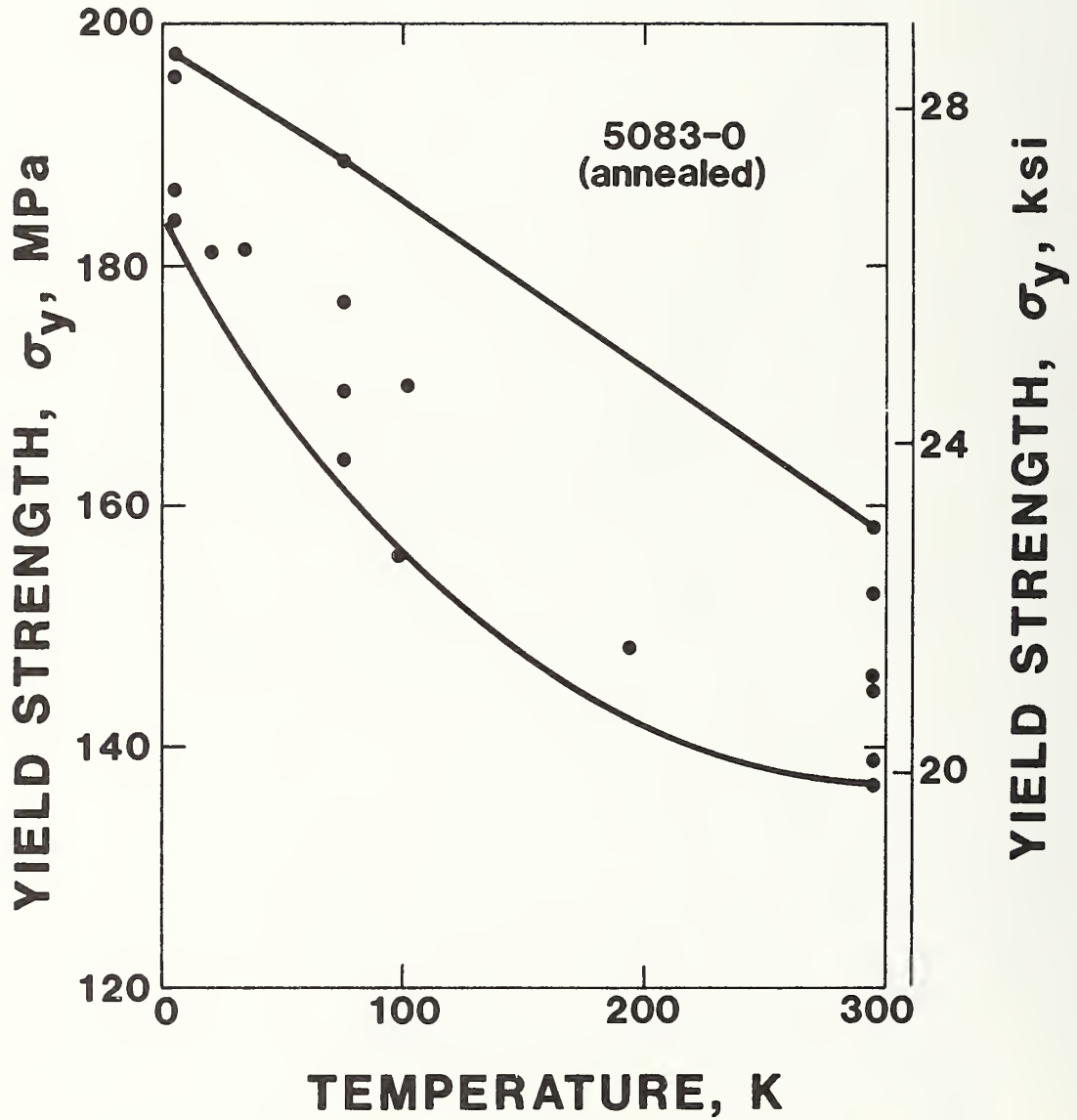


Figure 2. Tensile yield strength of 5083-0 aluminum alloy at low temperatures.

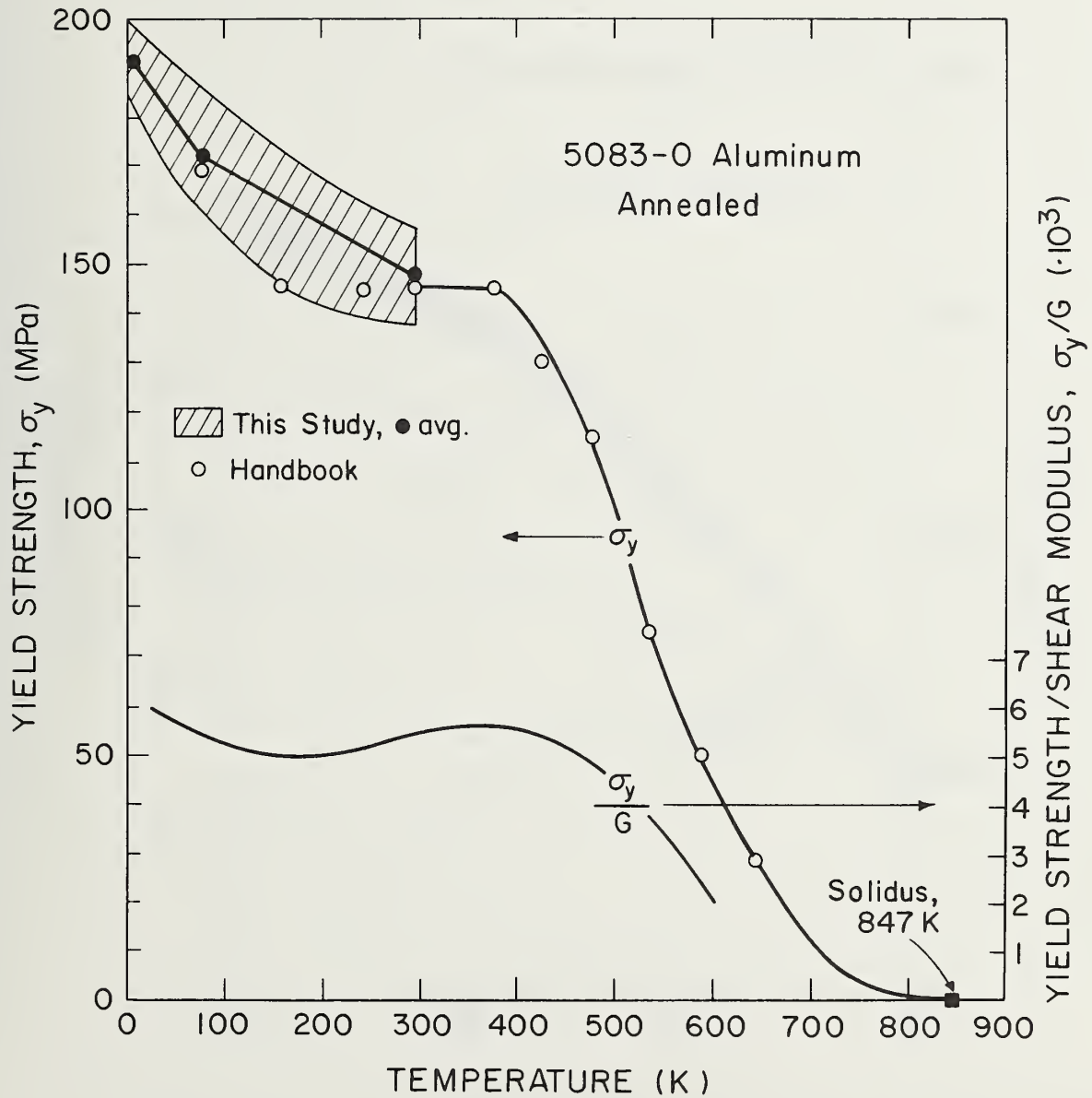


Figure 3. Variation of temperature dependence of tensile yield strength of 5083-0 aluminum alloy from 4 K to the melting temperature.

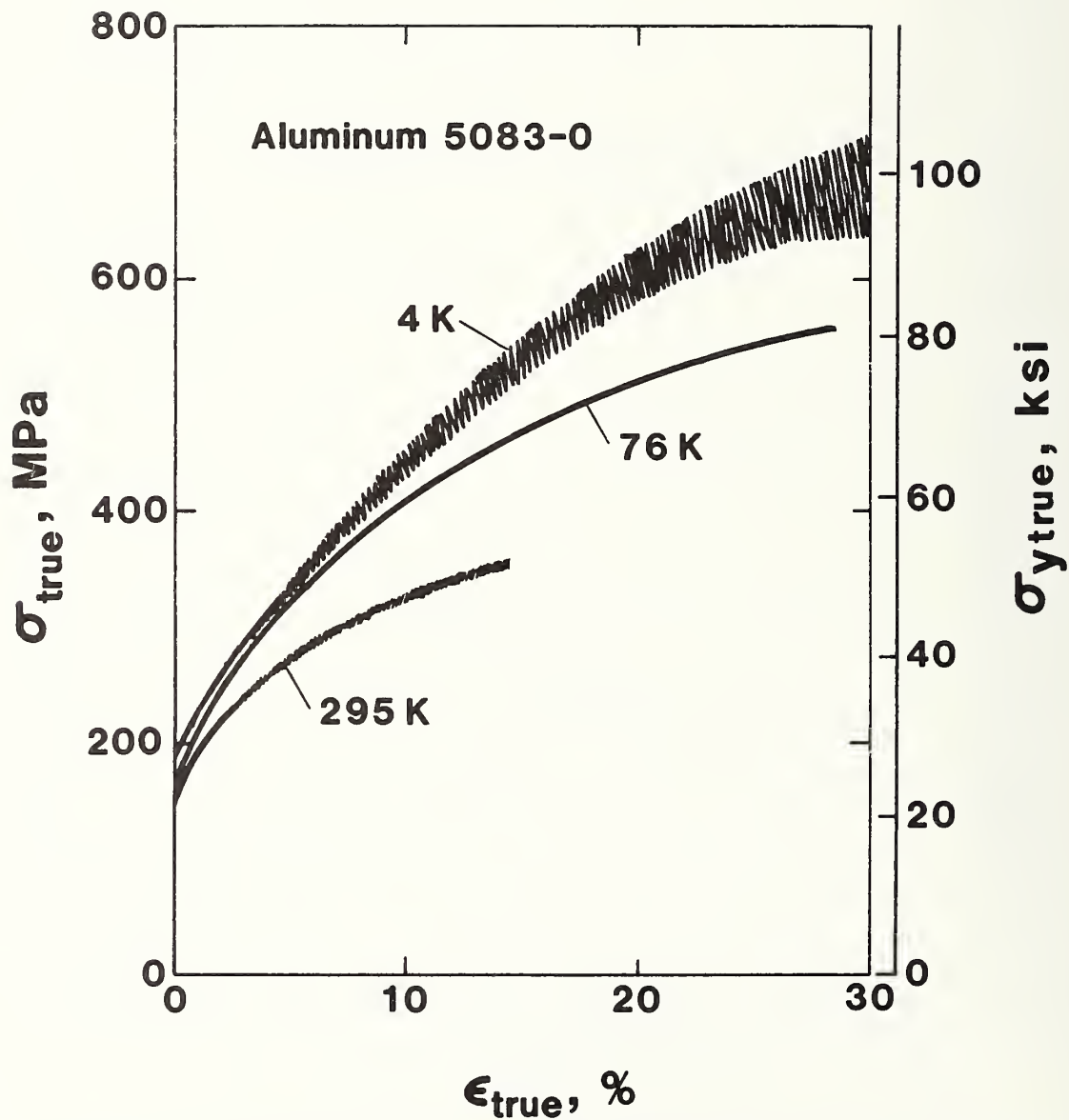
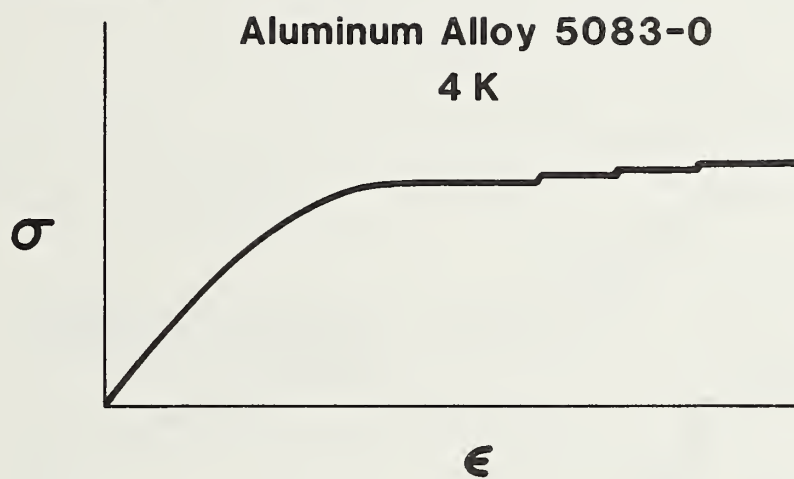


Figure 4. Tensile true stress-true strain curves of 5083-0 aluminum alloy at 295, 76, and 4 K.

Load Control



Displacement Control

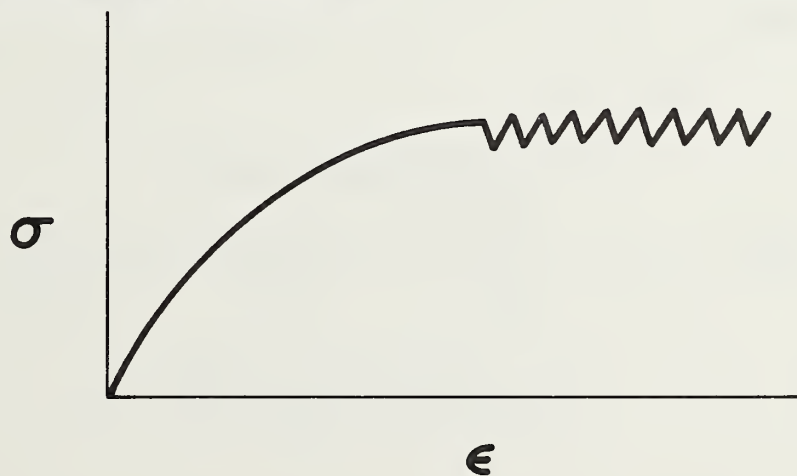


Figure 5. Load and displacement controlled tensile stress-strain behavior at 4 K.

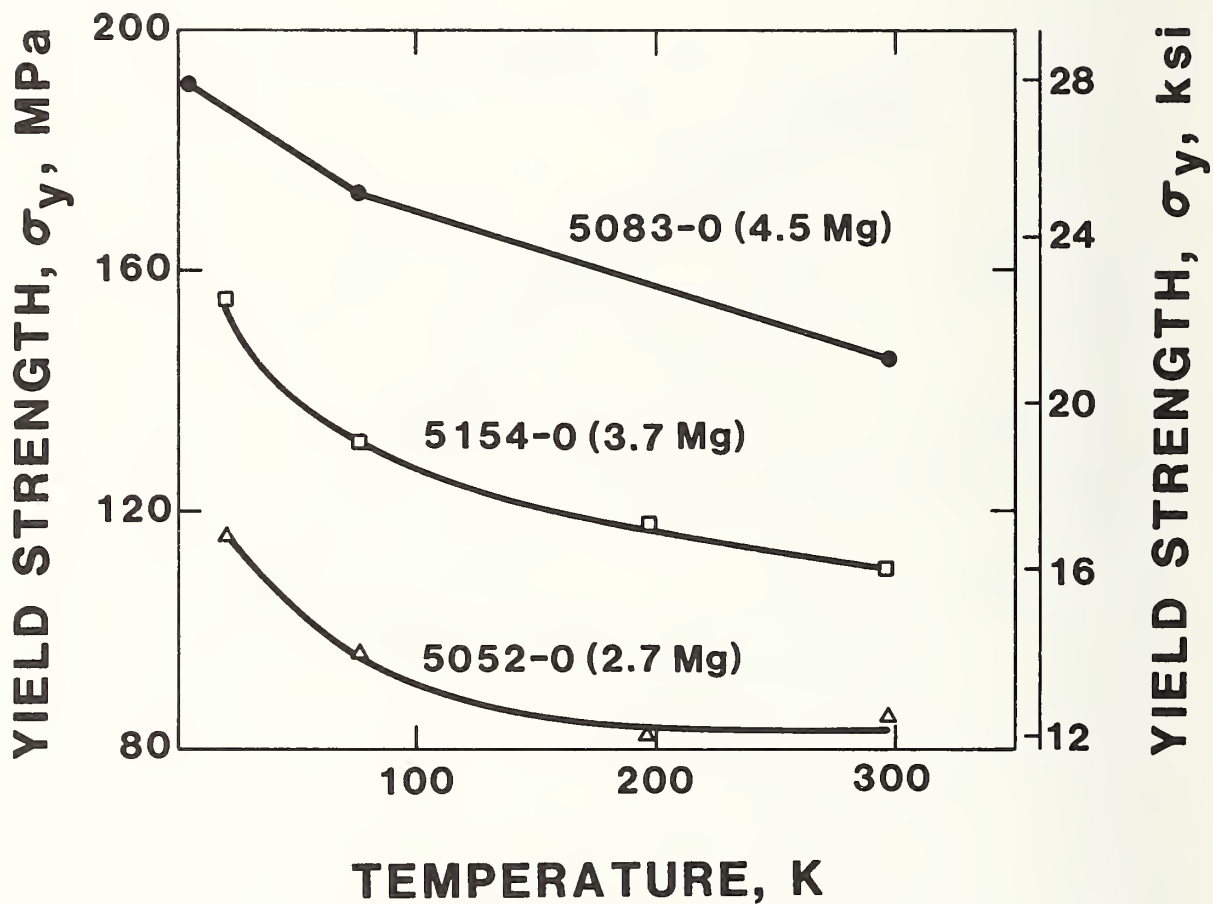


Figure 6. Tensile yield strength at low temperatures from aluminum-magnesium alloys 5083, 5154, and 5052 in the annealed condition.

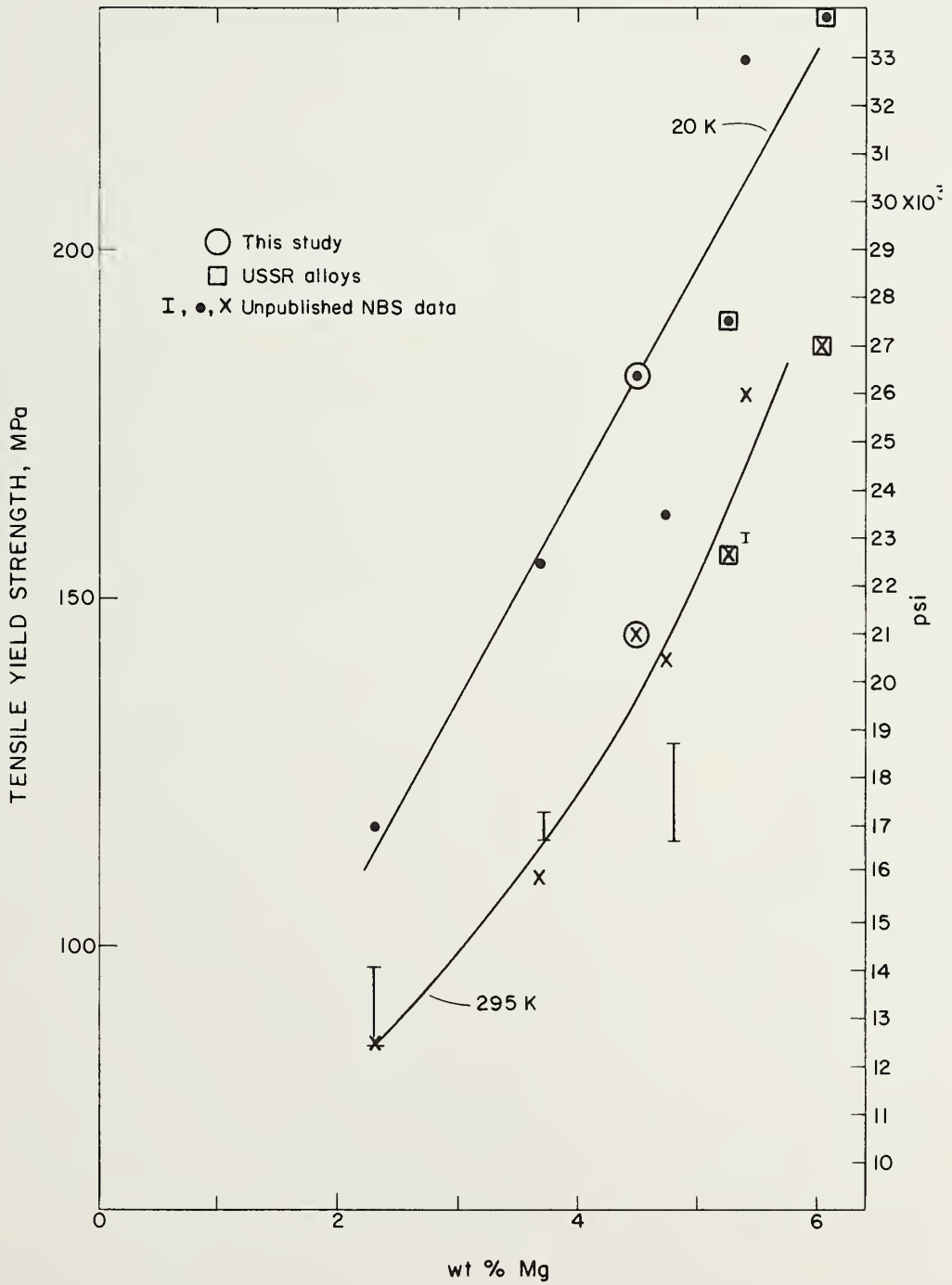


Figure 7. Influence of magnesium alloying additions in aluminum on tensile yield strength at 295 and 20 K.

EFFECTS OF CARBON AND NITROGEN ON THE ELASTIC CONSTANTS
OF STAINLESS STEEL 304

H. M. Ledbetter
Fracture and Deformation Division
National Bureau of Standards
Boulder, Colorado

ABSTRACT

Nine stainless-steel 304-type alloys were studied at room temperature. Carbon-plus-nitrogen contents of these alloys ranged from 0.067 to 0.325 weight percent (0.3 to 1.3 atomic percent). Five elastic constants--longitudinal modulus, Young's modulus, shear modulus, bulk modulus, and Poisson's ratio--were determined by a pulse-echo ultrasonic method. Within an experimental uncertainty of about 0.1 percent, all the elastic constants remain unaffected by carbon and nitrogen additions.

Introduction

This study sought to determine how carbon and nitrogen alloying additions affect the elastic constants of stainless-steel 304-type alloys.

Both carbon and nitrogen increase strength of austenitic Fe-Cr-Ni alloys. Nitrogen stabilizes the austenite, reducing the tendency at low temperatures toward martensitic transformations. Carbon functions similarly, but higher concentrations cause welding sensitization. The increasing popularity of these alloys together with a dearth of reliable physical-property measurements prompted the present study.

Being physical properties, elastic constants are relatively insensitive to details of internal structure related to thermomechanical treatment. However, when determined with sufficient sensitivity, they provide important parameters for indicating interatomic-force changes, which may occur during alloying. Indeed, small changes in elastic constants may indicate large changes in the nature of the interatomic bonding.

Experiment

Materials

Nine stainless-steel plates were purchased from the research laboratory of a U.S. steel manufacturer. All plates had nearly the same base composition, which fell within the limits of ASTM specification A240 for AISI-304 stainless steel, nominally Fe-18Cr-10Ni-1.5Mn-0.02P-0.02S-0.55Si-0.2Mo-0.2Cu weight percent. The carbon and nitrogen contents varied as shown in the mill chemical analyses in Table I. The nine plates were produced from three 136-kg vacuum-induction-melted heats, split with respect to carbon level, and teemed into 7.6 x 20 x 36 cm hot-topped cast-iron ingot molds. The ingots were reheated and

soaked at 1561 K (2350°F), hot-rolled into 2.54-cm plates, and air cooled. The plates were finally annealed at 1332 ± 7 K ($1937 \pm 13^\circ\text{F}$) for 1 h and water quenched. Hardness and grain size are also listed in Table I, and mass densities are given in Table II.

Methods

Room-temperature sound velocities were determined by a pulse-echo-overlap technique.¹ Quartz piezoelectric crystals with fundamental resonances between 4 and 7 MHz were cemented with phenyl salicylate to one end of a specimen with flat and parallel surfaces. An x-cut transducer was used for longitudinal waves and an ac-cut for transverse waves. The specimen in this case was a 1.59 x 1.59 x 1.27 cm parallelepiped with opposite faces ground flat and parallel within 2.5 μm . Ultrasonic pulses 1 to 2 cycles long were launched into the specimen by electrically exciting the transducer. The pulses propagated through the specimen, reflected from the opposite face, and propagated back and forth. The pulse echoes were detected by the transducer and displayed on an oscilloscope equipped with a time delay and a microprocessor for time-interval measurements. The sound velocity was computed by

$$v = 2\ell/t \quad (1)$$

where ℓ denotes specimen length, and t the round-trip transit time. On the oscilloscope, t was the time between adjacent echoes, the first and second echoes usually being measured, and within these the time between leading cycles. Elastic constants were computed from the general relationship

$$C = \rho v^2 \quad (2)$$

where ρ denotes mass density. The usual engineering elastic constants are related to the longitudinal and transverse sound velocities, v_ℓ and v_t , by

$$\text{longitudinal modulus} = C_\ell = \rho v_\ell^2 \quad (3)$$

$$\text{shear modulus} = G = \rho v_t^2 \quad (4)$$

$$\text{bulk modulus} = B = C_\ell - (4/3)G \quad (5)$$

$$\text{Young's modulus} = E = 3GB/(C_\ell - G) \quad (6)$$

$$\begin{aligned} \text{Poisson's ratio} = \nu &= (E/2G) - 1 \\ &= (1/2)(C_\ell - 2G)/(C_\ell - G) \end{aligned} \quad (7)$$

Results

Table II gives the principal results of the study: sound velocities and elastic constants for nine stainless-steel type-304 alloys with different carbon and nitrogen contents. Table III shows for one case, alloy 1, the directional variation of the ultrasonic wave velocities. Table III implies also that ultrasonic velocities can be measured in these alloys with an uncertainty of 0.05 percent or less.

Discussion

Results in Table II lead to the following conclusion: within our measurement capability (0.1 percent or less) all elastic constants of stainless-steel type-304 alloys remain unaffected by carbon-plus-nitrogen additions up to 1.3 atomic percent. Various statistical analyses of the results support this conclusion. And it can be seen quite simply by comparing the results for specimens 1 and 9, which have the lowest and

highest carbon-plus-nitrogen additions: the two sets of elastic constants are nearly identical; neither volume-deformation nor shear-deformation elastic constants change significantly nor show any trend versus composition. With the exception of specimen 4, all sound-velocity results fall within the one-standard-deviation range established for 304-type alloys by Ledbetter, Frederick, and Austin.¹ And specimen four is within 1.2 standard deviations.

Another strong reason for finding no alloying effect comes from comparing the variation of B and G among the nine alloys. Interstitial atoms, especially those in isotropic, octahedral positions, should affect B more than G because they cannot move under a dilation force. Yet, among the nine alloys B and G show the same variations from the mean.

Present results contrast sharply with observations reported for ferritic iron. Speich, Schwoeble, and Leslie² reported that carbon added to alpha iron reduces elastic stiffnesses such as E and G by about five percent per atomic percent carbon! Indeed, carbon is the most effective known alloying element in altering alpha iron's elastic constants. Quantitative results for nitrogen remain unreported, but one would expect nitrogen to behave similarly to carbon because their atomic diameters are similar. The essential distinction between the ferritic and austenitic cases is the crystal structure. Body-centered-cubic crystals are less accommodating to interstitials than are face-centered-cubic crystals. Carbon alloyed into bcc iron occupies octahedral interstices that have tetragonal symmetry, which produce a strong tetragonal distortion; no similar distortion occurs in fcc iron, where carbon occupies larger octahedral interstices and the lattice distortion is

isotropic. This distortion reflects also in the much higher solubility of carbon and nitrogen in fcc iron compared with bcc.

Present results dispute those of a previous study. Laddach and Schüller³ studied the influence of nitrogen on the elastic properties of an Fe-21Cr-20Ni alloy containing 0.02 and 0.29 weight percent nitrogen. They concluded that "nitrogen raises the modulus of elasticity as well as the modulus of rigidity, regardless of the nitrogen being either in interstitial solution or precipitated in the form of nitrides." No reconciliation of this conclusion and that of the present study seems apparent.

Conclusion

In the studied composition range, elastic constants are determined by interactions among atoms occupying lattice sites; carbon and nitrogen interstitial atoms play no significant part. Since elastic constants are determined by the interatomic force constants, they also must be independent of carbon and nitrogen content. Thus, the present result has importance also for other force-constant-determined physical properties, such as thermal expansivity and specific heat.

Acknowledgments

The DoE supported part of this study. R. L. Tobler of NBS contributed the materials and the grain-size measurements. J. Dahnke of NBS assisted in measurements.

References

1. H. M. Ledbetter, N. V. Frederick, and M. W. Austin, J. Appl. Phys. 51, 305-309 (1980).

2. G. R. Speich, A. J. Schwoeble, and W. C. Leslie, Metall. Trans. 3, 2031-2037 (1972).
3. H. Laddach and P. Schüler, DEW-Techn. Ber. 13, 85-88 (1973).

Table I. Chemical composition (weight percent), hardness, and grain size.

	Cr	Ni	Mn	P	S	Si	Mo	Cu	C	N	C+N	Hardness (Rockwell B)	Grain Size (μm)
1	18.3	10.1	1.57	0.021	0.019	0.50	0.20	0.210	0.028	0.039	0.067	73.4	85
2									0.058	0.039	0.097	74.1	78
3									0.089	0.039	0.128	78.5	90
4	18.0	9.91	1.50	0.022	0.017	0.57	0.205	0.197	0.037	0.120	0.157	81.9	105
5									0.067	0.120	0.187	83.5	85
6									0.094	0.120	0.214	84.2	78
7	20.3	9.97	1.42	0.024	0.016	0.55	0.195	0.200	0.030	0.240	0.270	87.3	98
8									0.057	0.240	0.297	88.0	82
9									0.085	0.240	0.325	88.5	90

Table II. Mass density, sound velocities, and elastic constants of nine carbon-plus-nitrogen-alloyed stainless-steel 304 alloys.

	Density (g/cm ³)	v_l (cm/ μ s)	v_t (cm/ μ s)	C_{ll} (GPa)	E (GPa)	G (GPa)	B (GPa)	ν
1	7.944	0.5751	0.3140	262.7	201.7	78.3	158.3	0.288
2	7.937	0.5757	0.3139	263.1	201.5	78.2	158.8	0.288
3	7.936	0.5751	0.3142	262.5	201.7	78.3	158.0	0.287
4	7.935	0.5743	0.3155	261.7	202.8	79.0	156.4	0.284
5	7.927	0.5747	0.3150	261.8	202.2	78.7	156.9	0.285
6	7.923	0.5748	0.3144	261.8	201.5	78.3	157.3	0.287
7	7.869	0.5769	0.3141	261.9	200.2	77.6	158.4	0.289
8	7.883	0.5764	0.3135	261.9	199.9	77.5	158.6	0.290
9	7.900	0.5766	0.3146	262.6	201.4	78.2	158.4	0.288
Mean		0.5755	0.3144	262.2	201.4	78.2	157.9	0.287
Std. dev.		0.0009	0.0006	0.5	0.9	0.5	0.8	0.002
Pct. std. error		0.2	0.2	0.2	0.4	0.6	0.5	0.7

Table III. Directional variation of ultrasonic wave velocities in specimen 1, where z direction is perpendicular to rolling plane.

Propagation direction	Polarization direction	v_l (cm/ μ s)	v_t (cm/ μ s)
x	x	0.5746	
x	y		0.3140
x	z		0.3143
y	y	0.5753	
y	x		0.3139
y	z		0.3138
z	z	0.5753	
z	x		0.3143
z	y		0.3140
Mean		0.5751	0.3141
Std. dev.		0.0004	0.0002
Pct. std. error		0.07	0.07

LOW-TEMPERATURE VARIABILITY OF STAINLESS-STEEL-304 ELASTIC CONSTANTS

H. M. Ledbetter
Fracture and Deformation Division
National Bureau of Standards
Boulder, Colorado

ABSTRACT

By measuring ultrasonic velocities, the elastic-constant behavior of four stainless-steel 304-type alloys was determined between ambient and liquid-helium temperatures. Despite their equivalence near room temperature, results show that cooling through the magnetic transition produces slightly different elastic constants in different alloys at low temperatures.

INTRODUCTION

Recently the author¹ collaborated in studying the room-temperature variability of stainless-steel 304-type elastic constants: Young's modulus, shear modulus, bulk modulus, Poisson's ratio. For twenty samples acquired randomly, the lot-to-lot variation was surprisingly small: 0.9 percent for Young's modulus, for example. Thus, for this commercial alloy, chemical-composition differences and thermomechanical-processing differences affect the elastic constants practically negligibly.

Because of many cryogenic applications for 300-series austenitic stainless steels, the author² recently determined accurately the low-temperature elastic constants of three such alloys: 304, 310, 316. At low temperatures all three alloys undergo a magnetic transition, which affects the elastic constants. The 304-alloy results given in that study were representative rather than comprehensive. Different 304 alloys actually behave slightly differently at low temperatures.

The present study determined approximately the low-temperature variability of stainless-steel-304 elastic constants. The longitudinal sound velocity was measured between 295 and 4 K for four steels: one regular 304 alloy, two low-carbon alloys, and one nitrogen-enriched alloy. The author³ showed recently that interstitial alloying elements such as carbon and nitrogen do not affect the room-temperature elastic constants of 304-type stainless steels. The longitudinal modulus manifests both volume and shear effects and is therefore sensitive to any change in the elastic constants.

EXPERIMENTS

Low-temperature ultrasonic velocities were determined similarly to room-temperature measurements made in our laboratory by a pulse-echo-superposition method.^{1,3} The notable difference was that for low temperatures the transducer-specimen bond consisted of stopcock grease rather than phenyl salicylate. The specimen was inserted into a probe,⁴ which was inserted into the ullage of a helium dewar. Measurements were made at 5-K intervals during continuous cooling or warming at rates of 1 to 2 K per minute. Temperature was monitored with a chromel-constantan thermocouple placed close to the specimen.

Table I shows the chemical compositions, hardnesses, and mass densities of the studied alloys.

RESULTS

Figure 1 shows the experimental results graphically: relative longitudinal modulus versus temperature for six alloys. To determine the slope dC/dT more accurately, phenyl salicylate bonds were used in two cases and cooled only to 245 K. Table II gives quantitative characteristics of the cooling curves (which reproduced during subsequent reheating, showing no hysteresis). "Max" indicates the maximum value of the $C(T)/C(295)$ curve, "min" indicates the minimum value at low temperatures, and Δ the difference between the two. The transition temperature, T_t , corresponds to $\Delta/2$. The slope dC/dT was determined by a linear-regression fit to eleven points between 245 and 295 K, and r^2 is the coefficient of determination.

DISCUSSION

Elastic constants reflect the magnetic-interaction energy of a system according to

$$C_{ijkl} = \partial^2 U / \partial \eta_{ij} \partial \eta_{kl} \quad (1)$$

where C_{ijkl} denotes the fourth-rank elastic-stiffness tensor, U denotes internal-energy density (including magnetic energy), and η_{ij} denotes Brugger strains. Four types of magnetic energy were discussed by Ledbetter and Collings⁵ in a study of Fe-Cr-Ni-Mn steels.

A priori, one expects strong magnetic interactions in these steels because they contain four magnetic elements: iron, chromium, nickel, and manganese. Fundamental calculations by Moruzzi, Janak, and Williams⁶ show that for these elements, especially Mn, magnetic energy affects properties: cohesive energy is reduced, bulk modulus reduced, and volume increased. At lower temperatures, because lattice vibrations are reduced and because magnetic atoms move closer together because of thermal contraction, magnetic interactions become stronger. Stronger magnetic interactions manifest themselves in physical-property changes.

The existence and complexity of low-temperature magnetic transitions in 304-type alloys have been discussed especially by Collings and Hart.⁷ They view austenitic stainless steels as completely paramagnetic at high temperatures. At some lower temperature, clustered ferromagnetic ordering leads to

superparamagnetism; at still lower temperatures, the paramagnetic matrix undergoes spin-glass condensation. Interactions among spin clusters and with the matrix lead to further possible complexities. In principle, all these magnetic transitions affect the elastic constants.

The reversible two-percent elastic-constant softening during cooling shown in Fig. 1 near $T = 47$ K results from a magnetic transition, probably the spin-glass condensation.

Why should spin-glass condensation cause elastic softening? Landau and Lifshitz⁸ proved for second-order phase transitions that "compressibility drops for a transition from an unsymmetrical to a symmetrical phase." Thus, the bulk modulus drops for a transition from a symmetrical (paramagnetic) phase to an unsymmetrical (magnetic) phase. Magnetic in this case means spin-glass.

Spin-glass properties arise, apparently, from magnetic-moment interactions. Principal among these is the s-d or Rudermann-Kittel-Kasuya-Yosida (RKKY) indirect-exchange interaction. The energy function for this spin system is

$$E = -(1/2) \sum_{i < j} J_{ij} \vec{S}_i \cdot \vec{S}_j \quad (2)$$

where $J_{ij} = J(\vec{R}_{ij}) = J(\vec{R}_i - \vec{R}_j) \quad (3)$

$$J(R) = A \cos 2k_f R / (2k_f R)^3 \quad (4)$$

where the spin positions \vec{R}_i are random variables, k_f is the fermi-level wavevector of the host conduction electrons, and $J(0) = 0$. Interaction (4) alternates in sign and is long range, representing alternately ferromagnetic and antiferromagnetic spin coupling. This type of magnetic interaction can become important when the usual $\vec{S}_i \cdot \vec{S}_j$ direct exchange becomes insignificant, that is, when the magnetic ions are separated so widely that their overlap integral is zero. The basic idea in RKKY exchange is that an s conduction electron interacts with a localized d electron through a direct-exchange interaction $\vec{S}^s \cdot \vec{S}_i^d$, travels through the lattice, and then has a second such interaction $\vec{S}^s \cdot \vec{S}_j^d$. This amounts to an effective (indirect) interaction $\vec{S}_i \cdot \vec{S}_j$ between the two localized d electrons at \vec{R}_i and \vec{R}_j .

The anomalous elastic-constant behavior shown in Fig. 1 relates in the most general sense to magneto-elastic energy, to a mechanism that couples a crystal's elastic vibrations to its magnetic modes. Here we are especially concerned with the magneto-elastic energy arising from the strain dependence of the $J_{ij} \vec{S}_i \cdot \vec{S}_j$ indirect exchange interaction. From Hausch and Warlimont,⁹ who used a molecular-field approximation, and for simplicity using Voigt averaging, it follows that the magnetic-exchange-energy contributions to the bulk modulus, B , and the shear modulus, G , for the face-centered-cubic first neighbor-only case are:

$$B_{\text{ex}} = -4N \left(1 - \frac{T}{T_t}\right) (r_0^2 J'' - 2r_0 J') \quad (5)$$

and
$$G_{ex} = \frac{-12}{5}N(1 - \frac{T}{T_t}) (r_0^2 J'' + 4r_0 J') \quad (6)$$

where N = atoms/volume, T_t = transition temperature, r_0 = equilibrium atomic spacing, and J' and J'' are the first and second derivatives of J with respect to r evaluated at $r = r_0$. Since $J(r)$ is not known a priori for 3d metals and alloys, J' and J'' must be determined experimentally. In principle, J' and J'' can be estimated from measurements made in the present study. However, the many approximations and the alloy's complexity render this approach dubious. Equations (5) and (6) are set out mainly to give the flavor of a final explanation, which awaits an ab initio relationship for $J(r)$, discussions of which Dehlinger¹⁰ gave for alloys.

ACKNOWLEDGMENT

The Department of Energy supported this study. Several people contributed experimentally: M. W. Austin, J. Dahnke, and G. Maerz.

REFERENCES

1. H. M. Ledbetter, N. F. Frederick, and M. W. Austin, J. Appl. Phys. 51, 305-309 (1980).
2. H. M. Ledbetter, J. Appl. Phys., forthcoming.

3. H. M. Ledbetter, unpublished research.
4. E. R. Naimon, W. F. Weston, and H. M. Ledbetter, *Cryogenics* 14, 246-249 (1974).
5. H. M. Ledbetter and E. W. Collings, in The Metal Science of Stainless Steels (Met. Soc. AIME, New York, 1979), pp. 22-40.
6. V. L. Moruzzi, J. F. Janak, and A. R. Williams, Calculated Electronic Properties of Metals (Pergamon, New York, 1978), p. 6.
7. E. W. Collings and S. C. Hart, *Cryogenics* 19, 521-530 (1960).
8. L. D. Landau and E. M. Lifshitz, Statistical Physics (Pergamon, London, 1959), p. 438.
9. G. Hausch and H. Warlimont, *Z. Metallkd.* 63, 547-552 (1972).
10. U. Dehlinger, *Z. Metallkd.* 28, 116 (1936); 28, 194 (1936); 29, 388 (1937).
Reviewed in F. Seitz, The Modern Theory of Solids (McGraw Hill, New York, 1940), pp. 623-626.

Table I. Chemical composition (weight percent) and other properties

	Cr	Ni	Mn	Si	C	P	S	N	Cu	Mo	V	Co	Hardness (Rockwell B)	Mass Density (g/cm ³)
1	18.4	9.7	1.4	0.6	0.02	0.02	0.01						87	7.923
2	18.84	10.18	1.65	0.82	0.026	0.022	0.010		0.28	0.27			62	7.856
3	18.30	8.45	0.82	0.59	0.061	0.020	0.017						92	7.927
4	18.5	8.75	1.43	0.31	0.030	0.025	0.013	0.061					73	7.940
5	18.65	9.49	1.88	0.38	0.048	0.019	0.024	0.12	0.07	0.52	0.03	0.06	75	7.860
6													77	7.817

Table II. Results of low-temperature measurements of relative longitudinal modulus

	max	min	Δ	T_t (K)	$-dC/dT$ ($10^7 N/m^2K$)	r^2
1	1.0442	1.0248	0.0194	46	6.62	0.9909
2					6.55	0.9944
3	1.0436	1.0207	0.0229	45	6.97	0.9910
4	1.0421	1.0147	0.0274	51	7.37	0.9917
5					6.04	0.9978
6	1.0429	1.0184	0.0245	47	6.38	0.9912

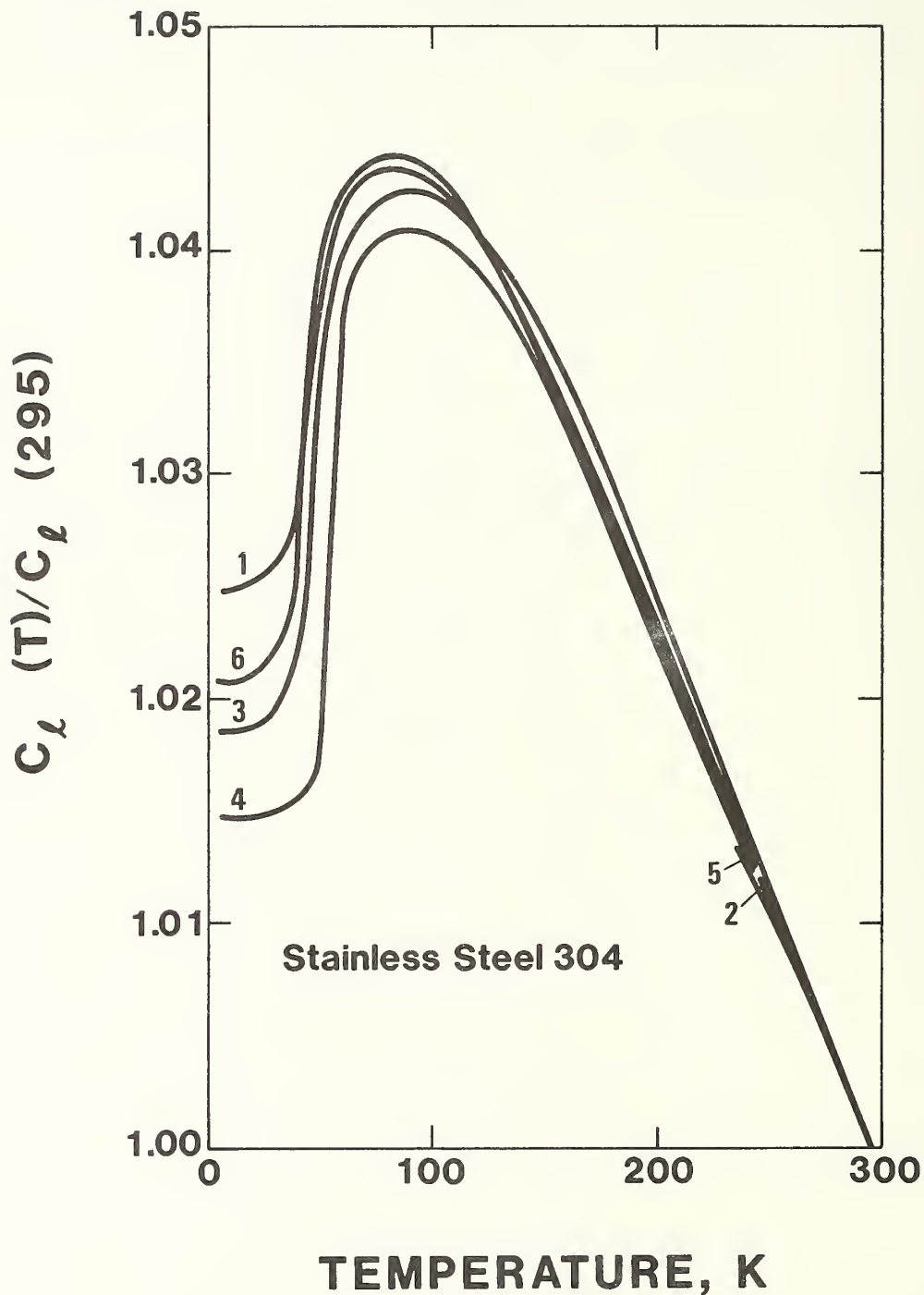


Fig. 1 Relative longitudinal modulus versus temperature for six stainless-steel type-304 alloys. This modulus reflects both dilation and shear deformation modes. As described in text, anomalous decrease at near 47 K arises from a paramagnetic-magnetic transition, probably spin-glass, which is usually described by an RKKY indirect exchange energy.

PREDICTED SINGLE-CRYSTAL ELASTIC CONSTANTS OF STAINLESS STEEL 304

H. M. Ledbetter
Fracture and Deformation Division
National Bureau of Standards
Boulder, Colorado

ABSTRACT

The three single-crystal elastic constants-- C_{11} , C_{12} , C_{44} --of stainless steel 304 are estimated from the polycrystalline bulk and shear moduli together with an empirical C_{12}/C_{11} value, which is discussed theoretically. The estimate involves a reverse Kröner method for relating single crystal and polycrystalline elastic constants.

A solid's engineering elastic constants, such as Young's modulus and Poisson's ratio, serve many practical purposes. Among these are calculations of load-displacement, thermoelastic stress, elastic stability (buckling), residual stress, and fracture-toughness plane-stress-to-plane-strain conversions.

A solid's single crystal (anisotropic) elastic constants, the C_{ij} 's and the S_{ij} 's, provide additional and more fundamental information than do the engineering (quasi-isotropic) elastic constants. The C_{ij} 's are essential, for example, for theory of point defects, anisotropic dislocation interactions, elastic-energy calculations, force-constant-related properties such as lattice vibrations, accurate determination of Debye characteristic temperatures, correlations with electronic theory of solids, and correlations with other physical properties.

Stainless steels form a key component of materials technology, and their basic properties are now being studied by methods applied formerly to elements or to simple binary alloys. Elastic constants comprise one subset of basic mechanical-physical properties, which must be known and understood before the metal physics of stainless steels can be carried very far.

Three existing experimental studies [1-3] of the single-crystal elastic constants of Fe-Cr-Ni alloys omit the Fe-18Cr-8Ni alloy, which is of most interest because of large tonnages and multifarious applications and because it provides a base material for developing many other special purpose stainless steels. In principle, these three studies on four alloys--Fe-12Cr-18Ni, Fe-18Cr-12Ni, Fe-18Cr-14Ni, Fe-18Cr-19Ni--should permit by linear-regression analysis the determination of the single-crystal elastic constants of Fe-18Cr-8Ni. But, this analysis

fails. Reasons for this probably include: a small sample set (four alloys for three independent coefficients), poor distribution of sample chemical compositions, experimental errors, nonlinear dependence on composition, and possible nonadditive, interactive composition effects.

The present study predicts the single-crystal elastic constants of Fe-18Cr-8Ni. The prediction depends on three ingredients: one observational, one theoretical, and one empirical, which has some theoretical basis. Observationally, Ledbetter, Frederick, and Austin [4] measured the polycrystalline elastic constants of twenty randomly acquired Fe-18Cr-8Ni alloys with the results that the bulk modulus, B , and the shear modulus, G , are well defined: $B = 1.582$ and $G = 0.774 \cdot 10^{11} \text{ N/m}^2$. Theoretically, Kröner [5] showed how the polycrystalline elastic constants (two independent, e.g., B and G) can be calculated from the single-crystal elastic constants (three independent for the cubic-symmetry case: C_{11} , C_{12} , and C_{44}). Empirically, as shown in table 1 for Fe, Ni, and the four Fe-Cr-Ni alloys described above, the dimensionless ratio $y = C_{12}/C_{11}$ is surprisingly constant for these materials: 0.635 ± 0.031 . In theory, y varies between zero and one. Both the upper and lower limits correspond to a mechanical instability. For the cubic elements, in practice y varies between 0.12 (diamond) and 0.85 (gold).

Before considering the above case, we consider a simple, familiar model: central forces between atoms, which require that $C_{12} = C_{44}$. Table 1 shows this assumption is not too bad for these materials. We will treat the results as approximate guidelines to a better calculation. Since we are computing three elastic constants (C_{11} , C_{12} , C_{44}) from two (B and G), we need another relationship among the C_{ij} 's. For central interatomic forces, this relationship is

$$C_{12} = C_{44} \quad (1)$$

For all cubic crystals, the bulk modulus relates to the C_{ij} 's according to

$$B = \frac{1}{3} (C_{11} + 2C_{12}) \quad (2)$$

Following Kröner, the shear modulus relates to the C_{ij} 's by

$$G^3 + \alpha G^2 + \beta G + \gamma = 0 \quad (3)$$

where

$$\alpha = (5C_{11} + 4C_{12})/8 \quad (4)$$

$$\beta = -C_{44}(7C_{11} - 4C_{12})/8 \quad (5)$$

and

$$\gamma = -C_{44}(C_{11} - C_{12})(C_{11} + 2C_{12})/8 \quad (6)$$

Solving eqs. (1) through (3) simultaneously gives the central-force (cf) results for Fe-18Cr-8Ni shown in table 1. All three C_{ij} 's and the bulk modulus fall within the ranges established by the four alloys. Both $C' = (C_{11} - C_{12})/2$ and $A = C_{44}/C'$ are outside these bounds. Thus, when fitted to observed values of B and G, a central-force model for stainless steel is not bad and fails mainly for the C' elastic constant.

We turn now to a more realistic noncentral-force model where $C_{12}/C_{11} = 0.635$. (The basis for this is described below.) Simultaneously solving eqs. (2) and (3) subject to this condition yields the results shown in table 1 in the bottom line. When combined with previous observations, these new theoretical results show how Ni affects elastic constants in the Fe-18Cr-8Ni region. Increasing Ni decreases C_{11} , C_{12} , B, and C' ,

but leaves C_{44} relatively unaffected, perhaps slightly increased; Zener anisotropy increases slightly, indicating a possible tendency toward instability. Except for C' and A , results of Salmutter and Stangler [1] suggest that Cr produces opposite effects from Ni.

Finally, it remains to try to understand why $y = 0.635$ for these alloys. If the two-body, central-force interatomic potential is denoted $\phi(r)$, then the Brugger elastic constants, which are fourth-rank tensors, are given at $T = 0$ K by:

$$C_{ijkl} = \frac{\partial^2 U}{\partial \eta_{ij} \partial \eta_{kl}} \quad (7)$$

$$= \frac{1}{2V^0} [\Sigma D^2 \phi(r) r_i^0 r_j^0 r_k^0 r_l^0]_{r = r^0},$$

where $D\phi(r)$ denotes $(1/r)[\partial\phi(r)/\partial r]$. The energy density U of the crystal is obtained by a sum over two-body atom-atom interaction energies:

$$U = (1/2V^0)\Sigma\phi(r), \quad (8)$$

where V^0 is the undeformed atomic volume. The η_{ij} are components of the Lagrangean elastic strain matrix

$$\eta = \frac{1}{2}(J^t J - I), \quad (9)$$

where I is the 3 x 3 identity matrix, t denotes transposition, and the deformation matrix J is defined by

$$r = Jr^0, \quad (10)$$

where r^0 and r are the interatomic spacings in the initial state and in the deformed state, respectively. Details concerning this approach to elastic constants can be found elsewhere [9].

Face-centered cubic crystals have twelve nearest neighbors at $\langle \pm 1, \pm 1, 0 \rangle a/2$, and six second-nearest neighbors at $\langle \pm 1, 0, 0 \rangle a$, where a is the unit-cell dimension. In this case one obtains from eq. (7):

$$C_{11} = \frac{1}{2V^0} \left[8 \left(\frac{a}{2} \right)^4 D^2_{\phi} \left(\frac{a}{\sqrt{2}} \right) + 2a^4 D^2_{\phi}(a) + \dots \right] \quad (11)$$

and

$$C_{12} = C_{44} = \frac{1}{2V^0} \left[4 \left(\frac{a}{2} \right)^4 D^2_{\phi} \left(\frac{a}{\sqrt{2}} \right) + \dots \right], \quad (12)$$

where ... indicates contributions from pairs farther than second neighbors. Clearly, summing over only nearest neighbors gives $y = 0.500$ for the f.c.c. case. The effects of second-nearest neighbors depend on whether $D^2_{\phi}(r)$ is already negative at $r = a$. If so, then y is increased because C_{11} is decreased while C_{12} remains unaffected. Equation (7) represents both structure-dependent and volume-dependent contributions to the C_{ij} 's. But there may be other, purely volume-dependent terms in the energy, often represented as

$$U(V) = AV^n \quad (13)$$

where V denotes volume and A and n are positive adjustable parameters. It follows simply that these terms (denoted by asterisks) contribute to the C_{ij} 's as follows:

$$C_{11}^* = nA(n-2) = n^2A - 2nA \quad (14)$$

$$C_{12}^* = n^2A \quad (15)$$

$$C_{44}^* = nA \quad (16)$$

Thomas [10] showed that for f.c.c. lattices

$$-nA = \sqrt{2}a(\partial\phi/\partial r) \quad (17)$$

evaluated at the nearest-neighbor spacing. Since $\partial\phi/\partial r$ is negative there, nA is positive. (If the volume-dependent energy arises, for example, entirely from the electron gas, then $n = -2/3$ in a Sommerfeld model.) Thus, C_{12}^* exceeds C_{11}^* and y is increased above 0.50 by volume-dependent energy terms. For cubic metals, only four (Cr, Ir, Mo, W) have C_{12}/C_{11} ratios less than 0.5, and only one of these is f.c.c. Values exceeding 0.50 are expected for metals because their electron gas contributes a volume-dependent energy. The near constancy of y among Fe, Ni, and these Fe-Cr-Ni alloys suggests that for some purposes the potential-energy function of d-band transition metals can be treated similarly to the simpler sp-band metals: a sum of pair potentials and a purely volume-dependent energy term.

ACKNOWLEDGMENT

This study was supported partly by the DoE Office of Fusion Energy and partly by the NBS Office of Standard Reference Data.

REFERENCES

- [1] K. Salmutter and F. Stangler, *Z. Metallkd.* 51, 1-4 (1960).
- [2] M. Kikuchi, *Trans. Jap. Inst. Met.* 12, 417-421 (1971).
- [3] M. C. Mangalick and N. F. Fiore, *Trans. Metall. Soc. AIME* 242, 363-2364 (1968).
- [4] H. M. Ledbetter, N. V. Frederick, and M. F. Austin, *J. Appl. Phys.* 51, 305-309 (1980).

- [5] E. Kröner, Z. Phys. 151, 504-518 (1958).
- [6] R. A. Johnson, Phys. Rev. 145, 423-433 (1966).
- [7] D. Diesburg, Ph.D. Thesis, Iowa State University (1971).
- [8] G. A. Alers, J. R. Neighbors, and H. Sato, J. Phys. Chem. Solids, 13, 40-55 (1960).
- [9] R. A. Johnson, Phys. Rev. B 6, 2094-2100 (1972).
- [10] J. F. Thomas, Scripta Metall. 5, 787-790 (1971).

Table 1
 Single-Crystal Elastic Constants of Several
 Face-Centered-Cubic Materials

Material	C_{11}	C_{12}	C_{44}	B	C'	A	ν	Ref.
	10^{11}N/m^2							
Fe	2.51	1.57	1.12	1.88	0.47	2.38	0.625	6
Fe	2.760	1.735	1.363	2.077	0.513	2.41	0.629	7
Ni	2.516	1.544	1.220	1.868	0.486	2.51	0.614	8
Fe-12Cr-18Ni	2.332	1.626	1.225	1.862	0.353	3.48	0.697	1
Fe-18Cr-12Ni	1.912	1.179	1.386	1.423	0.367	3.78	0.617	2
Fe-18Cr-14Ni	1.98	1.25	1.22	1.49	0.365	3.34	0.631	3
Fe-18Cr-19Ni	1.91	1.19	1.24	1.43	0.360	3.44	0.623	3
Fe-18Cr-8Ni (cf)	1.99	1.38	1.38	1.58	0.306	4.50	0.692	Present
Fe-18Cr-8Ni	2.09	1.33	1.21	1.58	0.382	3.17	0.635	Present

ELASTIC-CONSTANT/TEMPERATURE BEHAVIOR OF THREE HARDENED MARAGING STEELS

H. M. Ledbetter and M. W. Austin
Fracture and Deformation Division
National Bureau of Standards
Boulder, Colorado

ABSTRACT

Elastic constants of three maraging steels were determined by measuring ultrasonic velocities. Annealed steels show slightly lower bulk moduli and considerably lower shear moduli than hardened steels. All the elastic constants -- Young's modulus, shear modulus, bulk modulus, and Poisson's ratio -- show regular temperature behavior between 76 K and 400 K. Young's and shear moduli increase with increasing yield strength, but the bulk modulus and Poisson's ratio are relatively unchanged. Elastic anisotropy is quite small.

INTRODUCTION

Elastic constants find many uses. In technological materials they assume importance whenever problems arise concerning deflections, elastic stability (buckling), excessive elastic deformation (jamming), thermoelastic stress, residual stress, fracture, and so on. Ratios of elastic modulus to density or to thermal conductivity provide well-known structural-design parameters. Elastic constants correlate empirically with many practical properties such as strength, hardness, and wear. Because they relate intimately to both the interatomic potential and the lattice-vibration spectrum, elastic constants relate in turn to many fundamental solid-state phenomena such as diffusion, theoretical strength, and lattice-defect energies. Elastic constants appear as coefficients in thermodynamic equations of state where their relationships to free energy, specific heat, and thermal expansivity become especially clear. Since they can be measured accurately (typically within 1 percent or less) and small changes can be detected easily (typically 1 in 10^5 or better), elastic constants are useful physical properties for characterizing and comparing materials and for detecting changes in material properties. In the present case, the variation of elastic constants with composition and microstructure is of special interest.

Ledbetter and Read¹ recently reported the elastic-constant behavior of an annealed 300-grade maraging steel between 4 and 300 K. [The 300-grade steel has a yield stress near 2.07 GPa (300,000 psi).] They reported four elastic constants -- Young's modulus, shear modulus, bulk modulus, and Poisson's ratio. Besides corresponding closely to the elastic constants of an Fe-18Ni alloy, all these constants showed regular temperature behavior.

The present report describes a similar, extended study. Three maraging steels -- 200-grade, 250-grade, and 300-grade, both annealed and hardened -- were studied between 76 and 400 K. Elastic anisotropy was studied at room temperature. Despite their relatively poor low-temperature fracture toughness in the hardened condition, these steels occur in many cryogenic applications because of their exceptionally high strength. Because they are relatively new structural alloys, their elastic properties have received little attention.

EXPERIMENT

Tables I and II characterize the alloys obtained from a commercial source as 2.7-cm and 4.2-cm diameter bars. The pycnometric mass-density determination used distilled water as a standard.

Sound velocities were determined on two sizes of cubes -- 1.3 cm and 1.6 cm -- whose opposite faces were flat and parallel within 3 μm . Pulse-echo and pulse-echo-superposition techniques for room-temperature and low-temperature measurements, respectively, are described elsewhere.^{2,3} Measurements between 300 and 400 K were done in a stirred, heated mineral-oil bath using the oil as the transducer-specimen couplant; a mercury-in-glass thermometer indicated the temperature.

Elastic constants were obtained from longitudinal and transverse sound velocities, v_l and v_t , by the relationships:

$$\text{longitudinal modulus} = C_{\ell} = \rho v_{\ell}^2 \quad (1)$$

$$\text{shear modulus} = G = \rho v_t^2 \quad (2)$$

$$\text{bulk modulus} = B = C_{\ell} - \frac{4}{3}G \quad (3)$$

$$\text{Young's modulus} = 9GB/(G + 3B) \quad (4)$$

and

$$\text{Poisson's ratio} = (E/2G) - 1 \quad (5)$$

where ρ denotes mass density.

RESULTS

Table III gives, for the hardened steels, the room-temperature elastic constants and their directional variation. Table IV gives the averaged (over three orthogonal directions) room-temperature elastic constants for the annealed specimens. Table V and Figs. 1-5 give the temperature dependence of the elastic constants. Curves in these figures represent best fits of the data to Varshni's⁴ relationship:

$$C = C^{\circ} - s/(e^{t/T} - 1) \quad (6)$$

which contains three adjustable parameters: C° is the zero-temperature elastic constant, $-s/t$ is the high-temperature slope dC/dT , and t is an approximate Einstein temperature. Figures 1-5 contain only the 76 to 300 K results; the 300 to 400 K data form linear extensions of the 76 to 300 K curves.

DISCUSSION

In their annealed (Fe-Ni-martensite) condition, these alloys show decreasing E and G and increasing B and ν upon progressing from lower to higher yield strength (see Table IV). Since only Mo content increases systematically in this series and its bulk modulus exceeds considerably that of Fe, Ni, and Co, it may cause these property variations. Takeuchi's⁵ elastic-constant results confirm that Mo additions decrease Fe's shear modulus. Molybdenum effects on the bulk modulus remain uncertain. Ledbetter and Read¹ found that, except for the bulk modulus, an annealed 300-grade maraging steel has elastic constants similar to those of Fe-18Ni. The present study confirms this.

Hardening increases Young's modulus, shear modulus, longitudinal modulus, and bulk modulus but decreases Poisson's ratio (see Tables III and IV). These changes increase upon progressing from 200-grade to 250-grade to 300-grade. These elastic-constant changes suggest their possible use as an indicator of the precipitation process.

The elastic-constant temperature behavior is hardly remarkable. It shows all the features of regular behavior: tendency toward zero slope at zero temperature, as required by the third law of thermodynamics; continuous decrease with increasing temperature, consistent with the softening of interatomic bonding forces caused by increased thermal vibrations; and a linear slope at high temperatures. High-temperature linearity is consistent with the theoretical result of Leibfried and Ludwig⁶ that the elastic constant depends on temperature according to

$$C(T) = C(0) (1 - DU) \quad (7)$$

where U denotes mean energy and D is a parameter that depends on the type of crystal and the type of oscillator model used (Einstein, Debye, etc.). At high temperatures U varies as kT.

ACKNOWLEDGMENT

This study was supported by NASA Langley Research Center and by the DoE Office of Fusion Energy.

REFERENCES

1. H. M. Ledbetter and D. T. Read, *Metall. Trans. A* 8A, 1805-1808 (1977).
2. E. R. Naimon, W. F. Weston, and H. M. Ledbetter, *Cryogenics* 14, 246-250 (1974).
3. H. M. Ledbetter, N. F. Frederick, and M. W. Austin, *J. Appl. Phys.* 51, 305-309 (1980).
4. Y. P. Varshni, *Phys. Rev.* 2, 3952-3955, (1970).
5. S. Takeuchi, *J. Phys. Soc. Jpn.* 27, 929-940 (1969).
- 6.. G. Leibfried and W. Ludwig, in Solid State Physics, Volume 12 (Academic, New York, 1961), pp. 275-444.

Table I. Chemical compositions of studied steels, weight percentage, balance Fe.

	Ni	Co	Mo	C	Si	Mn	S	P	Al	Ti	B	Zr	Ca
200-grade	18.83	8.55	3.32	.014	.07	.08	.003	.003	.13	.20	.003	.010	.05
250-grade	18.34	8.03	4.69	.027	.04	.06	.004	.005	.12	.40	.002	.011	.05
300-grade	19.00	9.50	4.95	.026	.05	.01	.002	.006	.14	.58	.003	.011	.05

Table II. Metallurgical characterization of studied alloys.

	Density (g/cm ³)		Hardness (Rockwell C)		Hardening Heat Treatment
	Annealed	Hardened	Annealed	Hardened	
200-grade	8.068	8.030	28	43	489°C, 4.5 h, air cool
250-grade	8.076	8.066	29	51	same
300-grade	8.087	8.087	31	54	same

Table III. Room-temperature elastic constants
of three hardened maraging steels.

	B (10^{11} N/m ²)	E (10^{11} N/m ²)	G (10^{11} N/m ²)	ν
200-grade x ^a	1.654	1.853	0.706	0.313
y	1.657	1.848	0.703	0.314
z	1.656	1.852	0.705	0.314
250-grade x	1.666	1.885	0.719	0.311
y	1.664	1.884	0.718	0.311
z	1.663	1.888	0.720	0.310
300-grade x	1.680	1.902	0.725	0.311
y	1.681	1.899	0.724	0.312
z	1.686	1.899	0.724	0.312

^a_z = bar axis; x and y are perpendicular to z.

Table IV. Room-temperature elastic constants of three annealed maraging steels.

	B	E	G	ν
	(10^{11} N/m ²)	(10^{11} N/m ²)	(10^{11} N/m ²)	
200-grade	1.655	1.773	0.671	0.321
250-grade	1.656	1.749	0.661	0.324
300-grade	1.664	1.729	0.652	0.327

Table V. Elastic constants of three hardened maraging steels at selected temperatures.

T(K)	B (10^{11} N/m ²)	E (10^{11} N/m ²)	G (10^{11} N/m ²)	ν
<u>200-grade</u>				
400	1.63	1.794	0.681	0.317
350	1.643	1.822	0.693	0.315
300	1.655	1.849	0.704	0.314
250	1.667	1.875	0.714	0.313
200	1.678	1.900	0.724	0.311
150	1.687	1.920	0.733	0.310
100	1.694	1.935	0.739	0.310
75	1.696	1.938	0.740	0.309
<u>250-grade</u>				
400	1.645	1.826	0.695	0.315
350	1.654	1.855	0.706	0.313
300	1.664	1.883	0.718	0.311
250	1.673	1.910	0.729	0.310
200	1.682	1.935	0.740	0.308
150	1.691	1.956	0.748	0.307
100	1.698	1.971	0.754	0.307
75	1.701	1.976	0.756	0.306
<u>300-grade</u>				
400	1.664	1.841	0.700	0.316
350	1.674	1.870	0.712	0.314
300	1.684	1.898	0.723	0.312
250	1.694	1.925	0.734	0.311
200	1.704	1.949	0.744	0.309
150	1.713	1.971	0.753	0.308
75	1.72	1.986	0.759	0.308
75	1.722	1.990	0.761	0.307

LIST OF FIGURES

- Fig. 1. Temperature variation of longitudinal modulus of three hardened maraging steels.
- Fig. 2. Temperature variation of shear modulus of three hardened maraging steels.
- Fig. 3. Temperature variation of Young's modulus of three hardened maraging steels.
- Fig. 4. Temperature variation of bulk modulus of three hardened maraging steels.
- Fig. 5. Temperature variation of Poisson's ratio of three hardened maraging steels.

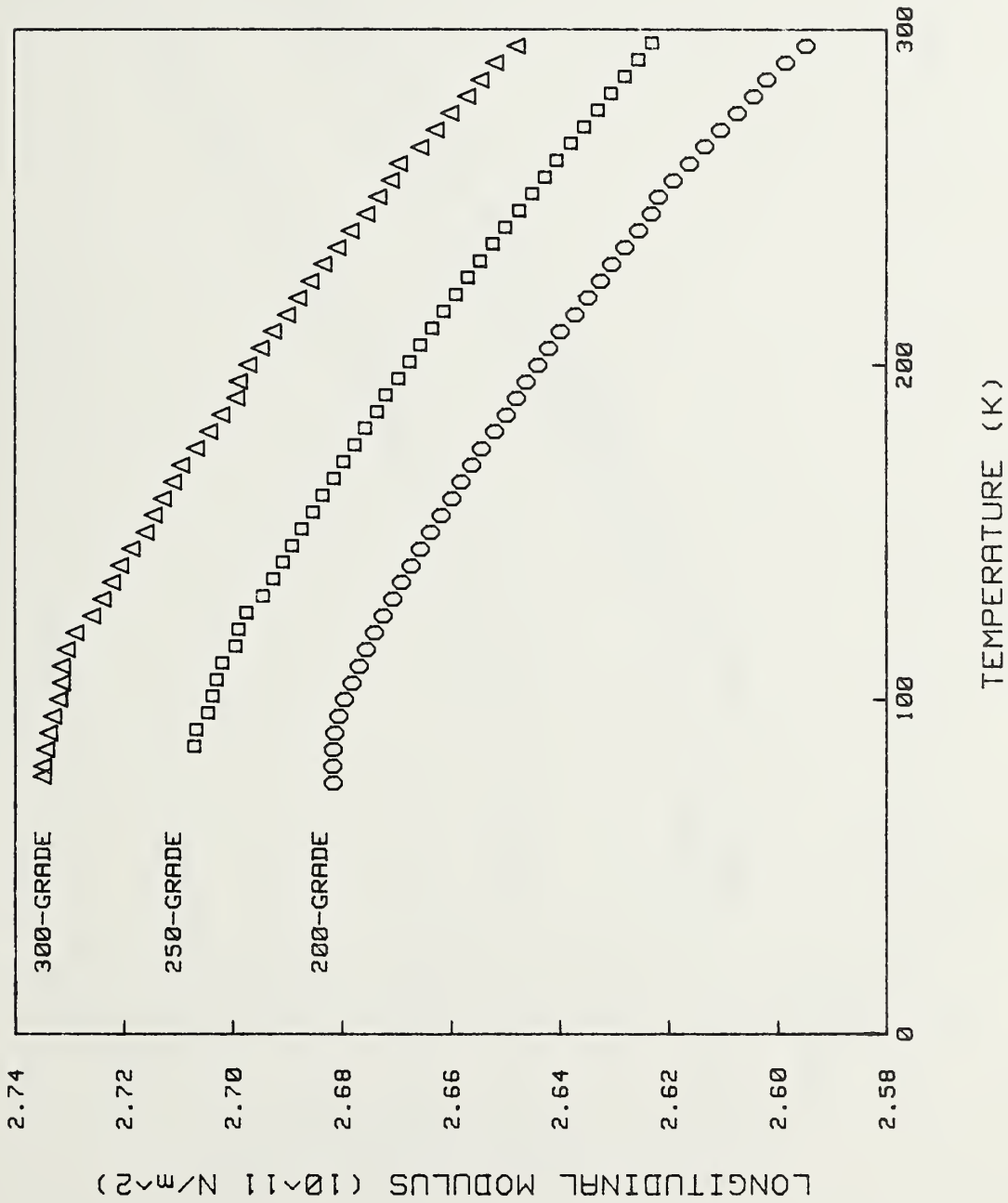


Fig. 1. Temperature variation of longitudinal modulus of three hardened maraging steels.

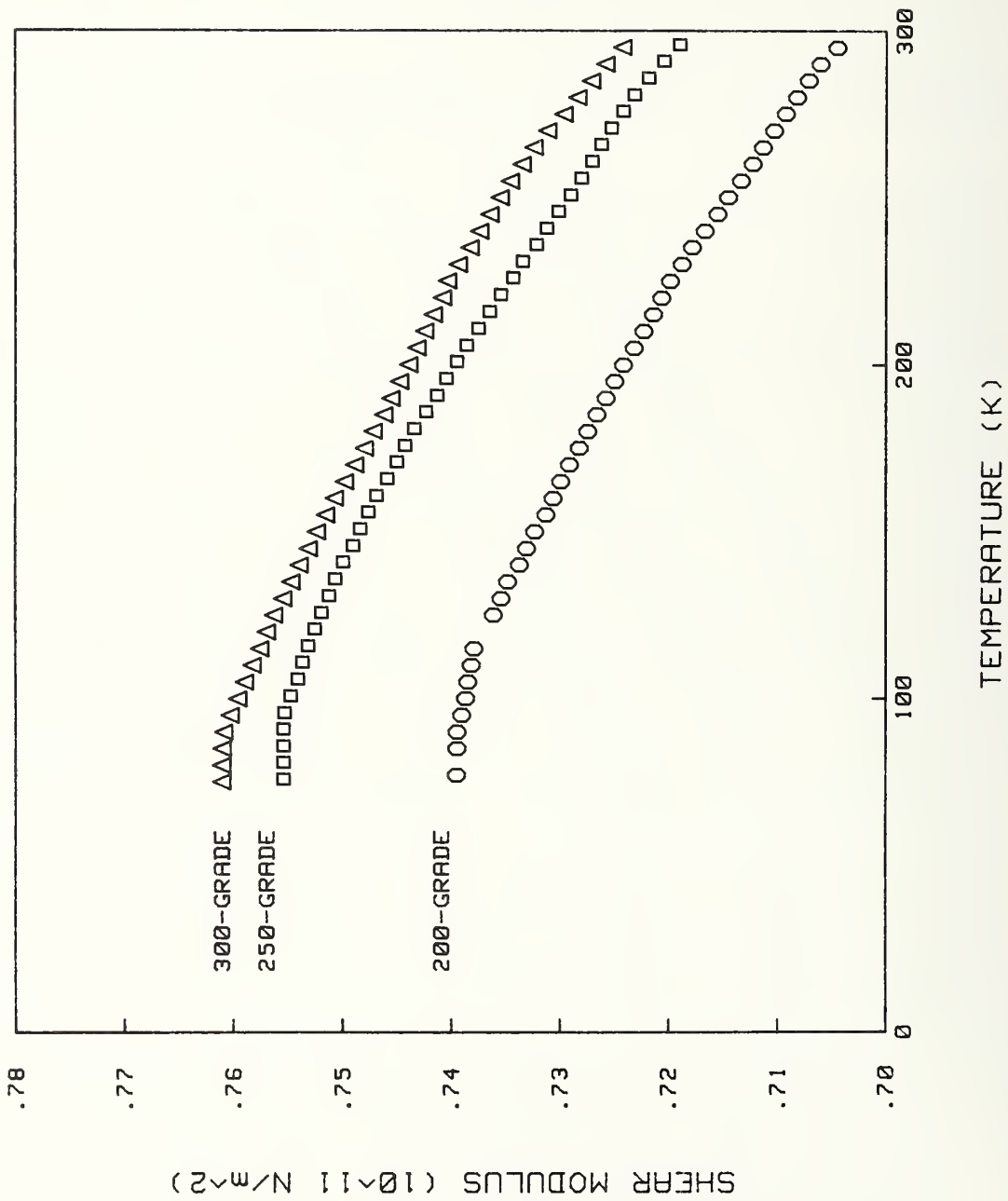


Fig. 2. Temperature variation of shear modulus of three hardened maraging steels.

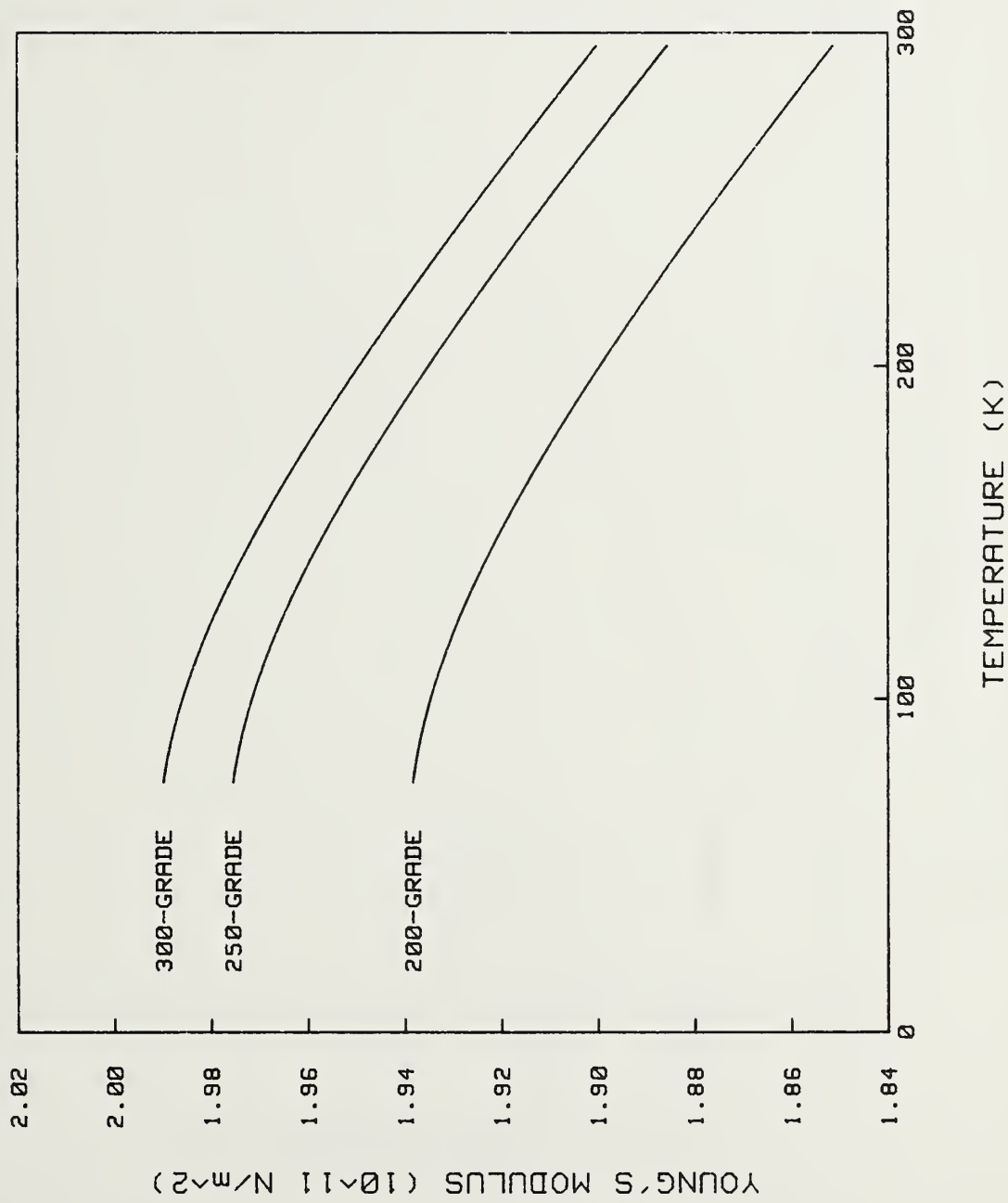


Fig. 3. Temperature variation of Young's modulus of three hardened maraging steels.

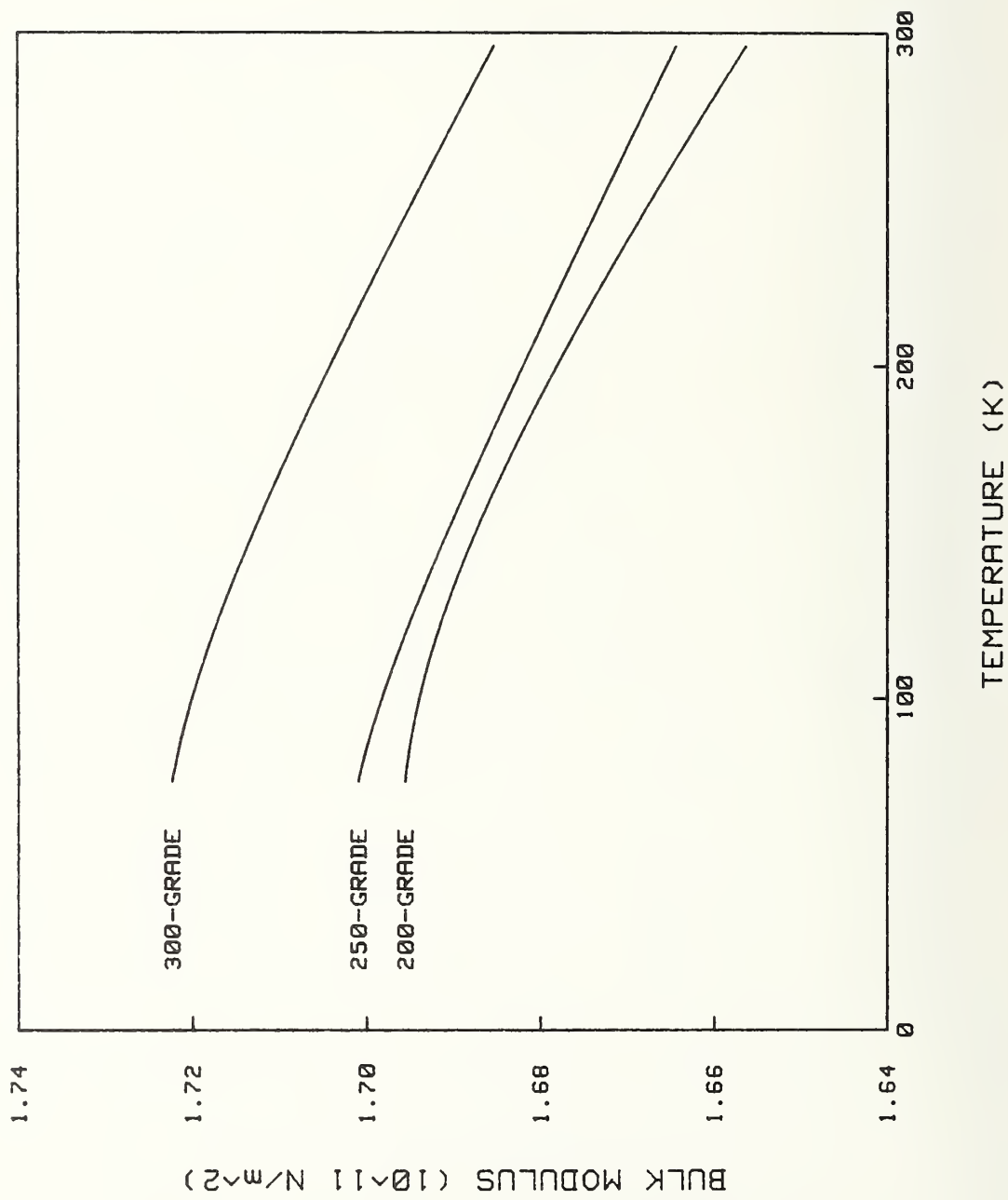


Fig. 4. Temperature variation of bulk modulus of three hardened maraging steels.

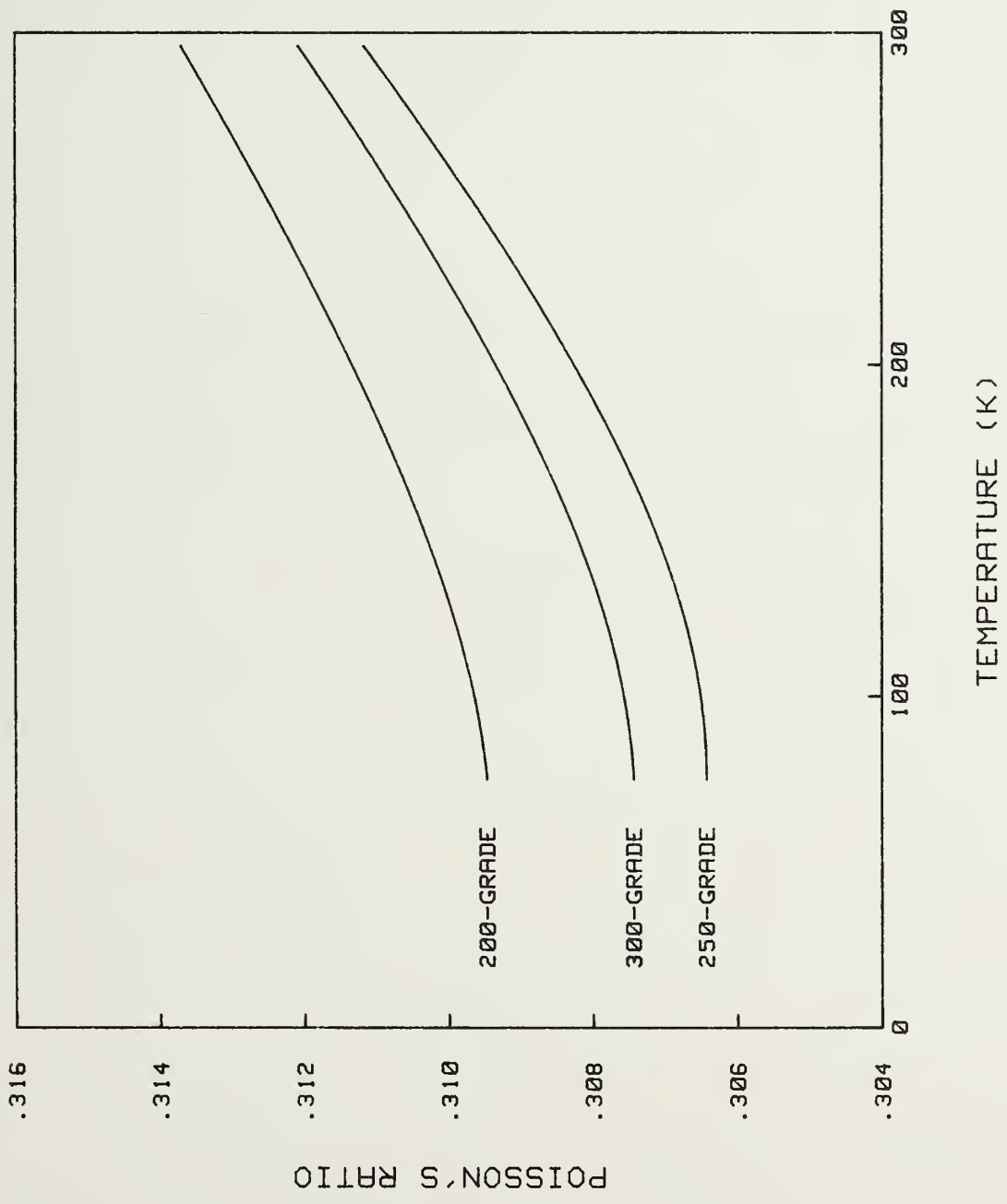


Fig. 5. Temperature variation of Poisson's ratio of three hardened maraging steels.

TEMPERATURE BEHAVIOR OF YOUNG'S MODULI OF FORTY ENGINEERING ALLOYS

H. M. Ledbetter
Fracture and Deformation Division
National Bureau of Standards
Boulder, Colorado

ABSTRACT

Young's-modulus and temperature data are collected graphically and tabularly for forty alloys that have technological applications. Alloy base metals include: aluminum, copper, iron, and nickel. Sources of data are: handbooks, original research at NBS, and the scientific-engineering literature. The temperature range 0 to 590 K (-460 to 600° F) is covered.

Introduction

Data are collected on Young's modulus and its temperature variation (0 to 590 K, -460 to 600° F) for forty engineering alloys. Criteria for including an alloy are: commercial availability, workability and joinability, suitability for low-temperature applications, and sufficient data to define the temperature dependence of the Young's modulus. The considered alloys represent four base metals: aluminum, copper, iron, and nickel.

The paper's main purpose is to provide a single source of reliable (\pm five percent) Young's-moduli values for a variety of common alloys over a wide temperature range. In many cases, Young's moduli of similar alloys can be deduced from the values reported here.

Data were acquired from three types of sources:

1. Handbooks
 - 1.1 Cryogenic Materials Data Handbook
 - 1.2 Handbook on Materials for Superconducting Machinery
 - 1.3 Metals Handbook
 - 1.4 Aerospace Structural Metals Handbook
 - 1.5 NERVA Handbook
2. Experimental studies at NBS/Boulder using dynamic methods
3. The scientific-engineering literature

In the second category of sources, dynamic Young's-modulus values between 4 and 300 K have been published for eighteen alloys: Inconel 600^{1,*}, Inconel 718², Inconel X-750¹, nickel steel (5 Ni)³, nickel steel (9 Ni)³,

*Tradenames are used to describe adequately the considered material. No endorsement of a particular product by NBS is implied.

invar⁴, AISI 304⁵, AISI 310⁵, AISI 316⁵, stainless A286⁵, cupernickel 10⁶, cupernickel 30⁶, aluminum 1100⁷, aluminum 2014⁸, aluminum 2219⁸, aluminum 5083⁷, aluminum 7005⁷, and aluminum 7075⁷. Thus, low-temperature data from the same laboratory are available in eight of the twelve alloy groupings used in the study. As described below, reliable high-temperature values can often be predicted from low-temperature data because of the linearity of the modulus-temperature curves at higher temperatures.

Description of Young's Modulus

Young's modulus has many pseudonyms: extension modulus, tensile modulus, tension modulus, elastic modulus, and modulus. Sometimes a compressive Young's modulus is described. Despite occasional contrary reports, this is a misnomer. For metals and alloys there is no difference, theoretically or experimentally, between Young's modulus in extension and in compression.

Young's modulus, E , is usually defined as the ratio of the stress σ_z applied along a rod with axis z to the strain component ϵ_z along the same axis. Thus,⁹

$$E = \sigma_z / \epsilon_z \quad (1)$$

Bending of rods is also characterized by Young's modulus. Thus, the stress along a bent rod with axis z is¹⁰

$$\sigma_z = E\epsilon_z = \frac{Ex}{r} \quad (2)$$

where x is a coordinate perpendicular to z , and r is the radius of curvature of the neutral surface near the origin.

Velocities of extensional waves in rods are given by¹¹

$$v = (E/\rho)^{1/2} \quad (3)$$

where ρ is the mass density.

The shear modulus G is related to Young's modulus by the empirical relationship¹²

$$G \approx 3E/8 \quad (4)$$

Young's modulus can be correlated with other solid-state parameters. For example,¹³

$$E = KM\theta^2/d \quad (5)$$

where K is a constant, M is the average atomic mass, θ is the Debye temperature, and d is the interatomic nearest-neighbor distance.

Results

Various base metals exhibit a relatively wide range of elastic moduli, and it is well known that chemical composition is usually the principal determinant of an alloy's elastic constants. Most other metallurgical variables have smaller effects on Young's modulus. Thus, alloys with similar compositions can be grouped. In the present study, alloys were grouped if their Young's modulus varied less than \pm five percent from the group average over the entire temperature region. In a few accidental cases, different types of alloys could be grouped within a \pm five percent band. Results of the study are shown in figure 1 and in table 1. The Monel K curve shows an unusual flatness that probably indicates inadequate experimental measurements rather than actual material behavior.

Modulus-Versus-Temperature Curve Fitting

Almost all data considered in this study were fitted to a theoretical relationship proposed by Varshni:¹⁴

$$E(T) = E(0) - s/[\exp (t/T) - 1] \quad (6)$$

This relationship follows from an Einstein-oscillator model of solids. It contains three adjustable parameters: $E(0)$, the Young's modulus at zero temperature; t , the Einstein characteristic temperature in the absence of electronic effects; and $-s/T$, the high-temperature limit of the temperature derivative dE/dT . T is the temperature in kelvin. Equation (6) was proposed originally to describe the temperature behavior of single-crystal elastic constants of pure metals. It was shown¹⁵ that it also describes the temperature dependence of the macroscopic elastic constants, such as Young's modulus of alloys.

Materials described by eq. (6) are called regular, and most materials are. As a class, ferromagnetic materials are irregular; they exhibit modulus-temperature anomalies that can be quite large. The most irregular material considered in the present study is invar. Because of magnetostrictive effects, it has a positive value of dE/dT over a large temperature region. Several other materials considered show smaller anomalies in their temperature dependence. These include: Inconels 600 and X750; austenitic stainless steels 304, 310, 316, and A286. However, these deviations from regular behavior were less than the \pm five percent bandwidth described above, and they were neglected. In these materials, most deviations occur at lower temperatures where magnetic effects are relatively less important.

Once parameters in eq. (6) are determined, which requires at least four good (or three excellent) data points, E values can be computed for the entire temperature range. Because of the approximate linearities of the E/T curves at higher temperatures, extrapolation of low-temperature data is quite reliable. The reverse extrapolation is not. In fact, fitting eq. (6) to data usually requires at least one reliable low-temperature point below 75 K. Also extrapolation to high temperatures is less reliable for materials with lower melting points, T_m . At high values of T/T_m , polycrystalline materials tend to soften elastically because of grain-boundary relaxations. Thus, copper-alloy moduli, which are extrapolated, may be slightly high.

Once groupings were determined by comparing curves for individual materials, the group-average curve was determined by refitting eq. (6) to all the alloys in the group. Each alloy was represented by the same number of points from its fitted-curve values.

Goodness-of-fit (average difference between observed value and curve value) varied considerably among various data sets. Ultrasonic data were usually excellent, 0.05 percent or less. Static data were usually poor, several percent or more. In many cases, sets of static data were discarded because eq. (6) could not be fitted to them. In general, all readily available data were included unless the data set was highly scattered, significantly different from the average of all these data available for the alloy, or showed irregular temperature behavior. For almost all alloys considered, room-temperature Young's moduli and dE/dT values are known reliably. Thus, there are criteria for rejecting poor data sets.

Static and Dynamic Values

For most engineering applications, the appropriate Young's moduli are the static (or zero-frequency) values. These values are obtained in conventional stress-strain-type experiments associated with mechanical-property measurements. Dynamic Young's-modulus values are now being determined more often because less inaccurate values are required, more physicists are studying mechanical properties of engineering alloys, and the advantages of dynamic methods are becoming better understood. These methods, which typically use kHz frequencies for resonance studies or MHz frequencies for pulse studies, yield dynamic (adiabatic) moduli that always exceed static (isothermal) moduli. For Young's modulus the interrelationship is¹⁶

$$E_d = E_s / (1 - E_s T \alpha^2 / C_p) \quad (7)$$

where subscripts d and s denote the dynamic and static modulus, T is temperature, α is linear thermal expansion, and C_p is specific heat per unit volume at constant pressure. Clearly, the difference between E_d and E_s vanishes at zero temperature for all materials and is small at all temperatures for low-thermal-expansion materials such as invar. In the present collection of Young's moduli, no static-dynamic corrections were applied to the data. The magnitudes of such corrections are shown for various base metals and various temperatures in table 2. For the materials and temperatures of concern here this correction is insignificant, never exceeding one percent.

Observations and Conclusions

(1) Except for invar, all considered alloys have regular temperature behavior: linear at higher temperatures, decreasing slope with decreasing temperatures, and relative flatness approaching zero temperature.

(2) For the considered temperature region, except for invar, the modulus-temperature curves are similar and the high-temperature dE/dT values cluster around -0.06 GPa/K with a 1σ standard deviation of 20 percent.

(3) Aluminum-base alloys have a smaller alloying dependence than alloys based on nickel, iron, or copper.

(4) Copper-base alloys have the largest alloying dependence, although many copper alloys can be grouped in a \pm five percent band.

(5) Only copper-nickel alloys have higher Young's moduli than the base metal. Alloying usually reduces Young's modulus.

(6) If a magnetic transition occurs, the anomaly size is related to the magnetic-transition temperature. Invar undergoes a Curie transition near 550 K and shows a large elastic anomaly. The stainless steels undergo Néel transitions near 50 K and show much smaller elastic anomalies.

Acknowledgment

The study was supported partially by the NBS Office of Standard Reference Data. A. F. Schmidt of NBS encouraged the study and commented on the manuscript. Both the tabular and graphical data contained in this paper were contributed by NBS to the American National Standards Committee B31.10 for inclusion in the ANSI B31.10 Code for Cryogenic Piping.

References

1. Weston, W. F., Ledbetter, H. M., and Naimon, E. R., Mater. Sci. Eng. 20, 185-194 (1975).
2. Weston, W. F. and Ledbetter, H. M., Mater. Sci. Eng. 20, 287-290 (1975).
3. Weston, W. F., Naimon, E. R., and Ledbetter, H. M., in Properties of Materials for Liquefied Natural Gas Tankage, ASTM STP 579, Amer. Soc. Test. Mater., Philadelphia (1970), pp. 397-420.
4. Ledbetter, H. M., Naimon, E. R., and Weston, W. F., in Advances in Cryogenic Engineering, Vol. 22, Plenum, New York (1977), pp. 174-181.
5. Ledbetter, H. M., Weston, W. F., and Naimon, E. R., J. Appl. Phys. 46, 3855-3860 (1975).
6. Ledbetter, H. M. and Weston, W. F., in Ultrasonics Symposium Proceedings, IEEE, New York (1975), pp. 623-627.
7. Naimon, E. R., Ledbetter, H. M., and Weston, W. F., J. Mater. Sci. 10, 1309-1316 (1975).
8. Read, D. T. and Ledbetter, H. M., J. Eng. Mater. Technol., forthcoming.
9. Landau, L. D. and Lifshitz, E. M., Theory of Elasticity, Pergamon, London (1959), p. 13.
10. Ref. 9, p. 73.
11. Ref. 9, p. 110.
12. Ledbetter, H. M., Mater. Sci. Eng. 27, 133-136 (1977).
13. Grimvall, G. and Sjodin, S., Phys. Scr. 10, 340-352 (1974).
14. Varshni, Y. P., Phys. Rev. B 2, 3952-3958 (1970).
15. Naimon, E. R., Weston, W. F., and Ledbetter, H. M., Cryogenics 14, 246-249 (1974).
16. Ref. 9, p. 17.

Table 1. Young's modulus of groups of engineering alloys in units of GPa.

Temp. (°C)	Nickel	Nickel Alloys	Inconels	Nickel Steels	Stainless Steels	Monel K	Cu-30Ni	Cu-10Ni	Invar	Copper	Copper Alloys	Aluminum Alloys
-270	240	222	215	207	207	180	164	148	134	139	114	79
-260	240	222	215	207	207	180	164	148	133	139	114	79
-240	240	222	215	207	207	180	164	148	132	138	114	79
-220	240	222	215	207	207	180	164	148	132	138	114	79
-200	239	222	215	206	206	180	164	148	132	138	114	79
-180	238	222	214	207	206	180	164	148	133	137	113	78
-160	237	221	213	206	205	180	163	148	133	136	112	78
-140	236	221	212	205	203	180	163	147	134	136	112	77
-120	234	220	211	204	202	180	162	147	135	135	111	76
-100	233	220	210	204	201	180	162	146	136	134	110	76
-80	232	219	209	203	199	180	161	145	137	133	109	75
-60	230	218	208	201	198	180	160	144	138	132	108	74
-40	229	217	206	200	196	180	159	144	139	131	107	73
-20	228	216	205	199	195	180	158	143	141	130	106	73
0	226	215	204	198	193	180	157	142	142	130	105	72
20	225	214	203	197	192	179	156	141	143	129	104	71
40	224	213	201	196	190	179	155	139	144	128	104	70
60	222	212	200	195	189	179	154	138	146	127	103	69
80	221	211	199	193	187	178	153	137	147	126	102	68
100	219	210	198	192	185	178	152	136	148	125	101	67
120	218	209	196	191	184	177	151	135	150	124	100	67
140	217	208	195	190	182	177	150	134	151	123	99	66
160	215	206	194	189	181	176	149	133	152	122	98	65
180	214	205	192	187	179	175	148	132	153	121	97	64
200	213	204	191	186	177	174	147	130	155	120	96	63
220	211	203	190	185	176	173	145	129	155	119	95	62
240	210	202	188	184	174	172	144	128	156	118	94	61
260	208	200	187	183	173	171	143	127	156	117	93	60
280	207	199	186	181	171	170	142	126	157	116	92	59
300	206	198	185	180	169	168	141	125	156	115	91	59
320	204	197	183	179	168	167	140	123	156	114	90	58

Table 2. Ratios of dynamic (adiabatic) and static (isothermal) Young's moduli, E_d/E_s .

Temp. (K)	Nickel	Iron	Copper	Aluminum
100	1.000	1.000	1.001	1.001
200	1.002	1.001	1.001	1.003
300	1.003	1.003	1.003	1.005
400	1.004	1.004	1.004	1.007
500	1.005	1.005	1.006	1.008
600	1.006	1.006	1.007	1.010

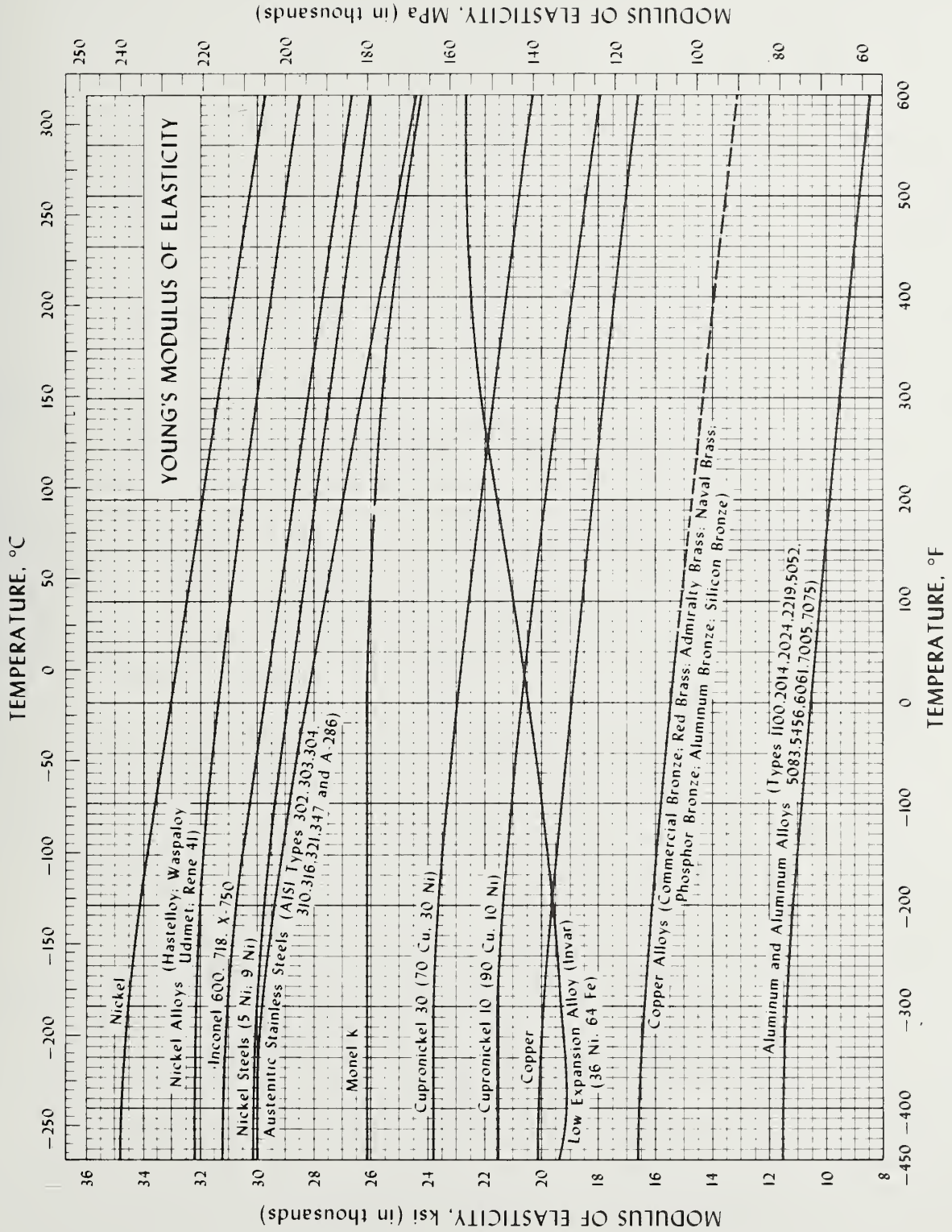


Figure 1. Temperature variation of Young's modulus for forty engineering alloys.

WELDING AND CASTING

EVALUATION OF WELDMENTS AND CASTINGS
FOR LIQUID HELIUM SERVICE

T. A. Whipple and H. I. McHenry
Fracture and Deformation Division
National Bureau of Standards
Boulder, Colorado

ABSTRACT

In this paper the FY80 results of the NBS program on the evaluation of weldments and castings for liquid helium service are reviewed. The welding process study for stainless steel castings and the study on the toughness of 5183 aluminum weldments were completed during FY80, and studies on the toughness of stainless steel castings and the fracture and deformation phenomena in duplex austenite/ferrite structures were begun. The research planned for FY81 is also reviewed.

Introduction

The program to evaluate weldments for structural applications in superconducting magnet systems [1,2,3] was continued in FY80. Except for the addition of the evaluation of stainless steel castings for liquid helium service, the objectives for the program have remained unchanged from those of FY79:

1. To investigate the metallurgical factors that affect the toughness of stainless steel weldments and castings at cryogenic temperatures.
2. To contribute to the development of improved filler metals for welding stainless steels for liquid helium service.
3. To evaluate the strength and toughness of stainless steel weldments and castings and aluminum weldments at 4 K.

Research began this year on a study that will take a more fundamental approach to the first objective, and work has continued on the evaluation of experimental stainless steel filler metals, evaluation of aluminum weldments and support of superconducting magnet construction programs. This report summarizes the results obtained in FY80 and outlines the research to be conducted in FY81.

Stainless Steel Weldments

Since previous studies [4,5] have shown that ferrite in weldments substantially reduces the fracture toughness at cryogenic temperatures, substantial work is being conducted on the development of 0% ferrite filler materials. A number of weldments made with experimental filler alloys have been tested at 4 K over the past year. The results of

these tests are presented later in this report by Elmer, McHenry and Whipple. Some of these experimental weldments have shown excellent combinations of strength and fracture toughness. However, some of the alloys have considerable problems with microfissuring and none are as yet commercially available.

The study on the effects of the welding process on the cryogenic properties of 316L weldments, which was begun in FY79 [6], was completed during the past year. The results of 4 K mechanical property testing are presented later in this report by Whipple and Kotecki. The weldment made by gas tungsten arc welding (GTAW) was found to have the highest toughness followed by gas metal arc welding (GMAW) and submerged arc welding (SAW). This order of weld metal toughness is the same as the expected order of weld metal cleanliness, indicating that impurities in the weld metal may have a significant influence on cryogenic properties.

As in past years, a number of qualification and test weldments were tested for tensile and fracture toughness at 4 K in support of the LCP magnet design and construction programs. These weldments included a 316L shielded metal arc (SMA) weldment, which was annealed, and 308L flux core metal arc (FCMA) weldments. The results of these tests are presented in Tables 1 and 2. In addition, these tables contain data obtained on a 316L electroslag (ES) weldment and a 308 SMA weldment (in the as-welded and annealed conditions), which were tested under separate contracts with the MFTF and the ANL-MHD projects, respectively. These data are included here because the weldments are being used as part of the overall study of 4 K fracture and deformation of stainless steel weldments at 4 K, which is included in this program.

As mentioned previously, a major fundamental study of fracture and deformation in duplex austenite/ferrite stainless steels at cryogenic temperatures has been undertaken. The objective of this investigation is to relate the structure of these materials to the cryogenic properties. During FY80 two initial parts of this investigation were completed and are presented later in this report. The first, by Brown, presents a detailed literature review, critical analysis and observations concerning structure development in duplex austenite/ferrite stainless steel weldments and castings. This study is necessary to define structural parameters to be used in deformation modeling and to understand effects that may arise due to such factors as microsegregation. This knowledge will also be necessary for the eventual modification of structural parameters to optimize mechanical properties. The second paper, by Whipple and Brown, presents the results of a metallographic investigation of deformation and fracture mechanisms in duplex austenite/ferrite stainless steel weldments and castings. In this study, the role of ferrite in 4 K deformation and fracture is examined with particular emphasis on possible fracture modes. The fracture-mode study has pointed out the advantages to be gained in studying castings as a model material that will give indications of the behavior of weldments. Because castings have a much coarser ferrite structure than weldments, their deformation and fracture phenomena are much more easily observed.

Stainless Steel Castings

The increased interest in the use of stainless steel castings for structural components of superconducting magnets has resulted in a program to evaluate castings for cryogenic service. Ferrite content and

nitrogen concentration have been found to have a significant influence on the cryogenic properties of stainless steel weldments [4,5] and it seems reasonable to expect that the same will be true of castings because of the similarities in their microstructures. Therefore, the program has been designed to test both of these effects. Two series of CF8M castings have been produced, one with a constant nitrogen content and varied ferrite content and one with a constant ferrite content and a varied nitrogen content. The production and initial testing of these castings is presented later in this report by Finch.

In FY80, 4 K mechanical property tests were conducted on some CF8M and CF8 castings under separate contracts. The data from these tests are presented in Tables 3 and 4. These castings have been used as part of the deformation and fracture mechanism study being conducted in this program, the results of which are presented later in this report by Whipple and Brown.

Aluminum Weldments

The program on the evaluation of 5183 welds in 5083 aluminum, which was begun in FY79 [7], was completed this year with 4 K fracture toughness testing. It was found that the toughness of aluminum weldments is not sensitive to welding procedure or supplier. The results of this program are presented later in this report by Elmer and McHenry.

Test-Method Development

In FY79 work had begun on the evaluation of a simple test method for estimating J_{IC} [8]. The aim of that work was to develop a simple and inexpensive test method for weld qualification for 4 K service. The initial results indicated that the test worked well for the base metals tested. In the past year the test method was evaluated for use on weldments. The weldments tested were those from the welding process study,

mentioned previously. The results are shown graphically in figure 1, which is a plot of the J_{IC} estimated by this procedure versus the J_{IC} measured by the single-specimen J-integral procedure. From this figure it is evident that, in the case of weldments, the correlation between the estimated J_{IC} and the actual J_{IC} is very poor. On the basis of these results, it was determined that the test method is not useful for weld property evaluation. This is probably due to the large grain size of weldments compared with the small ligament of the specimens used for this test.

Future Work

The major portion of the research effort in FY81 will be devoted to the previously mentioned deformation and fracture study on duplex austenite/ferrite stainless steel weldments and castings at 4 K. The objective of this work is to gain a much more comprehensive understanding of factors influencing the mechanical properties, including the causes of the observed large variability in weld metal properties. Specifically, this research will include the following efforts:

1. A theoretical model of duplex austenite/ferrite stainless steel deformation at 4 K will be developed from a two-phase deformation modeling approach. This model is intended to define quantitatively the effects of ferrite content, ferrite morphology, and phase properties on deformation.
2. The CF8M castings produced in FY80 will be used to verify and refine the above model and to make additional fracture and deformation mechanism observations.

3. Weldments of 316L stainless steel weldments will be made and tested with different welding processes and ferrite contents to extend the model to the finer structure in weldments.
4. Extensive metallographic investigations will be conducted in support of the above program. Optical microscopy will be used to define and measure microstructural parameters. Transmission electron microscopy will be used extensively to investigate factors such as orientation relationships, interface structures and dislocation substructures or deformed and undeformed specimens. Scanning electron microscopy will continue to be used to correlate microstructure to fracture and deformation micromechanisms.
5. Microstrain tensile testing, using high-sensitivity strain measuring equipment, will be conducted to establish microdeformation phenomena further.

In addition to and as part of the above program, a COD test methodology will be developed. This test method will use three-point bend specimens and will be capable of measuring J_{IC} . It is expected that this form of testing will significantly reduce the cost of 4 K fracture toughness testing. The 4 K mechanical property testing in support of superconducting magnet design and construction programs will continue in FY81.

REFERENCES

1. H. I. McHenry, "Evaluation of Stainless Steel Weld Metals at Cryogenic Temperatures," in Materials Studies for Magnetic Fusion Energy Applications at Low Temperatures-I, NBSIR 78-884 (1978), pp. 159-166.
2. H. I. McHenry, D. T. Read, and P. A. Steinmeyer, "Evaluation of Stainless Steel Weld Metals at Cryogenic Temperatures," in Materials Studies for Magnetic Fusion Energy Applications at Low Temperatures II, NBSIR 79-1609 (1979), pp. 299-308.
3. H. I. McHenry and T. A. Whipple, "Weldments for Liquid Helium Service," in Materials Studies for Magnetic Fusion Energy Applications at Low Temperatures-III, NBSIR 80-1627 (1980), pp. 155-165.
4. D. T. Read, H. I. McHenry, P. A. Steinmeyer, and R. D. Thomas, Jr., "Metallurgical Factors Affecting the Toughness of 316L SMA Weldments at Cryogenic Temperatures," Material Studies for Magnetic Fusion Energy Applications at Low Temperatures-II, NBSIR 79-1609 (1979) pp. 313-352.
5. E. R. Szumachowski and H. F. Reid, "Cryogenic Toughness of SMA Austenitic Stainless Steel Weld Metals: Part I - Role of Ferrite," Weld. J., Weld. Res. Suppl. 57, (1978) pp. 325-s-333-s.
6. D. J. Kotecki, "Weld Process Study for 316L Stainless Steel Weld Metal at Cryogenic Temperatures," in Materials Studies for Magnetic Fusion Energy Applications at Low Temperatures-III, NBSIR 80-1627 (1980), pp. 197-204.
7. R. A. Kelsey and L. N. Mueller, "Tensile and Notch-Tensile Properties at Room Temperature and 4K of Welds in Aluminum Alloy 5083-0 Plate," in Material Studies for Magnetic Fusion Energy Applications at Low Temperatures-III, NBSIR 80-1627, (1980) pp. 217-244.

8. T. A. Whipple and H. I. McHenry, "Note on a Simple Test Method for Estimating J_{IC} ," in Materials Studies for Magnetic Fusion Energy Applications at Low Temperatures-III, NBSIR 80-1627 (1980), pp. 245-256.

Table 1. Tensile properties of qualification weldments tested at 4 K.

Weld Type	Ferrite, %	Yield Strength, MPa (ksi)	Ultimate Strength, MPa (ksi)	Elongation, %	Reduction in Area, %
316L SMA	0	636	939	13	11
		685	1349	40	24
		650	919	13	20
		<u>727</u>	<u>1315</u>	<u>46</u>	<u>43</u>
		674 (97.8)	1130 (164.0)	28	25
316L Electroslag	4.5	700	1436	34	23
		<u>680</u>	<u>1294</u>	<u>38</u>	<u>25</u>
		690 (100.0)	1365 (197.4)	36	24
308L FCMA 0.60N	3	483	1168	22	16
		431	1395	29	19
		<u>460</u>	<u>1374</u>	<u>32</u>	<u>21</u>
		458 (66.4)	1312 (190.3)	28	19
308L FCMA 0.8N	3	541	1418	31	22
		<u>574</u>	<u>1219</u>	<u>21</u>	<u>16</u>
		558 (80.9)	1319 (191.3)	26	19

Table 2. Fracture properties of qualification weldments at 4 K.

Weld	Ferrite, %	J_{IC} , kJ/m ² (in·lb/in ²)	$K_{IC}(J)$, MPa√m (ksi√in)	Fatigue Crack Growth ¹	
				C	n metric units ² (English units) ²
316L SMA (annealed)	0	241 288 <u>272</u> 267 (1526)	247 (224)	0.501 x 10 ⁻⁸ (0.263 x 10 ⁻⁹)	2.83
316L Electroslag	4.5	174 140 <u>157</u> (897)	189 (172)		
308L FCMA 0.8N	3	80.3 77 <u>80.3</u> 79.2 (453)	134 (122)	0.489 x 10 ⁻⁹ (0.281 x 10 ⁻¹⁰)	3.69
308 SMA	12	46.0 <u>32.2</u> 39.1 (224)	94.4 (85.9)	0.254 x 10 ⁻⁹ (0.163 x 10 ⁻⁹)	3.84 3.88
308 SMA Annealed	0	328 <u>350</u> 339 (1938)	278 (253)	0.196 x 10 ⁻⁹ (0.846 x 10 ⁻⁹)	3.78 3.34

1. Constants fit the equation: $da/dN = C\Delta K^n$

2. Metric units: ΔK in MPa√m, da/dN in mm/cycle
 English units: ΔK in ksi√in, da/dN in in/cycle

Table 3. Tensile properties of stainless steel castings at 4 K.

Material	Ferrite, %	Yield Strength, MPa (ksi)	Ultimate Strength, MPa (ksi)	Elongation, %
CF8	0	413 (60)	125 (181)	46.1
	8	689 (100)	920 (133)	20.2
	14.5	470 (68)	1512 (219)	47.6
	12	578 (84)	753 (109)	10.7
CF8M	9.0	621 (90)	1317 (191)	41.0
		469 (68)	1338 (194)	44.0

Table 4. Fracture properties of stainless-steel castings at 4 K.

Material	Ferrite, %	J_{IC} , kJ/m ² (in·lb/in ²)	K_{IC} (J), MPa√m (ksi√in)	Fatigue Crack Growth ¹ C metric units ²	n
CF8	0	481 (2750)	331 (301)	--	--
	8	175 (1000)	199 (181)	--	--
	14.5	69.3 (396)	125 (114)	--	--
	12	31.5 (180)	84.5 (76.9)	--	--
CF8M	9.0	302		2.35 x 10 ⁻¹²	5.21
		403			
		280			
		372			
		339 (1938)	278 (253)		

1. Constants fit the equation: $da/dN = C\Delta K^n$

2. Metric units; ΔK in MPa√m, da/dN in mm/cycle

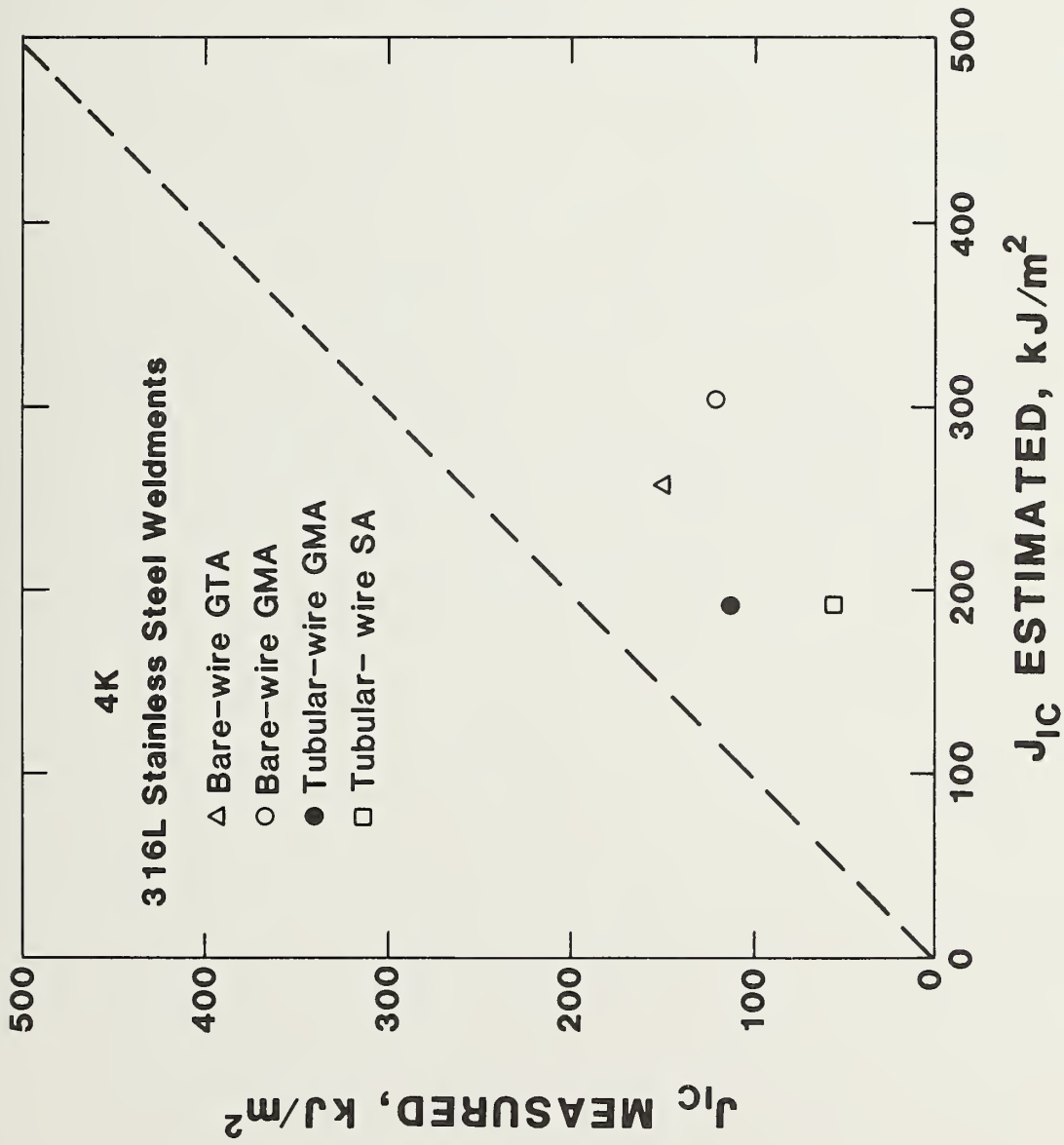


Figure 1. Comparison of actual and estimated J_{IC} for 316 L weldments.

STRENGTH AND TOUGHNESS OF FULLY AUSTENITIC STAINLESS STEEL
FILLER METALS AT 4 K

J. W. Elmer, H. I. McHenry, and T. A. Whipple
Fracture and Deformation Division
National Bureau of Standards
Boulder, Colorado

ABSTRACT

Several experimental fully austenitic stainless steel welds have been prepared by filler metal suppliers in the United States, Austria, Sweden and the Soviet Union. The strength and toughness of these welds have been tested and are reported at 4 K. Some Charpy impact toughness and tensile data at temperatures other than 4 K are presented. These data were reported by the suppliers. Four of the eight welds that were tested had strength-toughness combinations comparable to that of austenitic base metals. Of these four welds, three did not exhibit microfissuring that is generally present in fully austenitic welds.

INTRODUCTION

Stainless steel weldments are used for the main structural members of the superconducting magnet systems for fusion energy devices. Annealed austenitic stainless steels of the AISI 300 series are currently being used in weldments with thicknesses up to 125 mm. The weldments operate at high stress levels in liquid helium at 4 K. The weld metal that has been most thoroughly evaluated and is most frequently used for liquid helium service is AWS 316L deposited by the shielded metal-arc (SMA) process. Fracture toughness tests on 316L welds at 4 K indicate that toughness decreases with increasing ferrite content¹ and with increasing grain size in ferrite-free welds.² In general, the toughness of 316L welds varies significantly for the different welding processes,³ and the best assurance of satisfactory toughness is obtained with a ferrite-free weld deposited with a low-heat input. Problems arise because ferrite-free welds are susceptible to microfissuring^{4,5} and low-heat inputs result in low deposition rates.

The purpose of this program is to conduct a preliminary evaluation of the strength and toughness at 4 K of several proprietary fully austenitic weld metals provided in the form of as-welded test plates by filler metal suppliers in the United States, Austria, Sweden, and the Soviet Union. The evaluation is limited to the specific welding process and procedures chosen by the suppliers to prepare the test plates. Promising grades will be identified, but further evaluation will be needed to assess their suitability for structural members of superconducting magnets.

MATERIALS

Test weldments were provided for evaluation by five filler metal suppliers. The chemistry of the weld metals is summarized in Table I. The welds are identified by their chemistry: the numbers indicate the Cr-Ni-Mn content and any additional characteristic alloying elements follow, e.g., alloy 18-20-6 Nb is 18% Cr, 20% Ni, 6% Mn, and contains Nb. The welding process and procedures used to prepare the test weldments were selected by the suppliers. The available information is summarized in Table II. Tensile and Charpy impact data provided by suppliers 4 and 5 are summarized in Table III. Microfissuring was observed on the fracture surface of all the welds except for the 20-16-7 Mo-W submerged arc weld (SAW), 17-16-4 Mo (SMA), and 18-20-6 Nb gas metal-arc (GMA) welds.

PROCEDURES

Tensile Testing

Tensile testing was conducted on all-weld-metal specimens by means of a screw-driven testing machine equipped with a cryostat to perform the tests in liquid helium. A 0.635-cm (0.250-in)-diameter tensile bar was used, and the strain was measured over a 25-mm-gage length with a clip-gage extensometer mounted on the tensile specimen. A constant crosshead displacement rate of 0.008 mm/s was used for all specimens.

Fracture Toughness Testing

All fracture toughness testing was performed using the computer-aided, single-specimen, J-integral test facility described by Read.⁶ The testing was done in liquid He at a temperature of 4.0 K using a standard 2.54-cm (1.00-in)-thick ASTM E399 compact tension specimen. The specimen was removed with the plane of the notch perpendicular to

the surface of the plate and centered along the fusion zone. In some instances, the weldment was not thick enough to remove a 2.54-cm-thick compact tension specimen. In these cases, the planar dimensions were kept the same as for a 2.54-cm-thick specimen and only the thickness was reduced. The specimens were precracked in tension-tension fatigue to a depth of 3.05 cm (1.20 in) prior to testing. Displacements were measured with a clip-gage extensometer mounted at the load line.

RESULTS AND DISCUSSION

The tensile properties of the fully austenitic welds at 4 K are summarized in Table IV. The yield strength ranged from 606 to 1110 MPa. Much of the variation in yield strength can be attributed to variations in the C-and-N contents. These interstitials are effective strengtheners at low temperatures. However, the correlation of yield strength with interstitial content reported by Tobler and Reed⁷ for AISI 304 base metal was not observed. Apparently, other factors such as grain size, oxygen content, and overall chemistry are important contributors to strength. For example, four welds with the same carbon plus nitrogen (0.08%) had yield strengths ranging from 606 to 814 MPa. Similarly, the weld ductility, as measured by reduction of area, generally decreased with increasing C plus N. For example, the three welds with less than 20% reduction of area had the highest C-plus-N contents.

The fracture toughness values of the fully austenitic welds at 4 K are summarized in Table V. As a group, these welds had high fracture toughness relative to previous results on AWS 316L welds with and without ferrite.^{1,2} A comparison of the present results with the trend line of Read and Reed⁸ is shown in Figure 1, a plot of fracture toughness versus yield strength. Note that the strength and toughness combinations

for 20-16-7 Mo-W (SAW), 17-16-4 Mo (SMA), 18-20-6 Nb (GMA) and 16-16-4 Mo (FCAW) each are close to the base-metal trend line. This is noteworthy because four different welding processes are used, a wide range of strengths is covered, and three of the alloys (all except 16-16-4 Mo) did not exhibit microfissures. The similarity in chemistry of these alloys suggests that a fully austenitic alloy with 16 to 20% each of Cr and Ni, 4 to 7% Mn and refractory elements may provide the properties needed for liquid helium service.

SUMMARY AND CONCLUSION

A preliminary evaluation of the strength and toughness of several proprietary fully austenitic weld metals has been conducted. The results for 20-16-7 Mo-W, 17-16-4 Mo, 18-20-6 Nb and 16-16-4 Mo indicate that strength and toughness combinations comparable to the properties of austenitic stainless steel base metals are possible in fully austenitic weld deposits. Further investigation is needed to identify the optimum chemistry and welding process for achieving microfissure-free welds that have strength and toughness properties needed for structural applications in superconducting magnets.

REFERENCES

1. D. T. Read, H. I. McHenry, P. A. Steinmeyer, and R. D. Thomas, Jr., "Metallurgical Factors Affecting the Toughness of 316L SMA Weldments at Cryogenic Temperatures," *Weld. J. Res. Suppl.*, Vol. 59, No. 4, pp. 104s-113s (1980).
2. T. A. Whipple, H. I. McHenry, and D. T. Read, "Fracture Behavior of Ferrite Free Stainless Steel Welds in Liquid Helium," Materials Studies for Magnetic Fusion Energy Applications at Low Temperatures-III, NBSIR 80-1627, National Bureau of Standards, Boulder, Colorado, pp. 167-194 (1980).
3. T. A. Whipple and D. J. Kotecki, "Weld Process Study for 316L Stainless Steel Weld Metal for Liquid Helium Service," this volume, pp. 303-321 (1981).
4. C. D. Lundin, W. T. DeLong, and D. F. Spond, "Ferrite-Fissuring Relationship in Austenitic Stainless Steel Weld Metals," *Weld. J. Res. Suppl.*, Vol. 54, No. 8, pp. 241s-246s (1975).
5. C. D. Lundin and D. F. Spond, "The Nature and Morphology of Fissures in Austenitic Stainless Steel Weld Metals," *Weld. J.*, Vol. 55, No. 11, pp. 3565-3675 (1976).
6. D. T. Read, "The Computer-Aided J-Integral Test Facility at NBS," Materials Studies For Magnetic Fusion Energy Applications at Low Temperatures-III, NBSIR 80-1627, National Bureau of Standards, Boulder, Colorado pp. 205-216 (1980).
7. R. L. Tobler and R. P. Reed, "Interstitial Carbon and Nitrogen Effects on the Tensile and Fracture Parameters of AISI 304 Stainless Steels," Materials Studies for Magnetic Fusion Energy Applications at Low Temperature-III, NBSIR 80-1627, National Bureau of Standards, Boulder, Colorado pp. 17-48 (1980).

8. D. T. Read and R. P. Reed, "Fracture and Strength Properties of Selected Austenitic Stainless Steels at Cryogenic Temperatures," Materials Studies for Magnetic Fusion Energy Applications at Low Temperature-II, NBSIR 79-1609, National Bureau of Standards, Boulder, Colorado pp. 79-122 (1979).

Table I. Chemical Analysis of Test Welds*

Supplier	Designation	Process**	Cr	Ni	Mn	Mo	N	C	S	P	Si	Other
1	20-16-7 Mo-W	SAW	19.5	16.1	6.7	2.8	0.23	0.03	0.003	0.01	0.09	2.1 W
2	17-16-4 Mo	SMA	17.3	15.9	4.0	2.2	0.05	0.03	0.007	0.022	0.39	
3	18-20-6 Nb	GMA	18.0	20.3	5.8	0.02	0.04	0.04	0.007	0.005	0.32	.27 Nb
3	18-20-5	GMA	18.1	20.4	5.4	0.11	0.16	0.03	0.007	0.006	0.26	
3	18-20-6 Ti	GMA	18.2	20.3	5.7	0.03	0.024	0.03	0.007	0.006	0.28	.19 Ti
4	18-16-9	GMA	18.1	15.8	8.6		0.08	0.05	0.021	0.004	0.44	
5	16-16-4 Mo	FCMA	16.1	15.9	4.4	1.5	0.05	0.03	0.012		0.25	
5	16-15-4 Mo	SMA	15.7	15.0	3.7	1.8		0.024	0.012	0.020	0.22	

*Chemical Analyses provided by the suppliers of the test weldments

**SAW = Submerged arc weld

SMA = Shielded metal arc

GMA = Gas metal arc

FCMA = Flux core metal arc

Table II. Welding Parameters

Supplier	Process	Passes	Thickness, mm	Current, A	Voltage, V	Travel Speed, mm/s
1	SAW	2	19	---	---	---
2	SMA	18	25	130	22	---
3	GMA	---	13	220	30	5
4	GMA	20	25	150	---	0.5
5	FCMA	---	---	---	---	---
5	SMA	---	---	---	---	---

Table III. Mechanical Property Data Provided By the Suppliers
of the Test Weldments

Supplier	Alloy	Temperature, K	Tensile Strength, MPa	Tensile Strength, (ksi)	Yield Strength, MPa	Yield Strength, (ksi)	Elongation, % in 25 mm	Reduction of Area, %	Charpy Impact Toughness (Average)		
									Energy J	Energy (ft lb)	Lateral Expansion, mm
4	18-16-9	RT	651	(94.5)	431	(62.6)	17	49	---	---	3
		77	1228	(178.)	929	(135.)	10	35	---	---	3
5	16-16-4Mo FCAW	RT	494	(71.7)	344	(49.9)	42	46	---	---	3
		77	103	(76)	63	(46)	---	---	---	---	3
3	18-20-5	RT	119	(88)	---	---	---	---	---	---	3
		195	117	(87)	---	---	---	---	---	---	3
3	18-20-6 Ti	RT	137	(101)	---	---	---	---	---	---	3
		195	124	(92)	---	---	---	---	---	---	3
3	18-20-6Nb	77	93	(69)	---	---	---	---	---	---	9
		77	103	(76)	---	---	---	---	---	---	9
4	18-16-9	RT	103	(76)	---	---	---	---	---	---	3
		77	63	(46)	1.40	1.60	---	---	---	---	3
5	16-16-4 Mo FCAW	172	87	(64)	1.58	---	---	---	---	---	3
		144	86	(64)	1.47	---	---	---	---	---	3
5	16-16-4 Mo FCAW	116	85	(62)	1.28	---	---	---	---	---	3
		77	70	(51)	1.02	---	---	---	---	---	3

Table IV. Tensile Properties of Fully Austenitic Welds at 4 K.

Supplier	Alloy	Process	Tensile Strength, MPa	Tensile Strength, (Ksi)	Yield Strength, MPa	Yield Strength, (Ksi)	Elongation, % in 25 mm	Reduction of Area, %
1	20-16-7 Mo-W	SAW	1427	(207)	1110	(161)	10	16
2	17-16-4 Mo	SMA	1262	(183)	814	(118)	43	36
3	18-20-6 Nb	GMA	1048	(152)	696	(101)	36	30
3	18-20-5	GMA	1186	(172)	889	(129)	26	19
3	18-20-6 Ti	GMA	979	(142)	686	(99.5)	29	23
4	18-16-9	GMA	1434	(208)	1076	(156)	27	19
5	16-16-4 Mo	FCMA	1131	(164)	606	(87.9)	30	26
5	16-15-4 Mo	SMA	1345	(195)	717	(104)	26	24

Table V: Fracture Toughness of Fully Austenitic Welds at 4 K.

Supplier	Alloy	Process	J_{IC} ,		K_{IC} ,	
			J/m^2	(in·lb/in ²)	MPa√m	(ksi√in)
1	20-16-7 Mo-N	SAW	116	(660)	163	(148)
			77	(440)	132	(120)
		AVERAGE	<u>97</u>	<u>(550)</u>	<u>148</u>	<u>(148)</u>
2	17-16-4 Mo	SMA	240	(1370)	234	(213)
			306	(1748)	264	(240)
		AVERAGE	<u>273</u>	<u>(1560)</u>	<u>250</u>	<u>(227)</u>
3	18-20-6 Nb	GMA	130	(740)	171	(156)
			350	(2000)	282	(257)
		AVERAGE	<u>240</u>	<u>(1370)</u>	<u>227</u>	<u>(207)</u>
3	18-20-6 Ti	GMA	362	(2070)	287	(267)
4	18-16-9	GMA	65	(370)	121	(110)
5	16-16-4 Mo	FCMA	238	(1362)	239	(217)
5	16-15-4 Mo	GMA	114	(650)	170	(155)

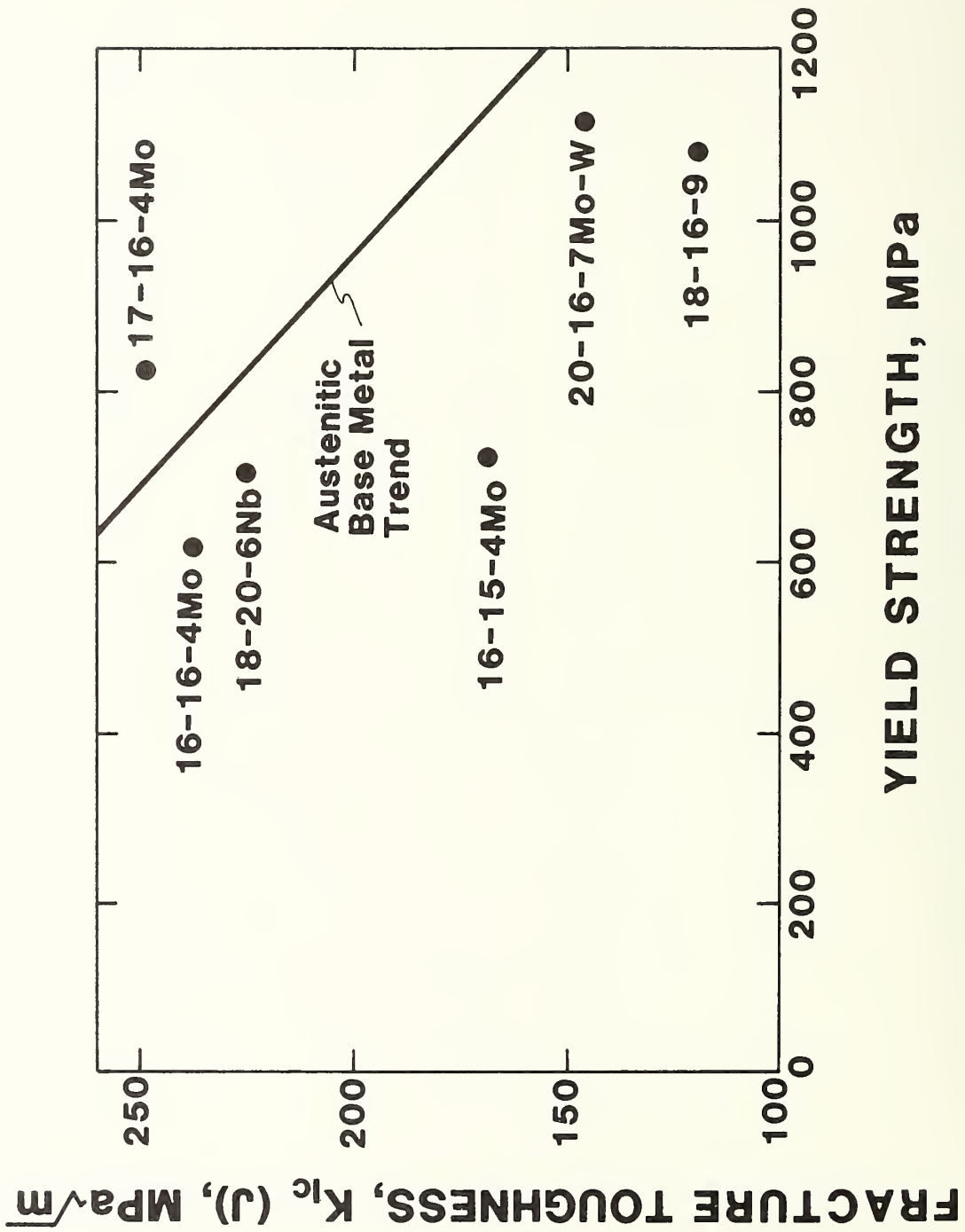


Figure 1. 4 K fracture toughness versus yield strength for fully austenitic welds. Data are compared with the 4 K austenitic base metal fracture toughness trend from a separate investigation.

WELD PROCESS STUDY FOR 316L STAINLESS STEEL
WELD METAL FOR LIQUID HELIUM SERVICE

T. A. Whipple
Fracture and Deformation Division
National Bureau of Standards
Boulder, Colorado

D. J. Kotecki
Teledyne McKay
York, Pennsylvania

ABSTRACT

This study was conducted to determine the effects of welding process choice on the cryogenic properties of 316L stainless steel welds. Six weldments were produced using two welding wires and three welding processes. The weldments were impact tested down to 77 K and tensile and fracture toughness tested down to 4 K. The best properties obtained were from a GTA weld, followed by GMA welds; SA welds had the poorest properties. This variation in properties was attributed to the cleanliness of the weld metal, which is dependent on the welding process and parameters selected.

INTRODUCTION

To date, most structures intended for liquid helium service have been welded with the shielded metal arc (SMA) welding process. This is mainly due to the lack of cryogenic mechanical property data on stainless steel weldments using higher deposition rate processes. The purpose of this program was to assess the effect of welding process choice and, to a lesser extent, the effect of welding parameter choice on the cryogenic toughness of type 316L weld metal at two nominal ferrite levels--approximately 5 ferrite number (FN) and 0 FN. This was intended to add to the data base on different welding processes and to assess the factors which cause differences between welding processes.

MATERIALS

Type 316L bare wire is fairly easy to obtain with ferrite calculated by the DeLong Diagram [1] at about 5 FN. But unless high-nitrogen content is acceptable, type 316L bare wire calculated to have 0 FN is rare. From previous work [2,3], it is apparent that high-nitrogen content has a detrimental effect on cryogenic toughness. In order to begin with a low nitrogen wire of calculated 0 FN, a tubular wire of special composition was produced for this work.

For the weldments intended to contain 5 FN, a heat of 0.24 cm (3/32 in) diameter 316L stainless steel bare wire with the following composition was selected:

<u>C</u>	<u>Mn</u>	<u>Si</u>	<u>Cr</u>	<u>Ni</u>	<u>Mo</u>	<u>P</u>	<u>S</u>	<u>N</u>	<u>Co</u>	<u>Cu</u>
0.021	1.58	0.50	18.61	12.79	2.17	0.019	0.002	0.033	0.08	0.11

The ferrite number calculated from the mill analysis using the DeLong Diagram is 5.2 FN.

A tubular wire was produced deliberately aiming to exceed the 11.0 to 14.0 percent nickel range for type 3]6L wire in AWS A 5.9, so that 0 FN might be obtained. The aim composition of the wire was:

<u>C</u>	<u>Mn</u>	<u>Si</u>	<u>Cr</u>	<u>Ni</u>	<u>Mo</u>	<u>N</u>
0.02	2.3	0.4	18.5	15.5	2.3	0.02

The calculated ferrite by the DeLong Diagram for this composition is 0.2 FN. Samples were taken from four locations within this lot. Gas tungsten arc (GTA) melts were prepared and checked for nickel, chromium, and molybdenum homogeneity, which proved to be satisfactory.

PROCEDURES

Welding

Six weldments were produced for cryogenic testing. All welds were made in 2.54 cm (1.0 in) thick 304L stainless steel plate in the flat position. The basic joint preparation was a 90° included angle double vee which was symmetrical about the plate midthickness. Three weldments were made with each of the welding wires described above. The bare wire was used for a GTA weldment, a gas metal arc (GMA) weldment, and a submerged arc (SA) weldment. The tubular wire was used for a GMA weldment and two SA weldments, one with normal heat input and one with high-heat input. Details of the welding procedures, ferrite measurements, and fissure bend testing have been reported previously [4].

Mechanical Testing

The weldments were evaluated using tensile tests, Charpy V-Notch (CVN) impact tests and fracture toughness tests. The tensile tests were conducted at 295 K and 4 K; CVN tests were conducted at 77 K, 116 K, 144 K, and 172 K, and fracture toughness tests were done at 4 K.

Tensile tests were conducted at 4 K using 2.5 cm (1 in) gage length and 0.64 cm (0.25 in) diameter specimens. The specimens were oriented along the length of the weldment so that the entire sample was welded metal. The test procedures and the cryostat for the low temperature tests have been described by Reed [5]. The 295 K tensile tests were done on standard 1.28 cm (0.505 in) diameter all weld metal specimens.

CVN impact tests were conducted on 12 specimens from each weldment. The specimens were machined such that the notch was perpendicular to the plate surface and the crack propagated along the weld centerline.

Fracture toughness tests were conducted at 4 K using the ASTM E399 compact specimen with a 5.1 cm (2 in) width and a 2.5 cm (1 in) thickness. The specimens were oriented so that loading was perpendicular to the weldment and crack extension was along the weldment centerline. The single-specimen J-integral procedure [6] was used to determine J_{IC} , the value of J at the onset of crack extension. The plane strain fracture toughness, $K_{IC}(J)$, was determined from J_{IC} using the relationship proposed by Begley and Landes [7]:

$$K_{IC}(J) = \left(\frac{J_{IC} E'}{1-\nu^2} \right)^{1/2}$$

where E is Young's modulus and ν is Poisson's ratio. Tests were conducted in an electrohydraulic fatigue machine equipped with the cryostat described by Fowlkes and Tobler [8].

All tests were conducted using the computer aided J-integral testing facility described by Read [9].

RESULTS AND DISCUSSION

Chemical composition and ferrite measurements were made on all weld metal deposits. The results of these measurements are given in table 1. Note that the SA weldments generally have higher concentrations of residual elements; of particular interest are silicon and oxygen. The higher concentration of these elements results from the flux used in SA welding. Also, note that the ferrite numbers do not correlate well with either the ferrite numbers calculated from the all-weld-metal deposit composition or the ferrite numbers calculated from the chemical composition of the welding wire. As a result of this unpredictability in ferrite contents, the original objective of obtaining three weldments with 5 FN and three with 0 FN was not achieved.

Ferrite measurements made on the actual double-vee weldments, which were tensile and fracture toughness tested at 4 K, are shown in table 2. These measurements were made with a ferrite meter that samples only a small area for ferrite content. (Note: These measurements were made in percent ferrite, which at these ferrite levels is approximately equal to FN.) By using this instrument, it is possible to see the variation in ferrite content through the thickness of the weldment. These results show that, although the average ferrite content of the double-vee weldment is very close to that of the all weld-metal pad, there is a significant variation in ferrite content through the thickness of the weldment. Generally, higher ferrite contents are found in the center of the weldment, as would be expected from the higher degree of base metal

dilution in this area. However, two of the weldments deviated from this expected trend. The 316L bare wire GMA weldment had higher ferrite on one side of the double-vee than on the other side. The 316L tubular wire SA weldment with high heat input had higher ferrite near the plate surfaces than in the center of the weldment. In the case of the high heat input SA weldment this effect can be explained by the fact that this weldment had very large passes, which resulted in considerable remelting of the previous pass and good mixing of the fused base metal. As a result of the primary austenite solidification mode, ferrite stabilizing elements were segregated to the top of the weldment. No explanation is offered for the curious result seen in the GMA weldment.

The above results on ferrite distribution were qualitatively confirmed by metallographic examination. Figures 1a and 1b show micrographs from locations C and E, respectively (see table 2). This sample was prepared using an electrolytic 10 N KOH etch, which selectively deposits a film on the ferrite phase. The weldments were also examined after color etching with a solution of 125 ml H₂O, 50 ml HCl, and 2 g Na₂SO₄, which was used to show whether the solidification mode was primary austenite or primary ferrite. The solidification mode is generally considered to be important with regard to microfissuring in the weldment [10] and it may also have an important effect on cryogenic toughness because it affects the continuity of the ferrite phase [11]. In general, the examination with the color etch showed that the areas that contained greater than two percent ferrite solidified as primary ferrite and those areas with less than two percent ferrite solidified as primary austenite.

The results of CVN impact tests are shown in table 3. From the very low lateral expansion it is evident that the two normal heat input

SA weldments have a low toughness. Although CVN impact results at 77 K are not a good indication of 4 K fracture toughness [12], it was decided that the lateral expansions of these two SA weldments were so poor that 4 K testing was unwarranted.

The 295 K and 4 K tensile properties of all weld metal specimens are shown in table 4. The 316L bare wire weldments had higher 4 K yield and ultimate strengths than the tubular wire weldments. This difference was large at 4 K and was probably due to the extremely low nitrogen content of the tubular wire weldments (see table 1).

The results of 4 K fracture toughness tests are shown in table 5. The highest toughness was achieved with the 316L bare wire GTA weldment. The two GMA weldments had almost the same fracture toughness even though the bare wire GMA weldment had a significantly higher strength. The tubular wire high heat input SA weldment had poor fracture toughness as well as a low yield strength.

As noted previously, the 4 K fracture toughness of stainless steel weldments has been correlated with both ferrite content and nitrogen concentration. The weldments tested in this study do not have significantly different ferrite contents, and the weldments with lower nitrogen concentrations also had lower fracture toughness, which is against the expected trend. The major difference in the weldments is the welding process used and it seems likely that this is the cause of the wide variation in fracture toughness.

Of the three processes used, GTA, GMA, and SA, it would be expected that the GTA process would produce a "clean" weld and the SA process would result in a "dirty" weld. In this case, clean and dirty refer to the amount of nonmetallic inclusions in the weld metal. The SA welding

process uses a flux that should result in a higher inclusion count than processes that use gas shielding. Micrographs on unetched samples from the bare wire GTA and the tubular wire SA weldment are shown in figures 2a and 2b, respectively. This figure qualitatively demonstrates that the SA weldment had a much higher inclusion count. It is well known that a high concentration of hard second phase particles can significantly reduce fracture toughness, and this appears to be the cause of the observed variation in fracture toughness of the welds tested in this study.

SUMMARY

Six 316L stainless steel weldments, which were produced by three welding processes with two welding wires, were evaluated for cryogenic mechanical properties. The best combination of 4 K yield strength and fracture toughness was achieved with the GTA process using 316L bare wire. This weldment had both the highest strength and highest fracture toughness of the welds tested. SA welding was found to result in both low strength and low toughness, attributed to the significantly "dirtier" weld produced by this process.

REFERENCES

1. W. T. DeLong, "Ferrite in Austenitic Stainless Steel Weld Metal," *Weld. J., Res. Suppl.* 53, 273s-275s (1974).
2. E. R. Szumachowski and H. F. Reid, "Cryogenic Toughness of SMA Austenitic Stainless Steel Weld Metals: Part I: Role of Ferrite," *Weld. J., Res. Suppl.* 58, 325s-333s (1978).
3. E. R. Szumachowski and H. F. Reid, "Cryogenic Toughness of SMA Austenitic stainless Steel Weld Metals: Part II: Role of Nitrogen," *Weld. J., Res. Suppl.* 58, 34s-44s (1979).
4. D. J. Kotecki, "Weld Process Study for 316L Stainless Steel Weld Metals at Cryogenic Temperatures," in Materials Studies for Magnetic Fusion Energy Applications at Low Temperatures-III, NBSIR 80-1627, National Bureau of Standards, Boulder, Colorado, pp. 195-204 (1980).
5. R. P. Reed, "A Cryostat for Tensile Tests in the Temperature Range 300 to 4 K," in Advances in Cryogenic Engineering, Vol. 7, Plenum Press, New York pp. 448-454 (1962).
6. G. A. Clarke, W. R. Andrews, P. C. Paris, and D. W. Schmidt, in Mechanics of Crack Growth, Proceedings of 1974 National Symposium on Fracture Mechanics, ASTM STP 590, American Society for Testing and Materials, Philadelphia, Pennsylvania, pp. 27-42 (1976).
7. J. A. Begley and J. D. Landes, in Fracture Toughness, Proceedings of 1971 National Symposium on Fracture Mechanics, Part II, ASTM STP 51, American Society for Testing and Materials, Philadelphia, Pennsylvania, pp. 1-20 (1972).
8. C. W. Fowlkes and R. L. Tobler, "Fracture Testing and Results for a Ti 6Al-4V Alloy at Liquid Helium Temperatures," *Eng. Fract. Mech.*, 8, 487-500 (1976).
9. D. T. Read, "The Computer-aided J-integral Test Facility at NBS," in Materials Studies for Magnetic Fusion Energy Applications at Low Temperatures-III, NBSIR 80-1627, National Bureau of Standards, Boulder Colorado, pp. 205-216 (1980).
10. T. Takalo, N. Suntala, and T. Moision, "Austenitic Solidification Mode in Austenitic Stainless Steel Welds," *Met. Trans. A*, 10A, pp. 1173-1181 (1979).
11. T. A. Whipple and E. L. Brown, "Deformation and Fracture of Stainless Steel Weldments and Castings at Low Temperatures," in Materials Studies for Magnetic Fusion Energy Applications at Low Temperatures-IV, NBSIR 81-1645, National Bureau of Standards, Boulder, Colorado pp. 415-451 (1981).
12. T. A. Whipple, H. I. McHenry, and D. T. Read, "Fracture Behavior of Ferrite-free Stainless Steel Welds in Liquid Helium," in Materials Studies for Magnetic Fusion Energy Applications at Low Temperatures-III, NBSIR 80-1627, National Bureau of Standards, Boulder, Colorado, pp. 167-194 (1980).

LIST OF TABLES

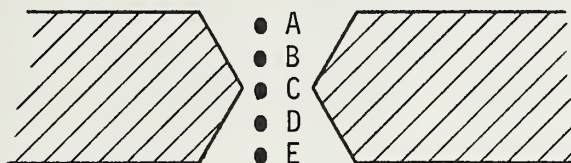
- Table 1. All-weld metal composition and ferrite content.
- Table 2. Delta-ferrite measurements on double-vee 316L stainless steel weldments.
- Table 3. CVN impact test results on 316L weldments.
- Table 4. Tensile properties of 316L stainless steel weldments.
- Table 5. Fracture toughness properties of 316L stainless steel weldments at 4 K.

Table 1

All-Weld-Metal Composition and Ferrite

Element	316L Bare			316L Tubular		
	GTA	GMA	SA	GMA	SA	SA High-Heat Input
C	0.017	0.017	0.023	0.014	0.016	0.017
Mn	1.39	1.40	1.97	2.17	2.50	2.43
Si	0.45	0.47	0.84	0.46	1.03	0.84
Cr	18.02	17.95	18.95	18.68	19.61	19.07
Ni	11.89	11.76	12.75	15.15	15.32	14.59
Mo	2.12	2.12	2.08	2.31	2.21	2.22
S	0.003	0.003	0.005	0.013	0.011	0.011
P	0.020	0.020	0.031	0.010	0.021	0.021
N	0.069	0.069	0.065	0.030	0.016	0.018
O	0.053	0.066	0.110	0.072	0.106	0.087
Co	0.092	0.090	0.095	0.012	0.025	0.020
V	0.063	0.063	0.06	0.013	0.017	0.016
Nb	0.02	0.02	0.02	0.02	0.02	0.02
Ti	0.021	0.022	0.024	0.15	0.092	0.104
Cu	0.089	0.086	0.10	0.037	0.043	0.042
FN measured	1.5	3.0	7.4	0.9	2.2	1.8
FN calculated by diagram	4.4	4.1	5.7	0.8	6.8	5.2

Table 2

Delta-ferrite Measurements on Double-vee 316L
Stainless Steel Weldments

Wire	Process	Percent Delta-ferrite*					Avg.
		A	B	C	D	E	
316L	GTA	0.0	0.6	1.9	0.7	0.0	0.6
Bare Wire	GMA	3.5	3.0	2.8	0.6	0.0	2.0
316L	GMA	0.5	3.2	2.3	3.2	0.6	2.0
Tubular Wire	SA (high-heat input)	4.7	0.2	0.7	0.6	2.7	1.8

*Measurements by ferrite meter at indicated locations.

Table 3
CVN Impact Test Results^{1,2} on 316L Weldments

Temperature, K	316L Bare Wire			316L Tubular Wire		
	GTA	GMA	SA	GMA	SA	SA High Heat Input
172	102 (0.91)	114 (1.17)	49 (0.41)	58 (0.91)	24 (0.30)	45 (0.53)
144	89 (0.99)	109 (1.19)	43 (0.41)	47 (0.69)	19 (0.18)	40 (0.53)
116	75 (0.69)	92 (0.99)	37 (0.28)	39 (0.43)	18 (0.18)	33 (0.36)
77	58 (0.46)	77 (0.81)	29 (0.05)	31 (0.43)	16 (0.08)	39 (0.38)

¹Results given are energy absorbed in joules and lateral expansion in (mm).

²All values are the average of three tests.

Table 4

Tensile Properties of 316L Stainless Steel Weldments

Wire	Process	Temperature, K	Yield Strength, MPa (ksi)	Ultimate Strength, MPa (ksi)	Elongation, %	Reduction in Area, %
316L Bare Wire	GTA	295	430 (62.4)	602 (87.3)	32	55
		4	807 (117.0)	1549 (224.6)	34	27
	GMA	295	355 (52.0)	554 (80.3)	45	55
		4	779 (113.0)	1510 (219.0)	37	27
	SA	295	441 (63.9)	587 (85.1)	36	54
	316L Tubular Wire	GMA	295	332 (48.1)	503 (73.0)	30
4			608 (88.2)	1162 (168.6)	29	20
SA		295	387 (56.1)	542 (78.6)	32	41
SA (high heat input)		295	322 (46.7)	555 (80.5)	34	38
		4	606 (87.9)	1122 (162.7)	21	18

Table 5

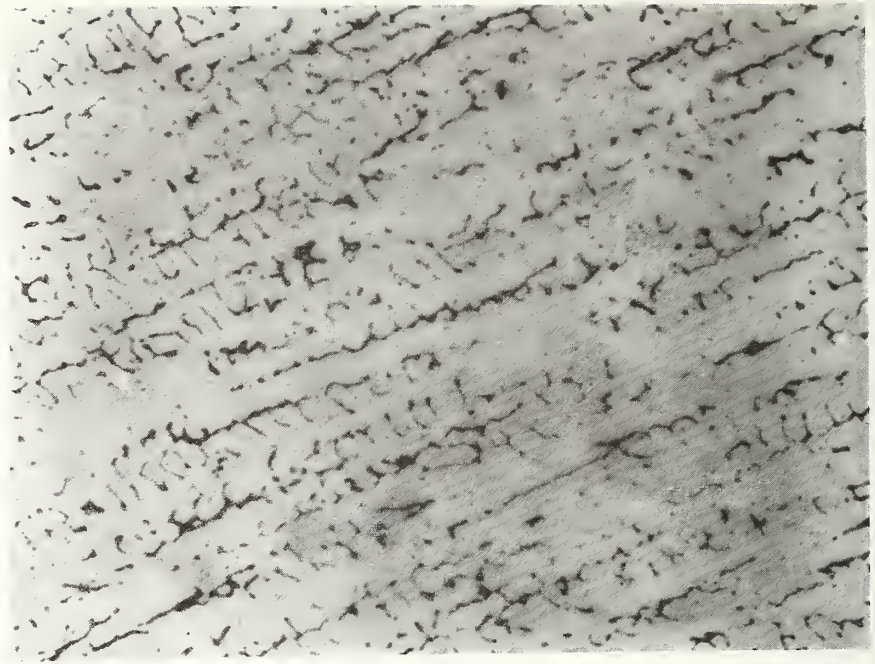
Fracture Toughness Properties of 316L Stainless Steel Weldments at 4 K

Wire	Process	J_{Ic} ,	$K_{Ic}(J)$
		kJ/m^2 ($\text{in}\cdot\text{lb/in}^2$)	$\text{MPa}\sqrt{\text{m}}$ ($\text{ksi}\sqrt{\text{in}}$)
316L Bare Wire	GTA	138 <u>148</u> 143 (818)	181 (165)
	GMA	103 <u>130</u> 116 (666)	163 (148)
316L Tubular Wire	GMA	111 (635)	159 (145)
	SA (High heat input)	47 (270)	103 (94)

LIST OF FIGURES

Figure 1 Micrographs of locations C and E on the 316L bare-wire GTA weldment, showing the variation in ferrite content through the thickness of the weldment. KOH etch, 400X.

Figure 2 Micrographs showing the difference in the cleanliness of the weldments (a) 316L bare-wire GTA weldment (b) 316L tubular-wire SA weldment. Unetched, 200 X.



(a)



(b)

Figure 1. Micrographs of locations C and E on the 316L bare wire GTA weldment, showing the variation in ferrite content through the thickness of the weldment. KOH etch, 400X.



(a)



(b)

Figure 2 Micrographs showing the difference in the cleanliness of the weldments (a) 316L bare wire GTA weldment (b) 316L tubular wire SA weldment. Unetched, 200X.

FRACTURE TOUGHNESS PROPERTIES OF WELDS IN ALUMINUM ALLOY 5083-0 AT 4 K

J. W. Elmer and H. I. McHenry
Fracture and Deformation Division
National Bureau of Standards
Boulder, Colorado

ABSTRACT

A series of weldments was prepared by five cooperating companies in 51-mm thick 5083-0 aluminum plate using 5183 filler metal and the gas metal arc (GMA) welding processes. The J-integral fracture toughness and fatigue crack growth rates of the weldments were measured at 4 K and found to be similar to base metal properties. In a related study, the tensile and notched tensile properties of the same weldments were obtained at room temperature and 4 K. Data for each of the mechanical properties did not vary significantly from weld to weld. It is concluded that the mechanical properties of 5183 welds at 4 K do not depend on the GMA welding parameters and procedures.

INTRODUCTION

Aluminum alloy 5083-0 is a solid-solution-strengthened alloy frequently used for cryogenic storage tanks for service to 76 K. Alloy 5083-0 derives its limited strength from the solid-solution-strengthening contributions of 4.4% Mg and 0.7% Mn. It is readily weldable with alloy 5183 filler metal and has outstanding toughness at low temperatures. New applications for 5083-0 aluminum in magnetic fusion energy systems are being examined; these place additional requirements on the alloy since it is necessary to retain favorable mechanical properties down to 4 K. To date, few mechanical property data are available for 5083-0 weldments at 4 K. [1,2]

In this study, fracture toughness and fatigue crack growth rate data were obtained for 5083-0 weldments at 4 K. This study was preceded by an evaluation of the tensile and notched tensile properties of the same weldments at room temperature and 4 K by Kelsey and Mueller. [1] The objectives were as follows:

1. Develop fracture toughness and fatigue crack growth rate data for 5083 aluminum weldments at 4 K.
2. Compare the 4-K toughness of 5183 aluminum weldments produced by different companies using different welding parameters and processes.

WELDING PROCEDURES

Weldments were prepared and donated by five different companies. Each company was asked to weld 51-mm (2-in) thick 5083-0 aluminum plate using 5183 filler wire and the gas metal arc (GMA) welding process. All welding was performed in the flat position using a double-vee joint

preparation; however, specific welding parameters were the choice of the individual company. In addition, two companies supplied high deposition rate (HDR) GMA weldments of the same material to determine if high heat input influences the mechanical properties. The welding parameters used are listed in Table 1. The welding parameters varied considerably; for example, the number of passes varied from 2 for an HDR weld to 55 for one of the conventional welds. A total of seven welds were made, five by the conventional GMA welding process and two by the HDR-GMA welding process.

TESTING PROCEDURE

All fracture toughness testing was performed in liquid helium at 4 K using a standard 2.54-cm (1-in) thick ASTM E399 compact tension specimen. The specimen was removed from the center of the 51-mm welded plate with the plane of the notch perpendicular to the plate and centered in the fusion zone, such that the 5183 weld metal was tested. The specimens were precracked in tension-tension fatigue to a depth of 3.05 cm (1.20 in) prior to testing. The fracture toughness was measured using a computer-aided, single-specimen J-integral test, described by Read.^[3] Fatigue crack growth rate measurements were made using the same specimen configuration and were tested in liquid helium with an R ratio of 0.1.

RESULTS

Tensile properties of the 5083 weldments at room temperature (Table 2) and at 4 K (Table 3) are provided to include additional information about the weldments.^[1] Table 3 also shows the 4-K fracture toughness properties for each of the seven weldments as measured by the

J-integral technique. In Table 3, $K_{IC}(J)$ refers to the plane strain fracture toughness as estimated from the J-integral test results. Fatigue crack growth rate data at 4 K (Table 4) compares conventional and HDR weld metal properties with 5083-0 base metal properties measured by Tobler and Reed.^[4] The empirical constants n and C refer to the Paris equation of fatigue crack growth rate:

$$\frac{da}{dN} = C(\Delta K)^n$$

C has metric units corresponding to da/dN in mm/cycle and ΔK in $\text{MPa}\sqrt{\text{m}}$.

DISCUSSION

A comprehensive summary of the tensile data indicates that welding parameters do not influence the yield strength or tensile strength to any significant extent. Except for the generally lower tensile properties of the GMA weldment of supplier 2, the tensile properties of the GMA weldments were quite consistent. The HDR weldments proved to be only slightly lower in strength than the conventional weldments. The notch yield ratios at 4 K and room temperature are all greater than 1.6, which suggests that the weld metal is very tough.

Results of the fracture toughness testing at 4 K show the average fracture toughness, $K_{IC}(J)$, determined by the J-integral method, to be $45.1 \text{ MPa}\sqrt{\text{m}}$. The $K_{IC}(J)$ data are consistent for the seven weldments and all the data lie within one standard deviation of the mean except for that of the HDR weldment from supplier 4. The tensile data are also consistent indicating that the mechanical properties of weldments in 5083-0 aluminum are relatively insensitive to welding parameters.

The average toughness of $45.1 \text{ MPa}\sqrt{\text{m}}$ at 4 K is low when compared with those of other tough materials used at low temperatures and seems to be in conflict with the notch-yield-ratio results. Actually the $K_{IC}(J)$ values for the welds are the same as the 5083-0 base plate (TL orientation) results at 4 K reported by Tobler and Read.^[3] The low values are due to the testing technique used and do not reflect the true fracture resistance of the material. The problem with measuring the toughness of the 5183 aluminum weldments using the J-integral technique is that the aluminum tears at low J-levels where $K_{IC}(J)$ is measured and thus the $K_{IC}(J)$ value is low. However, 5183 aluminum weldments are able to sustain much higher J-levels under stable crack propagation conditions, which is an indication of toughness. This is shown in Figure 1, which is a load-displacement curve recorded during one of the tests. The point indicated is the point of initial tearing, determined from the J- Δa curve. This occurs at a low load, but the specimen was able to sustain loads past the peak load without fracturing. Thus, 5183 aluminum weldments are tough even though their $K_{IC}(J)$ values are low.

Fatigue crack growth rates for 5183 weld metal deposited by conventional and HDR-GMA processes are compared with the fatigue crack growth rate of 5083-0 base metal at 4 K in Figure 2. The fatigue crack growth rates for the conventional and HDR welds are similar and generally faster than the base metal rates; however, without further study the differences between them cannot be considered significant.

SUMMARY AND CONCLUSION

Tensile properties at room temperature and at 4 K for 5183 aluminum weld metal were shown to be consistent for welds made with large variations in welding parameters.^[1] The $K_{IC}(J)$ values and fatigue crack

growth rates at 4 K for the welds were also shown to be insensitive to welding process and parameters. Therefore, it can be concluded that the mechanical properties of 5183 weld metal do not depend upon the GMA welding parameters to any great extent.

REFERENCES

1. R. A. Kelsey and L. N. Mueller, "Tensile and Notch-Tensile Properties at Room Temperature and 4 K of Welds in Aluminum Alloy 5083-0 Plate," in Material Studies for Magnetic Fusion Energy Applications at Low Temperatures-III, NBSIR 80-1627, 219-244 (1980).*
2. F. G. Nelson, J. G. Kaufman, and E. T. Wanderer, "Tensile Properties and Notch Toughness of Groove Welds in Wrought and Cast Aluminum Alloys at Cryogenic Temperatures," Advances in Cryogenic Engineering, Vol. 14, 1969, pp. 71-82.
3. D. T. Read, "The Computer-Aided J-Integral Test Facility at NBS," in Materials Studies for Magnetic Fusion Energy Applications at Low Temperatures-III, NBSIR 80-1627, 205-216 (1980).
4. R. L. Tobler and R. P. Reed, "Fracture Mechanics Parameters for a 5083-0 Aluminum Alloy at Low Temperatures," Journal of Engineering Materials and Technology, Vol. 99, (October 1977).

*NOTE: A slightly revised version of Reference 1 (same authors and title) has been published: Report Number 57-80-02, Alcoa Laboratories, Alcoa Center, PA 15069, March 14, 1980.

Table 1
Welding Procedures [1]

Supplier	Process Weld	Current (A)	Voltage (V)	Gas (L/min)	Number of Passes
1	GMA	230-250	26-29	15.5 Ar 31.0 He	55
2	GMA	250-300	26-29	11.7 Ar 35.2 He	--
3	GMA	240-300	24-26	28.2 Ar	25
4	GMA	335-365	33-34	9.4 Ar 18.8 He	16
5	GMA	380-390	28	---	18
4	HDR*	580	34	70.5 Ar 47.0 He	4
5	HDR	740-750	33	11.7 Ar 35.2 He	2

*High Deposition Rate

Table 2

Room-Temperature Mechanical Properties of 5083 Welds [1]

Supplier	Process	0.2% Yield Strength (MPa)	Notch Tensile Strength (MPa)	Notch* Yield Ratio
1	GMA	166	312	1.88
2	GMA	148	315	2.13
3	GMA	166	314	1.89
4	GMA	167	327	1.96
5	GMA	178	356	2.00
4	HDR	152	312	2.06
5	HDR	146	306	2.09

$$*NYR \equiv \frac{\text{Tensile Yield Strength}}{\text{Notch Tensile Strength}}$$

Table 3

Mechanical Properties of 5083 Welds at 4 K [1]

Supplier	Process	0.2% Yield Strength (MPa)	Notch Tensile Strength (MPa)	Notch Yield Ratio	K_{Ic} (J) (MPa \sqrt{m})
1	GMA	202	363	1.80	41.7
2	GMA	177	344	1.94	46.9
3	GMA	213	347	1.63	41.3
4	GMA	200	362	1.81	42.8
5	GMA	214	391	1.83	49.0
4	HDR	202	343	1.69	51.9
5	HDR	200	337	1.69	42.0

Table 4
Fatigue Crack Growth Rate at 4 K

Material	Condition	n	C	ΔK Range MPa \sqrt{m}
5083-0	annealed	5.2	1.3×10^{-10}	10-30
5183	HDR weld	6.5	3.8×10^{-12}	15-31
5183	GMA weld	4.6	7.3×10^{-10}	14-32

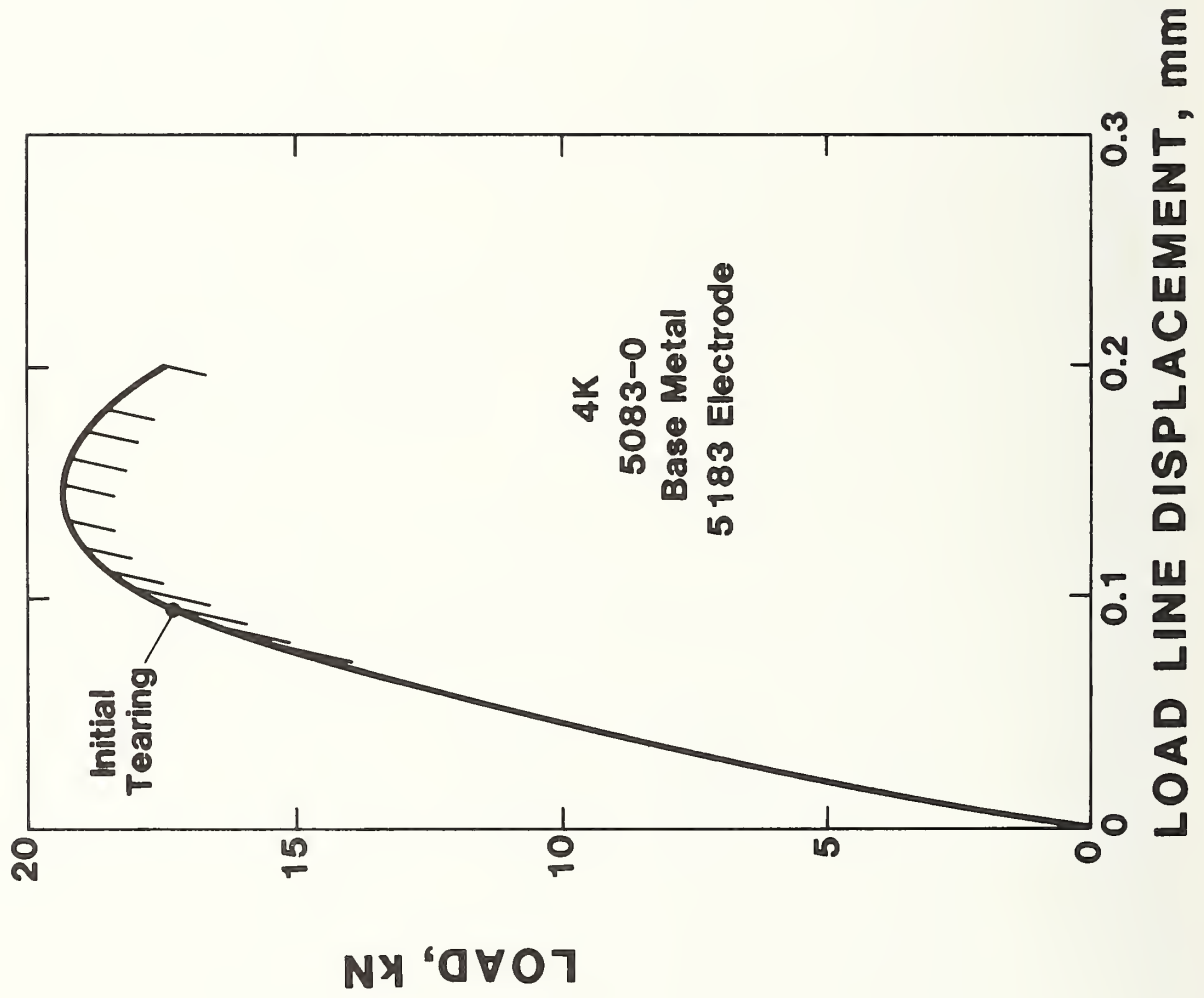


Figure 1. Load-displacement curve for one of the conventional welds indicating the point of initial tearing.

← TENSILE AXIS →



Figure 1

Micrograph of a 316L SA weld metal tensile specimen deformed at room temperature, taken near the fracture surface and showing the elongation of the ferrite. KOH etch.

THE INFLUENCE OF FERRITE AND NITROGEN ON MECHANICAL PROPERTIES
OF CF8M CAST STAINLESS STEEL

Leroy Finch
ESCO Corporation
Portland, Oregon

ABSTRACT

The production and mechanical-property testing of a cast molybdenum stainless steel are described.

THE INFLUENCE OF VARIABLE FERRITE AT A CONSTANT NITROGEN LEVEL
AND OF VARIABLE NITROGEN AT A CONSTANT FERRITE LEVEL ON
MECHANICAL PROPERTIES OF CF8M CAST STAINLESS STEEL

INTRODUCTION

---The National Bureau of Standards in Boulder desired to study the effect of a) variable ferrite content at a constant nitrogen level and b) a variable nitrogen content at a constant ferrite level in cast molybdenum stainless steel, CF8M.

---These materials were to be tested in tension at room temperature and 77°K (liquid nitrogen) at ESCO and at 4°K (liquid helium) at NBS in Boulder. Impact resistance values were also to be determined at room temperature and 77°K at ESCO and at 4°K at NBS.

---Tables 1 and 2 note the aim chemical analysis of the ten compositions decided on, five with variable ferrite content from 0%, fully austenitic, to 28% with a nitrogen content of 0.05% and five with a calculated ferrite content of 10% with variable nitrogen contents from 0.02 to 0.20%.

---The ferrite contents were calculated using the data and curve reported at the recent ASTM symposium on cast stainless steels, "Ferrite Measurement and Control in Cast Duplex Stainless Steels" by L. S. Aubrey et al.

---Figure 1 is the curve used to estimate the ferrite content from the chemical compositions.

---Pattern X3829 was used to make the molds for the casting to be used by NBS for the tests to be made at 4°K. The final casting is 4"x12"x24". The test bars tested at ESCO were from a conventional keel bar which has a diameter of 1½" at the bottom.

PRODUCTION

---Ten one thousand pound heats were melted in an induction furnace with a monolithic magnesia lining and powered by a motor generator having a 960 Hertz output.

---The sand mix used to form the molds was 33% zirconium silicate, 66% silica bonded with bentonite. This was washed with an alcohol base silica wash and torch dried. When the metal was all melted a preliminary sample was sent to the laboratory for spectrographic analysis. A "suck-up" sample was also sent for analysis of nitrogen content.

---When the results of these analyses were received back at the melting location, additions were calculated to bring the composition to the desired level. These additions were carefully weighed out and added to the molten metal. When the proper temperature was reached as measured with a platinum rhodium thermocouple, the metal was tapped into a magnesia lined ladle and transported to the mold. Final chemical analysis samples were taken from the ladles full of metal. When the proper pouring temperature was reached the metal was poured into the mold.

---After the metal had cooled down the castings were removed from the molds, heated to 2000°F, water quenched and the risers burned off using an oxyacetylene-powder torch. After the risers were removed the castings were again heated to 2000°F and water quenched. This double heat treatment was used because it has been found that CF8M is susceptible to sigma formation during cooling in the mold and if the risers are cut from material with sigma present in the microstructure cracking is likely to occur in the areas subjected to thermal shock.

---By heating to 2000°F the sigma is converted to ferrite and this ferrite is retained by the rapid water quench. After the risers are removed the material is again heat treated to redissolve any carbide which may have precipitated during the removal of the riser and also to dissolve any sigma that may have formed.

--Conventional tension test bars were machined from keel bars poured with metal from each heat. These were heat treated with the castings. Charpy V notch impact test specimens were also machined from the keel bars. The ferrite content of each heat was calculated using the Schoefer ratio and curve, Figure 1. It was also measured with a calibrated Magna gage and a Ferritescope. A portion of the end of each of the tension test bars was polished, etched and a point count made of the ferrite present using the procedure given in ASTM-E 562-76.

---The spectrographic chemical analyses of the heats produced are listed in Tables 3 and 4. The nitrogen contents included in the tables were obtained by vacuum fusion using a Leco rapid nitrogen analyzer. Also included in the tables are the ferrite contents determined by the methods noted above. The heat which was designed to have 0.02% nitrogen was melted in an argon atmosphere in order that the metal would not absorb nitrogen from the air and finish with a nitrogen content higher than 0.02%. The ferrite contents of four of the original heats were lower than desired. They were not used. The nitrogen content of another was higher than desired so it also was not used.

---Five more heats were produced in a similar manner as described above. In order to insure that the ferrite contents of these were satisfactory before the molten metal was tapped the spectrographic sample poured into the copper chill mold was measured with the calibrated Ferritescope. When the ferrite content was that desired the metal was tapped and poured as before.

MECHANICAL PROPERTIES

---Table 5 notes the room temperature mechanical properties obtained at ESCO for the ten heats which will be tested by the NBS. Table 6 lists the impact properties obtained to date. The tensile properties of the heats have not been obtained at 77°K at this time nor have the impact tests been completed for the last four heats. They will be reported when obtained. Figure 2 is a plot of the tensile and yield strengths (at 0.2% offset) at room temperature of the variable ferrite content heats versus the ferrite content. The ferrite content is expressed as the Cr^1/Ni^1 ratio. Figure 3 is the plot of the tensile and yield strengths (at 0.2% offset) at room temperature of the variable nitrogen content heats versus the nitrogen contents.

---In Figure 3 the numbers above each point plotted show the ferrite content of the material expressed by its ratio. The variable nitrogen heats did not have exactly the same ferrite contents. Heat 48987 was not used in these plots since the ferrite was 14% while the others were 8-10%. Heat 48988 with 8% ferrite and 0.05% nitrogen was used.

---Figure 4 is a plot of the average impact strength at room temperature and 77°K versus the ferrite content. Figure 4 is a similar plot of impact strength versus nitrogen contents.

DISCUSSION

---From Figure 2 and Table 5 it can be said that the ultimate tensile strength increases 940 psi per 1% ferrite when the ferrite varies from 0%, fully austenitic, to 29%. The yield strength increases 890 psi per 1% ferrite over the same range of ferrite.

---From Figure 3 and Table 5 it can be said that increasing the nitrogen content from 0.02 to 0.05% has little or no effect on mechanical properties. When the nitrogen content increases from 0.05 to 0.14% the tensile strength increases 855 psi per 0.01% of nitrogen. When it increases from 0.14 to 0.20% the increase in tensile strength averages 1250 psi per 0.01% of nitrogen.

---From Figure 2 and Table 6 it will be noted that the increase in tensile strength between 8 and 10% ferrite, 1.14 and 1.19 ratio is 2100 psi so if 2100 is subtracted from 93.7 the tensile strength of the heat with 1.19 ratio and 0.20% nitrogen the tensile strength of the material if it had had 8% ferrite and 0.20% nitrogen could have been 91.6 ksi, so $91.6 - 84.1 = 7500$ psi, which could have been due to the increase in nitrogen content or 1250 psi per point of nitrogen.

---It will be noted with similar calculation that the tensile strength of the heat with 0.10% nitrogen would have fallen on the line if its ferrite content had been 8%, 1.14 ratio, instead of the 10%, 1.17 ratio. The effect of the nitrogen content increase on yield strength appears to be linear, 1160 psi per 0.101% nitrogen. It will be noted in Figure 4 that the impact strength decreases as ferrite content increases. This is true at room temperature as well as at 77°K. Figure 5 shows that the impact strength at room temperature and 77°K is also lowered by increasing the nitrogen content. Of course this would be expected with the tensile strengths increased.

---When the mechanical property data is completed the results will be reported.

Table 1 - Aim Chemical Analysis in Percent of Five Heats of CF8M with Variable Ferrite and Constant Carbon and Nitrogen Contents

Ferrite %	0	7	14	21	28
C	0.06	0.06	0.06	0.06	0.06
Mn	1.20	0.40	0.40	0.40	0.40
Si	0.50	1.25	1.25	1.25	1.25
Cr	18.25	18.35	18.65	19.20	20.50
Ni	13.00	10.75	9.05	8.20	8.20
Mo	2.15	2.15	2.15	2.15	2.15
N ₂	0.05	0.05	0.05	0.05	0.05
Cr ¹ /Ni ¹	0.90	1.12	1.27	1.39	1.485

Table 2 - Aim Chemical Analysis in Percent of Five Heats of CF8M with Variable Nitrogen Contents at a Constant Ferrite Level, 10%

C	0.06	0.06	0.06	0.06	0.06
Mn	0.40	0.40	0.40	0.40	0.40
Si	0.75	1.25	1.25	1.25	1.50
Cr	18.55	18.90	19.25	21.20	21.00
Ni	10.10	10.00	9.25	9.45	9.25
Mo	2.15	2.15	2.15	2.15	2.85
N ₂	0.02	0.06	0.10	0.15	0.20
Cre ¹ /Nie ¹	1.19	1.19	1.19	1.19	1.19

Table 3 - Final Spectrographic Analysis in Percent of Five Heats of CF8M with Variable Ferrite Content and a Constant Carbon and Nitrogen

Heat No.	C	Mn	Si	Cr	Ni	Mo	N ₂	Ferrite Content*		
								C	M	Pt Ct
47640	0.06	1.10	0.59	18.04	13.24	2.12	.05	.88	0	0
48988	0.06	0.38	1.16	19.62	10.61	2.12	.05	1.21	6	8
47521	0.06	0.36	1.13	19.23	8.25	2.16	.05	1.39	17	15
47552	0.06	0.35	0.95	20.40	8.22	2.13	.05	1.45	22	22
49021	0.05	0.39	1.11	22.54	9.84	2.26	.05	1.48	27	29

Table 4 - Final Spectrographic Analysis in Percent of Five Heats with Variable Nitrogen at a Constant Ferrite Content

Heat No.	C	Mn	Si	Cr	Ni	Mo	N ₂	Ferrite Content*		
								C	M	Pt Ct
49020	0.07	0.39	1.09	19.32	10.00	2.07	.02	1.25	8	8
48987	0.07	0.51	1.17	20.13	10.23	2.49	.06	1.27	11	14
47364	0.06	0.40	1.30	19.17	9.14	2.00	.10	1.18	8	9
47390	0.07	0.41	0.98	21.00	9.46	2.13	.144	1.16	7	8
47399	0.06	0.33	1.35	21.66	9.68	2.83	.20	1.19	9	10

*Ferrite Content

C - Calculated using Schoefer formula for ratio

$$Cr^1 = Cr + 1.5Si + 1.4Mo - 4.99$$

$$Ni^1 = 30xC + .5Mn + Ni + 26(N - 0.2) + 2.77$$

M - Measured with calibrated Ferritescope

Pt Ct - Metallographic point count, ASTM E 562

The Cr¹/Ni¹ ratios used in the plotting of the figures were obtained from the ferrite content determined by point count and taken from Figure 1.

Table 5 - Room Temperature Mechanical Properties of Heats Shipped to NBS Tested at ESCO

<u>Heat No.</u>	<u>UTS</u> <u>ksi</u>	<u>YS ksi</u> <u>(0.20% offset ksi)</u>	<u>E</u> <u>%</u>	<u>RA</u> <u>%</u>	<u>Ferrite</u>	
					<u>Ratio</u>	<u>%</u>
<u>Variable Ferrite, 0.05% N</u>						
47640	65.3	29.6	55.5	65	.9	0
48988	76.4	36.4	56.0	71	1.14	8
47521	87.2	48.5	48.0	64	1.30	15
47552	89.0	50.2	46.5	63	1.43	22
49021	92.6	55.4	42.0	64	1.53	29
<u>Variable Nitrogen Content, Constant Ferrite</u>						
49020	76.4	36.2	58.0	65	1.14	8
48987	82.9	41.0	47.0	69	1.28	14
47364	81.3	44.3	48.5	70	1.17	9
47390	84.1	47.6	51.0	66	1.14	8
47399	93.7	53.8	42.0	59	1.19	10

Table 6 - Impact Properties Obtained to date

<u>Heat No.</u>	<u>Impact Data, Ft-Lbs</u>		<u>77°K</u>	<u>Avg.</u>
	<u>R.T.</u>	<u>Avg.</u>		
47640	177-240-240	219	136-122-147	135
48988				
47521	156-140-151	149	74- 78- 76	76
47552	149-122-145	139	63- 66- 61	63
49021				
49020				
48987				
47364	167-232-223	207	66-101-110	92
47390	170-175-169	171	65- 68- 61	65
47399	190-175-172	179	38- 39- 22	33

ADDENDUM

The Influence of Variable Ferrite at a Constant Nitrogen Level
and of Variable Nitrogen at a Constant Ferrite Level
on Mechanical Properties of CF8M Cast Stainless Steel

This is an addendum to the original report which did not contain all of the data.

This report includes the missing data: impact test results at room temperature and 77°K and tensile properties at 77°K.

Table 6 reports the impact strength at room temperature and 77°K obtained on all of the alloys. Some of these were included in the original report.

Figure 4 is a plot of the impact strengths of the heats with variable ferrite content vs. the ferrite content at room temperature and 77°K.

Figure 5 is a plot of impact strength vs. the nitrogen contents for the variable nitrogen series at room temperature and 77°K.

The impact strength drops with increase in ferrite content at both room temperature and at 77°K.

At room temperature the loss per percent of ferrite is as follows:

0- 8%	3.9 ft-lbs
0-15%	4.7 ft-lbs
0-22%	3.6 ft-lbs
0-29%	3.4 ft-lbs

At 77°K the drop is:

0- 8%	3.9 ft-lbs
0-15%	3.9 ft-lbs
0-22%	3.3 ft-lbs
0-29%	3.1 ft-lbs

The rate of loss is nearly equal at both temperatures.

Table 7 reports the tensile properties obtained at 77°K.

Figure 6 is the plot of the tensile strengths at 77°K plotted against the ferrite content expressed as Cr^1/Ni^1 ratio and the nitrogen contents.

It will be noted that the tensile strength increases both with ferrite content and with nitrogen contents to maxima and drops off with further increases: 22% ferrite with a ratio of 1.43 has the greatest strength of the ferrite series and the nitrogen content of 0.10 percent was the strongest of the nitrogen series of heats.

LFinch
/nmo
2/25/81

Table 5 - Room Temperature Mechanical Properties of Heats Shipped to NBS Tested at ESCO

<u>Heat No.</u>	<u>UTS ksi</u>	<u>YS ksi (0.20% offset ksi)</u>	<u>E %</u>	<u>RA %</u>	<u>Ferrite</u>	
					<u>Ratio</u>	<u>%</u>
<u>Variable Ferrite, 0.05% N</u>						
47640	65.3	29.6	55.5	65	.9	0
48988	76.4	36.4	56.0	71	1.14	8
47521	87.2	48.5	48.0	64	1.30	15
47552	89.0	50.2	46.5	63	1.43	22
49021	92.6	55.4	42.0	64	1.53	29
<u>Variable Nitrogen Content, Constant Ferrite</u>						
49020	76.4	36.2	58.0	65	1.14	8
48987	82.9	41.0	47.0	69	1.28	14
47364	81.3	44.3	48.5	70	1.17	9
47390	84.1	47.6	51.0	66	1.14	8
47399	93.7	53.8	42.0	59	1.19	10

Table 6 - Impact Properties

<u>Heat No.</u>	<u>Impact Data, Ft-Lbs</u>		<u>77°K</u>	<u>Avg.</u>
	<u>R.T.</u>	<u>Avg.</u>		
47640	177-240-240	219	136-122-147	135
48988	203-162-199	188	98-108-107	104.3
47521	156-140-151	149	74- 78- 76	76
47552	149-122-145	139	63- 66- 61	63
49021	125-118-115	119.3	40- 45- 47	44
49020	162-137-139	146	73- 87- 85	81.7
48987	184-198-205	195.7	118-102- 93	104.3
47364	167-232-223	207	66-101-110	92
47390	170-175-169	171	65- 68- 61	65
47399	190-175-172	179	38- 39- 22	33

Table 7 - Mechanical Properties at 77°K of Heats Shipped to NBS
Tested at ESCO

<u>Heat No.</u>	<u>UTS, psi</u>	<u>E, %</u>	<u>RA, %</u>	<u>Ferrite</u>		
				<u>Ratio</u>	<u>%</u>	
<u>Variable Ferrite Content, 0.05% N</u>						
47640	142,300	38	47	.9	0	
48988	190,800	53	54	1.14	8	
47521	211,200	30	20	1.30	15	
47552	214,100	37	28	1.43	22	
49021	169,200	30	56	1.53	29	
<u>Variable Nitrogen Content, Constant Ferrite</u>						<u>N₂</u>
49020	183,100	35	55	1.14	8	.02
48988	190,800	53	54	1.14	8	.05
48987	186,000	53	61	1.28	14	.06
47364	202,700	35	25	1.17	8	.10
47390	173,300	39	52	1.14	8	.144
47399	170,500	25	36	1.19	10	.20

LFinch
/nmo
1/23/81

$$Cr^1 = \%CR + 1.5\%Si = 1.4\%Mo - 4.99$$

$$Ni^1 = 30(\%C) + \frac{\%Mn}{2} + \%Ni + 26(\%N - .02) + 2.77$$

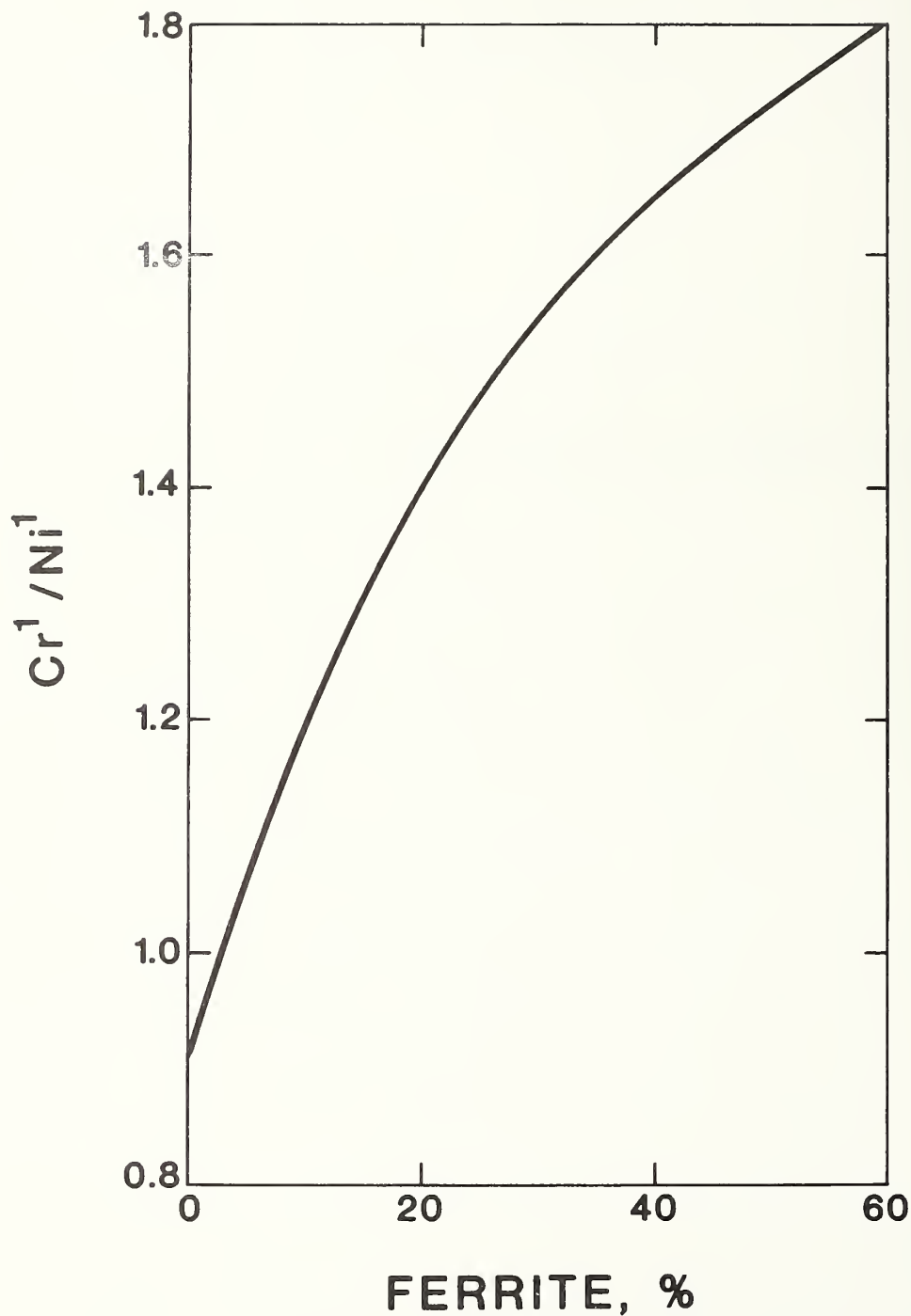


Figure 1 Relationship between Cr^1/Ni^1 and percent Ferrite in Cast Duplex Corrosion Resistant Stainless Steels

$$Cr^1 = \%CR + 1.5\%Si + 1.4\%Mo - 4.99$$

$$Ni^1 = 30(\%C) + \frac{\%Mn}{2} + \%Ni + 26(\%N - .02) + 2.77$$

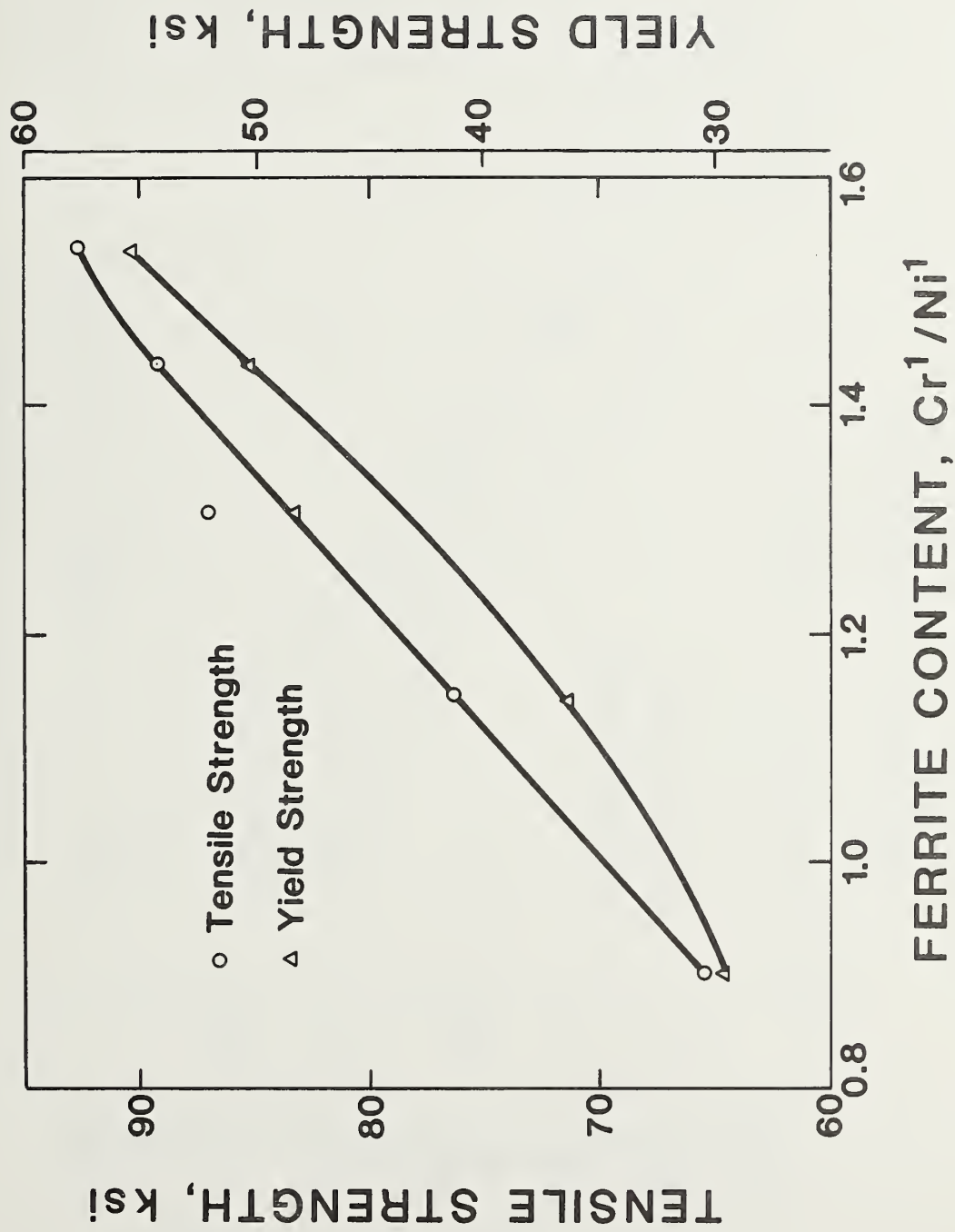
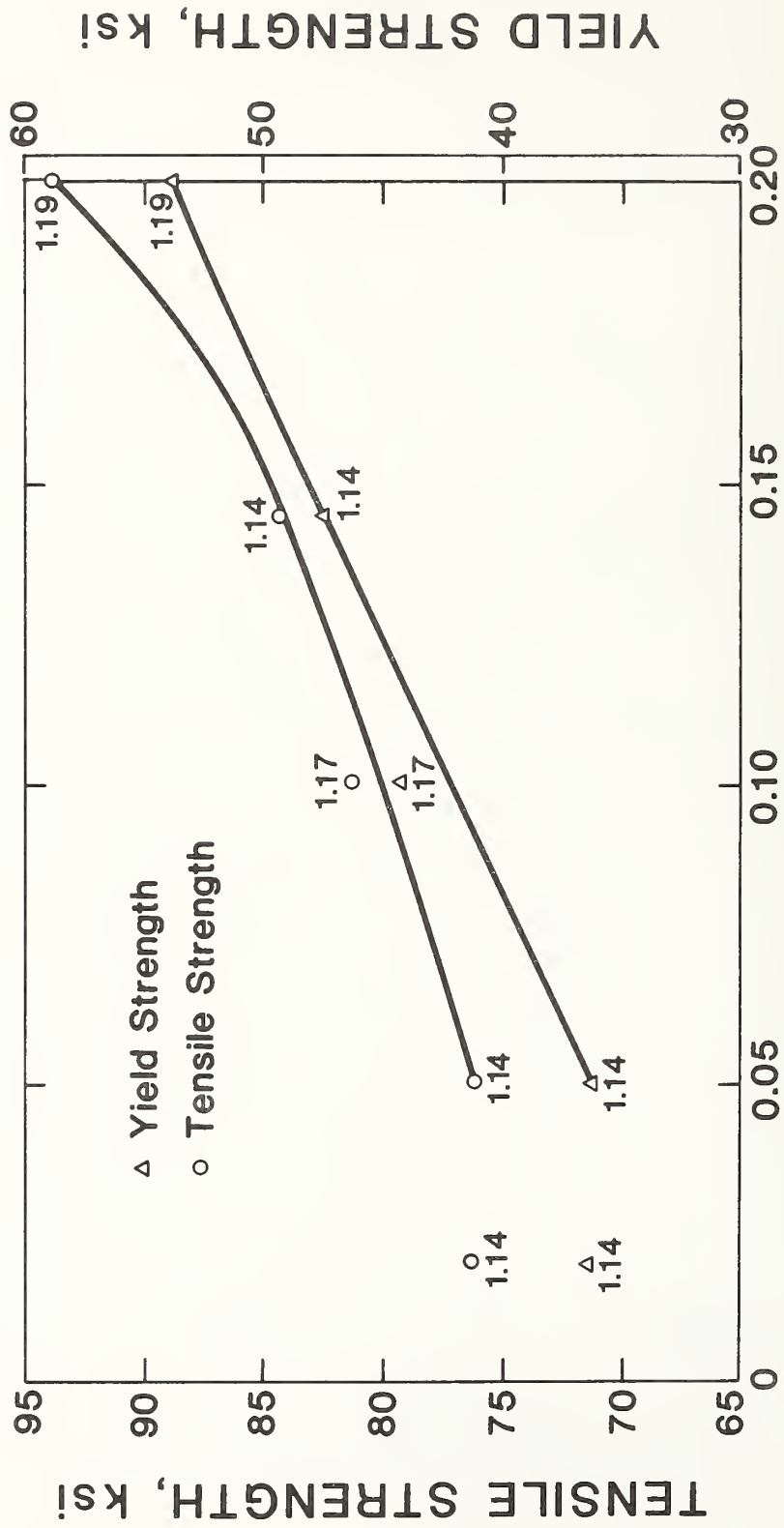


Figure 2 Relationship between RT Tensile and Yield Strength and Ferrite Content



NITROGEN CONTENT, %

Figure 3 Relationship between Tensile and Yield Strength and Nitrogen Content

$$Cr^1 = \%CR + 1.5\%Si + 1.4\%Mo - 4.99$$

$$Ni^1 = 30(\%C) + \frac{\%Mn}{2} + \%Ni + 26(\%N - .02) + 2.77$$

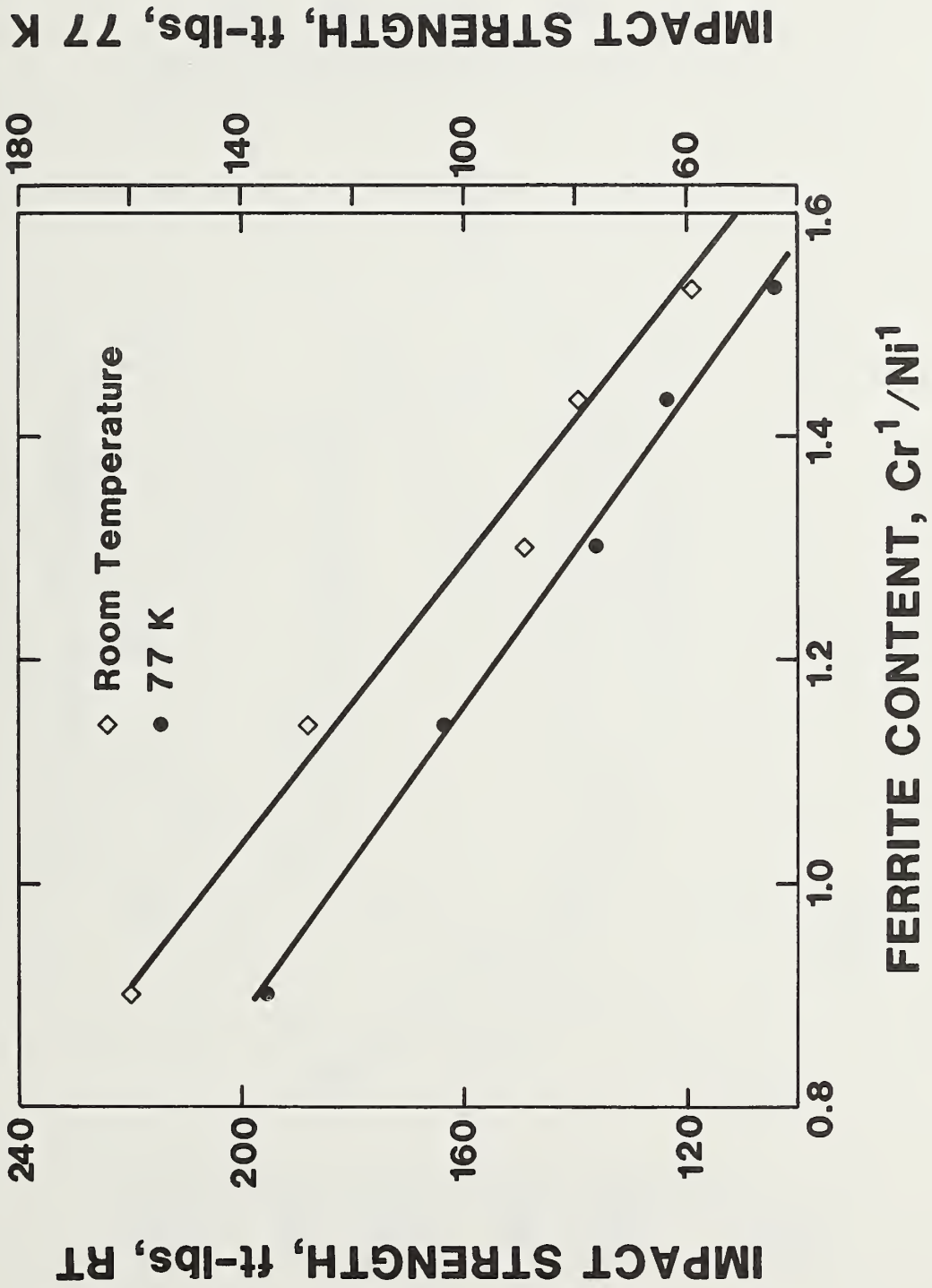


Figure 4 Relationship between Impact Strength at RT and 77 K and Ferrite Content expressed as Cr¹/Ni¹

IMPACT STRENGTH, ft-lbs, 77 K

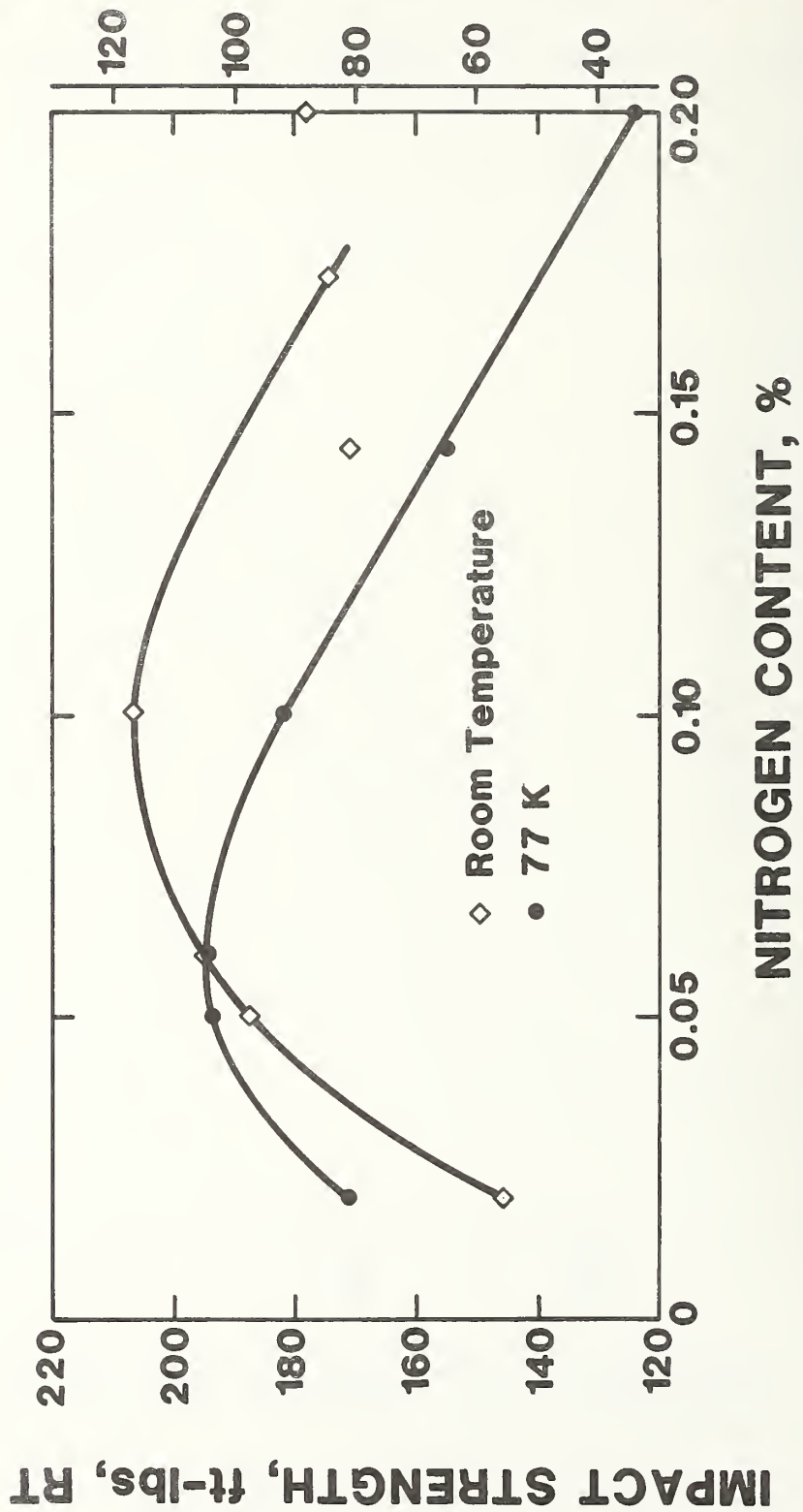
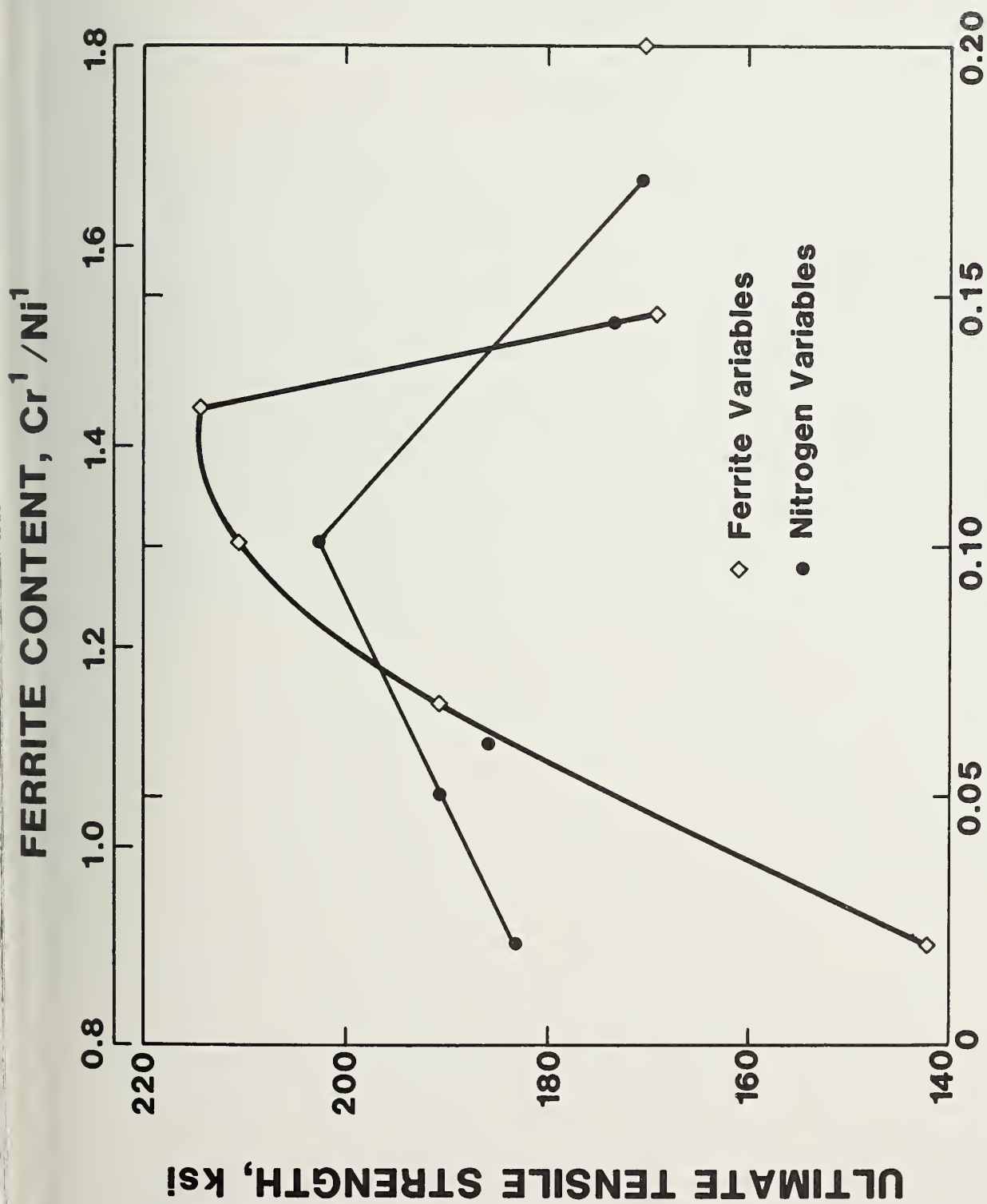


Figure 5 Relationship between Impact Strength at RT and 77 K and Nitrogen Content



NITROGEN CONTENT, %

Figure 6 Relationship between Tensile Strength at 77 K and Ferrite content expressed as Cr¹/Ni¹.

$$Cr^1 = \%Cr + 1.5\%Si + 1.4\%Mn - 4.99$$

$$Ni^1 = 30(\%C) + \frac{\%Mn}{2} + \%Ni + 25(\%N - .02) + 2.77$$

METALLOGRAPHY OF δ -FERRITE IN AUSTENITIC STAINLESS STEEL CASTINGS

Elliot L. Brown
Fracture and Deformation Division
National Bureau of Standards
Boulder, Colorado 80303

ABSTRACT

The volume fraction and morphology of δ -ferrite in austenitic stainless steel castings and welds profoundly influence their mechanical behavior over a wide range of temperatures. A review of the literature summarizes the effects of composition, solidification, and solid state ($\delta \rightarrow \gamma$) transformation on the resultant δ -ferrite microstructure in welds and castings. An optical metallographic study was performed on three ASTM A351 Grade CF8M alloy castings (e.g. 18-21Cr, 9-12Ni, 2-3Mo) that possessed different δ -ferrite contents. Metallographic techniques permitted distinction between the solidification and $\delta \rightarrow \gamma$ transformation behavior in these castings. All of the alloys solidify in a primary δ mode in which γ precipitates before solidification is complete. The residual δ -ferrite microstructure, owing to the $\delta \rightarrow \gamma$ transformation, is generally characterized by curved segments of δ/γ interface connected by straight or faceted segments. Frequently occurring interfacet angles are consistent with the facets being parallel to a $\{110\}_{\delta}$ crystallographic plane and an orientation relationship between δ and γ across the faceted δ/γ interface. The metallographic features of the δ -ferrite microstructure can be rationalized with the aid of a $\delta \rightarrow \gamma$ transformation model analogous to that proposed for the proeutectoid $\gamma \rightarrow \alpha$ transformation.

INTRODUCTION

The solidification behavior of austenitic stainless steels is of concern in both welding and casting technology. The term "austenitic" stainless steel is actually a misnomer with respect to weldment and casting microstructures, since they may contain significant amounts of delta-ferrite (δ -ferrite), the high temperature bcc phase of iron, as well as the fcc austenite phase (γ). The presence of δ -ferrite can significantly alter the physical and mechanical properties of austenite. Property variations due to δ -ferrite can be beneficial or deleterious depending upon the nature of the material application and its temperature range. For example, in the case of weldments the presence of 5 to 10% δ -ferrite has been reported to reduce the incidence of hot cracking^{1,2} and microfissuring³. At high temperatures (>973 K) δ -ferrite can transform to the brittle sigma (σ) phase, which results in a degradation of mechanical properties⁴⁻⁶. In highly corrosive environments σ -phase can provide a path for selective corrosion attack⁷ of welds and castings. Delta-ferrite in the austenite matrix also generally increases the strength and lowers fracture toughness of welds and castings⁸, especially in cryogenic applications⁹.

Since δ -ferrite profoundly affects the properties of austenitic stainless steel, it would obviously be advantageous to control its volume fraction and morphology in welds and castings. This report will consist of a review of δ -ferrite in austenitic stainless steel followed by a description and discussion of metallographic studies of δ -ferrite in stainless steel castings.

Composition Effects

Most research has been conducted in the area of welding austenitic stainless steels and, more specifically, on the effects of various filler metal compositions on δ -ferrite content. Some additional work has been performed to extend the concepts developed for weld metals to castings. Quantification of the effects of composition on δ -ferrite content are conveniently accomplished by Cr- and Ni-equivalents. The Cr-equivalents integrate the effects of ferrite formers (Cr, Mo, Si) and the Ni-equivalents, the effects of austenite formers (Ni, Mn, C, N). DeLong¹⁰ reviewed ferrite in austenitic stainless steel weld metal and traced the development of the Schaeffler¹¹ and DeLong¹² Diagrams (Figure 1). Both of these diagrams relate δ -ferrite content, in volume percent (v/o), to Cr- and Ni-equivalents. The Schaeffler Diagram was determined by quantitative metallographic techniques to within a ± 4 v/o accuracy. The δ -ferrite contents of the DeLong Diagram were determined magnetically to within ± 3 v/o, and a factor to account for the strong austenite forming effect of nitrogen was added to the Ni-equivalent. The DeLong Diagram predicts higher δ -ferrite contents than the Schaeffler Diagram for more highly alloyed materials. A recent modification of these diagrams has been made to account for the effects of precipitation in stabilized austenitic stainless steels, since precipitation removes carbon or nitrogen or both from solid solution, thus effectively reducing austenite stability.¹³ Despite the fact that cooling rates encountered during common welding practice do not exert a significant effect on total ferrite content, DeLong cautions against a literal translation of

data on welds to castings.¹⁰ Similar empirical correlations between δ -ferrite content and steel composition have been established for castings^{14,15} and are contained in the Schoefer Diagram (Figure 2). This diagram is actually derived from the Schaeffler Diagram and is supported by measurements made on castings.¹⁴

All of these diagrams refer to room temperature δ -ferrite formed in a nonequilibrium manner. In fact, the equilibrium microstructures of these austenitic stainless steels at room temperature do not contain any δ -ferrite. The departure from equilibrium can be effected by altering the solidification rate, the cooling rate subsequent to solidification, or the chemical composition.¹⁶ The following sections discuss the specific ways in which this departure from equilibrium affects the extent and morphology of δ -ferrite in austenitic stainless steels.

Solidification Effects

Numerous investigations have been conducted to elucidate the solidification behavior in austenitic stainless steel welds¹⁷⁻²⁶ and castings.^{16,27} Basically, the solidification behavior of this class of stainless steels can be divided into primary δ and primary γ modes according to the ratio of Cr- and Ni-equivalents. This division is frequently illustrated by construction of appropriate constant Fe pseudobinaries (isoplethes) of the Fe-Cr-Ni ternary.^{17,18,27} It is important to realize that pseudo-binary sections through ternaries are only qualitative, inasmuch as tie lines drawn across multiphase fields do not represent true equilibrium

tie-lines.²⁸ They are useful, however, for qualitatively illustrating solidification modes as a function of composition.

A typical pseudobinary of this sort is depicted in Figure 3. The two-phase, $\gamma+L$ and $\delta+L$ regions are separated by a eutectic triangle of $\gamma+\delta+L$ region. Below the triangle, a $\gamma + \delta$ phase field exists, enclosed by the γ and δ solvus lines. The $\gamma + \delta$ region broadens with decreasing iron content. Chromium- and Ni-equivalents are substituted for Cr and Ni to increase the generality of the ensuing review. If the nominal composition of the steel possesses a low Cr-equivalent (low proportion of ferrite formers) the primary solid phase is austenite. Similarly, in a steel with a high Cr-equivalent (high proportion of ferrite formers), ferrite is the primary solid phase. Therefore, solidification can be divided generally into primary γ and primary δ modes. The solidification mode becomes more complex in the vicinity of the eutectic triangle. For nominal compositions $C_3 > Cr_{eq} > C_1$, the primary solid phase is still austenite; however, ferrite precipitates before solidification is complete. Likewise, for nominal compositions $C_3 > Ni_{eq} > C_2$, the primary solid phase is ferrite but austenite precipitates prior to complete solidification. The microstructures that result from solidification and cooling in the vicinity of the eutectic triangle are also more complex. The classification of solidification modes has been variously described in the literature.^{16,19-22,27,29} Table I summarizes these classification schemes. Composition ranges and application (welding or casting) are included.

The ternary eutectic behavior described above is applicable to the majority of commercial austenitic stainless steel grades. In the materials

under consideration the eutectic has a divorced morphology since the amount of liquid at the eutectic composition is generally small.²³ In a divorced eutectic mixture one of the solidifying phases is discontinuous and present in smaller volume fraction (i.e. embedded in the continuous phase).^{30,31} In primary γ alloys the divorced phase at the subgrain and grain boundaries is δ . In primary δ solidified alloys the divorced phase is γ .²³

Studies of solidification in conventional ingots and by a directional solidification and quenching technique have identified three possible stages of solidification in an initially primary δ alloy.^{16,18,27,29,32} Initial precipitation of δ is interrupted by precipitation of γ , and at the end of solidification, a transition back to precipitation of δ is observed.³² This corresponds to the Type B solidification mode depicted in Table I, $L \rightarrow L + \delta \rightarrow L + \delta + \gamma \rightarrow \delta + \gamma$. In a conventional casting, the $L + \delta \rightarrow L + \delta + \gamma$ transition has been associated with the transition from a columnar or branched columnar solidification structure to an equiaxed structure. Segregation of alloying elements ahead of the solidification front as well as differences in cooling rate have been proposed as reasons for the interruption of initial solidification of δ by precipitation of γ from the melt and the transition back to δ precipitation at the end of solidification. The classification scheme of McTighe and Beech^{16,27} (see: Table I) will be used in the following descriptions. Schematic diagrams of Type A and Type B solidification extracted from the work of these investigators are shown in Figure 4. For Type A alloys, the primary δ dendrites grow out into the liquid and δ occupies close to 100 v/o of the as-solidified structure. With falling temperature γ forms by the solid state $\delta \rightarrow \gamma$ transformation, first in the primary grain boundaries

(γ_1) and then intragranularly at larger undercoolings (γ_2 and γ_3). The intragranular γ can possess more than one crystallographic orientation (e.g., difference between γ_2 and γ_3). For Type B alloys, the primary δ dendrites grow into the liquid and a γ envelope precipitates directly onto the δ from the liquid (γ_1). The $\delta \rightarrow \gamma$ transformation results in the growth of γ (γ_2) from the envelope into the δ dendrite. Some δ remains in the dendrite cores. The orientation of the δ is the same within a given grain or dendrite. Similar behavior has been observed by other investigators.²⁹

The columnar-to-equiaxed grain morphology transition often observed in conventional castings takes place in Types A and Type B solidification. However, in Type A alloys it is observable in both the primary and secondary structures, whereas in Type B alloys it is only observable in the primary structure²⁷ (Figure 8). Primary structure refers to the structure produced by solidification; secondary structure refers to that produced by the subsequent $\delta \rightarrow \gamma$ transformation.³³ The primary and secondary structures in Type B alloys can be differentiated by metallographic etching techniques.^{16,27,32,34}

Quenching techniques provide a powerful tool for analyzing the course of solidification by allowing the isolation of a particular stage of solidification.^{16,18,27,29,32} By quantitative metallography of specimens quenched from various points on a cooling curve, the volume fraction of primary δ has been determined as a function of time or temperature and composition for a cooling rate of 20 K/min.²⁹ At this cooling rate the maximum volume fraction of primary δ was 0.5 prior to the start of austenite growth in Type B alloys, and decreased monotonically with increasing C- equivalent (C + 0.65 N) until the onset of primary γ freezing. The maximum volume fraction of primary δ could be increased

further by alloying in the Type A alloy region (high Ni-equivalent). Other investigators have reported the ability to retain increasingly larger amounts of residual δ (subsequent to $\delta \rightarrow \gamma$ transformation) by increasing the cooling rate.^{16,21,32,35} The observed increase in residual δ -ferrite may reflect, at least partially, an increase in primary δ with increasing cooling rate. This has been attributed to an increase in departure from equilibrium conditions with increasing cooling rate.^{16,27} In contrast, work done on austenitic stainless steel arc welds has demonstrated only a small effect of cooling rate on total ferrite content,¹⁰ but a significant effect on ferrite scale and morphology.^{10,24}

Concomitant with the evolution of a solidification structure is the redistribution of solute elements, commonly referred to as solute segregation. Reference to the equilibrium phase diagram indicates the various possibilities, which have been described in detail elsewhere.³⁶⁻³⁸ Under conditions of equilibrium (slow cooling), diffusion in the solid and liquid and complete mixing in the liquid allow for complete solute redistribution, so that the composition of the solid formed is always that defined by the tie-line intersection with the solidus curve. The solid composition at the solidus temperature is the nominal composition. A more realistic situation is one in which solid-state diffusion is minimal so that coring or microsegregation occurs during solidification.^{37,38} Perfect mixing in the liquid and mixing in the liquid by only diffusion represent extreme situations. Real cases probably exist between these two extremes. For the cases described above, the final distribution of solute after normal freezing is depicted in Figure 5. The theoretical analyses of segregation are easily applied to planar interfaces, but it has already been implied

that more complex growth forms, such as cellular, cellular-dendritic, and dendritic, are the case in most castings and welds. These solid-liquid interface types are mainly due to the constitutional supercooling produced by solute redistribution.³⁶ However, they do not affect the generality of the statements made with respect to planar interfaces since the cell or dendrite can be viewed as composed of a series of small volume elements that grow into the liquid as a planar interface.¹⁷

A generalized theory of solidification of austenitic stainless steel as primary δ -ferrite has been formulated for weldments by assuming mixing in the liquid by diffusion only.¹⁷ A schematic diagram in Figure 6, extracted from this work, depicts the solute distributions of Ni and Cr across a subgrain following solidification. The gradients in composition are associated with the subgrain (dendrite) core and the subgrain boundary (interdendritic) region.

Attempts to analyze the solute distribution in these alloys have relied on electron microprobe and scanning transmission electron microscopy (STEM) analyses. The STEM possesses a higher spatial resolution capability. Analyses have been performed on actual welds^{17,18,20-22,24,25} and specimens in which solidification has been interrupted by quenching.^{18,29,32} In conventional welds and castings difficulties arise in separating the parts of the total solute redistribution due to solidification and the $\delta \rightarrow \gamma$ transformation. Assumptions regarding the nature of solidification and the $\delta \rightarrow \gamma$ transformation are generally necessary; e.g., no solute redistribution during the $\delta \rightarrow \gamma$ transformation.^{17,24,25} Reasonably independent assessments of the solute distribution coefficients and the solute profiles due to solidification have only been made in interrupted solidification studies.

Solid State $\delta \rightarrow \gamma$ Transformation and Residual δ -ferrite Morphologies

As-cast and as-welded austenitic stainless steel microstructures do not generally represent an equilibrium state. Treatments that promote equilibrium tend to dissolve δ -ferrite, e.g. wrought grades possess virtually no δ -ferrite at room temperature and the δ -ferrite levels in castings and welds can be substantially reduced by annealing at temperatures of approximately 1400K.^{26,39} A primary δ alloy may contain in excess of 50 v/o δ upon solidification. Since the room temperature microstructure of such an alloy contains substantially less δ -ferrite, it is obvious that the $\delta \rightarrow \gamma$ transformation plays a major role in the evolution of microstructure in duplex austenitic stainless steel welds and castings.

A $\delta \rightarrow \gamma$ transformation only occurs for alloys that undergo primary δ solidification, and the nature of the transformation appears to vary with composition, cooling rate, and perhaps with solidification behavior. It is important to note that a number of labels have been associated with the various observed residual ferrite morphologies that are descriptive in nature but may not describe the source of the morphology accurately. This section attempts to describe the various ferrite morphologies, and associate them with labels commonly employed in the literature.

Primary δ alloys can be classified further into alloys remote from the eutectic triangle that solidify with almost 100 v/o δ (forming γ interdendritically) and alloys that intersect the eutectic triangle, in which solidification to γ occurs directly from the melt after some δ has solidified. In the former type of alloy, the resultant room temperature microstructure is completely determined by the solid state transformation. The character of the phase transformation depends on the degree of undercooling, which in turn, depends upon the cooling rate.^{16,17} For

relatively rapid cooling, the $\delta \rightarrow \gamma$ transformation has been referred to as either a Widmanstätten^{18,23,24,32} or an acicular^{19,22} transformation, but the former is probably a more accurate description. The Widmanstätten phase transformation can be described as a thermally activated and diffusion controlled reaction in which an orientation relationship exists between the parent and product phases.⁴⁰ In this case, the residual δ -ferrite has been termed 'lathy'.^{19,20,22} Although the residual δ -ferrite morphology has been termed 'lathy', it is actually the austenite that forms laths by the $\delta \rightarrow \gamma$ transformation. Microstructural investigation of the lathy morphology in welds²⁰ has indicated the presence of several differently oriented lath bundles in a given large growth unit. The model for Type A alloys, depicted in Figure 4a, describes this case. The association of lathy δ -ferrite morphology with a Widmanstätten transformation on quenching allows for the metallographic delineation of regions in a specimen that have solidified as primary δ .^{18,32} At slower cooling rates the mode of $\delta \rightarrow \gamma$ transformation has been termed 'equiaxial'.^{19,22} It is not exactly clear what δ -ferrite morphology this type of $\delta \rightarrow \gamma$ transformation produces.

Many primary δ alloys of interest solidify so that γ envelops the primary δ prior to completion of solidification. This mode is depicted in the model of Figure 4b and refers to the sequence $L \rightarrow L+\delta \rightarrow L+\delta+\gamma$. In this case there is already solid γ present in the microstructure in the form of the γ envelope, as a result of a $L \rightarrow \gamma$ transformation. The solid γ envelope allows for heterogeneous nucleation of γ during the $\delta \rightarrow \gamma$ transformation with less undercooling (higher temperature) than for the Widmanstätten $\delta \rightarrow \gamma$ transformation. Therefore, the residual δ exhibits

less of the Widmanstätten type morphology.^{16,18,19,22,27,32} The morphology of the residual δ -ferrite in this case has been termed 'vermicular' because of its roundish appearance.^{17,22,23} The residual δ -ferrite morphology in primary δ alloys has also been described as a cell-like network.^{22-24,27} It is unclear whether this morphology is associated with the vermicular or lathy δ morphologies or is a transition morphology between the two. A continuous spectrum of ferrite morphology, from vermicular to lathy, has been observed with increasing Cr_{eq}/Ni_{eq} .²²

Regardless of the observed morphology, the residual δ -ferrite in primary δ alloys is definitely located at the cores or spines of dendrite arms (subgrains).^{16,18,19,22,23,27} The progressive growth of γ into the primary δ (see Figure 4) results in segregation of 'ferritizers' to the δ at the dendrite or subgrain core, thus stabilizing it against transformation.^{18,23,24,32} The formation of a γ envelope occurs with attendant segregation of alloying elements. Since diffusion, and hence homogenization, of alloying elements is more difficult in austenite the segregation persists. The segregation of alloying elements permits etching and hence, observation of the prior dendritic form at room temperature.²⁷ In alloys that solidify as virtually 100 v/o δ , the ease of diffusion in the bcc lattice minimizes segregation at high temperature, and therefore the prior dendritic structure is not observable. Transmission electron microscopy (TEM) observations have shown that lathy δ possesses a Kurdjumov-Sachs (K-S) type orientation relationship⁴¹ with austenite, whereas vermicular δ possesses no crystallographic relationship with austenite.²² Angular faceting of δ/γ interfaces in primary δ alloys has also been observed and noted in castings.²³

The observations of primary δ alloys described above have all implied a diffusion-controlled mechanism for the $\delta \rightarrow \gamma$ transformation.^{18,22} Other investigations, in welds, suggest that the rapid cooling rates attendant with relatively low heat input welding precludes the high temperature residence time necessary for a diffusion controlled transformation.^{17,23-25} They propose, instead, a massive phase transformation that would allow the bcc \rightarrow fcc crystal structure transition to occur at constant composition. The massive transformation is a thermally activated, partitionless phase transformation.⁴² Lippold and Savage¹⁷ have proposed that most of the δ dendrite solidifies at constant composition (Figure 6). These workers are suggesting that this region of constant composition δ transforms to γ by a massive transformation.^{17,23,29} The assertion that the Ni and Cr segregation profiles characteristic of solidification are preserved when a massive $\delta \rightarrow \gamma$ transformation occurs is supported by quantitative chemical microanalysis (STEM) across a dendrite.²⁵ The concentration profiles measured are also cited as evidence for short-range diffusion across the interphase boundary as the mechanism of transformation (i.e., local depletion of Cr in γ and excess in δ).²⁵ Other investigations have shown that a significant amount of microsegregation results from the solid state $\delta \rightarrow \gamma$ transformation.^{18,29,32} Thus, it is uncertain whether all the microstructural observations of residual δ -ferrite in these investigations are consistent with or peculiar to the occurrence of a massive transformation. Perhaps a massive $\delta \rightarrow \gamma$ transformation occurs only under conditions of rapid cooling. It is possible that an alternative explanation of the observed concentration profiles in welds lies in the enhanced homogenization associated with finer dendrite spacings.^{16,27}

Some of the observations described above have been used to explain the behavior of larger castings and ingots. In Type A alloys the first γ precipitates in the primary grain boundaries and as the temperature drops, intragranularly as well. All of these regions of γ have different orientations and the columnar-to-equiaxed transition is thus observable in the primary (solidification) and secondary (solid state) microstructures.²⁷ In Type B alloys, where γ begins to solidify from the melt after initial δ solidification and prior to completion of solidification, columnar γ crystals nucleate at high temperature and grow under steep temperature gradients across the entire ingot cross section. With the high driving force for γ growth produced by the temperature gradient, changes in the original δ orientation present no barrier to that growth.^{21,32,33} Mixtures of Type A and Type B behavior are frequently observed in the same ingot. Once δ has solidified, the γ envelope is difficult to form at high freezing rates.²⁷ Therefore, Type A solidification might be expected in the vicinity of the mold wall and Type B solidification in the ingot interior. Variations in δ -ferrite level across an ingot cross section must be rationalized in light of the fact that higher δ -ferrite levels, associated with higher cooling rates, can be offset by rapid homogenization in the finer solidification structures, which lowers the δ -ferrite content.^{26,39} As the δ -ferrite levels in welds and castings increase, the δ phase becomes more continuous.^{43,44} Spheroidization of δ can also take place during the $\delta \rightarrow \gamma$ transformation.²⁶

Measurement of δ -ferrite Content

There are a number of methods that have been employed to determine the δ -ferrite levels in duplex austenitic stainless steels and most have

been reviewed recently.^{10,45} The commonly employed methods are magnetic measurements and quantitative metallography. Quantitative metallography is not as useful for measurements of the fine δ -ferrite structures of welds, and extensive counting is necessary to compensate for the wide intrinsic variations in δ -ferrite content within a given microstructure.¹⁶ Several more exotic techniques for δ -ferrite measurement have been attempted. Of these, integrated Mossbauer spectra¹⁵ and electrolytic separation⁴³ may prove particularly useful because they are not dependent on the shape, size, orientation or distribution of the δ -ferrite.

RESULTS OF METALLOGRAPHIC INVESTIGATIONS OF CASTINGS AT NBS

The bulk of metallographic investigations on castings conducted at NBS to date has been performed on CF8M material (ASTM A351).⁴⁶ These alloys are a cast version of AISI 316 stainless steel. Alloy designation, ferrite level, and chemical composition of the CF8M alloys are contained in Table II. These castings were keel blocks, shown in Figure 7. All keel blocks were annealed at approximately 1400 K.

The macrostructure of these alloy castings is typified by the CF8M-9 alloy. The macrostructure, delineated by a light color etch,* is shown in Figure 8 and is characterized by a region of columnar dendritic grain growth perpendicular to the casting surface, followed by a transition to an equiaxed dendritic growth form. The color etch delineates the solidification structure by depositing a blue interference film on the regions of the original δ dendrites (high Cr) and a gold film on the interdendritic regions (low Cr). When viewed in color, the columnar region to the left of the transition boundary possesses a blue cast

*Color Etch - A deposition etch composed of: 100 cc³ distilled water, 20 cc³ hydrochloric acid, and 2 g potassium metabisulphite.

whereas the equiaxed region to the right possesses a gold cast, indicative of a greater volume of interdendritic liquid in the latter region. A series of higher magnification micrographs depicts the nature of the transition in solidification growth morphology (Figure 9a, b, and c). Note that the dark gray areas correspond to the blue original δ -ferrite dendrites and the light gray areas correspond to the gold interdendritic liquid regions. The region adjacent to the casting surface is composed almost completely of δ -ferrite dendrites, aligned perpendicular to the casting surface (Figure 9a). The microstructure in the transition region is characterized by δ -ferrite dendrites that grow at angles to the heat flow direction, effectively blocking columnar dendritic growth in this direction (Figure 9b). The transition also appears to signal an increase in the volume of interdendritic liquid in the as-solidified structure. This correlates with the gold appearance of the central zone of the keel block casting when viewed at lower magnification. The structure in the central portion of the casting is characterized by randomly oriented columnar dendrites as well as equiaxed dendrites (Figure 9c). The finer network structure observed inside the original δ -ferrite dendrites is the residual δ -ferrite present at room temperature subsequent to the $\delta \rightarrow \gamma$ transformation.

When a heavier color etch is applied to the same casting section a coarse columnar grain structure parallel to the direction of heat flow is observed (Figure 10). The columnar grain structure appears to grow across the previously described columnar-to-equiaxed grain morphology transition. A higher magnification macrograph of the columnar crystals

shows that the dendritic structure, as defined by the residual δ -ferrite, possesses the same orientation across many of the columnar grain boundaries (Figure 11). The columnar grain boundaries also appear faceted on a microscale.

A 10% oxalic acid electro-etch is employed to examine the residual δ -ferrite morphology since this etch preferentially attacks the δ/γ interphase boundaries. Some characteristic features of the δ -ferrite morphology are immediately apparent from observations of the CF8M-9 alloy (Figure 12). On a given plane of polish the δ -ferrite appears composed of either relatively long, filamentary particles (e.g., at A in Figure 12A) or equiaxed cell-like networks (e.g., at B in Figure 12a). The δ -ferrite at this volume fraction also appears to be composed of discrete particles that are faceted in many instances. A facet is defined as a straight segment of δ/γ interphase boundary. There are many regions of apparently fine, equiaxed δ particles (e.g. at C in Figure 12a) and other regions where δ/γ interfaces are tangent to one another (e.g., at D in Figure 12a). The latter regions would seem to be locations of incipient spheroidization of larger δ -ferrite particles. A less prevalent feature of the microstructure is the apparent twinning of the γ matrix between the regions of residual δ -ferrite (Figure 12b). The location and morphology of the δ -ferrite is obscured in these regions when the oxalic acid etch is employed.

The faceted δ -ferrite particles also seem to be characterized by definite angles that frequently occur between different facet variants (Figure 13). The frequently occurring intervariant angles are 60° and 90° . Although no independent assessment was made of the crystallographic

plane in the δ -ferrite parallel to the plane of polish, these intervariant angles are consistent with the interplanar angles of different 110 δ -ferrite planes ($\{110\}_\delta$). This means that faceted δ/γ interfaces could be parallel to $\{110\}_\delta$. Comparison of the residual δ -ferrite microstructure with the original δ -ferrite dendrite morphology provides some independent confirmation of this notion. A micrograph of a color etched region of the CF8M-9 alloy illustrates this relationship for facet traces with a 60° angle between them (Figure 14). The primary dendrite axis has been established parallel to a $\langle 100 \rangle_\delta$ easy growth direction by other investigators.⁴⁷ The measured angle between the primary dendrite axis and the facet trace is 45° (see the schematic diagram in Figure 14). The assumption of the facet plane parallel to $\{110\}_\delta$ is then consistent with the measured angle of 45° since this is one of the tabulated angles between $\{110\}_\delta$ and $\{100\}_\delta$ in a bcc crystal. X-ray and TEM determination of the crystallographic orientations of δ and γ are planned to confirm the accuracy of this analysis.

The residual δ -ferrite distribution was employed to define the orientation of the original δ -ferrite dendrite spines in Figure 11. As shown in Figure 15, the δ -ferrite located at the dendrite spines is actually composed of a network of δ -ferrite.

As the δ -ferrite content of the CF8M alloys is increased, the δ -ferrite microstructure on a given plane of polish becomes coarser while still possessing many of the characteristics observed in the CF8M-9 alloy, i.e., facets, points of interface tangency, networks (Figure 16). A 10N KOH electro-deposition etch is employed to deposit a light blue to light brown film on the δ -ferrite. This provides greater contrast between the δ and γ phases while eliminating the etching of γ twins. The coarser δ -ferrite microstructures are also characterized by a greater apparent continuity. The δ/γ interface morphology is quite intricate and can generally be described as straight facets connecting curved segments of interface. Closer scrutiny of the δ/γ interfaces indicates the presence of ledges on both faceted and curved segments (Figure 17).

DISCUSSION

The metallography of the CF8M alloys is consistent with the Type B solidification sequence: $L \rightarrow L+\delta \rightarrow L+\delta+\gamma \rightarrow \delta+\gamma$. In addition to residual δ -ferrite located at dendrite spines, this sequence is distinguished metallographically by a secondary structure, due to solid state transformation, in which the columnar-to-equiaxed grain morphology transition of solidification is not observed (Figures 8 and 10). Figure 8 shows the primary (solidification) structure with its columnar-to-equiaxed transition;

Figure 10 shows the secondary ($\delta \rightarrow \gamma$) structure composed of completely columnar crystals that bend parallel to the direction of heat flow. The fact that dendrites are observed to grow across the columnar grain boundaries of the secondary structure also supports the assertion that the columnar γ structure is a secondary structure produced by the $\delta \rightarrow \gamma$ transformation (Figure 11). In the case of a solidification sequence where a γ envelope begins to solidify from the melt, columnar γ crystals can nucleate heterogeneously at high temperature and grow with the aid of very steep temperature gradients. Once nucleated under these conditions, a columnar γ crystal will grow right across misorientations between δ -ferrite dendrites and parallel to the path of maximum heat flow (Figure 10). These metallographic observations are also consistent with respect to the various Ni- and Cr-equivalent ranges specified for primary δ alloys in Table I.

The larger volume fraction of primary δ -ferrite near the casting surface is partly attributable to the higher cooling rate in this region and the difficulty in forming the γ envelope at high solidification rates.²⁷ The interruption of δ solidification by γ solidification has been associated with the columnar-to-equiaxed transition, in which large pockets of liquid exist between settling δ crystals³² (Figure 9).

The level of residual δ -ferrite does not appear to vary significantly with distance from the casting surface and neither does the dendrite arm spacing (Figure 9). The latter is a monitor of local solidification time⁴⁸ and determines the time available for a diffusion controlled transformation to occur. Finer spacings might be expected to promote

the $\delta \rightarrow \gamma$ transformation and thereby decrease the level of residual δ -ferrite. Therefore, the constancy of both residual δ -ferrite content and δ dendrite arm spacing implies that the cooling rate does not vary sufficiently within the casting to affect these parameters significantly, although it still might affect the interruption of δ solidification by γ solidification.

A general model for the $\delta \rightarrow \gamma$ transformation is proposed to rationalize the observed microstructural features of the residual δ -ferrite in primary δ alloys. The model assumes that the $\delta \rightarrow \gamma$ transformation is thermally activated and diffusion controlled. A nucleus of γ forms either at solidification subgrain boundaries or on the γ envelope formed by direct γ solidification from the melt. These alternative modes of solid state γ nucleation would affect the nucleation rate and distribution of γ nuclei but not the basic morphological evolution. The shape of a nucleus and the implications of faceted nucleation and growth have been considered generally and with specific regard to proeutectoid α .⁴⁹⁻⁵² Analogous nucleation and growth is assumed to occur during the $\delta \rightarrow \gamma$ transformation. The occurrence of a facet on a nucleus is associated with formation of a low-energy interface between parent and product phase. The low energy interface, furthermore, is associated with a high degree of lattice matching (coherency) across the interface and a crystallographic orientation relationship between the abutting phases. The segment or segments of low energy interface minimize the total surface energy of the nucleus and thereby minimize the activation barrier for nucleation.

This type of nucleus has been used in models of Widmanstätten-type proeutectoid α formation (saw teeth and side plates).⁴⁹⁻⁵² In this kind of proeutectoid $\gamma \rightarrow \gamma$ transformation, the nucleus and precipitate faceting is associated with a Kurdjumov-Sachs (K-S) type of orientation relationship.⁴¹ A K-S orientation relationship, between bcc and fcc phases, involves a parallelism between planes and directions of densest atomic packing in the product and parent phases. For the K-S orientation relationship the following parallelisms exist:

$$\{111\}_{\gamma} // \{110\}_{\alpha}$$

$$\langle 110 \rangle_{\gamma} // \langle 111 \rangle_{\alpha}$$

Faceting is definitely an aspect of δ/γ interface morphology in the castings of the present investigation. Furthermore, optical metallographic evidence suggests that the facet plane in the δ -ferrite parent phase is a $\{110\}_{\delta}$ (Figures 13 and 14). This is a plane of densest packing in a bcc phase and is highly suggestive of a K-S orientation relationship existing between γ and the δ it is growing into. As mentioned in the previous section, X-ray and TEM will be employed to confirm whether or not a K-S orientation relationship exists between δ and γ in these alloys. This orientation relationship has been observed for so-called 'lathy' δ .²⁰

Once γ nucleus formation has been considered, it remains to demonstrate the γ growth process necessary for the observed evolution of δ -ferrite microstructure. Assuming a distribution of γ nuclei and facet morphologies, growth is accomplished mainly through the movement of the curved, incoherent segments of δ/γ interface. These are high energy and high mobility

boundaries. The faceted, coherent segments possess low mobility since atom jumping across the interface is energetically infeasible.⁴⁹⁻⁵² Movement of a faceted boundary perpendicular to itself can be envisioned as proceeding by the movement of ledges or steps parallel to the boundary.⁴⁹⁻⁵² These steps are actually incoherent boundary segments that possess high mobility. The presence of ledges in a macroscopically curved interface moving along specific crystallographic planes can also provide a means for maintaining an orientation relationship between the parent and product phases separated by the interface. Therefore, a faceted interface is not necessary for observation of a crystallographic orientation relationship between parent and product phases. Ledges have been observed on both faceted and curved δ/γ interfaces in this investigation (Figure 17). The features of the residual δ -ferrite microstructure can then be viewed as evolving through the rapid movement of incoherent segments of δ/γ interface with coherent segments being dragged along behind. The coherent segments move outwards as well, by a ledge mechanism, but more slowly. Points of tangency between transformation fronts after impingement are commonplace and accelerate spheroidization processes. A schematic diagram showing the evolution of the residual δ -ferrite morphology is shown in Figure 18. It is important to note that for both the model and the actual δ -ferrite microstructures observed in this study, observations on a given plane of polish can be deceiving. These types of observation might lead one to the erroneous conclusion that discrete δ -ferrite particles are formed, even at high volume fraction. In fact, observations

in the author's laboratory and by other investigators⁴³ suggest that a continuous δ -phase exists at contents greater than about 7 v/o. Therefore, although spheroidization of δ -ferrite certainly does take place at high temperature, the "discrete" particles and points of interfacial tangency observed may be peculiar to only that plane of polish (Figure 18). The characteristic filamentary δ -and cell-like δ -ferrite morphologies observed (Figure 16B) could then be considered as two views of a continuous δ -phase (Figure 18). The ferrite network can be more equiaxed if impingement of incoherent segments occurs more uniformly, and this will certainly occur if the solidification structure is finer and the γ nucleation rate higher. These conditions might be expected with welding and other higher cooling rate processes. Observations of the residual δ -ferrite microstructures in primary δ weld metals show them to be more equiaxed, i.e., to exhibit a higher volume of cell-like than filamentary δ -ferrite. The cell-like networks still possess faceted δ/γ interfaces (Figure 19). The similarities between residual δ -ferrite microstructures in welds and castings indicate potential similarities in their solidification and $\delta \rightarrow \gamma$ transformation behavior.

RECOMMENDATIONS FOR FURTHER WORK

The following are recommendations for further work:

- 1) TEM, selected area electron diffraction and X-ray diffraction studies to determine the fine structure of δ/γ interfaces and the crystallographic orientation relationships that exist between δ and γ .
- 2) Scanning transmission electron microscopy (STEM) studies to determine the concentration gradients of Ni and Cr that exist within the microstructures of duplex austenitic stainless steels. Knowledge of the

Ni and Cr concentration profiles across δ/γ interphase boundaries may assist in elucidating the nature of the $\delta \rightarrow \gamma$ transformation.

- 3) Quantification of the proposed model for $\delta \rightarrow \gamma$ transformation to confirm its ability to predict observed volume fractions of residual δ -ferrite within the constraints of normally encountered cooling rates.

CONCLUSIONS

1. The CF8M castings in this study are primary δ solidification alloys with the following transformation sequence: $L \rightarrow L + \delta \rightarrow L + \delta + \gamma \rightarrow \delta + \gamma$
2. The primary structure of these alloys is characterized by a columnar-to-equiaxed grain morphology transition in the casting interior.
3. The secondary structure, owing to the $\delta \rightarrow \gamma$ transformation, is characterized by columnar crystals that extend through the entire casting cross section, bending in the direction of heat flow. The secondary structure completely masks the presence of the primary structure, as noted in previous investigations.
4. The residual δ -ferrite microstructure is generally characterized by curved segments of δ/γ interface connected by straight or faceted segments of δ/γ interface. The δ -ferrite becomes coarser and appears to possess greater continuity as the δ -ferrite content increases.
5. Frequently occurring interfacet angles of 60° and 90° are consistent with a $\{110\}_\delta$ crystallographic plane parallel to the facet plane and the establishment of a Kurdjumov-Sachs orientation relationship between δ and γ across the faceted δ/γ interface.
6. The observation of ledges on curved and faceted δ/γ interfaces demonstrates the possibility of interface movement via a ledge mechanism that could maintain an orientation relationship across any type of δ/γ interface.
7. The features of the residual δ -ferrite morphology in this type of alloy can be rationalized with the aid of a transformation model analogous to that proposed for the proeutectoid $\gamma \rightarrow \alpha$ transformation.

REFERENCES

1. H. F. Reid and W. T. DeLong: "Making Sense Out of Ferrite Requirements in Welding Stainless Steel," Met. Prog., Vol 84 (1973), p. 73.
2. H. Fredriks and L. J. VanderToorn: "Hot Cracking in Austenitic Stainless Steel Weld Deposits," Br. Weld. J., Vol. 15 (1968), p. 178.
3. C. D. Lundin and D. F. Spond: "The Nature and Morphology of Fissures in Austenitic Stainless Steel Weld Metals," Weld. J. Res. Suppl. Vol. 55 (1976), p. 356-s.
4. R. T. King, N. C. Cole, and G. M. Goodwin, "Creep Behavior of SMA Type 316 Weld Metal with Controlled Residual Elements," J. Pressure Vessel Technol., Vol. 98 (1976), p. 194.
5. L. R. Poole: "An Unwanted Constituent in Stainless Weld Metal," Met. Prog., Vol. 65 (1954), p. 108.
6. O. H. Henry, M. A. Cordovi, and G. J. Fischer, "Sigma Phase in Austenitic Stainless Steel Weldments," Weld. J. Res. Suppl., Vol. 34 (1955), p. 75-s.
7. K. E. Pinnow and A. Moskowitz: "The Corrosion Resistance of Stainless Steel Weldments," Weld. J. Res. Suppl., Vol 49 (1970), p. 278-s.
8. V. N. Zemzin and G. L. Petrov: "Influence of Ferrite Content on the Properties of Austenitic Weld Metal," Svar. Proizvod., No. 5 (1967), pp. 6-8.
9. D. T. Read, H. I. McHenry, P. A. Steinmeyer, and R. D. Thomas, Jr. "Metallurgical Factors Affecting the Toughness of 316L Weldments at Cryogenic Temperatures," Weld. J. Res. Suppl., Vol. 59 (1980), p. 104-s.

10. W. T. DeLong: "Ferrite in Austenitic Stainless Steel Weld Metal," Weld. J. Res. Suppl., Vol. 53, (7), (1974), p. 273-s.
11. A. Schaeffler: "Constitution Diagram for Stainless Steel Weld Metal", Metal Progress, Vol. 56, (5), (1949), pp. 680-680B.
12. C. Long and W. T. DeLong: "The Ferrite Content of Austenitic Stainless Steel Weld Metal," Weld. J., Res. Suppl., Vol. 52, (7), (1973), pp. 281-s-297-s.
13. G. Molinder: "Ni Requirements for Equivalent Structures in Austenitic Stainless Steels", Met. Prog., Vol. 86, (11), (1979), pp. 56-59.
14. F. H. Beck, E. A. Schoefer, J. W. Flowers, and M. G. Fontana, "New Cast High Strength Alloy Grades by Structure Control," in Advances in the Technology of Stainless Steels and Related Alloys, ASTM STP 369, American Society for Testing and Materials, Philadelphia (1965), pp. 159-174.
15. L. J. Schwartzendruber, L. H. Bennett, E. A. Schoefer, W. T. DeLong, and H. C. Campbell, "Mossbauer-Effect Examination of Ferrite in Stainless Steel Welds and Castings", Weld. J. Res. Suppl. Vol. 53, (1), (1974), p. 1-s.
16. J. Beech: Personal Communication.
17. J. C. Lippold and W. F. Savage: "Solidification of Austenitic Stainless Steel Weldments: Part 1-A Proposed Mechanism," Weld. J. Res. Suppl., Vol. 58, (11), (1979), p. 330-s.
18. S. A. David, G. M. Goodwin, and D. N. Braski, "Solidification Behavior of Austenitic Stainless Steel Filler Metals," Weld. J. Res. Suppl., Vol. 58, (11), (1979), p. 330.

19. N. Suutala, T. Takalo, and T. Moisisio, "The Relationship Between Solidification and Microstructure in Austenitic and Austenitic-Ferritic Stainless Steel Welds," Met. Trans. A, Vol. 10A, (4), (1979), p. 512.
20. N. Suutala, T. Takola, and T. Moisisio, "Single-Phase Ferritic Solidification Mode in Austenitic-Ferritic Stainless Steel Welds," Met. Trans. A, Vol. 10A, (8), (1979), p. 1183.
21. T. Takalo, N. Suutala, and T. Moisisio, "Austenitic Solidification Mode in Austenitic Stainless Steel Welds," Met. Trans. A, Vol. 10A, (8), (1979), p. 1173.
22. N. Suutala, T. Takato, and T. Moisisio, "Ferritic - Austenitic Solidification Mode in Austenitic Stainless Steel Welds", Met. Trans. A, Vol. 11A, (5), (1980) p. 717.
23. M. J. Cieslak and W. F. Savage: "Weldability and Solidification Phenomena of Cast Stainless Steel," Weld. J. Res. Suppl., Vol. 59, (5), (1980), p. 136-s.
24. J. C. Lippold and W. F. Savage: "Solidification of Austenitic Stainless Steel Weldments: Part 2-The Effect of Alloy Composition on Ferrite Morphology," Weld. J. Res. Suppl., Vol. 59, (2), (1980), p. 48-s.
25. C. E. Lyman: "Analytical Electron Microscopy of Stainless Steel Weld Metal," Weld. J. Res. Suppl., Vol. 58, (7), (1979), p. 189-s.
26. V. S. Raghunathan, V. Seetharaman, S. Venkadesan, and P. Rodriguez, "The Influence of Post Weld Heat Treatments on the Structure, Composition and the Amount of Ferrite in Type 316 Stainless Steel Welds," Met. Trans A, Vol. 10A, (11), (1979), p. 1683.

27. J. M. McTighe and J. Beech: "The Structure of As-Cast Austenitic Stainless Steels," J. Res., SCRATA, No. 37, (June 1977), p. 43.
28. G. Masing: Ternary Systems: Introduction to The Theory of Three Component Systems, Dover, New York, (1960).
29. O. Hammar and U. Svensson: "Influence of Steel Composition on Segregation and Microstructure During Solidification of Austenitic Stainless Steels," in Solidification and Casting of Metals, Proceedings of an International Conference on Solidification, University of Sheffield, England (July 1977), p. 401.
30. G. A. Chadwick: "Eutectic Alloy Solidification," Progress in Materials Science, Vol. 12, No. 2 (1963) Pergamon Press.
31. W. Kraft: "Solidification Structures of Eutectic Alloys," ASM Metals Handbook, Vol. 8, 8th Edition, p. 157.
32. H. Fredriksson: "The Solidification Sequence in an 18-8 Stainless Steel, Investigated by Directional Solidification," Met. Trans., Vol. 3, (11), (1972), p. 2989.
33. A. Hultgren: "Crystallization and Segregation Phenomena in 1.10% Carbon Steel Ingots of Smaller Sizes," J.I.S.I., Vol. 70 (1929), pp. 69-113.
34. P. Lichtenegger and R. Bloch: "Color Etching of High Alloy Steels," Prak. Metall. Vol. 12, (1975), p. 567.
35. J. C. Lippold: PhD Thesis, Rensselaer Polytechnic Institute, Troy, NY, (1978).
36. J. W. Rutter and B. Chalmers: "A Prismatic Substructure Formed During Solidification of Metals," Can. J. Phys., Vol. 31 (1973) p. 15.

37. J. W. Christian: "The Theory of Transformations in Metals and Alloys," Pergamon Press, New York (1965), p. 566.
38. W. A. Tiller, K. A. Jackson, J. W. Rutter, and B. Chalmers, "The Redistribution of Solute Atoms during the Solidification of Metals," Acta Metall., Vol. 1 (1953), p. 428.
39. Y. Kinoshita, S. Tadedo, and H. Yoshimura, "On the Dissolution of δ -ferrite into Austenite in Continuously Cast Slabs of 18-8 Stainless Steel," Tetsu-to-Hagane, Vol. 65, (8), (1979), pp. 1176-1185.
40. J. B. Newkirk: "General Theory, Mechanism and Kinetics" in Precipitation from Solid Solution ASM Seminar, American Society for Metals, (Nov. 1957).
41. G. Kurdjumov and G. Sachs: "Crystallographic Orientation Relationship between α - and γ -Fe," Ann. Phys., Vol. 64 (1930), p. 325.
42. T. B. Massalski: "Massive Transformation, Chapter 10" in Phase Transformations, ASM Seminar, American Society for Metals, Metals Park, Ohio, October 1968, p. 433.
43. T. P. S. Gill, R. K. Dayal, and J. B. Gnanamoorthy, "Estimation of Delta Ferrite in Austenitic Stainless Steel Weldments by an Electrochemical Technique," Weld. J. Res. Suppl., Vol. 58, (12), (1979), p. 375-s.
44. R. G. Berggren, N. C. Cole, G. M. Goodwin, J. O. Stiegler, G. M. Slaughter, R. J. Gray, and R. T. King, "Structure and Elevated Temperature Properties of Type 308 Stainless Steel Weld Metal with Varying Ferrite Contents," Weld. J. Res. Suppl., Vol. 57, (6), (1979), p. 167-s.

45. R. B. Gunia and G. A. Ratz: "The Measurement of Delta Ferrite in Austenitic Stainless Steel," Weld. Res. Council. Bull. 132, (1968).
46. L. Genens, S. T. Wang, S. H. Kim, and E. L. Brown, "Design and Fabrication of the Cold Bore Tube for a Large Superconducting CFFF MHD Magnet", paper presented at the 1980 Superconducting MHD Magnet Design Conference, MIT, Cambridge, Massachusetts, March 26-27, 1980.
47. J. W. Christian: "Solidification and Melting," Chapter 14 in The Theory of Transformations in Metals and Alloys, Pergamon Press, New York (1965), pp. 562-566.
48. M. C. Flemings: "Solidification Processing," Met. Trans., Vol. 5, (2), (1974), p. 121.
49. W. C. Johnson, C. L. White, P. E. Marth, P. K. Ruf, S. M. Tuominen, K. D. Wade, K. C. Russell, and H. I. Aaronson, "Influence of Crystallography on Aspects of Solid-Solid Nucleation Theory," Met. Trans. A , Vol. 6A, (4), (1975), p. 911.
50. H. I. Aaronson: "The Pro-Eutectoid Ferrite and the Pro-Eutectoid Cementite Reactions" in Decomposition of Austenite by Diffusional Processes, The Metal Society, American Institute of Mining, Metallurgical, and Petroleum Engineers, New York (1962), p. 387.
51. H. I. Aaronson, C. Laird, and K. R. Kinsman, "Mechanisms of Diffusional Growth of Precipitate Crystals, Chapter 8", in Phase Transformations, ASM Seminar, American Society for Metals, Metals Park, Ohio, (October 1968) p. 313.
52. H. I. Aaronson, J. K. Lee, and K. C. Russell, "Diffusional Nucleation and Growth," in Precipitation Processes in Solids, Proceedings of a Symposium sponsored by The Metal Society, American Institute, Fall Meeting, Niagara Falls, New York (1976).

Table I. Classification of Solidification Modes in Austenitic Stainless Steels

Investigation	Classification	Classification	Composition	Application
References 16, 27	$L \rightarrow L + \delta \rightarrow \delta$	Type A	$Cr_{eq} = 18.2-24.2$ $Ni_{eq} = 8.6-11.2$	Castings
	$L \rightarrow L + \delta \rightarrow L + \delta + \gamma \rightarrow \delta + \gamma$	Type B	$Cr_{eq} = 18.1-21.7$ $Ni_{eq} = 10.1-13.6$	
	$L \rightarrow L + \gamma \rightarrow L + \gamma + \delta \rightarrow \delta + \gamma$	Type C	$Cr_{eq} = 18.9-20.3$ $Ni_{eq} = 13.9-26.6$	
	$L \rightarrow L + \gamma \rightarrow \gamma$	Type D		
References 19-22	$L \rightarrow L + \gamma \rightarrow \gamma$	Type A	$Cr_{eq}/Ni_{eq} \leq 1.48$	Welds
	$L \rightarrow L + \delta \rightarrow \delta$	Type C	$Cr_{eq}/Ni_{eq} \geq 1.95$	
	$L \rightarrow L + \delta \rightarrow L + \delta + \gamma \rightarrow \delta + \gamma$	Type B	$1.48 \leq Cr_{eq}/Ni_{eq} \leq 1.95$	
Reference 29	$L \rightarrow L + \delta \rightarrow L + \delta + \gamma \rightarrow \gamma + \delta$	$\Phi < 0$		Castings
	$L \rightarrow L + \gamma + \delta \rightarrow \gamma + \delta$	$\Phi = 0$	$\Phi = Ni_{eq} - 0.75Cr_{eq}$	
	$L \rightarrow L + \gamma \rightarrow \gamma$	$\Phi > 0$	$+ 0.257$	

Table II. Alloy Designation, Chemical Composition,
 δ -ferrite Level

Alloy Designation	Chemical Composition (w/o)						v/o δ -ferrite
	C	Mn	Si	Cr	Ni	Mo	
CF8M-9	.02	1.06	1.10	19.33	11.67	2.14	9
CF8M-14	.05	.83	1.25	19.50	12.20	2.69	14
CF8M-24	.07	.52	1.32	21.48	9.48	3.18	24

List of Figures

- Figure 1 (a) Schaeffler Diagram (b) DeLong Diagram.
- Figure 2 Schoefer Diagram.
- Figure 3 Constant Fe pseudobinary phase diagram.
- Figure 4 Schematic diagrams of primary δ -ferrite solidification modes.
- Figure 5 Schematic diagram of solute distribution after normal freezing.
- Figure 6 Schematic diagram of solute distribution across a subgrain, following primary δ solidification of a weld.
- Figure 7 Schematic diagram of keel block casting.
- Figure 8 Keel block cross section showing columnar-to-equiaxed grain morphology transition in solidification structure, light color etch..
- Figure 9(a) Keel block cross section in columnar grain region near edge, light color etch.
- Figure 9(b) Keel block cross section near columnar-to-equiaxed grain morphology transition in solidification structure, light color etch.
- Figure 9(c) Keel block cross section in equiaxed grain region, light color etch.
- Figure 10 Keel block cross section showing columnar γ crystals formed during $\delta \rightarrow \gamma$ phase transformation, heavy color etch.
- Figure 11 Columnar γ crystal structure in relation to solidification structure delineated by residual δ -ferrite, heavy color etch.
- Figure 12 Residual δ -ferrite morphology in CF8M-9 alloy (a) filamentary and cell-like δ -ferrite, (b) twinning in γ , oxalic acid electro-etch.
- Figure 13 Residual δ -ferrite faceting, oxalic acid electro-etch.
- Figure 14 Residual δ -ferrite in relation to δ -ferrite dendritic solidification structure, light color etch.
- Figure 15 Residual δ -ferrite networks at δ -ferrite dendrite spines, light color etch.

- Figure 16 Residual δ -ferrite morphology (a) CF8M-14, (b) CF8M-24, 10N KOH electro- deposition etch.
- Figure 17 Residual δ -ferrite in CF8M-24 alloy showing ledge morphology, 10N KOH electro-deposition etch.
- Figure 18 Schematic diagram of evolution of residual δ -ferrite morphology via $\delta \rightarrow \gamma$ phase transformation.
- Figure 19 Residual δ -ferrite in weld metal; ~3v/o δ -ferrite, 316L GMA, oxalic acid electro-etch.

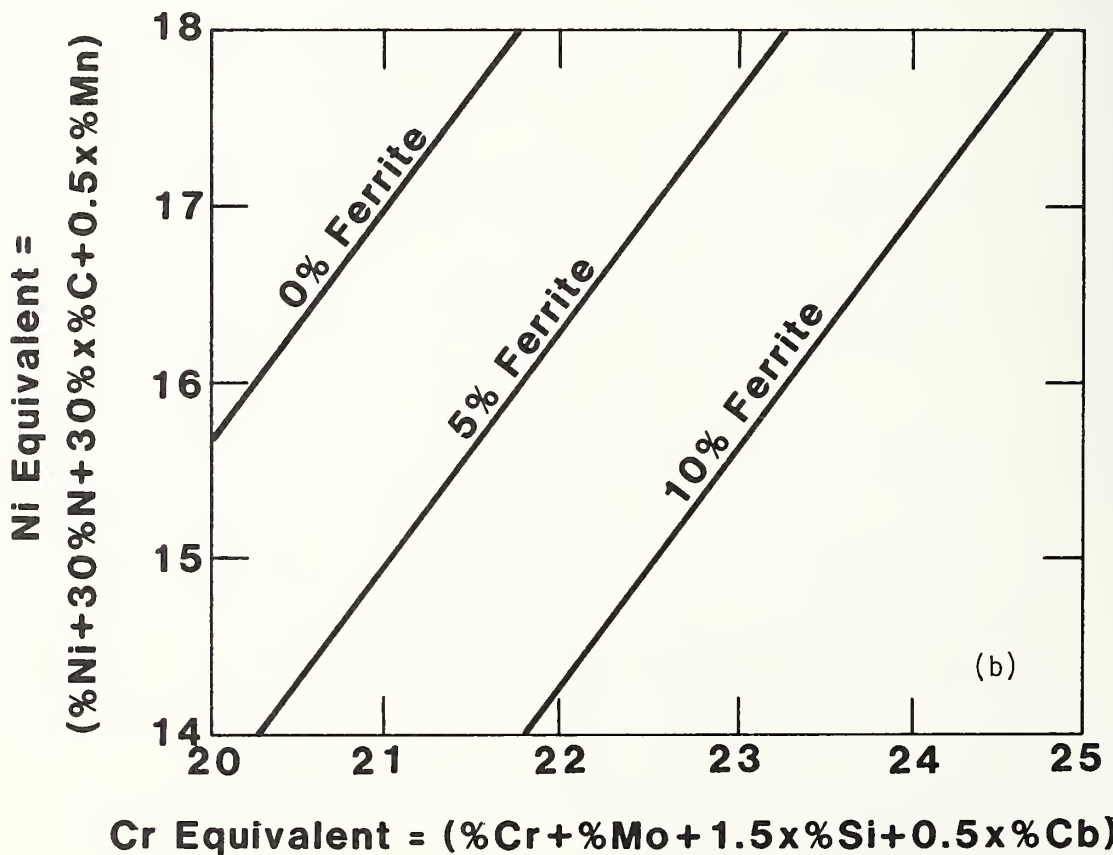
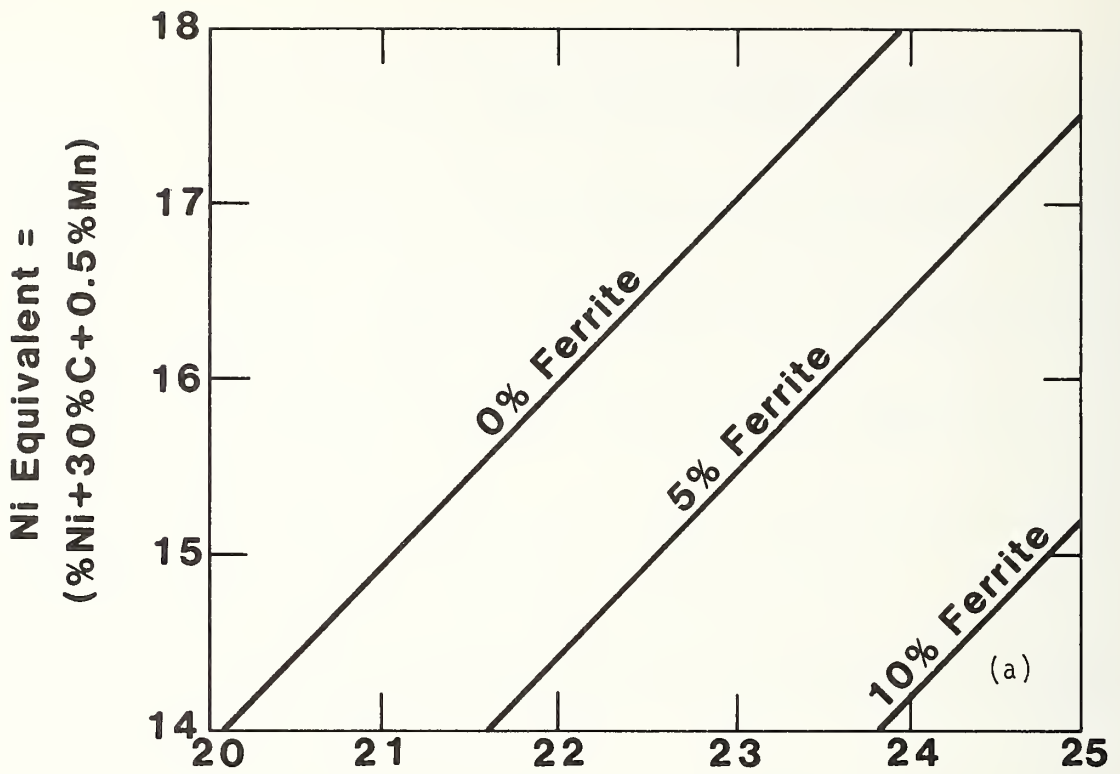
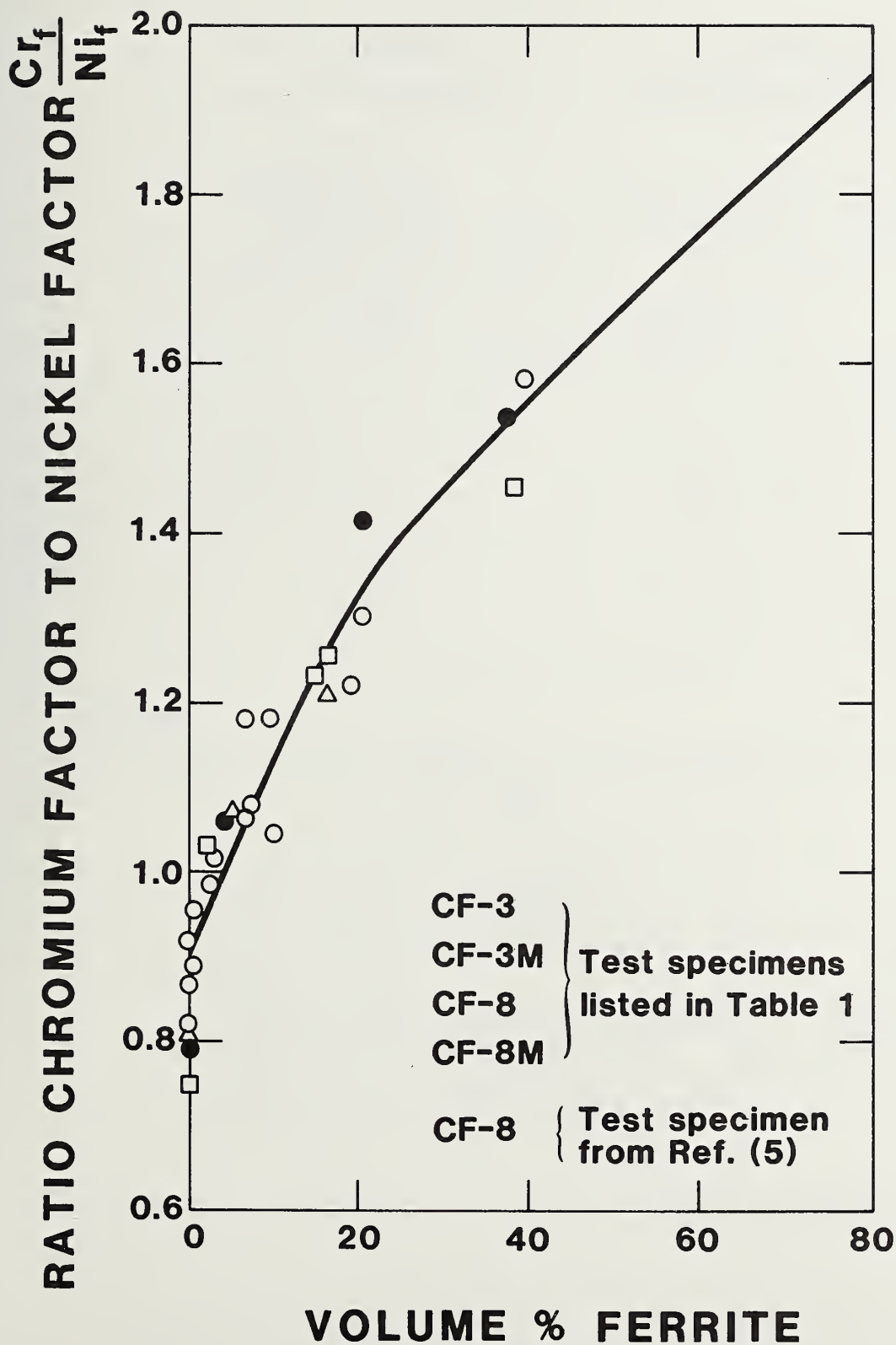


Figure 1 (a) Schaeffler Diagram (b) DeLong Diagram.



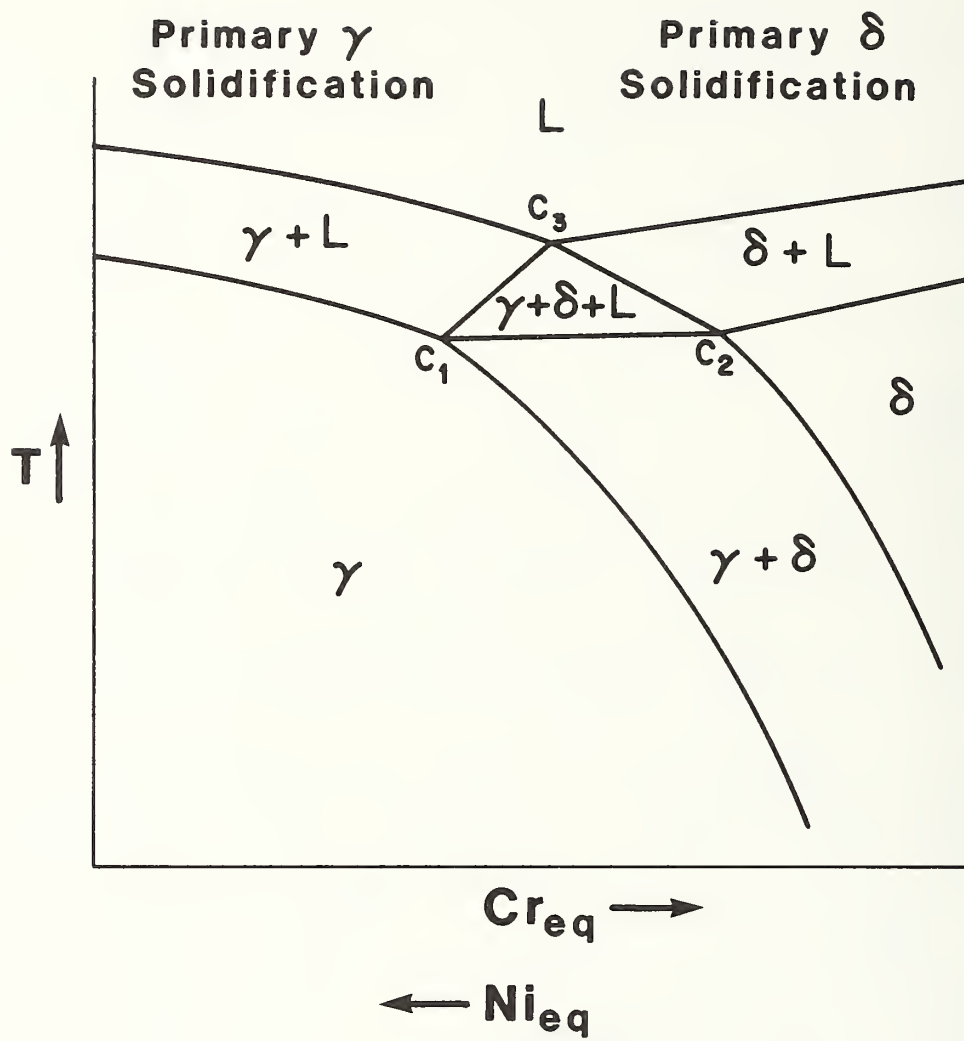
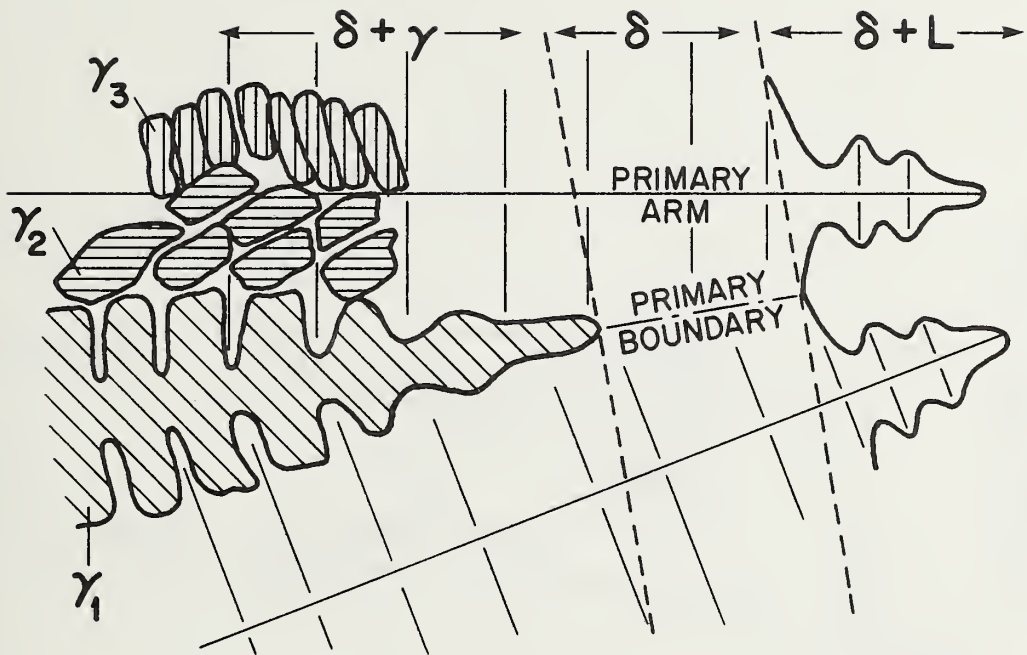
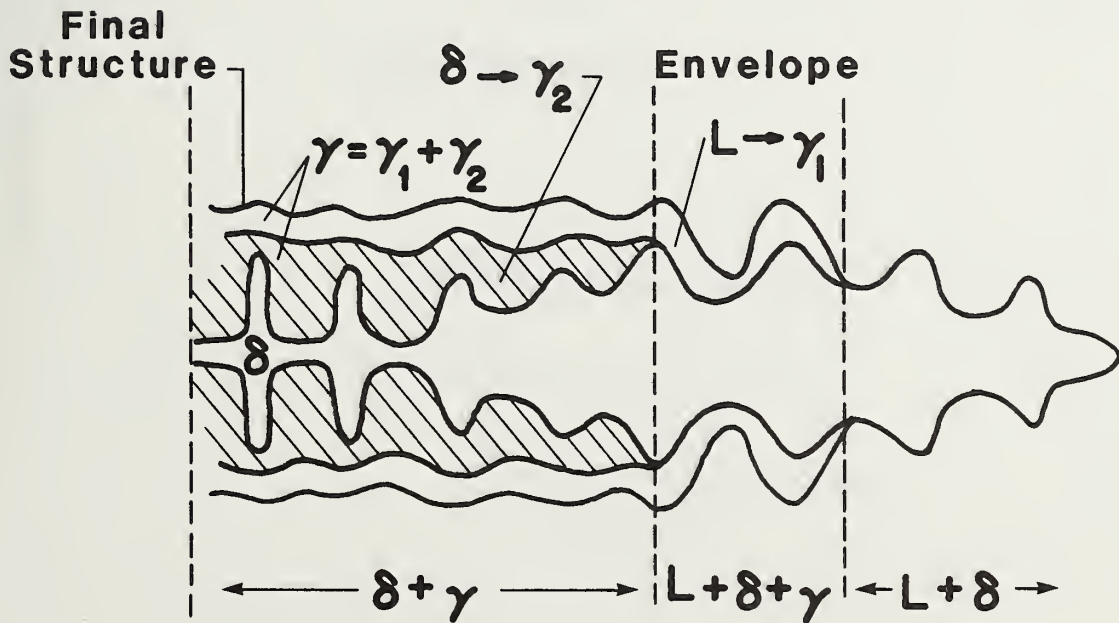


Figure 3 Constant Fe pseudobinary phase diagram.



(a) Type A ($L \rightarrow L + \delta \rightarrow \delta + \delta + \gamma$)



(b) Type B ($L \rightarrow L + \delta \rightarrow L + \delta + \gamma \rightarrow \delta + \gamma$)

Figure 4 Schematic diagrams of primary δ -ferrite solidification modes.

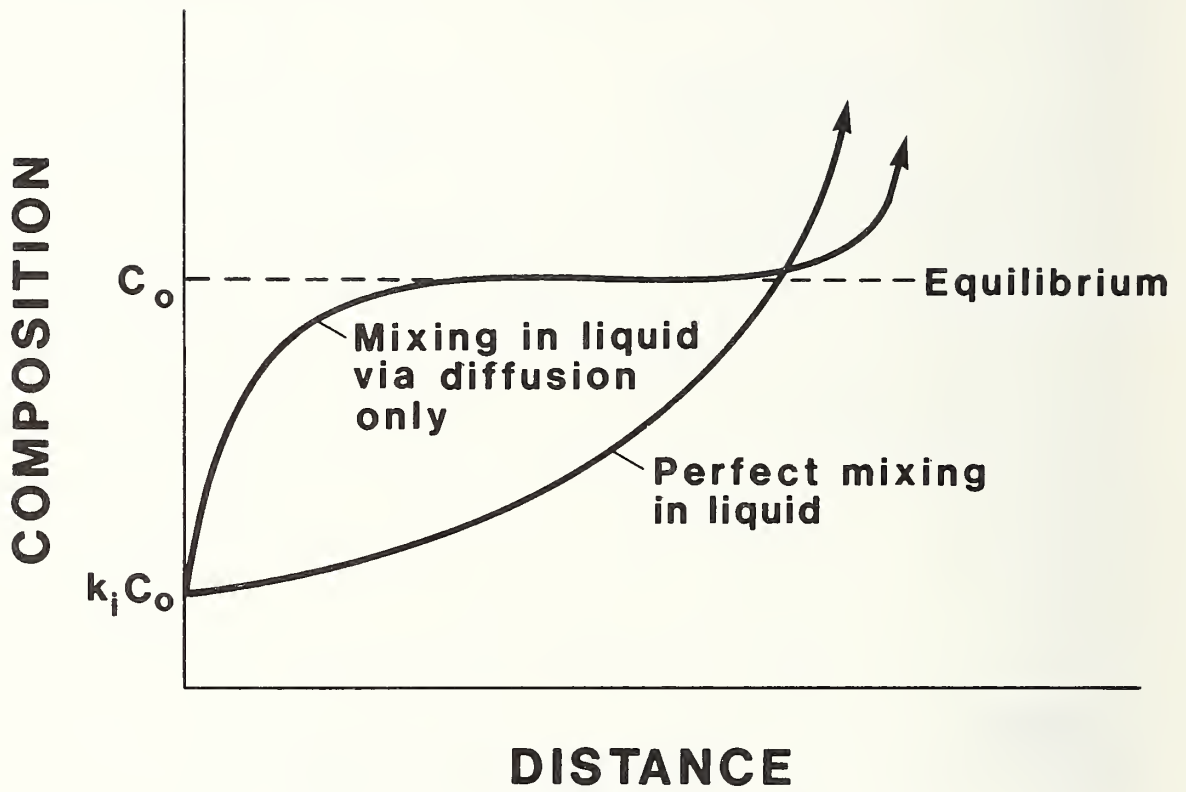


Figure 5 Schematic diagram of solute distribution after normal freezing.

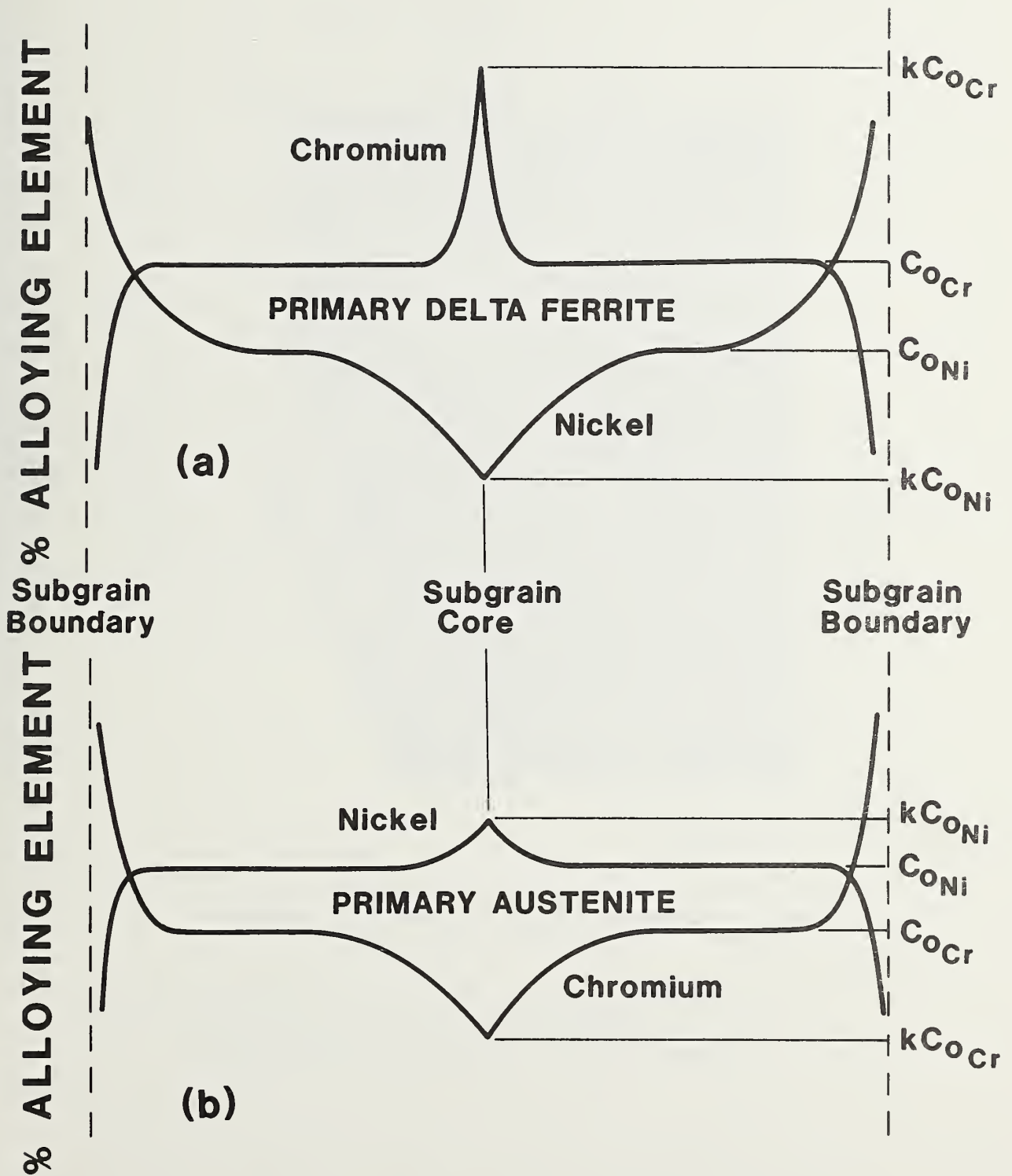


Figure 6 Schematic diagram of solute distribution across a subgrain, following primary δ solidification of a weld¹⁷.

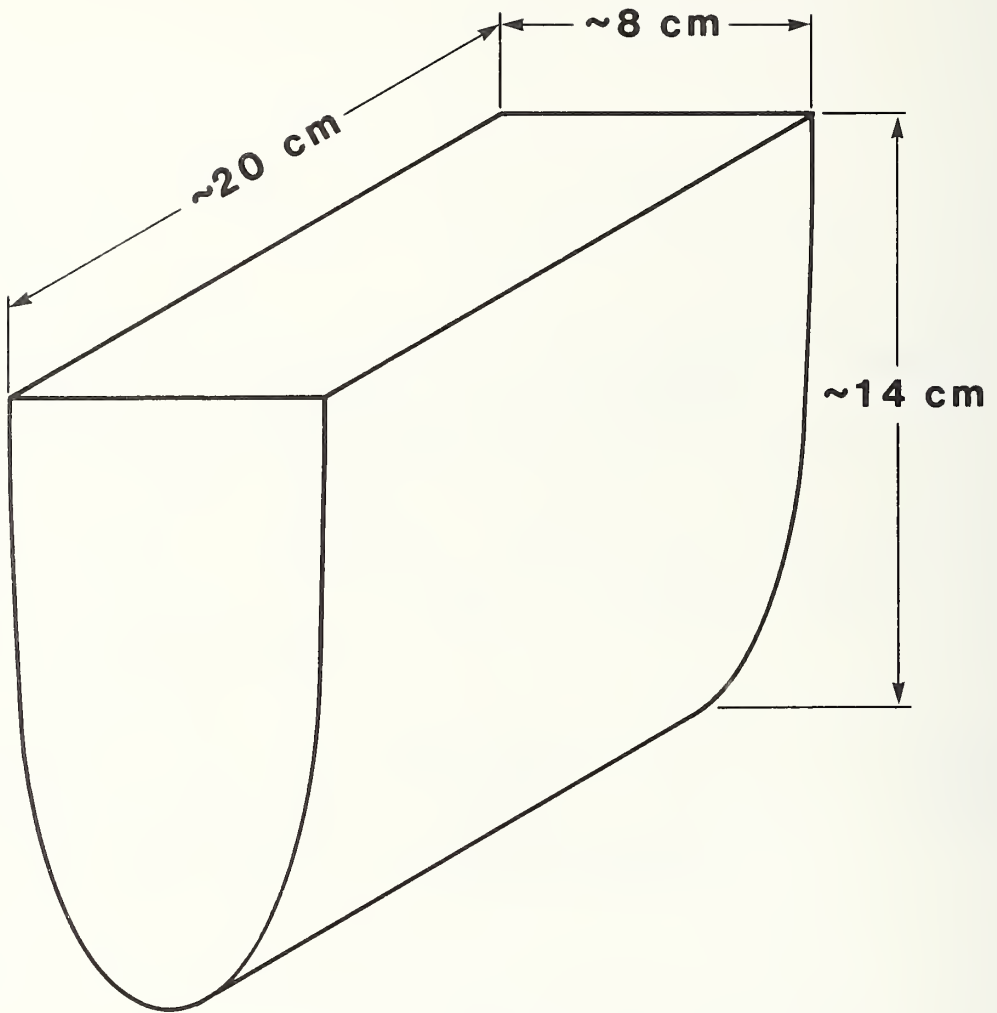


Figure 7 Schematic diagram of keel block casting.



Figure 8 Keel block cross section showing columnar-to-equiaxed grain morphology transition in solidification structure, light color etch.

Columnar Grain Growth Dir



500 μm

Figure 9(a) Keel block cross section in columnar grain region near edge, light color etch.

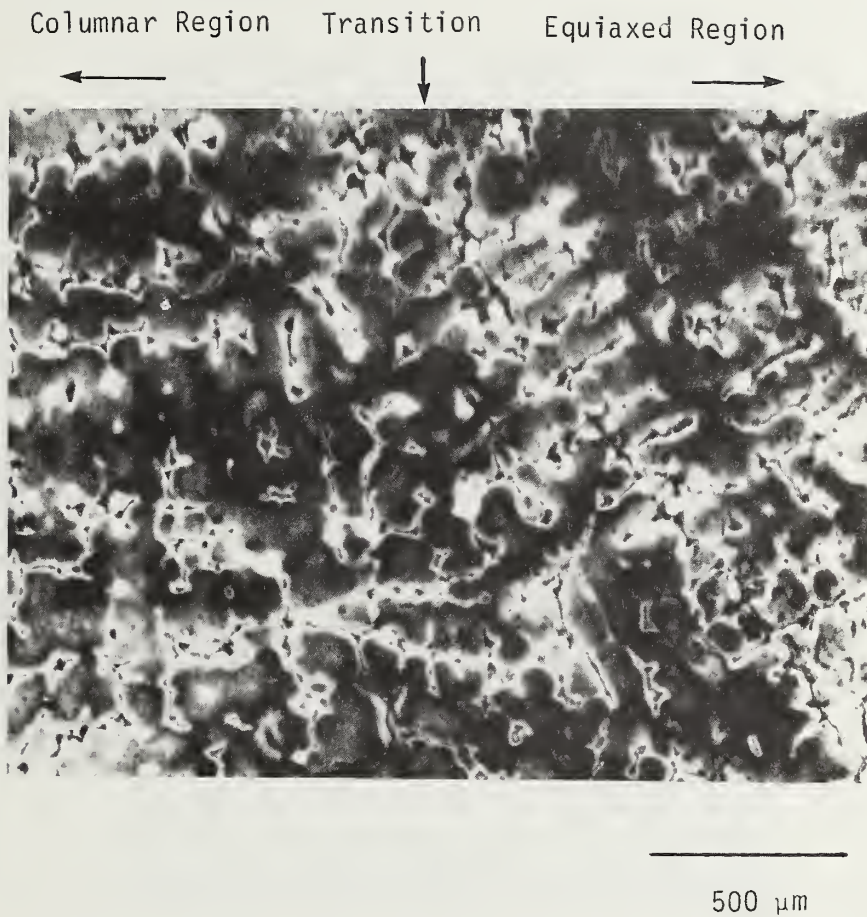
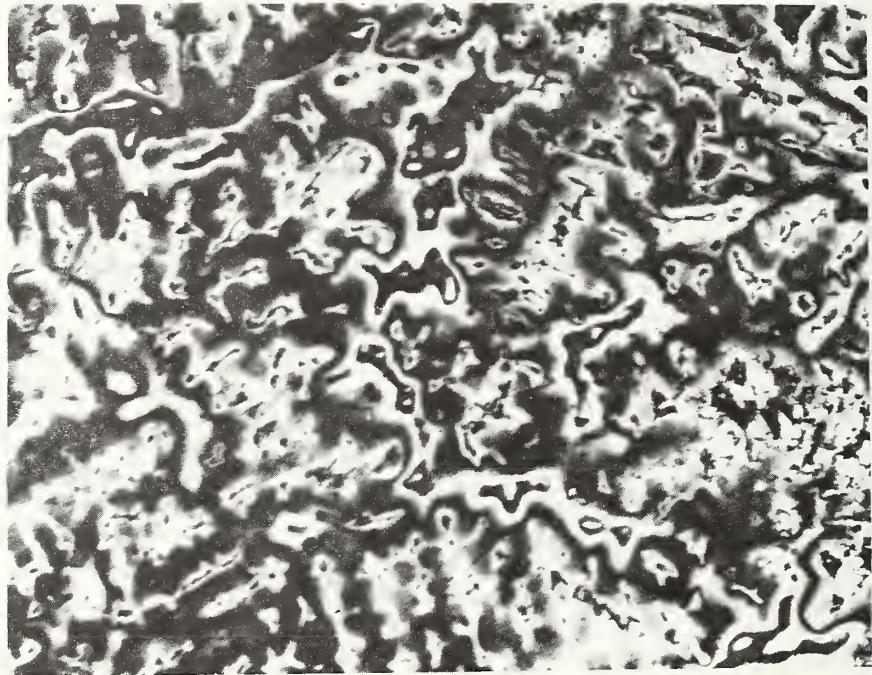
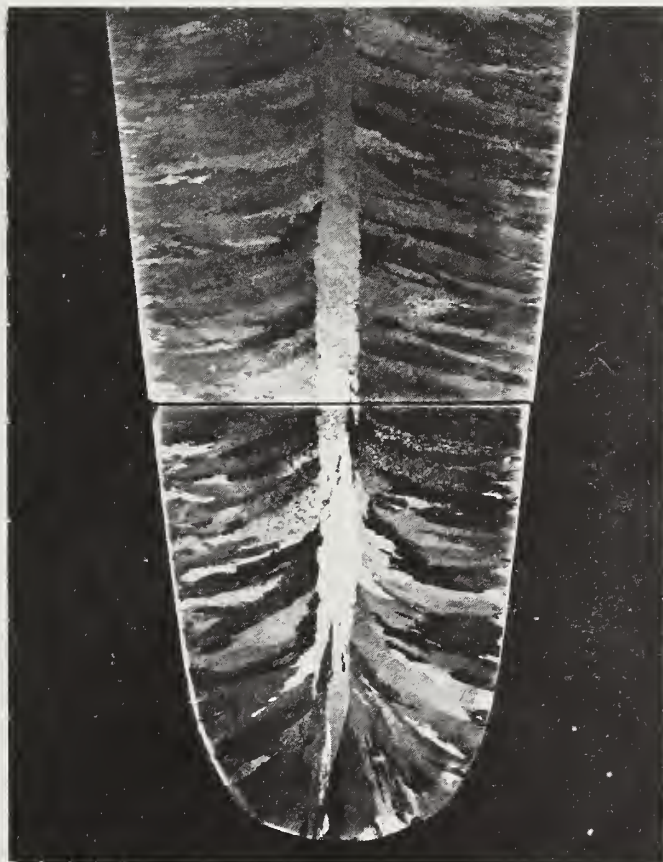


Figure 9(b) Keel block cross section near columnar-to-equiaxed grain morphology transition in solidification structure, light color etch.



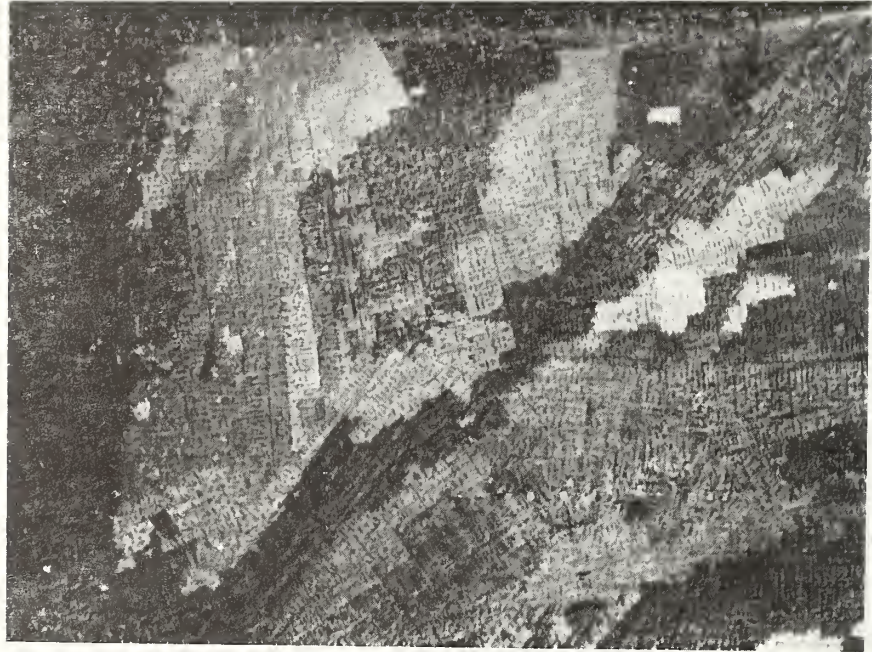
500 μm

Figure 9(c) Keel block cross section in equiaxed grain region, light color etch.



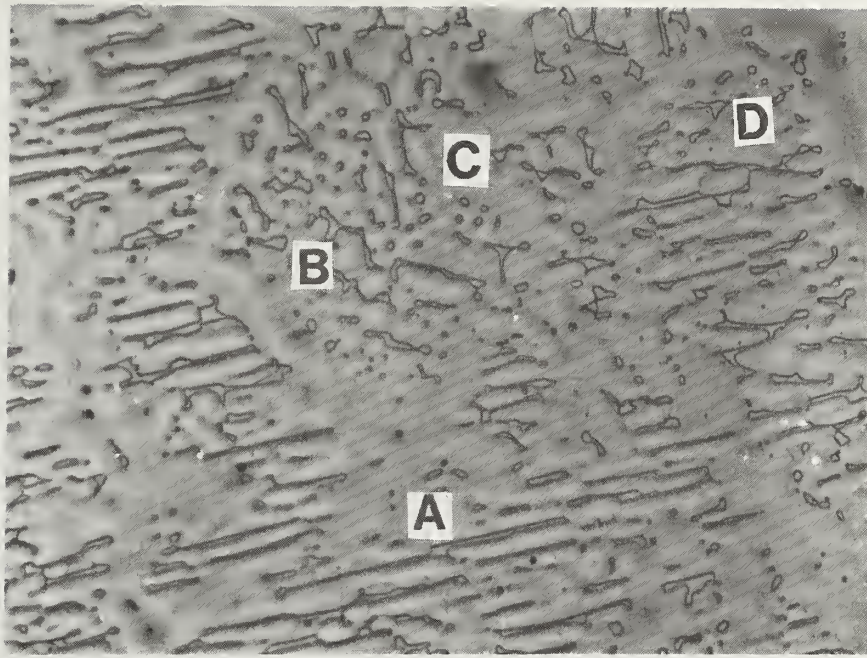
2 cm

Figure 10 Keel block cross section showing columnar γ crystals formed during $\delta \rightarrow \gamma$ phase transformation, heavy color etch.

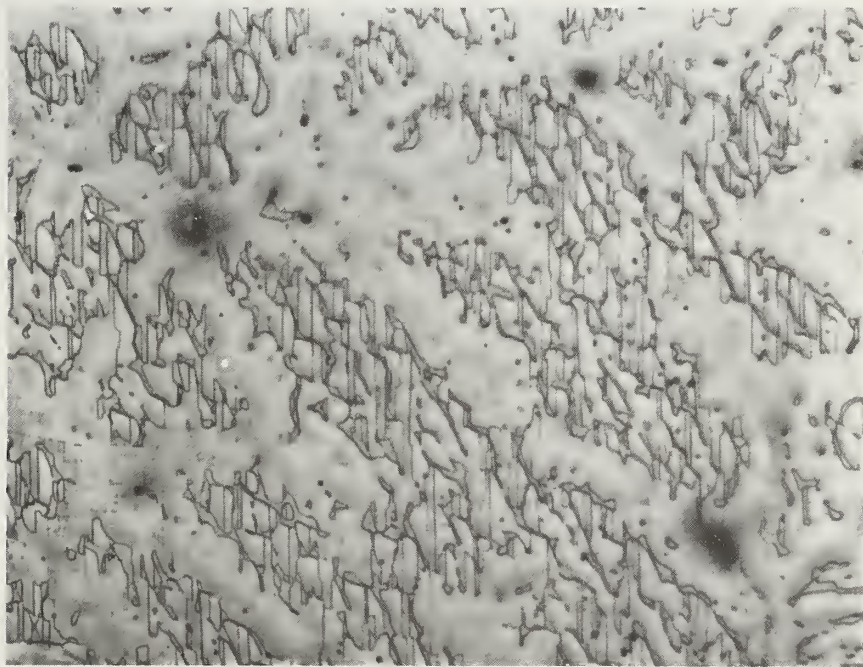


20 cm

Figure 11 Columnar γ crystal structure in relation to solidification structure delineated by residual δ -ferrite, heavy color etch.



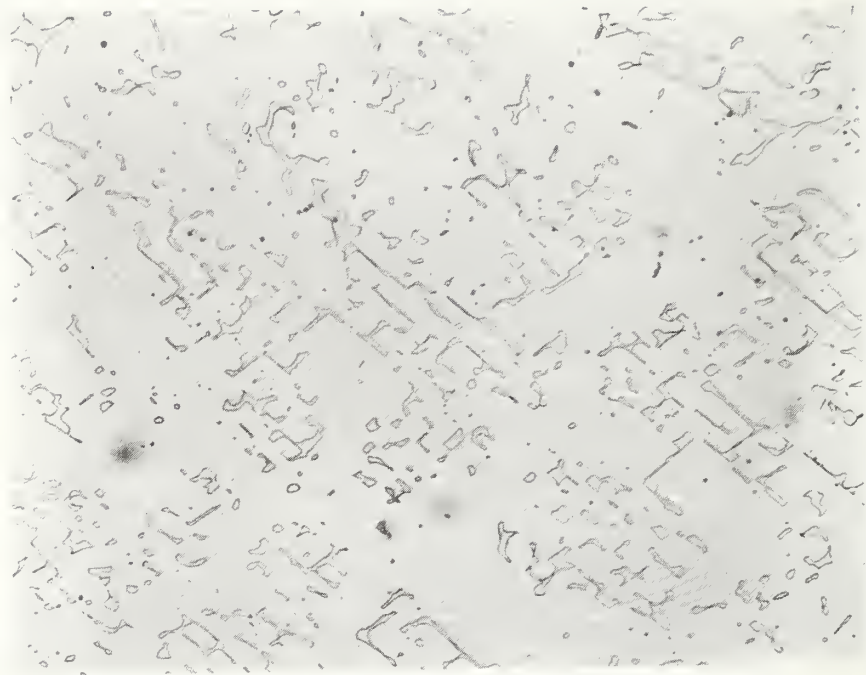
(a)



(b)

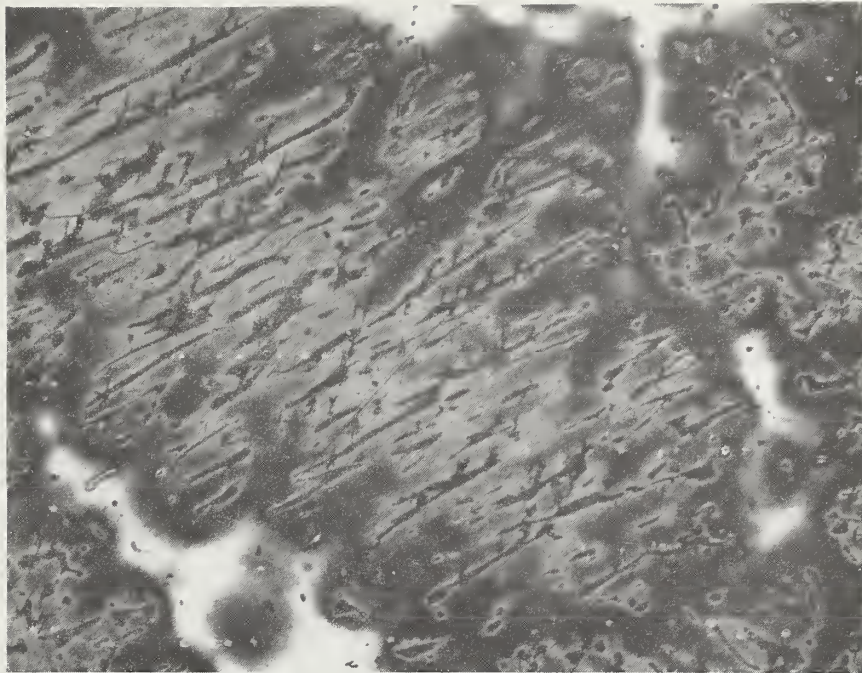
250 μm

Figure 12 Residual δ -ferrite morphology in CF8M-9 alloy (a) filamentary and cell-like δ -ferrite, (b) twinning in γ , oxalic acid electro-etch.



250 μm

Figure 13 Residual δ -ferrite faceting,
oxalic acid electro-etch.



250 μm

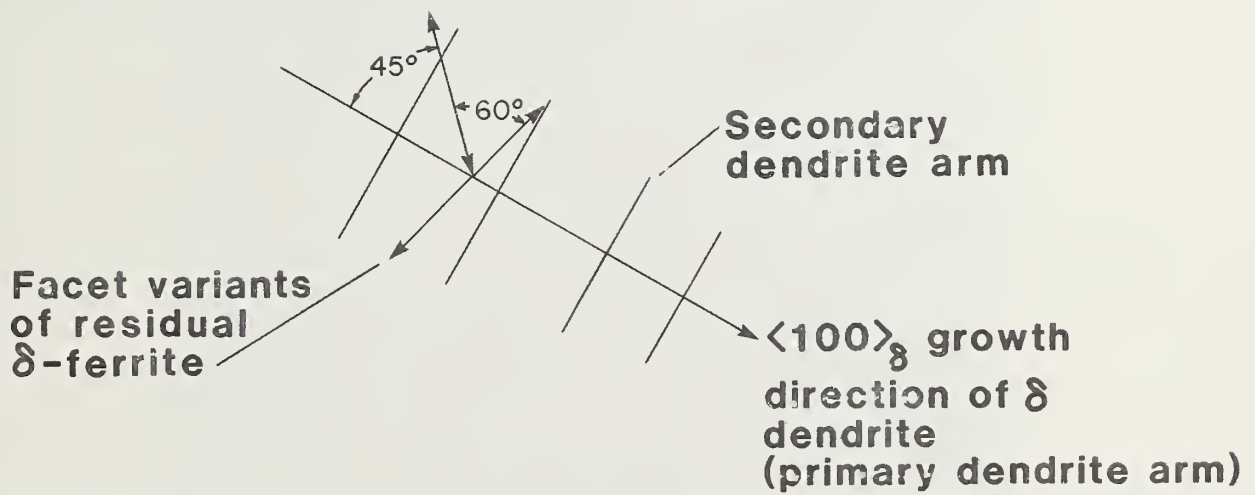
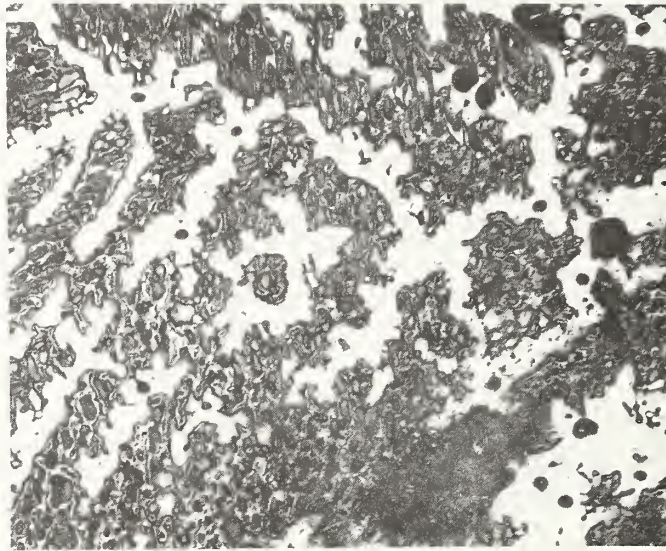


Figure 14 Residual δ -ferrite in relation to δ -ferrite dendritic solidification structure, light color etch.



500 μm

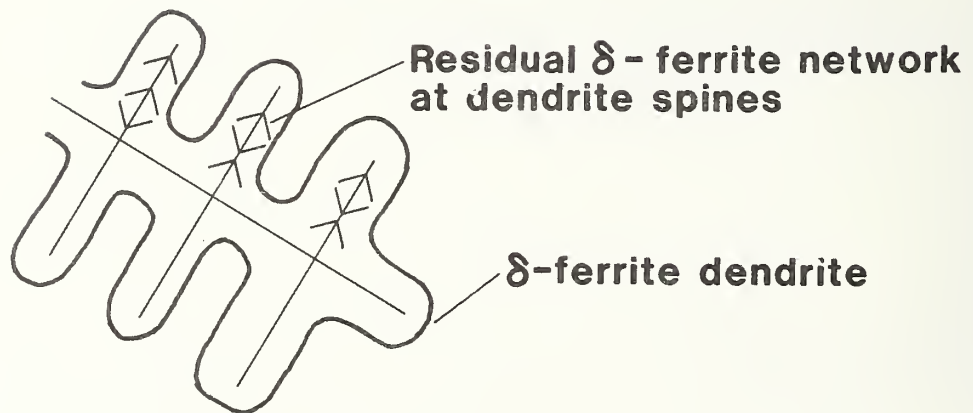
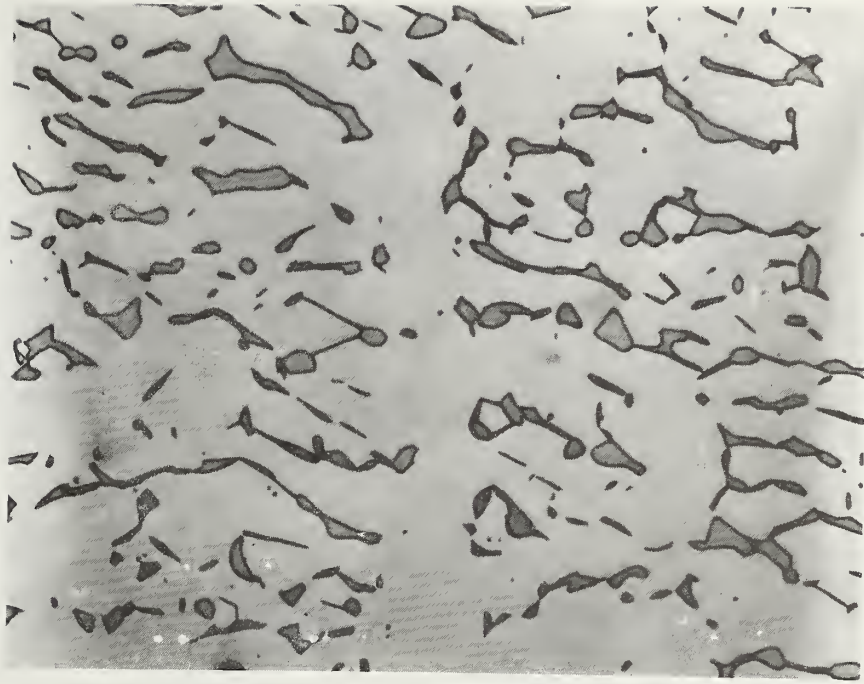
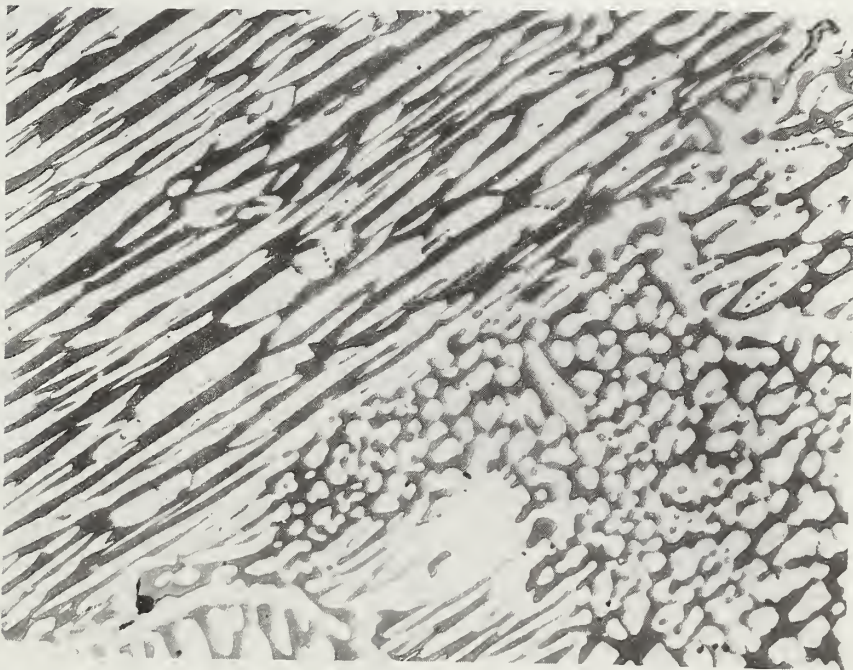


Figure 15 Residual δ -ferrite networks at δ -ferrite dendrite spines, light color etch.



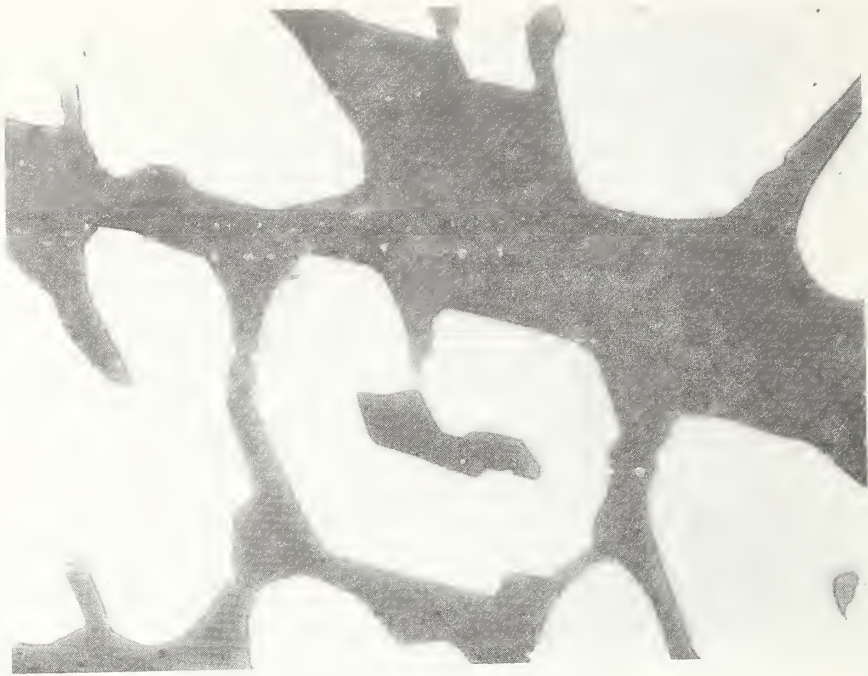
(a)



(b)

250 μm

Figure 16 Residual δ -ferrite morphology (a) CF8M-14, (b) CF8M-24, 10N KOH electro-deposition etch.



(a)



(b)

31 μm

Figure 17 Residual δ -ferrite in CF8M-24 alloy showing ledge morphology, 10N KOH electro-deposition etch.

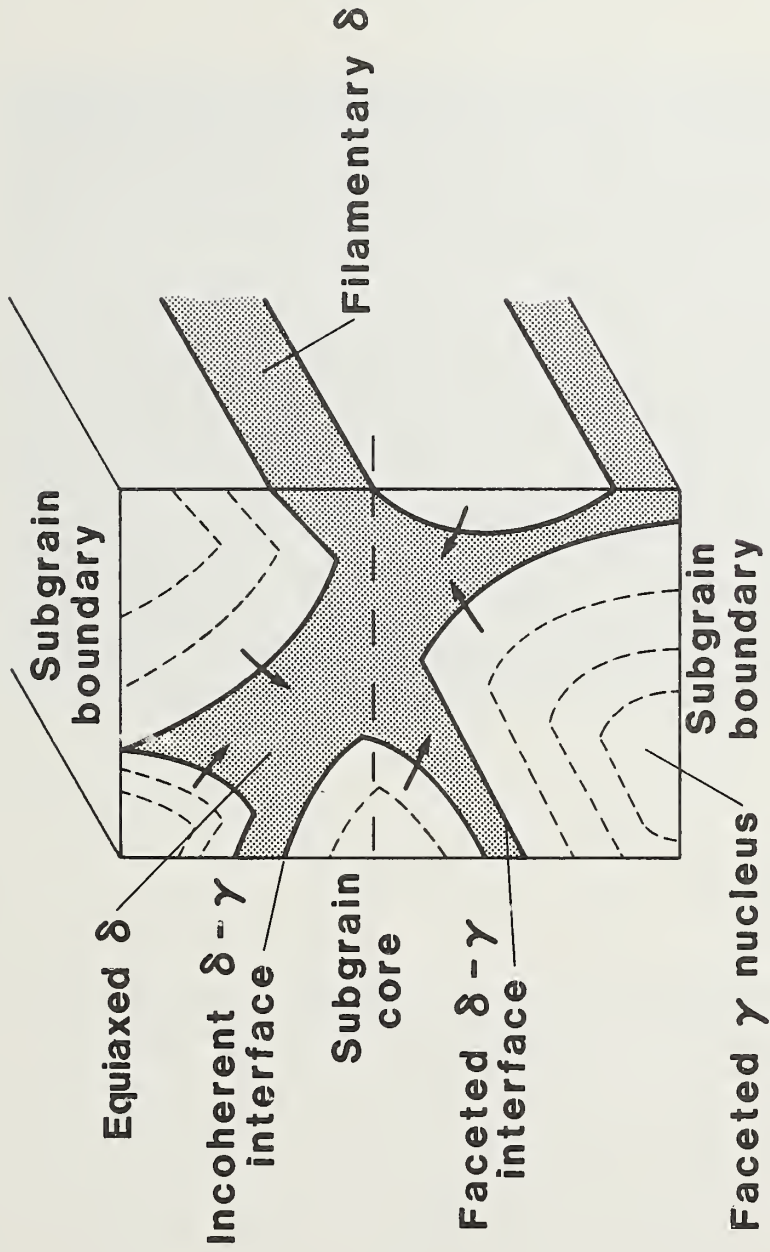


Figure 18 Schematic diagram of evolution of residual δ -ferrite morphology via $\delta \rightarrow \gamma$ phase transformation.



125 μ m

Figure 19 Residual δ -ferrite in weld metal; ~3v/o
 δ -ferrite, 316L GMA, oxalic acid electro-etch.

DEFORMATION AND FRACTURE OF STAINLESS STEEL CASTINGS AND
WELDMENTS AT 4 K

T. A. Whipple and E. L. Brown
Fracture and Deformation Division
National Bureau of Standards
Boulder, Colorado

ABSTRACT

A number of stainless steel weldments and castings that were deformed at 4 K have been examined with optical and electron microscopy. The purpose of this investigation was to assess qualitatively the effects of residual delta-ferrite on the deformation and fracture mechanisms of these materials at cryogenic temperatures.

Weldments and castings have very similar microstructures, but the ferrite in castings is much coarser as a result of slower solidification and cooling rates. This wide variation in the scale of the structure provides a good opportunity for the study of structure and property relationships in these materials.

It has been found that deformation and fracture are greatly influenced by the ferrite morphology. The study of the coarser structure in castings has allowed more direct observation of fracture, which has led to some preliminary conclusions concerning fracture mechanisms. Cleavage fractures of ferrite particles have been observed in some castings and in an electraslag weldment. It appears that these fractures, although not forming a continuous crack path, assist in the void formation in the ductile austenite matrix. Another observed crack propagation mechanism is that of void nucleation near the austenite/ferrite interface. Although interface separation has not been observed, the inhomogeneous deformation near the interface appears to cause premature void nucleation and growth. The occurrence of one of the above mechanisms rather than the other depends on a number of factors, including ferrite morphology and the properties of the two phases. The morphology and properties, in turn, depend on both the alloy composition and solidification conditions.

INTRODUCTION

The structural components for most superconducting magnets are being made of stainless steels. Because of the large structures, high stresses and low operating temperature, welded construction is the most attractive fabrication method. Since the structures are being made of thick plate, fracture toughness is an important consideration. It has been found that stainless steel weldments generally have a much lower fracture toughness than the stainless steel base metal.^{1,2}

To date, three factors have been established that have an effect on the cryogenic fracture toughness of stainless steel weldments: the delta-ferrite content of the weldment,^{1,3} the nitrogen concentration in the weld,⁴ and the fusion zone grain size of fully austenitic weldments.² Nevertheless, it still is not possible to predict the toughness of a stainless steel weldment on the basis of these factors. Apparently there are factors beyond those stated above that cause the observed wide variations in fracture toughness.^{2,5,6} This paper contains the results of the initial stage of an investigation that is intended to define more precisely the role of ferrite and to identify other factors that have an influence on the cryogenic toughness of stainless steel weldments and castings.

In many structural applications it would be advantageous to use stainless steel castings to facilitate fabrication and to eliminate the need for welding. There are presently very few 4 K mechanical property data on castings, but a few initial tests have shown a wide variation in fracture toughness similar to weldments.⁵ This is not surprising

because weldments are actually rapidly solidified castings. Stainless steel castings also generally contain a certain percentage of delta-ferrite, although on a much coarser scale than that of weldments, owing to the slower solidification of castings.

This paper presents the results of a metallographic and fractographic investigation of deformation and fracture mechanisms in duplex austenite/ferrite structures at 4 K.

MATERIALS

The materials examined in this study are stainless steel weldments and castings that have been tensile and fracture toughness tested at 4 K. These materials did not come from a controlled series, however, they all fall into the AISI type 304 or 316 stainless steel composition ranges. These variations in composition, as well as variations in the casting or welding process, are appropriate since the intent of this study was to investigate the possible deformation and fracture mechanisms in duplex austenite/ferrite structures at 4 K and not just the mechanism for a specific material. The available chemical composition and mechanical property data for the materials used in this study are presented in Tables 1 and 2.

PROCEDURES

For this investigation a number of sectioning, metallographic and fractographic techniques were employed. Each technique allows the observation of different phenomena. Macroscopic examination, optical microscopy, and scanning electron microscopy (SEM) were used for making observations.

Sectioning

Many of the figures presented in this paper are taken from samples that were sectioned perpendicular to the fracture plane of tensile and compact tension specimens. This sectioning method allows the observation of crack propagation paths and deformation around the crack tip and provides insight into the crack propagation mechanisms.

Metallographic Specimen Preparation

For the most part metallographic specimens were prepared by using standard mechanical grinding and polishing techniques, but in a few cases electrolytic polishing was used.

A 10% oxalic acid electrolytic etch was used as a general purpose etch to reveal ferrite morphology and grain boundaries. This etch can also reveal strain-induced martensite if the etching time is increased; however, if the specimen contains ferrite, this procedure leads to considerable surface relief and pitting, which make metallography difficult.

A 10 N KOH electrolytic etch was used to reveal ferrite structure only. This is a deposition etch that colors the ferrite light blue to brown. The main attribute of this etchant is that it does not remove any material; therefore, it will not round the edges of cracks or produce pitting and other etching artifacts. The KOH etch is sometimes used prior to oxalic acid etching because it tends to passivate the ferrite and allow deeper oxalic acid etching of the austenite with less overall damage.

A solution of 50 ml HCl, 125 ml H₂O and 2g Na₂SO₄ was used to color etch stainless steel weldments and castings. This etchant is useful in

revealing the original solidification pattern after the solid-state ferrite-to-austenite transformation has occurred.

A magnetic etching procedure was used to reveal the magnetic phases, ferrite, and bcc martensite. For this procedure a suspension of fine magnetic particles is spread on the surface of the specimen and the specimen is placed in a magnetic field; the magnetic particles will then migrate to the magnetic phases. This etch was used mainly in conjunction with the KOH etch to reveal bcc martensite which is an indication of plastic deformation in the austenite matrix.

DISCUSSION

Low Temperature Deformation

It is generally true that bcc materials, such as delta-ferrite, go through a ductile-to-brittle transition at low temperatures, whereas fcc materials, such as austenite, do not. This is due to the difficulty of operating non close-packed slip systems at low temperatures. The temperature at which this transition occurs in steels is influenced mainly by alloy content and microstructure; a higher nickel content and a smaller grain size lead to a lower transition temperature. Another factor to consider is the increase in strength with a reduction in temperature; bcc materials have a much more dramatic increase in yield strength than fcc materials at low temperatures.

These general observations lead to some expectations for the behavior of duplex stainless steels. At higher temperatures, both austenite and ferrite are ductile and have similar strengths; in this case the amount

or morphology of the ferrite is not expected to significantly affect the strength or toughness of the material. At temperatures below the transition temperature of the ferrite, it becomes a strong, brittle second phase. Factors that influence the inhomogeneity of deformation in the ductile austenite matrix will influence the strength and toughness of the material. This means that the amount, morphology and properties of the ferrite can all have significant influences. Observations that support these hypotheses have been made by Read et al.¹

Figures 1 and 2 are micrographs of 316L stainless steel weld metal tensile specimens that were tested at room temperature and 4 K, respectively. Note that at room temperature (Figure 1) the ferrite is highly elongated in the direction of the tensile axis and at 4 K (Figure 2) the ferrite maintains its original dendritic morphology and shows no indication of elongating with the matrix.

During deformation at low temperatures, austenite can go through a strain induced martensitic transformation. The degree of transformation and the critical strain at which it occurs are a function of the alloy content. Although the stability of the austenite matrix will quantitatively effect the strength and toughness of duplex austenitic stainless steel castings and weldments, it is only of interest in this qualitative discussion in that it provides a method of observing deformation in the austenite.

Figures 3 and 4 are micrographs of areas near the crack tips in two CF8* stainless steel castings tested at 4 K. The intent of these micro-

*CF8 and CF8M are ASTM A351 grades of cast stainless steel and are analogous to AISI 304 and 316, respectively.

graphs is to show the inhomogeneity in deformation caused by the presence of ferrite. Figure 3 is from a 0% ferrite casting; the straight lines near the crack tip are strain-induced martensite. Note that the lines are straight and fairly uniform, only changing direction at grain boundaries. This can be contrasted with Figure 4, which is a similar region in a 14.5% ferrite casting. In this case, the martensite formation is extremely nonuniform and seems to be concentrated in association with the ferrite morphology. Another example of the effect of the presence of ferrite on deformation patterns in the austenite matrix is shown in Figures 5 and 6. In Figure 5, bending of martensite bands near the ferrite particles can be seen in a CF8M* casting with 9% ferrite, indicating that the ferrite is nondeforming and the matrix is flowing around it. Figure 6 is from a 316L electroslag weldment; this micrograph shows the reinforcement of the austenite matrix by the ferrite in a low strain area. Note that there is little martensite formation between the parallel ferrite plates and more extensive martensite formation where the matrix is not as well reinforced.

All of the above evidence lends support to the observations cited at the beginning of this discussion: (1) at low temperatures ferrite is a very strong nondeforming phase and (2) the ferrite content and morphology are important influences on how the ductile austenite matrix deforms.

Low Temperature Fracture

As a result of the above discussion on low-temperature deformation, it appears appropriate to classify duplex austenitic stainless steel, at

*CF8 and CF8M are ASTM A351 grades of cast stainless steel and are analogous to AISI 304 and 316, respectively.

low temperatures, as a ductile matrix composite with hard, brittle particles or discontinuous fibers. This is not an exact classification, since the ferrite is very seldom in the form of spherical particles and can be either continuous or discontinuous depending on solidification and cooling conditions, but this classification does provide a good starting point for the discussion of fracture mechanisms. There are three possible mechanisms for the fracture of ductile matrix/hard-discontinuous fiber composites.⁷

1. Brittle fracture of the fibers.
2. Matrix/fiber interface separation.
3. Fiber pull-out.

Brittle fracture of the fibers occurs when the local stress in the fiber exceeds its fracture strength. The local stress in the fiber is not necessarily the same as the macroscopic stress on the sample, but can be considerably higher owing to inhomogeneous plastic deformation in the matrix. Interface separation is an important consideration with artificial composites and with metal-matrix/particulate composites; however, the interface between austenite and ferrite is a very strong one and no evidence of interfacial separation has been observed. Fiber pull-out is sometimes associated with interface separation, but for the purpose of this discussion it means a ductile failure of the matrix near the matrix/fiber interface. This occurs when the fiber does not fracture, but the highly inhomogeneous deformation of the matrix near the fiber results in void nucleation at this location. The occurrence of one of these mechanisms over the others depends on fibre strength, content and morphology.

In this study evidence was found for both fiber fracture and fiber pull-out. Until this investigation there had been no direct observation of the brittle fracture of ferrite in weldments and castings at 4 K. Although this had long been assumed to be the cause of the reduction in toughness of stainless steel weldments with increasing ferrite content, direct observation was difficult because of the extremely small size of the ferrite in weldments. In this investigation observations were made on both castings and weldments made with high heat input processes. The much slower solidification and cooling rates of these materials results in a coarser structure, which is more easily observed.

With these materials extensive evidence was found of brittle fracture of ferrite in weldments and castings deformed at 4 K. Figure 7 is a micrograph of a 316L electroslag weldment taken near the fracture surface of a tensile specimen. In this specimen, numerous brittle fractures of ferrite particles are evident. The fact that the fractures are at 90° to the tensile axis lends further support to the conclusion that they are brittle cleavage fractures. Additional evidence for cleavage fracture of ferrite is shown in Figure 8 (a graph from the 14.5% ferrite CF8 casting). This micrograph shows consistent angular relationships between the fractures, indicating that fracture is occurring on a specific set of crystallographic planes, i.e., cleavage planes.

Figure 9 and 10 are crack profiles for two stainless steel castings. Figure 9 is a CF8M casting that contains 9% ferrite and has a very high toughness at 4 K, similar to that of wrought base metals. Figure 10 is a CF8 casting containing 14.5% ferrite; this casting has a low toughness comparable to that of a weldment with a similar ferrite content.

In both cases the crack path is associated with the ferrite morphology, but Figure 10 has a much more brittle appearance and significant cracking not associated with the ultimate crack path. Also, it can be seen in Figure 4 (a higher magnification of the crack tip) that there is significant ferrite cracking in advance of the crack tip, which was not observed in the CF8M casting of Figure 9. A definitive explanation of the difference in these two castings cannot be offered at this time; however, two factors appear to have contributed the difference in the amount of ferrite cracking. First, the ferrite morphology is different; the tougher CF8M casting was a sand casting with a slower solidification and cooling rate than the centrifugally cast CF8 casting. This resulted in a coarser and discontinuous ferrite morphology, which provided less restriction to deformation in the austenite matrix than the finer more continuous ferrite in the CF8 casting. The second contributing factor may be the toughness of the ferrite phase: CF8M has a higher nickel content than CF8, and it is well known that nickel increases the cryogenic toughness of ferritic materials.

Weldments differ from castings mainly in that the solidification and cooling rates are much greater. This results in a more directional solidification pattern and a much finer structure. The greater cooling rate results in less diffusion during the ferrite-to-austenite transformation causing the ferrite to be more closely associated with the original dendritic solidification pattern. Therefore, the residual ferrite of weldments is more likely to be continuous. When fracture is associated with cracking of the residual ferrite, having continuous ferrite can provide

a preferred crack path and lower toughness than occurs for a material of the same ferrite content in a discontinuous morphology.

An example of this preferred crack path is shown in Figure 11 in the crack profile of a fracture toughness specimen from a 316L electroslag weldment. An electroslag weldment experiences a cooling rate greater than that of a casting, but much less than that of other welding processes. This results in a relatively coarse but continuous ferrite morphology. Figure 11(a) shows that the dendritic growth direction determined the crack propagation direction even though the stress state was such that the crack should propagate straight. The closer view, Figure 11(b), shows the crack was propagating down dendrite cores and secondary dendrite arms. The crack periodically moved to an adjacent dendrite owing to the stress state. Figure 12(a) is a micrograph of the crack tip of this weldment, showing that the crack is indeed propagating in a brittle manner through the ferrite. Although this fracture does have a very brittle appearance, the measured fracture toughness was above average for a weldment of this ferrite content. Figure 12(b) shows the same area using the magnetic etch to reveal strain-induced martensite. Even though the ferrite fractures in a brittle manner, there was still considerable plastic deformation in the austenite matrix. This matrix deformation and the fact that energy was consumed in the crack propagating off-line accounts for the relatively high toughness of this weldment. Further evidence that the ferrite in this weldment fractured in a brittle manner is provided by the SEM fractographs in Figure 13. These fractographs demonstrate the mixture of brittle ferrite fracture and ductile matrix failure.

Behavior similar to that described above can also be seen in the rapidly solidified 308L flux-cored metal arc (FCMA) weldment shown in Figures 14 and 15. Because of the rapid solidification, the ferrite is extremely fine and it was not possible to observe brittle fracture of the ferrite directly. Figure 14 shows that the crack propagation again followed the dendrite growth direction. The closer view of Figure 15 shows that the crack path was determined by the local ferrite morphology, which varies considerably from the bottom to the top of a weld pass.

As mentioned previously, two possible discontinuous fiber composite fracture mechanisms are of interest: fiber fracture and fiber pull-out. The evidence already presented has shown that fiber fracture does occur in coarse duplex structures. In the case of weldments with much finer structures, limited evidence has been found for both fracture mechanisms. Figure 16 is a stereo fractograph of the fracture surface of the 308L FCMA weldment described previously. The area indicated by the arrow appears to be a subsurface ferrite dendrite, where the inhomogeneous deformation nucleated a ductile failure near the ferrite/austenite interface. Composite fracture theory predicts that, for a discontinuous fiber composite, there is a critical aspect ratio (fiber length-to-diameter ratio) at which a transition from fiber fracture to fiber pull-out fracture mechanisms occurs; a high aspect ratio favors fiber fracture. The aspect ratio of a fiber is dependent on orientation to the tensile axis: the same fiber will have a high aspect ratio if it is aligned with the tensile axis and a low one if it is perpendicular to the tensile axis. In Figure 16 it is apparent that the dendrite was perpendicular to the tensile axis; therefore fiber pull-out occurred.

Figure 17 shows a case where the fibers were apparently parallel to the tensile axis and fiber fracture occurred.

SUMMARY

Samples of stainless steel castings and weldments that had been deformed and fractured at 4 K were examined. The thrust of the investigation was to determine the mechanisms by which residual delta-ferrite affects the deformation and fracture of duplex austenite/ferrite structures at cryogenic temperatures. Evidence was presented that indicates that at low temperatures the ferrite acts as a hard, brittle second phase particle. The manner in which these particles affect the mechanical properties of the material depends on the amount, properties and morphology of the second-phase particles. It was observed that the ferrite reinforces the austenite matrix and causes the deformation to be inhomogeneous. Evidence was found for two fracture mechanisms: (1) brittle fracture of the ferrite mixed with ductile failure of the matrix between ferrite fractures and (2) ductile failure in the matrix near the austenite/ferrite interface, which was caused by the highly inhomogeneous deformation in this region. The occurrence of one of these mechanisms over the other depends on the morphology and properties of the ferrite.

Future work in this area will concentrate on obtaining a more quantitative description of the role of ferrite in the deformation and fracture of duplex austenite/ferrite materials at liquid helium temperatures.

REFERENCES

1. D. T. Read, H. I. McHenry, P. A. Steinmeyer, and R. D. Thomas, "Metallurgical Factors Affecting the Toughness of 316L SMA Weldments at Cryogenic Temperatures," Weld. J. Res. Suppl. 59, 104s-113s (1980).
2. T. A. Whipple, H. I. McHenry, and D. T. Read, "Fracture Behavior of Ferrite-Free Stainless Steel Welds in Liquid Helium," to appear in Weld. J. Res. Suppl. 60 (4), 1981.
3. E. R. Szumachowski and H. F. Reid, "Cryogenic Toughness of SMA Austenitic Stainless Steel Weld Metals: Part I - Role of Ferrite," Weld. J. Res. Suppl. 57, 325s-333s (1978).
4. E. R. Szumachowski and H. F. Reid, "Cryogenic Toughness of SMA Austenitic Stainless Steel Weld Metals: Part II - Role of Nitrogen," Weld. J. Res. Suppl. 58, 34s-44s (1979).
5. T. A. Whipple and H. I. McHenry, "Evaluation of Weldments and Castings for Liquid Helium Service," in Materials Studies for Magnetic Fusion Energy Applications at Low Temperatures-IV, NBSIR 81-1645, pp. 273-287 (1981).
6. T. A. Whipple and D. J. Kotecki, "Weld Process Study for 316L Stainless Steel Weld Metal for Liquid Helium Service," in Materials Studies for Magnetic Fusion Energy Application at Low Temperatures-IV, NBSIR 81-1645, pp. 303-321 (1981).
7. A. Kelly, "Particle and Fibre Reinforcement," in Strengthening Methods in Crystals, Halsted Press Division, John Wiley & Sons, New York, pp. 433-484 (1971).

LIST OF TABLES

Table 1. Process and chemical composition data on stainless steel weldments and castings.

Table 2. Mechanical properties of stainless steel weldments and castings.

Table 1. Process and chemical composition data for stainless steel weldments and castings.

Alloy	Form	Ferrite,	Chemical Composition, wt.%										
			C	Mn	Si	Cr	Ni	Mo	S	P	N		
CF8	Centrifugal casting	0	0.02	1.0	.72	18.0	11.0	0.10	0.04	0.04	0.04	0.04	0.044
CF8	Centrifugal casting	14.5	0.006	0.19	1.62	19.6	8.4	0.08	0.02	0.02	0.02	0.02	0.049
CF8M	Sand casting	9.0	0.02	1.06	1.10	19.33	11.67	2.14	0.018	0.018	0.030		--
316L	Electroslag weld	4.5	0.025	1.75	0.37	18.8	11.0	1.60	0.012	0.012	0.021	0.021	0.045
308L	Submerged arc weld	4.7	--	--	--	--	--	--	--	--	--	--	--
308L	Flux-cored metal-arc weld	8.2	--	--	--	--	--	--	--	--	--	--	--

Table 2. Mechanical properties of stainless steel weldments and castings at 4K.

Alloy	Form	Ferrite, %	Yield Strength, MPa (ksi)	Ultimate Strength, MPa (ksi)	Elongation, %	Reduction in Area, %	K_{Ic} (J), MPa \sqrt{m} (ksi \sqrt{in})
CF8	Centrifugal casting	0	413 (60)	1250 (181)	46	--	331 (301)
CF8	Centrifugal casting	14.5	470 (68)	1512 (219)	48	--	125 (114)
CF8M	Sand casting	9.0	545 (79)	1328 (193)	43	--	278 (253)
316L	Electroslag weld	4.5	690 (100)	1365 (197)	36	24	189 (172)
316L	Submerged	4.7	918 (133)	1188 (172)	18	22	132 (121)
308L	Flux-cored metal arc weld	8.2	855 (124)	1354 (196)	24	21	79 (72)

LIST OF FIGURES

- Figure 1 Micrograph of a 316L SA weld metal tensile specimen deformed at room temperature, taken near the fracture surface and showing the elongation of the ferrite. KOH etch.
- Figure 2 Micrograph of a 316L SA weld metal tensile deformed at 4 K, showing that the ferrite does not deform at low temperatures. Oxalic acid etch.
- Figure 3 Area near the crack tip of a 0% ferrite CF8 casting. Oxalic acid etch.
- Figure 4 Area near the crack tip of a 14.5% ferrite CF8 casting. KOH and oxalic acid etch.
- Figure 5 Micrograph of a 9% ferrite CF8M casting deformed at 4 K, showing the deformation of the austenite matrix around a ferrite particle. Color etch.
- Figure 6 Micrograph of a 316L electroslag weldment deformed at 4 K, showing the reinforcement of the austenite matrix by the ferrite particles. KOH and magnetic etch.
- Figure 7 Area near the fracture surface of a tensile specimen from a 316L electroslag weldment. Oxalic acid etch.
- Figure 8 Area near the crack of a 14.5% ferrite CF8 casting. KOH and oxalic acid etch.
- Figure 9 Crack profile of a 9% ferrite CF8M casting. Color etch.
- Figure 10 Crack profile of a 14.5% ferrite CF8 casting. KOH and oxalic acid etch.
- Figure 11 Crack profile of a 316L electroslag weldment. Oxalic acid etch.

- Figure 12 Micrographs of the crack tip of a 316L electroslag weldment.
a) KOH etch, b) KOH and magnetic etch.
- Figure 13 SEM fractographs of the fracture surface of a 316L
electroslag weldment.
- Figure 14 Macroscopic crack profile of a 308L FCMA weldment. Oxalic
acid etch.
- Figure 15 Micrograph of the crack tip region of a 308L FCMA weldment.
Oxalic acid etch.
- Figure 16 SEM stereo fractograph of a 308L FCMA weldment.
- Figure 17 SEM fractograph of a 308L FCMA weldment.

← TENSILE AXIS →



Figure 1

Micrograph of a 316L SA weld metal tensile specimen deformed at room temperature, taken near the fracture surface and showing the elongation of the ferrite. KOH etch.

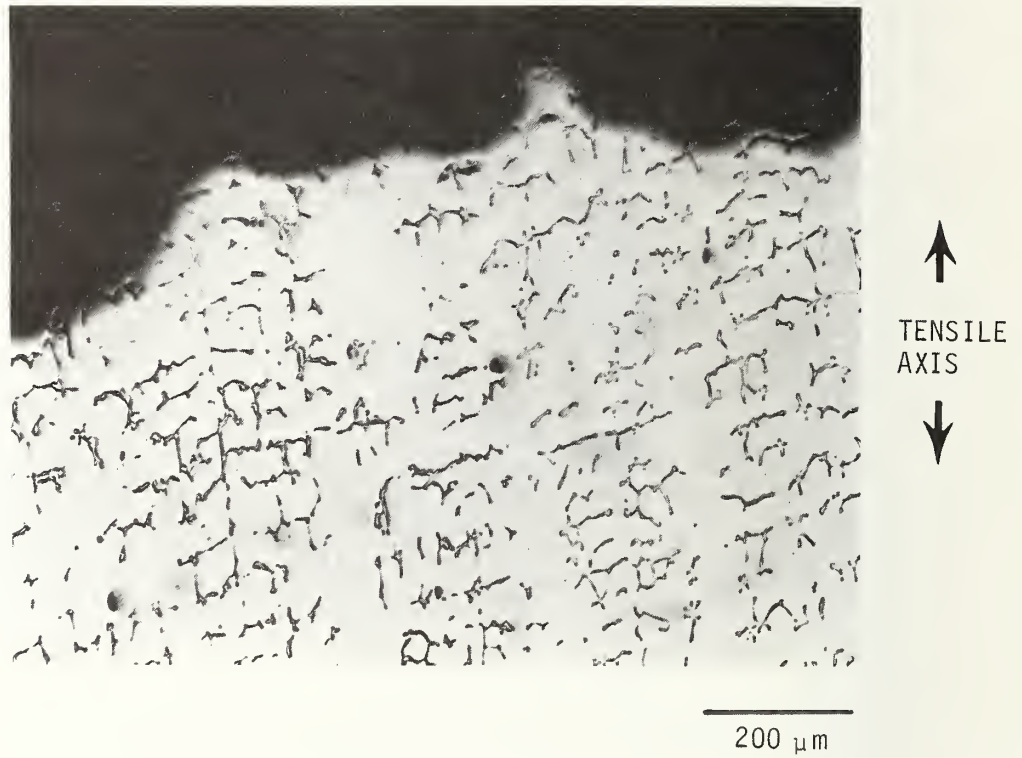


Figure 2

Micrograph of a 316L SA weld metal tensile specimen deformed at 4 K, showing that the ferrite does not deform at low temperatures. Oxalic acid etch.

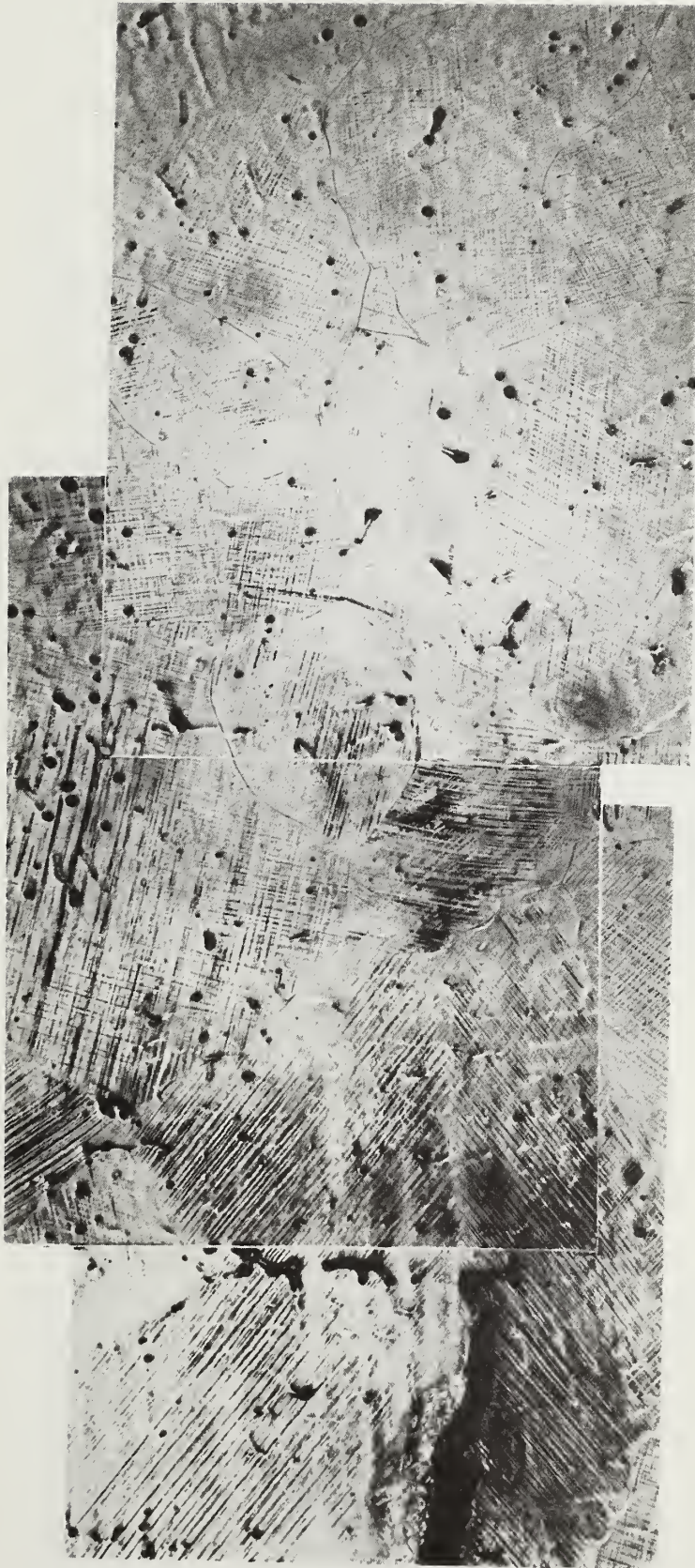


Figure 3 Area near the crack tip of a 0% ferrite CF8 casting. Oxalic acid etch.



Figure 4 Area near the crack tip of a 14.5% ferrite CF8 casting. KOH and oxalic acid etch.



50 μm

Figure 5 Micrograph of a 9% ferrite CF8M casting deformed at 4 K, showing the deformation of the austenite matrix around a ferrite particle. Color etch.



100 μm

Figure 6 Micrograph of a 316L electroslag weldment deformed at 4 K, showing the reinforcement of the austenite matrix by the ferrite particles. KOH and magnetic etch.



Figure 7 Area near the fracture surface of a tensile specimen from a 316L electroslag weldment. Oxalic acid etch.



Figure 8 Area near the crack of a 14.5% ferrite CF8 casting. KOH and oxalic acid etch.

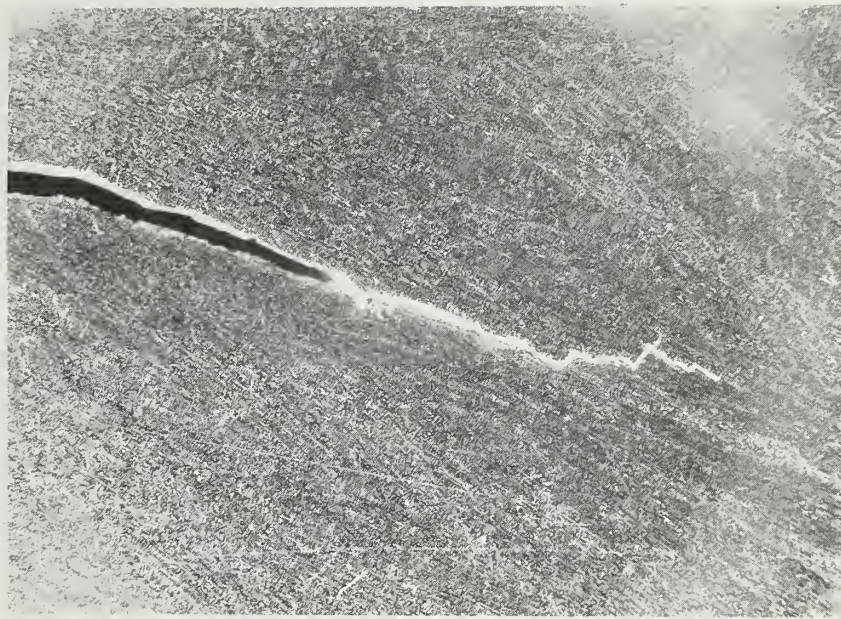


800 μm

Figure 9 Crack profile of a 9% ferrite CF8M casting.
Color etch.



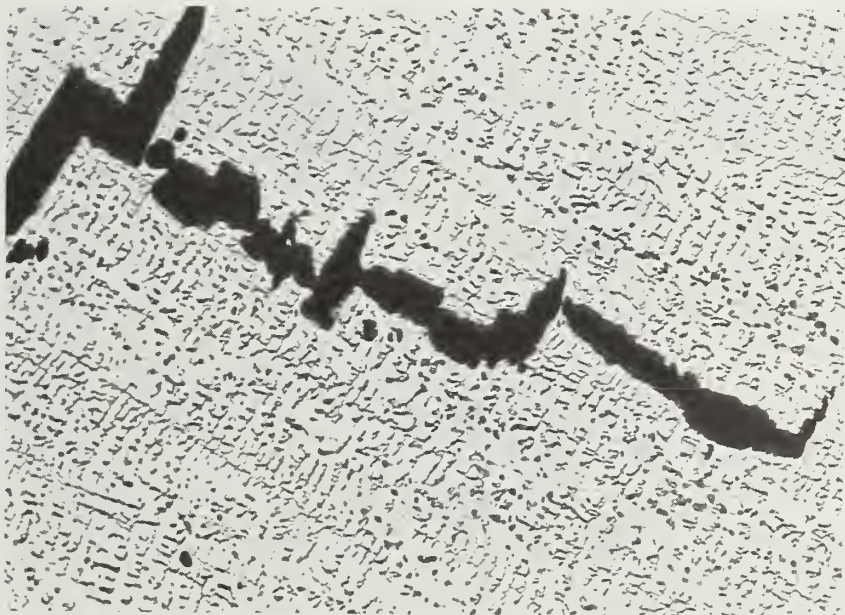
Figure 10 Crack profile of a 14.5% ferrite CF8 casting. KOH and oxalic acid etch.



↑
LOADING
DIRECTION
↓

5 mm

(a)



400 μm

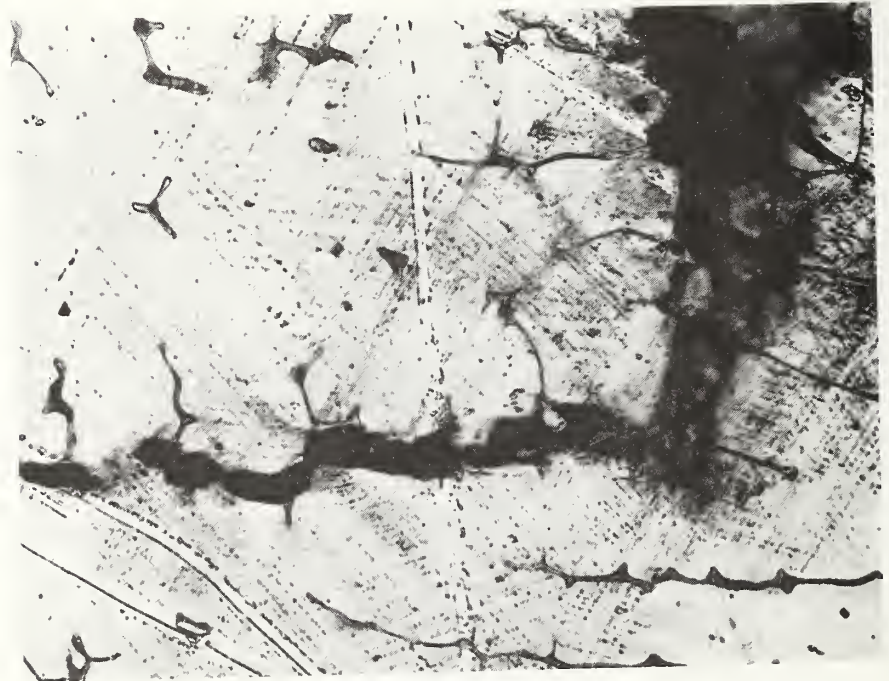
(b)

Figure 11 Crack profile of a 316L electroslag weldment. Oxalic acid etch.



(a)

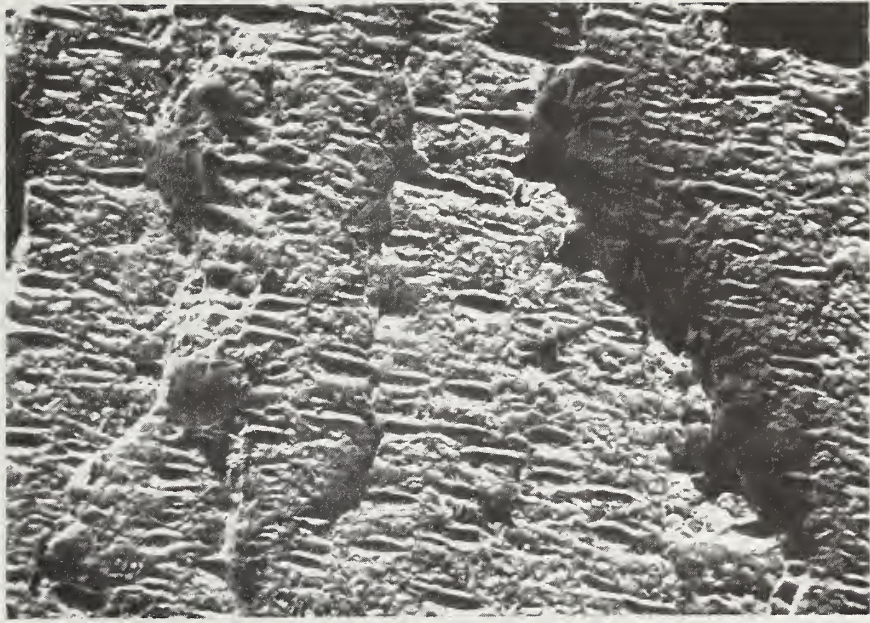
50 μm



(b)

50 μm

Figure 12 Micrographs of the crack tip of a 316L electroslag weldment. a) KOH etch, b) KOH and magnetic etch.



(a)

400 μm



(b)

50 μm

Figure 13 SEM fractographs of the fracture surface of a 316L electroslag weldment.



↑
LOADING
DIRECTION
↓

(a)

3 mm



(b)

1 mm

Figure 14 Macroscopic crack profile of a 308L FCMA weldment. Oxalic acid etch.

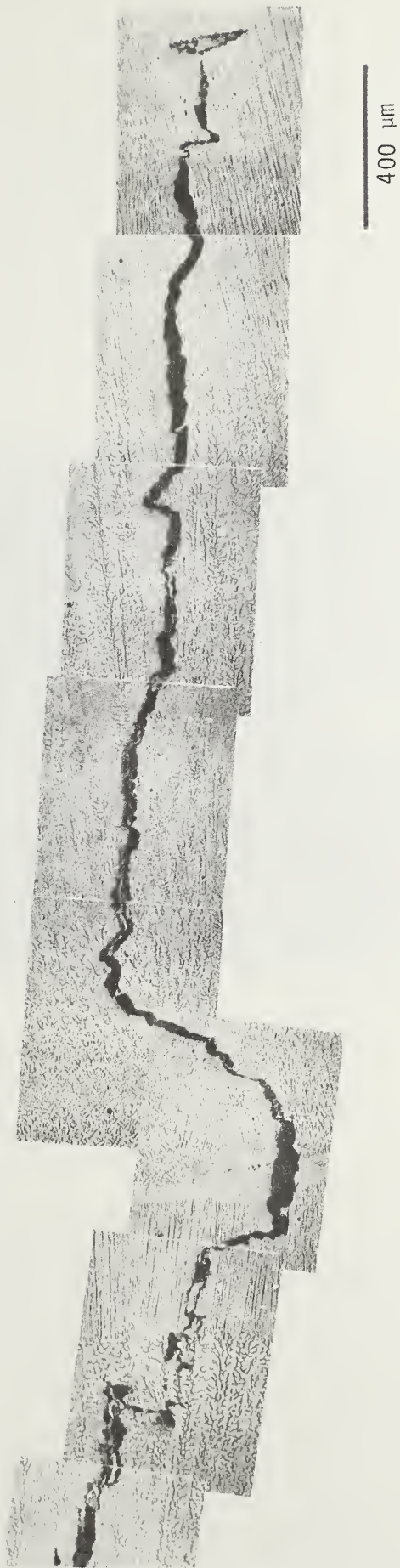


Figure 15 Micrograph of the crack tip region of a 308L FCMA weldment. Oxalic acid etch.

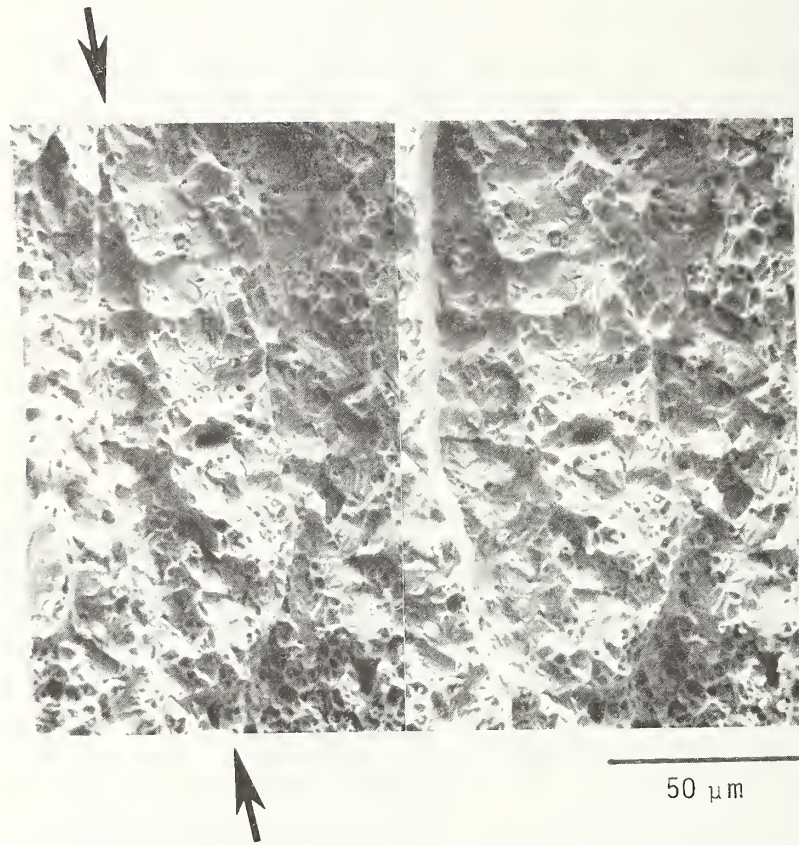
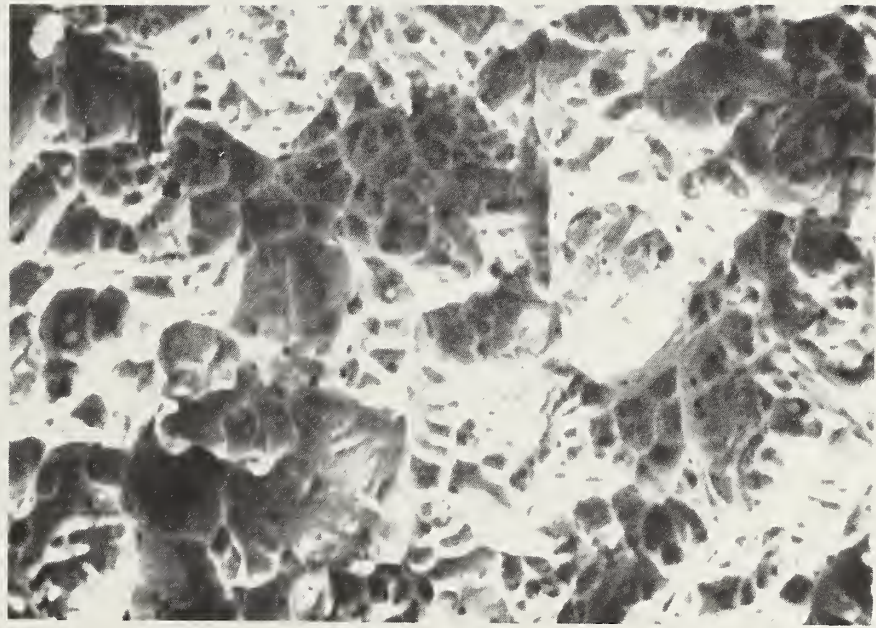


Figure 16 SEM stereo fractograph of a 308L FCMA weldment.



25 μm

Figure 17 SEM fractograph of a 308L FCMA weldment.

EVALUATION OF WELD FILLERS TO JOIN NITROGEN STRENGTHENED STAINLESS STEELS
FOR CRYOGENIC APPLICATIONS
(FUSION AND MHD ENERGY)

R. H. Espy
Armco Inc., Research and Technology
Middletown, Ohio

ABSTRACT

Tests are reported of austenitic stainless steel weldments that use filler materials manufactured outside the United States.

Evaluation of Weld Fillers to Join Nitrogen Strengthened
Austenitic Stainless Steels for Cryogenic Applications
(Fusion and MHD Energy)

R. H. Espy - Armco Research & Technology

US/USSR Technical Exchange Program
on Welding Stainless Steels

BACKGROUND INFORMATION

During the exchange visits of the Russian and United States Cryogenic Welding Groups both in the USA and Russia, information on weld fillers for joining the Nitrogen Strengthened Austenitic Stainless Steels was presented. While the weld compositions studied in the U.S.A. had acceptable strengths and toughnesses, there was some concern about the presence of micro fissure defects that were almost always present. The concern was mainly that of the effect of defects under cyclic loading conditions.

Initially the cooperative effort between the U.S. and USSR was to exchange sample weldments having defects typical of those encountered in welding fully austenitic stainless steels. During our first exchange it became evident that the defects we were talking about were metallurgical in nature (micro fissure) and the defects the Russian delegation was referring to were of the workmanship type like incomplete penetration, unfused or unwet areas, cold laps, entrapped slag, etc. Actually, we did not consider workmanship defects as being important because of our nondestructive test and repair practices which are very common and effective throughout the USA where high quality weldments are desired. On the other hand, the Russian group did not consider metallurgical defects like micro fissures because they did not occur with the weld fillers they were using. In general one might say that Russian weld metallurgy in this area appeared more advanced than in the U.S., but on the other hand that U.S. manufacturing technology appeared more advanced than the Russian manufacturing capability. The Russian approach of applying large numbers of people to technological problems appears to be the reason for this. In Russia's Paton Welding Institute alone there were, in 1979, 34 engineers and 17 technicians assigned to welding the stainless steels.

As a first step in resolving this major difference we inquired concerning the typical composition of the Russian weld filler. This was received along with a coil of bare wire for our laboratory evaluation. Just prior to our exposure to Russian technology in the exchange program, we at Armco decided to examine two foreign made weld fillers touted to be good for weldments used for

Cryogenics. One designated as Grinox 41 (stick electrodes) and Grinox 5 (bare wire) is made by Messer. Griesheim in Germany (distributed by MG Weld Products - Menomonee Falls, Wisconsin). The second designated as P6 (stick electrodes & bare wire) is made by Avesta in Sweden (distributed by A. Johnson & Co. - Lionville, Pennsylvania). The results of our work with these two wires are included with those of the Russian wire in this report.

COMPOSITION OF WIRES & WELD DEPOSITS

Analyses of the filler wires and weld deposits (for covered electrodes) showed them to have the following compositions. A typical composition of fully austenitic weld fillers studied in the U.S. is shown for comparison.

	<u>C</u>	<u>Mn</u>	<u>P</u>	<u>S</u>	<u>Si</u>	<u>Cr</u>	<u>Ni</u>	<u>Mo</u>	<u>W</u>	<u>N</u>
Russian Bare Wire	.027	6.7	.01	.003	.09	19.45	16.1	2.8	2.1	.23
German Grinox 41 Weld Deposit	.17	9.9	.012	.004	.80	15.6	12.4	-	2.3	-
Swedish Avesta P6 Weld Deposit	.03	4.9	.015	.001	.25	18.5	17.5	2.6	-	.17
U.S. Armco Weld Deposit	.05	9.0	.007	.009	.22	18.0	16.2	-	-	.18

PROCEDURE USED IN PREPARATION OF ALL-WELD TEST SPECIMENS

The weld geometry employed was as specified in AWS 5.4-79 except the base plate was 1" thick, the root opening was 3/4" and the buttered overlay was deposited as one layer using 5/32" ϕ Type 309 Stainless covered electrodes. The parameters for welding with the bare wire were as shown.

Weld Process - Automatic Gas Metal Arc (Pulse)
 Filler Wire - .062" ϕ X Coil
 Shield Gas - Argon + 2% O₂ at 30 CFH
 Weld Current - 160 amperes
 Volts - Average, 19.5
 Peak, 66.0
 Cycles - 120
 Weld Travel Speed - 15 IPM
 Stringer Bead Practice Used (No Oscillation)
 Weld Interpass Temperature RT/300°F

The parameters for welding with covered electrodes were as shown.

Weld Process - Shielded Metal Arc (Manual)
 Filler - 5/32" ϕ
 Weld Current - 100 amperes
 Weld Voltage - DCRP 24 volts
 Stringer Bead Practice Used
 Weld Interpass Temperature RT/300^oF

The .505" ϕ tensile and standard Charpy V-notch specimens were sectioned from the top center of each deposit. The notch in each Charpy specimen was oriented top to bottom of the weld deposit.

TEST RESULTS

All of the items welded in a satisfactory manner with the processes employed.

The room temperature and -320^oF tensile and Charpy data are shown below. Included again for comparison are data obtained with the U.S. weld filler.

Tests at Room Temperature

	Tensile				Toughness		
	UTS ksi	.2% YS ksi	% El 2"	% RA	Defects on Fracture Face	CVN '#	Defects on Fracture Face
Russian	104	73	41	56	None	114	1 ppt.
German Grinox 41	95	73	35	65	Some 11 ⁽¹⁾ Separations	116	None
Swedish Avesta P6	95	66	41	63	None	95	None
U.S. Armco	93	71	25	26	15% ⁽²⁾ M.C.	44	25% M.C.

Tests at -320^oF

Russian	186	133	19	26	5% ⁽²⁾ M.C.	68	3 small ppts.
German Grinox 41	173	118	31	31	Some 11 ⁽¹⁾ Separations	62	None
Swedish Avesta P6	179	123	40	40	None	37	None
U.S. Armco	162	134	10	12	10% ⁽²⁾ M.C.	13	20% M.C.

(1) Appear to be heat affected area grain boundary separations parallel to direction of welding.

(2) M.C. (Micro Condition) appear to be areas of grain boundary separations and weakness associated with the freezing pattern.

Metallographic examination of the weld structures to determine reasons for soundness or conversely lack of soundness, showed the molybdenum and tungsten bearing weld metals to contain coring or a phase that reacted sufficiently different to electrolytic etches so as to stand out significantly. These weld deposits were also free of grain boundary breaks in the high temperature heat affected areas of the multipass welds. The sensitized or lower temperature affected areas of the German Grinox weld contained many grain boundary precipitates of carbides. The tungsten and molybdenum free welds (U.S. - Armco) showed numerous grain boundary breaks in the high temperature heat affected zones. These structural conditions and their affect on tensile and impact tests are shown in Figures 1 to 4.

X-ray diffraction examination of the areas in the tungsten and molybdenum containing welds that showed a differential reaction to the etchants showed all areas to have the same crystal structures. The SEM analytical efforts were not successful in showing molybdenum and tungsten segregation, the elements believed responsible for the etching phenomena. Microprobe efforts with a Phillips AMI/3 Electron Microprobe to identify element separation were not successful. A new electron microprobe unit, Cameca CAMEBAS at Armco, with which it is believed that proper identification of the highlighted areas can be made will be in service shortly. The results from this effort will be reported separately when available.

DISCUSSION

The use of tungsten and molybdenum together as in the Russian wire or separately as in the German and Swedish electrodes is effective in controlling the high temperature hot short condition found to occur in the welds made with the U.S. - Armco electrodes.

All of the welds showed increased yield strengths at cryogenic temperatures confirming the fact that both N&C influence yield strengths as temperatures are lowered. The German Grinox electrode contained residual nitrogen (low) with C near .20% while all other Russian, Swedish and U.S. fillers contained N at about .20% with C at a low level.

While all of tungsten and molybdenum containing welds were acceptably sound and exhibited good properties at all temperatures there was a trend in the high carbon German alloy towards a tensile fracture pattern that reflected the presence of grain boundary carbides in lower temperature or sensitized areas of the multipass welds. While the Russian filler showed low indications of porosity and micro condition, both it and the Swedish alloy appeared overall quite good.

CONCLUSIONS AND COMMENTS

The use of tungsten and molybdenum in ferrite free stainless weld metal is effective in controlling the grain boundary breaks that have been found to occur in high N containing welds.

Normally ferrite in high nitrogen stainless welds is an effective means for producing sound defect-free welds, but ferrite when present has an adverse effect on toughness at cryogenic temperatures when associated with the high strength imparted by nitrogen.

While all ferrite-free stainless steel welds are prone to form some grain boundary breaks, the use of nitrogen for strength caused significant increases. The data reported shows that both tungsten and molybdenum are effective in controlling cracking with the processes used.

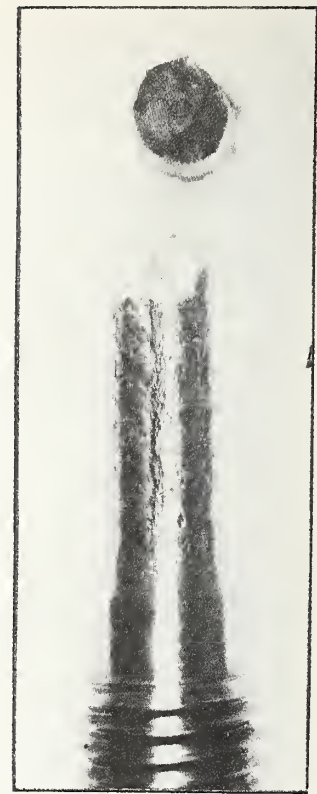
The German Grinox 41 (stick electrode) and Grinox S (bare wire) and Swedish Avesta P6 (stick electrode and bare wire) are commercially available for any added weld process work that may be desired. Armco is currently making an effort to produce the Russian wire so as to make it also available for additional weld process test work.

Overall the US/USSR exchange program has been beneficial in that the higher nitrogen stronger stainlesses like 304 LN (.15 N) and NITRONIC 40 (.30 N) can be considered for weldments at the liquid helium temperatures associated with fusion and MHD energy projects.

The initial objective of determining the effect of weld defects still remains to be addressed and should be considered in future exchanges. While the use of tungsten and molybdenum were effective in controlling the nitrogen induced grain boundary defect, there were indications that a small amount of the defect still occurred and this may vary with the weld processes employed. It is suggested that the program to determine the effect of defects be continued in future exchange visits.



Mag 8X
Fracture Face of CVN
Tested at -320°F



Mag 1.5X
Tensile Tested at
Room Temperature



Etchant NaOH Mag 500X
Coring or Phase in Ferrite-Free
Austenite

FIGURE 1: Impact, Tensile and Microstructure
for Weld Deposited Using Russian
Wire

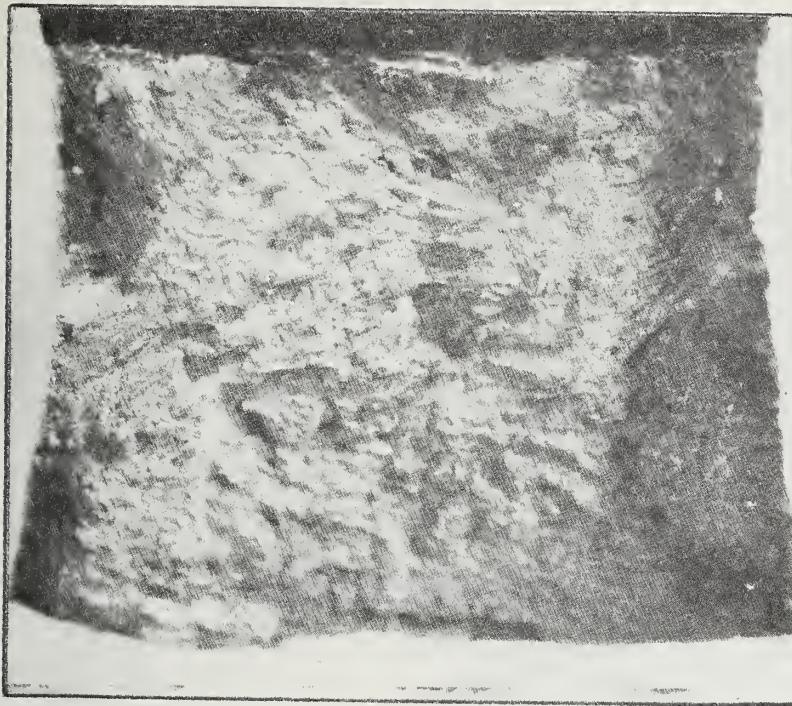
<u>C</u>	<u>Mn</u>	<u>P</u>	<u>S</u>	<u>Si</u>	<u>Cr</u>	<u>Ni</u>
.027	6.7	.01	.003	.09	19.5	16.1
		<u>N</u>	<u>Mo</u>	<u>W</u>		
		.23	2.8	2.1		

Toughness at -320°F

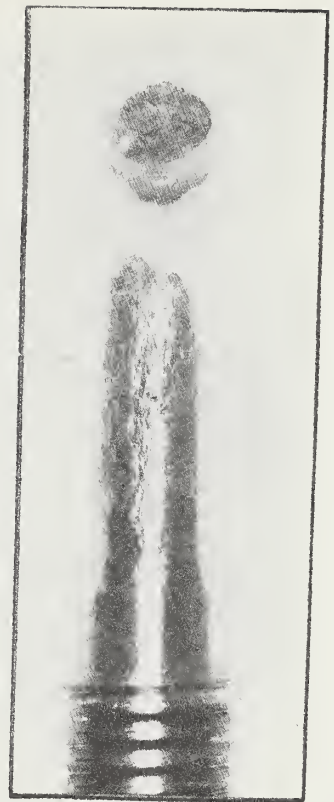
CVN Defects
68'# 3 small pts

Tensile at Room Temperature

<u>UTS</u>	<u>.2% YS</u>	<u>%El</u>		
<u>ksi</u>	<u>ksi</u>	<u>2"</u>	<u>%RA</u>	<u>Defects</u>
104	73	41	56	None



Fracture Face of CVN
Tested at -320°F



Mag 1.5X

Tensile Tested at
Room Temperature



Etchant NaOH Mag 500X

Coring or 2nd Phase in
Ferrite-Free Austenite

FIGURE 2: Impact, Tensile and Microstructure
for Weld Deposited Using German
Grinox 41 Electrodes

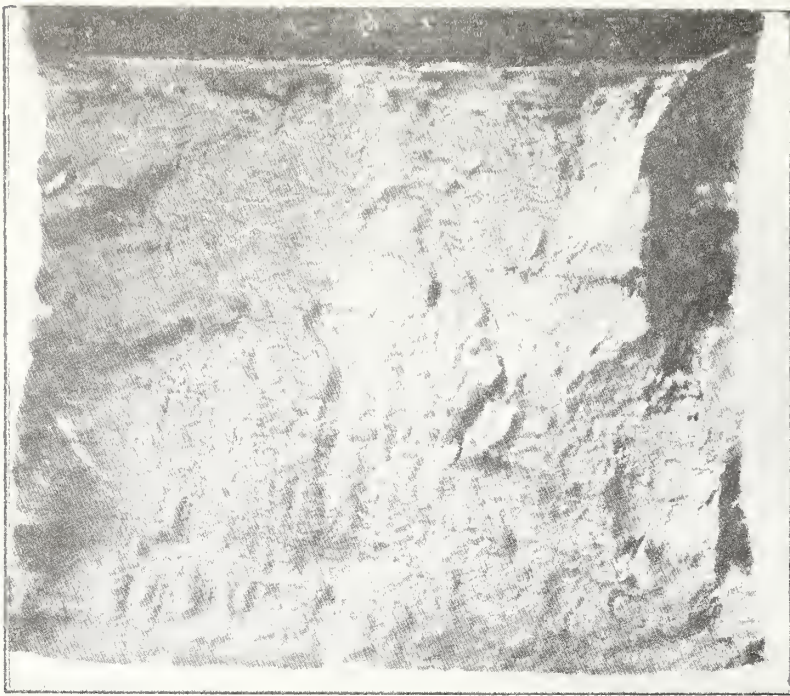
<u>C</u>	<u>Mn</u>	<u>P</u>	<u>S</u>	<u>Si</u>	<u>Cr</u>	<u>Ni</u>	<u>W</u>
.17	9.9	.012	.004	.80	15.6	12.4	2.3

Toughness at -320°F

<u>CVN</u>	<u>Defects</u>
62'#	None

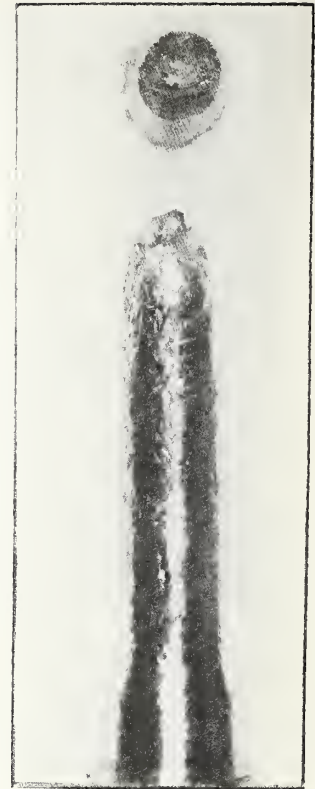
Tensile at Room Temperature

<u>UTS</u> <u>ksi</u>	<u>.2% YS</u> <u>ksi</u>	<u>%El</u> <u>2"</u>	<u>%RA</u>	<u>Defects</u>
95	73	35	65	Some ll Separations



Mag 8X

Fracture Face of CVN
Tested at -320°F



Mag 1.5X

Tensile Tested at
Room Temperature



Etchant NaOH Mag 500X

Coring or 2nd Phase in
Ferrite-Free Austenite

FIGURE 3: Impact, Tensile and Microstructure for Weld Deposited Using Swedish Avesta P6 Electrodes

<u>C</u>	<u>Mn</u>	<u>P</u>	<u>S</u>	<u>Si</u>	<u>Cr</u>	<u>Ni</u>
.03	4.9	.015	.001	.25	18.5	17.5
			<u>N</u>	<u>Mo</u>		
			.17	2.6		

Toughness at -320°F

<u>CVN</u>	<u>Defects</u>
37'#	None

Tensile at Room Temperature

<u>UTS</u>	<u>.2% YS</u>	<u>%El</u>	<u>%RA</u>	<u>Defects</u>
<u>ksi</u>	<u>ksi</u>	<u>2"</u>		
95	66	41	63	None

Mag 8X
Fracture Face of CVN
Tested at -320°F

Mag 1.5X
Tensile Tested at
Room Temperature

FIGURE 4: Impact, Tensile and Microstructure
for Weld Deposited Using U.S. -
Armco Electrodes

<u>C</u>	<u>Mn</u>	<u>P</u>	<u>S</u>	<u>Si</u>	<u>Cr</u>	<u>Ni</u>	<u>N</u>
.05	9.0	.007	.009	.22	18	16.2	.18

Toughness at -320°F

<u>CVN</u>	<u>Defects</u>
13'#	20% Micro Condition

Tensile at Room Temperature

<u>UTS</u>	<u>.2% YS</u>	<u>%El</u>		<u>Defects</u>
<u>ksi</u>	<u>ksi</u>	<u>2"</u>	<u>%RA</u>	
93	71	25	26	15% Micro Condition

Etchant Chromic Mag 500X
Grain Boundary Defects in
Ferrite-Free Weld Metal

NONMETALLICS

NONMETALLICS FOR MAGNET SYSTEMS

M. B. Kasen
Fracture and Deformation Division
National Bureau of Standards
Boulder, Colorado

ABSTRACT

An introduction to the nonmetallics program is presented. Topics discussed are: standard grades, radiation resistance, materials characterization, and technology transfer. Plans for FY 81 are presented.

The nonmetallics program has continued to respond to the needs of magnetic fusion energy (MFE) designers and fabricators by working with industry to provide commercial sources of standard grades of insulating laminates, emphasizing those grades that are most widely used in critical parts of superconducting magnets. The Annual Report for FY 79 (NBSIR 80-1627) reported the establishment of specifications for cryogenic grades of glass-fabric reinforced bisphenol A epoxy industrial laminates identified as G-10CR and G-11CR. The initial mechanical, elastic, electrical, and thermal property characterization data were reported to 4 K. This work has continued during FY 80, concentrating on refining the specification to achieve a balance between minimum performance variability at 4 K and minimum cost to the purchaser.

It was recognized at the outset that radiation resistance of the insulating laminates would be an important performance requirement. The G-11CR product was incorporated as an initial effort to achieve better radiation resistance than that of the more common and lower cost G-10 type laminates. Available data had indicated that the aromatic amine cure of the G-11 product should be beneficial. However, tests performed in the Oak Ridge reactor failed to confirm this expectation. Because this left the G-11CR, a fairly expensive material, with no overall performance advantage over the less expensive G-10CR, the G-11CR product was dropped from the list of standard laminate grades.

G-10CR is, therefore, the sole standard cryogenic grade at this time. Reception of this product by the cryogenic industry has been good, and it is presently being manufactured by three major U.S. laminating firms.

As originally conceived, the standard grades were to provide the basis for systematic material development in response to fabricators' needs, in addition to providing baseline materials having predictable cryogenic properties. Thus, a variant of the basic G-10CR product incorporating a lightweight glass cloth has been developed by one of the manufacturers. This variant, designated G-10CR-L, was required to increase the number of reinforcement layers in a thin wall thermal standoff for a Lawrence Livermore Laboratory magnet design.

Magnet fabricators also require a uniaxial glass-reinforced laminate product and would find it advantageous to have available a glass-mat-reinforced epoxy laminate having proven performance at 4 K. The uniaxial product would primarily serve in the fabrication of thermal standoff support straps, and the mat product would be, in many instances, a lower cost substitute for G-10CR, having the added advantage of isotropic properties in the plane of the laminate. Substantial progress has been made in working with industry to establish standard specifications for such materials.

Consideration has also been given to the possibility of establishing a laminate coding system that would permit the designer to specify the least expensive commercial material required to meet his needs without having to be intimately familiar with all of the parameters affecting insulating and structural laminate performance. This is long-range effort which, if successful, would encompass both standard cryogenic grades and the proprietary products of various manufacturers.

These considerations are further expanded in a publication "Standardization of Composites for Cryogenic Service" reproduced in this section of the report.

An example of industry interaction and participation is given by the discussions between NBS representatives and two industrial laminators during the NBS-DoE Vail Workshop that addressed refinement of the G-10CR specification. A copy of the Vail presentation by J. R. Benzinger entitled "The Manufacture of Radiation Resistant Laminates" is reproduced with the permission of Mr. Benzinger to provide background on the capability and limitations of industry in meeting the performance requirements of insulators for MFE magnets.

The materials characterization portion of the nonmetallics effort was continued in FY 80 with additional studies of the effects of cryogenic temperatures on the thermal conductivity of G-10CR and G-11CR laminates. An effort to measure conductivity of the epoxy matrices separately was only partly successful owing to inhomogeneity in the bulk resin. Such data would be of value in establishing models for predicting the conductivity of laminates of differing construction.

A glass-fabric-reinforced industrial laminate of European manufacture that had previously been evaluated at CERN was included in the NBS thermal conductivity program to provide a comparison of results between the two laboratories. For reasons not yet clarified, the NBS measurements indicated about a 45% higher conductivity at room temperature than did the experiment at CERN. It appears that the differences were due to experimental discrepancies between the laboratories rather than to specimen variabilities. Work to define the source of the differences is continuing.

The effect of temperature on the failure mode of insulating laminates must be understood if accurate predictions of the life-cycle performance of magnets are to be forthcoming. The document "Fracture Analysis of Compression Damage in Glass Fabric/Epoxy, G-10CR, 295 K to 4 K" included in this report reflects an initial effort in this direction. Compression failure was selected for study, since such stresses predominate in operating magnets.

The high anisotropy of composite laminates creates problems in measuring elastic constants by conventional strain gage methods. The effort to develop dynamic methods of obtaining such measurements has therefore been continued during FY 80. Such methods are attractive because the small specimen size facilitates the evaluation of anisotropic effects. But the necessary conditions for the dynamic moduli to be the technical equivalent of engineering moduli obtained by conventional techniques has not been established. The progress made during the past year in clarifying the equivalency is documented in the contribution entitled "Static and Dynamic Moduli of Two Fiber-Reinforced Composites".

The review paper entitled "Cryogenic Properties of Filamentary-Reinforced Composites: An Update" that appeared in the FY 79 report has been revised in part and submitted for publication to the journal Cryogenics. The major change was addition of a section on the radiation effects on composites, a copy of which is included in the present report.

Two miscellaneous contributions were made to the literature during FY80. A letter to the editor of the journal Composites comments on a contribution by K. Kadotani relating to the effect of cryogenic temperatures

on the performance of composite materials. Work at NBS has indicated that the authors' conclusions could lead to serious misjudgments in materials selection if they are misinterpreted. We also replied to an invitation from the American Society for Metals to contribute to their forthcoming issue "Technology Forecast '81". Copies of both these documents appear in this report.

We anticipate that the nonmetallics program for FY 81 will continue to emphasize the areas of materials standardization, materials research and characterization, and technology transfer. The standardization effort will pursue the introduction of standard cryogenic grades of glass mat and uniaxial glass-reinforced epoxy laminates. The characterization program will screen the performance of a G-10CR product from a third producer as well as that of a lightweight glass variant of this product. The performance of a polyimide-matrix variant of G-10CR will also be screened, because this laminate has shown substantially better radiation resistance than the epoxy grades. The research efforts will involve a cooperative program with industry to produce a cycloaliphatic epoxy resin variant of the basic bisphenol A G-10CR for future studies of radiation resistance. In-house research will attempt to resolve the noted discrepancy in laminate thermal conductivity and will continue to assess the validity of the dynamic method for determination of laminate elastic constants. Work will also begin on a system for precise measurement of viscoelastic effects in laminates as a function of temperature.

NONMETALLIC MATERIALS :
STANDARDIZATION

STANDARDIZING NONMETALLIC COMPOSITE MATERIALS
FOR CRYOGENIC APPLICATIONS

M. B. Kasen
Fracture and Deformation Division
National Bureau of Standards
Boulder, Colorado

ABSTRACT

The designer of superconducting magnet systems is confronted with a difficult task in specifying the nonmetallic insulating and structural support materials required for proper system functioning. He finds it necessary to select from a profusion of products identified by trade names, most of which were developed for other than cryogenic use and for which reliable cryogenic performance data are nonexistent. This paper describes the ongoing efforts by NBS and industry to provide a commercial supply of standardized cryogenic grades of the most widely used insulating laminates having well-characterized cryogenic performance. These laminates will also provide the basis for a systematic materials development program in response to user needs. The elements required for a more generalized laminate coding system incorporating all materials of interest to magnet designers are also considered.

INTRODUCTION

The technology of composite materials is presently at the state that metals technology was before being systematized by the establishment of industry standards. It is difficult to imagine working in metals technology in the United States without the ability to associate performance with designations such as 304L for stainless steel or 2024-T4 for aluminum. It would be equally difficult for individuals in other countries to perform effectively without similar national metal and alloy coding systems that transcend proprietary designations, but this is the situation presently confronting those working in the composite materials area, in the United States and elsewhere.

Up to the present time, the problem has not been of major concern because the consumption of high-performance composites has been relatively low. However, consumption is expected to increase greatly as escalating energy costs place premiums on lightweight, fuel-efficient transportation systems and the development of alternative energy sources. It will become increasingly difficult to meet the future needs of composite technology with proprietary systems or with laminates fabricated from the few formulations published in the literature.

The need for composite materials standards is therefore common to many industries. As reflected in the forum chaired by Evans at the 1979 ICMC/CEC conference,¹ the need of the cryogenic industry is particularly acute. This industry is already at the point where many of the nonmetallic materials needs of magnetic fusion energy (MFE), magneto-hydrodynamic (MHD), and rotating cryogenic machinery systems cannot be adequately met by existing commercial products.

A primary problem is the inability to associate reliably the cryogenic performance required for diverse applications with the profusion of products identified by trade names, most of which were developed for other purposes. This paper outlines the current thinking of the author on this overall problem and describes the efforts currently underway to meet the immediate industrial cryogenic requirements. The author hopes that these considerations may be combined with similar considerations based on European experience to contribute to the eventual establishment of workable international standards for nonmetallic materials.

The author will concentrate on nonmetallic composite materials, reflecting the current need for such materials in the fabrication of the cryogenic portions of new energy systems. It is recognized, however, that unreinforced polymers pose a similar standardization problem.

IMMEDIATE CONCERNS

The immediate task is to assist designers and fabricators in the selection of dependable insulating and structural nonmetallic laminates for MFE and MHD systems presently being built in the United States. The high costs of these systems and the substantial performance demands made on the laminates require that the selected materials be well characterized at cryogenic temperatures and the variability in performance be minimized. Because the present systems will provide experience that can be extrapolated to more sophisticated, larger systems, the selected materials must be commercially available over a period of years. Furthermore, they must lend themselves to a systematic materials development program in response to industry needs. These boundary conditions

imply that control over the constitutive elements, manufacturing processes, and performance characterization will be necessary.

Current construction will necessarily draw on state of the art, commercially available nonmetallic laminate materials developed for other than cryogenic service. In the past, many proprietary products have been used. However, this approach is inefficient for demanding applications since it requires that each group responsible for a design conduct an expensive in-house materials characterization program. It must also be assumed that the selected proprietary product will not be substantially altered in response to market forces outside the cryogenic area. The alternative of purchasing laminates to specified cryogenic performance criteria either requires the manufacturers to develop cryogenic quality-control procedures or assumes that room-temperature data can be confidently extrapolated into the cryogenic range. Unfortunately, the latter concept is rudimentary for most conventional properties and nonexistent for special-performance requirements under irradiation at cryogenic temperatures.

A third alternative is to establish uniform industry specifications for manufacturing a series of well-characterized nonmetallic laminates having the greatest application to cryogenic technology. This approach recognizes that many of the inexpensive commercial laminates developed for room-temperature applications are useful cryogenic materials, whose primary deficiencies are the lack of a cryogenic data base and an excessive variability when used in a temperature region for which they were not intended. Establishment and characterization of uniform specification laminates addresses these deficiencies and provides designers with materials having greatly improved cryogenic reliability at minimum

cost. Furthermore, the uniform specifications assure that the critical material factors affecting performance will be controlled by the cryogenic industry, providing the basis for a systematic materials development program that reflects the needs of the industry.

We have been following this approach in working with the United States laminating industry to develop a series of standard, high-pressure industrial laminates for cryogenic service. Both the industry and the coordinating standards group, the National Electrical Manufacturers Association (NEMA) have been most cooperative. Thus far, two grades of glass-fabric-reinforced epoxy laminates have been established, characterized, and placed in commercial production. These materials are designated G-10CR and G-11CR to distinguish them from the conventional NEMA G-10 and G-11 products. Performance data for these cryogenic grades have been published in the literature.² Acceptance by the cryogenic industry in the United States has been gratifying. Work is continuing at NBS in cooperation with industry to develop additional standard specifications for other laminate systems of interest to cryogenics, possibly including random-mat and uniaxial glass-reinforced epoxy-matrix laminates.

These developments are meeting the immediate needs of industry while providing the basis for systematic alteration in the performance of standard materials in response to developing industrial needs. The concept of the overall program is outlined by the flow chart of Fig. 1. Built-in iteration steps provide the open-ended type of program required to be responsive to continually developing needs. The sequence depicted for development of the CR grades of G-10 and G-11 illustrates the progress up to the present time. The characterization data indicate that these products will perform very well in most applications.

Studies at the Oak Ridge National Laboratory, however, have shown that the mechanical properties of these laminates are severely degraded by 4-K neutron and gamma irradiation at fluences comparable to those expected in a functioning MFE reactor.^{3,4} This deficiency is being addressed by a subprogram to develop laminates having improved radiation resistance. The first step will be to determine if radiation resistance will be significantly improved by replacing the epoxy matrix of the G-10CR laminate with a polyimide matrix.

It appears to the author that such a program would also entail an iterative cycle like the one illustrated in Fig. 2. Because the cryogenic radiation resistance of a polymer is likely to be a strong function of the exact molecular structure,⁵ an essential part of the cycle is a correlation of molecular-level damage with radiation level and property change. Only in this way will the required scientific basis be established. The program envisions the development of methods for preliminary screening of 4-K radiation resistance in the laboratory prior to confirmatory testing in a reactor. It is evident that considerable new ground will have to be broken in solving the radiation problems in nonmetallic materials.

A major deficiency in the approach thus far discussed is the absence of an industry standards group having the responsibility for coordinating, updating, and disseminating information on developed standards. The NEMA organization is performing the disseminating function for the CR-grade laminates through their Industrial Laminates Subcommittee, but NEMA interest is confined to high-pressure, bulk laminates. An organization responsive to the broader interests of the composite materials industry is required.

LONG-RANGE STANDARDIZATION NEEDS

The above approach lacks the comprehensiveness required to assure orderly overall composite materials development and implementation in the long run. The author agrees with Evans that the most effective way of alleviating the present chaotic state of nonmetallic materials technology would be to introduce a numerical classification system based upon key elements of a material that affect performance.¹ Here, the cryogenic industry has much in common with other industries exploiting composite technology.

There seems no a priori reason why such an approach would not be feasible for composite laminates, when one recognizes that the significant engineering properties of a laminate at any temperature are largely defined by relatively few parameters. For example, the intrinsic mechanical, elastic, thermal, and electrical properties of a laminate should be defined within relatively narrow limits by a numerical classification system that establishes the type and flexibility of the matrix, the type and configuration of the reinforcement, and the reinforcement volume fraction. At the very least, it should be possible to establish meaningful lower bounds on such properties. Special properties, such as radiation resistance, could continue to be associated with controlled-specification products that could be incorporated into the basic coding system.

It is beyond the scope of this paper to suggest a definitive system, but it is worthwhile to consider the general form that such a coding or classification system might take. One possibility, paralleling metals practice, is illustrated in Fig. 3. Here, the first

letter(s) and number define the matrix and reinforcement class, identifying the composite as being in a general category, such as epoxy-glass or polyimide-graphite. A following letter defines the reinforcement configuration, e.g., E1U would define a uniaxially reinforced, epoxy-glass composite. The next two digits define the nominal fiber volume fraction. A $\pm 3\%$ range would be sufficiently precise and would be compatible with existing manufacturing practice. An E1U60 coding thus defines a $60 \pm 3\%$ volume fraction uniaxial glass-epoxy laminate. The performance of such a laminate could be quite definitively established by adding general information on the degree of matrix flexibility and specific information on the type of reinforcement. Thus, a designation E1U60U-E would not only define a 60% volume fraction uniaxial E-glass reinforced, fully reacted epoxy-matrix laminate but would simultaneously establish meaningful intrinsic performance bounds on the laminate performance. Extrinsic factors related to laminate quality, such as void content and interply bond integrity, will affect performance, but such factors must be independently assessed for all laminates.

The fabric used to reinforce laminates is frequently unbalanced, usually having a lower fiber content in the fill direction of the weave than in the warp direction. For example, a type of 7628 glass weave commonly used in the United States has a fill/warp ratio of 32/42. In the scheme of Fig. 3, information on this unbalance is provided by a two-digit number defining the fill/warp fraction, or 76 in the cited case.

This type of system offers flexibility in establishing coding at the specific level required for the application of interest. The cryogenic industry would probably be reasonably well served by the categories listed in Table I. The list could be expanded or individual

designations could be made more or less specific as need arises. Some cryogenic data already exist for most of the materials on this list, although in no case are the data sufficient for establishment of statistically significant lower performance bounds.

A standardization scheme of this type would simplify materials selection and purchase; furthermore, it would minimize costs by providing the maximum flexibility to the laminating industry in meeting the requirements.

Consider, for example, the purchase of a G-10 type of laminate widely used in superconducting magnet construction in the United States. Under the present system, the cryogenic performance of this type of laminate purchased on the open market can vary by 30%, if produced by a reliable laminator, or more, if produced by marginal fabricators. Specifying the CR grade would solve the problem for critical applications; however, the premium paid for this grade may not be justified for many applications. Here, the illustrated classification system provides a solution by allowing the purchaser to specify an E1F48U-E/76 laminate if the generic equivalent to the CR grade was desired or to specify an E1F40U-E/76 laminate as a minimum requirement if greater property variability is acceptable. An E1F40U-E/XX specification would result in still further economy by removing the requirement for a specific fill/warp ratio.

SUMMARY

The author has described the ongoing efforts in the United States to provide a commercial supply of specific controlled-performance laminates required to meet the short-term needs of the cryogenic industry.

This approach also provides the basis for a systematic materials development program required to meet future needs, but the current effort addresses only the most demanding usage of nonmetallic laminates in cryogenic construction. The overall long-range requirements of the cryogenic industry justify consideration of a more comprehensive system of nonmetallic laminate classification that would simplify materials selection while minimizing costs. An example of such a system is provided to illustrate its potential benefits to both the consumer and the producer.

ACKNOWLEDGMENT

This work was supported by the Office of Magnetic Fusion Energy, United States Department of Energy.

REFERENCES

1. D. Evans, in Advances in Cryogenic Engineering, Vol. 26, Plenum Press, New York (1980), p. 83 (in publication).
2. M. B. Kasen, G. R. MacDonald, D. H. Beekman, and R. E. Schramm, in Advances in Cryogenic Engineering, Vol. 26, Plenum Press, New York (1980), p. 235 (in publication).
3. R. H. Kernohan, R. R. Coltman, and C. J. Long, Radiation Effects on Insulators for Superconducting Magnets, ORNL/TM-6193, Oak Ridge National Laboratory, Oak Ridge, TN (1978).
4. R. H. Kernohan, R. R. Coltman, and C. J. Long, Radiation Effects on Organic Insulators for Superconducting Magnets, ORNL/TM-7077, Oak Ridge National Laboratory, Oak Ridge, TN (1979).
5. B. S. Brown, Radiation Effects in Superconducting Fusion Magnet Materials, submitted to J. Nucl. Mater. (1980).

Table 1. Laminate Classifications of Primary Interest to Cryogenic Technology[#]

Laminate Category	Suggested Coding
Uniaxial Glass-Epoxy	E1U55U-E* E1U55U-S2 E1U55U-S
Glass Fabric-Epoxy	E1F48U-E/76* E1F40U-E/76 E1F40U-E/XX
Glass Mat-Epoxy	E1M35U-E*
Glass Fabric-Polyester	PE1F45U-E/76 PE1F40U-E/76 PE1F40U-E/XX
Glass Mat-Polyester	PE1M35U-E
Glass-Polyester Pultrusion	PE1F45U-E/11(P)*
Cotton Fabric-Phenolic	PH5XXU
Glass Fabric-Melamine	M1F45U-E/76 M1F40U-E/XX
Uniaxial Aramid-Epoxy	E2U60U-49
Aramid Fabric-Epoxy	E2F50U-49/94
Uniaxial, High-Strength Graphite-Epoxy	E3U60U-HS
Fabric, High-Strength Graphite-Epoxy	E3F60U-HS/100
Uniaxial, Medium-Modulus Graphite-Epoxy	E3U60U-M
Uniaxial, High-Modulus Graphite-Epoxy	E3U60U-HM
Uniaxial, 5.6-mil Boron-Epoxy	E4U50U-56

[#]For illustration purposes only.

*Classifications meriting development of special cryogenic grades.

List of Figures

- Fig. 1. Flow chart depicting a proposed approach to meeting immediate needs of nonmetallic laminate development for the MFE, MHD, and rotating cryogenic machinery industries. Dashed lines depict the present state of development of the G-10CR and G-11CR grades of industrial laminates.
- Fig. 2. Suggested flow chart for development of radiation-resistant nonmetallic laminate insulators.
- Fig. 3. Possible coding system for classifying nonmetallic composite laminates.

List of Tables

- Table 1. Laminate Classifications of Primary Interest to Cryogenic Technology.

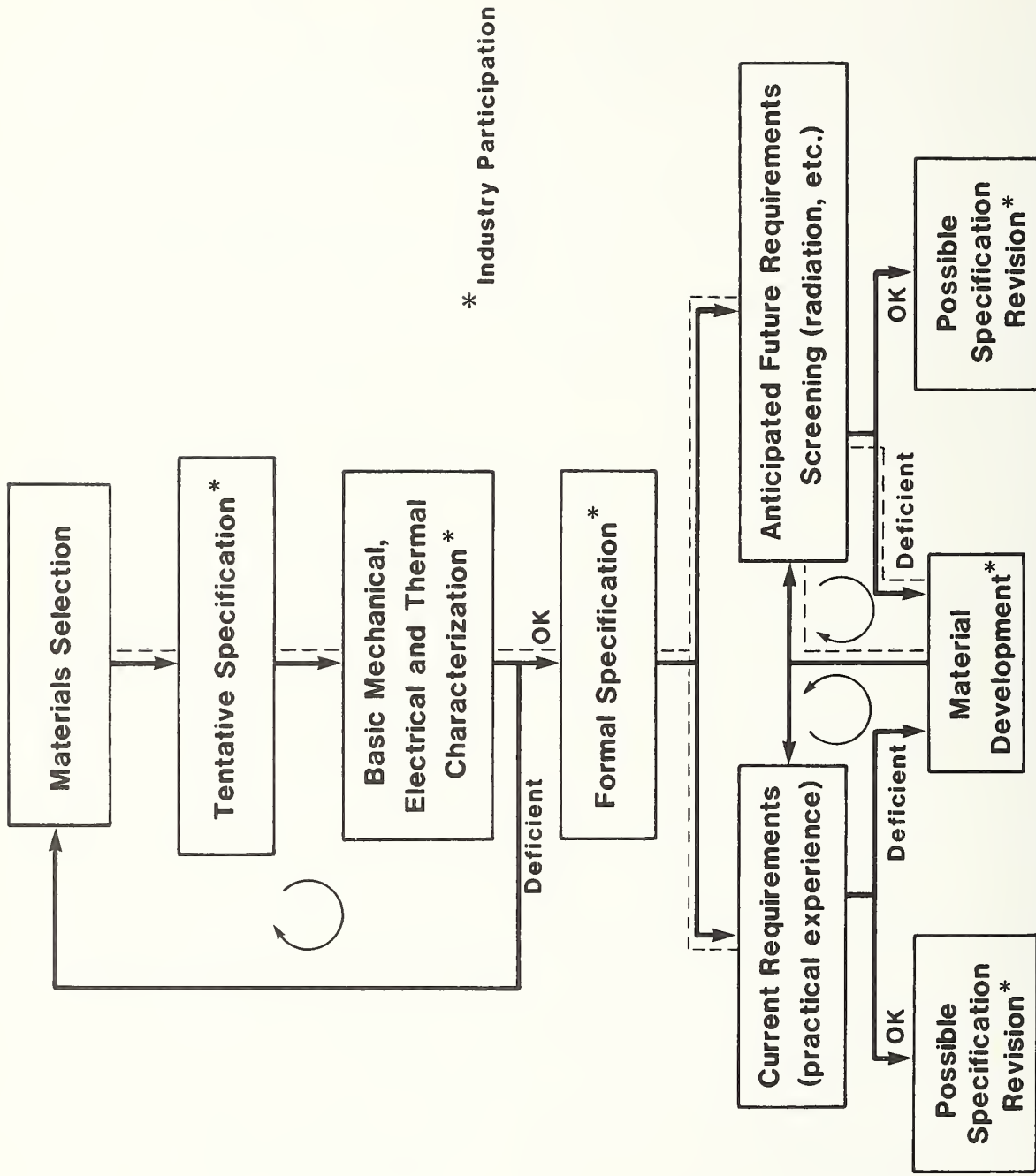


Fig. 1. Flow chart depicting a proposed approach to meeting immediate needs of nonmetallic laminate development for the MFE, MHD, and rotating cryogenic machinery industries. Dashed lines depict the present state of development of the G-10CR and G-11CR grades of industrial laminates.

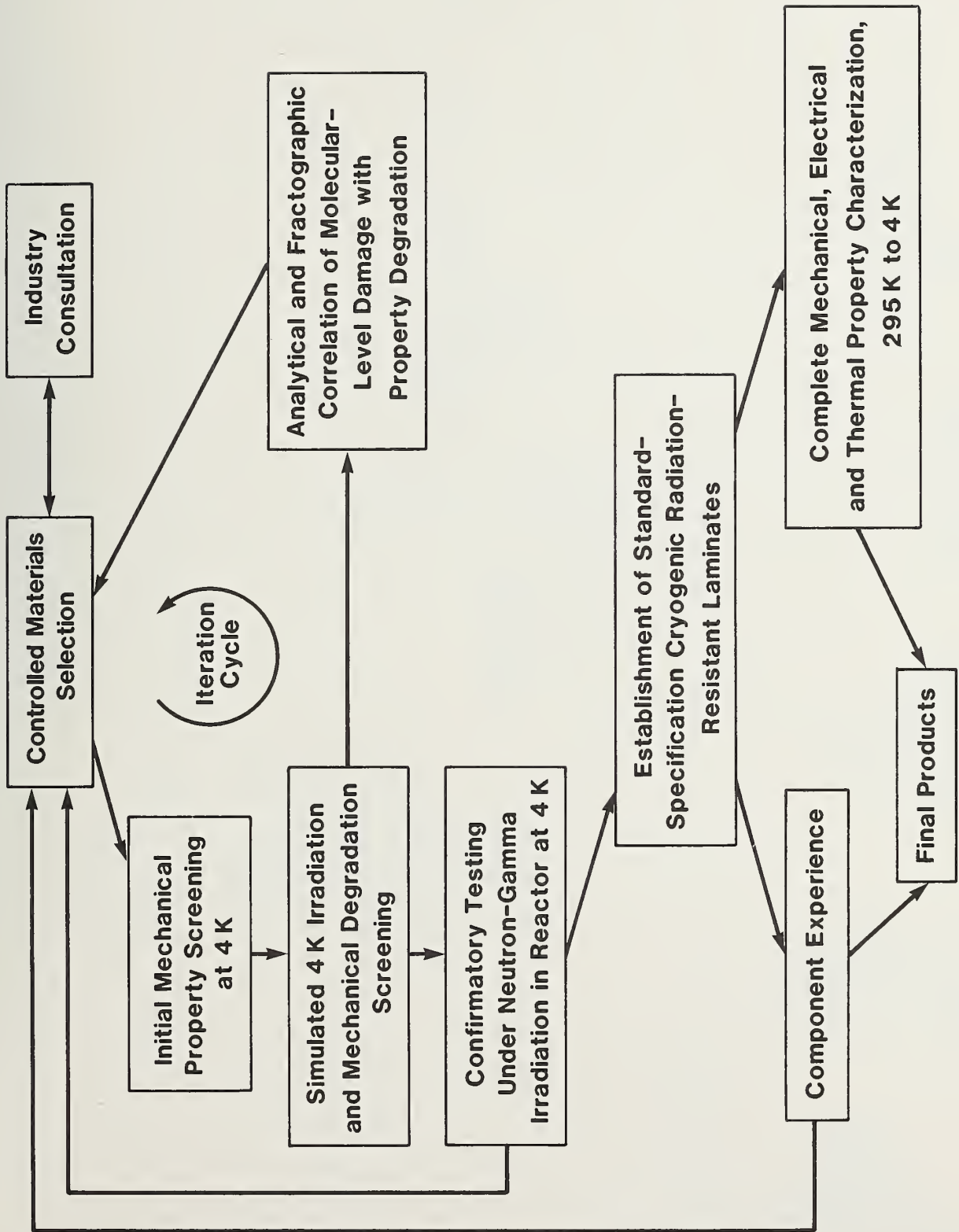


Fig. 2. Suggested flow chart for development of radiation-resistant nonmetallic laminate insulators.

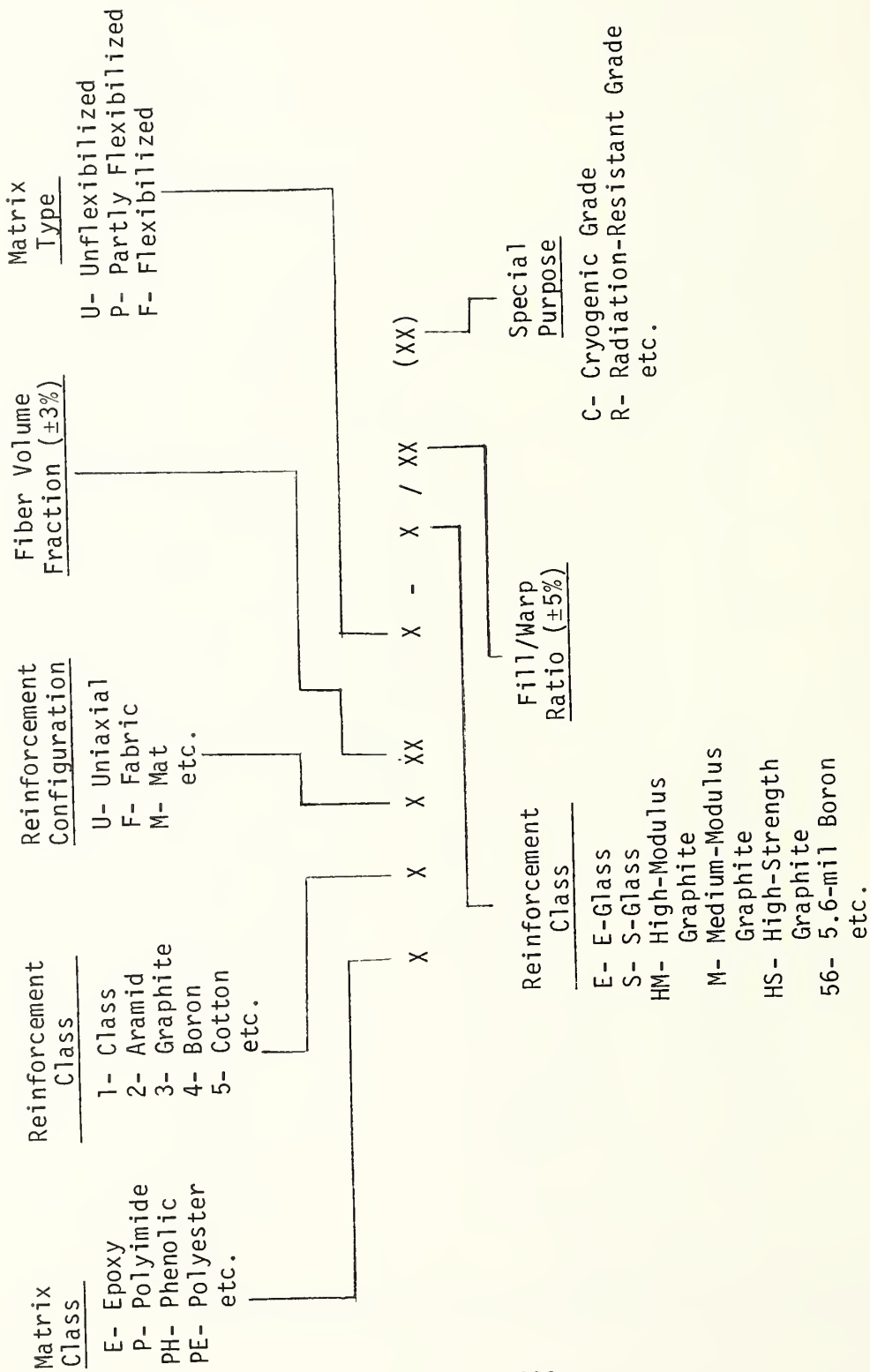


Fig. 3. Possible coding system for classifying nonmetallic composite laminates.

NONMETALLIC MATERIALS:
RESEARCH AND CHARACTERIZATION

THERMAL CONDUCTIVITY OF G-10CR AND G-11CR INDUSTRIAL
LAMINATES AT LOW TEMPERATURES (PART III)

J. G. Hust and R. Boscardin
Thermophysical Properties Division
Continuous Process Technology Programs
National Bureau of Standards
Boulder, Colorado

ABSTRACT

Thermal conductivity measurements from 2 to 300 K were made on the resins used in two cryogenic grades of fiberglass/epoxy composites, G-10CR and G-11CR. Effects of specimen thickness and inhomogeneity of the bulk sample were studied.

Also, the thermal conductivity of a European glass-fiber/epoxy composite was measured to assess the variation between measurements at CERN and at NBS. The accuracy of the NBS measurements was checked by measurements on a standard reference material.

INTRODUCTION

Extensive low-temperature electrical, thermal, and mechanical properties characterization of cryogenic grades of G-10 and G-11 fiberglass epoxy composites are being performed at the National Bureau of Standards. These special laminate grades, referred to as G-10CR and G-11CR, meet NEMA Grades G-10 and G-11, MIL-P-18177C, and federal specification LP-509.

In a previous report (Part I),¹ thermal conductivity data were presented for G-10CR and G-11CR at temperatures from 2 to 300 K for heat flow in both the normal and warp directions. These data indicated that the two laminates, produced by a single manufacturer (manufacturer A), had the same conductivity within about 10%. Also, it was found that the warp direction conductivity was about 20% higher than that in the normal direction.

In Part II of these reports,² data were presented showing the differences in thermal conductivity on specimens obtained from another manufacturer (B) and the effect of large strain. Preliminary data were also presented for thermal conductivity of the resins used in G-10CR and G-11CR. Further measurements on these resins and the conclusions are presented here.

In addition, this report (Part III) contains data on a European glass fiber/epoxy composite (Vetronite* 432.81).³ The purpose of these measurements is to clarify the cause of apparently large differences between NBS and CERN data on materials expected to be quite similar. The Vetronite was measured at both laboratories for direct comparison on a single sheet of material. The NBS measurements were also performed on various thicknesses to illustrate the absence of significant systematic errors due to interfaces and radial heat losses.

*Tradenames are used to describe adequately the materials studied. No endorsement of a particular product by NBS is implied.

MATERIAL AND SPECIMEN CHARACTERIZATION

G-10CR resin is a heat-activated amine-catalyzed bisphenol A, solid-type, epoxy resin. G-11CR resin is an aromatic amine bisphenol A liquid-type epoxy resin. The G-10CR resin has an uncured density of $1.10 \pm 0.01 \text{ g/cm}^3$ and the G-11CR resin has an uncured density of $1.04 \pm 0.01 \text{ g/cm}^3$.

The resin specimens were cut from blocks supplied by the manufacturer. The dimensions, masses, and calculated densities of these specimens are given in Table 1. The resin density calculated from data for the composites (reported earlier) is $1.25 \pm 0.01 \text{ g/cm}^3$ for both resins. Note that the measured densities of the G-10CR and G-11CR resins are 1.180 g/cm^3 and 1.227 g/cm^3 , respectively. The specimens designated as G-10CR resin (a) and (b) are the two obtained by cutting the original specimen in two, to study the effect of thickness and inhomogeneity.

A sheet of the Vetronite material, measured by K. D. Peterson of CERN, was obtained and twelve square specimens were cut from it. These were fabricated by cutting two 1.9 cm wide strips from the supplied sheet. Each of the two strips were further sectioned into six equal pieces. The twelve resulting pieces were machined to their final dimensions. Their dimensions, masses, and densities are given in Table 1. Measurements were performed on selected groups of these specimens to obtain thermal conductivity values as a function of thickness.

EXPERIMENTAL PROCEDURE AND DATA ANALYSIS

The thermal conductivity of the test specimens is determined using a thermal conductivity integral apparatus. This apparatus is described in detail by Hust and Arvidson.⁴ The estimated uncertainty of the results is 5%, unless

otherwise noted, as verified by measurements on NBS standard reference material SRM 735.

The data range is normally 2 to 300 K and the data are normally spaced approximately logarithmically within this range. The measured thermal conductivity integrals are fit by a special least squares technique (see Hust and Arvidson [1]) to yield the parameters for the following equation:

$$K(T) = \sum_{i=1}^n A_i [\ln(T + 1)]^i \quad \text{Eq. 1}$$

RESULTS AND DISCUSSION

To facilitate future analysis of composite data, measurements were performed on specimens fabricated from the pure resins used in G-10CR and G-11CR (see Table 1). These specimens were prepared from cured pieces supplied by the manufacturer. Twenty-one data points between 2 and 304 K were obtained on the original G-10CR resin specimen and sixteen data points were obtained from 4 to 304 K on the G-11CR resin specimen. The results, essentially the same within the precision of the data (+4%) for both resins, are illustrated in Figure 1. These values, however, are more uncertain and imprecise than usual because the specimen thicknesses were too large for optimum accuracy. Because of this potential problem with these first sets of data and because of the possibility of thermal radiation effects in these nearly transparent specimens, it was decided to section the G-10CR resin specimen to produce two thinner specimens. The thinnest specimen, about 1/3 the original thickness (see Table 1), was measured at 18 temperatures from 4 to 300 K. The results, appreciably lower (25%) than the original G-10CR resin data, are illustrated in Figure 1. This large difference was not understood and led to a series of measurements near

room-temperature. The results of the room temperature measurements are given in Table 2.

The conclusion reached from these measurements is that there is a significant inhomogeneity in the G-10CR resin specimen. The source of this inhomogeneity is uncertain but it is likely to be found in the original resin-mixing and block-curing procedure. The results of the measurements on specimens #1, (a), (b) and (a + b) suggest that the thermal conductivity is greater near the middle of the specimen, since both the results of the original measurement on the whole specimen and the later measurement on the reassembled specimen (a + b) were higher than (a) or (b) measured separately. It is also noted that the reassembled specimen resulted in an intermediate value, which is consistent with the above conclusion, since the center section was partly removed by cutting. The average thermal conductivity of nonhomogeneous specimens can be direction dependent, i.e., the results can depend on whether the hot face is on the low-conductivity side or the high-conductivity side. This effect is not quantified, because the orientation of the specimen in the chamber was not recorded in all cases. Whether the G-11CR resin specimen contains similar inhomogeneities is unknown because it was not sectioned. Since the percentage difference in thermal conductivity between the small and large G-10CR resin specimens is essentially independent of temperature, the thermal radiation component to total heat transfer is small compared with the conduction component.

One Vetronite specimen was measured near room temperature for comparison with the CERN data. In addition, as a check on the possibility of systematic errors due to interface resistance, radial heat losses, and the calibration constant of the probe, measurements were performed on randomly selected pieces

in the form of stacks (2 thick, 4 thick, and 12 thick). The results of the measurements are given in Table 3. These data reveal only a very small systematic deviation as a function of thickness. The constancy of the results over the extremes of thickness used here illustrate that boundary layer resistance (at the smallest thickness) and radial heat losses (at the largest thickness) are not significant experimental errors. In all cases, these results are about 45% higher than the results from CERN. This confirms that the differences are truly experimental in nature and not specimen differences. The possibility of systematic errors in the NBS thermocouple calibrations and other instrumentation calibrations has been ruled out by measurements on SRM 735.⁴

REFERENCES

1. J. G. Hust, "Thermal Conductivity of G-10CR and G-11CR Industrial Laminates at Low Temperatures," in Materials Studies for Magnetic Fusion Energy Applications at Low Temperatures - II, NBSIR 79-1609, F. R. Fickett and R. P. Reed, Eds., National Bureau of Standards, Boulder, CO (1979), pp. 417-436.
2. J. G. Hust, "Thermal Conductivity of G-10CR and G-11CR Industrial Laminates at Low Temperatures (Part II)," in Materials Studies for Magnetic Fusion Energy Applications at Low Temperatures - III, NBSIR 80-1027, R. P. Reed, Ed., National Bureau of Standards, Boulder, CO (1980), pp. 395-404.
3. K. Dahlerup-Petersen and A. Perrot, "Properties of Organic Composite Materials at Cryogenic Temperatures: CERN ISR-BOM/79-39." (November 1979).
4. J. G. Hust and J. Arvidson, "Thermal Conductivity of Glass Fiber/EPOXY Composite Support Bands for Cryogenic Dewars," unpublished report 275.03-78-2, National Bureau of Standards, Boulder, CO.

TABLE 1

DIMENSIONS, VOLUMES, WEIGHTS, AND DENSITIES
OF THE THERMAL CONDUCTIVITY SPECIMENS

SPECIMEN	DIMENSIONS (cm)			VOLUME (cm ³)	WEIGHT (g)	DENSITY (g/cm ³)
	X ^a ₁	X ^b ₂	X ^a ₃			
G-10CR RESIN #1	1.915	1.913	1.781	6.524	7.698	1.180
(a)	1.915	0.652	1.781	2.224	2.615	1.176
(b)	1.915	1.041	1.781	3.550	4.175	1.176
(a+b)	1.915	1.693	1.781	5.774	6.790	1.176
G-11CR RESIN	1.915	1.915	1.915	7.023	8.620	1.227
VETRONITE 432.81 (A1)	1.786	0.199	1.770	0.629	1.200	1.91
(single pieces) (A2)	1.780	0.198	1.768	0.623	1.194	1.92
(A3)	1.783	0.196	1.768	0.618	1.189	1.92
(A4)	1.780	0.196	1.765	0.616	1.186	1.92
(A5)	1.780	0.198	1.765	0.622	1.190	1.91
(A6)	1.780	0.199	1.765	0.625	1.193	1.91
(B1)	1.780	0.201	1.768	0.632	1.202	1.90
(B2)	1.775	0.200	1.768	0.628	1.200	1.91
(B3)	1.778	0.197	1.765	0.618	1.189	1.92
(B4)	1.775	0.196	1.763	0.613	1.183	1.93
(B5)	1.770	0.198	1.760	0.617	1.180	1.91
(B6)	1.768	0.200	1.753	0.620	1.176	1.90
(stacked groups)						
A3 & B3	1.780	0.393	1.766	1.235	2.328	1.92
A3, A5, B1, and B3	1.780	0.792	1.766	2.490	4.770	1.91
all 12 specimens	1.778	2.378	1.765	7.462	14.282	1.91

a - Values of X₁ and X₃ for the stacked groups are averages of the dimensions of the individual pieces.

b - Values of X₂ for the stacked groups are the sums of the thicknesses of the individual pieces.

TABLE 2

MEASURED THERMAL CONDUCTIVITY VALUES AT 280 K OF THE G-10CR RESIN SPECIMENS [SPECIMEN #1 REFERS TO THE ORIGINAL SPECIMEN, (a) AND (b) ARE THE SPECIMENS OBTAINED AFTER SECTIONING SPECIMEN #1]

Specimen Identification and Thickness (cm)		Thermal Conductivity (W m ⁻¹ K ⁻¹)
G-10CR Resin #1	1.913	0.296
G-10CR Resin (a)	0.652	0.230 ± 0.008 ^a
G-10CR Annealed 15 h @ 100°C (a)	0.630	0.232
G-10CR Resin (b)	1.041	0.246
G-10CR Annealed 15 h @ 100°C (b)	1.026	0.238
After Annealing (a + b)	1.656	0.252
G-11CR Resin	1.915	0.282 ± 0.005 ^b
G-11CR Annealed 15 h @ 100°C	1.915	0.278

a Range of 4 measured values

b Range of 2 measured values

TABLE 3

THERMAL CONDUCTIVITY VALUES FOR VETRONITE 432.81 NORMAL
TO THE FIBERS AS A FUNCTION OF THICKNESS AT 284 K.

Specimen Identification (see Table 1)	Thermal Conductivity $\text{W m}^{-1} \text{K}^{-1}$
B3	0.447
B3, A3	0.450
B3, A3, B1, A5	0.451
All 12 Specimens	0.480

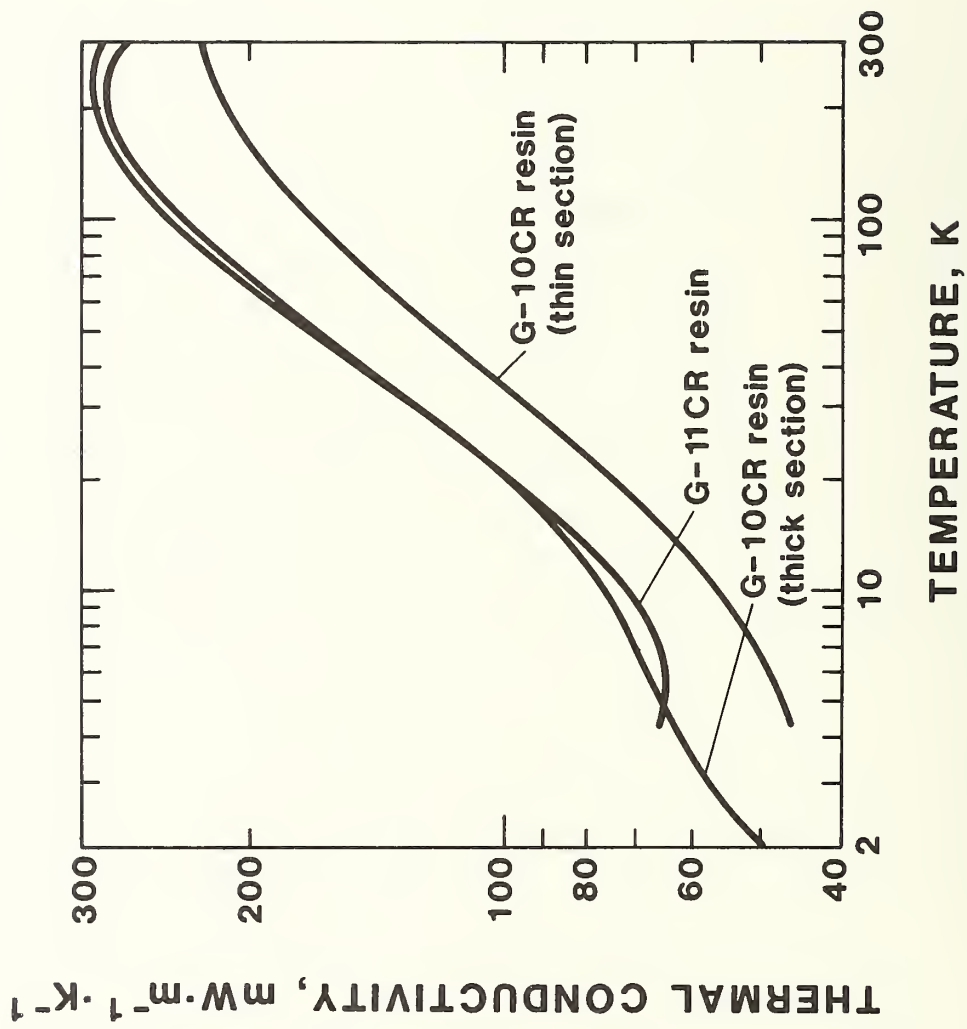


Figure 1. Thermal conductivity data from 2 to 300 K for G-10CR and G-11CR resins.

FRACTURE ANALYSIS OF COMPRESSION DAMAGE
IN GLASS FABRIC/EPOXY, G-10CR, 295 K to 4 K

Betty A. Beck
Fracture and Deformation Division
National Bureau of Standards
Boulder, Colorado 80303

ABSTRACT

This report describes scanning electron and optical microscope fractographic and modeling studies of G-10CR compression fracture at room and cryogenic temperatures. The primary objective of the investigation has been to assess the effect of cryogenic temperature on the failure behavior of these composite materials. Macromechanical analysis in terms of gross composite fracture has been designated as primary. Micromechanical (or constituent) analysis has been specified as secondary. This identification has been used for descriptive and comparative purposes rather than to indicate the level of importance in the fracture process. Results of the fractography have shown that the failure events included three kinds of primary fracture patterns which, to varying degrees, are temperature-related. These fractures have been identified as: 1) a 55° slant mode; 2) a chisel or V-notch mode; and, 3) a complex or mixed mode. The influence of constituent properties and behavior have been integral considerations in assessing the fracture mechanism and in analytical interpretations of the fracture behavior. As in other materials, the damage zone in these composites is the result of either discrete or interactive constituent failure processes (or both) occurring in a highly strained region of the specimen. Fiber microcracking or fracture, matrix yielding or cracking, and interface failure are examples of such events. Nucleation and propagation of fracture, as in other fiber-reinforced composites, is a function of microstructure, microdeformation, and the structural interaction of the constituents. Compressive strength data variability has been graphically correlated with primary and secondary fracture characteristics in order to understand the low temperature effects better.

Contents

	<u>Page</u>
Abstract	
A. Introduction	511
B. Previous Studies	512
1. Introduction	512
2. Constituent Properties and Behavior	515
(a) matrix resin	
(b) glass reinforcement	
(c) reinforcement/matrix interface	
3. Composite Room Temperature Behavior and Failure	518
(a) general	
(b) toughness	
(c) compression	
4. Studies of Glass Reinforced Nonmetallics at Low Temperature	526
5. In Summary and Concluding Remarks	531
C. Low Temperature Effects on Fracture Modes of G-10CR Tested in Compression at 295 K, 76 K, and 4 K.	532
1. Introduction	532
2. Material Specifications, G-10CR	534
3. Test Procedures	535
4. Fracture Analysis	535
5. Results and Discussion	540
(a) general	
(b) fractographic observations and analysis	
(c) conclusions	

Contents (continued)

	<u>Page</u>
6. Recommendations for Future Studies	551
7. References	552
8. Tables	557
9. Illustrations	561

A. Introduction

In general, composite failure is complex because of the interrelated behavior and properties of the constituents, i.e., the matrix, the reinforcement, the reinforcement/matrix interface as well as the variability resulting from the fabrication process. Fracture analysis experience has shown that no single failure mechanism stands out as a primary cause of composite fracture. Rather, there seems to be a sequence of failure events that lead to total composite failure (1-7).

Studies have shown that the predominant primary mechanism of composite fracture as well as the sequence of constituent failure events varies significantly for different composite types (6). Included with this failure pattern variability are the energy dissipative mechanisms at fracture initiation and growth which also differ from one material system to another. This lack of failure behavior continuity and the inherent complexity of fabric-reinforced nonmetallics emphasize the need for systematically building a theory of failure based in part and initially, on detailed observations of fractured specimens.

Numerous investigators have studied and described failure and fracture behavior in both discontinuous and uniaxially continuous glass-fiber reinforced nonmetallic composite materials (1-7). For the most part analytical interpretations, methods, and models, where they exist, have been developed around some theoretical or experimental aspect of a composite's room temperature behavior. Low temperature studies have had a characterization orientation primarily.

Fabric-reinforced nonmetallic composites possess a very complex geometry and behavior, and as such, are more difficult to describe both qualitatively and analytically. These materials have, to date, eluded conventional analysis

and modeling. Most of the difficulty seems to be in the inherent complexity of modeling the reinforcement. Because of the dearth of analytical studies for these materials at both room and low temperatures, there is essentially no analytical base on which to build a theory of failure.

In this study and through exploratory data analysis, a detailed description of primary and secondary fracture patterns has been developed to elucidate basic mechanisms of fracture and to determine temperature-related modes of failure. The results of this investigation will provide a foundation for developing failure analysis techniques based on correlating fractographic features with fracture properties and stress analysis at fracture.

B. Previous Studies

1. Introduction

A summary of information from the published literature has been included in this report. In order to identify, interpret, and analyze failure patterns in the G-10CR specimens, the literature review has provided a basis for developing a fractographic and an analytic frame of reference. Some of the published results have been modified or extended in part to this composite system which involved a different reinforcement geometry and type and loading condition. In utilizing and synthesizing the information on the behavior of matrices, reinforcements, and to some extent, interfaces, a rationale has been established for the systematic analysis of failure in the G-10CR specimens. The state of the present study would be significantly less complete without the direction provided by the earlier studies. Because there are so few published quantitative or even qualitative analyses about failure behavior in fabric reinforced nonmetallics, this approach has seemed necessary.

Most investigators agree, that, to formulate a better analytical understanding of the fracture process in all composite materials, knowledge, not only of the predominant mode of failure but of the sequence of failure events and their probability of occurrence is a primary consideration in the difficult task of reconstructing the fracture process from initiation through propagation to final failure (1-3, 6-14). Similarly there is a consensus about the importance of fractographic analysis in advancing a comprehensive theory of failure and failure analysis techniques (14).

There seems to be a lack of a well-ordered knowledge base that can be used to develop low-temperature strength theories of failure as well as predictions for the onset of failure. This has been particularly true for the glass-fabric-reinforced nonmetallics. There have been only a few studies of the low-temperature behavior of glass-reinforced nonmetallic composites. Constituent behavior, the matrix resins, and glass reinforcement have received somewhat more attention. The structural dependence of Young's modulus, Poisson's ratio, and strength, for example, has been shown to be rather small in epoxy resins. On the other hand, their fracture energy shows significant room- and low-temperature dependence on structure (15). For the composites made up of these materials, the low-temperature changes in strength, moduli, and other properties are incompletely understood structurally. Correlation of changes in static mechanical properties of glass-reinforced-epoxy composites with macrolevel fracture characteristics at cryogenic temperatures is almost nonexistent.

A prevailing idea among the many studies is the need to relate fracture modes to structure and states of stress in the development of valid failure criteria. Morgan et al., for example, point out that the network structure and void characteristics of epoxy resins control their mechanical response (16).

The network structure, which varies with chemical composition and curing conditions, imparts rigidity to the resin. Voids act as stress concentrators and, as such, degrade mechanical response by adversely affecting the effective shear strength. The structure and properties of the resin are significant to the load transfer function of the matrix. Low temperatures can adversely affect this load-transfer mechanism.

Fracture analysis of all composite systems is a function of the deterioration of the unit structure. Glass-reinforced materials are no exception. The constituents impart a major effect to the breakdown under an applied load.

Rosen, as well as other investigators, has shown that there is no unique mechanism that will adequately describe failure in all fiber-reinforced non-metallics (1-3, 4, 5, 9). The individual properties and characteristics of the constituents (the matrix, reinforcement, and interface) and their interactions in the process of degradation and failure yield a complex, coupled behavior in total composite fracture that is difficult to trace to its origins. The contributions of the variety of interacting mechanisms are not easily discernible in the complexity of general composite failure (10). To a great extent, for example, composite strength, which is related to how effectively the stress can be transmitted from one fiber to the next, is a function of the individual constituents (17).

Kelly, in discussing uniaxially reinforced composites subjected to an applied load parallel to the fiber, emphasizes a modulus mismatch that causes displacements in fiber and matrix to differ and leads to stress concentrations proportional to the difference in moduli. Shear stresses and strains resulting from the stress concentrations are the mechanism for load distribution between matrix and fiber via the interface (17, 18). The major part of the load is

carried by the reinforcement if the matrix modulus is such that a matrix displacement is greater than that of the fiber reinforcement.

Matrix and interface characteristics (void content and shear properties) are primary to an effective load-transfer mechanism (19). Cracking in the resin matrix can result in a poorer distribution of the load or abrasion of the glass. Most investigators agree that the load is transferred by shear stresses at the fiber/matrix interface and that the rate of load transfer is limited by the strength of either the interface, the matrix, or the reinforcement, whichever is least (3, 17). A strong interface (low void and crack content) provides a more effective load-transfer effect than a weak interface (high void and crack content that degrade bonding and shear strength) (17). The load-transfer effectiveness of the matrix is adversely affected by increased resin brittleness, increased Young's modulus, and the existence of residual stresses in the composite because of resin contraction and shrinkage during cure (3, 20).

The matrix resin protects the fibers and provides a shear rigidity between fibers and lamina, strength and stiffness to the reinforcement, and a coupling effect to the constituents in response to tensile, compressive, bending, and shear loads. Additionally, it sustains a high level of strain concentration that occurs as the result of the high-modulus, brittle fibers in the glass-reinforced-epoxy composites.

2. Constituent Properties and Behavior

(a) Matrix Resin

In general, polymer failure occurs by excessive deformation, crazing or cracking, and tensile or shear fracture. Cross-linked polymers fail by cracking

and fracture (21). Structurally, there is evidence to indicate that stress concentrations can lead to cracking at the cross-links if the cross-link length is too short for plastic flow. Shear fracture for polymers can occur on either a single plane or simultaneously along two planes of maximum resolved shear stress lying at 45° to the longitudinal axis of testing. Fracture results when deformation, due to a concentration of large shear strains, is restricted to the one or two planes of shear failure.

Strength and elasticity of epoxy resins show little or no dependence on cross-link distance for temperatures in the range above 50 K to less than 20 K. Energy at fracture, however, for these same resins, is strongly dependent on cross-link distance, increasing as the distance increases (15).

The response mechanism of a polymer to an applied mechanical stress is a function of the ability of the molecules to move past or over one another. At cryogenic temperatures there is an increase in the rigidity of these materials owing to an increased rigidity in the molecular structure.

Epoxy resins, in general, exhibit room-temperature glasslike textures typical of brittle materials that have characteristic low-energy-absorbing properties, low viscosity, and low shrinkage when cured (5, 22, 23). They don't form bubbles, which minimizes buildup of internal stresses in the cured resin.

(b) Glass Reinforcement

The high-strength, stiff glass fibers, in the form of a rigid molecular network with no mechanism for ductility, are subject to a statistical distribution of flaws and defects characteristic of brittle materials. As such, fiber failure is by random microcracking and fracture inherent to brittle

failure. An accumulation of fiber breaks is considered by many investigators to be a major mechanism in total composite failure. A strong, stiff matrix contributes to a greater probability of a statistical failure mode of the glass fibers (1-3, 7, 8, 11).

(c) Reinforcement/Matrix Interface

Debonding of the fiber from the matrix and delamination of one lamina from another are interface failure modes. Most composite studies have shown that the fiber/matrix interface is primary to load distribution from matrix to fibers. Strength, mode of failure, and work at fracture are a function of the behavior of the interface. Interface shear strength is a function of the density of voids formed during fabrication. High void content results in low shear strength and leads to a weak interface that can be split by stresses set up ahead of an advancing crack (17).

There is some evidence to indicate that fiber/matrix debonding and matrix cracking can interact to reduce load concentrations and result in an increased composite stress. Studies have also indicated that, where there is an increase in composite strain at fracture, it may be due to deterioration of the fiber/matrix interface.

In synthesizing fracture information for glass-reinforced-plastic composite systems, constituent characteristics and their highly coupled nature and behavior relative to the failure process must be integrated with the analysis. The degradation and failure mechanisms may occur independently, simultaneously, or consecutively in total failure.

Energy-dissipative mechanisms and levels thereof are integrally important in sequence analyses of failure events (4, 24, 25). Crack branching, for

example, in fiber-reinforced-composites extends the size of the fracture surface and results in a large dissipation of energy. Debonding, for brittle fibers enclosed by a semibrittle matrix resin, seems to occur first along an interface, and the debonding work done is stored in the fiber as elastic strain energy. When a debonding sequence is completed, the fiber pulls out of the matrix. This occurs because the load on the fiber, in order to split it from the matrix, is higher than the load for pullout. As a result, the energy dissipated at fiber pullout is higher than the work done in debonding (4).

3. Composite Room Temperature Behavior and Failure

(a) General

Primary, considerations in composite fracture and fractographic analyses include the identification and description of: (1) the predominant failure mode of the composite; (2) the failure modes of the constituents; (3) their probability of occurrence in the failure of a specific composite material under a well-defined loading condition; and, (4) a probable sequence of failure events from initiation to propagation and final fracture. Collins et al., for example, conclude that, in determining which mode dominates failure behavior, fractographic analysis is a function of which model is assumed (11). Their study identifies and summarizes two approaches: (1) a cumulative fracture propagation model and (2) a noncumulative model. These models have also been described and expanded upon in other investigations (2, 9).

The cumulative model assumes that the total applied load is borne by the fibers. The matrix acts only as a mechanism for redistribution of the stresses when a fiber breaks locally. This model is based on a statistical strength distribution due to inherent defects characteristic of the brittle glass

fibers. Total composite fracture occurs after enough fiber fractures have resulted in a weakened cross section so that it can no longer support the applied load. This model is valid if an assumption is made either that (1) the load is distributed uniformly over the remaining fibers after one breaks or (2) surviving fibers are subjected to static and dynamic load concentrations. The noncumulative mode identifies composite failure as a function of crack propagation through the matrix, interface, and reinforcement. As a result, the failure loads are considerably below those which would cause a significant number of fibers to break.

According to these investigators, fractographic analysis will be approached differently depending on which mode is assumed. The cumulative mode implies, for example, that interface debonding of fiber and matrix and fiber pullout result in an ineffective fiber length, which carries little of a tensile load in a failed area. The noncumulative mode, on the other hand, implies that interface debonding and fiber pullout determine an optimum path of crack propagation through the matrix, including crack branching at the interface.

Zweben has determined that such factors as fiber/matrix debonding, interface cracking, matrix plasticity and cracking, and the three-dimensional nature of the material act as energy-absorbing mechanisms that tend to reduce load concentrations, effectively increasing composite stress. On the other hand, a lack of uniformity in the spacing as well as cracks in the fibers tends to increase stress concentrations and decrease composite failure stress (2, 9, 11, 24).

Early studies of the tensile failure of a uniaxially reinforced matrix identified a simple failure model based on a uniform strain throughout the composite. As a result, fracture occurred at the failure strain of the fibers alone (2,7). More recently most investigators

have postulated a nonuniform strain distribution, which has directed consideration of the influence of flaws in the brittle reinforcement on composite failure (4, 5, 7, 9).

Rosen, and others, have developed a rather comprehensive description of failure in fiber-reinforced composites (2, 6, 7). This model assumes that because of flaws inherent to the brittle fibers, initial fracture will most likely occur in the fibers causing a local perturbation of the stress field. The way the load is redistributed near the broken fiber ends and the resulting stress concentrations may result in: (1) separation along an interface (i.e., fiber debonding or lamina-to-lamina delamination); (2) fracture of nearby fibers (since they are subjected to a greater stress intensity than those at some distance); (3) propagation of transverse cracks; (4) immediate composite fracture; or (5) no further fracture. Because the strengths of the brittle fibers are not uniform, they will break randomly throughout the material as the applied stress is increased. The fractured fibers are then reloaded to some level before being pulled out of the matrix. There is, however, a critical length at which the fibers will no longer support the load. As fractures accumulate, the end result is a number of fibers of ineffective lengths interacting to produce a weakened cross section of the composite, which leads to total failure. Since the shortened fibers can no longer effectively transmit the increasing load, composite fracture occurs as the maximum shear strength of the matrix is exceeded. A strong, stiff matrix, the nonuniform strength of the fibers, and a statistical accumulation of flaw-related fiber fractures are the controlling factors in the failure characterization of this model. Because the fibers do not have uniform strengths, strong fibers will carry an increasingly greater load as weaker fibers break. Additionally, the average strength of some of the individual fibers may

be greater than the coupled strength of fiber bundles, which can significantly affect the fracture sequence. Because of the lack of uniformity in the glass-fiber strengths, investigators have utilized the Weibull distribution as statistically descriptive of the strength variability (4, 5, 7, 9, 26).

There is a distinction between the failure processes (including stress distribution and level) that control the onset or initiation of failure and those that control the fast propagation of a crack. The former is more difficult to reconstruct fractographically and has thus received less study. Because of the variety of micromechanisms of failure occurring and interacting, failure mechanisms at the onset of damage must be distinguished from those close to fracture in terms of stress levels and states. Rosen feels that, in developing a failure criterion, it's initially important to understand internal irregularities in the state of stress (7).

Tetelman has determined that composite fracture initiates either by: (1) fiber fracture, (2) interface shear fracture (debonding or delamination), or (3) matrix tensile or shear fracture, depending on which of the above occurs first at a lower value of applied strain. Final fracture may be the result of some or all of the above mechanisms (3).

Mullin has analyzed energy-absorbing mechanisms in high-modulus fiber composites (24). His analysis indicates that, at a fiber fracture site, strain energy will be increased in adjacent fibers by a stress-transfer mechanism acting through the interface and the matrix. The localized redistribution of load can produce either matrix cracking perpendicular to the fiber or debonding at the interface. The probability of the former mechanism occurring reflects a strong interface bond; the latter, a weak one. Debonding can

result in a localized sliding of the fiber in the interface socket accompanied by fiber fracture and pullout. Beaumont has identified postdebond sliding, rather than fiber fracture and pullout, as a major toughening mechanism in fiber-reinforced composites (27). Vinson and Chow associate fiber pullout with the flaws in the brittle fibers that lead to nonuniform strengths (4). They assume that the matrix has cracked completely. As a result, fibers in the cracked regions become stressed more than the remaining ones, which are firmly fixed in the matrix.

Zweben cites a study of composite failure that associates fracture sequence with a propagating stress wave that fractures the fibers destroying their load-carrying capability (25). The matrix, as a result, cannot sustain the applied load level without the strengthening effects of the reinforcement. This leads to total composite failure with most of the energy being dissipated by the matrix.

Additional models for describing failure initiation and propagation with associated energy dissipative mechanisms have been proposed. One of these indicates initiation is the result of debonding brought about by increasing fiber fracture strength or decreasing matrix or interface shear strength (3). Voids introduced during fabrication degrade interfacial shear strength and significantly influence debonding. Deformations that develop during initial impairment of a fiber-reinforced material can lead to a tensile fracture of the reinforcement, which is most probably due to bending followed by a final shear mode of composite failure (5, 27). Materials with a high void content can fail by crack extension parallel to the fibers, whereas those with low void content and high fracture toughness have a characteristic shear final-failure mode. Residual stresses and strains introduced during fabrication are

the result of differential thermal expansion characteristics between reinforcement and matrix. The existence of these stresses can complicate the analysis of failure initiation. If, as some investigations have assumed, failure first occurs in the brittle matrix and the crack propagates toward the fibers, it can propagate across the fibers if the interface is strongly bonded and continue to brittle failure. If, however, the propagating crack approaches a weak interface, debonding of fiber/matrix interface occurs. Debonded fibers then fracture as a function of the defect distribution in the imperfect fibers. Stress concentrations ahead of an advancing crack can cause the interface to fail. When a propagating crack reaches a fiber, it is diverted along the cracked interface and blunted. In order for the crack to continue to propagate, it must be reinitiated by increasing the load. Some investigators have emphasized that this sequence of events is the primary toughening mechanism in fiber-reinforced nonmetallics (4, 5, 27).

(b) Toughness

Toughness in a metal is the ability to absorb energy during plastic deformation without fracturing. In a static tensile test this energy can be measured by the area under a stress-strain curve, which represents the work required to fracture a specimen.

In glass-reinforced epoxy composites there is no direct toughness analogy with a metallic system because of the plastic nature of the metal. If, however, toughness is considered to be the ability to redistribute stresses in the presence of a notch to reduce the effects of high stress concentrations by dissipating the energy, then the work required to fracture a composite specimen should represent toughness properties analogous to a metal. Toughness in a

glass-fiber-reinforced plastic seems to be a function of the interfaces and their ability to deflect cracks propagating normal to them (4, 5, 12, 17, 22, 27). If there is a strong interfacial bond, there is a high probability that stress concentrations set up by failure of one fiber will nucleate cracks in nearby fibers leading to progressive fiber failure. If the bond is weak, interfacial shear strength will be degraded and stress concentrations ahead of a crack advancing normal to the fibers can split the interface. As the crack reaches a flawed boundary, it will be blunted or diverted parallel to the interface. For the crack to continue to propagate, it must be reinitiated by a sufficient stress buildup as the applied load is increased. If this process can be repeated as the cracking spreads, large amounts of energy can be absorbed.

Some investigators have indicated that toughness relates to the energy dissipated as fiber/matrix debonding occurs. The toughness mechanism becomes a sliding action between fiber and socket, accompanied by friction effects and eventual fiber pullout (24, 27).

Fiber-reinforced nonmetallics are considered to be tough and not notch sensitive.

(c) Compression

Compressive stresses are the result of either an externally applied load or are due to shrinkage stresses developed during cooling because of differential thermal expansion characteristics between matrix and fiber. Rosen and others have developed models for uniaxial continuous-filament composites subjected to an externally applied compression load parallel to the fibers (1, 7, 28-30). The model postulates that failure occurs by microbuckling of the fibers on an elastic foundation. The analysis identifies two fiber buckling

modes, a shear mode and extension mode, each descriptive of matrix deformation. For this model the matrix shear modulus controls composite compression strength. Buckling can be prevented by a stiff matrix and strong bonding at the interface (5, 7, 20, 31, 32). There seems to be little evidence to show whether, under compressive loading, local buckling precedes and causes crack propagation or follows crack initiation and propagation (5).

There is a study cited in Broutman that investigated a linear relation between interlaminar shear strength and compressive strength for flat filament-wound panels. That analysis showed compression strength as a function of resin properties and either high interlaminar or horizontal shear strengths (5).

For his investigation on compressive fracture Chaplin has expanded the development of the shear mode to a shear instability in a volume of material rather than failure in a plane as a function of a resolved shear stress. The shear instability produces significant shear deformation in the matrix and bending of the reinforcement (32).

Externally applied compressive loads parallel to the fibers in a unidirectional fiber-reinforced composite can result in failure by: fiber microbuckling in a shear mode; tensile or compressive fiber fracture; shear failure of the matrix; interfacial failure due to delamination or debonding or both; or compression-induced bending accompanied by secondary tensile and shear stresses (4, 5, 7, 31-33). Fiber pullout and fracture are failure events in the debonding sequence. A major characteristic of composite shear failure is lack of damage to the fibers in the direction of shear.

A compressive stress will not propagate internal cracks nor will it produce crazing, a failure phenomenon characteristic of many matrix resins. Rather, a compressive stress normal to a crack tends to close the crack.

Secondary tensile and shear stresses, however, will propagate internal cracks and are significant to the resulting fracture behavior.

Ryder and Black, in discussing types of compression testing, indicate that there are several possible compression failure modes in fiber-reinforced composites. Each has a different ultimate strength. For each testing procedure, failure occurs at the lowest strength with a corresponding failure mode. The range of possibilities suggests that compressive strength for these materials is not a precise term, but rather, is one of definition (34).

Extensive work on static compressive behavior of glass-epoxy composites has shown that test results and the failure mode are sensitive to the method of gripping (misalignment causing the specimen to bend), type of reinforcement, and fiber volume fraction. Three major compressive failure modes have been identified: (1) fiber buckling, (2) shear, and (3) interfacial, with the shear mode predominating (7, 28, 33). Total brittle compression fracture of a composite specimen results in separation of the specimen into two or more parts with little or no measurable inelastic deformation.

If deformations develop initially, they can lead to either (1) tensile fracture of the reinforcement due to bending with final fracture of the composite in a shear mode or (2) shear displacement in the matrix, which can cause stress concentrations and crack extension along the fibers if voids are present in a contiguous area.

4. Studies of Glass Reinforced Nonmetallics at Low Temperature

Fiber and matrix characteristics have a significant influence upon the mechanics of deformation and fracture of fiber reinforced nonmetallics at both room and cryogenic temperatures. As such, temperature-related behavior and

properties of the constituents are important in the analysis of temperature effects on failure modes for these composites.

Polymer behavior is a function of a molecular chain response mechanism, which can experience a temperature-related change as temperatures are decreased to those representing cryogenic environments. Such change can have strong effects on material properties and fracture behavior. At room temperature the molecular chain is in thermal motion around an equilibrium position. At this temperature the molecular response to an external stress (that is, the coiling and uncoiling of the chains and their moving over and past one another) is easier because there is no fixed molecular position. In this configuration, the polymer chain provides an energy-absorbing mechanism for stress waves transmitted through the material. As the temperature is decreased, the thermal energy of the molecules decreases and the elastic mobility of the polymer chain slows down. As a result, the chain becomes more rigid, the energy-absorbing alternatives become more restricted, and attractive forces become more effective in the resistance of materials to deformation. Under an applied load the decreasing ability to dissipate energy through the molecular structure leads to an increased resin rigidity until the cohesive strength of the polymer has been exceeded, ultimately leading to fracture as a dissipative mechanism. This molecular rigidity results in a stronger, stiffer material at low temperatures because the polymer chains are unable to slide over one another effectively (3, 15, 16, 23, 35).

For epoxy resins, there are cross-linking effects in the molecular structure as well as the effects of molecular anisotropy of the binding forces owing to the directional nature of the primary covalent bonds and secondary

Van der Waals forces, which act along and across the molecular chains. The cross-linked structure imparts some degree of rigidity to the polymer.

Epoxy resins do not seem to be subject to changes in structure with decreasing temperature. They exhibit elastic-plastic stress-strain behavior at room temperature but have nearly linear stress-strain characteristics at low temperature. Strength (tensile, compressive, and shear) and modulus increase with decreasing temperature. Fracture strain, a function of molecular cross-linking, approximates 2% at 77 K and 4 K.

Soffer and Molho tested a Bisphenol-A epoxy resin at cryogenic temperatures (77 K and 20 K). Their results indicate that, in comparison with room-temperature properties, (1) there is an increase in strength and modulus in tension and compression; (2) there is a change in elastic-plastic behavior at room temperature to essentially linear elastic behavior at 77 K and 20 K; and (3) there is a decrease in fracture strain and resin toughness (as measured by the area under the stress-strain curve) with decreasing temperatures. The rate of decrease for (2) and (3) moderates between 77 K and 4 K. The resin exhibited a maximum notch toughness (the capacity of the resin system to sustain loads in spite of defects in the matrix) value at 77 K and decreased to below the room temperature value at 20 K. Their assessment of the fracture-surface examination of this particular resin specimen indicated a smooth, almost glasslike texture typical of low-energy, absorbing, brittle materials (23).

Hartwig's low-temperature analysis indicates, in general, that the chemical structure of epoxy resin chains, including cross-link density, does not have a marked effect on elastic mechanical parameters. Poisson's ratio seems to be entirely independent of structure. Energy at fracture, on the other hand, decreases with higher cross-link density at cryogenic as well as higher

temperatures (15). Other investigators have noted a relation between the degree of cross-linking and void density and their detrimental effects on matrix and interface shear strength. This effect, however, was not investigated below room temperature, probably because low-temperature factors were not a part of the study (21).

Kadotani determined in his low-temperature studies that the lower the glass transition temperature, T_g , of a resin, the larger its tensile elongation at 77 K. The larger the elongation at 77 K, the higher the strength and elongation of the composite at 77 K (36).

Glass materials used for reinforcement are brittle at room temperature and below. Their rigid silica network structure and lack of molecular order is such that there is no inherent structural mechanism for ductile behavior characteristics. Because of their brittle nature, strengths are not uniform and their failure modes at room and cryogenic temperatures reflect these brittle characteristics.

Glass-fabric-reinforced epoxy composites exhibit significant increases in tensile, compressive and shear strength, tensile modulus, Poisson's ratio, and tensile strain to failure with decreasing temperature compared with room-temperature values (20, 36, 37). There is considerable evidence to indicate that:

1. A stiffer resin holds the reinforcement more firmly fixed for loading parallel to the principal direction of fabric-reinforced composite. As a result, there is a greater resistance of the fibers to displacement or deformation.
2. Fiber-to-fiber progressive fracture leading to final composite fracture provides an enhanced energy-absorbing mechanism, the

characteristics of which reflect the sum of the energies of the individual fibers. As a result, more energy can be absorbed at room and low temperatures.

3. The increase in strength at low temperatures is the result of interface failure and crack blunting, a progressive mechanism that imparts toughness to the material.
4. The high strain of the composite at fracture at the lower temperatures is a direct function of the low-temperature, high-fracture strain characteristics of the glass reinforcement.
5. The increase in composite fracture strain may reflect a deterioration of the fiber/matrix interface.
6. The glass-reinforced plastics are the only composites that exhibit increased elongation at 77 K.
7. Tear-type fractures seem to be more evident at low temperature for epoxy matrix materials.

For glass-fabric-reinforced epoxy composites stressed parallel to the principal fiber direction, there is a transition in the stress-strain (20, 22, 36, 37) behavior below room temperature that results in both an initial and secondary modulus characteristic, termed a "knee" of the stress-strain curve. Figure 1 is a typical illustration of this effect. Initially the knee seems to be due to interface failure and matrix cracking. There is some evidence to indicate that the decrease in secondary modulus with decreasing temperature, as illustrated in Figure 1, reflects a decrease in the shear strength of the resin matrix or fiber/matrix interface.

5. In Summary and Concluding Remarks

For glass-fabric-reinforced nonmetallics this review has demonstrated, not only a dearth of adequate test and analysis techniques for predicting strengths and determining mechanisms of deformation and failure, but also, a need for such analyses and tests.

The "rule of mixtures" was an early and relatively simple model for relating fiber and matrix strength and stiffness to estimates of composite strength. Implicit in the model was the assumption that, under an applied load, there was a constant strain throughout the composite. The interpretation based on that assumption indicated that the first fiber to fracture led to crack propagation to failure for the composite with fracture occurring at the failure strain of the fibers.

More recently some investigators (1, 5, 26) have pointed out that the "rule of mixtures" analysis is inadequate for composites reinforced with very brittle materials such as glass fibers. Failure for these materials has statistical features that reflect the nonuniform strength distribution of the fibers' inherent flaws and imperfections.

Cryogenic testing of these composite materials has been limited to characterization studies which show strength and stiffness increases with decreasing temperatures. These effects seem to be more a reflection of changes in the reinforcement than the matrix. There are, however, significant structural changes going on in the resin at cryogenic temperatures that may or may not be important in trying to deduce how a glass fabric reinforced epoxy will fail.

Since the fracture strengths of the individual fibers or fiber bundles - covers a range of values, determination of an appropriate stress for describing the failure stress of the reinforcement - and ultimately the composite - is a

complex problem still to be addressed. Adding to this complexity are important considerations relative to the sequence of constituent failure events, their interaction, and contributions to total composite failure.

The initial part of this report has been directed toward a comprehensive synthesis of behavior and properties information as well as failure models derived from published investigations of glass-reinforced plastic composites.

The analytical and descriptive material and models included herein have served as an excellent basis for the low-temperature fractographic analysis of G-10CR that follows in this report.

C. Low-Temperature Effects on Fracture Modes of G-10CR Tested in Compression at 295 K, 76 K, and 4 K

1. Introduction

To provide an initial data base for engineering applications a cryogenic-temperature-characterization program was conducted at the National Bureau of Standards (1978-79) for the cryogenic-grade glass-fabric/epoxy composite, G-10CR (37). These experimental studies included electrical, thermal, and mechanical property characterizations of CR-grade materials over the 295 K to 4 K temperature range.

The objective of the present study, described in this paper, is to assess the effect of cryogenic temperatures on the failure behavior of the G-10CR specimens tested in compression under the program described above. The following specific activities were directed toward achieving this objective:

1. Examination and analysis of fracture surfaces of G-10CR specimens previously tested in compression at 295 K, 76 K, and 4 K with fractographic methods.

2. Identification and characterization of primary composite failure and secondary constituent failure as well as the interactive effects of the constituents that led to gross composite failure.
3. Correlation of failure morphology with room and cryogenic compressive strength characteristics. As a result, the development of an interpretation of the experimental results, which shows compressive strength and data variability increasing with decreasing temperature.
4. Comprehensive review of the literature of existing failure analysis information and models that can be used as a frame of reference for identifying and elucidating G-10CR compression failure behavior at room and cryogenic temperatures.

Generically failure was considered to be the occurrence of any discernible discontinuity in the response of the composite and constituent material to a mechanically applied external compressive load. Gross composite failure was determined to be primary, constituent failure to be secondary for comparative and descriptive purposes rather than to designate order of importance. Several kinds of failure mechanisms within this classification were used to identify failure in the G-10CR specimens. Breakdown of the unit structure leading to failure of the constituents or the bond between them; reduction in the load-carrying capacity due to localized damage or separation; significant loss of strength due to crack growth; or total composite fracture were considered to be identifiable failure processes in this analysis.

This study involved an after-the-fact critical examination and analysis of the fractured specimens. In the analysis it was important to determine:

1. What constituted failure.
2. What was the predominant composite failure mode.

3. What were the modes of constituent failure and the probable occurrence of each.
4. What was the probable sequence of failure events in total composite failure.
5. How do the above (i.e., 1-4) correlate with decreasing temperature, 295 K to 4 K.

2. Material Specifications, G-10CR

Specimen configuration with adhesively bonded end caps is shown in Figure 2 (37). The end caps were designed for and used to eliminate premature specimen failure and to assure uniform load transfer as well as good vertical alignment of specimen ends to avoid column buckling. Figure 2 also shows diagrams of laminate configurations.

The reinforcement is a silane-finish, E-glass, 7628 woven glass fabric, plain weave with interlaced warp (length) threads (43/in) and fill (width) threads (32/in). This type of reinforcement results in a high-volume fraction of fibers in the resin with a correspondingly high strength and modulus and different strength properties in directions parallel and perpendicular to the warp.

The matrix is a heat-activated, amine-catalyzed bisphenol A solid-type epoxy resin, a cross-linked molecular system. Resin content ranges from 32 to 35%.

The composite specimen is made up of layers of similar parallel lamina, as illustrated in Figure 2. Material for the specimens was obtained from two producers. Tables 1 and 2 contain typical property values for the E-glass reinforcement and an epoxy resin (9, 22, 23).

3. Test Procedures

Static compression testing was done by applying a compressive load in the plane of the cloth. The compression test fixture is shown in Figure 3. The testing environment included air at 295 K, liquid nitrogen at 76 K, and helium at 4 K. Tests were performed parallel to both warp and fill, and compressive strength values were determined for both directions at the above temperatures.

4. Fracture Analysis

Fractured specimens of G-10CR tested in compression at 295 K, 76 K, and 4 K were subjected to a critical examination using optical microscope and scanning electron microscope (SEM) fractography to assess damage and determine failure modes, both primary and secondary, for each specimen. Failure was defined in the preceding part of this report. Both macrolevel and microlevel observations and analysis were considered to be important to the results of the study. The former assumed the composite to be a homogeneous solid and an averaging process was utilized to assess damage and failure. The latter was based on the assumption that the material is a heterogeneous solid and that constituent (fiber, matrix, and interface) characteristics are integral considerations in composite fracture.

For both primary and secondary failure mode analyses, location and direction of failure and failure-surface morphology were stages considered important to fracture characterization. Determining individual constitutive failure events as well as their relation to total composite fracture were subsets in the major focus of the study. Although there seemed to be a significant degree of consistency in the G-10CR fracture morphology, it still became an

extremely difficult task to establish the path of fracture and trace it to initiation.

In general, damage modes of importance to this analysis were considered to be cohesive failure of the matrix and reinforcement and adhesive failure of the fiber/matrix interface.

Constituent damage and failure types, which combine in a variety of ways as they affect the response of a material to the applied compression load, are consistent with the numerous published studies summarized in an earlier part of this report. Those failure modes identified as important to this study were:

1. Matrix (epoxy) cracking and fracture
2. Reinforcement (glass fabric) microcracking and fracture
3. Fiber/matrix interface, debonding, delamination, and fiber pullout.

Primary compressive failure modes were either (1) an approximate 55° slant type; (2) a V-notch or chisel type, or (3) a mixed mode or complex type. Types (1) and (2) have been diagrammed and are illustrated in Figure 4. Figure 5 correlates each of these three modes [i.e., (a), (b) or (c)] with temperature for warp and fill directions.

Tables 3 and 4 are temperature-related summaries of significant factors in the characterization and fracture analysis of these materials. These tables represent the same information, except that one is a summary for the warp direction and the other, for the fill direction.

In the first part of the table, failure modes at each testing temperature have been correlated with the lowest and highest values of compressive strength. The second part is a summary of the percentages of each primary failure mode

for each testing temperature. Several factors became apparent in organizing the summaries. There is more variability in the primary failure mode in the warp direction than in the fill direction. In the fill direction, the single-plane $\sim 55^\circ$ slant-type mode was the predominant mode. This mode represented 100% of the lowest compression strength-vs.-temperature values in the fill direction, but only 33% of those values in the warp direction. Highest compressive strength-vs.-temperature values were identified as either a single- or a double-slant (shear-type) failure for the fill tests. The warp-test fracture modes, in this case, were not representative of any highest value mode except a complex type indicating considerable variability.

The third part of the table identifies the fracture edge for the primary mode when that mode is either the $\sim 55^\circ$ slant or V-notch. This edge is a transverse crack across the specimen with some evidence of tearing at the lower temperatures (Figs. 4, 6-20).

Part four of the table is a summary of constituent damage or failure-vs.-temperature. The next part of this report emphasizes in more detail some of the fractographic analysis that integrates with and documents certain aspects of the fracture interpretations.

Property measurements determined during the initial characterization tests are graphically presented for inclusion in this part of the report in Figures 21 through 23 (35). These diagrams serve as a basis for analysis in the development of this failure-analysis study. Also, results determined from these graphs have directed construction of additional graphical comparisons considered to be significant and illustrated in Figures 24 through 26.

Figure 1, as previously indicated, illustrates a typical tensile stress-strain diagram for some of the G-10CR specimens tested in the warp direction

at room temperature and 76 K (37). The diagram, even though it represents a typical tensile property, has been included with the report because it is representative of the stress-strain behavior for this material. The work required to fracture a specimen can be related to the area under the stress-strain curve and is an indication of the toughness of a material. Using this area as a measure, the work at fracture shows an increase when the temperature is lowered to 76 K. At 76 K there is a discontinuity in the configuration of the curve, considered to be a "knee" at about 300 MPa with an accompanying change in the modulus. Initial and secondary moduli reflect this transition at low temperatures but not at room temperature. This type of behavior can be correlated with specific failure occurrences i.e., beginning matrix cracking at the knee and a degradation in interface shear strength reflected by the lower secondary modulus.

Figure 21 has been included to provide a graphic comparison of the range of measured test values for compressive strength, Young's modulus, and tensile strain to failure for room temperature, 76 K, and 4 K in both warp and fill directions. The number of specimens for each test condition are shown in Tables 3 and 4. The bars at each temperature in Figure 21 are representative of the highest and lowest test value and thus illustrate the variability in the data for each of the properties shown. Figure 22 diagrams all measured values for Young's modulus vs. temperature and Figure 23 is a graph of all the measured data for compressive strength vs. temperature. The outer straight lines have no physical meaning other than to indicate upper and lower bounds for the data and to present a graphical comparison of the scatter in the data at each temperature; the center straight line connects the average value at

each temperature. The temperature-related vertical line delineates the calculated standard deviation for the range of values.

It's interesting to note the significant increase in strengths for warp and fill directions compared with those at room temperature. Figure 24 illustrates a graphical comparison for warp and fill tests of the low temperature-room temperature percentage increase in compressive strength, Young's modulus, and tensile strain to failure.

Another interesting factor to be noted in Figure 23 is that the low temperature variability (i.e., the scatter in the data) is reversed for measured compressive strength values in the warp and fill directions. At 76 K the scatter is very large for the warp direction and is significantly less in the fill direction. At 4 K the reverse is true. Variability (as expressed in the standard deviation and coefficient of variation for compressive strength, Young's modulus, and tensile strain to failure) has been addressed in Figures 25 and 26. These graphs summarize and compare variability as a function of temperature.

The graph illustrating Young's modulus vs. temperature (Figure 22) was determined and presented in a manner similar to the one for compressive strength. Earlier studies have indicated that the low-temperature related increase in composite strength and modulus primarily reflect similar changes in the glass reinforcement. Plotted values for Young's modulus in warp and fill directions indicate, as was also illustrated for compressive strength, that there is significantly greater scatter for the data in the warp direction. Variability at 4 K does not appear to be a significant factor for either warp or fill directions.

Optical and scanning electron microscopes were used to examine details of the fracture surfaces to identify and evaluate constituent failure. Figures 6 through 15 are typical photographs obtained with the optical microscope. Figures 16 through 20 are typical SEM photographs of fracture details for specimens tested in the warp direction at various temperatures. Significant details have been identified and delineated on each of the photographs. These illustrations can, in turn, be correlated with the summaries in Tables 3 and 4.

5. Results and Discussion

(a) General

As indicated in an earlier part of this report, previous studies have shown that the response of a glass-reinforced laminated nonmetallic tested in static compression is a function of the type, orientation, and volume fraction of the reinforcing material; matrix characteristics; precision of alignment of the test specimen; and direction of loading (e.g., load-path distribution as a function of the anisotropy of the material). A woven glass-reinforced epoxy-matrix composite subjected to an externally applied compressive load parallel to the fibers (either warp or fill) can undergo in-plane shear deformation (affecting both the lamina and the interlaminar areas), longitudinal and transverse bending of the reinforcement, and possible bending of the specimen. The matrix undergoes shear deformation. Bending of the fibers results in secondary tensile and shear stresses that may be highly significant to the failure mechanism.

Published studies on the compressive strength of laminates have identified shear and interface (debonding, delamination, and pullout) failure and fiber buckling as primary failure modes. The shear mode, however, has seemed

to predominate. A propagating shear mode of failure across a specimen can be the result of compression-induced bending or shear stresses (4, 5, 28, 31, 33).

There are several constituent structurally related responses to the low-temperature environment that are significant to the behavior of glass-reinforced nonmetallics. Failure modes of the composite are in some way related to interacting molecular and microstructural (constituent) events. An increased rigidity in the polymer chain degrades its ability to dissipate energy. Chemical structure, in terms of cross-linking and directional characteristics inherent in primary covalent bonds and secondary Van der Waals forces, characterizes a molecular anisotropy in the matrix resin, which can be significant to composite behavior. Hartwig has shown that for an epoxy resin: (1) Young's modulus and Poisson's ratio show little or no dependence on chemical structure at low temperature; (2) tensile strength shows some dependence on cross-link distance at temperatures below 76 K; and (3) the energy of fracture shows significant structure sensitivity at both normal and cryogenic temperatures. The energy of fracture is released locally and can lead to a significant temperature rise in the specimen. Hartwig points out that epoxy resins behave viscoelastically at or near the transition temperature and linearly elastic to fracture with an accompanying low fracture strain (approximately 2%) at cryogenic temperatures. Increased strength, brittleness, and resin rigidity characterize the matrix at the low temperatures (15, 35). Increased strength and fracture strain are the cryogenic effects on the glass reinforcement.

The topography of a fracture surface is largely a function of the stress conditions at fracture. An analogy with metals would indicate that lower stress levels are generally identified with a lower level of energy being dissipated at fracture and a smooth, regular fracture surface.

(b) Fractographic Observations and Analyses

With the above as an introduction, the following relates to the specific compression tests of G-10CR specimens at 295 K, 76 K, and 4 K and the fractographic examination and analysis of those specimens that comprised this study.

There were two significantly different testing conditions for the G-10CR specimens compression tested at each of the indicated temperatures. Specimens were oriented with the compression load parallel to warp threads for one series of tests and to the fill threads for the other group. (There was a third test orientation normal to the fabric reinforcement. These specimens however, were not included in this fractographic assessment.) The ratio of fill-to-warp threads is approximately 0.75. Measured values of Young's modulus, E , and compressive strength, σ^{CU} , for the various testing temperatures correlated well with this ratio.

As the summary in Tables 3 and 4 indicates a single-plane, slant-type primary fracture configuration occurred most frequently for both warp and fill tests at all temperatures but more frequently for the fill tests. This investigation has identified that mode as an approximate 55° slant-type mode ($\sim 55^\circ$), see Figure 4. A second slant-type configuration occurred and was identified as two intersecting planes showing a "V" or chisel appearance. This configuration was designated as either a V-notch or chisel type (Figure 4). There were more V-notch failures for the warp tests than the fill tests. For the former, all occurred at 295 K and 76 K. At 295 K these failures generally occurred (1) within the gage section but near the face of one of the grips and (2) with considerable longitudinal delamination. At 76 K the fractures occurred (1) at the face of the grip, (2) with delamination, and (3) with considerable general damage and surface roughness.

There were more complex or mixed-mode fractures in the warp direction than in the fill direction and more evidence for this at 4 K. There was significantly more variability in the primary fracture mode for tests performed in the warp direction than in the fill direction, and this variability increased at the lower temperatures. High values of compressive strength for warp tests generally correlated with complex fracture modes at cryogenic temperatures; low values of compressive strength for these tests correlated with either $\sim 55^\circ$ slant type or V-notch at 295 K and 76 K and was mixed at 4 K.

For the fill tests at all temperatures, the lowest values of compressive strength correlated 100% with the $\sim 55^\circ$ slant mode. Whereas high values of compressive strength at all temperatures correlated with either the $\sim 55^\circ$ slant or V-notch mode.

For all tests, both warp and fill, damage and surface roughness generally increased at the lower temperatures. This damage was manifest in matrix cracking and greater transverse fiber damage. Individual fiber and fiber-bundle fracture, debonding, and pullout were characteristic of the latter. Increased damage and surface roughness at low temperatures has been correlated with energy or work to fracture at 76 K, a measure of which is the area under the stress-strain curve in Figure 1. Published studies have indicated increased work to fracture is a function of the interface and its ability to deflect or blunt a crack propagating normal to the reinforcement (4, 5, 12, 17, 22, 27). For the present study, the low-temperature significance of this effect, in part, can be associated with changes taking place at the interface, which probably intensify the mechanism for occurrence.

Another characteristic that has been identified with primary fracture in both warp and fill directions for slant-type failures at all temperatures is a

major transverse crack across the specimen, which has been determined to be the primary fracture edge. This crack, illustrated in Figure 4, shows evidence of being initially a transverse crack in the matrix of the outer lamina (Figures 6-10 and 14). Fractography shows this edge is deflected very slightly at fiber interfaces (for those fibers parallel to the applied load) but reinitiates in a transverse direction, propagating and deflecting intermittently across the specimen face. Reinitiation and propagation are such that the pattern of the fracture edge is primarily at right angles to the applied load. At cryogenic temperatures the fracture edge is similarly transverse but there is evidence of tearing (Figures 8 and 13).

Several factors complicate fractographic analysis in general and the determination of an initiating failure mode in particular. Composite anisotropy contributes significantly to variability at the interfaces. As this study shows, there has been more interface damage variability transverse to the applied load than there has been parallel to it. In conjunction with this effect is the fact that load-path and stress distributions are a function of the inherent anisotropy of the composite material. Moreover, the determination of an initiating failure mode is complicated by the differential stiffness, expansion and contraction characteristics, and subsequent residual curing stresses developed in fabrication. And, the load-bearing capabilities of matrix and reinforcement, although integral in forming the unit structure of the composite, represent a significantly important differential in the load-support effect. Thus, the reinforcement carries more of the load than the matrix because of its higher strength and modulus. The high volume fraction of the glass reinforcement represents another parameter that makes a significant contribution to the failure mode in compression.

Constituent behavior, properties, and interactions have received equal emphasis in this fractographic study to describe G-10CR fracture behavior. In examining the fracture surfaces, the analysis was based first on discrete damage events (i.e., matrix, fiber, and interface failure) and second on the constituent interaction, which determined a most probable sequence of failure events. The former was developed in considerable detail and has been typically illustrated in Figures 12 through 20. The latter is more complex and requires detailed techniques of analysis, which will direct efforts in future studies. It has received initial coverage here.

(c) Conclusions

When glass-fabric-reinforced systems such as the G-10CR materials are subjected to an externally applied compressive load parallel to the fibers at either room or cryogenic temperatures, the stiff epoxy resin holds the fibers firmly fixed, constraining deformation which leads to strong stress and strain concentrations (5, 31, 34). As in other composites under an applied stress, different displacements occur in the matrix resin and glass reinforcement owing to an inequality in the moduli (18). The stiffness differential results in shear strains and stresses, a primary mechanism for distributing the load between matrix and reinforcement. Because the matrix will deform more than the fibers and because of the difference in elastic moduli, the latter support most of the load at all levels. Previous studies (3-15, 18) have shown that an axial load, parallel to the fibers, is transmitted directly to the reinforcement for continuous-filament composites and via shear stresses at the interface for discontinuous-fiber laminates. The epoxy matrix acts primarily as a mechanism for load transfer and stress redistribution. Although the

G-10CR materials are considered to be continuous, in actuality, as with other continuous glass-fiber-reinforced composites, continuity characteristics can be disrupted by fabrication flaws or early fiber fracture at low levels of applied stress. The latter is the result of the lack of uniformity in glass strengths owing to defects inherent in all very brittle materials. The shortened fibers, the weaker ones that fracture at low applied-stress levels, characterize a discontinuous effect in what is normally considered to be a continuous-filament-reinforced material. Stress perturbations and stress concentrations ultimately result in weakened zones in the composite that lead to total composite fracture.

An increase in strength and strain properties of the G-10CR specimens with decreasing temperatures seems to be more a reflection of changes taking place in the reinforcement (i.e., an increase in strength and modulus) than in the matrix.

A fractographic assessment of the specimens has shown some rather specific consistencies as well as differences in the appearance of the glass fabric with decreasing temperature. First and most general, the evidence indicates that the reinforcement fractures by tension or bending. Second and more specifically, there is a brush-type fracture of fiber bundles at the crossovers and parallel to the applied compressive load for both warp and fill tests (with little or no debonding of individual fibers); see Figures 14 through 20. There are more of these fractures visible on the fracture surface at the higher temperatures than at 4 K. Alternatively, there are less visible brush fractures at low temperatures for tests performed in the fill direction. A significant number of the brush fractures are accompanied with delamination outermost of the fiber crossover area (Figure 24-26). To a lesser extent, some of the bundle fractures remain embedded (little or no delamination) with

only the brush ends showing (Figures 22 and 24). This effect is apparent at low temperatures when there is a transverse matrix crack contiguous to a transverse fiber bundle. For both warp and fill tests, fractographic evidence points to an elastic bending of the fibers with resulting fracture at the crossovers for those fibers parallel to the applied load. There is a characteristic consistency to this type of fracture mode at all temperatures. The only temperature-related difference seems to be that fewer of these are visible on the fracture surface at the lower temperatures, particularly for the fill tests. A low-temperature-related effect is that more matrix shows on the fracture surface at 4 K. The fractography has provided strong evidence that longitudinal bending fracture (i.e., for fibers parallel to the applied load) occurs as a result of stress concentrations at the fiber crossovers, where the dissipative mechanism with the highest probability for relieving the stress buildup is the bending fracture of the bundles. Published fracture studies reviewed for this report have shown no evidence of the brush fracture mechanism observed in the G-10CR specimens.

For both warp and fill tests, examination of the fracture surfaces of the specimens showed a significantly greater degree of randomness for damage and fracture (individual fiber and fiber bundle, debond, and pullout) transverse to the applied load, at cryogenic temperatures in particular. Room-temperature random effects were significantly less. At room temperature, evidence of shear failure was apparent for transverse fibers in that damage was primarily limited to delamination with little or no damage to the fibers in the shear direction. The undulating nature of the transverse fibers was not destroyed at the fracture edge (Figures 16 and 17).

Finally, as in other published studies, fiber cracking and fracture appears to be due, in part, to cracks at the surface as well as to intrinsic defects. As the fibers fractured in the composite, the increasing load was redistributed by the matrix via the interface to the shortened, weaker as well as the remaining, stronger, long fibers. Initial fractographic analysis indicates that this process continued until a significant number of fibers were reduced to ineffective lengths, causing a weakened region in the composite which, in part, led to total composite fracture.

Matrix fracture was characteristically either tensile or shear, with the latter predominating. Since the matrix resins serve primarily as a mechanism for load transfer and stress redistribution, there are certain temperature-related factors that directly or indirectly determine the effectiveness of those functions. On the molecular level, for example, the energy dissipative mechanisms inherent in the mobility of the polymer chain were more constrained with decreasing temperatures. Changes that occurred in the resin at low temperatures affected the load transfer function, a parameter that is sensitive to residual stresses developed during fabrication, to resin brittleness, and to a change in resin modulus. The ductility of the resin matrix decreased rapidly with cryogenic cooling. Resin strength and modulus increased; strain capability was reduced; toughness decreased; and, stress-strain behavior changed from viscoelastic to linearly elastic at 4 K. At cryogenic temperatures there was evidence that the epoxy resin matrix of the G-10CR materials cracked before the glass reinforcement (Figures 1, 9b, 10b).

Although there has been extensive consideration in the published literature about which constituent (the matrix or the reinforcement), fails first, this study indicates that the most probable first failure event for these

testing conditions was the fracture of the outer layer of the epoxy matrix. As the matrix crack in the outer lamina developed and propagated transverse to the applied load and across the specimen, a less effective distribution of the load resulted. Fibers contiguous to the matrix crack became more highly stressed than those firmly embedded, and some bending of the fibers occurred in the vicinity of the cracked matrix. This process continued as the load increased and contiguous regions were weakened. Several factors lend support to matrix cracking preceding significant fiber fracture: First, epoxy strength is lower than that of the glass reinforcement. Second, the nonuniform strengths characteristic of glass fibers signify a randomness in their total fracture pattern for which there is little or no evidence in the constituent failure modes parallel to the applied load at any temperature. There was, however, a distinct randomness in failures transverse to the applied load with a more irregular effect becoming apparent at the lower temperatures. Finally, typical tensile stress-strain curves at 295 K and 76 K for these specimens show a transition in the configuration occurring at 76 K, a "knee" with an accompanying secondary modulus (Figure 1). The appearance of a "knee" has been correlated with initial matrix cracking and the secondary modulus, with interfacial failure.

There were several fractographic features that provided evidence of changing matrix damage at the lower temperatures. The increased brittleness of the matrix resulted in opaqueness. Tear features were apparent at the lamina interface and tear ridges showed in the matrix (Figure 19). A number of matrix cracks, both external and internal were visible. There was more matrix on the fracture surface for the low temperature specimens and there was some evidence of hacklelike marks of the matrix at the fracture surface (21).

Finally, interface failures at all temperatures for these specimens were identified as delamination (of the lamina) and debonding and pullout of the fibers and fiber bundles. Debonding and pullout were most characteristic of failures transverse to the applied load. There was significantly more of this type of damage at the lower temperatures. Delamination was identified in several ways. First, there were the short delamination steps associated with brush fracture of the longitudinal bundles (Figure 17). Second, there was almost total delamination of the lamina in a direction parallel to the applied load for some of the mixed mode failures. Third, there was the transverse delamination at the primary fracture edge for the warp tests at 295 K, which left the undulating surface of the fill bundles intact (Figure 17).

There is some evidence in the published literature to indicate that an increased fiber fracture strength or a decreased matrix or interface shear strength lead to debonding rather than fracture in the debond/fracture subsequence of events. There seems to be some support for this sequence at the lower temperatures of the present study.

In conclusion, examination and analysis of the fracture surfaces of the G-10CR specimens fractured in compression at 295 K, 76 K and 4 K have provided a basis for the identification and characterization of primary composite failure and secondary constituent failure. As the summaries in Tables 3 and 4 indicate there are identifiable temperature-related failure effects. Figures 6-20 correlated with Tables 3 and 4 emphasize the major effects. Figures 21-26 illustrate temperature related increases in strength stiffness, and variability or scatter in the data (in terms of standard deviation and coefficient of variation). This information is also reflected in Tables 3 and 4 and can be correlated with Figures 6-20.

6. Recommendations for Future Studies

There has been little or no fractographic or modeling studies of the low-temperature compression failure behavior for glass-fabric-reinforced epoxies. The in-depth review of published studies that comprised the initial part of this report has been synthesized to provide a comprehensive survey of relevant information that can be used to support and direct the investigative efforts of this study. The literature review has been immeasurably helpful in the development and organization of this report and the failure studies that preceded it. The explanations, interpretations, and extrapolations have provided an invaluable documentary information base.

A logical follow-up of this temperature fracture-mode study should include reconstruction of the fracture process from initiation, through propagation, and on to final fracture developed in terms of a most probable sequence of failure events by using a Fault-free Analysis, which has been described in other publications (10).

Concurrent with a sequence-of-events analysis should be a stress analysis describing material behavior just prior to fracture. The fractography and modeling developed in the present report will provide support information for the analyses suggested above.

These stages, in turn, can serve as a logical supplement to the systematic development of a theory of failure for analyzing the low-temperature behavior of glass-fabric-reinforced nonmetallics under a static compression load.

REFERENCES

1. Rosen, B. W., "Strength of Uniaxial Fibrous Composites," Mechanics of Composite Materials, Wendt, F. W., H. Liebowitz, and Perrone, N., Eds., Pergamon, New York (1970) 621-49.
2. Zweben, C., "Tensile Strength of Fiber-Reinforced Composites: Basic Concepts and Recent Developments," Composite Materials: Testing and Design, ASTM, STP 460, American Society for Testing and Materials, Philadelphia (1969) 528-39.
3. Tetelman, A. S., "Fracture Processes in Fiber Composite Materials," Composite Materials: Testing and Design, ASTM, STP 460, American Society for Testing and Materials, Philadelphia (1969) 473-502.
4. Vinson, J. R., and Chow, T. -W., Composite Materials and Their Use in Structures, John Wiley & Sons, New York (1973).
5. Broutman, L. J., and Krock, R. H., Eds. Modern Composite Materials, Addison-Wesley Publishing Co., Reading, MA (1967).
6. Rosen, B. W., Kalkaini, S. V., and McLaughlin, P. V., Jr., "Failure and Fatigue Mechanisms in Composite Materials," Inelastic Behavior of Composite Materials, American Society of Mechanical Engineers, Applied Mechanics Division, (AMD, Vol. 13), New York (1975) 17-38.
7. Rosen, B. W., "Mechanics of Composite Strengthening," Fiber Composite Materials, American Society for Metals, Metals Park, OH (1965) 37-75.
8. Williams, R. S., and Reifsnider, K. L., "Fracture Analysis of Fatigue Damaged Mechanisms in Fiber Reinforced Composite Materials Using Scanning Electron Microscopy," Report to the Air Force Office of Scientific Research, College of Engineering, Virginia Polytechnic Institute and State University.

9. Zweben, C., "Tensile Failure of Fiber Composites," AIAA J., Vol. 6, No. 12, (December 1968) 2325-31.
10. Masters, J. W., Yeow, Y. T., Louthan, M. R., Jr., Reifsnider, K. L., and Brinson, H. F., "A Qualitative Fault Tree Analysis for the Tensile Failure of Fibrous Laminated Composites," Composites, (April 1977) 111-17.
11. Collins, B. R., Brentnall, W. D., and Toth, I. J., "Properties and Fracture Modes of Borsic-Titanium," Failure Modes in Composites, I. J. Toth, Ed., the Metallurgical Society of AIME, New York (1972) 103-29.
12. Kanninen, M. F., Rybicki, E. F., and Griffith, W. I., "Preliminary Development of a Fundamental Analysis Model for Crack Growth in a Fiber Reinforced Composite Material," Composite Materials: Testing and Design (fourth conference), ASTM, STP 617, American Society for Testing and Materials, Philadelphia (1977) 53-69.
13. Schramm, R. E., and Kasen, M. B., "Cryogenic Mechanical Properties of Boron-, Graphite-, and Glass-Reinforced Composites," Mater. Sci. Eng., 30, (1977) 197-204.
14. Jones, R. C., "Fractography of Aluminum-Boron Composites," Composite Materials Testing and Design, ASTM, STP 460, American Society for Testing and Materials, Philadelphia (1969) 513-27.
15. Hartwig, G., "Mechanical and Electrical Low Temperature Properties of High Polymers," Nonmetallic Materials and Composites at Low Temperatures, A. F. Clark, R. P. Reed, and G. Hartwig, Eds., Plenum Press, New York (1979) 33-50.
16. Morgan, R. J., O'Neal, J. E., and Miller, D. B., "The Structure Modes of Deformation and Failure, and Mechanical Properties of Diaminodiphenyl Sulphone - Cured Tetraglycidyl 4.4' Diaminodiphenyl Methane Epoxy," J. Mater. Sci., 14, (1979) 109-24.

17. Salkind, M. J., "The Role of Interfaces in Fiber Composites," Surfaces and Interfaces II, Physical and Mechanical Properties, 14th Sagamore Army Materials Research Conference, J. J. Burke, N. L. Reed, and V. Weiss, Eds., Syracuse University Press (1968) 417-45.
18. Kelly, A., Strong Solids, Second Edition, Clarendon Press, Oxford (1973) 157-236.
19. Sih, G. C., Hilton, P. D., Badaliance, R., Shenberger, P. S., and Villarreal, G., "Fracture Mechanics for Fibrous Composites," The Test Methods for High Modulus Fibers and Composites, ASTM, STP 521, American Society for Testing and Materials, Philadelphia (1973) 98-132.
20. Hertz, J., "The Effect of Cryogenic Temperatures on the Mechanical Properties of Reinforced Plastic Laminates," Soc. Plast. Eng. J., 21, (February 1965) 181-89.
21. Hull, D., "Nucleation and Propagation Processes in Fracture," Polymeric Materials, American Society for Metals, Metals Park, OH (1975) 487-550.
22. Wigley, D. A., "The Properties of Nonmetals," Mechanical Properties of Materials at Low Temperatures, Plenum Press, New York (1971).
23. Soffer, L. M., and Molho, R., "Mechanical Properties of Epoxy Resins and Glass/Epoxy Composites at Cryogenic Temperatures," NASA-CR-84451, NTIS, Springfield, VA (1967).
24. Mullin, J. V., "Influence of Fiber Property Variations on Composite Failure Mechanisms," Analysis of the Test Methods for High Modulus Fibers and Composites, ASTM, STP 521, American Society for Testing and Materials, Philadelphia (1973) 349-66.
25. Zweben, C., "Fracture Mechanics and Composite Materials: A Critical Analysis," Analysis of the Test Methods for High Modulus Fibers and Composites, ASTM, STP 521, 1973. 65-97.

26. Harlow, D. G., and Phoenix, S. L., "Bounds on the Probability of Failure of Composite Materials," Int. J. Fract., Vol. 15, Nov. 4, (August, 1979) 321-36.
27. Beaumont, P. W. R., and Tetelman, A. S., "Fracture Strength and Toughness of Fibrous Composites," Failure Modes in Composites, Istavan Toth, Ed., AIME, New York (1972) 49-80.
28. Greszczuk, L. B., "Compressive Strength and Failure Modes of Unidirectional Composites," Analysis of the Test Methods for High Modulus Fibers and Composites, ASTM, STP 521, American Society for Testing and Materials, Philadelphia (1973) 192-217.
29. Lanir, Y., and Fung, Y. C. B., "Fiber Composite Columns Under Compression," J. Compos. Mater., Vol. 6, (July 1972) 387-95.
30. Davis, J. G., Jr., "Compressive Strength of Fiber Reinforced Composite Materials," Composite Reliability, ASTM, STP 580, American Society for Testing and Materials, Philadelphia (1975) 364-77.
31. Jones, R. M., Mechanics of Composite Materials, McGraw-Hill, New York (1975) 134-45.
32. Chaplin, C. R., "Compressive Fracture in Unidirectional Glass-Reinforced Plastics," J. Mater. Sci., 12, (1977) 347-52.
33. Chou, T.-W., and Kelly, A., "The Effect of Transverse Shear on the Longitudinal Compressive Strength of Fiber Composites," J. Mater. Sci., 15, (1980) 327-31.
34. Ryder, J. T., and Black, E. D., "Compression Testing of Large Gage Length Composite Coupons," Composite Materials: Testing and Design (fourth conference), ASTM, STP 617, American Society for Testing and Materials, Philadelphia (1977) 170-89.

35. Hartwig, G., "Low Temperature Properties of Epoxy Resins and Composites," Advances in Cryogenic Engineering, Vol. 24, K. D. Timmerhaus, R. P. Reed, and A. F. Clark, Eds., Plenum Press, New York (1978) 17-36.
36. Kasen, M. B., "Mechanical and Thermal Properties of Filamentary-Reinforced Structural Composites at Cryogenic Temperatures, 1: Glass-Reinforced Composites," Cryogenics, Vol. 15, No. 6, (June 1975) 327-49.
37. Kasen, M. B., MacDonald, G. R., Beekman, D. H., and Schramm, R. E., "Mechanical, Electrical, and Thermal Characterization of G-10CR and G-11CR Glass Cloth/Epoxy Laminates Between Room Temperature and 4 K," Advances in Cryogenic Engineering, Vol. 26, A. F. Clark and R. P. Reed, Eds., Plenum Press, New York (1980) 235-44.

List of Tables

Table 1. Typical Values, E-glass

Table 2. Typical Values, General Purpose Epoxy Resin

Table 3. G-10CR Fracture Analysis Summary, Warp Tests (Compression)

Table 4. G-10CR Fracture Analysis Summary, Fill Tests (Compression)

Table 1. Typical Values, E-Glass (9, 22, 33)

E-glass		Temperature			
Properties	295 K	~230 K	~205 K	~83 K	
Tens. St., MPa	3447	5171	5343	5654	
Young's Modulus, E, GPa	72.4	Modulus increases approximately 3% between 295 K and 76 K.			
% Fracture Elongation	~2.5%				

Table 2. Typical Values, General Purpose Epoxy Resin

Epoxy Properties	Temperature		
	295 K	77 K	20 K
Tens. St., MPa	41	103	100
Compress. St., MPa	90-138		
Young's Modulus, E, GPa	21	47	66
% Fracture Elongation	4.5%	2%	1.8%

Table 3 G-10CR Fracture Analysis Summary, Warp Tests (Compression)

295 K (8 specimens)	76 K (7 specimens)	4 K (3 specimens)
<p><u>σ^{CU} vs. Failure Mode:</u>*</p> <p>(a) low σ^{CU}: ~55° slant</p> <p>(b) high σ^{CU}: V-notch (chisel)</p>	<p><u>σ^{CU} vs. Failure Mode:</u>*</p> <p>(a) low σ^{CU}: V-notch (chisel)</p> <p>(b) high σ^{CU}: mixed mode</p>	<p><u>σ^{CU} vs. Failure Mode:</u>*</p> <p>(a) low σ^{CU}: mixed (Failed at grip--no gage section separation)</p> <p>(b) high σ^{CU}: mixed (55° slant, delamination, and bending.)</p>
<p><u>Primary Mode:</u></p> <p>37% ~55° slant 25% V-notch</p> <p>38% Miscellaneous (broke in gage section, mixed or missing)</p>	<p><u>Primary Mode:</u></p> <p>14% ~55° slant 43% V-notch at face of grip 43% other (mixed and saw-tooth)</p>	<p><u>Primary Mode:</u></p> <p>67% mixed 33% failed at grip--no gage section separation</p>
<p><u>Primary Fracture Edge</u></p> <p>Major transverse crack across specimen. Initially cracked through matrix of outer lamina.</p>	<p><u>Primary Fracture Edge</u></p> <p>Major transverse crack across specimen; same as 295 K. Some tearing-type damage at edge.</p>	<p><u>Primary Fracture Edge</u></p> <p>2 specimens show major transverse crack similar to 295 K and 76 K. No gage-section separation of third specimen.</p>
<p><u>Constituent Failure</u></p> <p>(a) Longitudinal Direction (warp) Brush fracture of fiber bundles with some slight delamination at fabric crossovers</p> <p>(b) Transverse Direction (fill) some fiber microcracks, breaks and pullout.</p> <p>Many fiber bundles show delaminated outer surface but imbedded in inner matrix resulting in an undulating surface.</p> <p>(c) Interface Damage Primarily delamination</p> <p>(d) Matrix</p> <p>Glassy and transparent. Smooth at fracture edge. No evidence of matrix cracks outside the fractured area</p>	<p><u>Constituent Failure</u></p> <p>More general damage and more random in nature than 295 K. Rough fracture surface</p> <p>(a) Longitudinal Direction (warp) some brush fracture and delamination of fiber bundles</p> <p>(b) Transverse Direction (fill) Considerable damage to transverse bundles and individual fibers fracture, debond, and pullout. Bundles pulled out--not imbedded in inner matrix as they were at 295 K.</p> <p>(c) Interface Damage Debonding, delamination and pullout</p> <p>(d) Matrix</p> <p>Opaque. Microcracks in gage section on reverse side of fracture surface.</p>	<p><u>Constituent Failure</u></p> <p>Considerable damage at primary transverse crack.</p> <p>(a) Longitudinal Direction (warp) some brush fracture longitudinal fiber bundles with some microcracks in fibers and delamination.</p> <p>(b) Transverse Direction (fill) microcracks in fibers. Some debonding, fiber fracture and pullout.</p> <p>(c) Interface Damage Considerable delamination some fiber debonding</p> <p>(d) Matrix</p> <p>Opaque. Significant matrix damage--cracking and roughness. More matrix showing on fracture surface than at higher temperature. Cracks showing on external specimen surface at warp and fill crossovers.</p>

*Note: σ^{CU} refers to ultimate compressive strength.

Table 4. G-10CR Fracture Analysis Summary, Fill Tests (Compression)

295 K (3 specimens)	76 K (3 specimens)	4 K (3 specimens)
<p><u>σ^{CU} vs. Failure Mode:</u></p> <p>(a) low σ^{CU}: ~55° slant</p> <p>(b) high σ^{CU}: ~55° slant</p>	<p><u>σ^{CU} vs. Failure Mode:</u></p> <p>(a) low σ^{CU}: ~55° slant</p> <p>(b) high σ^{CU}: V-notch</p>	<p><u>σ^{CU} vs. Failure Mode:</u></p> <p>(a) low σ^{CU}: ~55° slant</p> <p>(b) high σ^{CU}: ~55° slant</p>
<p><u>Primary Mode:</u></p> <p>67% ~55° slant 33% Missing Spec.</p>	<p><u>Primary Mode:</u></p> <p>67% ~55° slant 33% V-notch at grip</p>	<p><u>Primary Mode:</u></p> <p>100% ~55° slant</p>
<p><u>Primary Fracture Edge</u></p> <p>Major transverse crack across specimen Initially cracked through matrix of outer lamina</p>	<p><u>Primary Fracture Edge</u></p> <p>Major transverse crack across specimen; see 295 K. More tearing-type damage</p>	<p><u>Primary Fracture Edge</u></p> <p>Major transverse across specimen; see 295 K.</p>
<p><u>Constituent Failure</u></p> <p>(a) Longitudinal Direction (fill) Brush fracture with some delamination at crossovers of fiber bundles.</p> <p>(b) Transverse Direction (warp) More random fiber damage than warp tests. Considerable damage of fibers debond, fracture and pullout.</p> <p>(c) Interface Damage Delamination. Debonding and pullout of bundles and individual fibers.</p> <p>(d) Matrix Glassy and translucent</p>	<p><u>Constituent Failure</u> (more surface damage than at 295 K)</p> <p>(a) Longitudinal Direction (fill) Brush fracture of fiber bundles with more delamination than room temperature. Microcracks in fibers.</p> <p>(b) Transverse Direction (Warp) More transverse fiber bundle debonding, fracture and pullout. Less individual fiber debonding fracture and pullout. Considerable transverse damage at fracture edge.</p> <p>(c) Interface Damage Delamination, debond, and pullout</p> <p>(d) Matrix Opaque. More broken up and cracked than at 295 K. Significant matrix cracks undercutting transverse fibers. Transverse crack of matrix on reverse side of fracture surface.</p>	<p><u>Constituent Failure:</u> (Not as much visible fiber damage on fracture face; more matrix showing compared to that at 295 K)</p> <p>(a) Longitudinal Direction (fill) Few bundle fractures with some delamination-mostly at fracture edge.</p> <p>(b) Transverse Direction (warp) Considerable fiber damage; irregular and random damage of individual fibers and bundles; debonding, fracture and pullout.</p> <p>(c) Interface Damage Some longitudinal delamination. Transverse fiber and bundle debond and pullout.</p> <p>(d) Matrix Opaque. More matrix showing on fracture surface Small number of glassy regions. Irregular surface Some internal cracks showing on reverse side.</p>

LIST OF FIGURES

- Figure 1. Typical tensile stress-strain diagram G-10CR, Warp (37).
- Figure 2. Laminate and specimen configurations used in determining static compressive properties of G-10CR at 295 K, 76 K, 4 K.
- Figure 3. Fixture for static compression testing at cryogenic temperatures (13).
- Figure 4. Typical primary fracture modes in compression. G-10CR at 295 K, 76 K, 4 K.
- Figure 5. G-10CR. Primary compression fracture mode vs. temperature. See Tables 3 and 4 for information on the number of specimens in each machine mode.
- Figure 6. G-10CR, warp test, 295 K, $\sim 55^\circ$ slant mode fracture (37).
- Figure 7. G-10CR, fill test, 295 K. $\sim 55^\circ$ slant mode fracture (37).
- Figure 8. G-10CR, warp test, 76 K. (a) $\sim 55^\circ$ slant mode (b) and (c) mixed-mode fracture. (a), (b), and (c) are different specimens (37):
- Figure 9. G-10CR, warp test, 76 K. (a), (b), and (c) are different specimens (37).
- Figure 10. G-10CR, fill test, 76 K. (a) and (b) are different specimens (37).
- Figure 11. G-10CR, warp test, 4 K mixed mode failure (37).
- Figure 12. G-10CR, warp test, 4 K. (a) and (b) are different examples of mixed mode failure (37).
- Figure 13. G-10CR, fill test, 4 K. $\sim 55^\circ$ slant mode failure (37).
- Figure 14. G-10CR, warp test, 295 K. (a) and (b) are different specimens.

- Figure 15. G-10CR, warp test, 295 K. Fracture surface (35).
- Figure 16. G-10CR, warp test, 295 K. SEM of fracture surface (37).
- Figure 17. G-10CR, warp test, 295 K. SEM of fracture surface (37).
- Figure 18. G-10CR, warp test, 76 K. SEM of fracture surface (37).
- Figure 19. G-10CR, warp test, 4 K. SEM of fracture surface (37).
- Figure 20. G-10CR, warp test, 4 K. SEM of fracture surface (37).
- Figure 21. G-10CR. Compressive strength, Young's modulus, tensile strain to failure vs. temperature (37).
- Figure 22. G-10CR. Young's modulus vs. temperature (37).
- Figure 23. G-10CR. Compressive strength vs. temperature (37).
- Figure 24. G-10CR. Percent increase in tensile strain to failure, Young's modulus, and compressive strength at cryogenic temperatures relative to room temperature. Calculated from results in reference 37.
- Figure 25. G-10CR. Standard deviation vs. temperature (37).
- Figure 26. G-10CR. Coefficient of variation in percent vs. temperature (37).

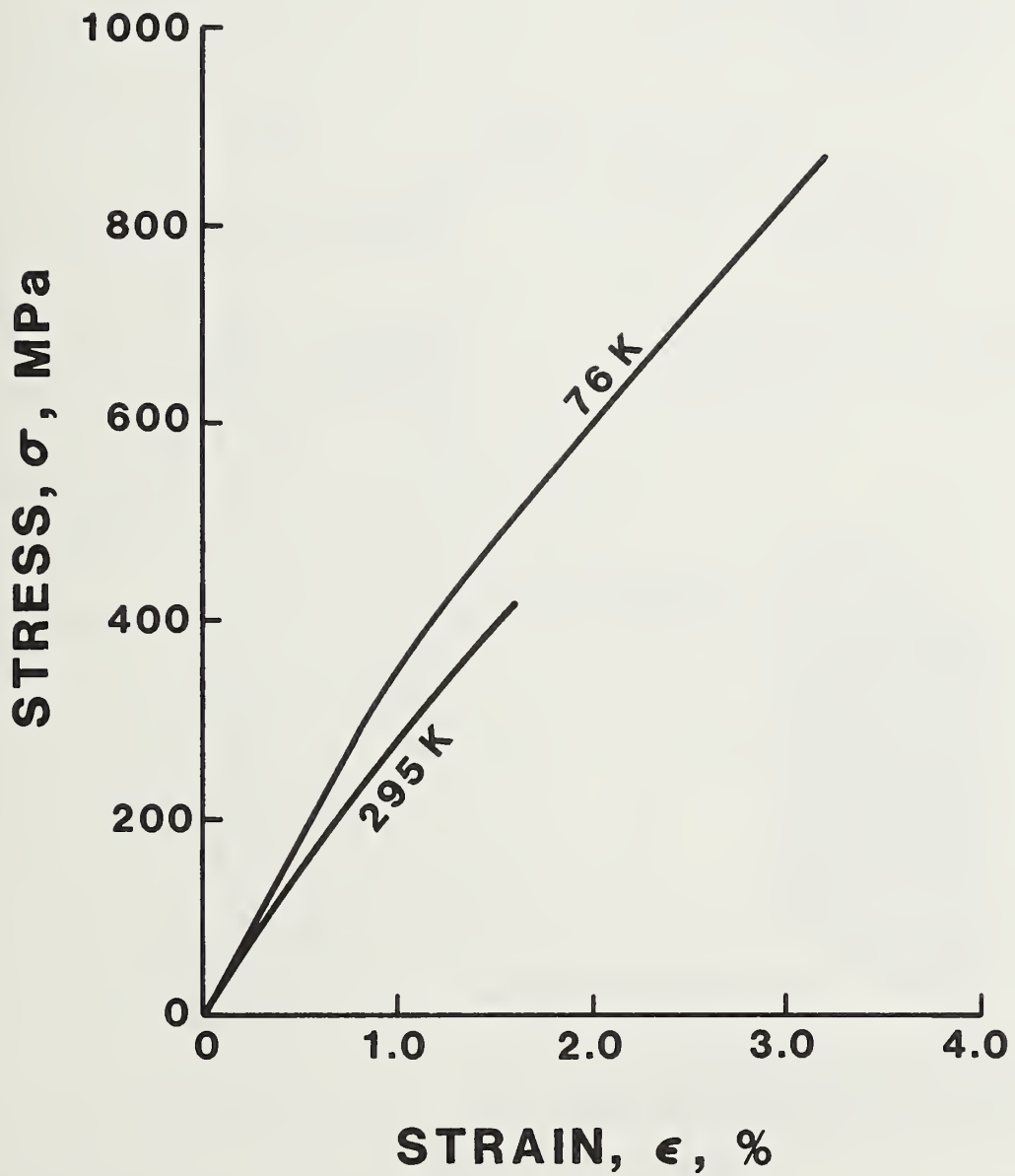


Figure 1. Typical tensile stress-strain diagram, G-10CR, warp (37).

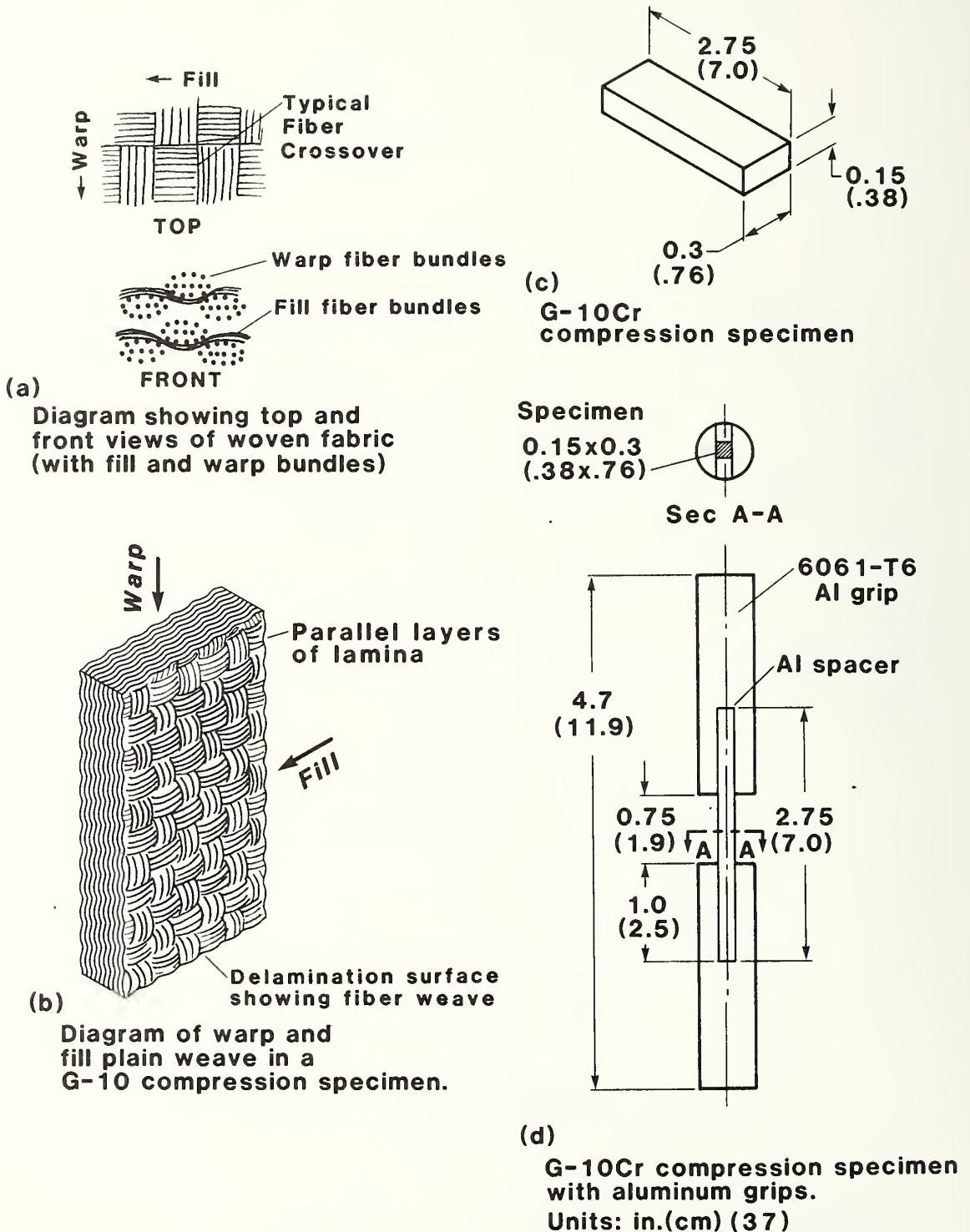


Figure 2. Laminate and specimen configurations used in determining static compressive properties of G-10CR at 295K, 76K and 4K.

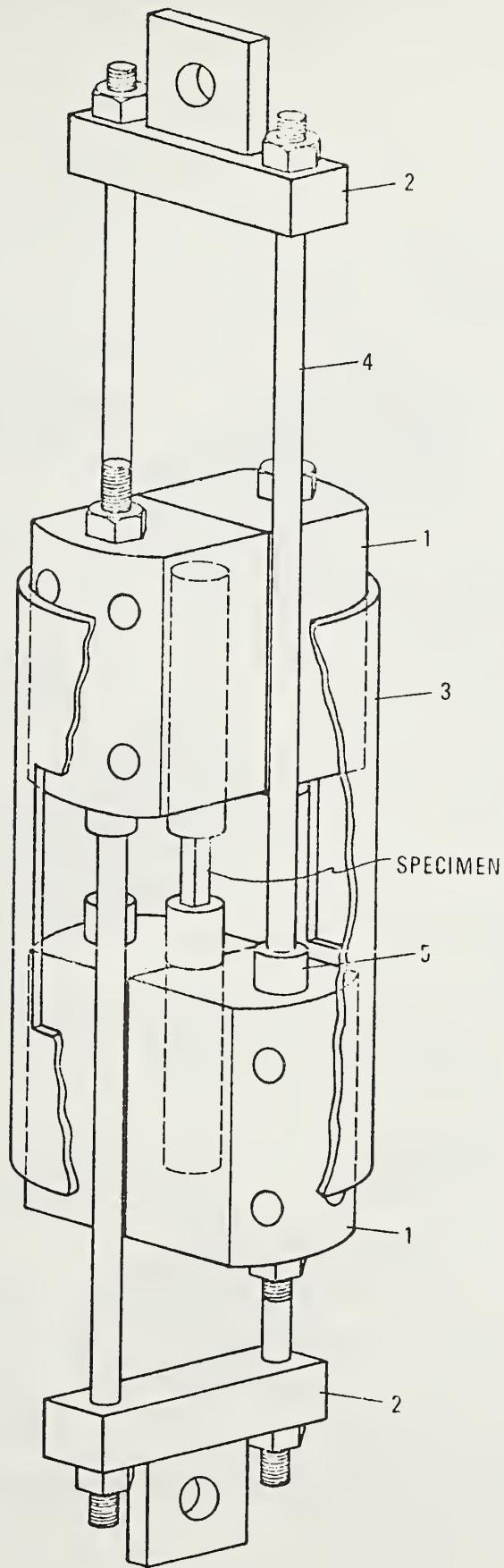


Figure 3 Fixture for static compression testing at cryogenic temperatures (13).

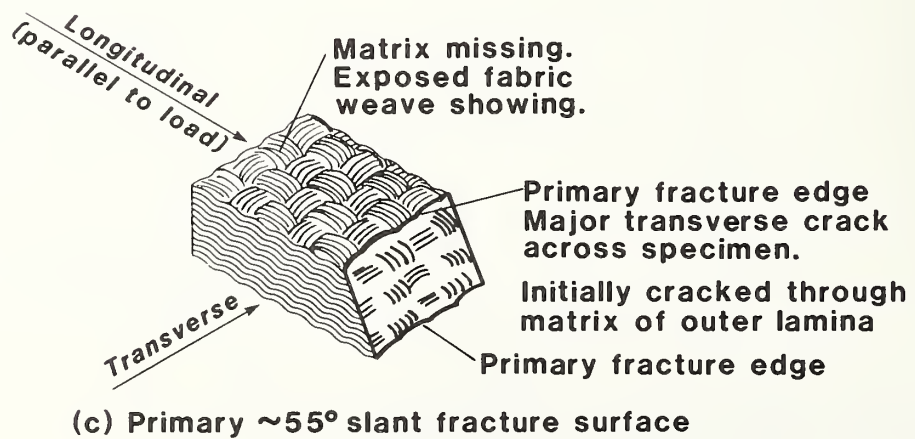
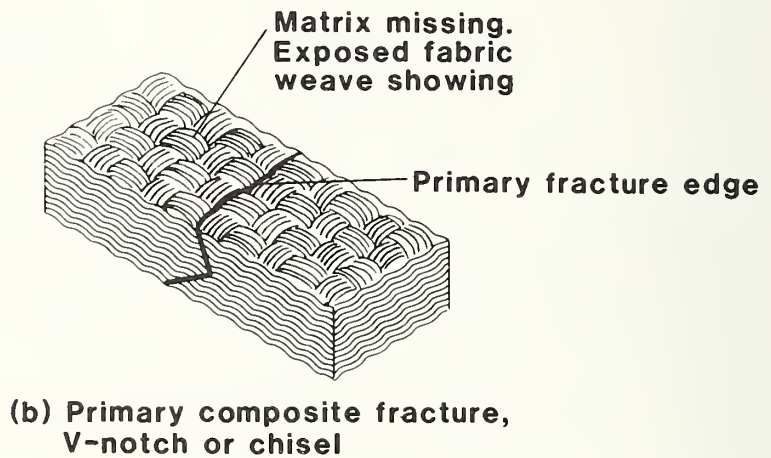
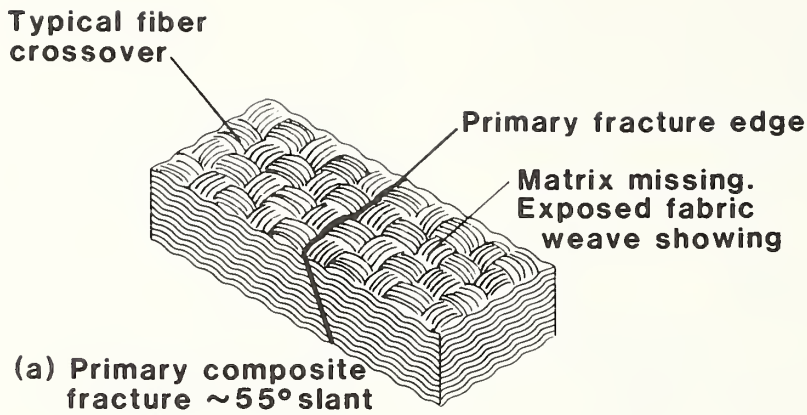


Figure 4. Typical primary fracture modes in compression. G-10CR at 295K, 76K, 4K.

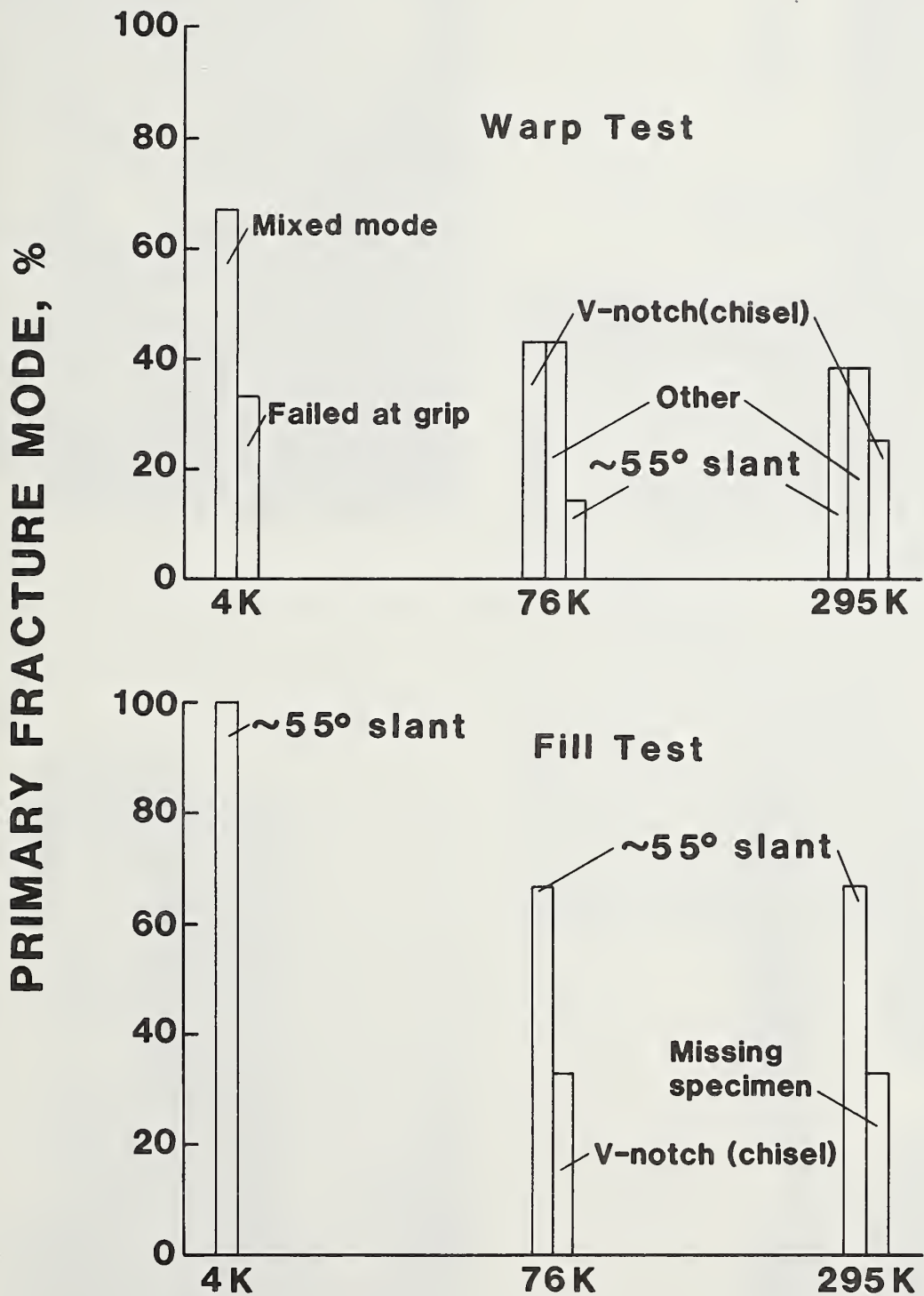
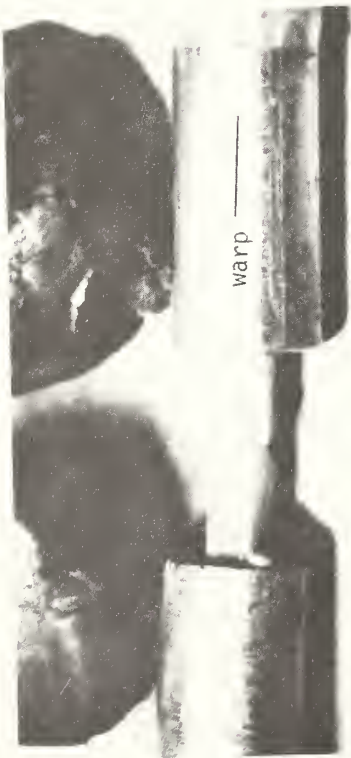


Figure 5. G-10CR. Primary compression fracture mode vs. temperature. See Tables 3 and 4 for information on the number of specimens in each fracture mode.



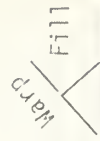
(a) $\sim 55^\circ$ Slant Mode
 $\sigma_{cu} = 357.7$ Mpa



(b) Fracture surfaces of (a)



(c) Enlarged view of (a) showing undulating characteristic of the fabric



Primary Fracture Edge



(d) Enlarged view of the fracture surface (a) showing relatively little transverse (fill) damage

Figure 6. G-10CR, warp test, 295K, $\sim 55^\circ$ slant mode fracture (37)



(a) Fracture Surfaces
 $\sigma_{CU} = 239.7 \text{ Mpa}$



(b) Fracture surfaces of (a) from the side

Test direction



(c) Enlarged view of the fracture surface, (a)

longitudinal
 (test) direction; fill.

Figure 7. G-10CR, fill test, 295 K. $\sim 55^\circ$ slant-mode fracture (37)



(a) $\sim 55^\circ$ slant mode. Some evidence of tearing at primary fracture edge
 $\sigma_{Cu} = 790.4 \text{ Mpa}$

test direction



(b) Mixed Mode Failure. $\sigma_{Cu} = 778.1 \text{ Mpa}$

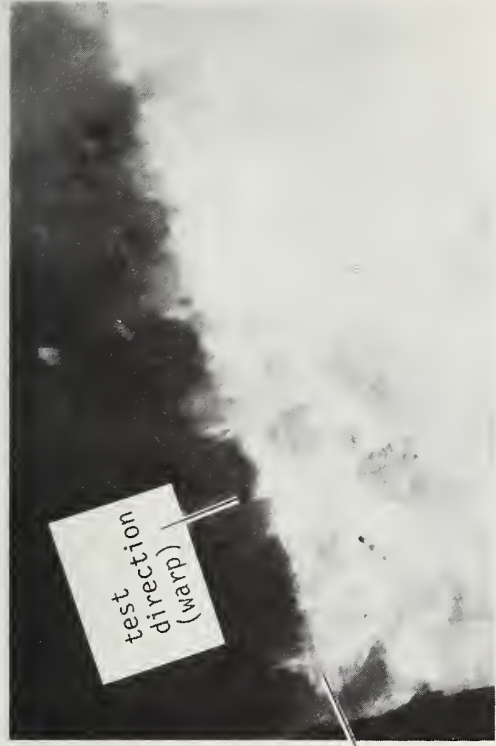


(c) Mixed Mode Failure. $\sigma_{Cu} = 682.0 \text{ Mpa}$

Figure 8. G-10 CR, warp test, 76K. (a) $\sim 55^\circ$ slant-mode (b) and (c) mixed-mode fracture (a), (b), and (c) are different specimens (37).



(a) Typical Fracture Surface, Warp Test, 76K.
 $\sigma_{Cu} = 790.4 \text{ Mpa}$

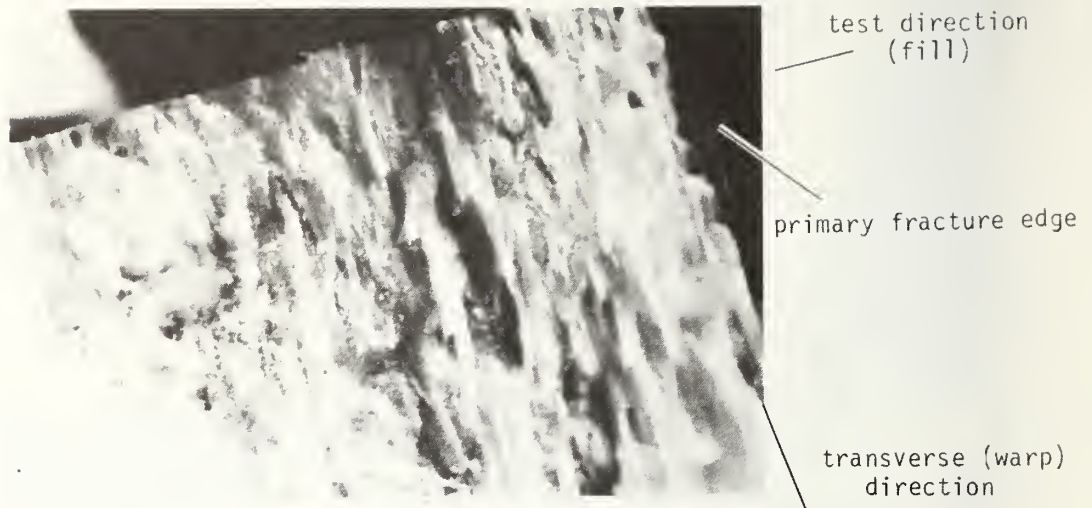


(b) Matrix cracking across specimen gage section face. $\sigma_{Cu} = 832.6 \text{ Mpa}$



(c) Mixed Mode Failure. $\sigma_{Cu} = 703.5 \text{ Mpa}$

Figure 9. G-10Cr, warp test, 76 K (a), (b), and (c) are different specimens. (37)



(a) $\sim 55^\circ$ slant mode. Considerable transverse (fill) damage. $\sigma_{cu} = 536.6$ Mpa



(b) Matrix cracking across specimen gage section face $\sigma_{cu} = 561.6$ Mpa

Figure 10. G-10CR, Fill Test, 76K (a) and (b) are different specimens. (37).



(a) Mixed mode: $\sim 55^\circ$ slant, longitudinal delamination, and bending. Test direction is parallel to axis of end caps. $\sigma_{cu} = 854.5$ Mpa



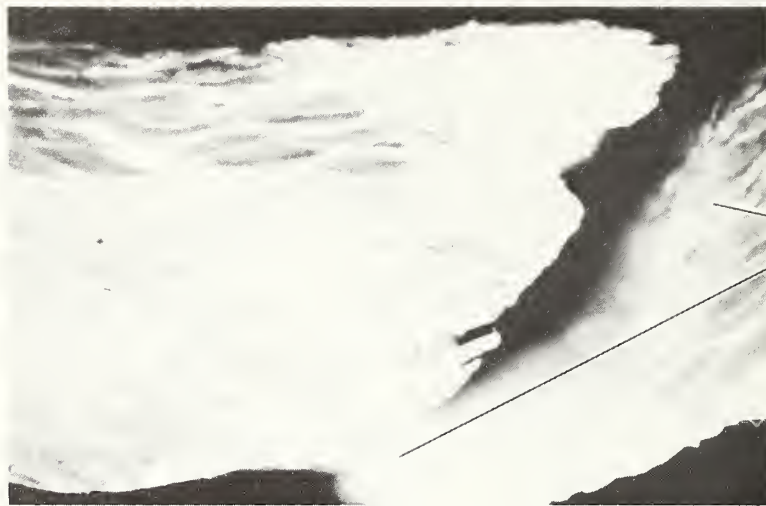
(b) Enlarged view at left end cap.



(c) Enlarged view of fracture at right end cap

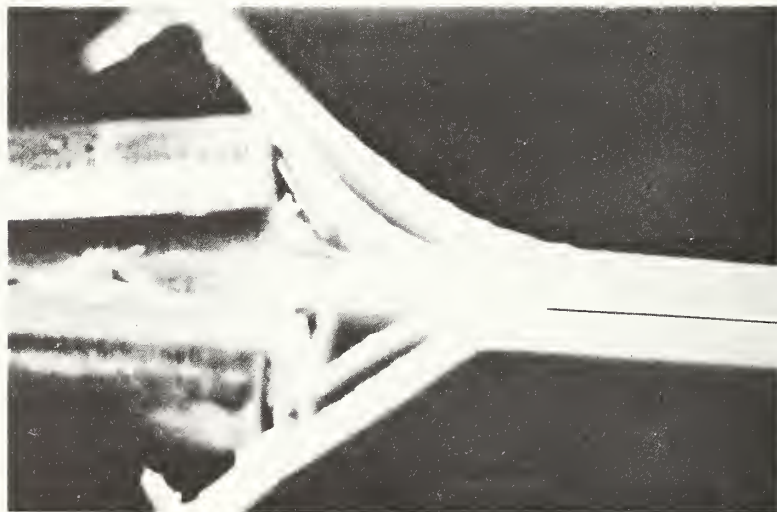
Figure 11. G-10CR, warp test, 4K mixed mode failure (37)

test
direction



bending

(a) Mixed mode failure: delamination, bending of the specimen, and slant mode fracture.
 $\sigma_{CU} = 881.9 \text{ Mpa}$



test (warp)
direction

(b) Mixed Mode Failure. No gage section separation. $\sigma_{CU} = 849.9 \text{ Mpa}$

Figure 12. G-10CR, Warp Test, 4K. (a) and (b) are different examples of mixed mode failure (37).



(a) $\sim 55^\circ$ slant mode with longitudinal delamination parallel to the specimen surface. $\sigma_{Cu} = 507.1$ Mpa



(b) Fracture surface of (a)

warp
(transverse)
direction

test (fill)
direction

primary fracture edge

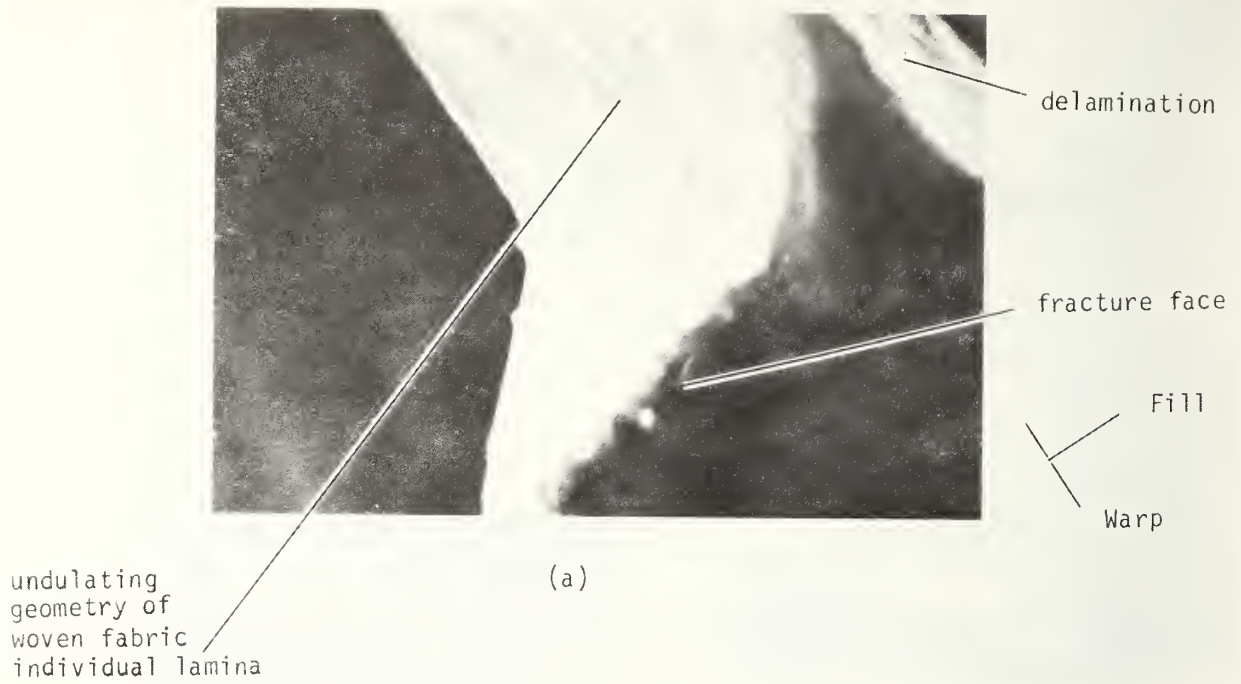


(c) Enlarged view of the fracture surface of another specimen. $\sigma_{Cu} = 593.3$ Mpa

primary
fracture
edge

longitudinal
(test) direction.
Fill

Figure 13. G-10CR, fill test, 4K. $\sim 55^\circ$ slant mode failure (37)



fill (transverse) fiber bundle fracture and pullout.

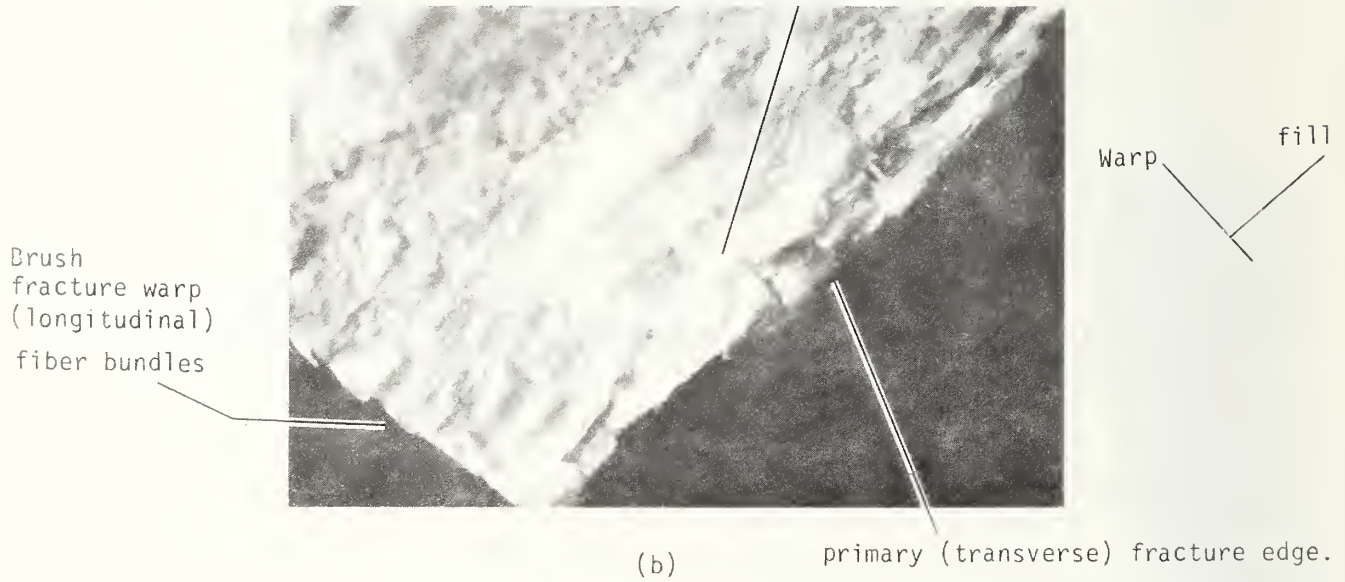
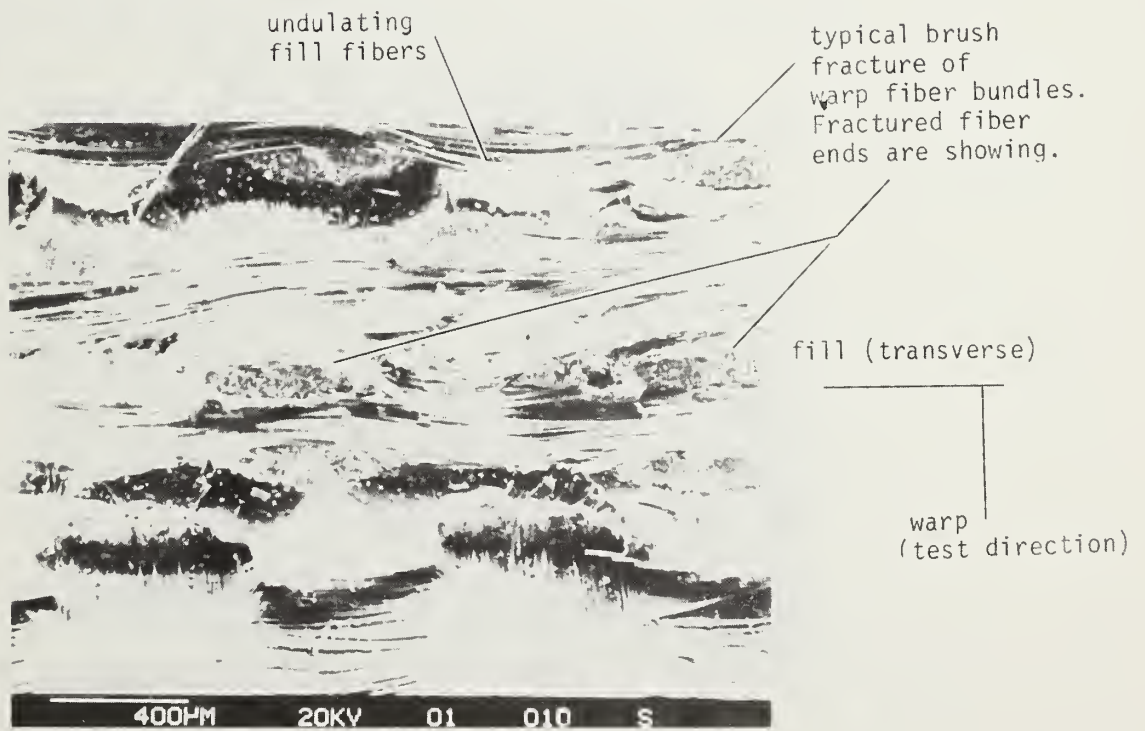
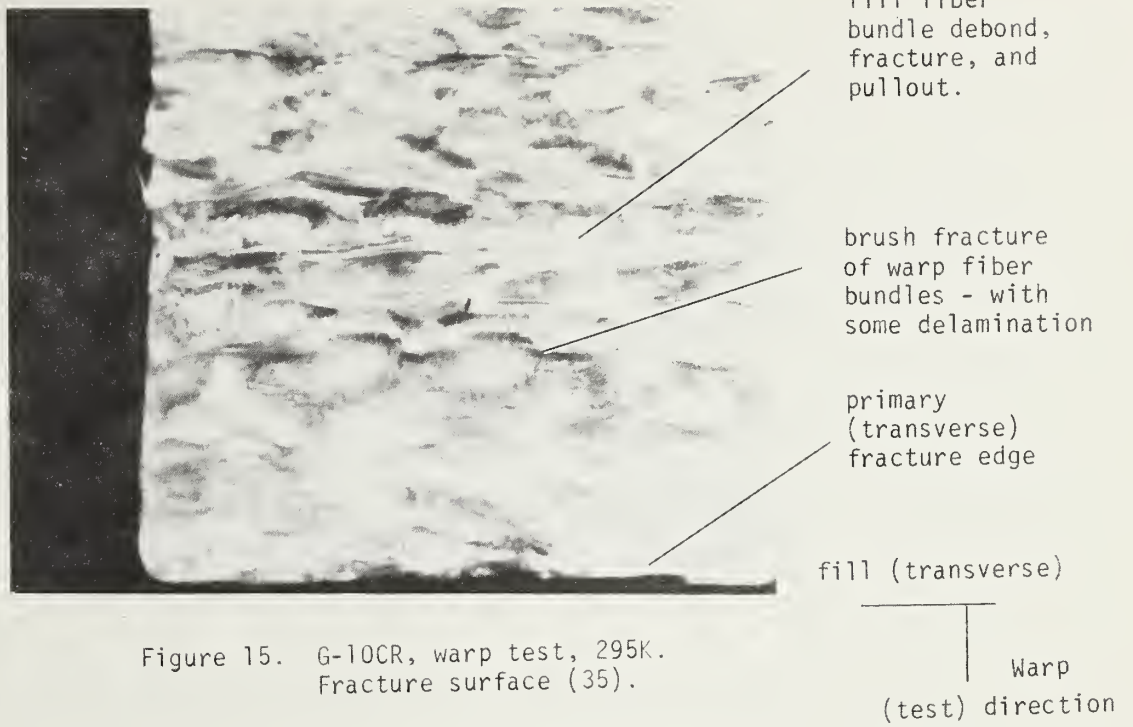
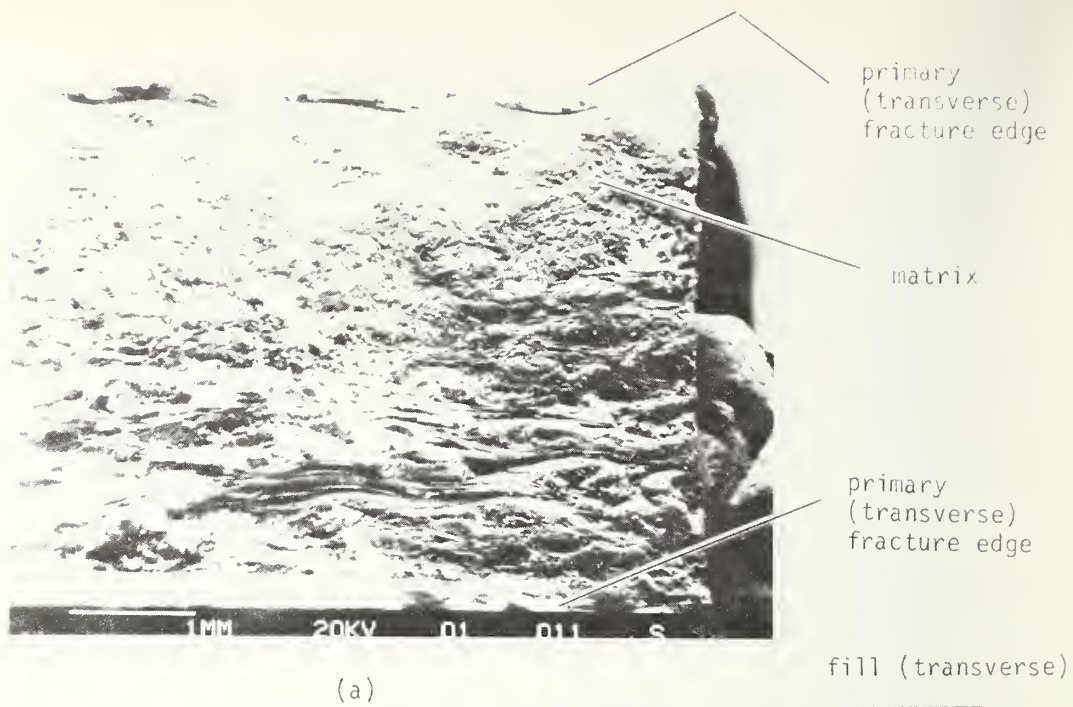


Figure 14. G-10CR, warp test, 295 K.
 (a) and (b) are different specimens.

(37)





Matrix steps. Delaminated regions showing missing warp bundles. End views of fractured warp bundles are visible at rear boundaries of matrix steps.

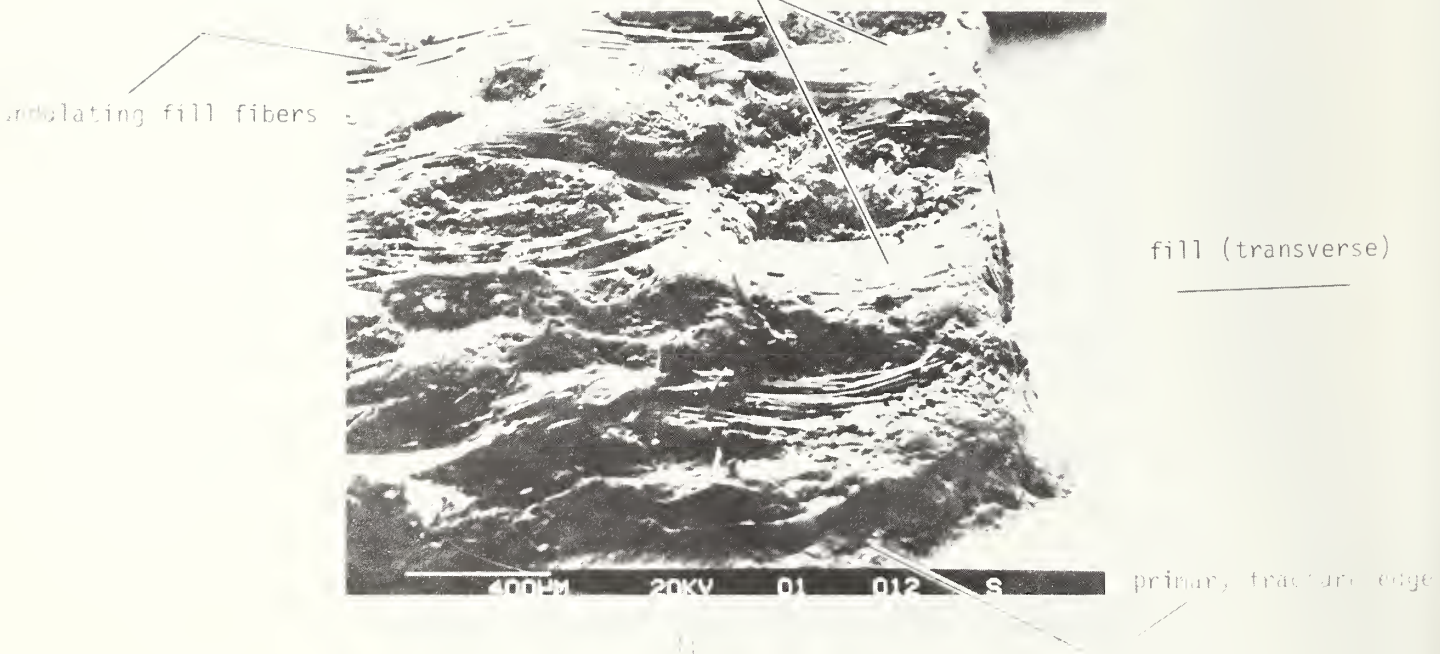


Figure 1. SEM, 20KV, warp to fill, 95% TEM of fracture surface (a)

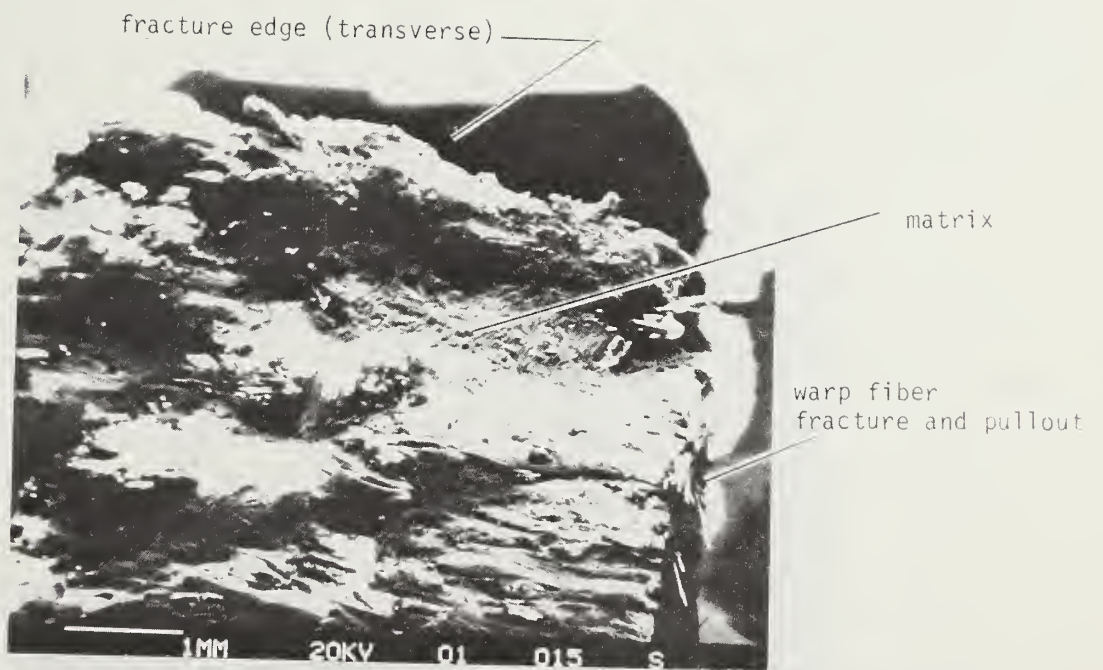


fill fiber
debond, fracture,
and pullout

brush fracture
warp fiber
bundles

fill (transverse)

(a)



fracture edge (transverse)

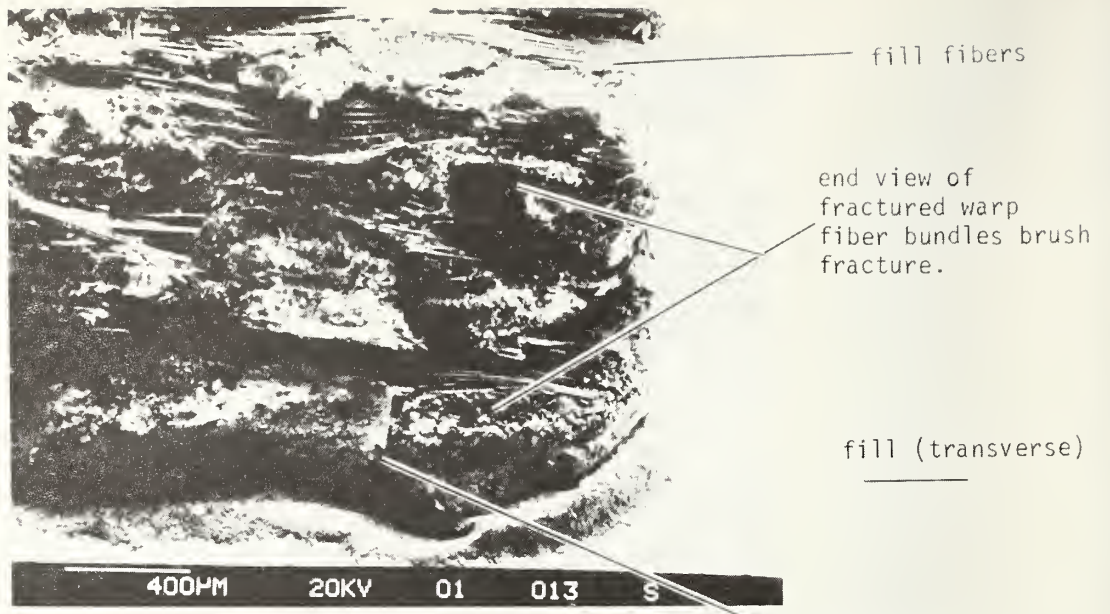
matrix

warp fiber
fracture and pullout

1MM 20KV 01 015 S

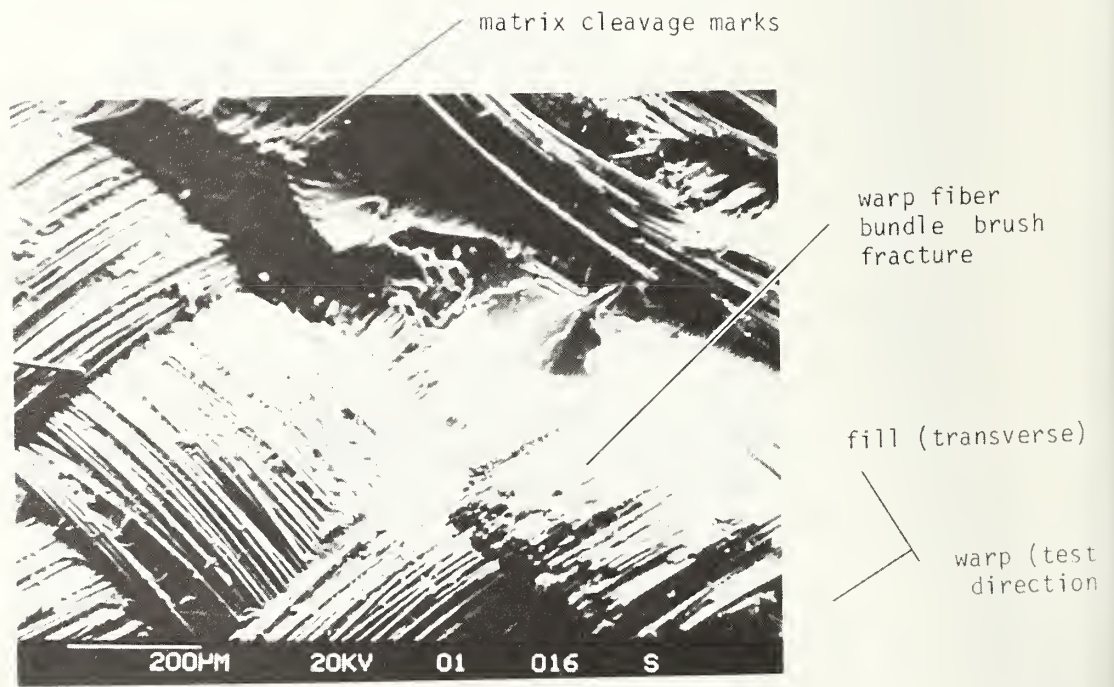
(b)

Figure 10 G-10CR, warp test, 76P. SEM of fracture surface (a).



(a)

Primary fracture edge



(b)

Figure 10-11-11-11 warp test, 4K. SEM of fracture surface (37)

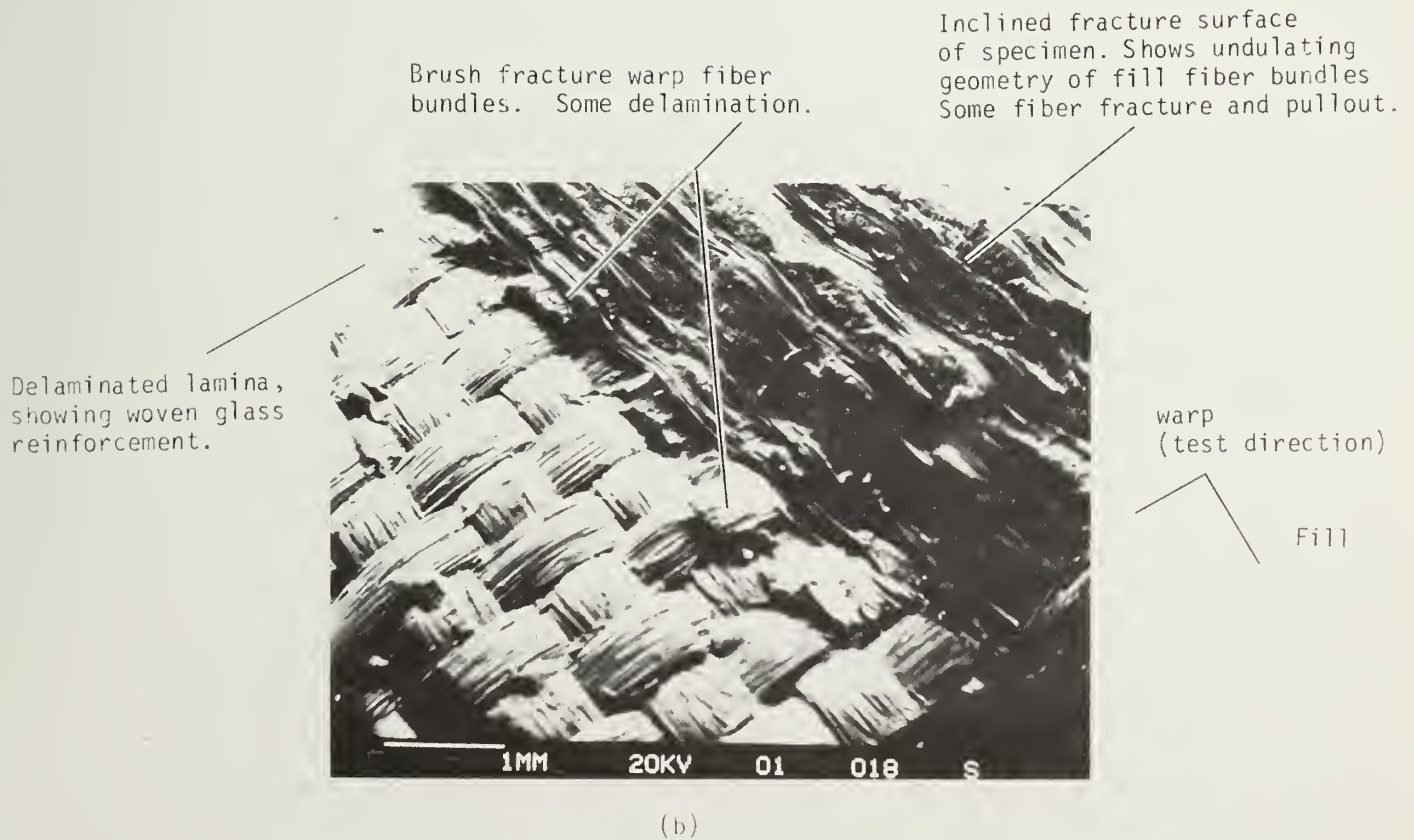
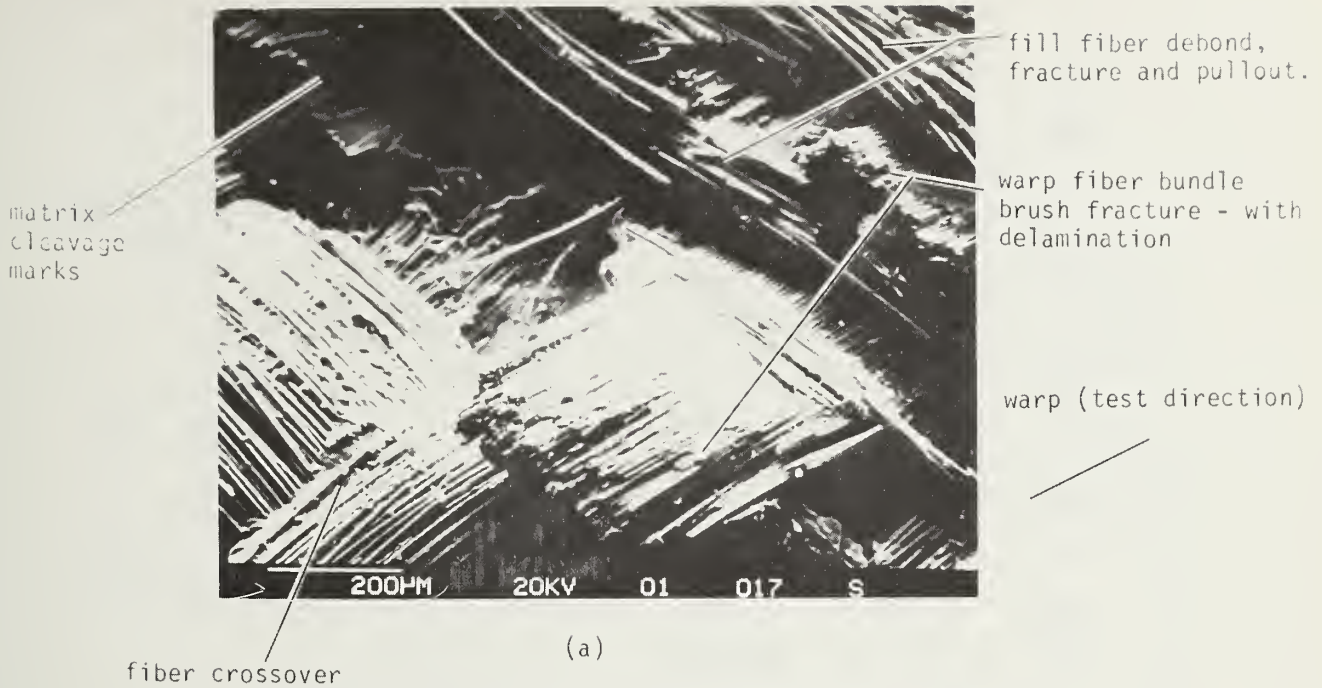


Figure 20. G-10CR, warp test, 4K. SEM of fracture surface (37)

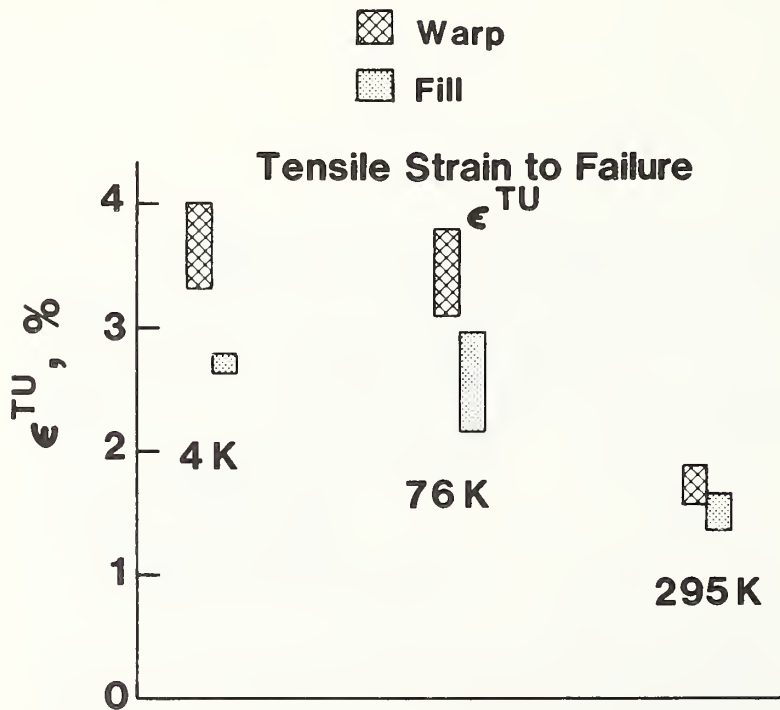
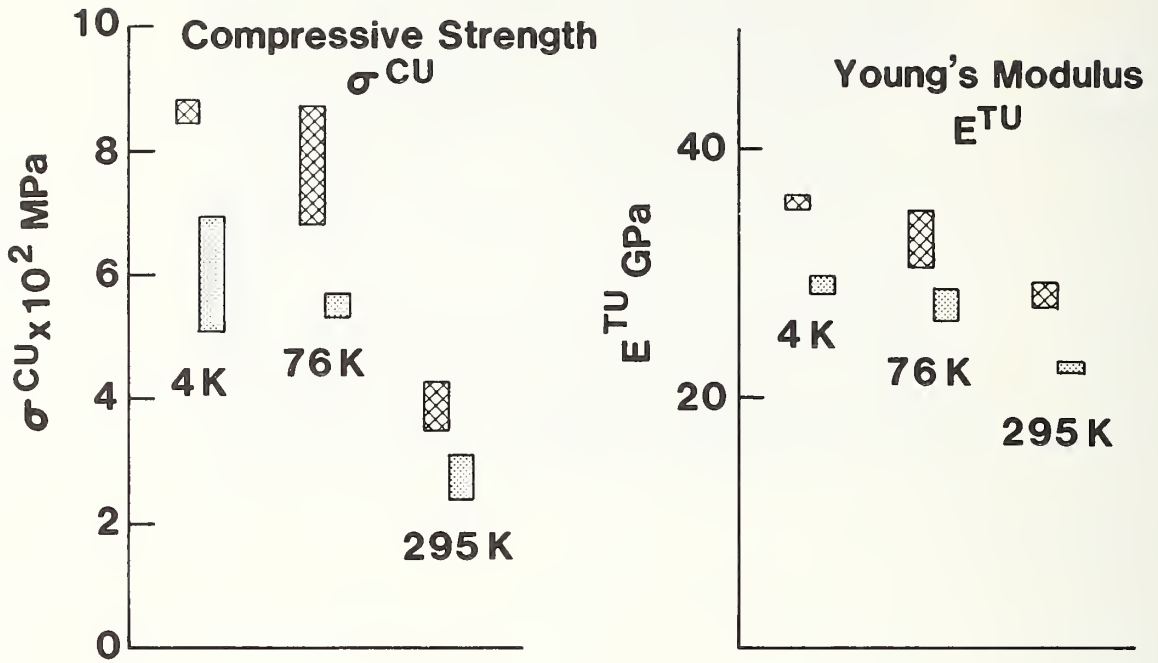


Figure 21. G-10CR. Compressive strength, Young's modulus, tensile strain to failure vs. temperature (37).

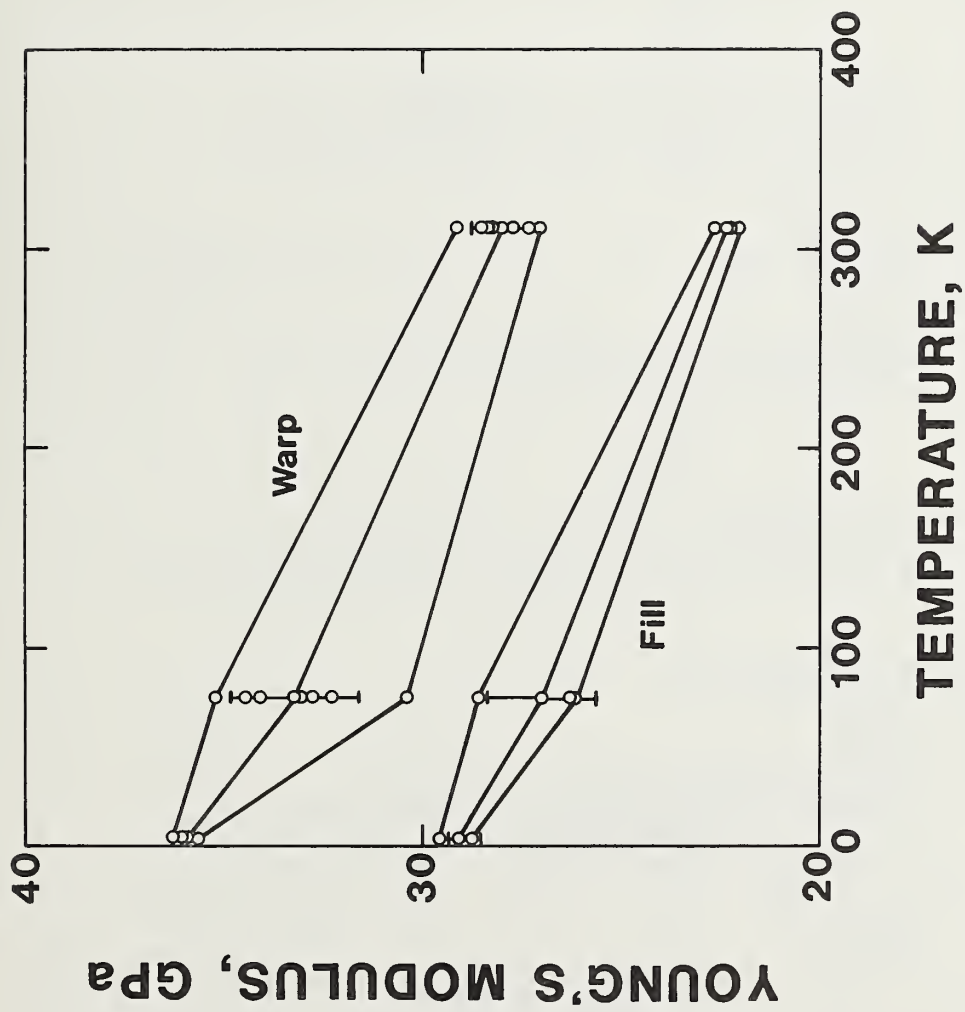


Figure 22. G-10CR. Young's modulus vs. temperature (37).

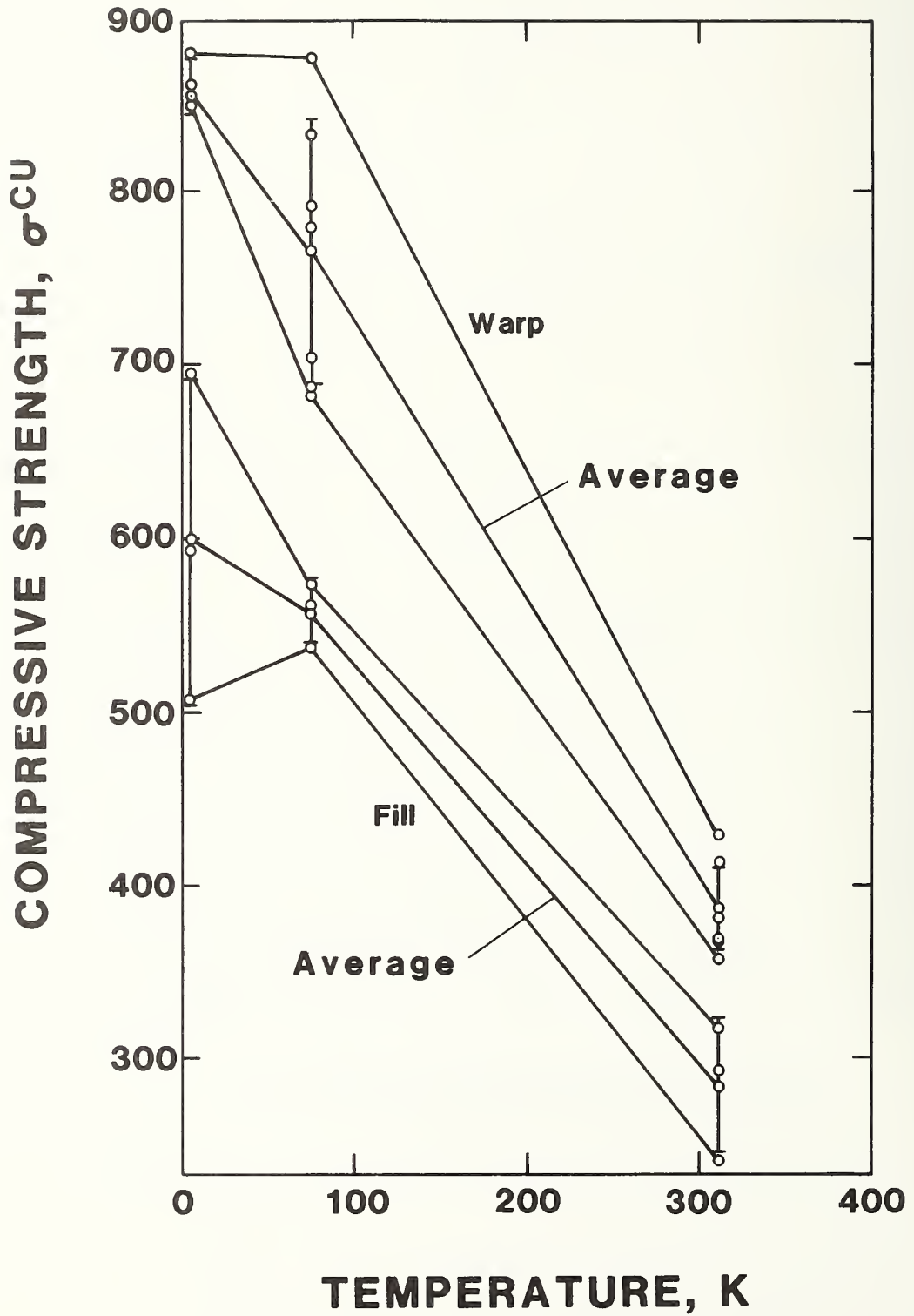


Figure 23. G-10CR Compressive strength vs. temperature (37).

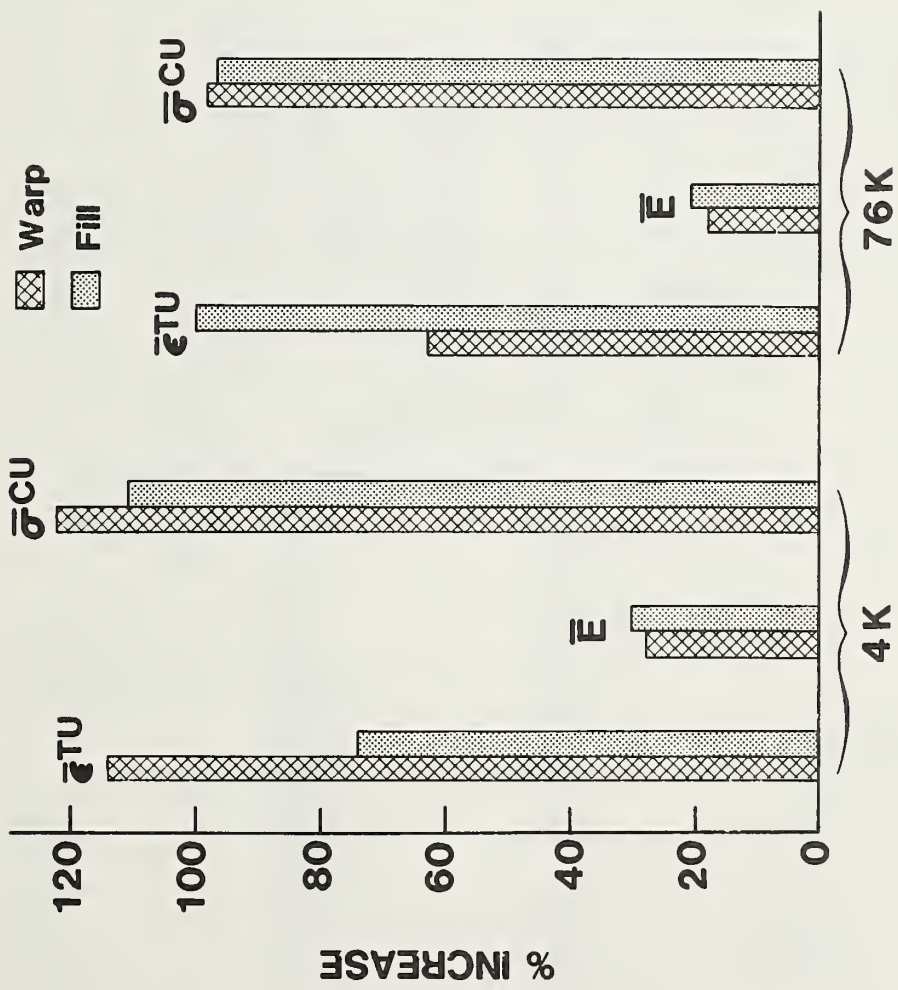


Figure 24. G-10CR. Percent increase in tensile strain to failure, Young's modulus, and compressive strength at cryogenic temperatures relative to room temperature. Calculated from results in reference 37.

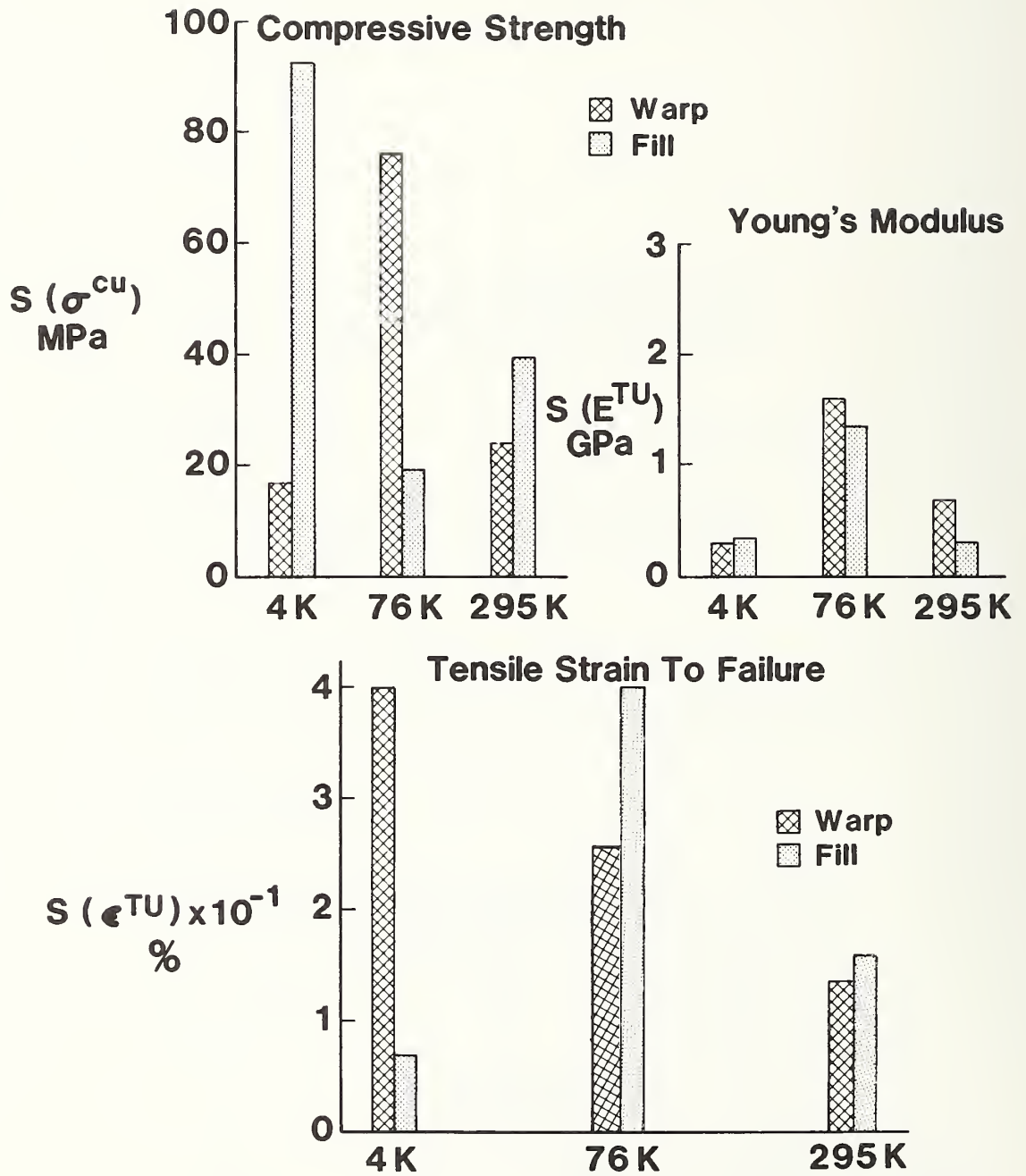


Figure 25. G-10CR. Standard deviation vs. temperature (37).

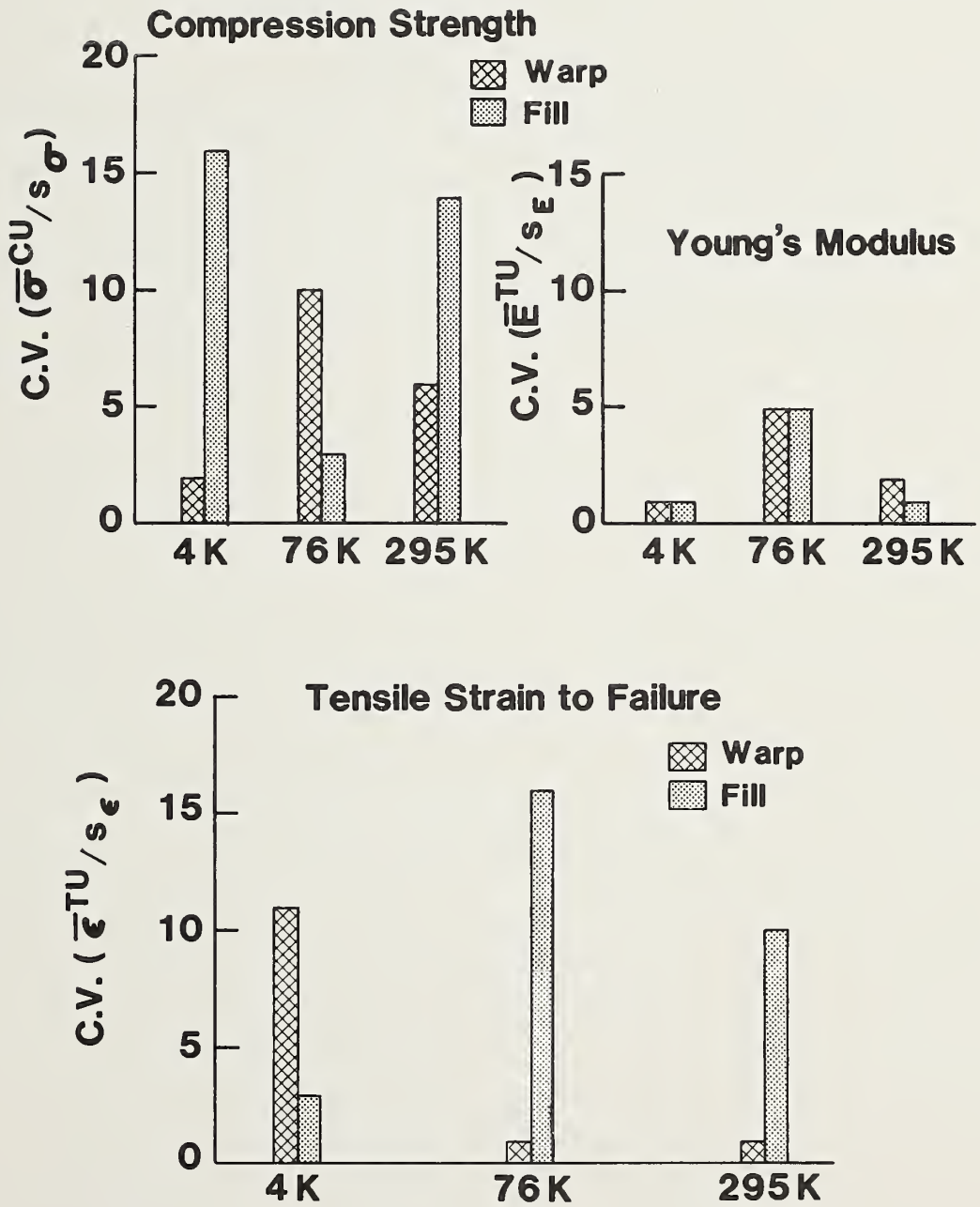


Figure 26. G-10CR. Coefficient of variation in percent vs. temperature (37).

STATIC AND DYNAMIC YOUNG'S MODULI OF TWO
FIBER-REINFORCED COMPOSITES

H. M. Ledbetter
Fracture and Deformation Division
National Bureau of Standards
Boulder, Colorado

ABSTRACT

Two uniaxially fiber-reinforced composites were studied: graphite/epoxy and E-glass/epoxy. Dynamic Young's modulus was determined at kHz frequencies using a Marx three-component oscillator. Comparison with the static Young's modulus determined in compression shows agreement within experimental error.

Elastic constants find many uses. In technological materials they assume importance whenever problems arise concerning deflections, elastic stability (buckling), excessive elastic deformation (jamming), thermoelastic stress, residual stress, fracture, and so on. Ratios of elastic modulus to density or to thermal conductivity provide well-known structural design parameters. Elastic constants correlate empirically with many practical properties such as strength, hardness, and wear. Because they relate intimately to both the interatomic potential and the lattice-vibration spectrum, elastic constants relate in turn to many fundamental solid-state phenomena such as diffusion, theoretical strength, and lattice-defect energies. Elastic constants appear as coefficients in thermodynamic equations of state where their relationships to free energy, specific heat, and thermal expansivity become especially clear. Since they can be measured accurately (typically within one percent or less) and small changes can be detected easily (typically 1 in 10^5 or better), elastic constants are useful physical properties for characterizing and comparing materials and for detecting changes in material properties.

Elastic constants are especially important for composites. These materials exhibit elastic deformation at all stress levels up to rupture.

Methods for measuring elastic constants fall into two categories: static and dynamic. Static measurements tend to be made in engineering laboratories at high stress levels. Dynamic measurements tend to be made in physics laboratories at very low stress levels. The dynamic test frequency varies considerably: near 1 Hz for torsional-pendulum and forced-vibration measurements; up to several hundred kHz for resonance measurements; up to 100 MHz for pulse-echo measurements.

Dynamic and static elastic-constant measurements remain unreconciled among many engineers and scientists who use these properties. Engineers tend to be more familiar with static measurements and tend to avoid using results determined dynamically. This situation is unfortunate for several reasons. First, dynamic results are more accurate by approximately an order of magnitude. Second, dynamic measurements are quicker and less expensive. Third, dynamic measurements on small specimens, including sheet and wire, are relatively simple. Fourth, complete sets of elastic constants, including anisotropy effects, are determined with little difficulty.

Theoretically, dynamic-static elastic-constant differences arise from three sources: the adiabatic-isothermal difference,^[1] the stress-level (strain-level) difference,^[2] and the role of higher-order elastic constants at high-strain levels.^[2] However, all these differences are relatively small and relatively well understood so that the existing static-dynamic controversy among practitioners surprises the theorist.

One feels the controversy will never be resolved except through comparisons of carefully obtained static and dynamic results on the same materials. Previously, the principal problem has been the dearth of reliable static measurements.

This situation changed recently in round-robin Young's-modulus measurements made at six laboratories on two composites.^[3] Table 1 shows the static Young's moduli, which are averages of measurements on five specimens. Table 1 also shows the moduli determined dynamically at 60 and 30 kHz, respectively, by a three-component Marx-oscillator method.^[4] Three static methods were used: ASTM D695, ASTM D3410, and sandwich-

beam. The six laboratories participating in the round-robin testing are designated by letters A through F in table 1. Two composites were studied in this series of tests: (1) a unidirectional graphite/epoxy (AS/3501) of high strength and medium modulus, and (2) a unidirectional glass/epoxy laminate (E-glass/1002). Panels of both composites were prepared by autoclave curing according to the manufacturer's recommendations at the University of Delaware. The panels were cut into blocks that were sent to participants who prepared specimens.

For both composites, results in table 1 show that the static (determined compressively) and dynamic results agree within experimental and/or material uncertainties. Thus, in these cases no basis exists for distinguishing between static and dynamic Young's moduli. All three theoretical factors listed above predict a dynamic elastic stiffness that slightly exceeds the static. Although the graphite/epoxy results show this relationship, the glass/epoxy results do not; there, the seven-percent error for the static value masks this relationship.

Within our laboratory, we expect several further studies, theoretical and experimental, on the static-dynamic elastic-constant question for composites. This will include design and construction of apparatus for accurate static values as a function of strain (stress).

Acknowledgment

This study was supported partly by the DoE Office of Fusion Energy and partly by the NBS Office of Standard Reference Data.

REFERENCES

- [1] L. D. Landau and E. M. Lifshitz, Theory of Elasticity (Pergamon, London, 1959), p. 19.
- [2] F. D. Murnaghan, Amer. J. Math. 59, 235 (1937).
- [3] N. R. Adsit, Compos. Tech. Rev. 2 (No. 2), 32 (1980).
- [4] H. M. Ledbetter, in Nonmetallic Materials and Composites at Low Temperatures, (Plenum, New York, 1979), pp. 277-281.

Table 1
 Static and Dynamic Young's Modulus,
 in Units of GPa, for Two Fiber-reinforced Composites

	AS/3501 [0°]	E-glass/1002 [0°]
Static A	115	41
B	130	45
C	125	43
D	119	50
E	128	48
F	123	46
Static Avg.	123 ± 6	46 ± 3
Dynamic	130.4 ± 1.3	44.3 ± 0.5

RADIATION EFFECTS ON COMPOSITES AND
NONMETALLIC MATERIALS

M. B. Kasen
Fracture and Deformation Division
National Bureau of Standards
Boulder, Colorado

ABSTRACT

This discussion of radiation effects is part of a review paper on composites. The other parts of the review appeared last year, in Volume III of this series.

The resistance of nonmetallic materials and composites to damage by neutron and gamma irradiation of 4 K is an important consideration in selecting insulating and structural support materials for superconducting magnets of magnetic fusion energy systems. Current designs anticipate that glass-reinforced polymers and other nonmetallics could be exposed to lifetime dose rates equivalent to about 10^{10} rads in some critical areas.¹ The ability of conventional organic-matrix materials to withstand such doses is significant concern.

A number of studies have been conducted on the effect of irradiation on the room-temperature properties of nonmetallic insulators, but few studies have extended into the cryogenic range.² In addition to degrading mechanical, thermal, and electrical properties, the low thermal conductivities of the nonmetallics might also result in nuclear heating, which places an added burden on the refrigeration system.

Extrapolating from room-temperature experience suggests that bisphenol A epoxy systems cured with aromatic amines should have better radiation resistance than systems cured with dicyandiamide. Cycloaliphatic epoxies may be superior to bisphenol A, polyimides should be better than epoxies, and filled resin systems superior to unfilled resins, but confirmation is lacking. Complexities of the processes involved do not permit a theoretical estimate to be made of the effect of irradiation at cryogenic temperature on the various properties of nonmetallic insulators-- an experimental data base must be acquired. Because the radiation resistance of a polymer is strongly affected by the exact molecular structure, such experiments must be carried on with materials characterized on the molecular level.²

The Oak Ridge National Laboratory has recently screened the effect of 4 K gamma and neutron irradiation on the stability of eight types of organic insulation.³ The volume resistivities of a bisphenol A epoxy, an inorganic-filled epoxy, an aromatic-polyimide sheet material, a polyvinyl formal wire coating and an FR-5 type glass-epoxy laminate were found to be very little affected by a dose of 2×10^8 rads (γ). The effectiveness of a filled epoxy and of a B-staged glass-epoxy adhesive for joining Cu-Be lap-shear tensile specimens was also relatively unaffected, as was the flexural strength of a filled epoxy, a G-10 laminate, and an FR-5 laminate.

When doses were increased to higher levels, the mechanical and electrical properties of glass-reinforced epoxy laminates and filled epoxy resins were found to be significantly deteriorated.¹ Residual flexural and compressive strengths of G-10CR and G-11CR laminates were reduced to 10 to 15% of original values after exposure to 2.4×10^9 rads (γ) and to 6 to 10% after exposure to 1.0×10^{10} rads (γ). These doses were accompanied by fast neutron doses of 2.2×10^{20} n/m² and 8.7×10^{20} n/m², respectively. The strength retention of the aromatic-amine-cured G-11CR product appeared better than that of the dicyandiamide-cured G-10CR after the lower dose, but no difference is noted after the higher dose. A variant of the G-10CR product containing boron-free E-glass reinforcement performed much like the G-11CR laminate.

The relatively high fraction of initial flexural modulus retained by the laminates indicates that the glass reinforcement did not sustain major damage. The low strain to failure indicates that deterioration of the matrix--

and possibly of the Fiber-matrix bond--accounts for most of the property degradation.

The mechanical properties of the filled resins were relatively unaffected by the lower level of radiation, but were substantially degraded at the higher level. These materials appear to be essentially at the end of their useful life after the higher level of radiation.¹ Despite the larger percentage of strength reduction, the high initial strength of the glass/epoxy laminates permitted retention of sufficient residual strength (100 MPa, 15×10^3 psi flexural strength; 55 MPa, 8×10^3 psi compressive strength) for some magnet applications.

Except for one of the filled epoxies, no significant dimensional changes were observed as a result of the irradiation.

Warming of the specimens to room temperature after 4-K irradiation simulated periodic warming of the magnet structures throughout their lifetime and incorporated additional damage anticipated from defect recombination at higher temperatures--the Wigner energy.

It is apparent that much work remains to be done before reliable radiation-resistant insulators are developed. Current programs are examining the type of molecular damage incurred during irradiation of bisphenol A epoxy-matrix laminates and testing is being extended to include glass-reinforced laminates having other resin matrices.

REFERENCES

1. Coltman, R. R., Klabunde, C. E., Kernohan, R. H. and Long, C. J. "Radiation effects on organic insulators for superconducting magnets," Oak Ridge National Laboratory Report ORNL/TM-7077 (1979).
2. Brown, B., "Low Temperature radiation effects on superconducting magnets" submitted to Journal of Nuclear Materials (1980).
3. Kernohan, R. H., Coltman, R. R., and Long, C. J. "Radiation effects on organic insulators for superconducting magnets," Oak Ridge National Laboratory Report ORNL/TM-6708 (1979).

NONMETALLIC MATERIALS :
TECHNOLOGY TRANSFER

CONTRIBUTIONS TO TECHNOLOGY FORECAST '81[†]
PLASTICS, CERAMICS AND COMPOSITES

M. B. Kasen
Fracture and Deformation Division
National Bureau of Standards
Boulder, Colorado

[†]Submitted to Metal Progress

Nonmetallic composites perform critical structural, thermal, and electrical insulation functions in large superconducting magnets required for magnetic fusion energy (MFE), magnetohydrodynamic (MHD), rotating cryogenic machinery and energy storage systems required to meet future energy requirements of the United States and other countries. Large quantities of these materials--up to a thousand tons for a storage magnet--must perform reliably over a thirty-year lifetime while subjected to large electromagnetic stresses, thermal stresses, and intense radiation in some applications.

Studies at NBS have shown that the variability in cryogenic properties of conventional nonmetallic composites is a primary problem. This variability reflects both the intrinsic embrittlement of the polymer matrix at cryogenic temperatures and the extrinsic variability of cryogenic properties among laminates produced to similar commercial designations by a variety of producers.

NBS personnel are working with magnet designers, industrial laminators, and the polymer industry to establish standard grades of non-metallic laminates for high technology cryogenic applications. The principle is to establish specifications for components and manufacturing procedures that will minimize the property variability while providing a basis for systematic development of improved laminates in response to demonstrated needs. This has resulted in the establishment of two commercial glass-fabric-reinforced epoxy laminate types identified as NEMA G-10CR and G-11CR. The specifications have been distributed to all U.S. laminators through the NEMA organization and are presently being manufactured by three concerns.

Organic-matrix laminates are unable to retain required mechanical and electrical properties after exposure to radiation levels on the order of 10^{10} rads (γ) plus a significantly fast neutron fluence at 4 K. Therefore, ceramics may be chosen over nonmetallic composites for insulation in MHD superconducting magnets, but ceramic use entails substantially higher magnet construction cost. On behalf of the Department of Energy, NBS is cooperating with industry and with other federal laboratories to define the extent of the problem and to pursue development of improved radiation resistant laminates. Studies at the Oak Ridge National Laboratory have shown that the anticipated radiation levels reduce the compressive and flexural strengths of conventional glass-fabric epoxy laminates to 6 to 10% of their original values. Polyimide matrices are presently being evaluated. Cycloaliphatic epoxy systems and filled-resin laminates are primary candidates for future studies.

A significant detriment to the expanded use of composite materials in all areas of consumer technology is the difficulty of associating performance with the profusion of products identified by trade names. Composite technology would greatly benefit from the establishment of an industry standards group who would establish a numerical composite classification system based on the key elements affecting performance. Such a system has been proposed by NBS, in which lower bound mechanical, electrical and thermal properties are defined by a number-letter combination defining type and flexibility of the matrix, the type and configuration of the reinforcement and the reinforcement volume fraction. The AISI designations for steel and the Aluminum Association designations for aluminum alloys serve as models.

[†]COMMENT ON "MECHANICAL PROPERTIES OF PLASTIC COMPOSITES..."

M. B. Kasen
Fracture and Deformation Division
National Bureau of Standards
Boulder, Colorado

[†]To appear as a letter to the editor, Composites.

Comment on "Mechanical Properties of Plastic Composites Under Low Temperature Conditions" by K. Kaotani, Composites, V. 11, No. 2, April 1980, pp. 87-94

The author's conclusion that composites fabricated with a highly flexibilized epoxy matrix provide better cryogenic properties than those fabricated with nonflexibilized systems may be valid for laminates containing 32% by volume reinforcement, but is not valid for the higher volume fractions typical of laminates in industrial usage. Literature reviews and work in our laboratory¹⁻³ indicate that residual stresses created by the large thermal contraction of highly flexibilized systems negate any advantage provided by the intrinsically higher strain capability of the matrix when fiber contents approach 50 to 60% by volume in glass, graphite, or aramid laminates. We find, for example, that the flexible Resin 2 formulation⁴ decreases the 4-K uniaxial longitudinal tensile strength of an S-901 glass-reinforced laminate to a level about equal to that of a nonflexibilized matrix laminate at 295 K. The transverse strength of a uniaxial graphite-reinforced laminate at 4 K is reduced by about 60% by a highly flexibilized matrix, while the transverse failure strain is reduced about 90%. When used with aramid fiber, the flexibilized matrix reduces the uniaxial transverse strength to an extent rendering the laminate almost useless for structural applications.

Additionally, the intrinsic weakness of highly flexibilized resin systems near room temperature has resulted in the catastrophic failure of several structures designed for cryogenic use but necessarily subjected to moderate stresses at room or slightly elevated temperatures.

The author quite correctly points out the limitation imposed on the effective cryogenic strength of glass-reinforced laminates owing to the strain limitations of conventional bisphenol A epoxies at such temperature (the "knee point" in the stress-strain curve). But the solution requires a resin system providing reasonably high room-temperature strength and reasonably low thermal contraction as well as cryogenic toughness. Possible approaches have been discussed in the recent literature.⁵ Until such systems are developed and proven, it appears most prudent to utilize conventional resin systems for cryogenic laminates.

REFERENCES

1. Kasen, M. B., "Mechanical and thermal properties of filamentary-reinforced structural composites at cryogenic temperatures" Part I: glass-reinforced structural composites, Cryogenics 15, No. 6 (June 1975), pp. 327-349; Part II: advanced composites, Cryogenics, 15, No. 12 (December 1975), pp. 701-719.
2. Kasen, M. B., "Cryogenic properties of filamentary-reinforced composites: An update," National Bureau of Standards, Boulder, Colorado (in preparation).
3. Schramm, R. E. and Kasen, M. B., "Cryogenic mechanical properties of boron-, graphite-, and glass-reinforced composites," Materials Science and Engineering, 30 (1977), pp. 197-204.
4. Soffer, L. N. and Molho, R., "Cryogenic resins for glass-filament-wound composites," NASA CR-72114 (Final).
5. Nonmetallic Materials and Composites at Low Temperatures, A. F. Clark, R. P. Reed, and G. Hartwig, eds. (Plenum Press, 1979).

THE MANUFACTURE OF RADIATION RESISTANT LAMINATES

J. R. BENZINGER
CORPORATE TECHNOLOGY
SPAULDING FIBRE COMPANY, INC.
TONAWANDA, NEW YORK 14150

PRESENTED AT THE NBS/DOE WORKSHOP ON MATERIALS AT
LOW TEMPERATURE, OCTOBER 8, 1980, VAIL, COLORADO

THE MANUFACTURE OF RADIATION RESISTANT LAMINATES

J. R. BENZINGER
Corporate Technology
Spaulding Fibre Company, Inc.
Tonawanda, New York 14150

INTRODUCTION

There have been many studies on the irradiation effects of polymers and insulators, but only a few on high pressure thermo-setting laminates¹. There was virtually no published information on radiation at cryogenic temperatures on polymers, let alone laminates, until the recent work at Oak Ridge on the Spauldite® CR grade laminates, some particle filled epoxies and films of Mylar and Kapton². One conclusion of the 1979 ORNL report was that, at a dose of 1×10^{10} rads, particle filled epoxies are at "end of life" in terms of mechanical strength while CR grade laminates, although showing severe degradation, still retained usable strength. Further testing was suggested to determine margins of safety. In some locations of the magnet, such as adjacent to the injector of neutron beams, higher doses would require additional shielding or redesign at considerable expense³. A more prudent approach it is claimed would be to improve the radiation resistance of the insulation.

Inorganic insulators like ceramics are much more resistant to radiation but tend to be very brittle. This rules them out

for most fusion reactor applications since these magnets are subject to extreme mechanical and magnetically induced forces⁴. Consequently, the critical applications can only be satisfied by the use of tough, high pressure thermosetting laminates⁵. It is the purpose of this paper to demonstrate the capability of industry to modify high pressure thermosetting laminates for improved radiation resistance.

Mechanical strength testing of some of the experimental G-10CR variants designed for improved radiation resistance yielded some surprising results. Also to be reviewed are the design rationale, materials of construction, and method of manufacture of some polyimide and epoxy laminates prepared for MIT and ORNL irradiation effect studies. In conclusion, cost comparisons, availability and anticipated manufacturing problems associated with some raw materials and laminates will be discussed.

MIT AND ORNL PROGRAMS

In response to requests from H. Becker and E. Erez of MIT and J. Long of ORNL, several experimental laminates were prepared in the laboratory with the intent to improve radiation resistance. Some of them were variants in some manner to Spauldite® G-10CR or G-11CR.

The program at ORNL, sponsored by DOE is an ongoing special purpose materials program on "Radiation Effects On Organic

Insulators For Superconducting Magnets". The MIT work was performed in the MIT Plasma Fusion Center also under DOE auspices. This work was part of an investigation of material properties for an ignition test reactor (ITR) subject to high neutron fluence and gamma radiation⁶. The radiation effect results on the laminates of these programs will be reported by their respective authors at the NBS/DOE Workshop On Materials At Low Temperature at Vail, October 7-9, 1980.

MATERIALS OF CONSTRUCTION

Fabric Reinforcements

Listed in Table I is a description and cost of the five woven fabrics used as reinforcements in the experimental laminates. The low cost plain weave E glass 7628 A-1100 was selected as a control based on an extensive test data base and a long history of successful use in laminates⁷.

S glass was selected not only because of its high strength, but also because it is boron free. Table II lists the chemical composition of the various glasses. E glass which contains boron may present a problem in reactors in that it retains residual radioactivity for longer periods of time than boron free glasses. Quartz was chosen because it tested the best of several inorganic insulators for resistance to irradiation.

The standard finish available on the commercial S and quartz fabrics was A-1100, the same finish as used in the CR

grade laminates. At least one investigator has concluded that A-1100 was the best of a variety of coupling agents evaluated⁸. It is suggested that some future program include an update study of coupling agents when time permits ordering and preparing special samples.

Although all of the five fabrics used in this program were commercial grades, availability and cost of quartz and S glasses could present problems in delivery. As for manufacturing, there are less problems associated with the manufacture of high pressure laminates with plain weaves. However, the satin weaves tend to perform better in low pressure molding where curvatures are involved. See Figure 1 for a schematic of the comparisons of construction.

Resins and Curing Agents

It has been reported by several early researchers that aromatic compounds such as polyimides and aromatic epoxies have good radiation resistance⁹. They are many times more stable than aliphatic compounds to radiation owing primarily to the greater bond strength and the resonance energy of the aromatic structure. Substituted aromatics are more resistant than non-substituted aromatics and saturated aliphatics are more stable than unsaturated aliphatics. Other investigators have reported that the aromatic amine curing agent diaminodiphenyl sulphone was best when used with epoxies of the diglycidyl ethers of bisphenol A type and that diaminodiphenyl methane gave the best

results when used with multi-functional glycidyl amines¹⁰. It was also observed that the more highly functional and cross-linked polymers that perform well at high temperatures also tend to fair best at high levels of radiation. Listed in Table III are the epoxies, curing agents and polyimides selected for the program.

The polyimide, Kerimid 601, was selected for its ease of processing, modest cost as far as polyimides are concerned and because it has been reported to be unaltered after a 10^{10} rad exposure. The other polyimide used in the program was DuPont NR-150B2 polyimide precursor solution. Shortly after the experiments were underway, DuPont withdrew this resin from the market.

LAMINATE PREPARATION

The laminates prepared for the MIT and ORNL programs are listed in Tables IV and V. Most of the laminates were very thin and consisted of only two or three sheets of prepreg. For this reason the laminate specimens were prepared by laboratory "hand treating" rather than using the pilot facility.

This process involved hand dipping of the reinforcements in solutions consisting of the resin polymer, its curing agent and compatible solvents. The resin treated webs were then passed through motor driven squeeze rolls. The rolls were preset so that pressure was applied to the treated web forcing the resin into the interstices of the fabric. The force of the

rolls also squeezed off excess resin, leaving a uniform application.

After saturation, the treated webs were placed in an air-circulating oven at 280-300°F. The purpose of the drying operation for the polyimides was to remove the solvent. In the case of epoxies and phenolics, additional polymerization takes place in the drying oven in addition to the removal of solvent. All of the prepregs were subsequently pressed between steel plates at a pressure of 500 psi and a temperature of 360°F with the exception of one of the Kerimid laminates which was pressed at 440°F.

Two of the polyimide laminates supplied to ORNL were post cured at 450°F for five hours to insure adequate cure. The epoxy based laminates were not post cured. Results of some radiation effects by R. Sheldon on one wet lay-up epoxy laminate indicated that higher temperature post cure tended to improve radiation resistance⁸. Subsequent designed experiments at different post cure temperatures by D. Evans indicated no significant differences could be detected in radiation resistance⁹. Therefore, for this reason and because the process is irreversible, the epoxy laminates were not post cured. Based on initial radiation results, a post cure study, if deemed advisable, could be undertaken simply by post curing replicate samples of the laminates.

Also included for controls were the commercially available laminate, Spauldite® G-11CR and a phenolic cured epoxy novolac.

G-10CR VARIANTS

GEM-CR, Quartz Filled

As part of an ongoing research program at Spaulding Fibre Company, Inc. several variants of G-10CR and G-11CR were investigated with a view toward improvements in radiation resistance, mechanical strength and cost. One of these was a continuous filament E glass epoxy mat laminate (GEM-CR) which was constructed using the G-10CR resin system.

Last year Dr. Olinger of OCF reported on the good results he had achieved at liquid nitrogen temperatures using mat epoxy laminates¹¹. Also several investigators have reported improved radiation stability by incorporating particle fillers in epoxy resin castings and moldings¹². Other improved properties reported for filled resins are less thermal contraction, reduced cracking or crazing, increased or reduced thermal conductivity based on the type and amount of filler and cost¹³. Therefore, a combination of reinforcement, resin and filler seemed like a good approach to improve radiation resistance and other properties of laminates as was the case with castings.

The initial experiment was conducted with glass mat rather than fabric for three reasons: (a) lower cost, (b) random and wide spacing of the fibers for reception of the filler, and (c) prior success in GPO laminates. Although several fillers were considered as possible candidates, see Figure 2, the filler selected for experimentation was Quartz (SiO_2) because, as

stated previously, it tested the best of several inorganic insulators for resistance to irradiation¹⁴. Shown in Figure V are some mechanical strength properties of both filled and unfilled GEM-CR. The properties of the filled GEM-CR laminate were not as good as the unfilled GEM-CR, but this is believed due to the high loading of SiO₂, 80 parts to 100 parts of resin. A high loading was used to reduce costs as well as improve radiation stability. Dr. Kasen has suggested that while the optimum amount is unknown, it is possible that a small amount, well distributed, could be effective.

The bar graph in Figure 3 compares the compressive strength edgewise at ambient (293 K) and liquid nitrogen (77 K) temperatures of the unfilled GEM-CR laminate versus a NEMA GPO-1. (glass mat polyester). The GEM-CR variant like G-10CR increases considerably in strength at cryogenic temperatures. The bar graph in Figure 4 is similar to Figure 3 in all respects except that it compares interlaminar shear (unsupported) as a function of temperature.

S Glass And High Glass Content

Some mechanical properties of the S glass variant of G-10CR are shown in Table V compared with the average test data of Spauldite® G-10CR. This laminate was made identical to G-10CR with the only variant being S in place of E glass. The weave, finish and resin were the same as G-10CR. The two properties that stand out are compressive strength normal to laminations

and bond strength. Both tests when repeated gave the same identical results. The high E glass content variant of G-10CR demonstrates another way to achieve higher strengths.

Both of the above laminates, one because of the absence of boron oxide and other because of less organic content, would be expected to provide improved radiation resistance.

Polyimide And Phenolic-Epoxy

Also listed in Table V are the properties of the polyimide laminate submitted to Joe Long at Oak Ridge for irradiation effects. This laminate is grouped with an aniline phenolic cured epoxy novolac epoxy. Both laminates contain high temperature, highly aromatic polymers which like G-11CR are considered key elements for resistance to radiation. These resins are harder and tend to be a little brittle as evidenced by the reduced interlaminar shear and bond strengths when compared with G-10CR (epoxy resin) laminates.

G-10CR Quartz Filled

Based on the good results achieved with the particle filled glass epoxy mat laminate, a quartz filled variant of G-10CR was planned. Several changes were made, one of which was to reduce the amount of quartz (SiO_2) added to the epoxy resin from 80 to 40 parts by weight to 100 parts epoxy. The selection of a finer particle size SiO_2 filler, half the size used in the mat, was considered another improvement. In order to improve the bond of the filler to the epoxy with resultant expected increase in

strength a filler was obtained that had been pretreated with A-1100 coupling agent.

Another reason to explain the lower strength of the filled GEM-CR laminate is that the percentage of glass fiber mat reinforcement was reduced by the exact amount of the loading of filler while the amount of resin remained the same as in the unfilled laminate. In the case of the SiO_2 filled fabric laminate, the resin, rather than the reinforcement was displaced by the filler, and the amount of glass fabric reinforcement was not reduced but kept the same as the unfilled G-10CR.

Test data on mechanical strength properties of this latest variant of G-10CR is not available for inclusion in this report, but will be reported verbally at the workshop. It should be emphasized that all of the laminates reviewed in this paper, with the exception of G-10CR and G-11CR, are laboratory developments and not commercially available at this time. Also, most of the reported data are based on one time testing of laboratory specimens.

CONCLUSION

It has been demonstrated that laminates can be modified in many ways to make them more resistant to radiation. The success of these endeavors will be largely unknown until and when the laminates can be properly tested and evaluated. Higher temperature irradiations can serve as a guide, but as concluded by B. Brown only irradiations performed near the temperature of the

magnet are realistic¹⁵. If it is deemed necessary that a more comprehensive program be established, it seems more than likely that a significant improvement in radiation resistance can be successfully achieved with high pressure laminates.

ACKNOWLEDGEMENT

The author wishes to gratefully thank E. Erez of MIT for the test data used to generate the graphs in Figures 3 and 4.

REFERENCES

1. M. G. Young, "Radiation Effects On Laminated Plastic Materials", UD-NEMA Facility, April 1965
2. R. H. Kernohan, R. R. Coltman and C. J. Long, "Radiation Effects On Organic Insulators For Superconducting Magnets", Oak Ridge National Laboratory Report ORNL/TM-6708 (1979)
3. R. T. Santaro, J. S. Tang, R. G. Alsmiller, Jr. and J. M. Barnes, Nucl. Tech. 37, 65 (1978)
4. R. P. Reed, F. R. Fickett, M. B. Kasen and H. I. McHenry, "Materials Studies For Magnetic Fusion Energy Applications At Low Temperature - 1", Report No. NBSIR 78-884, National Bureau of Standards, Boulder, Colorado (1978), p. 243
5. M. B. Kasen, G. R. MacDonald, D. H. Beekman and R. E. Schramm, "Mechanical, Electrical And Thermal Characterization Of G-10CR And G-11CR Glass Cloth/Epoxy Laminates Between Room Temperature And 4 K", Advances In Cryogenic Engineering, V 26 Plenum Press N.Y. (1980)

6. E. A. Erez, H. Becker, "Radiation Damage In Thin Sheet Fiberglass Insulators", Non-metallic Materials And Composites At Low Temperature - II, Plenum Press 1981
7. J. R. Benzinger, "Advances In Cryogenic Engineering", Volume 26 Plenum Press, New York 1980 pp. 252-258
8. R. Sheldon and G. B. Stapleton, "The Effect Of High Energy Radiation On The Mechanical Properties Of Epoxy Resin Systems Used For Particle Accelerator Construction", Rutherford Laboratory, Chilton, Didcot, England (1968)
9. M. H. Van de Voorde, IEEE Trans. Nucl. Sci. 18, 784 (1970), and IBID 20, 693 (1973)
10. D. Evans, J. T. Morgan, R. Sheldon, G. B. Stapleton, "Post-Irradiation Mechanical Properties Of Epoxy/Glass Composites" RHEL/R200 Chilton, Berkshire, England, 1970
11. J. Olinger, "Cryogenic Grade Glass Mat Epoxy Laminates", NBS/DOE Workshop On Materials At Low Temperature", Vail, Colorado, October 1979
12. H. Brechna, "Effect Of Nuclear Radiation On Organic Materials; Specifically Magnet Insulations In High-Energy Accelerators", SLAC Report No. 40, 1965
13. G. Claudet, F. Disdier and M. Locatelli, "Interesting Low Temperature Thermal And Mechanical Properties Of A Particular Powder-Filled Polyimide", Non-Metallic Materials And Composites At Low Temperatures, Plenum Press pp. 131-140, 1979

14. C. L. Hanks and D. J. Hamman, "Report On The Effect Of Radiation On Electrical Insulating Materials", REIC Report No. 46, Battelle Institute, Columbus, Ohio (1969)
15. B. S. Brown, "Radiation Effects In Superconducting Fusion Magnet Materials", May 1980, submitted to Journal Of Nuclear Materials

LIST OF TABLES

TABLE I	Description Of The Woven Fabric Reinforcements
TABLE II	Chemical Composition Of The Reinforcements
TABLE III	Polymeric Materials Of Construction
TABLE IV	Fabric Reinforced Polyimide Laminates Prepared For Irradiation
TABLE V	Fabric Reinforced Epoxies Prepared For Irradiation
TABLE VI	Mechanical Strength And Physical Properties Of Some G-10CR Variants

TABLE OF FIGURES

Figure 1.	Comparison Of Weaves, Style 7628 And Style 181
Figure 2.	Relative Radiation Resistance Of Inorganic Insulating Materials, Based Upon Changes In Physical Properties
Figure 3.	Compressive Strength Edgewise As A Function Of Temperature Spauldite® GEM-CR Versus NEMA GPO-1

Figure 4. Interlaminar Shear Strength ASTM Guillotine
(Unsupported) As A Function Of Temperature
GEM-CR Versus GPO-1

TABLE I - DESCRIPTION OF THE WOVEN FABRIC REINFORCEMENTS

STYLE	SUPPLIER	FINISH CHEMICAL NAME	ABBREVIATION	TYPE	WEAVE	COUNT	WEIGHT OZ./YD.	COST \$/LB.
7628 A-1100*	Clark-Schwebel	gamma - amino- propyl - tri- ethoxysilane	amino silane	E	plain	44x32	5.9	2.0
6528 A-1100	Burlington	gamma - amino- propyl - tri- ethoxysilane	amino silane	S-2	plain	44x32	6.1	7.8
Astro Quartz 527 A-1100	J. P. Stevens	gamma - amino- propyl - tri- ethoxysilane	amino silane	quartz	plain	42x32	5.6	80.0
181 CS-272A	Clark-Schwebel	gamma - gyl- cidoxypropyl trimethoxysilane	epoxy silane	E	8H satin	57x54	8.9	2.8
6581 GB-770B	Burlington	proprietary epoxy compatible silane	modified epoxy silane	S-2	8H satin	57x54	8.99	8.0

*Control fabric used in Spauldite® G-11CR

TABLE II - CHEMICAL COMPOSITION OF THE REINFORCEMENTS

COMPONENTS, % BY WEIGHT	E GLASS	S GLASS	QUARTZ
Silicon dioxide	52-56	64-66	99.9
Calcium oxide	16-25	---	--
Aluminum oxide	12-16	24-26	--
Boron oxide	8-13	---	--
Sodium & potassium oxide	0-1	---	--
Magnesium oxide	0-6	9-11	--
Density, g/cc	2.54	2.48	2.65

TABLE III - POLYMERIC MATERIALS OF CONSTRUCTION

TRADE NAME	SUPPLIER	GENERIC CHEMICAL NAME	ABBREVIATION	TYPE	APPROX. COST \$/LB.
<u>EPOXY RESINS</u>					
Araldite 0500	Ciba-Geigy	Triglycidyl ether of p-amino phenol	TGPAP	Aromatic epoxy resin high functionality *E.E.W. 110	6.8
Araldite 6010	Ciba-Geigy	Diglycidyl ether of Bisphenol A	DBEBA	Liquid epoxy resin *E.E.W. 190	1.1
<u>EPOXY CURING AGENTS</u>					
HT 972	Ciba-Geigy	4,4'-diaminodiphenyl methane	DDM	Aromatic amine hardener	1.8
Eporal	Ciba-Geigy	4,4'-diaminodiphenyl sulphone	DDS	Aromatic amine hardener	6.1
<u>POLYIMIDE RESINS</u>					
Kerimid 601	Rhodia	Maleic N,N'-4,4'-diphenyl-methane-bis-imide + bis-(4-aminophenyl) methane		Aromatic diamine bismalcomide	15.0
DuPont NR-150B2	DuPont	2,2-bis(3,4-dicarboxyphenyl)hexa-fluoropropane/p-phenylenediamine/m-phenylenediamine		Polyimide precursor solution	70.0 (no longer available)

*Epoxide Equivalent Weight

TABLE IV - FABRIC REINFORCED POLYIMIDE LAMINATES PREPARED FOR IRRADIATION

EXPERIMENTAL NUMBER	DESCRIPTION FABRIC/RESIN SYSTEM	STYLE	FINISH	WEAVE	% RESIN BY WEIGHT	THICKNESS, MILS
21-1, 2	E-Glass/Kerimid 601	7628	A-1100	Plain	29	19
37-7					30	55
38-1					30	260
21-3	S-Glass/Kerimid 601	6528	A-1100	Plain	31	19
27-22A	Quartz/Kerimid 601	527	A-1100	Plain	34	20
27-21A	Quartz/DuPont NR-150B2	527	A-1100	Plain	29	19

TABLE V - FABRIC REINFORCED EPOXIES PREPARED FOR IRRADIATION

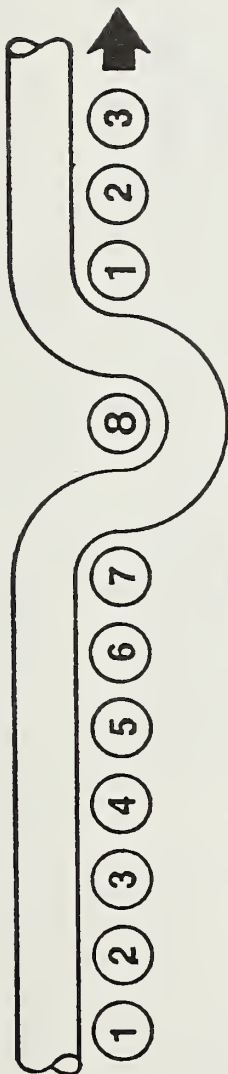
EXPERIMENTAL NUMBER	DESCRIPTION FABRIC/RESIN SYSTEM	STYLE	FINISH	WEAVE	% RESIN BY WEIGHT	THICKNESS, MILS
25-10D	E-Glass/DGEBA + DDS	181	Epoxy Silane	Satin	32	18
25-11D	S-Glass/DGEBA + DDS	6581	GB-770B	Satin	30	19
G-11CR*	E-Glass/DGEBA + DDS	7628	A-1100	Plain	28	18
28-26A	E-Glass/TGPAP + DDS	181	Epoxy Silane	Satin	27	18
28-27	S-Glass/TGPAP + DDS	6581	GB-770B	Satin	29	19
29-30	E-Glass/TGPAP + DDM	181	Epoxy Silane	Satin	25	18
29-31A	S-Glass/TGPAP + DDM	6581	GB-770B	Satin	26	19
29-32A	Quartz/TGPAP + DDM	527	A-1100	Plain	33	21
29-33A	S-Glass/TGPAP + DDM	6581	GB-770B	Satin	27	17
43-1	E-Glass/PNE + APF	7628	A-1100	Plain	28	19

*Spaldite® G-11CR Control

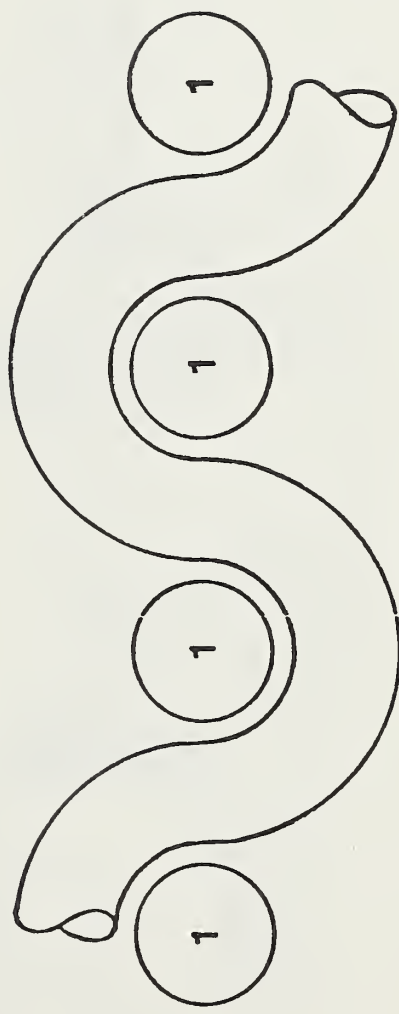
TABLE VI - MECHANICAL STRENGTH AND PHYSICAL PROPERTIES OF SOME G-10CR VARIANTS*

MECHANICAL STRENGTH PROPERTIES AT 293 K	GLASS MAT		GLASS FABRIC				CONTROL** G-10CR
	UNFILLED GEM-CR	PARTICLE FILLED GEMF-CR	ANILINE PHENOLIC EPOXY NOVOLAC	POLYIMIDE	EPOXY "S" GLASS	HIGH GLASS CONTENT	
Compressive, psi Edge Warp Fill Normal	53,600	49,200	69,500	73,200	61,500	64,000	59,000
	-	-	61,500	58,300	50,700	55,900	48,000
	84,200	57,600	92,800	83,300	92,900	91,900	70,000
Interlaminar Shear, Guillotine, psi Warp Fill	6,800	4,000	5,600	4,500	-	6,500	6,800
	-	-	4,800	-	6,700	-	6,700
Bond; 10mm Ball psi	2,900	-	1,950	-	3,800	3,100	2,900
Flexural, psi Warp Fill	71,400	31,800	78,800	86,500	-	-	72,000
	-	-	63,800	-	-	-	54,000
<u>PHYSICAL PROPERTIES</u>							
Density, g/cc	1.93	1.93	2.07	2.03	1.83	1.99	1.85
Thickness	1/2"	1/4"	1/2"	1/4"	1/2"	1/2"	1/2"
Percent Glass	71	47	77	72	68	75	67
Percent Resin	29	29	23	28	32	25	33
Percent SiO ₂	-	24	-	-	-	-	-

* One time data based on laboratory sample laminates
 ** Average data based on three years of production of Spauldite® G-10CR



STYLE 181
B-HARNES SATIN



STYLE 28
PLAIN WEAVE

FIGURE 1. COMPARISON OF WEAVE

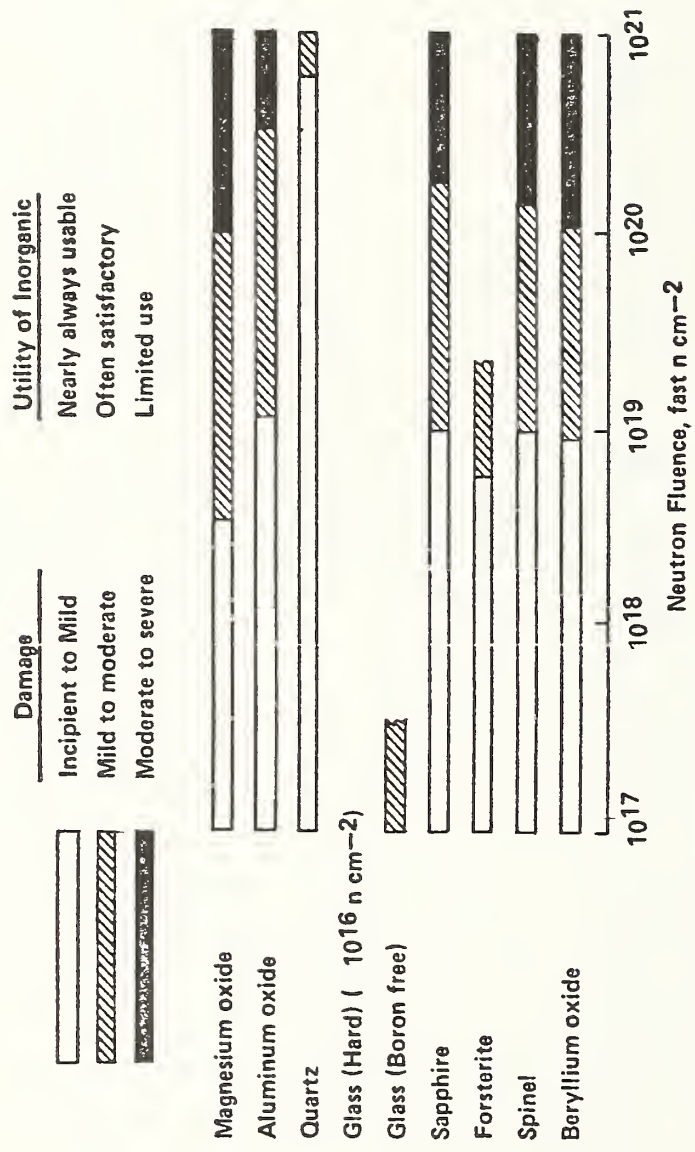


FIGURE 2. RELATIVE RADIATION RESISTANCE* OF INORGANIC INSULATING MATERIALS. BASED UPON CHANGES IN PHYSICAL PROPERTIES

*Varies greatly with temperature.

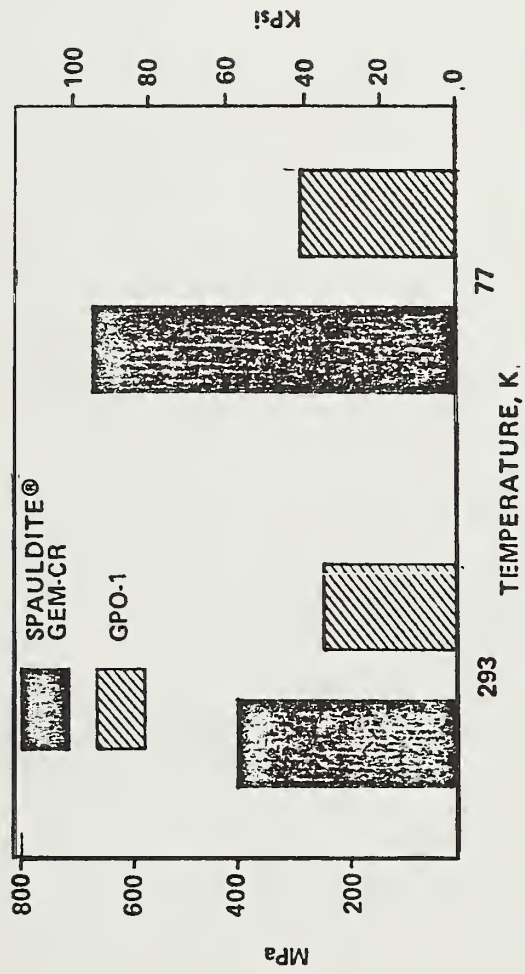


FIGURE 3 COMPRESSIVE STRENGTH EDGEWISE AS A FUNCTION OF TEMPERATURE

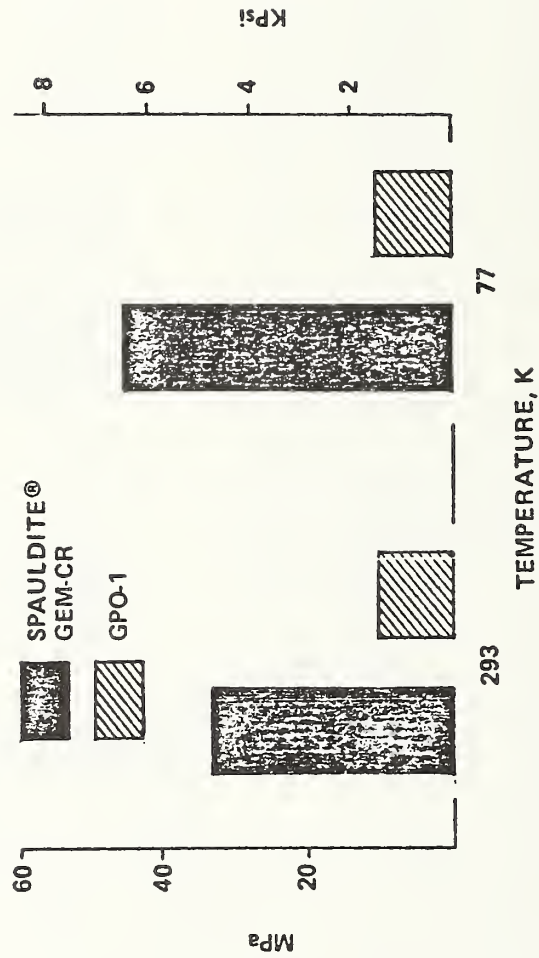


FIGURE 4. INTERLAMINAR SHEAR STRENGTH (UNSUPPORTED) AS A FUNCTION OF TEMPERATURE

TECHNOLOGY TRANSFER

NBS-DoE WORKSHOP: MATERIALS AT LOW TEMPERATURES

October 7-9, 1980, Vail, Colorado

N. J. Simon
Fracture and Deformation Division
National Bureau of Standards
Boulder, Colorado

ABSTRACT

The subject matter and format of this annual workshop are discussed. During fiscal year 1980, this workshop constituted the chief formal activity of the technology transfer program. However, starting with the present fiscal year, a second major activity will be undertaken: the production of handbook pages for low-temperature mechanical and physical properties of materials for magnets in fusion energy systems.

The workshop discussions concerned structural and insulating materials to be used at low temperatures in superconducting magnets for fusion reactors and MHD systems. Each year, a major purpose of the workshop is to bring together representatives from the community of users and suppliers of materials for low temperature magnet applications with those engaged in development and characterization of these materials. Participants this year came from industry, the national laboratories, the magnetic fusion energy programs, NBS, DoE and several universities. A list of attendees is given in the following pages. The technical presentations were informal, with many opportunities for comments and questions.

Initially, overviews of the large superconducting magnet programs for fusion energy and MHD were given. Presentations regarding the Large Coil Projects and the ORNL test facility followed. Then, recent measurements of properties of structural alloys, welds and castings were presented. In the next session, fracture, fatigue and radiation damage in composites were considered. In the last session, codes and standards for fusion energy magnets were discussed. A detailed list of all the technical papers presented is attached. The proceedings of the workshop are not published, but abstracts or short summaries of all the presentations are provided to those who attend.

Meetings of several advisory groups were held during the workshop. For example, the CCP conductor sheath advisory committee met, as did the joint NBS-industry group which is working on specifications for CR-grade laminates.

PROGRAM

NBS/DoE Workshop on Materials at Low Temperatures
October 7-9, 1980
Vail, Colorado

Tuesday, October 7

Session 1 (9:00-12:00): Large Superconducting Magnet Programs
R. P. Reed, Chairman

DoE Office of Fusion Energy - Overview
NBS Program
Magnetic Fusion Test Facilities, A and B
Engineering Test Facility
MHD Magnets

D. Beard, DoE
R. P. Reed, NBS
E. N. C. Dalder, LLL
R. J. Hooper, ORNL
V. Der, DoE

Session 2 (2:00-5:00): Large Coil Projects
D. Beard, Chairman

Oak Ridge National Laboratory
General Dynamics
General Electric
Westinghouse
Japan Atomic Energy Research Institute
Kernforschungszentrum Karlsruhe

C. J. Long, ORNL
J. L. Christian, GD
C. L. Linkinhoker, GE
C. J. Heyne, W
E. Tada, JAERI
A. Ulbricht, KfK

Wednesday, October 8

Session 3 (8:30-12:00): Structural Alloys, Welds and Castings
H. I. McHenry, Chairman

Cr-Ni-Mn-N Stainless Steels
Japanese Studies
Conductor Sheath Materials
Welding Research at Lawrence Berkeley
Stainless Steel Weldments
Aluminum Weldments
Stainless Steel Castings

R. L. Tobler, NBS
R. Ogawa, KOBE
R. Gold, W
J. W. Morris, LBL
T. A. Whipple, NBS
J. W. Elmer, NBS
R. Finch, ESCO

Session 4 (1:30-5:00): Insulating and Structural Composites
M. B. Kasen, Chairman

Fracture Modes of G-10CR in Compression
Fatigue of Fibrous Glass/Epoxy Laminates in LN₂
Multiaxial Fatigue Damage in Fiberglass
Radiation Damage in Fiberglass Insulators
Radiation Effects in Organics at 4 K
Manufacturing of Radiation Resistant Laminates
Low Temperature Irradiation Studies

B. A. Beck, NBS
J. L. Olinger, Owens Corning
S. Wang, UI
H. Becker, MIT
C. J. Long, ORNL
J. Benzinger, Spaulding
B. Brown, ANL

6:00 - 8:00 P.M. COCKTAIL PARTY

Thursday, October 9

Session 5 (8:30-12:00): Codes and Standards
E. N. C. Dalder, Chairman

Structural Design Basis for Superconducting Magnets
The Development of Codes and Standards
Cooperative Research for Codes and Standards
Code Approaches to Fracture Control
Material Suppliers Viewpoint
Filler Metal Suppliers Viewpoint

H. Becker, MIT
W. E. Cooper, TES
M. Prager, MPC
H. I. McHenry, NBS
E. H. Espy, Armco
D. J. Kotecki, McKay

NBS/DOE WORKSHOP ATTENDANCE
October 6-9, 1980

39. Harry McHenry, National Bureau of Standards
40. A. J. Moorhead, Oak Ridge National Lab.
41. Ralph Neiman, Argonne
42. R. Ogawa, KOBE Steel, Japan
43. John Olinger, Owens Corning
44. John O'Meara, Fermilab
45. David Parker, General Electric
46. Martin Prager, MPC
47. Harry Reid, McKay
48. Dick Reed, National Bureau of Standards
49. Blaine Roberts, Combustion Engineering
50. Bill Roden, Convair Div. of G. D.
51. Stu Rosenwasser, General Atomic
52. R. N. Sampson, Westinghouse
53. Phillip Sanger, Airco
54. Joseph Schrub, 3 M Company
55. Oscar Seth, Chicago Bridge and Iron
56. Nancy Simon, National Bureau of Standards
57. Jan Smolders, Sandvik
58. Michael Strum, Lawrence Berkley Lab.
59. E. Tada, Oak Ridge National Lab.
60. Philip Thullen, Los Alamos Scientific Lab.
61. Ralph Tobler, National Bureau of Standards
62. Albert Ulbricht KFK, Karlsruhe
63. Norman Wamack, Combustion Engineering
64. S. S. Wang, University of Illinois
65. Tom Whipple, National Bureau of Standards
66. Jerry Wille, McDonnell Douglas
67. Dingan Yu, University of Wisconsin

Late Arrivals:

- Smitty Gause, Westinghouse
Ted Kiefer, Martin Marietta Aerospace
J. W. Morris, Materials Science & Engineering
John Shepic, Martin Marietta Aerospace
Ron Kriz, National Bureau of Standards

1. Frank Babish, Sandvik
2. Bob Baysinger, Welk Bros.
3. Don Beard, DOE
4. Betty Beck, National Bureau of Standards
5. Herb Becker, MIT
6. James Benzinger, Spaulding Fibre Co.
7. Bruce Brown, Argonne
8. Bruce Christ, National Bureau of Standards
9. Jack Christian, General Dynamics
10. W. E. Cooper, Teledyne
11. Kenneth Crooks, Armco
12. Ed Dalder, DOE
13. Victor Der, DOE
14. John Elmer, National Bureau of Standards
15. Harry Espy, Armco
16. Richard Elsley, Rockwell
17. Leroy Finch, ESCO Corp.
18. Chris Fortunko, National Bureau of Standards
19. A. L. Gaines, Combustion Eng.
20. James Gauchel, Owens Corning
21. Lyle Genens, Argonne
22. Robert Gold, Westinghouse
23. Don Hackworth, Westinghouse
24. Kyung Han, Univ. of Wisconsin
25. Don Hanson, Welk Bros.
26. Jeff Hodges, Lawrence Livermore Lab
27. Richard Hooper, ETF Design Center
28. Cy Kano, Teledyne
29. Bud Kasen, National Bureau of Standards
30. D. Kotecki, McKay
31. Robert Krenzer, Rockwell
32. Carl Linkinhoker, General Electric
33. Don Litz, Westinghouse
34. C. J. Long, Oak Ridge National Lab.
35. Thomas Luhman, Brookhaven National Lab.
36. Finley Markley, Fermilab
37. Harold McCaskey, Westinghouse Micarta
38. David McColskey, National Bureau of Standards



ORGANIZATIONAL CONTACTS

The people responsible for the various major aspects of the program are listed below so that specific technical questions may be directed to them.

Department of Energy, Office of Fusion Energy, Washington, D.C. 20545		
Program Monitor	D. Beard	(301) 353-4958 (FTS) 233-4958
National Bureau of Standards, Boulder, Colorado 80303		
Program Manager	R. P. Reed	(303) 497-3870 (FTS) 320-3870
Welding and Casting	H. I. McHenry T. A. Whipple E. L. Brown	(303) 497-3268 497-5795 497-5790
Elastic Properties	H. M. Ledbetter	(303) 497-3443
Nonmetallics	M. B. Kasen	(303) 497-3558
Structural Alloys	R. P. Reed, R. L. Tobler	(303) 497-3421
Technology Transfer	N. J. Simon	(303) 497-3687
ESCO Corporation, 2141 N.W. 25th Avenue, P. O. Box 10123, Portland, Oregon 97210		
Program Manager	L. Finch	(503)228-2141,X520
University of Wisconsin, Engineering Research Building, Madison, Wisconsin 53706		
Program Manager	D. Larbalestier	(608)262-2194

ACKNOWLEDGMENT

The editors wish to express their appreciation to JoAnne Wilken for preparing much of the manuscript. They are also grateful for the assistance of Carole Montgomery and Vickie Grove.

Marilyn Stieg removed many of the inconsistencies, grammatical errors, and awkward usages of language. The editors are responsible for those errors that remain.

U.S. DEPT. OF COMM. BIBLIOGRAPHIC DATA SHEET <i>(See instructions)</i>	1. PUBLICATION OR REPORT NO. NBSIR 81-1645	2. Performing Organ. Report No.	3. Publication Date April 1981
4. TITLE AND SUBTITLE Materials Studies for Magnetic Fusion Energy Applications at Low Temperatures-IV			
5. AUTHOR(S) R. P. Reed and N. J. Simon, Editors			
6. PERFORMING ORGANIZATION <i>(If joint or other than NBS, see instructions)</i> NATIONAL BUREAU OF STANDARDS DEPARTMENT OF COMMERCE WASHINGTON, D.C. 20234		7. Contract/Grant No.	8. Type of Report & Period Covered
9. SPONSORING ORGANIZATION NAME AND COMPLETE ADDRESS <i>(Street, City, State, ZIP)</i> Department of Energy Office of Fusion Energy Washington, D.C. 20545			
10. SUPPLEMENTARY NOTES Related earlier reports: NBSIR 80-1627, NBSIR 79-1609, NBSIR 78-884 <input type="checkbox"/> Document describes a computer program; SF-185, FIPS Software Summary, is attached.			
11. ABSTRACT <i>(A 200-word or less factual summary of most significant information. If document includes a significant bibliography or literature survey, mention it here)</i> This report contains results of a research program to produce material property data that will facilitate design and development of cryogenic structures for the superconducting magnets of magnetic fusion energy power plants and prototypes. The program was conceived and developed jointly by the staffs of the National Bureau of Standards and the Office of Fusion Energy of the Department of Energy; it is managed by NBS and sponsored by DoE. Research is conducted at NBS and at various other laboratories through subcontracts with NBS. The reports presented here summarize the fourth year of work on the low temperature materials research program. Highlights of the results are presented first. Research results are given for the four main program areas: structural alloys, weldings and castings, nonmetallics, and technology transfer. Objectives, approaches, and achievements are summarized in an introduction to each program area. The major portion of the program has been the evaluation of the low temperature mechanical and physical properties of stainless steel base metal and welds, with particular emphasis on the nitrogen-strengthened stainless steels. Aluminum alloys have received some consideration also. Work has been done on the production and standardization of nonmetallics, primarily industrial laminates, for low temperature applications and on the measurement of their properties at cryogenic temperatures. A brief description is given of the fourth NBS/DoE Vail workshop held in October 1980.			
12. KEY WORDS <i>(Six to twelve entries; alphabetical order; capitalize only proper names; and separate key words by semicolons)</i> Alloys; aluminum alloys; castings; composites; cryogenic properties; low temperature; mechanical properties; nonmetallics; physical properties; stainless steels; structural alloys; welding.			
13. AVAILABILITY <input checked="" type="checkbox"/> Unlimited <input type="checkbox"/> For Official Distribution. Do Not Release to NTIS <input type="checkbox"/> Order From Superintendent of Documents, U.S. Government Printing Office, Washington, D.C. 20402. <input checked="" type="checkbox"/> Order From National Technical Information Service (NTIS), Springfield, VA. 22161		14. NO. OF PRINTED PAGES 604	15. Price \$41.00



